Qing Jiang
Zi Wen

Thermodynamics of Materials

Qing Jiang
Zi Wen

Thermodynamics of Materials

Qing Jiang
Zi Wen

Thermodynamics of Materials

With 91 figures

高等教育出版社
HIGHER EDUCATION PRESS

Springer

Authors:

Prof. Qing Jiang
Department of Materials and Engineering
Jilin University
Changchun 130022, P.R. China
E-mail: jiangq@jlu.edu.cn

Prof. Zi Wen
Department of Materials and Engineering
Jilin University
Changchun 130022, P.R. China
E-mail: wenzi@jlu.edu.cn

Preface

As a classic theory dealing with energy and its transitions in matter, thermodynamics has always been a valuable theoretical tool, providing useful insights into all fields of science and technology since the 19th century. In this book, the basic underlying principles of thermodynamics are introduced concisely and their applicability to the behavior of all classes of materials, such as metals and alloys, ceramics, semiconductors, and polymers, is illustrated in detail. The book accentuates more physical thermodynamics and statistical physics closely tied to computer simulation results, which could deepen our present understanding of material's properties on a physical basis. This book acts also as an authored advanced text, including authors' findings on the new topics of nanothermodynamics or the size effect of thermodynamic functions. Thus, the book intends to provide an integrated approach to macro- (or classical), meso- and nano-, and microscopic (or statistical) thermodynamics within the framework of materials science, which helps us to see a natural connection between the molecular and nanometer level properties of systems and their collective properties on macroscopic scales, benefiting our current understanding of nanoscience and nanotechnology in 21st century. Since nanothermodynamics has only been recently developed, we emphasize the close relationship between the text and the new literature on this subject.

This book is intended for scientists, engineers and graduate students engaged in all disciplines of materials science.

Qing Jiang and Zi Wen
Jilin University, May 2010

Contents

Nomenclature

a_l	lattice constant
a_B	activity of material B
a_{emf}	thermal emf
a_{lc}	the lattice constants of cubic phase
a_{lt}	the lattice constants of tetragonal phase
A	surface or cross-sectional area
A'	material constant
A_0	surface atom density
$A_{AFM}(\infty)$	the exchange stiffness; $A_{AFM}(\infty) = 2J_{AFM}(\infty)s^2/a_l$
A_f	austenite transition finish temperature
A_L	area of two-dimensional unit cell of liquid
A_S	area of two-dimensional unit cell of solid
A_s	austenite transition start temperature
b	Burgers length
$\mathbf{b}$	Burgers vector
b'	cut-off distance
B	magnetic induction
$\boldsymbol{B}$	Bucky diamond
B'	$2S_{vib}(1-\theta)/(3R\theta)$
B_m	bulk modulus
bcc	body centered cubic structure
c	$c = c'H_v'/H_v$
c_1	additional condition for different surface states
c_e	equilibrium concentration of vacancy
C	heat capacity
C'	concentration in the fluid for a particle of radius r
C_0'	bulk saturation concentration
C_B	magnetic contribution to the heat capacity
C_{Curie}	Curie constant
C_d	concentration for diffusion
$C_{H_{mag}}$	heat capacity at constant magnetic field
C_m	molar heat capacity
C_M	heat capacity at constant magnetic moment
$C_{P,m}$	molar heat capacity at constant pressure
$C_{V,m}$	molar heat capacity at constant volume
CN	coordination number
CNT	classical nucleation theory

ΔC_{pss}	heat capacity difference between polymorphous solid phases of the same substance
d	dimension of crystal
D	diameter
$\boldsymbol{D}$	diamond
dc	diamond-type structure
e	$e = -4u'\Delta S/(3\lambda N_{\mathrm{A}}^{1/3}V_{\mathrm{s}}^{2/3})$
E	total energy
E^*	migration energy for diffusion
E_0	FM/AFM interfacial energy
E_{c}	bulk cohesive energy
$E_{\mathrm{ci}}(N)$	cohesive energies of atoms at interior of cluster
E_{cr}	crystalline field
$E_{\mathrm{cs}}(N)$	cohesive energies of atoms at surface of cluster
E_{e}	electric field in vacumm
E_{el}	elastic energy
E_{exc}	spin-spin exchange interaction energy
E_{fr}	frictional energy
E_{g}	band gap width
E_{mp}	magnetic potential energy
E_{p}	potential energy
E_{PA}	photoabsorption energy
E_{PL}	photoluminescence energy
E_{s}	energy for electron-phonon coupling
$E_{\mathrm{th}}(T)$	thermal energy
E_{v}	van der Waals interlayer attraction
$E_{\mathrm{v}x}$	the vacancy formation energy of the x site
E_{Y}	Young's modulus
f	surface or interface stress
$\overline{f}$	$\overline{f} = (f_{\mathrm{f}} + f_{\mathrm{r}})/2$
f_{B}	activity coefficient of material B
f_{c}	fraction of electrons in the crystal
f_{e}	elastic force
f_{f}	interface stress of forward transition
f_{o}	force
f_{r}	interface stress of reverse transition
F	Helmholtz function
$\boldsymbol{F}$	fullerenes
fcc	face centered cubic structure
fi	number of degree of freedom
g	degeneracy of the level
g'	geometry factor of the lattice type considered
$g_{\mathrm{L}}(r)$	liquid radial distribution function
g_{m}	Gibbs free energy difference between bulk liquid and crystal
G	Gibbs function or Gibbs free energy
$\boldsymbol{G}$	graphite
G'	magnetic Gibbs function
G_{d}	misfit dislocation energy

G_{el}	elastic Gibbs free energy
G_{i}	non-coherent interface Gibbs free energy
G_{s}	surface free energy
G_{shear}	shear modulus
G_{v}	volume Gibbs free energy
ΔG	Gibbs free energy change
h	atomic diameter
h and l	subscripts for high and low pressure phases
h_{f}	atomic diameter of films
h_{P}	Planck's constant (6.62×10^{-34} J·s)
h_{s}	atomic diameter of substrate
H	enthalpy
H'	magnetic enthalpy
H_{e}	exchange bias field
H_{e0}	exchange bias field at 0K, $E_0/(M_{\text{FM}}t_{\text{FM}})$
H_{eTb}	exchange bias at T_{bl}
H_{mag}	magnetic field intensity
H_{s}	critical or threshold field required to destroy superconductivity in a metal
$H_{\text{s,0}}$	critical field at 0K
hcp	hexagonal close packed structure
hr	hour
ΔH_{s}	solid transition enthalpy
ΔH_{sn}	superconductor transition enthalpy
ΔH_{v}	heat of evaporation at T_{m} or T_{b}
$\Delta H_{\text{v}}'$	heat of evaporation at $T = 0$ K
i	i-th level
I	current
I_{r}	moment of inertia
J	diffusing flux
J'	spin interact energy
J_{AFM}	the exchange integral
J_{d}	diffusing coefficient
J_{int}	interface coupling exchange between the FM and AFM spins
$J_{\text{i}}, J_{\text{s}}, J_{\text{sub}}$	exchange constant or exchange coefficient where subscripts "i", "s", and "sub" show interface, surface and substrate, respectively and $J_{\text{i}} = J_{\text{s}} + J_{\text{sub}}$
k	Boltzmann's constant
$\boldsymbol{k}$	scaling exponent
k'	rate of adsorption
k_{-1}	rate of evaporation from the completely covered surface at a certain T
k_{m}	a given macrostate
k_{r}	ratio of C_P and C_V
k_{s}	spring constant
K	$K = k'/k_{-1}$
K_{AFM}	the magnetic anisotropy constant
l_{ed}	electric displacement
l_{s}	length of step

L	liquid
ΔL	thickness of surface layer of nanoparticles
m^*	effective mass
m'	$m = (2 - \upsilon_1 - \upsilon_1^{1/2})/2$
M	magnetic moment
M_{f}	martensite transition finish temperature
M_{FM}	fixed saturation magnetization of the FM layer
M_{s}	martensite transition start temperature
M_{w}	molecular or atomic weight
min and max	minimum and maximum value
n	number of atoms in a molecule
n'	layer number of epitaxially grown films
n_0	number of energy level
n_{c}'	critical layer number
n_{e}	equibrium number of vacancy
n_{s}	symmetry number
N	number of particles
N_{A}	Avogadro constant
N_{d}	dislocation number
$\boldsymbol{O}$	carbon onions
P	pressure
$\overline{P}$	$\overline{P} = (P_{\mathrm{f}} + P_{\mathrm{r}})/2$
P_{d}	electric polarization
P_{e}	external pressure
P_{f}	forward transition pressure
P_{in}	internal pressure
P_{n}	necessary pressure for the solid transition in thermodynamic equilibrium
P_{r}	reverse transition pressure
P_{s}	macroscopic spontaneous polarization
P_{ss}	surface spontaneous polarization
P_{sv}	interior spontaneous polarization
P_{w}	static pressure hysteresis width
q	$q = (\mathrm{d}\rho_{\mathrm{L}}/\mathrm{d}T)[T_{\mathrm{m}}/\rho_{\mathrm{L}}(T_{\mathrm{m}})]$
Q	heat
Q_{ij}	electrostrictive coefficient
Q_P	heat at constant pressure
Q_V	heat at constant volume
r	radius, half thickness of film
r^*	critical radius of the nucleation
r_0	critical radius between solid and liquid
r_{c}	critical radius of nanocarbon for phase transition
r_{e}	effective dislocation stress field radius
r_{g}	grain size
r_{h}	radius of the hollow part of cylinder
$\mathbf{r}_i$	denote the vector position of the i-th link in the chain
R	ideal gas constant
$\mathbf{R}$	end-to-end vector
R_{b}	net displacement magnitude

R_c	radius of cylinder
R_e	equimolar radius
R_s	radius of surface tension
$\mathfrak{R}$	cell position
s	solid
s	spin value
s_{11}, s_{12}	elastic compliance constants
S	entropy
sa	atoms/molecules at the surface
sc	simple cubic structure
ΔS_b	bulk solid-vapor transition entropy
ΔS_{el}	electronic entropy
ΔS_m	melting entropy
ΔS_{pos}	positional entropy
ΔS_s	solid transition entropy
ΔS_{sn}	superconductor transition entropy
ΔS_{vib}	vibrational entropy
t	time
t_0	thickness of film that has firmly attached to a substrate
t_C	Celsius temperature
t_f	thickness of a monolayer
t_{FM}	thickness of FM layer
t_h	isotropic film of thickness
t_r	molecular relaxation time
t_s	surface melting layer thickness
T	absolute temperature
T_0	temperature at which the Gibbs free energy of austenite and martensitic phase are equal
T_{0b}	temperature at which the austenite and ferrite of the same composition have an identical G value
T_b	bulk solid-vapor transition temperature
T_{bl}	blocking temperature
T_c	the critical temperature
T_C	Curie temperature
T_f	freezing temperature
T_g	glass transition temperature
T_K	Kauzmann temperature
T_m	melting temperature
T_{mh}	melting temperature of high pressure phase
T_{ml}	melting temperature of low pressure phase
$T_m(r)$	size dependent melting temperature
T_n	critical temperature of the nucleation
T_N	the Néel temperature
T_r	reduced temperature
T_{room}	room temperature
T_s	solid transition temperature
$T_{s,0}$	superconductor transition temperature in the absence of a magnetic field
T_t	triple point temperature

u	potential difference
u'	$u' = (\mathrm{d}\rho_\mathrm{L}/\mathrm{d}T)/\rho_\mathrm{L}(T_\mathrm{m})$
$u(r)$	potential energy function
u_d	misfit dislocation energy of a single dislocation
u_e	elastic free energy of unit volume
U	internal energy
υ	vibrational quantum number
υ_1	$\upsilon_1 = Z_\mathrm{s}/Z_\mathrm{b}$
υ_1'	$\upsilon_1' = Z_\mathrm{s}'/Z_\mathrm{b}'$
υ_u	ultrasound propagation velocity
V	volume
V_L	g-atom volume of liquid
V_s	g-atom volume of crystal
V_f	g-atom volume of the film
va	atoms/molecules within the particle
w	a critical exponent
w	$w = \gamma_\mathrm{sv0}/\gamma_\mathrm{Lv0}$
w'	weight fraction of the second polymer component
w_r	reversible work
W	mechanical work
W^*	useful work
Y	biaxial modulus, $Y = E_\mathrm{Y}/(1 - \nu_\mathrm{P})$
Y_s	stability parameter
z	a number of order unity
z_b	coordinates without CN imperfection
z_i	coordinates with CN imperfection
Z	partition function
Z_b	coordination number (CN) of interior atom
Z_b'	next nearest CN of interior atom
Z_{hkl}	broken bond number
Z_s	coordination number of surface atom
$Z_\mathrm{s'}$	next nearest CN of surface atom
α	coefficient of thermal expansion
α'	Lagrangian multiplier
α_F	ferrite phase
α_M	martensitic phase
α_r	$\sigma_\mathrm{s}^2/\sigma_\mathrm{v}^2$
α_s	$\sigma_\mathrm{s}^2/\sigma_\mathrm{v}^2$ for glass transition
β	compressibility
β'	Lagrangian multiplier
γ_A	austenitic phase
γ_exp	experimental values of interface energy
γ_i	non-coherent interface
γ_Lv0	bulk liquid-vapor interface energy
$\gamma_\mathrm{Lv0}'(T)$	$\gamma_\mathrm{Lv0}'(T) = \mathrm{d}\gamma_\mathrm{Lv0}(T)/\mathrm{d}T$
γ_sL0	bulk solid-liquid interface energy
γ_ss0	bulk solid-solid interface energy
γ_sv0	bulk solid-vapor interface energy

γ_{TS}	solid-liquid interface energy based on the Turnbull-Spaepen relation
δ	Tolman's length, $\delta = R_{\mathrm{e}} - R_{\mathrm{s}}$
$\delta_{\min}$	minimum value of δ
δ_{v}	vertical distance from the surface of tension to the dividing surface
δ_{∞}	Tolman's length when $r \to \infty$
ε	bond energy
ε_0	permittivity of free space
ε_{a}	actual permittivity
ε_{e}	electronic energy
$\varepsilon_{\mathrm{emf}}$	electromotive force
ε_{F}	Fermi energy
ε_i	the energy in level i
ε_{n}	nuclear energy
$\varepsilon_{\mathrm{n}'}$	kinetic energy of the electrons
ε_{p}	kinetic energy of the holes
ε_{r}	relative permittivity
$\varepsilon_{\mathrm{rt}}$	rotational energy
ε_{t}	translational energy
ε_{v}	vibrational energy
ζ	ratio of the surface volume to the entire volume
η	packing density
η_{v}	dynamic viscosity
θ	order parameter
θ_1	angle between direction of the nearest atoms at neighbor planes and that of the film surface
θ_{a}	contact angle
θ_{c}	$(T_{\mathrm{m}} - T)/T_{\mathrm{m}}$, degree of undercooling
θ_{m}	rotation angle of the magnetic dipole from its zero energy position $\pi/2$ to θ_{m}
θ_{s}	fraction of the surface occupied by gas molecules
ϑ_{s} and ϑ_{L}	electrical conductivity of the crystal and the melt
Θ	characteristic temperature
Θ_{D}	Debye temperature
Θ_{E}	Einstein temperature
κ	$\kappa = 1/[m'\Delta H_{\mathrm{v}}/(T_{\mathrm{m}}\Delta S) - 1]$
κ_{s}	$\kappa_{\mathrm{s}} = \kappa - 2q/3$
λ	$2^{-1/6}h$
λ'	$\lambda' = (8^{1/2}/3)(6\eta/\pi)^{2/3}$
λ_{c}	critical misfit
Λ	critical exponent
μ	chemical potential
μ'	$\mu' \cong 1/[4\pi(1 - \nu_{\mathrm{P}})]$
μ_0	permeability of free space
μ_{B}	1 Bohr magneton
μ_{v}	magnetization or magnetic moment per unit volume
ν	$\nu = m'\Delta H_{\mathrm{v}} - T_{\mathrm{m}}\Delta S$
ν_{P}	Poisson's ratio

$\nu_{\mathrm{s}}, \nu_{\mathrm{L}}$	characteristic vibration frequencies of the particles in the crystal and melt
ξ	correlation length
ξ_0	microscopic length
ξ_1	$J_{\mathrm{int}}/(4K_{\mathrm{AFM}}ra_{\mathrm{l}})$
Π	the number of phases presented
ρ	density
σ	root-mean-square (rms) average amplitude of atomic thermal vibration
ς	strain
τ	Turnbull coefficient
τ_{ij}	$\tau_{ij} = \partial\gamma_{\mathrm{sv}}/\partial\varsigma_{ij}$
τ_{s}	shear stress
Γ	jump frequency of atom
Γ'	generic extensive property of a solution
υ	a constant related to CN
Υ	mean-square root error between the predicted and the experimental results
φ	total bond strength ratio between next-nearest neighbor and the nearest one
φ_{c}	volume fraction of clusters at T_{m}
ϕ	geometric factor
Φ	total flux
χ	electric susceptibility
ψ	effective dislocation stress field radius
ω	interaction parameter
ϖ	$\varpi = |\gamma_{\mathrm{Lv0}}(T_{\mathrm{m}}) - \gamma_{\mathrm{Lv0}}^{\mathrm{e}}(T_{\mathrm{m}})|/\gamma_{\mathrm{Lv0}}^{\mathrm{e}}(T_{\mathrm{m}})$
Ω	the number of microstates
б	stress
л	$1/\nu_{\mathrm{c}}$
$\Delta\cent$	Peltier heat
∞	bulk size

Chapter 1 Fundamentals of Thermodynamics

This chapter firstly looks back on the development of macroscopic thermo-dynamics during the last three hundred years and its historical contribution to the social evolvement. The present achievement and challenges are also discussed. To clearly understand the thermodynamic laws, the essential concepts of thermodynamics are defined and clarified. Further, the macroscopic thermodynamics of materials and the fundamental principles of four thermodynamics laws are introduced, which are the essential basis of the later chapters. The intrinsical relationships between these thermodynamics laws through a series of mathematical deductions are given, which additionally result in the acquirement of the most important physical amounts of materials.

1.1 Thermodynamics of Materials Science, Scope and Special Features of the Book

Classical thermodynamics is a branch of physics originating in the nineteenth century as scientists were first discovering how to build and operate steam engines [1], which primarily led to the industrial revolution. A steam engine is a heat engine that performs mechanical work using steam as its working fluid. Historically, thermodynamics developed just out of needs to understand the nature of these heat engines and to increase the efficiency of transition between heat and work [2]. With a deeper understanding of the relationship between heat, work and temperature, the design of engines of specific power output and efficiency became possible. Although the relationship between science and technology in this period is complex, it is fair to say that without the introduction of scientific thermodynamic methods, the development of the industrial revolution would not have been so swift.

The demands of the industrial revolution had put the "standard model" of physics in a crisis around the question of "what is energy?". Energy as the capacity to do work is essentially an abstract concept. It cannot be measured directly and thus has no definite value. Thermodynamics, dealing with energy and its transitions, is based on two laws of nature, namely the first and the second laws of thermodynamics [3]. Thermodynamics tells us that the energy differences can be measured by heat and work removed or added.

Heat and work are not stored as such anywhere, but are the two forms of energy transfer. Such results of thermodynamics meant that physics could be rewritten in terms of energy. Therefore, thermodynamics is one of the most basic sciences with applications in all fields of science and technology since its results are essential for physics, chemistry, materials science, chemical engineering, aerospace and mechanical engineering, cell biology, biomedical engineering, and economics [4].

In wide range of applications of thermodynamics, the scientific discipline that intersects the areas of materials science and thermodynamics is commonly known as thermodynamics of materials. Materials science involves investigating relationships of materials between manufacture, compositions and structures, properties, and performance [5]. The major determinants for materials structures and thus their properties are their constituent elements and the way in which they have been processed into their final forms as well as their activity between the manufactured parts and working surroundings. The development of thermodynamics both drove and was driven by atomic theory and even by quantum mechanics. The development of thermodynamics also motivated new directions in probability statistics. Atomic theory tells us that the electrons in the constituent elements occupy a set of stable energy levels and can transform between these states by absorbing or emitting photons that match the energy differences between the levels. Such electron structure of the individual atoms in turn determined various types of atomic interaction bondings that exist among constituent atoms or molecules. Without a doubt, materials store energy through the arrangement and motion of the constituent atoms, and so the way that a material changes its atomic structure during undergoing a change in thermodynamic state is governed by the laws of thermodynamics. Thermodynamics thus affects materials microstructures, defect concentration, atomic ordering, etc. Altogether, energy has to do with materials science. Thermodynamics of materials just deals with the relationships between energy and matters and describes how the properties of materials are affected by thermodynamic processes. In many cases, thermodynamics of materials is a crucial factor to good engineering design and performance forecast of manufactured components, parts, devices, tools, machines, etc. [6].

The last 50 years witnessed progressive miniaturization of the components employed in the construction of devices and machines [7]. One of the most striking significance of miniaturizing a solid to nanometer scale is the tunability in physical and chemical properties compared with the corresponding more bulky solids. Miniaturization itself has also achieved evident progress in the fields of microelectronics or super-large-scale integration circuits (SLIC) along with constant speed of scaling to maximize transistor density due to the requirements for electrical and functional performances. As predicted by Moore's law, new technology generations have been introduced with a 2-year or 18-month cycle, and packing density and device speed have increased exponentially at rapidly decreasing cost per function [8]. Today,

45 nm process technology is the world's normal chip-manufacturing technology, where on-chip interconnect networks include eleven metal levels and connect more than $10^7/\text{mm}^2$ transistors for 70 Mbit static random access memory (SRAM) chips [9]. Moreover, in one of the biggest advancements in fundamental transistor design, Intel used different transistor materials to build 731 million transistors inside the present generation of the company's Intel Core i7 family in November, 2008 with 45 nm technique. Minimum feature sizes of the silicon technology are reduced to 32 nm in 2009. It is further envisioned that this size will be 22 nm in 2011 and 15 nm in 2013, while the ultimate feature sizes could be below 10 nm [8]. Nanomaterials have also been and will be widely utilized in medicine fields. For instance, nanoparticles have properties that are useful for the diagnosis and treatment of cancer, including their size-dependent properties, stability in solvent, ideal size for delivery within the body, and tunable surface chemistry for targeted delivery. Several different nanoparticle building blocks possessing varied functionalities can be assembled into one multifunctional composite nanoparticle, further expanding their potential use in cancer diagnostics and therapeutics [10]. With the large surface-to-volume ratio, the surface, interface, and quantum effects make such microscopic and mesoscopic systems differ substantially from isolated atoms of their constituent elements or the corresponding bulk counterparts in performance. The quantities, such as the phase transition temperature, the Young's modulus, and the extensibility of a solid, are no longer constant but change with the materials size. Properties of nanomaterials determined by their shapes and sizes are indeed fascinating and form the basis of the emerging field of nanoscience and nanotechnology that have been recognized as the key area being of significance in science, technology, and economics in the 21st century. Thus, as the bridge between the atomic and macroscopic scales, the microscopic and mesoscopic systems have attracted tremendous interest in recent years because of their novel mechanical, thermal, acoustic, optical, electronic, dielectric, and magnetic properties from a basic scientific viewpoint, as well as from their great potential in upcoming technological applications such as SLIC and nano-electromechanic systems (NEMS). Accordingly, a huge experimental database has been generated for nanothermodynamics in past decades [10 − 13].

The physical and chemical properties of a macroscopic system can be well described using the classical thermodynamics in terms of the Gibbs free energy or the continuum medium mechanics. At the atomic scale, the quantum effect becomes dominant and the physical properties of a small object can be reliably optimized in computations by solving the Schrödinger equations for the behavior of electrons or the Newtonian motion of equations for the atoms with a sum of averaged interatomic potentials as key factors to the single body systems. However, for a small system at the nanometer regime, called mesoscopic or furthermore microscopic system, both the classical and quantum approaches encountered severe difficulties [10, 11].

Unfortunately, the unusual behavior of a nanostructure goes beyond the

expectation and description of the classical theories in terms of the continuum medium mechanics and the statistic thermodynamics. As the nanothermodynamics is an emerging field of study, fundamental progress is lagging far behind the experimental exploitations. Many questions and challenges are still open for discussion. Extending the validity of thermodynamics into nanometer size range thus becomes an urgent task. It is fascinating that the new variable of size and its combination with various thermodynamic parameters not only offer us opportunities to tune the physical properties of nanomaterials, but also allow us to gain information that may be beyond the scope of conventional approaches. Therefore, to complement the classical and the quantum theories, a set of analytical expressions from the perspective of nanothermodynamics for the size dependence of the intrinsic physical properties of a specimen is necessary where the size should be introduced as an independent variant [12]. This technique to extend the suitability range of the classic thermodynamics is usually called "top-down method". It is noteworthy that since scientists and engineers in the long history have been familiar to the classic thermodynamic theory, for the most people, especially for materials scientists and engineers, using an extension of the classic thermodynamics theory is a much easy way compared with other theories to go into the nanoworld theoretically.

Based on the four thermodynamic laws, two essential and two additional, thermodynamics gives a number of exact relationships between many properties of materials. However, they are a theoretical construction, and new properties cannot be measured, but just be calculated. To get numerical answers, the theoretical framework has to be connected to the behavior of matters through properties that can be measured. However, before the advent of computers, only limited descriptions of matters were possible. Computer simulation as a new powerful technique could supply not only the details of atomic structures, but also the corresponding electronic states. Thus, computer simulation could support and make up the modeling results of nanothermodynamics. The use of computers starting around 1960 showed a gradual and even a dramatic change for thermodynamics, and is now practiced. It became increasingly possible to correlate data in proper models and then to use these models in combination with the rigorous thermodynamic relations with better answers. Almost all thermodynamic theories now rely on simulation techniques. This method has been named "bottom-up method" [14].

Some thermodynamic properties are easier to understand and explain based on the macroscale, while other phenomena are more easily illustrated at the microscale. Macro- and microscale investigations are just two views of the same thing. "Bottom-up method" together with "top-down method" guarantees development of nanothermodynamics or mesoscopic thermodynamics in recent years.

The book will start here in Chapter 1 with an introduction to the subject of macroscopic thermodynamics of materials and development of fundamental principle of four thermodynamics laws, which are essential for the

later chapters. Chapter 2 discusses the microscopic point of view: statistical mechanics, and how microscopic and macroscopic properties are connected. Chapter 3 shows the thermodynamic descriptions of heat capacity and entropy in solid, both are elementary parameters for many physical properties of matters. Alloying of elements and compounds leads to the presence of many interesting properties. In addition, some important chemical reactions take place not among pure elements or compounds, but among elements or compounds dissolved in one another as solution. A knowledge and understanding of phase diagrams are thus important to the engineers relating to the design and control of the heat treatment procedure. Furthermore, the development of a set of desirable mechanical characteristics for a material often results from a phase transition with the help of the heat treatment technique. Chapter 4 and Chapter 5 deal with thermodynamics of solution, phase diagrams, and phase transitions. Thermodynamic definitions of interface energy and interface stress are clarified to formulate surface thermodynamics [10, 11]. This theme becomes more and more important due to the appearance of nanotechnology. In Chapter 6, the interface thermodynamics is developed. In all later three chapters, the basic underlying principle of thermodynamics is applied to the behavior of all classes of materials, such as metals and alloys, ceramics, semiconductors and polymers. An important characteristic of this book is accentuation of a physical basis of thermodynamics. This is partly because of the development of physical theory, which makes it possible to analyze, illustrate and understand the physical nature of materials and materials properties. This book acts also as an authored advanced text, including authors' research production in the new topics of nanothermodynamics or size effect of thermodynamic functions. Thus, authors intend to provide integrated approach to macro-(or classical), meso- and nano-, and microscopic (or statistical) thermodynamics.

1.2 Concepts of Thermodynamics [6, 15 − 17]

Thermodynamics is one of the basic sciences, which mathematically and quantitatively deals with heat and work and their transfer of materials in equilibrium, materials transitions, and their relationships with properties of materials. The thermodynamics consists of four essential laws that govern the study of energetic transitions and the relationships between thermodynamic properties [2, 3]. Two of these – the first and the second laws – dispose energy, directly or indirectly. Consequently they are of fundamental importance in materials studies of energy transitions and usage. The remaining two statements – the zeroth and the third laws – refer to thermodynamic properties and possess a second importance. The power of thermodynamics is that everything follows from these laws although it is hard for people to clarify how this is followed. By logical reasoning and skillful manipulation of these laws, it

is possible to correlate many properties of materials and to gain insight into many chemical and physical changes that materials undergo. In this chapter, we shall develop the principles of thermodynamics and show how they apply to a system of any nature.

There are a number of terms used in the study of thermodynamics and these concepts and terms are basilic in thermodynamic studies, hence their physical meanings must be clear and will be introduced in the following section.

As the word used in thermodynamics, a system is a part of the universe under consideration. A real or imaginary boundary separates the system from the rest of the universe, which is referred to as the environment. A useful classification of thermodynamic system is based on the nature of the boundary and the flows of matter, energy and entropy through it. There are three kinds of systems, depending on the kinds of interchanges taking place between a system and its environment. If condition is such that no energy and matter interchange with the environment occurs, the system is said to be isolated. If there are interchanges of energy and matter between a system and its environment, the system is named being open. A boundary allowing matter exchange is called permeable. The ocean would be an example of an open system. If there is only interchange of energy (heat and work) crossing the boundary, the system is called closed. A greenhouse is for instance such a system where exchanging energy with its environment is present while substances keep constant. Whether a system interchanges heat, work or the both is usually thought to be a property of its boundary, which may be adiabatic (not allowing heat exchange) or rigid boundary (not allowing exchange of work). In reality, a system can never be absolutely isolated from its environment, because there is always at least some slight coupling, even if only via minimal gravitational attraction.

The state of a thermodynamic system at any instant is its condition of existence at that instant, which is specified by values of a certain number of state variables or properties. Different properties that can be used to describe the state of a system comprise energy, entropy, chemical composition, temperature, pressure, volume, external field and substance size. The specification of the state of the system must include the values of these properties. A state of the system, which can be reproduced, means that the state is well defined.

A property of a system depends only on the state of the system, and not on how that state was attained. The uniqueness in the value of a property at a state introduces naming state function for a property. By contrast, the so-called path functions are quantities, which concern the path of a process by which a system changes between two states. Since a property is a state function, its differential must be an exact or perfect differential in a mathematical term. The line integral of the differential of a property is independent of the path or curve connecting the end states, and this integral vanishes in the special case of a complete cycle.

Thermodynamic properties of a system may be classified as intensive and extensive properties. The former is independent of the extent or mass of the system and can be specified at a specific point in the system, such as pressure, temperature, and specific volume. The latter is not additive because it does not scale with the size of the system and cannot be specified at a particular point of space. Its value for the entire system is equal to the sum of its values for all parts of the system. Volume, energy, and mass are instances of extensive properties. To change the latter to the former is generally done by normalizing the former by the size of the system, namely, by making the property be a density.

For our purpose, the energy of a system can be divided into three categories: internal, potential, and kinetic energy. To take them in a reverse order, kinetic energy refers to the energy possessed by the system due to its overall motion, either translational or rotational. The kinetic energy to which we refer is that of the entire system, other than that of the molecules in the system. For instance, if the system is a gas, the kinetic energy is the energy due to the macroscopic flow of the gas, not the motion of individual molecules. A familiar form of this energy is the translational energy of $(1/2)mv^2$ possessed by a body of mass m moving at a velocity v.

The potential energy of a system is a sum of the gravitational, centrifugal, electrical, and magnetic potential energy. To illustrate this, the gravitational potential energy is taken as an example. A 1 kg mass, 10 m above the ground, clearly has a greater potential energy than the same mass on the ground. The potential energy can be converted into other forms of energy, such as the kinetic energy, if the mass is allowed to fall freely. The sizes of kinetic and potential energy lies in the environment in which the system exists. Particularly, the potential energy of a system depends on the choice of an arbitrarily chosen zero level. However, the difference in the potential energy, such as that between the mass at 10 m and that at the ground level, is the same and is independent of the datum plane.

The internal energy of a thermodynamic system, denoted as U, is the sum of all microscopic forms of energy of a system. It is related to the molecular structure and degree of molecular activity and may be viewed as the sum of kinetic and potential energy of the molecules. U includes the energy in all chemical bonds, and the energy of the free, conduction electrons in metals. U of a system depends on the inherent qualities, or properties, of materials in the system, such as composition and physical form, as well as the environmental variables (temperature, pressure, external fields, system size, etc.). U has many forms, including mechanical, chemical, electrical, magnetic, surface, thermal, and size ones. For example, a compressed spring has higher internal energy (mechanical energy) than a spring without compression because the former can do some work on changing (expanding) to the uncompressed state.

On the question of thermal energy, it is intuitive that U of a system increases as its temperature T increases. The form of U of a material relating to its T is called thermal energy, not heat. Note that heat is the energy in

transfer between a system and the environment. Thermal energy is possessed by the system, and is a state function of a system and an extensive quantity. The SI unit of the energy is the joule.

The entire structure of the science of classical thermodynamics is built on the concept of equilibrium states. When a system is in equilibrium, unbalanced potential (or driving force), which tends to promote a change of state, is absent. The unbalanced potential may be mechanical, thermal, chemical or any combination of them. When temperature gradient is absent in a system, the system should be in a state of thermal equilibrium, which is the subject of the zeroth law of thermodynamics. If there are variations in pressure or elastic stress within the system, parts of the system may move, either expand or contract. Eventually these motions (expansion or contraction) will cease. When this has happened, the system is in mechanical equilibrium. If a system has no tendency to undergo either a chemical reaction or a process such as diffusion or solution, the system is regarded as in a state of chemical equilibrium. If all these equilibrium is satisfied, the system is in a state of thermodynamic equilibrium.

In the most part of this book, we shall consider systems that are in thermodynamic equilibrium, or those in which the departure from thermodynamic equilibrium is negligibly small. The local state of a system at thermodynamic equilibrium is determined by the values of its intensive parameters, such as pressure P, T, and system size (radius) r, etc. Specifically, thermodynamic equilibrium is characterized by a minimum of a thermodynamic potential. Usually the potential is the Helmholtz free energy, i.e. system is in a state at constant T and volume V. Alternatively, the Gibbs free energy can be taken as the potential, where the system is at constants P and T.

When any property of a system is changed, the state of the system varies, and the system undergoes a process. A thermodynamic process may be defined as the energetic evolution of a thermodynamic system from an initial to a final state. Paths through the space of thermodynamic properties are often specified by holding certain thermodynamic variables as constants. It is useful to group these processes into pairs, in which each variable holding constant is one member of a conjugate pair. For instance, P-V conjugate pair is concerned with the transfer of mechanical or dynamic energy as the result of work.

An isobaric process is a thermodynamic process in which P stays constant: $\Delta P = 0$ where Δ shows the difference. The heat transferred to the system does work but also changes U of the system, such as a movable piston in a cylinder. In this instance, P inside the cylinder is always at atmospheric pressure, although it is isolated from the atmosphere. In other words, the system is dynamically connected, by a movable boundary, to a constant-pressure reservoir.

An isochoric process is one where V is held constant, meaning that the mechanical work done by the system W is zero. It follows that for a simple system of two dimensions, any heat energy transferred to the system

externally will be absorbed as U. An isochoric process is also known as an isometric or isovolumetric process. An example would be to place a closed tin can containing only air into a fire. To the first approximation, the can will not expand, and the only change is that the gas gains U, as evidenced by its increase in T and P. We may say that the system is dynamically insulated from the environment by a rigid boundary.

The temperature-entropy (T-S) conjugate pair is concerned with the transfer of thermal energy as the result of heating.

An isothermal process is a thermodynamic process where $\Delta T = 0$. This typically occurs when a system is in contact with an outside thermal reservoir (heat bath), and processes occur slowly enough to allow the system to continually adjust to T of the reservoir through heat exchange. Having a system immersed in a large constant-temperature bath is such a case. Any work energy performed by the system will be lost to the bath, but its T will remain constant. In other words, the system is thermally connected by a thermally conductive boundary to a constant-temperature reservoir.

An adiabatic process is a process where there is no heat transferred into or out of the system by heating or cooling. For a reversible process, this is identical to an isentropic process. Namely, the system is thermally insulated from its environment and its boundary is a thermal insulator. If a system has entropy which has not yet reached its maximum equilibrium value, S will increase even though the system is thermally insulated.

During a thermodynamic process, some unbalanced potential exists either within the system or between it and the environment, which promotes the change of state. If the unbalanced potential is infinitesimal so that the system is infinitesimally close to a state of equilibrium at all times, such a process is called quasistatic. A quasistatic process may be considered practically as a series of equilibrium states and its path can graphically be represented as a continuous line on a state diagram. By contrast, any process taking place due to finite unbalanced potentials is non-quasistatic.

A system has undergone a reversible process if at the conclusion of the process, the initial states of the system and the environment can be restored without leaving any net change at all elsewhere. Otherwise, the process is irreversible. A reversible process must be quasistatic, so that the process can be made to traverse in the reverse order the series of equilibrium states passed through during the original process, without change in magnitude of any energy transfer but only a change in direction.

The most natural processes known to be reversible are an idealization. Although real processes are always irreversible, some are almost reversible. If a real process occurs very slowly, the system is thus virtually always in equilibrium, the process can be considered reversible.

1.3 Temperature and Zeroth Law of Thermodynamics

We often associate the concept of T with how hot or cold a system feels when we touch it. Thus, our senses provide us with qualitative indications of T. However, our senses are unreliable and often misleading. We thus need a reliable and reproducible method, which makes quantitative measurements establish the relative "hotness" or "coldness" of systems that is solely related to T of the system.

After the three laws of thermodynamics were explained practically and theoretically, the scientists tried to make thermodynamics systematically logical. It was realized that a basic statement about T was important and even more fundamental. This statement is given the unusual name of the zeroth law of thermodynamics: When two systems are each in thermal equilibrium with a third system, the first two systems are in thermal equilibrium with each other.

The above statement implies that all systems have a physical property that determines whether or not they will be in thermal equilibrium when they are placed in contact with other systems. This property is called temperature. Two systems in thermal equilibrium with each other are at the same T. Thus, thermometers can be called the "third system" and used to define a temperature scale. The thermometer as a device is used to measure T of a system, with which the thermometer is in thermal equilibrium. All thermometers make use of some physical properties exhibiting a change with T that can be calibrated in order to make T measurable. Some of the physical properties used are (1) V of a liquid, (2) the length of a solid, (3) P of a gas held at constant V, (4) V of a gas held at constant P, (5) the electric resistance of a conductor, and (6) the color of a very hot object. For instance, V_{L}, the volume of a liquid, is taken as such physical property in the familiar liquid-in-glass mercury or alcohol thermometers. The thermometers used most widely in precise experimental work are however the resistance thermometer and the thermocouple.

Another important type of thermometer, although it is not suitable for routine laboratory measurements, is the constant volume gas thermometer. The behavior observed in this device is P variation with T of a fixed V of gas. When the constant volume gas thermometer was developed, it was calibrated using the ice and steam points of water. P and T values are then plotted on a graph, as shown in Fig. 1.1.

The line connecting the two points serves as a calibration curve for measuring unknown T. To measure T of a substance, we place the gas thermometer in thermal contact with the substance and measure P of the gas. Then, T of the substance from the calibration curve can be found.

If the curves in Fig. 1.1 are extended back toward negative T, we find a starting result. In any case, regardless of the type of gas or the value of the low starting P, P extrapolates to zero when the Celsius temperature t_{C} is $-273.15\,°C$. This suggests that this particular T is universal in its importance,
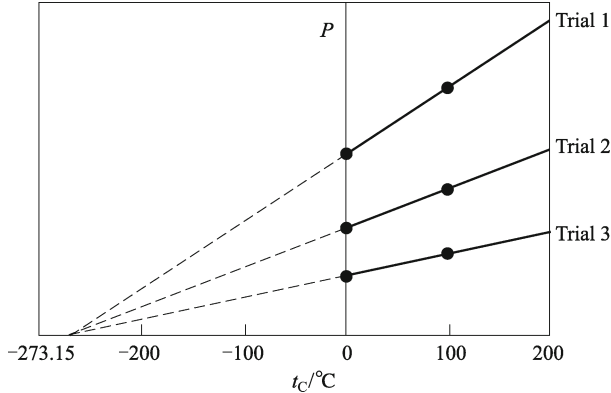
Fig. 1.1 *P-T* diagram of dilute gases where t_C denotes Celsius temperature.

which does not depend on the substance used in the thermometer. In addition, since the lowest $P = 0$, which would be a perfect vacuum, this T must represent a lower bound for physical processes. Thus, we define this T as the starting point of the absolute or the thermodynamic temperature, which is utilized as the basis for the Kelvin temperature scale $T = t_C - 273.15\ ℃ = 0\ K$. The size of one "degree" in the Kelvin scale (called a Kelvin or one K) is chosen to be identical to the size of a degree in the Celsius scale. Thus, the relationship that enables us to convert between t_C and T is

$$t_C = T - 273.15.$$

Early gas thermometers made use of ice and steam points according to the procedure just described. However, these points are experimentally difficult to duplicate because they are pressure-sensitive. Consequently, a procedure based on two new points was adopted in 1954 by the International Committee on Weights and Measures. They are 0 K and the triple point of water where water, water vapor, and ice coexist in equilibrium with a unique T and P. This convenient and reproducible reference T for the Kelvin scale is $t_C = 0.01\ ℃$ or $T = 273.16\ K$ and $P = 4.58\ mmHg$[①]. Thus, the SI unit of T is defined as $1/273.16$ of this triple point.

1.4 First Law of Thermodynamics [6, 17, 18]

The first law of thermodynamics is essentially the law of conservation of energy applied to thermodynamic systems. Through his famous experiments in 1843 Joule was led to the postulate that heat and work were of equivalent quantities, which is generally known as the first law of thermodynamics. This

---

① 1 mmHg = 1.33322×10^2 Pa.

law is most simply stated as "energy cannot be created or destroyed" or "the energy of the universe is a constant". More precise statement is for instances: "a given amount of energy in a particular form can be converted to energy of a different form and then transformed back into the same amount of the original form. The total energy during the conversion and reverse process is constant". Remember that the first law states that energy is conserved always. It is a universally valid law for all kinds of processes and provides a connection between microscopic and macroscopic worlds.

In thermodynamics of materials, we are most interested in the transitions of energy and how it governs the interaction of energy with materials. We know that as a material changes its structure or as individual atoms of the material increase their motion, the energy of the material changes. However, this energy change must be balanced by an equal and opposite variation in energy of the environment. Thus, although we haven't developed much detail of how energy and materials interact, we do know that the total energy is a constant throughout the process regardless of the details of their interaction.

According to the first law of thermodynamics, it is useful to separate changes to U of a thermodynamic system into two sorts of energy transfers: heat Q and work W. Both indicate path dependent quantities. They only have meaning when describing a property of the process, not the state of the system. We cannot tell what the heat of a system is. We can however tell what heat is associated with a well defined process. Neither heat nor work is the energy contained in a system and neither is a system property. The differential of a path function is inexact and is denoted by the symbol δ to distinguish from the symbol d for exact differentials.

Q is a form of energy exchange between a system and its environment. Heat flows from regions of high T to that of low T. So like P, T is a potential for transferring energy, specifically the potential to transfer energy as Q. Q is a mechanism by which energy is transferred between a system and its environment due to the existence of ΔT between them. The algebraic sign of Q is positive when heat flows from the environment into the system. The increase in T of the system is caused by an increase in the thermal energy of the system. In a thermodynamic sense, heat is never regarded as being stored within a system. When energy in the form of heat is added to a system, it is stored not as heat, but as kinetic and potential energy of the atoms or molecules making up the system.

From an atomic point of view, heat is the transfer of energy that occurs through the chaotic motion of matters at a molecular scale. The atoms in a hot region of a material vibrate chaotically more than that in a cooler region of the material. As atoms vibrate, they impart a force to their neighbors and cause them to move. The hotter the atoms, the more vigorous the motions and the larger the forces they impose on their neighboring atoms. This random motion passing from one point to another in the material results in energy transfer and eventually brings out a uniform amount of chaotic motion once the random motion of energetic atoms has flowed so that no

temperature gradients persist. This transfer of kinetic energy to neighboring atoms accomplished through flow of random atomic motion is called heat transfer. Random, chaotic motion is thus disordered and is classified as thermal motion, whereas work causes ordered, organized motion of the atoms in a system in a uniform manner.

The work-energy principle, in mechanics, is a consequence of Newton's law of motion. It states that the work of the resultant force on a particle is equal to the change in kinetic energy of the particle. If a force is conservative, the work of this force can be set to equal the change in potential energy of the particle, and the work of all forces exclusive of this force is equal to the sum of the changes in kinetic and potential energy of the particle.

Work can also be done in a process where there is no change in either the kinetic or potential energy of a system. Work is thus done when a gas is compressed or expanded, or when an electrolytic cell is charged or discharged, or when a paramagnetic rod is magnetized or demagnetized, even though the gas, or the cell, or the rod, remains at rest at the same elevation. Thermodynamics is largely (but not exclusively) concerned with processes of this sort where the work is defined as all other forms of energy transferred between the system and its environment by reasons other than a temperature gradient.

In mechanics, the work is defined as the product of a force and the displacement when both are measured in the same direction. When a thermodynamic system undergoes a process, the work in the process can always be traced back ultimately to the work of some force. Mechanical work W can be made on the system, say, by compressing the system (volume changes). Electrical work being done on the system is the moving charges in the system by the application of an external electric field. Thus, it is convenient to express the work in terms of the thermodynamic properties of the system and we first seek to derive the expression for work in relation to volume changes.

Consider the compression of a gas in a cylinder of an automobile engine. If the gas is taken as the system, work done on the system is by the face of the piston, whose magnitude is the force f_o, multiplied by the distance Δl through which the piston moved (Fig. 1.2).
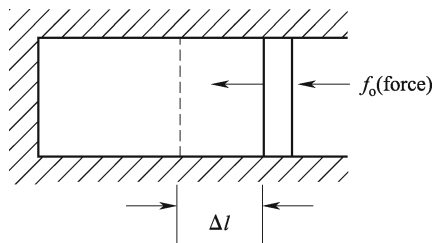

Fig. 1.2   Mechanical work.

If the cross-sectional area of the piston is taken as A, the gas pressure

against the piston is P, this work term W can be converted into

$$W = -f_\mathrm{o}\Delta l = -PA\Delta l = -P\Delta V, \text{ or } \delta W = -P\mathrm{d}V. \tag{1.1}$$

Note that W is done on a system when there is a pressure gradient where P is the potential to do the mechanical work. W is expressed in a unit J ($=$ N·m) when P is expressed in a unit N·m^{-2}, or pascal (Pa), and the volume change ΔV is expressed in unit m^3.

The direction of force and the distance moved establishes the algebraic sign of W, which is defined as being positive when work is done on a system by the environment. $W < 0$ when the system does work on the environment. Thus negative sign in Eq. (1.1) insures that when system is compressed, W is positive since Δl will be negative. The sign convention is the same for both Q and W, that is, these terms are considered to be positive when they add energy to the system.

There are a number of other work modes that occur frequently in thermodynamic analyses. Consider next a specialized mechanical system with work modes other than $-P\mathrm{d}V$. The work done in stretching an elastic thin solid rod or wire consists of A and l where $V_0 = Al$ is the volume of the rod at the unstrained state. If the stretching force f_o acts through an elongation $\mathrm{d}l$, the work input is $\delta W = f_\mathrm{o}\mathrm{d}l$. It is appropriate in the study of elastic solids to express work in terms of the stress δ and the strain ς where $\delta = f_\mathrm{o}/A$ and $\mathrm{d}\varsigma = \mathrm{d}l/l$. Upon substituting these equations into the expression for work, we get the work of elastic stretching $\delta W = Al\delta\mathrm{d}\varsigma$, or,

$$\delta W = V_0\delta\mathrm{d}\varsigma. \tag{1.2}$$

One important application of thermodynamics is the study of the behavior of paramagnetic substances at extremely low T. This issue will be considered more fully in Secs. 2.5.2 and 3.1.2, and for the present we discuss only the expression for the work in a process where the magnetic state of the material in a magnetic field is changed. To start with this theme, several essential concepts of the magnetism are simply clarified. Just as an electron current in a small loop produces a magnetic field, an electron revolving in its orbit around the nucleus and rotating around its own axis has associated a magnetic dipole with its motion. In the absence of an external magnetic field, all such dipoles cancel each other. In the presence of an external field, however, the frequencies and senses of orbiting and spinning of the electrons will be changed in such a manner as to oppose the external field. This is the diamagnetic nature of all materials. In some materials, however, there are permanent magnetic dipoles owing to unbalanced electron orbits or spins. These atoms behave like elementary dipoles, which tend to align with an external field and to strengthen it. When this effect in a material is greater than the diamagnetic tendency common to all atoms, this material is termed paramagnetic. Note that paramagnetism is T-dependent. When T is sufficiently lower, the atomic elementary dipoles are magnetically aligned within microscopic domains, which can be readily aligned by a relatively small external

field H_{mag} to form a large induction. This is referred to as ferromagnetic. A ferromagnetic material becomes paramagnetic above a T known as the Curie temperature T_{C}. T_{C} of Fe, Co, and Ni are far above room temperature; they are thus usually referred to as ferromagnetic. On the other side, some metallic salts with $T_{\mathrm{C}} < 1$ K are usually considered as paramagnetic. A paramagnetic material is not a magnet if there is no H_{mag} applied to it. Under an external field, it becomes slightly magnetized in contradistinction to a ferromagnetic material, which shows very strong magnetic effects.

In ferromagnetic materials, each atom has a comparatively large dipole moment caused primarily by uncompensated electron spins. Interatomic forces produce parallel alignments of the spins over regions containing large numbers of atoms. These regions or domains have a variety of shapes and sizes (with dimensions ranging from a micron to several centimeters), depending on materials and magnetic history. The domain moments are generally randomly oriented, the material as a whole has therefore no magnetic moment. Under H_{mag}, however, those domains with moments in the direction of the applied H_{mag} increase their sizes at the expense of their neighbors, and the internal field becomes much larger than H_{mag} alone. When H_{mag} is removed, a random domain alignment in the material does not usually occur, and a residual dipole field remains. This effect is called hysteresis. The magnetic effects on a ferromagnetic material are not reversible because the reverse process of demagnetization forms a hysteresis loop with the forward process of magnetization. Thus, the state of a ferromagnetic system relies on not only its present condition, but also its past history. A ferromagnetic system is thus not amenable to thermodynamic analyses. On the other hand, the magnetization process is reversible and the state of the system can be described by a few thermodynamic variables for a paramagnetic system (such as a paramagnetic salt) or a diamagnetic system (such as a superconducting material). Most experiments on magnetic materials are performed at constant P and involve insignificant volume changes. Hence, variations of P and V can be ignored.

When the system consists of a long slender rod in an H_{mag} parallel to its length l with cross-sectional area A, demagnetizing effects can be neglected. Suppose it is to be wound uniformly with a magnetizing winding of negligible resistance, having N turns and carrying a current I. $H_{\mathrm{mag}} = NI/l$ set up by I in the winding, which in turn produces a magnetic induction B, being the flux density in the rod. $\Phi = BA$ is the total flux. If I is changed by dI, and in time interval dt, the flux is varied by dΦ, there is an induced back electromotive force (emf) $\varepsilon_{\mathrm{emf}}$ according to the relation $\varepsilon_{\mathrm{emf}} = -N\mathrm{d}\Phi/\mathrm{d}t = -NA\mathrm{d}B/\mathrm{d}t$ in terms of Faraday's law of electromagnetic induction. A quantity of electricity dq is transferred in the circuit during dt, the work done by the system is thus $\delta W = -\varepsilon_{\mathrm{emf}}\mathrm{d}q = NA(\mathrm{d}q/\mathrm{d}t)\mathrm{d}B = NAI\mathrm{d}B$. Combining the preceding equation of $H_{\mathrm{mag}} = NI/l$, it gives $\delta W = VH_{\mathrm{mag}}\mathrm{d}B$ with $V = Al$.

If μ_{v} is the magnetization in the rod, or the magnetic moment per unit volume, B in the core becomes $B = \mu_0(H_{\mathrm{mag}} + \mu_{\mathrm{v}})$, where $\mu_0 = 4\pi \times 10^{-7}$

$N \cdot A^{-2}$ is permeability of free space. The magnetic moment is present since the originally random distribution of orbital and spin motions of electron under an H_{mag} reorientates. When this expression for B is inserted in the δW equation, $\delta W = \mu_0 V H_{\mathrm{mag}} dH_{\mathrm{mag}} + \mu_0 V H_{\mathrm{mag}} d\mu_{\mathrm{v}}$. When there is no material within the winding, $\mu_{\mathrm{v}} = 0$, and the right-hand side of the equation is reduced to the first term only, or $\mu_0 V H_{\mathrm{mag}} dH_{\mathrm{mag}}$ is the work required to increase the magnetic field of the empty space of V by an amount dH_{mag}. The second term on the right is therefore the work associated with the change in magnetization of the rod. Because we are interested in the thermodynamics of the material, the work of magnetization, exclusive of the vacuum work, is simply $\delta W = \mu_0 V H_{\mathrm{mag}} dp_{\mathrm{m}}$, which can be written in terms of the total magnetic moment $M = \mu_0 V \mu_{\mathrm{v}}$, namely,

$$\delta W = H_{\mathrm{mag}} dM. \tag{1.3}$$

Equation (1.3) indicates that work input is required to increase the magnetization of a substance.

Next, we take the work of polarization into account. In contrast with an electric conductor having a sufficiently large number of free electrons, a dielectric or electric insulator has none or only a relatively small number of free electrons. The major effect of an electric field on a dielectric is the polarization of the electric dipoles. Work is done by H_{mag} on the dielectric material during the polarization process.

For the purpose of deriving the equation of work in polarizing a dielectric, let us consider a parallel-plate capacitor or condenser. The two plates, each of area A with a distance of separation l, are charged with equal and opposite charges $\pm q$. According to electrostatics, when the space between the plates is a vacuum, the electric field intensity E_{e} created by the charges is given by $E_{\mathrm{e}} = q/(A\varepsilon_0)$, where $\varepsilon_0 = 8.85 \times 10^{-12}$ $C^2 \cdot N^{-1} \cdot m^{-2}$ is the permittivity of a free space. $u = E_{\mathrm{e}} l = ql/(A\varepsilon_0)$ where u is the potential difference between the plates.

Let a dielectric material be inserted between the plates. In the absence of E_{e}, in spite of the atomic irregularities, we can imagine the dielectric to be composed of generally uniform distributions of positive and negative charges. Under the influence of an E_{e}, a rearrangement of the charges in the dielectric takes place and it thus becomes polarized. The positive charges are displaced slightly in the direction of the field, while the negative charges are done in the opposite direction. Thus, because of the presence of the dielectric between the capacitor plates, the effective charge on each plate is reduced by a relative permittivity ε_{r}. The actual permittivity of dielectric is then calculated by multiplying the relative permittivity by ε_0, $\varepsilon_{\mathrm{a}} = \varepsilon_{\mathrm{r}} \varepsilon_0 = (1 + \chi)\varepsilon_0$, where χ is the electric susceptibility of the dielectric. Hence, the electric field and the potential difference between the plates are described by the equation $E_{\mathrm{e}} = q/(A\varepsilon_{\mathrm{a}})$ and $u = ql/(A\varepsilon_{\mathrm{a}})$.

The electric polarization P_{d} of a dielectric is defined as the electric dipole moment per unit volume and is related to E_{e} by $P_{\mathrm{d}} = \varepsilon_0 \chi E_{\mathrm{e}}$, while P_{d} and

E_e in turn are related to the electric displacement l_{ed}, which can be separated into a vacuum contribution and the one arising from the dielectric by $l_{ed} = \varepsilon_a E_e = \varepsilon_0 E_e + P_d = q/A$. The reversible work done in charging a capacitor is $\delta W = u dq$, which may be transformed to $\delta W = (E_e l)d(Al_{ed}) = (Al)E_e dl_{ed} = V E_e dl_{ed}$. Combining the preceding equation with $l_{ed} = \varepsilon_0 E_e + P_d$, it gives $\delta W = V\varepsilon_0 E_e dE_e + V E_e dP_d$.

When there is no material between the capacitor plates, $P_d = 0$, $\delta W = V\varepsilon_0 E_e dE_e$ and $V\varepsilon_0 E_e dE_e = d(V\varepsilon_0 E_e^2/2)$ is the work required to increase the electric field of the free space between the capacitor plates by an amount dE_e. This quantity is additive to U when the first law is used. Therefore, with $P_d' = V P_d$, the reversible work in the polarization of a dielectric material is

$$\delta W = V E_e dP_d = E_e dP_d'. \tag{1.4}$$

As a final example of a process, in which work other than mechanical one $(-PdV)$ is done, take into account the work of surface when the area of a surface A for a film with thickness $2r$ is changed,

$$\delta W = \gamma_{sv} dA = 2\gamma_{sv} dV/r \tag{1.5}$$

where γ_{sv} is surface energy or solid-vapor interface energy. Note that r could be extended as a radius for a particle or a wire. Equation (1.5) is especially important when material size is considered as a variant, which will come into contact with nanothermodynamics and will be discussed in detail in Chapter 6.

Since work can be done by many different kinds of forces, to find the total work, we add together the mechanical, magnetic, electrical, and surface work, etc. That is $\delta W_{total} = \delta W + \delta W' + \delta W'' + \cdots = -PdV + H_{mag}dM + EdP_d' + \gamma dA + \cdots$. Let us define δW^* as "useful" work exclusive of the PdV term, $\delta W_{total} = \delta W + \delta W^*$. Because we often focus on simple systems where only mechanical work is done on or by the system, $\delta W_{total} = \delta W = -PdV$.

If we have a closed system and it is carried out through a cycle, the first law is expressed by

$$\oint \delta Q + \oint \delta W = 0, \quad \text{or} \quad \oint (\delta Q + \delta W) = 0. \tag{1.6}$$

Since the cyclic integral of the quantity $(\delta Q + \delta W)$ is always zero, it is a differential of a property of the system and is a state function or a property of the system. This property is called the stored energy, which represents all energy of a system at a given state, such as the kinetic energy, potential energy and all other energy of the system. We call the energy the internal energy U. In the absence of motion and gravity effects, the first law for a closed system may be written in integrated form as

$$\Delta U = Q + W, \tag{1.7}$$

or in a differential form

$$\mathrm{d}U = \delta Q + \delta W. \tag{1.8}$$

The value of Q as a transfer quantity and a process variable depends on the process that the system undergoes during heat transfer. Q values of several simple processes are discussed here. From the first law and taking into account only mechanical work, we have

$$\delta Q = \mathrm{d}U + P\mathrm{d}V. \tag{1.9}$$

If $\mathrm{d}V = 0$, there is no work done between the system and the environment, $\delta W = 0$. Hence, the heat flow into the system is just equal to the change in internal energy,

$$\delta Q_V = \mathrm{d}U, \quad \text{or} \quad Q_V = \Delta U. \tag{1.10}$$

For an isometric process, the infinitesimal expression for heat forms an exact differential, but for processes involving work, it forms an inexact differential.

Although Eq. (1.10) is simple and convenient, many processes occur under a constant P, rather than with a constant V. This is because in many laboratory experiments a considered system is exposed to atmospheric pressure, rather than kept in vessel with a constant V. If the process is isobaric ($\mathrm{d}P = 0$), from the first law and considering only mechanical work, then the heat associated with this process is $\delta Q_P = \mathrm{d}U + (P\mathrm{d}V)_P = \mathrm{d}U + \mathrm{d}(PV) = \mathrm{d}(U + PV)$. The term $U + PV$ is defined as enthalpy H,

$$H \equiv U + PV. \tag{1.11}$$

H in Eq. (1.11) has the unit of energy. H is a state function since U, P, and V all are. Finally,

$$\delta Q_P = \mathrm{d}H, \quad \text{or} \quad Q_P = \Delta H. \tag{1.12}$$

For a system under a constant P, ΔH is the heat received by the system plus the useful work that has been done.

Although H is commonly used in engineering and science, it is impossible to directly measure it, while ΔH is measured instead. For exothermic and endothermic reaction at a constant P, ΔH equals the energy released (negative) and absorbed (positive) in the reaction, respectively.

If ΔV is little and P is not too big (these are the conditions of small $P\mathrm{d}V$),

$$\mathrm{d}H = \mathrm{d}U + P\mathrm{d}V \approx \mathrm{d}U. \tag{1.13}$$

This is exactly the case we find for processes involving condensed phases under a low to moderate P where $\Delta U \approx \Delta H$, which is often used in some theoretical calculations and computer simulations due to the simplicity.

When heat is transferred to a system, a change of U occurs, which can affect the kinetic energy or potential energy of the molecules, or both. We can define two types of heat: sensible and latent. Sensible heat Q causes a temperature change but the system does not change its phase. Latent heat

causes phase change with a constant T; for example, latent heat of boiling, latent heat of melting, etc.

Q transferred to or from a system causes its T changing from an initial value T_{in} to a final value T_{fi}, which is calculated as follows: $Q = C\Delta T = C(T_{fi} - T_{in})$ where the proportionality constant C is called the heat capacity. C is the amount of heat energy required to increase the unit temperature of a substance in a unit of J·K^{-1}. C is an extensive property because its value is proportional to the material amount in the system; for instance, a bathtub of water has a greater heat capacity than a cup of water. The heat capacity of a unit quantity of a substance is called specific heat capacity or specific heat, which becomes an intensive property and can be measured.

When the unit quantity is the mole, the term molar heat capacity C_m in J·mol^{-1}·K^{-1} may be used to describe the measure more explicitly. The equation relating heat energy to C_m is

$$Q = nC_m\Delta T \tag{1.14}$$

where n is the number of moles.

C is mathematically defined as the ratio of a small amount of heat δQ added to the system, to the corresponding small increase in its temperature dT,

$$C = \left(\frac{\delta Q}{dT}\right)_{cond.} \tag{1.15}$$

For a real system, the path through energy changes must be explicitly defined, since C_m value relies on which path from one T to another is chosen. C_m of substances are typically measured under constant P ($C_{P,m}$). However, fluids (gases and liquids) are typically also done at constant V ($C_{V,m}$). $C_{V,m}$ is determined by

$$C_{V,m} = \left(\frac{\delta Q_m}{dT}\right)_V = \left(\frac{\partial U_m}{\partial T}\right)_V. \tag{1.16}$$

Note that we have implicitly assumed that no other forms of work, such as electrical or magnetic, are involved. Accordingly,

$$dU = nC_{V,m}dT. \tag{1.17}$$

Measuring $C_{V,m}$ can be prohibitively difficult for liquid and solids. That is, dT typically requires large P to maintain a liquid or solid at constant V. This implies that the containing vessel must be nearly rigid or at least very strong. Instead it is easier to measure $C_{P,m}$ (allowing the material to expand or contract as it wishes). The thermal energy added to the material is accounted for by the increase in U plus W done by the material as it expands against the constant P imposed on it. As a result,

$$C_{P,m} = \left(\frac{\delta Q_m}{dT}\right)_P = \left(\frac{\partial H_m}{\partial T}\right)_P. \tag{1.18}$$

1.5 Entropy and Second Law of Thermodynamics [6, 17, 18]

It is well known that physical processes in nature proceed toward equilibrium spontaneously. Liquids flow from a region of high elevation to that of low elevation; gases expand from a region of high P to that of low P; heat flows from a region of high T to that of low one, and material diffuses from a region of high concentration to that of low one. A spontaneous process can proceed only in a particular direction. Everyone realizes that these reversed processes do not happen. But why? The total energy in each case would remain constant in the reversed process as it did in origin, and there would be no violation of the principle of conservation of energy. There must be another natural principle, in addition to the first law, not derivable from it, which determines the direction, in which a natural process will take place. This principle is contained in the second law of thermodynamics, which epitomizes our experience with respect to the unidirectional nature of thermodynamic processes.

The invention and improvement of the steam engine and internal combustion engine, the devices that convert Q into W, played an important role in the development of the second law. These devices also made industrial development possible, and greatly changed the nature of our everyday life. The first law accounts for the energy involved in such a conversion but places no limits on the amounts that can be converted. The second law is concerned with limits on the conversion of "heat" into "work" by heat engines. As one of the fundamental laws of nature, the second law cannot be derived from any other laws and may be stated in many different forms, but when its statement is accepted as a postulate, all other statements of it can then be proved. One of which, known as the Kelvin-Planck statement, is as follows: it is impossible to construct a heat engine that, operating in a cycle, produces no other effect than the absorption of energy from a reservoir and the performance of an equal amount of work. Its essence is that it is theoretically impossible to construct a heat engine that works with 100% efficiency.

Can we find some features all of the above dissimilar impossible processes have in common? What are the conditions under which no process at all can occur, and in which a system is in equilibrium? Is there any thermodynamic quantity that can help us to predict whether a process will occur spontaneously? These questions could be answered if some properties of a system, namely, some state functions of a system, have different values at the beginning and at the end of a possible process. A function having the desired property was devised by Clausius and is called entropy of the system S. The concept of S is developed using the properties of the Carnot cycle and then calculating entropy changes ΔS during reversible and irreversible processes.

The principles governing heat engines were investigated in 1824 by a French engineer Sadi Carnot. Through considering an idealized heat engine,

now called a Carnot engine, Carnot found that a heat engine operating in an ideal, reversible cycle – called a Carnot cycle – is the most efficient engine possible. Such an engine establishes an upper limit on the efficiencies of all real engines. That means not all the heat removed from a high T reservoir is converted into work. In fact, the amount that can be converted is governed by the temperatures of the two reservoirs.

The Carnot cycle consists of two reversible isothermal and two reversible adiabatic processes. From thermodynamic calculation, it was concluded that for any two temperatures T_2 and T_1, the ratio of the magnitudes of Q_2 and Q_1 and that of the magnitudes of T_2 and T_1 in a Carnot cycle have the same value for all systems, no matter whatever their nature is, where Q_2 is a heat flow into the system and Q_1 is a heat flow out of the system, namely,

$$\frac{T_2}{T_1} = -\frac{Q_2}{Q_1}, \quad \text{or} \quad \frac{Q_1}{T_1} + \frac{Q_2}{T_2} = 0. \tag{1.19}$$

A system undergoing a reversible cycle is presented by the continuous curve shown in Fig. 1.3. It is possible to subdivide this cycle into a number of small Carnot cycles as indicated. The isotherms and part of the adiabats of the small Carnot cycles form a zigzag curve which follows closely the path of the original cycle. The remaining parts of the adiabats of the small Carnot cycles cancel out because each section is traversed once in a forward direction and once in a reverse direction. As the number of Carnot cycles is increased, the zigzag curve can be made to approach the original cycle to any desired degree.
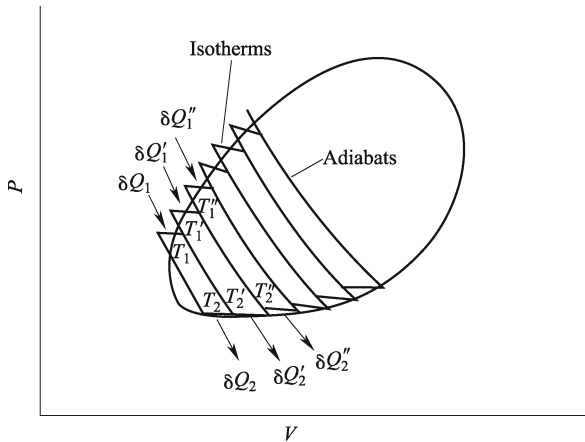

Fig. 1.3   A reversible cycle subdivided into infinitesimal Carnot cycles.

Let $\delta Q_1, \delta Q_1', \delta Q_1'', \cdots, \delta Q_2, \delta Q_2', \delta Q_2'', \cdots$ denote the respective algebraic amounts of heat exchanged, which are positive when absorbed and negative when given off by the system. Then for the small Carnot cycles as we may

write $\dfrac{\delta Q_1}{T_1} + \dfrac{\delta Q_2}{T_2} = 0$, and $\dfrac{\delta Q_1'}{T_1'} + \dfrac{\delta Q_2'}{T_2'} = 0, \cdots$, etc. Adding the preceding

equations gives $\dfrac{\delta Q_1}{T_1} + \dfrac{\delta Q_2}{T_2} + \dfrac{\delta Q_1'}{T_1'} + \dfrac{\delta Q_2'}{T_2'} + \cdots = \sum \dfrac{\delta Q}{T} = 0$. In the limit,

upon replacement of the summation of finite terms by a cyclic integral, we obtain

$$\oint \frac{\delta Q_{\mathrm{rev}}}{T} = 0 \tag{1.20}$$

where the subscript "rev" serves as a reminder that the result above is applied to reversible cycles only. The foregoing equation states that the integral of $\delta Q/T$ when carried out over a reversible cycles is equal to zero. It follows that the differential $\delta Q_{\mathrm{rev}}/T$ is a perfect differential and the integral $\oint \delta Q_{\mathrm{rev}}/T$ is a property of the system. This property is called entropy S, and

$$\mathrm{d}S = \frac{\delta Q_{\mathrm{rev}}}{T}, \quad \text{or} \quad \delta Q_{\mathrm{rev}} = T\mathrm{d}S. \tag{1.21}$$

Equation (1.21) is the defining expression for S. Integrating along a reversible path between two equilibrium states 1 and 2 gives

$$\Delta S_{12} = S_2 - S_1 = \int_1^2 \frac{\delta Q_{\mathrm{rev}}}{T}. \tag{1.22}$$

It cannot be overemphasized that S is a state function; it depends only on the state that the system is in, and not on how that state is reached. If a system goes from state 1 to 2, its entropy changes from S_1 to S_2. However, it is only when the system travels along a reversible path between the two end states that Eq. (1.22) is valid. If the path is irreversible, $\int_1^2 (\delta Q_{\mathrm{irr}}/T)$ differs from ΔS_{12}. The relation that does exist between the change in entropy and the integral $\int_1^2 (\delta Q/T)$ along any arbitrary path can be obtained as follows:

$$\mathrm{d}S \geqslant \frac{\delta Q_{\mathrm{rev}}}{T}, \quad \text{or} \quad \Delta S_{12} = S_2 - S_1 \geqslant \int_1^2 \frac{\delta Q}{T} \tag{1.23}$$

where the equality holds for a reversible process and so does the inequality for an irreversible process. This is one of the most important equations of thermodynamics. It expresses the influence of irreversibility on the entropy of a system.

For an isolated system, $\delta Q = 0$. Thus, in light of Eq. (1.23),

$$\mathrm{d}S_{\mathrm{isolated}} \geqslant 0. \tag{1.24}$$

This is the principle of increase of entropy. In accordance with the first law, an isolated system can only assume those states for which the total U remains

constant. Now according to the second law as expressed by Eq. (1.22) of the states of equal energy, only those states, for which the entropy increases or remains constant, can be attained by the system.

In addition to U and S of a system, several other useful quantities can be defined that are combinations of these and the state variables. One such quantity, already introduced, is $H = U + PV$. There are two combinations of thermodynamic properties involving the entropy being of great utility in thermodynamics, which are the Helmholtz function F and the Gibbs function G.

In light of the first law, when a system performs any process, reversible or irreversible, between two equilibrium states, the total work in the process is

$$W + W^* = \Delta U - Q. \tag{1.25}$$

We now derive expressions for the maximum amount of work that can do when a system undergoes a process between two equilibrium states, for the special case in which the only heat flow is from a single reservoir at a T and the initial and final states are at the same T. In light of Eq. (1.24), the sum of the increase in entropy of the system, ΔS, and that of reservoir, ΔS_{r}, is equal to or greater than zero, namely, $\Delta S + \Delta S_{\mathrm{r}} \geqslant 0$ and $\Delta S_{\mathrm{r}} = -Q/T$. Hence, $\Delta S - Q/T \geqslant 0$ and $T\Delta S \geqslant Q$. As a result, from the first law,

$$\Delta U - T\Delta S = \Delta(U - TS) \leqslant W + W^*. \tag{1.26}$$

Let us define a property of the system called Helmholz function F, by the equation

$$F \equiv U - TS, \tag{1.27}$$

then for two equilibrium states at the same T,

$$\Delta F = \Delta U - T\Delta S, \tag{1.28}$$

and from Eq. (1.26),

$$\Delta F \leqslant W + W^*. \tag{1.29}$$

That is, the decrease in F sets an upper limit to the work in any process between two equilibrium states at the same T, during which there is a heat flow into the system from a single reservoir at this T. If the process is reversible, the equality sign then holds in Eq. (1.29) and the work is a maximum. Against that, when the process is irreversible, the work is less than this maximum.

Equation (1.29) is perfectly general and applies to a system of any nature. The process may be a change of states, or a change of phases, or a chemical reaction.

If both V and T are constants, considering only mechanical work $P\mathrm{d}V$, then $W = W^* = 0$ and

$$\Delta F \leqslant 0, \quad \text{or} \quad F_2 \leqslant F_1. \tag{1.30}$$

Take into account next a process under a constant external P. W in such a process is $-P\Delta V = -\Delta(PV)$, and from Eq. (1.29),

$$\Delta F + \Delta(PV) = \Delta(F + PV) \leqslant W^*. \tag{1.31}$$

Let us define Gibbs function G as

$$G \equiv F + PV = U - TS + PV = H - TS. \tag{1.32}$$

Then for two states at the same T and P,

$$\Delta G \leqslant W^*. \tag{1.33}$$

The decrease in G therefore gives an upper limit to the useful work in any process between two equilibrium states at the same T and P where the process is reversible. Because its decrease in such a process equals the maximum energy that can be "freed" and can be the useful work done by a system, the Gibbs function has also been called the free energy of a system. We however shall use the term "Gibbs function" to avoid confusion with the Helmholtz function.

Similar to Eq. (1.30), if the only work is PdV, $W^* = 0$ and

$$\Delta G \leqslant 0, \quad \text{or} \quad G_2 \leqslant G_1. \tag{1.34}$$

That is, in such a process G either remains constant or decreases. Conversely, such a process is possible only if G_2 is equal to or less than G_1.

1.6 General Thermodynamic Relationships [6, 17, 18]

We have defined and used several thermodynamic properties by now. Some of them are directly measurable, but others cannot be measured and must be calculated from data of other properties and quantities, which can be measured. We are now ready to develop some useful general relationships between thermodynamic properties that shall facilitate such calculations. We will restrict our attention to simple systems which require only two independent properties to determine their thermodynamic states. Once the thermodynamic relations are developed for such systems, it is simple to write analogous relations for other simple systems.

We now combine the first and second laws to obtain several important thermodynamic relations. The analytical formulation of the first law, in a differential form, is $dU = \delta Q + \delta W$. The second law states that for a reversible process between two equilibrium states is $\delta Q = TdS$. Also, the work in a reversible process, for a PVT system, is $\delta W = -PdV$. It follows that in any infinitesimal reversible process for a PVT system,

$$dU = TdS - PdV. \tag{1.35}$$

This may be used in connection with the definitions of H, F and G functions to form three other important relations,

$$\mathrm{d}H = T\mathrm{d}S + V\mathrm{d}P, \tag{1.36}$$

$$\mathrm{d}F = -S\mathrm{d}T - P\mathrm{d}V, \tag{1.37}$$

$$\mathrm{d}G = -S\mathrm{d}T + V\mathrm{d}P. \tag{1.38}$$

Equations (1.35) to (1.38) are four basic relations of properties. They are applicable for any process, reversible or irreversible, between equilibrium states of a simple compressible system with a fixed mass.

A number of useful partial derivative relations can be readily obtained from the four basic relations. They are as follows:

$$\left(\frac{\partial U}{\partial S}\right)_V = T \quad \text{and} \quad \left(\frac{\partial U}{\partial V}\right)_S = -P, \tag{1.39}$$

$$\left(\frac{\partial H}{\partial S}\right)_P = T \quad \text{and} \quad \left(\frac{\partial H}{\partial P}\right)_S = V, \tag{1.40}$$

$$\left(\frac{\partial F}{\partial T}\right)_V = -S \quad \text{and} \quad \left(\frac{\partial F}{\partial V}\right)_T = -P, \tag{1.41}$$

$$\left(\frac{\partial G}{\partial T}\right)_P = -S \quad \text{and} \quad \left(\frac{\partial G}{\partial P}\right)_T = V. \tag{1.42}$$

Since U, H, F, and G are all thermodynamic properties and state functions, $\mathrm{d}U$, $\mathrm{d}H$, $\mathrm{d}F$, and $\mathrm{d}G$ are exact differentials. Applying these exact conditions to Eqs. (1.35) through (1.38), one obtains

$$\left(\frac{\partial T}{\partial V}\right)_S = -\left(\frac{\partial P}{\partial S}\right)_V, \tag{1.43}$$

$$\left(\frac{\partial T}{\partial P}\right)_S = \left(\frac{\partial V}{\partial S}\right)_P, \tag{1.44}$$

$$\left(\frac{\partial S}{\partial V}\right)_T = \left(\frac{\partial P}{\partial T}\right)_V, \tag{1.45}$$

$$\left(\frac{\partial S}{\partial P}\right)_T = -\left(\frac{\partial V}{\partial T}\right)_P. \tag{1.46}$$

The above equations are known as the four Maxwell relations. Note that in each of the Maxwell relations the cross product of the differentials has the dimensions of energy. The independent variable in the denominator on one side of an equation is the constant on the other side. They are of great usefulness in the transition of state variables, and particularly in the determination of change in entropy, which are not experimentally measurable, in terms of the measurable properties of P, V, and T.

The magnetic systems of primary interest in thermodynamics are paramagnetic crystals, whose volume change in a process or "$-PdV$" can be neglected. The only work interaction is due to the magnetization of the material, i.e., $\delta W^* = H_{\mathrm{mag}}dM$.

A system for which the only reversible work mode is the magnetization of the magnetic material is called a simple magnetic system. This will be taken as an example to illustrate the application of the above equations. The first law for a reversible process in a simple magnetic system is $dU = \delta Q + H_{\mathrm{mag}}dM$. Combination of this equation and the second law leads to

$$dU = T\mathrm{d}S + H_{\mathrm{mag}}\mathrm{d}M. \tag{1.47}$$

Eq. (1.47) is a very basic equation which combines the first and second laws as applied to a simple magnetic system.

It is helpful to define two new properties, the magnetic enthalpy H' and magnetic Gibbs function G', $H' = U - H_{\mathrm{mag}}M$ and $G' = H' - TS = U - TS - H_{\mathrm{mag}}M$. F takes the usual definition, $F = U - TS$. Comparing to $H = U + PV$ in a PVT system, the equations do have the same form, we can take over all of the equations previously derived for the enthalpy H, replacing H with H', V with $-M$, and P with H_{mag}. From these equations and Eq. (1.47) it follows that

$$\mathrm{d}H' = T\mathrm{d}S - M\mathrm{d}H_{\mathrm{mag}}, \tag{1.48}$$

$$\mathrm{d}F' = -S\mathrm{d}T + H_{\mathrm{mag}}\mathrm{d}M, \tag{1.49}$$

$$\mathrm{d}G' = -S\mathrm{d}T - M\mathrm{d}H_{\mathrm{mag}}. \tag{1.50}$$

Applying the condition of exactness to the four basic relations, Eqs. (1.47) to (1.50), results in the following four Maxwell relations,

$$\left(\frac{\partial T}{\partial M}\right)_S = \left(\frac{\partial H_{\mathrm{mag}}}{\partial S}\right)_M, \tag{1.51a}$$

$$\left(\frac{\partial T}{\partial H_{\mathrm{mag}}}\right)_S = -\left(\frac{\partial M}{\partial S}\right)_{H_{\mathrm{mag}}}, \tag{1.51b}$$

$$\left(\frac{\partial S}{\partial M}\right)_T = -\left(\frac{\partial H_{\mathrm{mag}}}{\partial T}\right)_M, \tag{1.51c}$$

$$\left(\frac{\partial S}{\partial H_{\mathrm{mag}}}\right)_T = \left(\frac{\partial M}{\partial T}\right)_{H_{\mathrm{mag}}}. \tag{1.51d}$$

A crystalline metal with the atoms lies on a regular repetitive lattice. When the crystal lattice is perfect, free electrons in the metal are able to pass through it without difficulty. However, there are two factors that generally ruin the perfect arrangement of a crystal lattice and thus give rise to electrical resistance. These are the thermal vibrations of the atoms and the impurities

or imperfections of the metal. As T falls, the thermal vibrations of the lattice atoms decrease, which bring out the decrease of the electrical resistance of metals. Since any real specimen of a metal cannot be perfectly pure and will inevitably contain some impurities, the effect of impurity on electrical resistance is more or less T-independent. Thus we can see that impurities and lattice imperfections (point defects, dislocations, interfaces or surfaces) are mainly responsible for the small constant residual resistivity of a metal at very low T.

However, many metals exhibit extraordinary behavior. After the residual resistivity of a metal has been reached, when T is further reduced, its electrical resistance suddenly disappears completely. Once a current is introduced in the metal at such low T, the current will continue to undergo flow undiminished for an indefinite period of time. This phenomenon was discovered in 1911 by Onnes and was given the name superconductivity. A material having superconductivity at low T is called a superconductor. Since its discovery, the superconductivity has been found in many metallic elements and in a very large number of alloys and compounds, and even in oxides or ceramics.

The superconductivity has many applications. For instance, it can be applied in journal bearings to eliminate friction, in electric motors to reduce internal losses, in electromagnets to obtain very high magnetic fields, and in high-speed computers to form the so-called cryotrons to be used as logic, memory, and comparison elements. There are two kinds of superconductivity, known as type I and type II. Most of those elements exhibiting superconductivity belong to type I, while alloys generally belong to type II. The two types have many properties in common, but there are considerable differences in their magnetic behavior. In 1957 an acceptable fundamental theory of superconductivity was formulated by Bardeen, Cooper, and Schrieffer (BCS theory) when quantum mechanics was applied to the free electrons in a crystal lattice. The complete treatment of the theory is extremely complicated. It requires an advanced knowledge of quantum mechanics and is beyond the scope of this book. It is our intention here to give only a brief descriptive introduction of the thermodynamics of superconductors.

The normal to superconductor transition occurs at a temperature $T_{s,0}$, which depends not only on P, but also on the size when the materials are low dimensional. For a strain-free pure bulk metal, $T_{s,0}$ is well defined and can be measured accurately.

Superconductivity can be destroyed by a magnetic field. A magnetic field-strength required to destroy superconductivity in a metal is called a critical or threshold field H_s. The uniqueness of H_s at a given T relies on the shape and orientation of the superconductor as well as on any impurity and strain in it. In an ideal case, when a strain-free pure type I superconductor in the shape of a long thin cylinder is placed longitudinally in a uniform magnetic field, the transition between normal and superconductivity is sharp and a unique value of H_s can be obtained at a given T, which is only a function of T. Figure 1.4(a) shows this dependence of a type I superconductor. It is

observed that H_s curve forms the boundary of superconducting states which divides the H_s-T plane into two regions. The area enclosed by H_s curve is the region in which the metal is superconducting. It is normal to go beyond the confines of the curve. $T_{s,0}$ values and the critical field at $T = 0$ K, $H_{s,0}$, for a number of elements are given in Table 1.1.
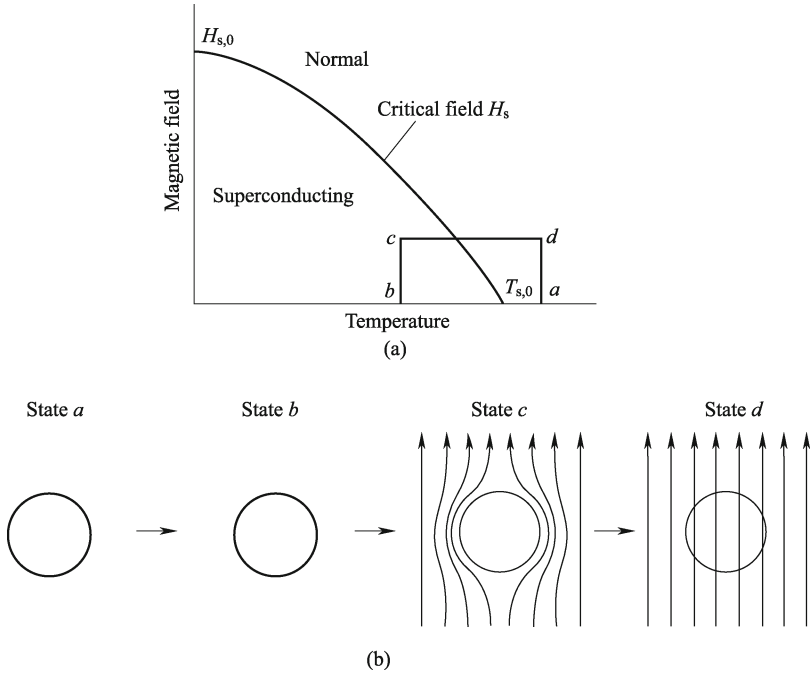
Fig. 1.4   (a) T-dependent H_s of a type I superconductor. (b) The effect of zero electrical resistance and zero magnetic induction.

Table 1.1   The superconducting elements [19]

Element	$T_{s,0}$	$H_{s,0}$	Element	$T_{s,0}$	$H_{s,0}$	Element	$T_{s,0}$	$H_{s,0}$
Al	1.2	0.79×10^4	Ir	0.1	$\sim 0.16 \times 10^4$	Ru	0.5	0.53×10^4
Cd	0.5	0.24×10^4	La-α	4.8		Ta	4.5	6.6×10^4
Ga	1.1	0.41×10^4	La-β	4.9		Tc	8.2	
In	3.4	2.2×10^4	Pb	7.2	6.4×10^4	Tl	2.4	1.4×10^4
Hg-α	4.2	3.3×10^4	Th	1.4	1.3×10^4	U-α	0.6	
Hg-β	4.0	2.7×10^4	Sn	3.7	2.4×10^4	U-β	1.8	
Mo	0.9		Ti	0.4		V	5.3	Type II
Nb	9.3	Type II	W	0.01		Zn	0.9	0.42×10^4
Os	0.7	$\sim 0.5 \times 10^4$	Zr	0.8	0.437×10^4	Re	1.7	1.6×10^4

Figure 1.4(a) reveals that every critical field curve has a negative slope, which increases in magnitude from zero at 0 K to a finite value at T_0. These curves may be approximated by a parabolic equation of the form

$H_s = H_{s,0}(1 - T^2/T_{s,0}^2)$.

In addition to the disappearance of electrical resistivity, a superconducting metal also shows a magnetic effect – the disappearance of magnetic induction. The phenomenon of zero magnetic induction was discovered by Meissner and Ochsenfeld in 1933 and is now commonly known as the Meissner effect. Its meaning can be understood by considering a type I superconducting metal going through a few processes as depicted in Fig. 1.4(a). The specimen is first cooled at zero magnetic field from a normal state a to a superconducting state b, and then is magnetized at constant T from state b to state c, which is well below the critical field curve. When the magnetic field is applied to the specimen in superconducting states, persistent currents induced on the surface of the specimen prevent the field from penetrating the metal. Thus, as illustrated in Fig. 1.4(b), at state c the magnetic lines of forces are bulging around the specimen. When the specimen is heated in a constant H_s from state c to state d, as H_s curve is passed, the persistent current on its surface dies out and magnetic flux penetrates into it. Thus, as illustrated in Fig. 1.4(b), H_s has uniformly penetrated the metal at state d since the metal is now in a normal state and is virtually nonmagnetic. The fact that the magnetic field is expelled from the metal when it becomes superconducting implies not only infinite electrical conductivity, but also perfect diamagnetism. This is the essence of the Meissner effect.

As a further illustration of the magnetic nature of superconductivity, let us consider the variations of the magnetic induction B and the magnetization μ_v of a type I superconductor as H_{mag} is increased isothermally across the critical field. In general, $B = \mu_0(H_{mag} + \mu_v)$. When the metal is in superconducting phase, we have

$$B = 0, \quad \text{and} \quad \mu_v = -H_{mag}, \qquad (1.52)$$

whereas beyond H_s corresponding to the given T, the metal is normal. Since normal metals (excluding ferromagnetic metals, such as Fe) are virtually nonmagnetic, it follows

$$\mu_v = 0, \quad \text{and} \quad B = \mu_0 H_{mag}. \qquad (1.53)$$

There is another property of a metal, which changes abruptly during transitions from normal to superconductivity. As we know, conduction heat transfer in a metal is mainly due to the mobility of free electrons. However, at a superconducting state the free electrons of a metal no longer interact with the lattice in such a way that the electrons can pick up heat energy from one part of the metal and deliver it to another part. Therefore when a metal becomes superconducting, its thermal conductivity decreases in general. At $T \ll T_{s,0}$, the decrease in thermal conductivity is abrupt at the crossing of the critical field curve. Since superconductivity can be destroyed by the application of a magnetic field, the thermal conductivity of a superconductor can be easily controlled by means of a magnetic field. This is the basic principle for a thermal valve.

A type I superconducting system at any values of H_{mag} and T within the superconducting region has a strictly fixed state and is independent of how the system got there. Hence a type I superconductor may be considered as a thermodynamic system whose equilibrium states can be described by a few thermodynamic properties, and the transitions between normal and superconducting states are reversible.

As plotted in Fig. 1.4, below H_s curve the system is in the superconducting phase. Otherwise, the normal phase is present. H_s curve itself is the equilibrium line for the phase coexistence. In general, the transition between normal and superconducting phases, taking place at constant T and H_s, involves a finite latent heat, denoting a first order phase transition. We now derive the equation for the latent heat as functions of T and H_s. According to Eq. (1.50), the differential of the magnetic Gibbs function is given by $dG' = -SdT - MdH_{\text{mag}}$. At $T = $ constant and $H_{\text{mag}} = H_s = $ constant, we must have $dG' = 0$, or $G'^{(n)} = G'^{(s)}$, where the superscripts (n) and (s) denote respectively normal and superconducting phases. When T and H_s are increased to $T + dT$ and $H_s + dH_s$ respectively, $G'^{(n)} + dG'^{(n)} = G'^{(s)} + dG'^{(s)}$, or $dG'^{(n)} = dG'^{(s)}$. Applying Eq. (1.50), we obtain $-S^{(n)}dT - M^{(n)}dH_s = -S^{(s)}dT - M^{(s)}dH_s$. Therefore, $-dH_s/dT = (S^{(n)} - S^{(s)})/(M^{(n)} - M^{(s)})$. In light of Eqs. (1.52) and (1.53), $M^{(n)} = \mu_0 V \mu_v^{(n)} = 0$ and $M^{(s)} = \mu_0 V \mu_v^{(s)} = -\mu_0 V H_s$. It follows

$$\Delta S_{\text{sn}} = S^{(n)} - S^{(s)} = -\mu_0 V H_s \frac{dH_s}{dT}. \tag{1.54}$$

Now since $\Delta H_s = T(S^{(n)} - S^{(s)}) = $ latent heat, we obtain finally

$$\Delta H_{\text{sn}} = -\mu_0 V T H_s \frac{dH_s}{dT}. \tag{1.55}$$

Since dH_s/dT is always negative, we see from Eq. (1.54) that $S^{(n)} > S^{(s)}$. Since entropy is physically an index of orderliness, we conclude that more orders exist in the superconducting than in the normal phase. From Eq. (1.55) we see that $\Delta H_{s,0} = 0$ at the two extremes of H_s curve, i.e., dH_s/dT at $T = 0$, and $H_s = 0$ at $T = T_{s,0}$. Between them, $\Delta H_{\text{sn}} > 0$, indicating that heat addition is required in changing from superconducting to normal phase.

Since the transition between normal and superconducting phases takes place at $T_{s,0}$ without latent heat evolution in the absence of a magnetic field while heat capacity shows a discontinuity at $T_{s,0}$, this phase transition is obviously of the second order.

There are some useful relationships concerning C and H_s. With simple mathematical treatment of Eq. (1.54), we obtain $TdS^{(n)}/dT - TdS^{(s)}/dT = -\mu_0 V T d(H_s dH_s/dT)/dT$. Since $C = TdS/dT$, it reads

$$C^{(s)} - C^{(n)} = -\mu_0 V T \frac{d}{dT}\left(H_s \frac{dH_s}{dT}\right), \tag{1.56}$$

or $C^{(s)} - C^{(n)} = \mu_0 V T (dH_s/dT)^2 + \mu_0 V T H_s d^2 H_s/dT^2$. Equation (1.56) can be used to determine $C^{(s)} - C^{(n)}$ from measurements of magnetic properties for an ideal type I superconductor. At $T = T_{s,0}$ and $H_s = 0$, Eq. (1.56) reduces to

$$\left(\frac{dH_s}{dT}\right)^2_{T=T_{s,0}} = \frac{1}{\mu_0 V T_{s,0}}(C^{(s)} - C^{(n)})_{T=T_{s,0}}. \qquad (1.57)$$

This equation could be utilized to determine the slope of H_s curve at $T_{s,0}$ from measurements on C. Conversely, the magnitude of C jump at $T_{s,0}$ decides the slope of H_s curve. Integrating Eq. (1.56) from $T = 0$ K and $H_s = H_{s,0}$ to $T = T_{s,0}$ and $H_s = 0$ along H_s curve, there is

$$\int_0^{T_{s,0}} (C^{(s)} - C^{(n)})dT = \mu_0 V \int_{H_s}^0 T d\left(H_s \frac{dH_s}{dT}\right)$$

$$= \mu_0 V T H_s \frac{dH_s}{dT}\Bigg]_0^{T_{s,0}} - \mu_0 V \int_{H_{s,0}}^0 H_s \frac{dH_s}{dT}$$

where the method of integration has been used in part. Now, since at $T = T_{s,0}, H_s = 0$, the first term in the last expression is zero, and therefore,

$$\int_0^{T_{s,0}}(C^{(s)} - C^{(n)})dT = \frac{1}{2}\mu_0 V H_{s,0}^2, \quad \text{or} \quad H_{s,0}^2 = \frac{2}{\mu_0 V}\int_0^{T_{s,0}}(C^{(s)} - C^{(n)})dT$$

which is useful to determine $H_{s,0}$ from heat capacity measurements.

Until 1986, physicists had believed that BCS theory forbade superconductivity at $T > 30$ K. In that year, Bednorz and Müller discovered superconductivity in a lanthanum-based cuprate perovskite material, which had a $T_{s,0}$ of 35 K without a magnetic field [20]. Particularly, the lanthanum barium copper oxides, an oxygen deficient pervoskite-related material, are proved to be promising. In 1987, Bednorz and Müller were jointly awarded the Nobel Prize in Physics for this work. Shortly after that, Chu and his co-workers found that replacing La with Y, often abbreviated to YBCO, raised $T_{s,0}$ to 93 K [21]. YBCO compound with the formula $YBa_2Cu_3O_7$ is a famous high-temperature superconductor because from a practical perspective, it was the first material to achieve superconductivity above T_b of N_2 of 77 K at atmospheric pressure. Their work led to a rapid succession of new high temperature superconducting materials, ushering a new era in the study of superconductivity. However, although many other cuprate superconductors have since been discovered, the theory of superconductivity in these materials is one of the major outstanding challenges of theoretical condensed matter physics.

Magnesium diboride (MgB_2) is another inexpensive and useful superconducting material. Although this material was first synthesized in 1953, its superconductivity had not been discovered until 2001 [22]. Magnetization and resistivity measurements established a $T_{s,0}$ of 39 K, which was believed to be the highest yet determined for non-copper-oxide bulk superconductors.

Though it is generally believed to be a conventional (phonon-mediated) superconductor, MgB_2 is rather an unusual one. In fact, it is a multi-band superconductor, that is, each Fermi surface has different superconducting energy gaps. This differs from usual theories of phonon-mediated superconductivity, which assume that all electrons behave in the same manner. Moreover, MgB_2 was regarded as behaving more like a low temperature metallic superconductor than a high temperature cuprate superconductor.

Very recently, researches have discovered a new family of high temperature superconductors. In 2008, Hosono and his colleagues reported that lanthanum oxygen fluorine iron arsenide $LaO_{1-x}F_xFeAs$ becomes a superconductor at 2.6×10^6 K [23, 24]. Thereafter, Chen and his colleagues found that samarium oxygen fluorine iron arsenide ($SmO_{1-x}F_xFeAs$) goes superconducting at 43 K [25]. Physicists consider the discovery of the new iron-and-arsenic compounds as a major advance, which are the only other high-temperature superconductors differing from the copper-and-oxygen compounds found in 1986. The mechanisms of the new superconductors are believed to be different from those of the old ones, since the latter evolves from a state with one electron per copper ion, whereas the former evolves from a state with two electrons per iron ion. Nowadays, the new materials are generating intense interest to synthesize higher quality samples consisting of a single pristine crystal in the next step.

1.7 Third Law of Thermodynamics [6, 17, 18]

A basic law of thermodynamics was born from the attempt to calculate equilibrium constants of chemical reactions entirely from thermal data (i.e., H and $C_{P,\mathrm{m}}$). What has come to be known as the third law of thermodynamics had its origin in the Nernst heat theorem. Nernst noted from the experimental results by Thomsen and Berthelot, and by careful experiments with galvanic cells. In the experiments, ΔG in a reaction generally approached ΔH more closely as T was reduced, even at quite high T. In 1906, he therefore proposed a general principle that as $T \to 0$, not only did ΔG and ΔH approach equality, but their rates of change with T approached zero. That is,

$$\lim_{T \to 0} \left(\frac{\partial \Delta G}{\partial T} \right)_P = 0, \quad \lim_{T \to 0} \left(\frac{\partial \Delta H}{\partial T} \right)_P = 0. \qquad (1.58)$$

In geometric terms this means that the graphs of ΔG and ΔH as a function of T both have the same horizontal tangent at $T = 0$ as shown in Fig. 1.5.

The first of Eq. (1.58) can be rewritten as

$$\lim_{T \to 0} \left(\frac{\partial (G_2 - G_1)}{\partial T} \right)_P = \lim_{T \to 0} \left[\left(\frac{\partial G_2}{\partial T} \right)_P - \left(\frac{\partial G_1}{\partial T} \right)_P \right] = 0. \qquad (1.59)$$
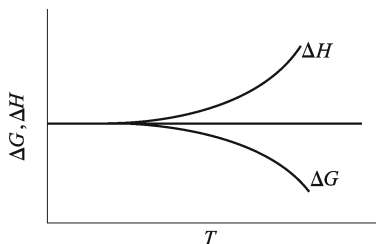
Fig. 1.5 ΔG and ΔH as a function of T for an isobaric process.

Since $(\partial G/\partial T)_P = -S$,

$$\lim_{T \to 0} (S_1 - S_2) = 0. \tag{1.60}$$

This is the Nernst heat theorem, which states that in the neighborhood of absolute zero, all reactions in a liquid or solid in internal equilibrium take place without change in entropy.

Planck, in 1911, made a further hypothesis that not only the entropy difference vanishes as $T \to 0$, but also that the entropy of every solid or liquid substance in internal equilibrium at absolute zero is itself zero, that is,

$$\lim_{T \to 0} S = 0. \tag{1.61}$$

This is named the third law of thermodynamics. If the substance is heated reversibly at constant V or P from $T = 0$ to $T = T$, its entropy at T is

$$S(V,T) = \int_0^T C_V \frac{\mathrm{d}T}{T}, \quad S(P,T) = \int_0^T C_P \frac{\mathrm{d}T}{T}. \tag{1.62}$$

Because entropy changes near room temperature are often needed in thermo-dynamic calculations, the integral of Eq. (1.62) has been evaluated for many substances at 298 K, which is generally called the "standard" entropies. The form in Eq. (1.62) assumes that no phase changes take place between 0 K and T. If there are phase transitions, such as solid to liquid and liquid to gaseous transitions in the region of 0 K and T, they must be considered in the integration,

$$S(P,T) = \int_0^{T_m} C_P \frac{\mathrm{d}T}{T} + \frac{\Delta H_m}{T_m} + \int_{T_m}^{T_b} C_P \frac{\mathrm{d}T}{T} + \frac{\Delta H_b}{T_b} + \int_{T_b}^{T} C_P \frac{\mathrm{d}T}{T} \tag{1.63}$$

where ΔH_m and ΔH_b are the molar enthalpies of melting and boiling, re-spectively, and T_m and T_b are the corresponding melting points.

Now since the third law asserts that the entropy of any substance must be finite or zero at 0 K, it follows that the entropy of a substance must be finite at any finite T. Consequently, from Eq. (1.62) we conclude that $\lim_{T \to 0} C_V = \lim_{T \to 0} C_P = 0$. However, $C_P/T = (\partial S/\partial T)_P$ may in fact diverge as

T approaches 0 K. The Nernst theorem implies that the change in entropy is zero in any process at 0 K. For example,

$$\lim_{T \to 0} \left(\frac{\partial S}{\partial P} \right)_T = \lim_{T \to 0} \left(\frac{\partial S}{\partial V} \right)_T = 0. \tag{1.64}$$

The derivatives of many thermodynamic properties are related to the derivatives of the entropy through the Maxwell relations. Using the relations, we obtain

$$\lim_{T \to 0} \left(\frac{\partial V}{\partial T} \right)_P = \lim_{T \to 0} \left(\frac{\partial P}{\partial T} \right)_V = 0. \tag{1.65}$$

Since coefficient of thermal expansion $\alpha = \dfrac{1}{V} \left(\dfrac{\partial V}{\partial T} \right)_P$ and V remains finite as $T \to 0$, we can also write the compressibility β as

$$\lim_{T \to 0} \beta = 0. \tag{1.66}$$

The third law also implies that it is impossible to reduce T of a system to 0 K in any finite number of operations.

References

1   Berlanstein L R. The Industrial Revolution and Work in Nineteenth-century Europe. Routledge, London (1992)

2   Van Ness H C. Understanding Thermodynamics. Dover, London (1969)

3   Pierre P. A to Z of Thermodynamics. Oxford University, New York (1998)

4   Smith J M, Van Ness H C, Abbott M B. Introduction to Chemical Engineering Thermodynamics. McGraw-Hill, New York (2005)

5   Callister W D Jr. Fundamentals of Materials Science and Engineering. John Wiley & Sons, New York (2000)

6   David V R. Thermodynamics of Materials. John Wiley & Sons, New York (1994)

7   Balzani V, Credi A, Venturi M. Molecular Devices and Machines. Wiley-VCH, Weinheim (2003)

8   Arden W. Future semiconductor material requirements and innovations as projected in the ITRS 2005 roadmap. Mater. Sci. Eng., B **134**, 104-108 (2006)

9   http://www.intel.com. Accessed 12 January 2008

10   Gil P R, Parak W J. Composite nanoparticles take aim at cancer. ACS Nano, **2**, 2200-2205 (2008)

11   Jiang Q, Lu H M. Size dependent interface energy and its applications. Surf. Sci. Rep., **63**, 427-464 (2008)

12   Sun C Q. Thermo-mechanical behavior of low-dimensional system: the local bond average approach. Prog. Mater. Sci., **54**, 179-307 (2009)

13   Sun C Q. Size dependence of nanostructures: impact of bond order deficiency. Prog. Solid Chem., **35**, 1-159 (2007)

14   http://www.nt.ntnu.no/users/haugwarb/History/development_of_
thermodynamics.pdf. Accessed 17 May 2008

15   Musgrave C B. Solid State Thermodynamics. Stanford University, Stanford (1998)

16   http://en.wikipedia.org/wiki/Theromodynamic_process

17   Francis W S, Gerhard L S. Thermodynamics, Kinetic Theory and Statistical Thermodynamics. Addison-Wesley Publishing Company, London (1975)

18   Hsieh J S. Principles of Thermodynamics. Scripta Book Company, (1975)

19   Rose-Innes A C, Rhoderick E H. Introduction to Superconductivity. Pergamon Press, London (1969), p. 46

20   Bednorz J G, Müller K A. Possible high T_c superconductivity in the Ba-La-Cu-O system. Z. Phys., B **64**, 189-193 (1986)

21   Wu M K, Ashburn J R, Torng C J, Hor P H, Meng R L, Gao L, Huang Z J, Wang Y Q, Chu C W. Superconductivity at 93 K in a new mixed-phase Y-Ba-Cu-O compound system at ambient pressure. Phys. Rev. Lett., **58**, 908-910 (1987)

22   Nagamatsu J, Nakagawa N, Muranaka T, Zenitani Y, Akimitsu J. Superconductivity at 39 K in magnesium diboride. Nature, **410**, 63-64 (2001)

23   Kamihara Y, Watanabe T, Hirano M, Hosono H. Iron-based layered superconductor La[$O_{1-x}F_x$]FeAs ($x = 0.05 - 0.12$) with $T_c = 26$ K. J. Am. Chem. Soc., **130**, 3296-3297 (2008)

24   Takahashi H, Igawa K, Arii K, Kamihara Y, Hirano M, Hosono H. Superconductivity at 43 K in an iron-based layered compound $LaO_{1-x}F_x$FeAs. Nature, **453**, 376-378 (2008)

25   Chen X H, Wu T, Wu G, Liu R H, Chen H, Fang D F. Superconductivity at 43 K in $SmFeAsO_{1-x}F_x$. Nature, **453**, 761-762 (2008)

Chapter 2 Statistical Thermodynamics

After the introduction of macroscopic thermodynamics of Chapter 1, the microscopic thermodynamics, or statistics thermodynamics, is introduced in this chapter. Three essential distribution functions of particles in statistics thermodynamics, namely, Maxwell-Boltzmann (MB), Bose-Einstein (BE), and Fermi-Dirac (FD) statistics, are described after introducing some basic concepts, such as energy levels, degeneracy and thermodynamic probability, distinguishability of particles, ways of arrangement of particles, etc. Based on the functions, the partition function is obtained, which results in achievements of all macroscopic thermodynamic functions. In addition, emphasis is given on the relationship between the macroscopic and microscopic functions and importance of microscopic functions related to essential physical meaning.

There are two approaches to the study of thermodynamics, macroscopic and microscopic thermodynamics. Macroscopic thermodynamics is concerned with relative changes of the macroscopic properties of matter, such as heats of transition, P, T, C_m, and vapor pressure. Except in the study of chemical reactions, where it is recognized that elements combine in simple proportions to form compounds, macroscopic thermodynamics does not require any knowledge of the atomistic nature of matters. Microscopic thermodynamics, on the other hand, attempts to compute absolute values of thermodynamic quantities based on a statistical averaging of such properties of individual atoms or molecules as the mass and volume of atoms, molecular bond strength, and vibration frequencies. Because of the characteristic of this statistical averaging, microscopic thermodynamics is usually called statistical thermodynamics. Macroscopic thermodynamics can ignore the existence of molecules, molecular complexity, and quantum mechanics. Statistical thermodynamics however relies heavily on quantum mechanics, and knowledge of molecular motion and structures.

The methods of statistical thermodynamics were first developed during the latter part of the 19th century, largely by Boltzmann and Gibbs. As the quantum theory was present in the early years of the 20th century, Bose and Einstein, and Fermi and Dirac introduced certain modifications of Boltzmann's original ideas and succeeded in clearing up some of the unsatisfactory features of the Boltzmann statistics. Statistical methods can be applied not only to molecules but also to photons, elastic waves in solids, and the more

abstract entities of quantum mechanics called wave functions. We shall use the neutral term "particle" to designate any of these.

2.1 Basic Concepts [1– 3]

A basic idea embodied in statistical thermodynamics is that even when a material is in equilibrium on a macroscopic scale, it is dynamic on a microscopic scale. This dynamic distribution and its consequences are derived using the methods of statistical thermodynamics. To establish the basis for the study of statistical thermodynamics, the one based on probabilities, we will distinguish between a macrostate and a microstate. A macrostate of a system in macroscopic thermodynamics is called a "state", which is characterized by a few state variables, such as T, V, and U, and is the state of all particles in the system.

A system in one macrostate passes very rapidly through many microstates during the observation time because atoms or molecules move and change direction quickly. An atom in a solid, for example, vibrates at a frequency in the order of 10^{13} s^{-1}. Gas molecules have velocities of order of 10^2 ms^{-1}. It is easy to see that we do not have the ability to track the movement of all atoms in time or to extract usable information from those trajectories. The picture of a material as a rapidly changing system leads us to the realization that when we observe a property of a system, we really see the average of this property in all of the microstates that the material passed through during the observation time. What we can do is to take advantage of the large number of atoms in the system to make statistical descriptions of the behavior of the atoms that make up the material based on their microscopic behavior.

In this chapter, we will deal with thermodynamic systems on the ideas that macroscopic systems are only the manifestation of microscopic behavior. The microscopic behavior gives us all needed information to analyze the macroscopic system because the macroscopic system behaves in an average way. An important premise to the statistical thermodynamics is that a system in a given macrostate can exist in every microstate consistent with the constraints of the macrostate. The ergodic hypothesis of the microscopic thermodynamics states that the time average of the properties of a system is equivalent to the instantaneous average over the ensemble of the microstates available to the system.

At atomistic or microscopic scales, the classical mechanics does not apply, and it must be replaced by the quantum mechanics. In order to describe matters from the atomistic, microscopic points of view, we are required to be aware of some of the main results of the quantum mechanics. The most important one for our purposes is that energy is quantized where the energy of a system can only take on certain discrete values. For example, we know from spectroscopy that molecules and materials emit and absorb light at

characteristic frequencies. These frequencies correspond to the differences in energy in the system and are discrete. Semiconductors offer another simple example. It is known that pure and perfect semiconductors have band gaps, which separate the valence electronic band from the conduction band. The energy of electrons between these two bands is forbidden. What is more difficult to see is that the energy levels within the bands are quantized as well, the energy spacing between the energy levels within the band is however extremely small.

Our consideration for particles is so restricted that the energy of each is independent of the energy of the others. Actually, because the atoms in materials collide with each other and exchange energy, the energy of an individual particle will vary with time as it is bumped up into higher energy levels or relaxes to a lower energy level by transferring some of its energy to neighbors. Just as we did not want to keep track of the trajectories (positions and velocities) of all 10^{23} atoms in a system, we also do not want to keep track of the energy of each particle. However, we find that collisions cease to influence the distribution of energy at equilibrium. Our statistical method therefore envisions an equilibrium array of particles without making reference to collisions. It is much easier if we could just keep track of how many particles have a particular energy.

Based on the quantum mechanics, it is frequently found that several quantum states have the same or nearly the same energy ε. These states are then grouped together and belong to the same energetic level. The number of these states with the equal energy is known as the degeneracy of the level, g. Although the energy of the states is equal, they still are distinct states. Shifting of particles from one state to another on the same level constitutes a new arrangement.

The meaningful specification of a finite array of microstates can only be made after means has been devised for breaking the energy of particles into finite increments. The energy is subdivided in the following arbitrary way: An array of N particles has a total energy E. The energy of N_i particles is assumed to take on the discrete value ε_i and

$$\sum_i N_i = N. \tag{2.1}$$

Also, since the particles in these states included in any level i all have the same energy ε_i, the total energy of the particles in level i is $\varepsilon_i N_i$, and the total energy E of the system is $\sum_i \varepsilon_i N_i = E$. If the system is in an external conservative force field such as a gravitational, electric, or magnetic field, E will consist in part of the potential energy E_p of the system. If $E_\mathrm{p} = 0$, E is then the internal energy U and

$$\sum_i \varepsilon_i N_i = U. \tag{2.2}$$

The word "macrostate" can now be applied to the gross (or observable) state

that corresponds with a given set of numerical values $N_1, N_2, \cdots, N_i$, and thus satisfies the above two constraints. The number of microstates for each macrostate will be equal to the number of ways in which we can choose these N_i from N particles.

The fundamental assumption in statistical mechanics is the principle of equaling a priori probabilities. In slightly restrictive form, we say that all microstates of motion occur with an equal frequency. This principle implies that all arrangements of a system of molecules in phase space are equally probable – a fact we have to use in writing the probability of a given macrostate. There is no definite information or logical reason to favor one particular arrangement, so this principle is indeed the only alternative. The validity of this principle, however, can only be supported by the aposteriori success of statistical mechanics in predicting the macroscopic behavior of thermodynamic systems.

In the later few sections, we will see how probability connects with thermodynamics. If we can take a macroscopic system, look at all the possible ways in which the individual atoms may be acting (as determined by their energy) and take the statistical average of their behavior, we will get a very accurate description of what the system is doing macroscopically. In other words, we would like to determine the probabilities of how energy is distributed among the individual particles in a system. From those probabilities, we determine how the system behaves, including how it evolves to other distributions of energy as we change the conditions of the system.

The number of equally probable microstates, corresponding to a given macrostate k_{m}, is called the thermodynamic probability of the macrostate Ω_k. For most macrostates of an assembly of a large number of particles, the thermodynamic probability is a very large number. The total number Ω of possible microstates of an assembly, or the thermodynamic probability of the assembly, equals the sum over all microstates of the thermodynamic probability of each macrostate,

$$\Omega = \sum_k \Omega_k. \tag{2.3}$$

To find the most likely configuration of a system or the most probable macrostate, we need to determine which macrostate has the most microstates and also has the right total energy and number of particles. Maximizing Ω_k can result in this macrostate with respect to changing N_i in the corresponding level ε_i under the constraints of the system with the total energy U and the total particle number N.

When we consider many particles, the question of distinguishability among them arises. There are two ways to distinguish different particles. The first relies on differences in the particles' intrinsic physical properties, such as mass, electric charge and spin. If there are differences in them, they can be distinguished by measuring the relevant properties. However, it is an empirical fact that particles of the same species have completely equivalent physical

properties. For instance, every electron in the universe has exactly the same electric charge. In this case, a second technique should be utilized, which is to track the trajectory of each particle. As long as we can measure the position of each particle with infinite precision (even when the particles collide), there would be no ambiguity about which particle is which. In a solid where atoms are localized, that is, they vibrate from some fixed locations, the particles (the atoms) are distinguishable.

The problem in this approach is that it contradicts the principles of quantum mechanics. According to quantum theory, the particles do not possess definite positions during the periods between measurements. Instead, they are governed by wave functions that give the probability of finding a particle at each position. As time passes, the wave functions tend to spread out and overlap. Once this happens, it becomes impossible to determine, in a subsequent measurement, which particle positions correspond to those measured earlier. The particles are then said to be indistinguishable or identical. In the case of atoms or molecules in a gas, the particles are not localized and are indistinguishable.

We shall analyze a number of widely different systems, which require the application of Maxwell-Boltzmann (MB), Bose-Einstein (BE), or Fermi-Dirac (FD) statistics. The subject matter includes a study of the properties of an ideal gas, the photon gas, the specific heat of a solid, and the electron gas in metals. These are some of the many uses of quantum-statistical mechanics, which lead to a broader understanding of the nature of matters.

To illustrate the difference between macrostates and microstates, we digress from the problem at hand to enumerate the solution of five combinational problems that we must subsequently use in discussing the probabilities of macrostates.

Problem 1. How many ways can we arrange N distinguishable objects? Let us suppose that, for example, we wish to arrange N books in various ways on a shelf. When the first book is placed in any one of N ways, there remain only $N-1$ ways of placing the second. There are thus $N(N-1)$ ways of placing the first two. When they are in position, there exist $N-2$ ways of placing the third. As a result, there are $N!$ ways of arranging N distinguishable objects.

Problem 2. How many ways can we put N distinguishable objects into r different boxes (regardless of order within the boxes), such that there are N_1 objects in the first box, N_2 in the second, $\cdots$, and N_r in the r-th box? Once more we have N books but now there are r shelves, and the order within any shelf is unimportant. There are again a total of $N!$ arrangements of books, but the arrangements that result from changing books on a given shelf must be divided off because they are not relevant. We must divide $N!$ by $N_1!$, $N_2!$, $\cdots$, $N_i!$, $\cdots$, $N_{r-1}!$, and $N_r!$ to account for the meaningless rearrangements. There are thus $N!/\prod_{i=1}^{r} N_r!$ ways of putting N_1, N_2, $\cdots$, N_r, distinguishable objects into r distinct boxes (regardless of order).

Problem 3. How many ways can we select N distinguishable objects from a set of g distinguishable objects? This is nothing more than putting N books on one of two shelves and $g - N$ books on the other. The distinguishable "books" are simply divided in two groups within which there is no concern for order. The answer to this problem can be written immediately, as a special case of Problem 2, in the form $g!/[N!(g - N)!]$ ways of selecting N distinguishable objects from g distinguishable objects.

Problem 4. If there is no limit on the number of objects in any box, how many ways can we put N indistinguishable objects into g distinguishable boxes? This is the first problem in which we must cope with the indistinguishability of objects. We might liken it to the problem of placing N copies of the same book among g shelves. The problem can be solved very simply when we reduce it to a more abstract form. Let us designate the books with identical dots, and separate shelves with slashes: $\cdots/\cdots\cdot/\cdot/\cdots\cdot/\cdot$. There are N dots and $g - 1$ slashes, denoting a total of g boxes. The "boxes" are distinguishable by virtue of their locations, and the apparent indistinguishability of the slashes is irrelevant to the problem. The problem can now be asked in the form: how many ways can we select N distinguishable dot locations and $g - 1$ distinguishable slash locations from $N + (g - 1)$ dot and slash locations? The problem is now to reduce to Problem 3 and the answer is $(N + g - 1)!/[N!(g - 1)!]$ ways of putting N indistinguishable objects into g distinguishable boxes.

Problem 5. How many ways can we put N distinguishable objects into g distinguishable boxes? Each of N different books can be put on any of g shelves. The first book can be placed in g ways, the second book can be placed also in g ways, and so on. There are thus g^N ways to place N distinguishable objects into g distinguishable boxes.

In science, the term "entropy" is generally interpreted in three distinct, but semi-related, viewpoints, i.e., from a macroscopic classical thermodynamics, a microscopic statistical thermodynamics, and an information theory. The statistical definition of entropy described below is the fundamental one while the other two can be mathematically derived from it, but not vice versa. All properties of entropy (including second law of thermodynamics) follow from this definition.

We can relate the number of microstates Ω of a system to its entropy S by considering the probability of a gas to spontaneously compress itself from the original volume V_i into a smaller volume V_f. The probability of finding N molecules in V_f is $\Omega_f/\Omega_i = (V_f/V_i)^N$ and $\ln(\Omega_f/\Omega_i) = N \ln(V_f/V_i) = nN_A \ln(V_f/V_i)$ where n is molar number of particles in a system, N_A is Avogadro constant. We have seen for a free expansion that $\Delta S = nR \ln(V_f/V_i)$. Thus, $\Delta S = (R/N_A) \ln(\Omega_f/\Omega_i) = k \ln(\Omega_f/\Omega_i)$ or, $S_f - S_i = k \ln \Omega_f - k \ln \Omega_i$ where $k = R/N_A$ is Boltzmann's constant. Thus, we arrive at an equation, first deduced by Boltzmann, relating the entropy of a system to the number of microstates,

$$S = k \ln \Omega. \tag{2.4}$$

Boltzmann was so pleased with Eq. (2.4) that he asked for it to be engraved on his tomb stone. From a statistical viewpoint, S of a system consisting of a very large number of particles is proportional to the natural logarithm of Ω. If we could prepare an assembly with unique microstate, $\Omega = 1$, $\ln \Omega = 0$, and $S = 0$. This system is perfectly ordered since the state of each particle is the same. If more energy states are available to the system, $\Omega > 1$ and $S > 0$. In this case it is impossible to specify uniquely the state of each particle since the state of the particle may be distinct in the system. The system is more disordered as Ω increases. Thus, S of a system may be thought of as a measure of the disorder of the system.

This statistical interpretation of entropy allows additional insight into the meaning of $T = 0$. According to the Planck statement of the third law, the entropy of a system in internal equilibrium approaches zero as $T \to 0$ where the system in internal equilibrium must be perfectly ordered.

2.2 Classical Statistic Thermodynamics of Independent Particles [1, 2, 4, 5]

In statistical mechanics, MB statistics describe the statistical distribution of particles over various energy states in thermal equilibrium, when T is high enough and density is low enough to render quantum effects negligible. MB statistics were developed in the late 1800s, before the advent of quantum mechanics. Therefore, this method of evaluation is not restricted to the rules of quantization of energy. In MB statistics, the particles of a system are considered distinguishable, but there is no restriction on the number of particles that can occupy the same energy state.

Consider a system of N particles and r' energy levels. The number of microstates, Ω, corresponding to a given macrostate, can be written by the answer to Problem 2 in Sec. 2.1, which tells the number of arrangements for placing N_1 particles in the first level, N_2 particles in the second level, etc.,

$$\Omega = N! \prod_{i=1}^{r'} \frac{1}{N_i!} \tag{2.5}$$

where N_i represents the number of particles in the i-th level. However, the number of arrangements is actually larger than this value, because we have not accounted for different arrangements within a given energy level. It is possible to rearrange the N_i distinguishable particles within g_i distinguishable quantum states at this level. This number of rearrangements is given by Problem 5 in Sec. 2.1 as $g_i^{N_i}$. Since the number of arrangements within a given energy level is independent of other levels, the total number of arrangements of the system due solely to rearrangement of particles within the levels is the product of $g_i^{N_i}$ terms at all the levels. The total number of distribution, or

the thermodynamic probability, for a given set of N_i values is the product of the two relations developed above. Thus,

$$\Omega = N! \prod_{i=1}^{r'} \frac{(g_i)^{N_i}}{N_i!}. \tag{2.6}$$

Since the most probable macrostate by definition is the one with the largest number of microstates, the relationship between N_i, g_i, and ε_i in the macrostate may be found by maximizing $\ln\Omega$ function of Eq. (2.6) of $\ln \Omega = \ln N! + \sum_i (N_i \ln g_i - \ln N_i!)$. Maximization of $\ln\Omega$ requires that it be differentiated with respect to N_i. To avoid differentiation of factorial quantities, we may replace $\ln N!$ and $\ln N_i!$ using Stirling's formula. The result after this treatment is

$$\ln \Omega = N \ln N + \sum_i (N_i \ln g_i - N_i \ln N_i). \tag{2.7}$$

Let g_i remain constant, $d(\ln\Omega) = \sum_i (\ln g_i - \ln N_i - 1)dN_i$. Maximizing $\ln\Omega$,

$$d(\ln \Omega) = \sum_i \ln(g_i/N_i)dN_i = 0. \tag{2.8}$$

Since N and U of a system are conserved, for a differential change in a state,

$$\sum_i dN_i = 0, \tag{2.9}$$

and

$$\sum_i \varepsilon_i dN_i = 0. \tag{2.10}$$

The maximization of Eq. (2.8) is accomplished using the method of Lagrangian multipliers. To pursue the Lagrangian method, we shall multiply Eqs. (2.9) and (2.10) by the arbitrary Lagrangian multipliers α' and β', respectively. That is,

$$\alpha' \sum_i dN_i = 0 \quad \text{and} \quad \beta' \sum_i \varepsilon_i dN_i = 0. \tag{2.11}$$

Subtracting Eq. (2.11) from Eq. (2.8), $\sum_i [\ln(g_i/N_i) - \alpha' - \beta'\varepsilon_i]dN_i = 0$ where $(i-2)dN_i$ terms are independent. Through selecting α' and β' with certain values, the remaining dN_i terms become independent. Hence, their coefficients may be set to be equal to zero for all i values with the same format,

$$\ln(g_i/N_i) - \alpha' - \beta'\varepsilon_i = 0. \tag{2.12}$$

With a simple mathematical treatment,

$$N_i = \frac{g_i}{e^{\alpha'+\beta'\varepsilon_i}}. \text{ (Maxwell-Boltzmann)} \tag{2.13}$$

This expression is known as MB distribution and is one of the most important results of statistical mechanics. It is the most probable distribution of particles among energy states for independent, distinguishable particles, noting the exponential nature of the distribution. The value of N_i/g_i (fractional occupancy) falls off rapidly as the value of ε_i increases for given values of α' and β'.

By employing the constraining Eq. (2.1), it is found

$$\mathrm{e}^{\alpha'} = \frac{1}{N} \sum_i g_i \mathrm{e}^{-\beta' \varepsilon_i}. \tag{2.14}$$

In any equilibrium state, the values of ε_i, g_i, and T are known for each energy mode, at least in theory. Consequently, the summation quantity that appears in Eq. (2.14) has a known value for a given energy mode. This summation is called the partition function Z, namely,

$$Z = \sum_i g_i \mathrm{e}^{-\beta' \varepsilon_i}. \tag{2.15}$$

The MB distribution law expressed in terms of Z function is now read,

$$\frac{N_i}{N} = \frac{g_i \mathrm{e}^{-\beta' \varepsilon_i}}{Z}. \tag{2.16}$$

The Z function is so named because it expresses the partition or distribution of energies over the various energy levels. The great value of Z function will be found to lie in its role as a generating function for the macroscopic thermodynamic properties.

One feature of Z function is that if the energy of the system is composed of contributions from different degrees of freedom, say, translational energy in the x, y and z directions, molecular rotations, molecular vibrations, etc. that are independent of each other, Z function is the product of the individual partition functions of each of these modes considered separately,

$$Z = \sum_t g_t \exp^{-\frac{\varepsilon_t}{kT}} \sum_r g_r \exp^{-\frac{\varepsilon_{rt}}{kT}} \sum_v g_v \exp^{-\frac{\varepsilon_v}{kT}}. \tag{2.17}$$

It should be noted that Z is a dimensionless number. We can anticipate that the multiplier α' (which arises from the constraint of constant N) should be related in some fashion to the absolute number of particles presented. The exact relation is related to the chemical potential μ,

$$\alpha' = -\mu/kT. \tag{2.18}$$

The constant β', on the other hand, is related in some way to the general level of particle energy. The entropy for a system of distinguishable particles can be expressed in terms of Z function with the help of the thermodynamic probability. The combination of Eqs. (2.4) and (2.7) yields

$$S = k \ln \Omega = k[N \ln N + \sum_i (N_i \ln g_i - N_i \ln N_i)]. \tag{2.19}$$

In light of Eq. (2.16), $\ln(g_i/N_i) = \ln(Z/N) + \beta'\varepsilon_i$. The substitution of this relation into Eq. (2.19) results in

$$S = kN \ln N + k \sum_i (N_i \ln Z - N_i \ln N + N_i \beta' \varepsilon_i)$$

$$= kN \ln N + kN \ln Z - kN \ln N + k\beta' U,$$

$$\text{or,} \quad S = kN \ln Z + k\beta' U. \tag{2.20}$$

β' is eliminated from Eq. (2.20) with the help of the definition of T, $(\partial S/\partial U)_{V,N} = 1/T = [(\partial(kN \ln Z + k\beta' U)/\partial U)]_{V,N}$, which gives

$$\frac{1}{T} = k\beta' + k \left[\frac{\partial}{\partial \beta'} \left(N \ln \sum_i g_i e^{-\beta' \varepsilon_i} \right) + U \right] \frac{\partial \beta'}{\partial U}. \tag{2.21}$$

However,

$$\frac{\partial}{\partial \beta'} \left(N \ln \sum_i g_i e^{-\beta' \varepsilon_i} \right) + U = -N \frac{\sum_i g_i e^{-\alpha'} \varepsilon_i e^{-\beta' \varepsilon_i}}{\sum_i g_i e^{-\alpha'} e^{-\beta' \varepsilon_i}} + U$$

$$= -\frac{N \sum_i N_i \varepsilon_i}{\sum_i N_i} + U = 0.$$

Therefore, in light of Eq. (2.21),

$$\beta' = 1/kT. \tag{2.22}$$

Substituting Eq. (2.22) into Eq. (2.20),

$$S = kN \ln Z + U/T. \tag{2.23}$$

All the thermodynamic properties of a system in MB statistics can be expressed in terms of $\ln Z$ and its partial derivatives. U associated with a given energy mode is given by $U = \sum_i N_i \varepsilon_i$. If Eq. (2.16) for N_i in terms of Z function is substituted into the above expression, it reads

$$U = \frac{\sum_i N g_i \varepsilon_i e^{-\beta' \varepsilon_i}}{Z}. \tag{2.24}$$

A further refinement of this equation is possible by comparing it with the derivative of $\ln Z = \ln \sum_i g_i e^{-\beta' \varepsilon_i}$ based in Eq. (2.15) with respect to β'. The

values of ε_i are held fixed during the differentiation. The result is

$$\left(\frac{\partial \ln Z}{\partial \beta'}\right)_V = -\frac{\sum_i g_i \varepsilon_i \mathrm{e}^{-\beta' \varepsilon_i}}{Z}. \tag{2.25}$$

Comparing Eqs. (2.24) and (2.25),

$$U = -N \left(\frac{\partial \ln Z}{\partial \beta'}\right)_V = NkT^2 \left(\frac{\partial \ln Z}{\partial T}\right)_V = nRT^2 \left(\frac{\partial \ln Z}{\partial T}\right)_V. \tag{2.26}$$

Then,

$$S = kN \ln Z + NkT \left(\frac{\partial \ln Z}{\partial T}\right)_V = nR \ln Z + nRT \left(\frac{\partial \ln Z}{\partial T}\right)_V. \tag{2.27}$$

With similar treatments in light of Eqs. (2.26) and (2.27), the Helmholtz free energy F is determined to be

$$F = U - TS = -nRT \ln Z. \tag{2.28}$$

The equations developed above permit the evaluation of pertinent thermodynamic properties where Z function should be determined by methods of statistics. Z function of each energy mode depends in turn upon the allowed energy levels for that mode. Hence we need, next, to investigate techniques to obtain values of the discrete energy levels.

2.3 Energy Mode and Energy Levels [2, 5]

The total energy of a molecule can be split into energy resulting from different modes of motion. Roughly speaking, a molecular energy state is the sum of electronic, vibrational, rotational, nuclear and translational components, consequently, $\varepsilon = \varepsilon_e + \varepsilon_v + \varepsilon_{rt} + \varepsilon_n + \varepsilon_t$. In the quantum mechanics, also known as the wave mechanics, the general method of attacking a problem is to set up and solve an equation known as Schrödinger's equation. For a single particle in three dimensions,

$$i\hbar \frac{\partial}{\partial t} \Psi(r,t) = -\frac{\hbar^2}{2m} \nabla^2 \Psi(r,t) + V(r) \Psi(r,t). \tag{2.29}$$

This Schrödinger equation for a system where $r = (x, y, z)$ is the particle's position in a three-dimensional space, $\Psi(r,t)$ denotes the wave function, which is the amplitude for the particle at a given position r at any given time t, m is the mass of the particle, and $V(r)$ is the potential energy of the particle at the position r.

In thermodynamics one is primarily concerned with particles which are restrained to certain regions of the space. In this case, time-independent standing waves are set up. Eq. (2.29) will generally yield to a separation-of-variables solution of the form $\Psi(r,t) = f(t)\psi(r)$. Thus, the equation becomes $\frac{i\hbar}{f}\frac{df}{dt} = \frac{1}{\psi}\left[V(r)\psi - \frac{\hbar^2}{2m}\nabla^2\psi\right]$. Since the left-hand side depends upon t alone and the right-hand side upon r only, each side must equal the same constant named ε. Thus,

$$V(r)\psi - \frac{\hbar^2}{2m}\nabla^2\psi = \varepsilon\psi. \qquad (2.30)$$

Suppose that a particle translates freely in a box. The motion is free where no external force fields or intermolecular forces act upon it except on the box walls. Such simplest case would be unidimensional motion in the interval $(0, L)$ with collisions on the "walls". Thus, $V(r) = 0$ in $(0, L)$ and infinite at $x = 0$ and L. Since no wave function can exist as $V \to \infty$, $\psi(0)$ and $\psi(L)$ must both vanish. And since ψ function should be continuous, it should still be close to zero at $x = 0$ and L, where $V(r) = 0$. We can therefore drop $V(r)$ from the consideration and write Schrödinger equation in the form

$$-\frac{\hbar^2}{2m}\frac{d^2\psi(x)}{dx^2} = \varepsilon_x\psi(x). \qquad (2.31)$$

The general solution of Eq. (2.31) is $\psi(x) = A\sin\sqrt{\frac{2m\varepsilon_x}{\hbar^2}}x + B\cos\sqrt{\frac{2m\varepsilon_x}{\hbar^2}}x$. Substitution of the first boundary condition of $\psi(0) = 0$ gives $B = 0$ and that of the second one of $\psi(L) = 0$ specifies the eigenvalues as $\varepsilon_x = \frac{h_P^2}{8mL^2}n_x^2$ with $n_x = 1, 2, 3, \cdots$. The term n_x is known as the translational quantum number in the x direction. Similar equations are valid in the y and z directions. For a free particle in a three-dimensional cubic box of volume, $V = L^3$, the total translational energy is

$$\varepsilon_t = \frac{h_P^2}{8mV^{2/3}}(n_x^2 + n_y^2 + n_z^2) = \frac{n_i^2 h_P^2}{8mV^{2/3}} \qquad (2.32)$$

where $n_i^2 = n_x^2 + n_y^2 + n_z^2$, and n_x, n_y, n_z are integers of $1, 2, 3, \cdots$, etc.

The degeneracy g_i of a level, or the number of energy states in the level, is calculated in terms of the translational quantum numbers. The result is

$$g_i = \frac{1}{8}\frac{4\pi}{3}n_i^2 = \frac{\pi}{6}n_i^3. \qquad (2.33)$$

In order to evaluate the translational partition function Z_t, the translational energy equation (2.32) is substituted into the expression for Z,

$$Z_t = \sum \exp\left(-\frac{\varepsilon_t}{kT}\right) = \sum_{n_x}\sum_{n_y}\sum_{n_z}\exp\left[\frac{-h_P^2}{8mkTV^{2/3}}\left(n_x^2 + n_y^2 + n_z^2\right)\right].$$

$$(2.34)$$

The value of Z depends upon the summation over all available levels of energy. Before trying to reduce this to a more compact form, let us look at the quantity, the so-called "characteristic temperature for translation", $\Theta_t \equiv h_P^2/8mkV^{2/3}$. For a hydrogen molecule in a 1 cm^3 cubic box, $\Theta_t \equiv 1.2 \times 10^{-14}$ K. Θ_t provides an indicator of the closeness of quantum spacing. Under normal conditions, the intervals in the above summations are very close to each other since h_P^2 is a very small number. When $\Theta_t \ll T$, the summation on the right-hand side of Eq. (2.34) may be evaluated as the product of three integrals of a similar form. Considering the x direction only,

$$Z_x = \int_0^\infty \exp\left[(-\Theta_t/T)\, n_x^2\right] dn_x = \int_0^\infty \exp(-Cn_x^2)dn_x \text{ where } C = \Theta_t/T.$$

Since $\int_0^\infty \exp(-Cn_x^2)dn_x = \sqrt{\pi/C}/2$ is well known, $Z_x = [\pi T/(4\Theta_t)]^{1/2} = (2\pi mkT)V^{1/3}/h_P$. Because $Z_t = Z_x Z_y Z_z$ according to Eq. (2.34), Z_t function is shown as

$$Z_t = \left(\frac{\pi T}{4\Theta_t}\right)^{3/2} = \frac{V}{h_P^3}(2\pi mkT)^{2/3}. \tag{2.35}$$

For a given chemical species, Z_t function is primarily a function of V and T of the system.

All diatomic gases and a number of triatomic gases (for examples, CO, CO_2, CS_2, N_2O) are linear molecules. The atoms of the molecule lie in a straight line. As a first approximation for these gases, it may be assumed that the interatomic distances are fixed. The assumption of a rigid rotator is valid generally at not too high T. Under these conditions, the solution of the wave equation shows the total energy of both rotational degrees of freedom of the j-th level ε_{rt} as

$$\varepsilon_{rt} = j(j+1)h_P^2/(8\pi^2 I_r) \tag{2.36}$$

where I_r is the moment of inertia of the molecule. The rotational quantum numbers j are integral values with $j = 0, 1, 2, 3, \cdots$. The order of magnitude for the spacing of $\varepsilon_{rt} \sim 5$ to 500 J·mol^{-1} is much larger than that for the translational mode. Excitation of the rotational levels thus would occur at much higher T than that of the translation.

In addition to the energy-level spacing, we need information on the number of energy states per level. Quantum mechanics demonstrates that there are $2j + 1$ of molecular quantum states which correspond approximately to the same magnitude of the rotational energy. Therefore, in rotation,

$$g_j = 2j + 1. \tag{2.37}$$

The degeneracy of a rotational level thus increases linearly with j. Both Eqs. (2.36) and (2.37) are substituted into the expression for the rotational partition function of a rigid rotator Z_{rt},

$$Z_{rt} = \sum_{j=0}(2j+1)\exp[-j(j+1)h^2/(8\pi^2 I_r kT)]. \tag{2.38}$$

Once again we wish to develop the limiting value of this sum. Let $\Theta_{\mathrm{rt}} \equiv h_{\mathrm{P}}^2/(8\pi^2 I_{\mathrm{r}} k)$ be the characteristic rotational temperature with a dimension of T, $Z_{\mathrm{rt}} = \sum_{j=0}(2j+1)\exp[-j(j+1)\Theta_{\mathrm{rt}}/T]$. Although the energy levels are more widely spaced in rotation than in translation, a continuum of energy often is a reasonable assumption. The summation of Z_{rt} with this approach becomes integration. The evaluation of the rotational partition function by integration may be justified when $\Theta_{\mathrm{rt}} \ll T$, $Z_{\mathrm{rt}} = \int_0^\infty (2j+1)\exp\left[-j(j+1)\Theta_{\mathrm{rt}}/T\right]\mathrm{d}j$. Note that $(2j+1)\mathrm{d}j$ is equivalent to $\mathrm{d}(j^2+j)$ and let $x = [(j^2+j)\Theta_{\mathrm{rt}}]/T$, the above expression can thus be rewritten as

$$Z_{\mathrm{rt}} = \int_0^\infty \exp\left[-(j^2+j)\Theta_{\mathrm{rt}}/T\right]\mathrm{d}(j^2+j) = \frac{T}{\Theta_{\mathrm{rt}}}\int_0^\infty \exp(-x)\mathrm{d}x. \quad (2.39)$$

The value of the integral in Eq. (2.39) is unity. Hence, $Z_{\mathrm{rt}} = T/\Theta_{\mathrm{rt}} = 8\pi^2 I_{\mathrm{r}} kT/h_{\mathrm{P}}^2$. This equation is valid for a heteronuclear diatomic molecule, assuming a continuum for the energy levels and behavior as a rigid rotator. For homonuclear molecules a symmetry number n_{s} is necessary in the denominator of the rotational partition. For homonuclear diatomic molecules, $n_{\mathrm{s}} = 2$, and for heteronuclear ones $n_{\mathrm{s}} = 1$. Therefore the above equation should be revised into the general form,

$$Z_{\mathrm{rt}} = 8\pi^2 I_{\mathrm{r}} kT/(n_{\mathrm{s}} h_{\mathrm{P}}^2) = T/(n_{\mathrm{s}}\Theta_{\mathrm{rt}}). \quad (2.40)$$

When the energy levels are not closely spaced, it may be necessary to carry out the actual summation of terms in Eq. (2.38), rather than to use an integration technique. This is accomplished through the Euler-Maclaurin summation formula. The result is

$$Z_{\mathrm{rt}} = \frac{T}{n_{\mathrm{s}}\Theta_{\mathrm{rt}}}\left[1 + \frac{1}{3}\left(\frac{\Theta_{\mathrm{rt}}}{T}\right) + \frac{1}{15}\left(\frac{\Theta_{\mathrm{rt}}}{T}\right)^2 + \frac{4}{315}\left(\frac{\Theta_{\mathrm{rt}}}{T}\right)^3 + \cdots\right]. \quad (2.41)$$

This approaches Eq. (2.40) rapidly as $T > \Theta_{\mathrm{rt}}$. However, Θ_{rt} is generally assumed between 2 and 100 K, Eq. (2.40) is thus valid in the range of practical interest.

The vibrational motion of a molecule can often be treated as the motion of a harmonic oscillator. A unidimensional harmonic oscillator is a particle moving about an equilibrium position ($x = 0$) subject to a restoring force f_{o} that is linearly dependent upon x. Thus, $f_{\mathrm{o}} = -k_{\mathrm{s}}x$, where k_{s} is the "spring constant." The potential energy for such a particle is defined for any conservative force field, consequently $f_{\mathrm{o}} = -\mathrm{d}V(x)/\mathrm{d}x$. Thus, we have, in this case, the scalar relation,

$$V(x) = -\int_0^x f_{\mathrm{o}}\mathrm{d}x = k_{\mathrm{s}}x^2/2. \quad (2.42)$$

Equation (2.42) is substituted into Eq. (2.30) to obtain the Schrödinger wave equation for a one-dimensional harmonic oscillator, $\dfrac{\mathrm{d}^2\psi}{\mathrm{d}x^2} + \dfrac{8\pi^2 m}{h^2}\left(\varepsilon - \right.$

$\frac{1}{2}k_sx^2\Big)\psi = 0$. The general solution of this differential equation is given by an infinite series. The allowed vibrational energy levels are quantized, and given by

$$\varepsilon_{\mathrm{v}} = \left(v + \frac{1}{2}\right)h_{\mathrm{P}}\nu \tag{2.43}$$

where $v = 0, 1, 2, 3, \cdots$ is the vibrational quantum number, and ν is the fundamental frequency of oscillation in s^{-1}. ν lies in the infrared region of the electromagnetic spectrum for diatomic gases. Recall that the equation for the rotational energy indicates the ground-level energy being zero. However, in the ground level, the vibrational energy is $h\nu/2$. The quantity $h\nu$ is referred to as a quantum of energy.

The energy spacing of the vibrational levels of $4000-40000$ J·mol^{-1} is extremely large. According to Eq. (2.43), the vibrational levels of a harmonic oscillator are equally spaced. The quantum mechanics also shows that the degeneracy of a one-dimensional harmonic oscillator is unity. That is $g_{\mathrm{vib}} = 1$.

The vibrational partition function may now be obtained by the usual summation process. In this case, the characteristic temperature of vibration Θ_{v} is large, being in the order of 10^3 K. One cannot pass from summation to integration at temperatures in the range of practical interest. It is unnecessary to do so, however, because in this case the partition function can be summed exactly. The multiplicity, or degeneracy factor, of the vibrational levels is unity. The partition function constructed from the energy given in Eq. (2.43) is $Z_{\mathrm{v}} = \sum_{v=0} \exp[-(v + 1/2)h_{\mathrm{P}}\nu/(kT)]$ where $h_{\mathrm{P}}\nu/k \equiv \Theta_{\mathrm{v}}$. This equation can be expanded as $Z_{\mathrm{v}} = \exp[-\Theta_{\mathrm{v}}/(2T)][1 + \exp(-\Theta_{\mathrm{v}}/T) + \exp(-2\Theta_{\mathrm{v}}/T) + \cdots]$ and summed. We recognize that the bracketed term is in the form of a binomial expansion. Thus Z_{v} is presented as

$$Z_{\mathrm{v}} = \frac{\exp[-\Theta_{\mathrm{v}}/(2T)]}{1 - \exp(-\Theta_{\mathrm{v}}/T)}. \tag{2.44}$$

In some instances it is convenient to suppress the ground-level energy $\varepsilon_{\mathrm{v},0}$ and then correct for this later. Equation (2.43) may be modified as

$$\varepsilon_{\mathrm{v}} - \varepsilon_{\mathrm{v},0} = vh_{\mathrm{P}}\nu. \tag{2.45}$$

If Eq. (2.45) is used as vibrational energy ε_{v} in the partition function of vibration, a constant multiplicative factor, $\exp[-h_{\mathrm{P}}\nu/(2kT)]$, has likewise been suppressed. The equation for the partition function of a harmonic oscillator is then

$$Z_{\mathrm{v}} = \left(1 - \exp\frac{-h_{\mathrm{P}}\nu}{kT}\right)^{-1}. \tag{2.46}$$

2.4 Bose-Einstein and Fermi-Dirac Statistics [2, 3, 5]

Calculations in statistical mechanics rely on probabilistic arguments, which are sensitive to whether the objects studied are identical. Uncertainty principle requires that we abandon the concept of distinguishability except in certain restrictive cases. As a result, identical particles exhibit markedly different statistical behavior from distinguishable particles.

There are two main categories of identical particles: bosons, which can share quantum states, and fermions, which are forbidden from sharing quantum states (this property of fermions is known as the Pauli Exclusion Principle). In statistical mechanics, BE and FD statistics determine the statistical distribution of identical indistinguishable bosons and fermions under the energy states in thermal equilibrium. Photons, phonons and helium-4 atoms, for example, are not bound by Pauli Exclusion Principle and will therefore be subject to BE statistics. This explains why, at low T, bosons can behave very differently from fermions; all the particles will tend to congregate together at the same lowest-energy state, forming what is known as a Bose-Einstein condensate. FD statistics describes the energy of identical particles with half-integer spin which comprises a system in thermal equilibrium, being most commonly applied to electrons.

Two particular situations will be of subsequent interest to us. Each will have a slightly different statistical description. Assume that an energy level ε_i has a degeneracy g_i. The number of ways of distribution N_i indistinguishable particles among the g_i sublevels of an energy level ε_i is given by the answer to Problem 4 in Sec. 2.1, as $(N_i+g_i-1)!/[N_i!(g_i-1)!]$. Thus the thermodynamic probability Ω_{BE} that a set of occupation numbers N_i can be realized is the product of the ways that each individual energy level can be populated,

$$\Omega_{\mathrm{BE}} = \prod_i \frac{(N_i + g_i - 1)!}{N_i!(g_i - 1)!}. \tag{2.47}$$

Again consider the i-th level, where there are g_i energy states and N_i indistinguishable particles available, which may be placed in g_i states. Now, however, $N_i \leqslant g_i$, and the number of particles in a given state must be unity or zero. A microstate consists of one way of arranging the N_i particles among the g_i places available. There are $g_i!/[N_i!(g_i - N_i)!]$ ways in which g_i quantum states can be divided into N_i that are occupied by a single particle and $g_i - N_i$ that are not. The total number of ways of arranging them is equivalent to the answer to Problem 3 in Sec. 2.1, as $g_i!/[N_i!(g_i - N_i)!]$. Since the number of arrangements of each level is independent of other levels, again the thermodynamic probability Ω_{FD} is given as the product of the number of arrangements for each level,

$$\Omega_{\mathrm{FD}} = \prod_i \frac{g_i!}{N_i!(g_i - N_i)!}. \tag{2.48}$$

It is a matter of great convenience that in dilute gases the degeneracies are largely unoccupied and $g_i \gg N_i$. In this case, $(g_i + N_i - 1)!/[(g_i - 1)!N_i!] = (g_i + N_i - 1)\cdots(g_i + 1)g_i/N_i!$ is a little larger than $g_i^{N_i}/N_i!$ and $g_i!/[(g_i - N_i)!N_i!] = g_i(g_i - 1)\cdots(g_i - N_i + 1)/N_i!$ is a little smaller than $g_i^{N_i}/N_i!$. As a result,

$$\Omega_{\mathrm{FD}} \cong \Omega_{\mathrm{BE}} \cong \frac{\Omega_{\mathrm{B}}}{N!} = \frac{g_i^{N_i}}{N_i!}. \tag{2.49}$$

Distribution functions for particles of the preceding two types are obtained using the same basic strategy that underlay the derivation of MB distribution. The particles must be distributed in such a way as to maximize the thermodynamic probability subject to the usual constraints that there is a fixed number of particles, and a fixed energy. The procedure, using the method of Lagrangian multipliers, will be the same as that outlined in Sec. 2.2. In the resulting distribution of the N_i's for bosons of BE function, the average occupation number per state in any level i, N_i/g_i, is

$$\frac{N_{i,\mathrm{BE}}}{g_i} = \frac{1}{\exp\left(\alpha' + \beta'\varepsilon_i\right) - 1} = \frac{1}{\exp\left(\frac{\varepsilon_i - \mu}{kT}\right) - 1}. \tag{2.50}$$

Einstein pointed out a curious phenomenon related to BE distribution in 1925. This subsequently received attention for its possible relevance to the λ transition of liquid helium. Suppose that a BE gas is cooled to a very low T. Since $\beta' \gg 1, \varepsilon_0 < \varepsilon_1 < \cdots$, and $\exp(\beta'\varepsilon_0) \ll \exp(\beta'\varepsilon_1) \ll \cdots$, it follows that $N = \sum\limits_{i=0}^{\infty} N_i = \dfrac{g_0}{\exp\left(\alpha' + \beta'\varepsilon_0\right) - 1} + \dfrac{g_1}{\exp(\alpha' + \beta'\varepsilon_1) - 1} + \cdots = N_0 + N_1 + \cdots$, or

$$N \approx \frac{g_0}{\exp\left(\alpha' + \beta'\varepsilon_0\right) - 1} = N_0. \tag{2.51}$$

The preceding result implies that at low T there can be a pileup of particles in the ground state ε_0, or the Bose-Einstein condensation. The transition temperature at which this takes place can be identified. This temperature is rather like a condensation point and, indeed, it is found to lie at $T = 3.2$ K, which is comparable with the observed λ transition for helium, $T = 2.19$ K.

The Pauli Exclusion Principle requires the development of a third type of quantum-statistical description. By the same reasoning as in MB statistics, the expected number of fermions in states with energy ε_i is

$$\frac{N_{i,\mathrm{FD}}}{g_i} = \frac{1}{\exp\left(\alpha' + \beta'\varepsilon_i\right) + 1} = \frac{1}{\exp\left(\frac{\varepsilon_i - \mu}{kT}\right) + 1.} \tag{2.52}$$

The distribution function for indistinguishable particles can all be represented by the single equation,

$$\frac{N_{i,\mathrm{FD}}}{g_i} = \frac{1}{\exp\left(\frac{\varepsilon_i - \mu}{kT}\right) + A} \tag{2.53}$$

where $A = -1$ in BE statistics, $A = +1$ in FD statistics, and $A = 0$ in MB statistics.

Note that when $\varepsilon_i = \mu$, the value of N_i/g_i in BE statistics becomes infinite, while for levels in which $\varepsilon_i < \mu$, it is negative and hence meaningless. That is, in this statistics, μ must be lower than the energy of the lowest permitted energy level. The particles like to concentrate in levels for which ε_i is only little greater than μ.

In FD statistics, on the other hand, all levels are populated down to the lowest and as ε_i decreases, $N_i/g_i \to 1$. That is, the low-energy levels are very nearly uniformly populated with one particle per state.

2.5 Application of Quantum Statistics

2.5.1   Spatial Configuration of Long Chain Polymers [6, 7]

The study of long chain polymers has been a source of problems within the field of statistical mechanics since about the 1950s. Disordered long chain polymers are too complex to be described using a deterministic method. However statistical approaches can yield results and are often pertinent since large polymers (that is to say, polymers containing a large number of monomers) can be described efficiently as systems at the thermodynamic limit. One of the reasons that scientists were interested in their study is that the equations governing the behavior of a polymer chain are independent of the chain chemistry. The statistical approach to polymer physics is based on an analogy between a polymer and either a Brownian motion, or some other types of random walks.

Random walks in space (or more exactly, random flights since we consider three dimensions) can be thought of as snapshots of the path taken by a random walker in time. The results of random walk analysis have been applied to computer science, physics, ecology, economics and a number of other fields as a fundamental model for random processes in time. For instance, the path traced by a molecule as it travels in a liquid or a gas, the spatial configuration of long chain polymers, and the topic of electronic transport in amorphous photoconductors can all be modeled as random walks. In the present section, we will illustrate such an application for rubber elasticity in polymers.

The freely joined chain is the simplest model of a polymer. In this model, fixed length polymer segments are linearly connected, and all bonds and torsion angles are equiprobable. The polymer can therefore be described by a simple random walk and an ideal chain. The ideal chain model assumes that there are no interactions between chain monomers and polymer segments can overlap each other as if it is a phantom chain. In reality, this occurs when a

single polymer chain is located in bulk polymer materials where the above interactions are effectively canceled out. The ideal chain model provides a good starting point for investigation of more complex systems and is better suited for equations with more parameters. Since two segments cannot occupy the same space at the same time, this interaction between segments can be modeled as excluded volume. This causes a reduction in the conformational possibilities of the chain, and leads to a self-avoiding random walk, which cannot repeat its previous path. This is present when a single polymer chain is in a dilute solution, whose statistics differs from the simple random walk where the idea of the fractal dimension should be introduced.

When the random walk is applied to polymer structures, the walk is reinterpreted as the physical configuration (static configuration in a glass) of a flexible long-chain molecule, rather than the transitory path of a diffusing particle. Each step of length b (for a uniformly stepping walk) is interpreted as a chemical unit–a monomer segment of the chain. The net displacement magnitude R_b is now the end-to-end length separating the first and last monomers at the two ends of the chain. Above the glass transition temperature T_g, the polymer chain oscillates and R_b changes over time. The net time average $\langle R_b \rangle$, or the root mean square (rms) end-to-end length $\langle R_b^2 \rangle^{1/2}(R_{rms})$ is a useful measure of the size of the chain.

By considering an ideal chain, we use N and r_i to denote the number of steps and the vector position of the i-th link in the chain ($|\boldsymbol{r}_i| = r_i = b$). Then the end-to-end vector $\boldsymbol{R}_b$ achieved in walks of N steps is $\boldsymbol{R}_b = \sum_{i=1}^{i=N} \boldsymbol{r}_i$ and

$$\langle R_b^2 \rangle = \sum_{i=1}^{N} \langle r_i \cdot r_i \rangle + \sum_{i \neq j} \langle r_i \cdot r_j \rangle \tag{2.54}$$

where the angle brackets means an average over all possible walks having exactly N steps, that is configuration average. The second summation is a double sum extending over all values of i and j except for those with $i = j$. All of the latter diagonal terms, corresponding to the appearance in $R_b^2 = \boldsymbol{R}_b \cdot \boldsymbol{R}_b$ of the self-products $\boldsymbol{r}_i \cdot \boldsymbol{r}_i$, which represents the square of the length of a given step of the walk, have been separately taken into account in the first sum of Eq. (2.54). Since there are N such self-product terms, and since each contributes b^2, the first sum is simply Nb^2. On the other hand, the second sum of Eq. (2.54), containing configuration averages over cross terms $\boldsymbol{r}_i \cdot \boldsymbol{r}_j$, necessarily vanishes because of the assured randomness of the walk. Since two different steps i and j are completely uncorrelated and all orientations of $\boldsymbol{r}_i$ and $\boldsymbol{r}_j$ occur with equal probability, the average $\boldsymbol{r}_i \cdot \boldsymbol{r}_j$ of their scalar products, taken over all possible configurations, must equal zero. Hence,

$$R_{rms} = \langle R_b^2 \rangle^{1/2} = N^{1/2} \cdot b. \tag{2.55}$$

In addition to R_{rms}, the full distribution function $P(\boldsymbol{R}_b)$ is also known for random walks. $P(\boldsymbol{R}_b)$ is the probability of finding configuration with $\boldsymbol{R}_b$.

As no direction is favored over any other, it is isotropic and depends only on the scalar $R_b = |\boldsymbol{R}_b|$. Thus the frequency of occurrence of end-to-end lengths lying in the range from R_b to $R_b + dR_b$ in configuration space is, in three dimensions, $4\pi R_b^2 P(R_b)dR_b$. Assuming that distribution of end-to-end vectors for a very large number of identical polymer chains is Gaussian, the probability distribution has the following form:

$$P(R_b) = \left(\frac{3}{2\pi N b^2}\right)^{3/2} \exp\frac{-3R_b \cdot R_b}{2Nb^2}. \tag{2.56}$$

Figure 2.1 shows $P(R_b)$ and $4\pi R_b^2 P(R_b)$ functions of an assembly of chains assumed to have random-walk conformations and an R_{rms} of 300 Å (a representative value for polymers with $N \approx 10^5$). $P(R_b)$ in Fig. 2.1 provides a linear section, along any radial line, of the spherically symmetric three-dimensional free endpoint distribution $P(\boldsymbol{R}_b)$. The function $4\pi R_b^2 P(R_b)$ amounts to the pair correlation function (i.e., the radial density function RDF) for connected chain ends. Its peak occurs at $(2/3)^{1/2}R_{rms}$ and its second moment is R_{rms}^2. Although other linear measures of the region encompassed by a random coil chain might be adopted (such as the rms distance of the chain segments from its center of gravity, called its "radius of gyration"), they scale each other in the same order.
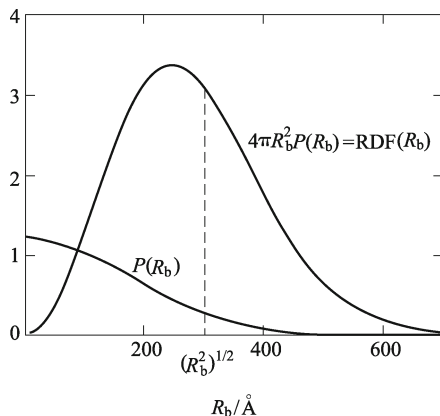
Fig. 2.1 Distribution functions for the end-to-end distance R_b of an assembly of "ideal" (i.e., random-walk configuration) chains for which R_{rms} is 300 Å.

Throughout this discussion, R_b has been employed as a fantastically abridged one-parameter characterization of chain conformation. For each R_b there exists an astronomical variety of possible configurations. The complete configuration of any particular chain, that is, the full sequence of r_i's of Eq. (2.54), is virtually unknowable, due to the complete atom-by-atom structure of any amorphous system. Precisely because of the large numbers involved, the statistical approach becomes both necessary and valid.

Upon stretching a material we are doing work on the system to exhibit a limited elastic region while the material regains its original dimensions if the stress is removed. As the resulting strain is related to the extent of movements of atoms from their equilibrium conditions, substances such as crystalline solids and amorphous glasses have elastic limits rarely exceeding 1% because atomic adjustments are localized. The elastic properties of elastomers, however, are truly exceptional. Elastomers are polymeric materials, natural or synthetic, that can be stretched to several times its original length without breaking owing to the ability of their constituent polymeric chains to rotate about the chain bonds. By far the most widely studied elastomer is the natural rubber, its deformation is reversible and instantaneous and it shows almost no creep. The reversible character of the deformation is a consequence of the fact that rubbers are lightly cross-linked, which prevent the chains from slipping past each other. The chains between adjacent crosslinks contain typically several hundred main chain atoms. The instantaneous deformation occurring in rubbers is due to the high segmental mobility and thus to the rapid changes in chain conformation of the molecules. The energy barriers between different conformational states must therefore be small compared to the thermal energy. Given our probability distribution function, there is a maximum corresponding to $\boldsymbol{R}_{\mathrm{b}} = 0$. Physically this amounts to that there are more microstates of chain conformations with an end-to-end vector of zero than any other microstate. Stress acting on the rubber network will stretch out and orient the chain between the crosslink joints. This will thus decrease the entropy of the chains and hence give rise to an entropic force. The change in chain conformation is expected to change the intramolecular internal energy. The packing of the chains may also change, affecting the intermolecular-related internal energy. Both the intramolecular and intermolecular potentials contribute to the energetic force. The following thermodynamic treatments yield expression differentiating between the entropic and energetic contributions to the elastic force f_{e}.

According to the first and second laws of thermodynamics, the internal energy change $\mathrm{d}U$ consisting of the chain exchanging heat (δQ), deformation and $P - V$ work (δW) is shown as $\mathrm{d}U = T\mathrm{d}S - P\mathrm{d}V + f_{\mathrm{e}}\mathrm{d}R_{\mathrm{b}}$, where $f_{\mathrm{e}}\mathrm{d}R_{\mathrm{b}}$ is the work done by the deformation. Physically what is more interesting is to consider deformation at constant V in order to view only the direct effects of orientation on entropy and internal intramolecular energy where $\delta W = -P\mathrm{d}V = 0$. The partial derivative of U with respect to R_{b} at constant T and V is $f_{\mathrm{e}} = (\partial U/\partial R_{\mathrm{b}})_{T,V} - T(\partial S/\partial R_{\mathrm{b}})_{T,V}$. $(\partial U/\partial R_{\mathrm{b}})_{T,V}$ vanishes for ideal chains, which means that the polymer chains can rotate freely and its U does not change with conformation. We are thus led to

$$f_{\mathrm{e}} = -T \left(\frac{\partial S}{\partial R_{\mathrm{b}}} \right)_{T,V}. \tag{2.57}$$

Equation (2.57) shows that the elastic force necessarily stems from a purely entropic effect. This entropic force is very similar to P of an ideal gas. U

of an ideal gas depends only on its T, and not on V of its container, so it is not an energy effect that tends to increase V like gas pressure does, or P of an ideal gas has a purely entropic origin. The elasticity of rubbers is predominantly entropy-driven, which brings out a number of spectacular phenomena. The stiffness increases with increasing T and Q is reversibly generated on deformation. What is the microscopic origin of such an entropic force? The most general answer is that the effect of thermal fluctuations tends to bring a thermodynamic system toward a macroscopic state that corresponds to a maximum in the number of microscopic states, which are compatible with this macroscopic state.

Return now to the probability distribution function (Eq. (2.56)) of finding configuration with $\boldsymbol{R}_\mathrm{b}$. Recall that according to the principle of equally likely a priori probabilities, Ω at some physical value is directly proportional to the probability distribution at that physical value, viz, $\Omega(\boldsymbol{R}_\mathrm{b}) = cP(\boldsymbol{R}_\mathrm{b})$, where c is an arbitrary proportionality constant. The entropy associated to a macrostate of an ideal chain is thus equal to

$$S(\boldsymbol{R}_\mathrm{b}) = k \ln \Omega(\boldsymbol{R}_\mathrm{b}) = k \ln P(\boldsymbol{R}_\mathrm{b}) + C_0 \qquad (2.58)$$

where C_0 is a fixed constant. By combining Eqs. (2.57) and (2.58), it reads

$$f_\mathrm{e} = -3kTR_\mathrm{b}/(Nb^2) = -k_\mathrm{s}R_\mathrm{b}. \qquad (2.59)$$

The above thermodynamic equation is the same as that for the conventional $P-V$ systems where P and V are substituted by $-f_\mathrm{e}$ and R_b. The resulting stress-strain relationship is called the equation of state of the ideal chain. It is only exact in the limit of polymers containing a large number of monomers, that is, the thermodynamic limit.

An analogous expression to Eq. (2.57) can be derived: $f_\mathrm{e} = (\partial F/\partial R_\mathrm{b})_{T,V} = (\partial \Omega^*/\partial R_\mathrm{b})_{T,V}$ at constant V and T where $F = U - TS$. Insertion of Eq. (2.59) into the above equation gives

$$F = \Omega^* = -3kTR_\mathrm{b}^2/(2Nb^2) = k_\mathrm{s}R_\mathrm{b}^2/2, \quad k_\mathrm{s} = 3kT/(Nb^2). \qquad (2.60)$$

Equations (2.59) and (2.60) are known as the entropic spring results. Namely, upon stretching a polymer chain we are doing work on the system to drag it away from its (preferred) equilibrium state and the chain behaves like a conventional spring. Particularly the work can be related entirely to the entropy change of the system.

2.5.2 Statistical Thermodynamics of a Paramagnetic Crystal [3, 8]

The properties of paramagnetic crystals are essential interest at extremely low T of a few Kelvin or less. A number of simplifying assumptions will be made, but the procedure is the same as in more complicated cases.

Paramagnetism results from the tendency of unpaired magnetic dipole moments associated with the electron orbital angular momentum, the electron spin, or the both, to align themselves parallel to the applied field. Paramagnetism occurs in compounds containing transition metal ions that have either incomplete d shells (the iron, palladium and platinum groups) or incomplete f shells (the lanthanide and actinide groups). Both of the net spin and orbital magnetic moments may contribute to paramagnetism, but for an ion with an incomplete d shell, the effective orbital moment may be quenched by electrostatic interactions with its neighboring ions, leading to a predominant spin moment. Paramagnetism is due mainly to the spin angular moments of the electrons. Every electron in an atom has not only an electric charge but also a magnetic moment μ_B of 1 Bohr magneton, being equal to $9.27 \times 10^{-24} A \cdot m^2$, as if the electron were a tiny sphere of electric charge spinning about an axis.

It was shown in Sec. 1.6 that the thermodynamic properties of a paramagnetic crystal could be calculated from a knowledge of $G' = H' - TS$. Using the methods of statistics, G' can be derived in terms of T and the parameters that determine the energy levels of the atoms in the crystal. In a paramagnetic material, because the atoms can be labeled according to the positions they occupy in a crystal lattice, the system obeys MB statistics. As usual, the first step is to calculate Z, defined as $Z = \sum_j \Delta g_j \exp(-\varepsilon_j/kT)$.

Because of their oscillatory motion, the molecules have the same set of vibrational energy levels as those of any solid, and the total vibrational energy constitutes the internal energy U_{vib}. In addition, the small interaction between the magnetic ions, and their interactions with the electric field set up by the remainder of the lattice, gives rise to an additional internal energy (of the ions only) U_{int}. Each magnetic ion in a paramagnetic crystal is a small permanent magnet and is equivalent to a tiny current loop as shown in Fig. 2.2.
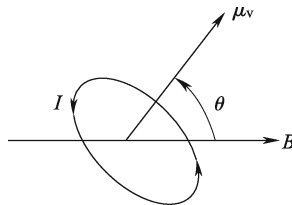
Fig. 2.2 Magnetic ion of the magnetic moment μ_v equivalent to a small current loop.

The ion has a magnetic moment μ_v, which can be represented by a vector perpendicular to the plane of the loop. If the paramagnetic crystal is placed in a magnetic field B, where the moment vector makes an angle θ with the direction of $\boldsymbol{B}$, a torque τ of magnitude $\mu_v B \sin\theta$ is exerted on the loop, in such a direction as to align μ_v in the same direction as $\boldsymbol{B}$. Finally, the

ions have a magnetic potential energy which, like the gravitational potential energy of particles in a gravitational field, is a joint property of the ions and the source of the field and cannot be considered as internal energy. The total magnetic potential energy is E_{mp}.

The vibrational energy levels associated with internal magnetic and electrical interactions, and the potential energy levels are all independent. Z can be expressed as the product of independent partition functions Z_{vib}, Z_{int}, and $Z_{H_{mag}}$. Thus, $Z = Z_{vib}Z_{int}Z_{H_{mag}}$. The magnetic ions constitute a subassembly, characterized by the partition functions Z_{int} and $Z_{H_{mag}}$ only, and they can be considered independent of the remainder of the lattice, and simply as a container of the subassembly.

The paramagnetic salts most widely used contain paramagnetic ions surrounded by large number of nonmagnetic particles. A typical example is $Cr_2(SO_4)_3 \cdot K_2SO_4 \cdot 24H_2O$ (chromium potassium alum). Its magnetic properties are due solely to the chromium ions existing in the crystal. Cr^{+++} has three unpaired electron spins and therefore a magnetic moment of $3\mu_B$. Besides the two chromium ions there are four sulphur ions, two potassium ions, forty oxygen ions, and forty-eight hydrogen ions. Hence there are a total of ninety-four nonmagnetic particles. The magnetic ions are so widely separated in the molecules that the interaction between them is negligibly small. At the same time, the effect of the orbital motions of the valence electrons is quenched by the fields of neighboring ions. What remains is a net electron spin. Although U_{int} and Z_{int} play important roles in the complete theory, we shall neglect them and consider that the total energy of the subassembly is its potential energy E_p only. Thus we solely consider $Z_{H_{mag}}$.

E_{mp} is the work that must be done to rotate the magnetic dipole from its zero energy position $\pi/2$ to θ_m,

$$E_{mp} = \int_{\pi/2}^{\theta_m} \tau d\theta_m = \mu_v B \int_{\pi/2}^{\theta} \sin\theta_m d\theta_m = -\mu_v B \cos\theta_m.$$

For simplicity, only a subassembly of ions having a magnetic moment of 1 Bohr magneton μ_B is considered. The principles of quantum mechanics restrict the possible values of θ_m, for such an ion, to either $0°$ or $180°$, so that the magnetic moment is either parallel or antiparallel to the field (other angles are permitted if the magnetic moment is greater than μ_B). As an example, for an electron with a single net electron spin, there would be two possible energy levels, with spin quantum number $m_s = 1/2$ (spin parallel to $\boldsymbol{B}$) and $m_s = -1/2$ (spin antiparallel to $\boldsymbol{B}$). The corresponding values of $\cos\theta_m$ are then $+1$ and -1, and the possible energy levels are $-\mu_B B$ and $+\mu_B B$. The energy levels are nondegenerate. There is only one state in each level, but there is no restriction on the number of ions per state. $Z_{H_{mag}}$ therefore reduces also to the sum of two terms,

$$Z_{H_{mag}} = \exp\left(\frac{\mu_B B}{kT}\right) + \exp\left(\frac{-\mu_B B}{kT}\right) = 2\cosh\left(\frac{\mu_B B}{kT}\right) \qquad (2.61)$$

since by definition the hyperbolic cosine is given by $\cosh x = (1/2)[\exp(x) + \exp(-x)]$.

The thermodynamic properties of a two-level system exhibit the same features as those of more complex systems and are easier to calculate. Let $N \uparrow$ and $N \downarrow$ represent respectively the number of ions whose moments are aligned parallel and antiparallel to $\boldsymbol{B}$. The corresponding energy is $\varepsilon \uparrow = -\mu_B B$ and $\varepsilon \downarrow = +\mu_B B$. The average occupation numbers in the two directions are then

$$\overline{N} \uparrow = \frac{N}{Z} \exp\left(\frac{-\varepsilon \uparrow}{kT}\right) = \frac{N}{Z} \exp\left(\frac{\mu_B B}{kT}\right),$$

$$\overline{N} \downarrow = \frac{N}{Z} \exp\left(\frac{-\varepsilon \downarrow}{kT}\right) = \frac{N}{Z} \exp\left(-\frac{\mu_B B}{kT}\right).$$

The excess of those ions in the parallel, over those in the antiparallel alignment, is

$$\overline{N} \uparrow - \overline{N} \downarrow = \frac{N}{Z}\left[\exp\left(\frac{\mu_B B}{kT}\right) - \exp\left(-\frac{\mu_B B}{kT}\right)\right] = \frac{N}{Z} 2 \sinh\left(\frac{\mu_B B}{kT}\right),$$

which reduces to $\overline{N} \uparrow - \overline{N} \downarrow = N \tanh(\mu_B B/kT)$.

The net magnetic moment M of the crystal is the product of μ_B of each ion and the excess number of ions aligned parallel to $\boldsymbol{B}$. Thus, $M = \left(\overline{N} \uparrow - \overline{N} \downarrow\right)\mu_B = N\mu_B \tanh(\mu_B B/kT)$. This is the magnetic equation of state of the crystal, expressing M as a function of B and T. Note that M depends only on the ratio B/T.

Since the limits of small and large x are $\tanh(x) = (\mathrm{e}^x - \mathrm{e}^{-x})/(\mathrm{e}^x + \mathrm{e}^{-x})\overrightarrow{x \to 0}(1-1)/(1+1) = 0$ and $\tanh(x) = (\mathrm{e}^x - \mathrm{e}^{-x})/(\mathrm{e}^x + \mathrm{e}^{-x})\overrightarrow{x \to \infty}\mathrm{e}^x/\mathrm{e}^x = 1$, in the case of $\mu_B B \gg kT$, $\tanh(\mu_B B \gg kT) \to 1$ and $M = N\mu_B$. This is simply the saturation magnetic moment M_{sat}, which would result if all ionic magnets were parallel to $\boldsymbol{B}$.

At the other extremes of weak $\boldsymbol{B}$ and high T, $(\mu_B B/kT) \ll 1$, $\tanh(\mu_B B/kT) \to \mu_B B/kT$, and $M = (N\mu_B^2/k)(B/T)$. This is just the experimentally observed Curie law, stating that $M \propto B/T$ or $M = C_{\text{Curie}} B/T$ in weak $\boldsymbol{B}$ and at high T where C_{Curie} is the Curie constant. The methods of statistics therefore not only lead to the Curie law, but also provide a theoretical value of $C_{\text{Curie}} = N\mu_B^2/k$.

We now calculate other thermodynamic properties of the system. E_{mp} can then be found from

$$E_{\text{mp}} = NkT^2\left(\frac{\partial \ln Z}{\partial T}\right)_B = -Nk\left(\frac{\mu_B B}{k}\right)\tanh\left(\frac{\mu_B B}{kT}\right). \qquad (2.62)$$

The energy is $-N\mu_B B$ at $T = 0$ and approaches zero asymptotically at high T. Here higher T produces increased randomization of the dipole moments and E_{mp} goes to zero.

The magnetic contribution to the heat capacity also has distinctive characteristics, which is given by

$$C_{\mathrm{B}} = \left(\frac{\partial E_{\mathrm{mp}}}{\partial T}\right)_{B,N} = Nk\left(\frac{\mu_{\mathrm{B}}B}{kT}\right)^2 \mathrm{sech}^2\left(\frac{\mu_{\mathrm{B}}B}{kT}\right). \qquad (2.63)$$

Figure 2.3 shows graphs of E_{mp} and C_{B} (both divided by Nk) as a function of $kT/(\mu_{\mathrm{B}}B)$. The curves differ from the corresponding curves for the internal energy and heat capacity of an assembly of harmonic oscillators because there are only two permitted energy levels and the energy of the subassembly cannot increase indefinitely with increasing T. C_{B} has a fairly sharp peak known as a Schottky anomaly. It is called anomalous because the heat capacity usually increases with increasing T, or stays constant. The anomaly is useful for determining energy level splitting of ions in rare-earth and transition-group metals.
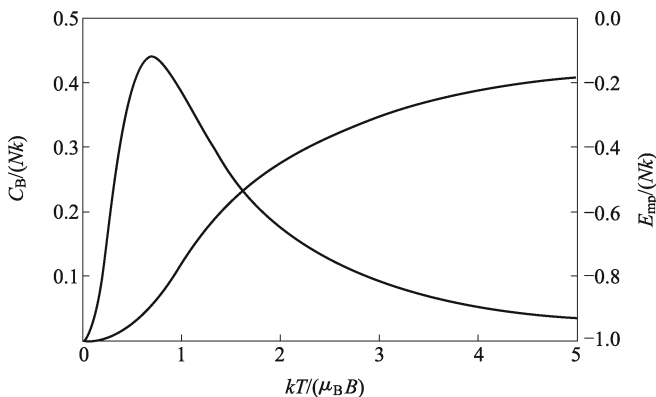
Fig. 2.3 The specific potential energy and specific heat capacity at constant magnetic intensity, both divided by Nk, for a paramagnetic crystal as a function of $kT/(\mu_{\mathrm{B}}B)$.

Now we compare C_{B} of the magnetic subassembly with C_V of the entire crystal. Letting $T = 1$ K and $B = 1$ T (a comparatively strong laboratory magnetic field), we have $(kT/\mu_{\mathrm{B}}B) \approx 1.5$, $\mathrm{sech}^2(\mu_{\mathrm{B}}B/kT) = 0.66$, and by Eq. (2.63), $C_{\mathrm{B}} \approx Nk(1.5)^{-2} \times 0.66 \approx 0.29Nk$. Assuming that there are 50 nonmagnetic particles for every magnetic ion, and taking a $\Theta_{\mathrm{D}} = 300$ K as a typical value, we have from the Debye T^3 law, $C_V \approx Nk(50) \times (12\pi^4/5)(1/300)^3 \approx 0.5 \times 10^{-5}Nk$. Hence, C_{B} at $T = 1$ K is about 100000 times C_V. Much more energy is required to orient the ionic magnets than to increase the vibrational energy of the molecules of the lattice. It is this energy of the orientation which allows the cooling of the lattice during the process of adiabatic demagnetization described in Sec. 3.1.2.

The most important thermodynamic property of two-level system is the

entropy. For MB statistics, $S = E_{mp}/T + Nk \ln Z$. Substituting Eqs. (2.61) and (2.62) into this expression, $S = Nk \left[\ln \left(2 \cosh \dfrac{\mu_B B}{kT} \right) - \dfrac{\mu_B B}{kT} \tanh \dfrac{\mu_B B}{kT} \right].$

Figure 2.4 is a graph of $S/(Nk)$, plotted as a function of $kT/\mu_B B$. At low T, $\ln[2 \cosh(\mu_B B/kT)] = \ln[\exp(\mu_B B/kT) + \exp(-\mu_B B/kT)] \rightarrow \ln[\exp(\mu_B B/kT)] = \mu_B B/kT$ and $(\mu_B B/kT) \tanh(\mu_B B/kT) \rightarrow \mu_B B/kT$. Thus, $S \rightarrow 0$ as $T \rightarrow 0$. As $T \rightarrow 0$ all the dipoles are in the lowest energy state pointing to a direction parallel to the applied magnetic field. There is only one possible microstate. As a result, $W = 1$ and $S = k \ln 1 = 0$. At high T, the second term in brackets approaches zero, $\cosh(\mu_B B/kT) \rightarrow 1$, and $S \rightarrow Nk \ln 2$. This is exactly what we would expect. At the upper temperature limit, $W = 2^N$, the number of equally probable microstates, and $S = Nk \ln 2$. This corresponds to a pattern of random dipole orientations, involving equal numbers of parallel and antiparallel magnets in any chosen direction. In this disordered state S as a function of B/T only reaches the maximum. In a reversible adiabatic demagnetization, S and hence B/T remain constants. Thus as B drops, T must decrease too, in agreement with the thermodynamic result.
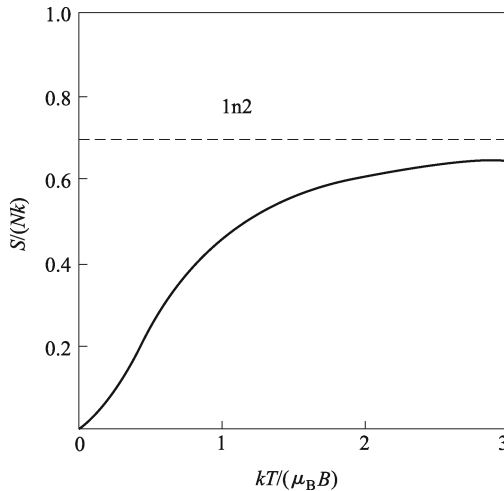

Fig. 2.4 The entropy of a paramagnetic crystal.

2.5.3 Negative Temperature [3]

Consider again a system with just two possible magnetic energy levels, in which μ_B of a particle can be either parallel ($\uparrow$) or antiparallel ($\downarrow$) to $\boldsymbol{B}$. In the equilibrium state at a T, the ratio of the average occupation numbers of

the levels is

$$\frac{\overline{N}\uparrow}{\overline{N}\downarrow} = \exp\left(\frac{\varepsilon\downarrow - \varepsilon\uparrow}{kT}\right), \quad \text{or} \quad T = \frac{1}{k}\left[\frac{\varepsilon\downarrow - \varepsilon\uparrow}{\ln\overline{N}\uparrow - \ln\overline{N}\downarrow}\right] \tag{2.64}$$

and we can consider this as the equation defining T, in terms of $\varepsilon\uparrow, \varepsilon\downarrow, \overline{N}\uparrow$, and $\overline{N}\downarrow$. If $\varepsilon\downarrow > \varepsilon\uparrow$ and $\overline{N}\uparrow > \overline{N}\downarrow$, the right side of the equation is positive and $T > 0$.

Now suppose the direction of the magnetic intensity is suddenly reversed. Those magnetic moments, which were parallel to the original field, and in the state of lower energy $\varepsilon\uparrow$, are opposite to the new field and are now in the higher energy state, while those opposite to the original field, and in the higher energy state $\varepsilon\downarrow$, are parallel to the new field and are now in the lower energy state. Eventually, the moments in the higher energy state will hop over to the new lower energy state, but immediately after the field has been reversed, and before any change in occupation numbers has taken place. The average occupation number $\overline{N}'\downarrow$ of the new upper state is the same as the number $\overline{N}\uparrow$ in the original lower state, and the occupation number $\overline{N}'\uparrow$ of the new lower state is the same as the number $\overline{N}\downarrow$ in the original upper state. We say that there has been a population inversion. The concept is of fundamental importance in laser science because the production of a population inversion is a necessary step in the workings of a laser. Now if the temperature of the system is defined by Eq. (2.64),

$$T' = \frac{1}{k}\left[\frac{\varepsilon\downarrow - \varepsilon\uparrow}{\ln\overline{N'}\uparrow - \ln\overline{N'}\downarrow}\right].$$

Since $\overline{N}'\downarrow > \overline{N}'\uparrow$, the denominator on the right side of the equation is negative and $T' < 0$.

Negative temperatures can be looked at from another viewpoint. At $T = 0$, all magnets are in their lower energy states. As T is increased, more and more magnets move to the state of higher energy. When $T \to +\infty$, both states are equally populated. Then one might say that if the number in the higher state is even greater than that in the lower state, as it is when there is a population inversion, the temperature must be hotter than infinity. We thus have the paradoxical result that a system at a negative T is even hotter than at an infinite T.

In paramagnetic substances, the interactions between the ionic magnets and the lattice are so great that the substance cannot exist in a state of population inversion for an appreciable time. However, it was found by Pound, Purcell, and Ramsey in 1951 that the nuclear magnetic moments of lithium atoms in LiF interact so slowly with the lattice that a time interval of several minutes is required for equilibrium with the lattice to be attained, a time long enough for experiments to be made showing actual existence of a population inversion.

References

1   David V R. Thermodynamics of Materials. John Wiley & Sons, New York (1994)

2   Chang L T, John H L. Statistical Thermodynamics. Hemisphere Publishing Corporation, Washington London (1979)

3   Francis W S, Gerhard L S. Thermodynamics, Kinetic Theory and Statistical Thermodynamics. Addison-Wesley Publishing Company, London (1975)

4   http://en.wikipedia.org/wiki/Maxwell%E2%80%93Boltzmann_statistics. Accessed 20 September 2008

5   Kenneth W. Thermodynamics. McGraw-Hill Book Company, New York (1977)

6   http://en.wikipedia.org/wiki/Statistical_mechanics. Accessed 6 October 2008

7   Zallen R. The Physics of Amorphous Solids. John Wiley & Sons, New York (1983) and references therein

8   http://ruelle.phys.unsw.edu.au/~gary/Site/PHYS3020_files/SM3_7.pdf. Accessed 5 December 2008

Chapter 3 Heat Capacity, Entropy, and Nano-thermodynamics

Two important thermodynamic parameters of heat capacity and entropy, and the constitutions of them are extensively introduced where different ways to deduce the above amount and the corresponding mathematical and physical relationships presented in the above deductions are given. Based on these results and related messages shown in Chapters 1 and 2, the recent progress in thermodynamics for materials in nanometer size range – Nanothermodynamics – and several typical applications are present where the functions of the size-dependent functions of cohesire energy and entropy are recommended.

3.1 Heat Capacity

3.1.1 Relations of Principal Heat Capacities [1, 2]

The thermodynamic properties of materials are intensive thermodynamic parameters, which are specific for a given material. Each is directly related to a second order differential of a thermodynamic potential. For a single component system, only three thermodynamic parameters are needed to derive all others, namely, heat capacity C_m, the coefficient of thermal expansion α, and the compressibility β, being the three possible second derivatives of G with respect to T and P or V.

C_m describes the ability of a given quantity of a substance to store energy (internal energy or enthalpy) while undergoing a given temperature change other than a phase change. C_m may be expressed in terms of Eqs. (1.16) and (1.18),

$$C_{P,m} = \left(\frac{\partial H}{\partial T}\right)_P = \left(\frac{\partial H}{\partial S}\right)_P \left(\frac{\partial S}{\partial T}\right)_P = T\left(\frac{\partial S}{\partial T}\right)_P$$

$$= T\left(\frac{\partial}{\partial T}\left(-\frac{\partial G}{\partial T}\right)_P\right)_P = -T\left(\frac{\partial^2 G}{\partial T^2}\right)_P,$$

$$C_{V,m} = \left(\frac{\partial U}{\partial T}\right)_P = T\left(\frac{\partial S}{\partial T}\right)_V = T\left(\frac{\partial}{\partial T}\left(-\frac{\partial F}{\partial T}\right)_V\right)_V = -T\left(\frac{\partial^2 F}{\partial T^2}\right)_V. \quad (3.1)$$

As T varies, the energy stored in the atomic bonds changes. When the stored energy increases, so does the length of the atomic bonds. As a result, solids typically expand in response to heating and contract on cooling; this dimensional response to temperature change is α, which can be written as

$$\alpha_V = \frac{1}{V}\left(\frac{\partial V}{\partial T}\right)_P = \frac{1}{V}\left(\frac{\partial}{\partial T}\left(\frac{\partial G}{\partial P}\right)_T\right)_P = \frac{1}{V}\frac{\partial^2 G}{\partial T \partial P}. \quad (3.2)$$

In thermodynamics and fluid mechanics, all one needs to know is how V changes when P is varied by a small amount, and this is described by the compressibility of the fluid or solid – either the isothermal compressibility, β_T, or the adiabatic compressibility, β_S, according to circumstances. They are mathematically expressed as

$$\beta_T = -\frac{1}{V}\left(\frac{\partial V}{\partial P}\right)_T = -\frac{1}{V}\left(\frac{\partial}{\partial P}\left(\frac{\partial G}{\partial P}\right)_T\right)_T = -\frac{1}{V}\left(\frac{\partial^2 G}{\partial P^2}\right)_T, \quad (3.3)$$

and

$$\beta_S = -\frac{1}{V}\left(\frac{\partial V}{\partial P}\right)_S. \quad (3.4)$$

For a solid, the distinction between the two is usually negligible. The inverse of the compressibility is called the bulk modulus.

There are two more important equations for C_P in relation to P-V-T data: one is the ratio of C_P to C_V and the other is their difference. The former k_r is shown as

$$k_\mathrm{r} = \frac{C_P}{C_V} = \frac{(\partial S/\partial T)_P}{(\partial S/\partial T)_V}. \quad (3.5)$$

According to the mathematical cyclic relations where the variables are permuted cyclically, $(\partial S/\partial T)_P = -(\partial P/\partial T)_S(\partial S/\partial P)_T$ and $(\partial S/\partial T)_V = -(\partial V/\partial T)_S(\partial S/\partial V)_T$. If we substitute the above expressions into Eq. (3.5), $C_P/C_V = [(\partial P/\partial T)_S(\partial S/\partial P)_T]/[(\partial V/\partial T)_S(\partial S/\partial V)_T]$. Taking together the two derivatives at constants S and T, $(\partial P/\partial T)_S/(\partial V/\partial T)_S = (\partial P/\partial T)_S$ $(\partial T/\partial V)_S = (\partial P/\partial V)_S = -1/(V\beta_S)$ and $(\partial S/\partial P)_T/(\partial S/\partial V)_T = (\partial S/\partial P)_T$ $(\partial V/\partial S)_T = (\partial V/\partial P)_T = -V\beta_T$. In light of Eq. (3.5), we have

$$k_\mathrm{r} = \frac{C_P}{C_V} = \frac{\beta_T}{\beta_S}. \quad (3.6)$$

$C_P - C_V = T(\partial S/\partial T)_P - T(\partial S/\partial T)_V$. In light of the mathematical relation, $(\partial S/\partial T)_P = (\partial S/\partial T)_V + (\partial S/\partial V)_T(\partial V/\partial T)_P$. Thus, $C_P - C_V = T(\partial S/\partial V)_T(\partial V/\partial T)_P = TV\alpha(\partial S/\partial V)_T$. Using Maxwell relation and mathematical cyclic relation, $(\partial S/\partial V)_T = (\partial P/\partial T)_V = -(\partial V/\partial T)_P(\partial P/\partial V)_T = \alpha/\beta_T$. Finally,

$$C_P - C_V = \frac{TV\alpha^2}{\beta_T}. \quad (3.7)$$

Equation (3.7) can be used for the conversion of C_P into C_V, or vice versa, when adequate P-V-T data are available. Since C_V values of solids and liquids are very difficult to determine experimentally, measured C_P values must be converted using these equations when solid-liquid transition is thermodynamically considered.

3.1.2 Magnetic Heat Capacity [3]

In an analogy to C_V and C_P, let us define the heat capacity at constant magnetic moment C_M and that at constant magnetic field $C_{H_{\mathrm{mag}}}$ for a simple magnetic system by the following equations:

$$C_M = \left(\frac{\partial U}{\partial T}\right)_M = T\left(\frac{\partial S}{\partial T}\right)_M, \tag{3.8}$$

and

$$C_{H_{\mathrm{mag}}} = \left(\frac{\partial H'}{\partial T}\right)_{H_{\mathrm{mag}}} = T\left(\frac{\partial S}{\partial T}\right)_{H_{\mathrm{mag}}}. \tag{3.9}$$

Taking the difference between Eqs. (3.8) and (3.9), one obtains, $C_{H_{\mathrm{mag}}} - C_M = T\left(\frac{\partial S}{\partial T}\right)_{H_{\mathrm{mag}}} - T\left(\frac{\partial S}{\partial T}\right)_M$. Thus, we have, $\left(\frac{\partial S}{\partial T}\right)_{H_{\mathrm{mag}}} = \left(\frac{\partial S}{\partial T}\right)_M + \left(\frac{\partial S}{\partial M}\right)_T\left(\frac{\partial M}{\partial T}\right)_{H_{\mathrm{mag}}}$. As a result, $C_{H_{\mathrm{mag}}} - C_M = T\left(\frac{\partial S}{\partial M}\right)_T\left(\frac{\partial M}{\partial T}\right)_{H_{\mathrm{mag}}}$. Substituting Maxwell relations into this equation leads to

$$C_{H_{\mathrm{mag}}} - C_M = -T\left(\frac{\partial H_{\mathrm{mag}}}{\partial T}\right)_M\left(\frac{\partial M}{\partial T}\right)_{H_{\mathrm{mag}}} = T\left(\frac{\partial M}{\partial T}\right)_{H_{\mathrm{mag}}}^2\left(\frac{\partial H}{\partial M}\right)_T.$$

The equation for entropy and internal energy for a simple magnetic system can be easily derived. When we consider $S = S(T, M)$ or $S = S(T, H_{\mathrm{mag}})$, we obtain two equations:

$$T\mathrm{d}S = C_M\mathrm{d}T - T\left(\frac{\partial H_{\mathrm{mag}}}{\partial T}\right)_M\mathrm{d}M, \tag{3.10}$$

and

$$T\mathrm{d}S = C_{H_{\mathrm{mag}}}\mathrm{d}T + T\left(\frac{\partial M}{\partial T}\right)_{H_{\mathrm{mag}}}\mathrm{d}H_{\mathrm{mag}}. \tag{3.11}$$

$\partial S/\partial H_{\mathrm{mag}}$ can be determined by Eq. (3.11) through $(\partial S/\partial H_{\mathrm{mag}})_T = (\partial M/\partial T)_{H_{\mathrm{mag}}}$. For a paramagnetic salt obeying Curie's law, $(\partial M/\partial T)_{H_{\mathrm{mag}}} < 0$ and S decreases as H_{mag} enhances. Such a magneto thermodynamic phenomenon is the cause of the magnetocaloric effect, in which a reversible change in temperature of a suitable material is achieved by exposing the

material to a changing magnetic field. This is also known as adiabatic demagnetization by low temperature physicists, due to the application of process specifically to affect a temperature drop.

The production of low temperatures by adiabatic demagnetization of a paramagnetic salt can be understood with the help of Fig. 3.1 where S is a function of T from the initial $H_{mag} = 0$ at T_1, by contacting a bath of liquid helium, to $H_{mag,1}$. The state of the system is represented by the point a. H_{mag} is now increased isothermally and reversibly, in the process $a - b$, to a value $H_{mag,1}$, forcing various magnetic dipoles of the salt to align and putting these degrees of freedom of the paramagnetic salt into a state of lowered entropy at a constant T_1.
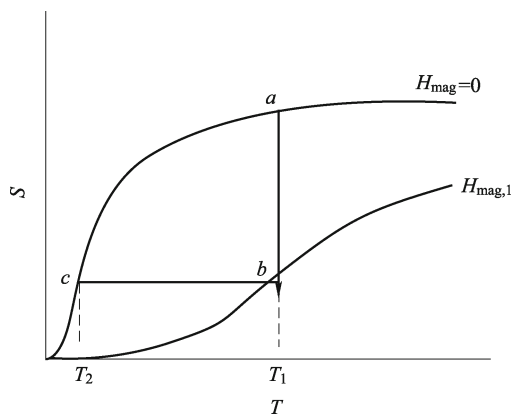
Fig. 3.1 S function of a magnetic system at $H_{mag} = 0$ and at $H_{mag} = H_{mag,1}$.

In the isothermal process $a - b$ where $dT = 0$, Eq. (3.11) yields

$$\delta Q_T = T dS_T = T \left(\frac{\partial M}{\partial T} \right)_{H_{mag}} dH_{mag,T}.$$

At constant H_{mag}, $(\partial M/\partial T)_{H_{mag}} < 0$. As H_{mag} increases, $\delta Q_T < 0$ and there is a heat flow out of the salt into the helium bath.

The next step is to isolate the system thermally from the surroundings and perform the reversible adiabatic process $b - c$ where H_{mag} is reduced to zero while S remains constant. The final temperature T_2, from Fig. 3.1, is evidently lower than T_1. In this process, since $dS = 0$, Eq. (3.11) becomes $dT_S = -(T/C_{H_{mag}})(\partial M/\partial T)_{H_{mag}} dH_{mag}$. Because $(\partial M/\partial T)_{H_{mag}}$ and dH_{mag} are both negative, dT_S is negative too. $T \rightarrow 10^{-3}$ K has been attained in this way.

3.1.3 Heat Capacity of Lattice Vibration of Solids [3, 4]

Thermal energy in a solid may exist in a variety of forms that correspond with various modes of motions in its fundamental particles. Some common modes of motion include internal vibration and rotation within the molecules, and the translation of free electrons. These modes, however, are absent in solids. For instance, there exists little or no free-electron contribution in nonmetals, and there is no internal vibration or rotation in monatomic crystals, such as metals. Furthermore, not all modes of motions are significant at all temperature levels. The free-electron contribution in metals, for example, becomes appreciable compared to the contribution of lattice vibration only at very low temperatures $-T < 30$ K. At room temperature however, it is almost negligible. One particular mode of motions, which always plays a significant role in the evaluation of the thermal properties of such solids, is the lattice vibration, which will be developed in this section by a statistical-mechanical description.

The statistical-mechanical description of the solid distinctly differs from that of the gaseous state in one essential point: The strong interactions between the molecules preclude a consideration of the dynamic behavior of each individual molecule which was possible in the theory of gaseous state. In solids, we consider the motions of the whole lattice and analyze these gross motions statistically.

When we add some thermal energy to an object, in most cases it is directly detectable as a small increase in T (the exception is during a phase transition). Therefore, C_m is one of the most important thermal properties of materials. Dulong and Petit noted in 1819 that $C_{V,m} \approx 3R (\approx 25 \text{ J} \cdot \text{mol}^{-1} \cdot \text{K}^{-1})$ for all elementary solids, which is named the law of Dulong and Petit. Neumann extended this law in 1831 to say that each molar atom in the molecule of a solid contributed 25 J·mol^{-1}·K^{-1} to $C_{V,m}$. Although these laws are by no means exact, they strongly suggest that some underlying physical principles might be responsible for the degree of success.

The atoms of a solid, unlike those of a gas, are constrained to oscillate about fixed points by the relatively large forces exerted on them by other atoms. Let us imagine that each executes harmonic motion. The atoms of a solid are free to move in three dimensions, not just one, so that an assembly of N atoms has $3N$ degrees of freedom. The potential energy associated with its harmonic motion, which could be neglected for the widely separated atoms of a gas, is on the average just equal to the kinetic energy. Hence, if the equipartition principle is valid for solids, we must assign an energy kT to each degree of freedom ($kT/2$ for kinetic energy, $kT/2$ for potential energy) rather than just $kT/2$ as for the atoms of a gas. The total molar energy of N atoms is then

$$U = 3NkT, \tag{3.12}$$

and $C_{V,\mathrm{m}}$ from the theory is

$$C_{V,\mathrm{m}} = (\partial U/\partial T)_V = 3N_{\mathrm{A}}k = 3R. \qquad (3.13)$$

Equation (3.13) verifies the empirical laws beautifully, but it fails to explain why certain substances deviate very strongly from this law.

Figure 3.2 shows $C_{P,\mathrm{m}}(T)$ and $C_{V,\mathrm{m}}(T)$ functions of Cu at $P = 0.1$ MPa. At low T, the two are nearly equal, and near absolute zero both drop rapidly to zero. While $C_{V,\mathrm{m}}(T) \approx 3R$ at high T, $C_{V,\mathrm{m}}(T)$ drops as T decreases. This behavior is the characteristic of the most solids, although T, at which the sharp drop occurs, varies widely from one substance to another. The above phenomenon cannot be understood in terms of partition functions of the kind used to describe ideal gases.
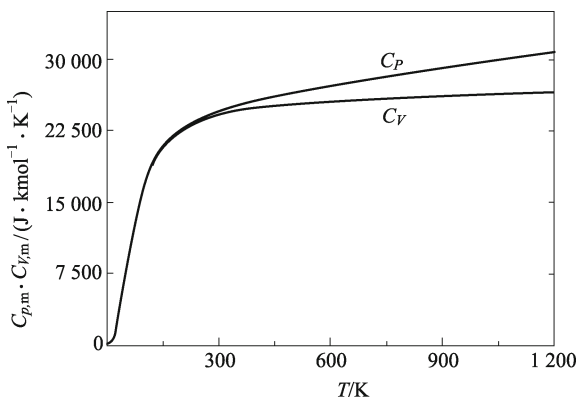
Fig. 3.2 Schematical graphs of $C_{V,\mathrm{m}}$ and $C_{P,\mathrm{m}}$ of Cu as a function of T at $P = 0.1$ MPa.

The first analysis of the thermodynamics of lattice vibrations was carried out by Einstein, who recognized that a quantum explanation might resolve the failure of the classical heat capacity theory and proposed that the atoms of a solid could be considered in the first approximation as an assembly of quantized oscillators. All vibrate with the same frequency ν. In an assembly of N_{A} atoms, applying Eqs. (2.26) and (2.46), the internal energy of $3N_{\mathrm{A}}$ oscillators is

$$U_{\mathrm{m}} = RT^2 \left[\frac{\partial(\ln Z)}{\partial T} \right]_V = 3R\Theta_{\mathrm{E}} \left[\frac{1}{\exp(\Theta_{\mathrm{E}}/T) - 1} \right] \qquad (3.14)$$

where $\Theta_{\mathrm{E}} \equiv h_{\mathrm{p}}\nu/k$ is the Einstein temperature. Since $C_{V,\mathrm{m}} = (\partial U_{\mathrm{m}}/\partial T)_V$, there is

$$C_{V,\mathrm{m}} = 3R \left(\frac{\Theta_{\mathrm{E}}}{T} \right)^2 \frac{\exp(\Theta_{\mathrm{E}}/T)}{[\exp(\Theta_{\mathrm{E}}/T) - 1]^2}. \qquad (3.15)$$

Equation (3.15) has two characteristics of the observed heat capacities: when $T \gg \Theta_{\mathrm{E}}$ or Θ_{E}/T is small, $C_{V,\mathrm{m}}$ approaches the Dulong-Petit value of $3R$.

When $T \ll \Theta_{\text{E}}$, the exponential term is large, we can neglect the 1 in the denominator, and

$$C_{V,\text{m}} = 3R \left(\frac{\Theta_{\text{E}}}{T} \right)^2 \exp(-\Theta_{\text{E}}/T). \tag{3.16}$$

When $T \to 0$, the exponential term goes to zero more rapidly compared with that $1/T^2$ goes to infinity, and $C_{V,\text{m}} \to 0$, being in agreement with experiments and the third law. However, because of the rapid decrease of the exponential term, the theoretical values of $C_{V,\text{m}}$, at very low temperature, decrease much more rapidly than the experimental values. It remained for Debye to suggest another form of the vibration equations for the individual atoms.

Debye realized that the individual vibrating atoms are not really independent, but are strongly coupled. He analyzed the situation by treating an entire crystal as an elastic medium with a range of frequencies, varying from zero to some maximum value ν_{m}, which is characteristic of solids. An alternative approach is to consider the elastic waves themselves as the "particles" of an assembly. Each wave can also be taken as a particle and is called a phonon, and the assembly is described as a phonon gas. Since the waves or phonons are indistinguishable, and there is no restriction on the number permitted per energy state, the assembly obeys BE statistics.

U of the assembly is now obtained by integrating the expression of $\text{d}U_\nu$, the internal energy of waves with frequencies between ν and $\nu + \text{d}\nu$. In the frequency interval over all values of ν from zero to ν_{m}, there is

$$U \equiv \frac{9N}{\nu_{\text{m}}^3} \int_0^{\nu_{\text{m}}} \frac{h_{\text{p}}\nu^3}{\exp(h_{\text{p}}\nu/kT - 1)} \text{d}\nu. \tag{3.17}$$

Let $\Theta_{\text{D}} \equiv h_{\text{p}}\nu_{\text{m}}/k$ be named Debye temperature, some Θ_{D} values are given in Table 3.1.

Table 3.1 Θ_{D} values of several metals and compounds

Substance	$\Theta_{\text{D}}/\text{K}$	Substance	$\Theta_{\text{D}}/\text{K}$	Substance	$\Theta_{\text{D}}/\text{K}$
Pb	88	KBr	177	Cu	315
Tl	96	Ag	215	Al	398
Hg	97	Ca	226	Fe	453
I	106	KCl	230	CaF_2	474
Cd	168	Zn	235	FeS_2	645
Na	172	NaCl	281	Diamond	1860

For convenience, we introduce the dimensionless quantities of $x = h_{\text{p}}\nu/kT$ and $x_{\text{m}} = h_{\text{p}}\nu_{\text{m}}/kT = \Theta_{\text{D}}/T$. Then $U = 9NkT \left(\frac{T}{\Theta_{\text{D}}} \right)^3 \int_0^{x_{\text{m}}} \frac{x^3 \text{d}x}{\exp(x) - 1}$. At the high temperature limit where $x = h_{\text{p}}\nu/kT$ is small, $\exp(x) - 1 \approx x$ and the integral becomes $\int_0^{x_{\text{m}}} x^2 \text{d}x = \frac{x_{\text{m}}^3}{3} = \frac{\Theta_{\text{D}}^3}{3T^3}$. $U_{\text{m}} = 3N_{\text{A}}kT$ and $C_{V,\text{m}} = 3R$, in agreement with the Einstein theory and the Dulong-Petit law.

At intermediate and low T, the value of the integral can be expressed only as an infinite series. To a good approximation, the upper limit of the integral at very small T can be taken as infinity instead of x_m since the integrand is small for values of $x > x_\mathrm{m}$. The definite integral then equals $\pi^4/15$, and hence at lower T,

$$U = \frac{3}{5}\pi^4 NkT \left(\frac{T}{\Theta_\mathrm{D}}\right)^3, \tag{3.18}$$

and by differentiation,

$$C_{V,\mathrm{m}} = \frac{12\pi^4}{5} R \left(\frac{T}{\Theta_\mathrm{D}}\right)^3. \tag{3.19}$$

Equation (3.19) is known as the Debye T^3 law. According to this law, $C_{V,\mathrm{m}}$ decreases with T^3 near $T = 0$, rather than exponentially as in the Einstein theory. The decrease is therefore less rapid and the agreement with experiments is much better.

Although the Debye theory is based on an analysis of elastic waves in a homogeneous, isotropic, continuous medium, experimental $C_{V,\mathrm{m}}$ values of many crystalline solids are in good agreement with the Debye theory at $T/\Theta_\mathrm{D} < 0.02$. As T increases, $C_{V,\mathrm{m}}$ increases somewhat faster than the theory would predict.
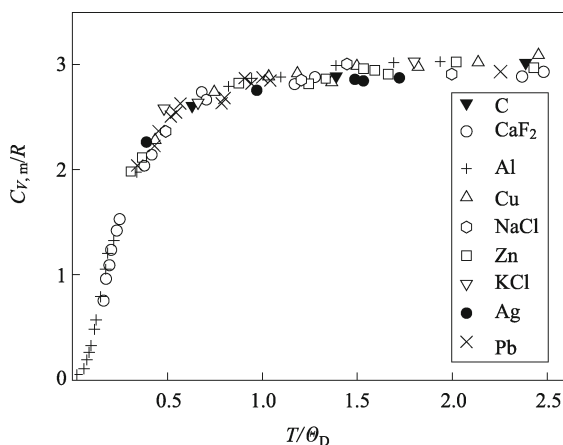
Fig. 3.3 $C_{V,\mathrm{m}}/R$ of various solids as a function of T/Θ_D.

Figure 3.3 shows a graph of $C_{V,\mathrm{m}}/R$ as a function of T/Θ_D, and the points are experimental values for a variety of metals or compounds. In light of Fig. 3.3, when $T/\Theta_\mathrm{D} > 1$, the system roughly behaves "classically" and $C_{V,\mathrm{m}}$ is nearly equal to the "classical" or "non-quantum" value of $3R$. When $T/\Theta_\mathrm{D} < 1$, quantum effects become significant and $C_{V,\mathrm{m}} \to 0$ as $T \to 0$. It is noteworthy that Θ_D is induced by Fig. 3.3, which leads to different locations

of room temperature compared with Θ_D. For Pb, "room temperature" is well above $\Theta_D = 88$ K, while for diamond, "room temperature" is much lower than $\Theta_D = 1860$ K and a "quantum solid" is present.

At intermediate T, there is good agreement between $C_{V,m}$ values calculated by the both theories. This agreement might be expected since the Dulong-Petit theory as a first order approximation works at high temperature. The Einstein theory is a second order approximation, which is valid for high and intermediate temperatures. The Debye theory is a third order approximation that is effective also at low temperatures when other effects do not dominate.

3.1.4 Electronic Heat Capacity of Metals [3]

The most important example of an assembly obeying FD statistics is the free electrons in metals. There is good reason to believe that each atom in metallic crystalline lattice parts with one or more of its outer electrons and that these free, or conducting, electrons behave essentially as a gas. Consequently, it is common to speak of them collectively as an electron gas. If these particles are free to move about, their behavior is similar to that of the translational motion of an ideal monatomic gas and the thermal and electrical conductivities of a metallic solid are the results of this motion within the solid. That is, this electron gas has translational degrees of freedom, which is quite independent of the metallic ions forming the crystal lattice.

Since free electrons have to obey the Pauli Exclusion Principle, a proper description of their behavior requires the use of FD statistics. That is, any energy state can be associated with no more than one electron. Nevertheless, the allowed ε_i, and g_i of electrons will still be those associated with translational motion such as Eqs. (2.32) and (2.33). From them, we can derive the differential relationships between the n_i, ε_i, and g_i,

$$\mathrm{d}n = \frac{1}{2}\left(\frac{8m}{\varepsilon}\right)^{1/2}\frac{V^{1/3}}{h_P}\mathrm{d}\varepsilon, \qquad (3.20)$$

and

$$\mathrm{d}g = \pi n^2 \mathrm{d}n/2. \qquad (3.21)$$

FD distribution for these electrons can also be expressed in a differential form,

$$\mathrm{d}N = \frac{\mathrm{d}g}{\exp[(\varepsilon - \mu)/kT] + 1}. \qquad (3.22)$$

With the help of Eqs. (3.20) and (3.21),

$$\frac{\mathrm{d}g}{\mathrm{d}\varepsilon} = \frac{\mathrm{d}g}{\mathrm{d}n}\frac{\mathrm{d}n}{\mathrm{d}\varepsilon} = \frac{\pi}{2}\frac{8mV^{2/3}\varepsilon}{h_P^2}\cdot\frac{1}{2}\left(\frac{8m}{\varepsilon}\right)^{1/2}\frac{V^{1/3}}{h_P} = 2\pi V\left(\frac{2m}{h_P^2}\right)^{3/2}\varepsilon^{1/2}. \quad (3.23)$$

Equation (3.23) is actually low by a factor of two. Electrons have a spin degeneracy of two because they can be spinning in either of two directions. Each mode of storage of translational energy can occur in combination with either mode of rotation. Equation (3.23) should accordingly be replaced, in this case, by $dg = 4\pi V (2m/h_P^2)^{3/2} \varepsilon^{1/2} d\varepsilon$. If for brevity we set $A \equiv 4\pi V (2m/h_P^2)^{3/2}$, $dg = A\varepsilon^{1/2} d\varepsilon$. The degeneracy therefore increases with the increasing square root of the energy. From FD distribution function of Eq. (3.22), replacing the sum with an integral, we have $N = A \int_0^\infty \dfrac{\varepsilon^{1/2}}{\exp[(\varepsilon - \mu)/kT] + 1} d\varepsilon$. The integral cannot be evaluated in closed form and the result can be expressed only as an infinite series. The result is, first obtained by Sommerfeld,

$$\mu = \varepsilon_F \left[1 - \frac{\pi^2}{12} \left(\frac{kT}{\varepsilon_F} \right)^2 + \frac{\pi^4}{80} \left(\frac{kT}{\varepsilon_F} \right)^4 + \cdots \right]. \qquad (3.24)$$

The Fermi energy ε_F is a constant for a given metal. As we shall show, ε_F is a function of N/V, the number of electrons per unit volume. Thus, μ in Eq. (3.24) is a function of T and N/V. When $T = 0$, $\mu^0 = \varepsilon_F$. The distribution function at $T = 0$ is then

$$N_i^0 = \frac{g_i}{\exp[(\varepsilon_i - \varepsilon_F)/kT] + 1}. \qquad (3.25)$$

The significance of ε_F can be seen as follows: In all levels for which $\varepsilon_i < \varepsilon_F$, $\varepsilon_i - \varepsilon_F$ is a negative quantity, and at $T = 0, (\varepsilon_i - \varepsilon_F)/(kT) \to -\infty$. Hence, $N_i^0 = g_i$. That is, the average number of electrons in a level equals the number of states in the level, and all levels with energy smaller than ε_F are fully occupied with their quota of one electron in each state.

In all levels for which $\varepsilon_i > \varepsilon_F$, the term $(\varepsilon_i - \varepsilon_F)$ is positive. Hence, the exponential term equals $+\infty$ and $N_i^0 = 0$ at $T = 0$. There are thus no electrons in these levels and ε_F is the maximum energy of an electron at $T = 0$ K. The corresponding level is called the Fermi level.

An expression for ε_F can now be obtained from the requirement that $\sum dN^0 = N$. Replacing the sum with an integral, introducing the distribution function at $T = 0$, and integrating over all levels from zero to ε_F, we have $N = A \int_0^{\varepsilon_F} \varepsilon^{1/2} d\varepsilon = \frac{2}{3} A \varepsilon_F^{3/2}$, or, after inserting the expression for A,

$$\varepsilon_F = \frac{h_P^2}{8m} \left(\frac{3N}{\pi V} \right)^{2/3}. \qquad (3.26)$$

Thus, as stated earlier, ε_F is a function of N/V, but is independent of T.

The solid curve in Fig. 3.4 is a graph of $dN^0/d\varepsilon = A\varepsilon^{1/2}$ at $T = 0$. The curve extends from $\varepsilon = 0$ to $\varepsilon = \varepsilon_F$, and is zero at all energetic levels being greater than ε_F.
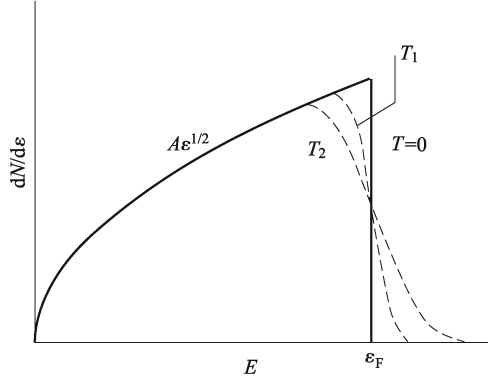
Fig. 3.4 Graphs of the distribution function of free electrons in a metal at $T = 0$ and at two higher temperatures T_1 and T_2.

As a numerical example, let the metal be Ag. Since Ag is monovalent, we assume one free electron per atom. The density of Ag is 10.5×10^3kg·m^{-3} with atomic weight of 107, $N/V = 5.86 \times 10^{28}$ m^{-3}. The mass of an electron is 9.11×10^{-31} kg and $h_P = 6.62 \times 10^{-34}$ J·s. Then $\varepsilon_F = 9.1 \times 10^{-19}$ J $= 5.6$ eV. $U = \sum \varepsilon_i N_i$ for the electrons or, replacing the sum with an integral, $U = A \int_0^\infty \dfrac{\varepsilon^{3/2}}{\exp[(\varepsilon - \mu)/kT] + 1} \mathrm{d}\varepsilon$. Again, the integral cannot be evaluated in a closed form and must be expressed as an infinite series. The result is

$$U = \frac{3}{5} N \varepsilon_F \left[1 + \frac{5\pi^2}{12} \left(\frac{kT}{\varepsilon_F} \right)^2 - \frac{\pi^4}{16} \left(\frac{kT}{\varepsilon_F} \right)^4 + \cdots \right]. \qquad (3.27)$$

When $T = 0, U^0 = (3/5) N \varepsilon_F$ where $\overline{\varepsilon^0} = U^0/N = 3\varepsilon_F/5 \approx 3.5$ eV for a single electron of Ag. The mean kinetic energy of a gas molecule at room temperature is only about 0.03 eV. If this value reaches 3.5 eV, $T \approx 28000$ K. Hence the mean kinetic energy of the electrons in a metal, even at absolute zero, is much greater than that of molecules of an ordinary gas at $T \sim 10^3$ K. At $T = 300$ K, $kT/\varepsilon_F = (1.38 \times 10^{-23} \times 300)/(9.1 \times 10^{-19}) = 4.58 \times 10^{-3}$ for Ag, which is very small. To a good approximation, one can consider that $\mu = \varepsilon_F$ at any T.

The dotted curves in Fig. 3.4 are $\mathrm{d}N/\mathrm{d}\varepsilon$ graphs at higher temperatures T_1 and T_2 with $T_2 > T_1$. The occupation numbers change appreciably with increasing T only in those levels near ε_F. The reason for this is the following. Suppose U of metals gradually increases from U^0 at $T = 0$, as T raises. In order to accept a small amount of energy, an electron must move from its energy level at $T = 0$ to a level of slightly higher energy. However, except for those electrons near ε_F, all states of higher energy are fully occupied. Thus, only those electrons near ε_F can move to a higher level. With increasing T, those levels just below ε_F become gradually depleted, electrons at still lower

levels can move to those that have been vacated, and so on.

For the particular level at which $\varepsilon = \mu$, and at $T > 0$, the exponential term in the distribution function is equal to 1, and the occupation number is $N_i = g_i/2$. If T is low, as a good approximation, $\mu = \varepsilon_F$ and the Fermi level is 50% occupied.

In light of Eq. (3.27), $C_V^e = \dfrac{\pi^2}{2}\left(\dfrac{kT}{\varepsilon_F}\right)Nk\left[1 - \dfrac{3\pi^2}{10}\left(\dfrac{kT}{\varepsilon_F}\right)^2 + \cdots\right]$. At low T, the high order terms of kT/ε_F can be neglected, and $C_{V,m}^e = (\pi^2/2) \cdot (kT/\varepsilon_F)R$, which is zero at $T = 0$ K and increases linearly with T. For Ag at 300 K, using kT/ε_F value previously calculated, $C_{V,m}^e = 2.25 \times 10^{-2}R$. On the other hand, $C_{V,m} = 3R/2$ for a monatomic ideal gas.

We therefore see that as a direct consequence of the Pauli Exclusion Principle, the mean kinetic energy of the electrons in metals is much smaller than that of the molecules of an ideal gas at the same T. But the excitation energy required to jar electrons into the unoccupied higher energy states is too big, except that near ε_F. As a result, only very few of electrons actually contribute to $C_{V,m}$. This result illustrates what had long been a puzzle in the electron theory of metallic conduction: the observed $C_{V,m}$ of metals is similar to that of isolators of about $3R$, as given by the Dulong-Petit law. The free electrons however, if they behave like the molecules of an ideal gas, should make an additional contribution of $3R/2$ to $C_{V,m}$, resulting in a value being larger than experimental results. The fact that only those electrons having energy near ε_F can increase their energy with increasing T let us understand why the electrons make only negligible contribution to $C_{V,m}$.

3.2 Entropy [5]

The concept of entropy is derived from the interpretation of the second law, which just summarizes our experience with those spontaneous happenings and millions of others: All kinds of energy spontaneously spread out from where they are localized to where they are more dispersed, if they are not hindered from doing so. The opposite does not occur spontaneously. Entropy just measures what happens in that kind of process (at a specific T) of energy dispersing. So, the words and meaning of "the entropy" and "the second law" are so closely related (entropy is the quantitative measure of the qualitative law) that they are often used interchangeably. Never forget that entropy must always be connected with energy in general, and specifically with energy that is being or has been dispersed. Actually, we should always say "entropy change" because we were measuring the difference in energy distribution "after" something happens versus the "before". Entropy change, ΔS, measures how much energy is dispersed in a system, or how wide spread of the energy of a system becomes (both always involving T). We take an example of melting ice process to illustrate ΔS. Ice is melted to water at 273 K

where $\Delta S = Q/T$. Thus, in that equation, it is easy to see that Q (the enthalpy of fusion) is how much "heat" energy is spread out in the ice to change it to water [6].

Melting is one of the most familiar natural phenomena. A common aspect of the melting of all types of crystals and the liquids formed from them is that, regardless of the physical and chemical nature of the condensed phases coexisting at the point of the phase transition, the regular repetition of lattice site in all three dimensions disappears upon melting. Any approach to describe the melting process must accordingly incorporate the existence of positional disorder that occurs as a result of the transition from the crystalline state to the liquid state. This aspect of the melting process distinguishes the entropy of melting from other thermodynamic parameters.

Melting is characteristic of any crystalline material, regardless of the particular features of its interatomic interaction. However, the fact that this phenomenon is common to different types of materials does not rule out a diversity of ways in which the transition occurs from the solid state to the liquid state. For example, the melting of semiconductors is characterized by fundamentally different types of transitions from the solid state to the liquid state, associated with the presence or absence of radical changes in the nature of the interatomic interaction upon the melting transition. This circumstance alone suggests that the positional disorder, which is common to all materials, cannot be the only source of an increase in entropy upon melting.

In calculating the heat of the phase transition by statistical methods, Frenkel and Mott started from the argument that a liquid, like a solid, is a system of oscillators, with the sole distinction that the equilibrium positions of these oscillators in the liquid are distributed at random. That approximation was based on many experimental results indicating similarities in the structure of liquids and solids near T_m. The vibrational spectrum of a crystal and a melt at T_m can be approximated well by the Einstein approximation, according to the ideas of Frenkel and Mott, since the condition $kT \geqslant h\nu$ usually holds here. From the standpoint of the change in the type of vibrational spectrum in the atomic subsystem, the melting process is characterized by a lowering of the maximum frequency of the vibrations of the particles due to a weakening of binding forces upon the melting transitions. In this case a basic parameter of the model is a characteristic frequency ν, and the partition function for each phase can be written in a much simpler way. Letting subscripts "s" and "L" denote solid and liquid, respectively, the entropy of melting ΔS_m has the expression,

$$\Delta S_m = 2R\ln(\nu_s/\nu_L). \tag{3.28}$$

This model of melting presupposes that the only reason for ΔS_m is a change in the nature of the vibration spectrum. This circumstance allowed Mott to link ΔS_m upon melting with corresponding changes in electrical conductivity

ϑ and to derive the well-known expression,

$$(\vartheta_{\mathrm{s}}/\vartheta_{\mathrm{L}}) = \exp(-335\Delta S_{\mathrm{m}}) \tag{3.29}$$

where ΔS_{m} is in $\mathrm{J \cdot mol^{-1} \cdot K^{-1}}$. Numerous tests have shown that there are significant deviations between Eq. (3.29) and experiments in several cases. Regel showed that Eq. (3.29) is satisfied by "good" metals, i.e., those have approximately the same values of ΔS_{m} (about R). By contrast, semimetals – Ga, Sb, and Bi, distinguished by high values of ΔS_{m} (about $2.5R$) – have anomalies in the changes in their physical properties upon melting.

For these materials, melting is accompanied by a significant increase in CN and by a strengthening of the "metallization bonds". The latter circumstance is seen directly in an increase in ϑ of Ga, Sb, and Bi upon melting. Equation (3.29) does not yield even an indirect hint of the direction of the changes in the electric properties upon melting. A more striking picture is observed in the semiconductors Ge and Si, whose melting is accompanied by radical changes in the short-range order and in the nature of the interatomic bonds. These materials are distinguished by anomalously large values of ΔS_{m} (about $3.5R$). These facts reflect, in addition to structural disorder and changes in the vibrational spectrum of particles upon melting, changes in the nature of the interatomic bonds, which go with this process. The latter changes are known to be intimately related to variations in states of the electronic subsystem.

This conclusion follows more clearly from an analysis of the behavior of ΔS_{m} of simple solids as a function of the atomic number of the corresponding elements, as shown in Fig. 3.5.

The features of this plot indicate that elements, which exhibit elevated values of ΔS_{m}, are specifically those elements whose melting is related with structure changes of the short-range order and the nature of the interatomic binding. Thus, the changes occurring in the vibrational spectrum of atoms during a melting contribute only a part of ΔS_{m}, and this part, even when summed with the positional component due to the structural disorder, often does not constitute the total ΔS_{m} of such crystals. Consequently, analysis of ΔS_{m} of simple substances in connection with the periodic table of elements leads to a completely rigorous law. Substances in which the type of interatomic binding changes upon melting are distinguished by elevated values of ΔS_{m}. All other simple substances have low values of this entropy (0.3–$1.5R$).

For the substance of this group, the absolute values of ΔS_{m} are associated with differences of ν in the solid and liquid phases and also with changes in the vacancy concentrations upon melting. Both are determined by the electronic configuration of the particles and by the concentration of free electrons. This case is ultimately responsible for subtle differences in ΔS_{m}. With regard to thermodynamic characteristics of the process by which chemical compounds, particularly, semiconductor compounds, undergo melting, we see the principle of chemical analogy, incorporating ideas of electronic analogs and second periodicity, in its full glory.
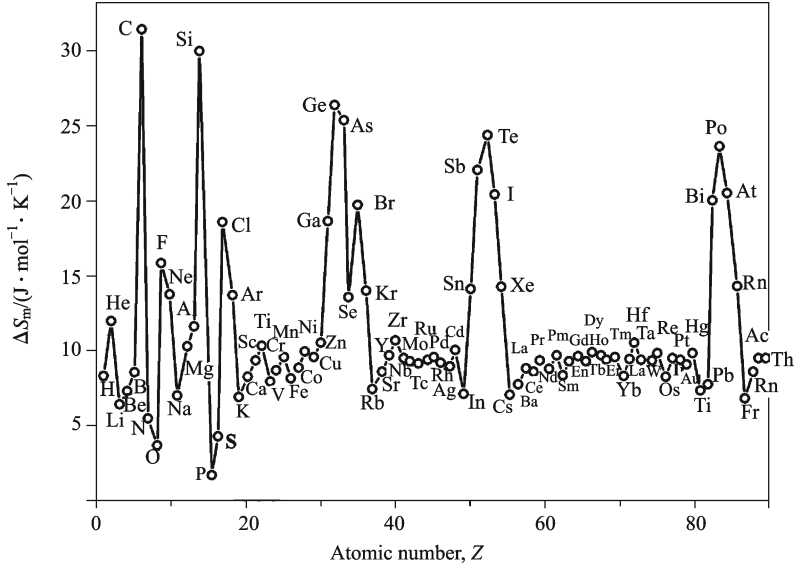
Fig. 3.5 ΔS_m of simple solids versus the atomic number of elements.

Table 3.2 shows values of T_m, ΔH_m, and ΔS_m of semiconductor compounds of various structural groups. Large values of ΔH_m and ΔS_m are indeed characteristics of compounds, which undergo a substantial change in the type of interatomic binding due to melting. This is true primarily of III-V compounds, whose melting is analogous to that of Si and Ge. When a compound melts, the process is complicated by thermal dissociation of the compound in the liquid phase. This circumstance can strongly influence ΔS_m.

Analyzing the data in Table 3.2, we see a correlation between thermodynamic characteristics of the melting process, on the one hand, and characteristics of the interatomic bonding strength, on the other. In this situation, it is quite natural that there would be a correlation between these thermodynamic characteristics and the extent to which the interatomic binding becomes ionic.

As an example, supporting the point of view discussed above, Fig. 3.6 gives the correlation between ΔS_m and the degree of ionicity of the bond, as calculated by the Pauling method for a group of Cu and Ag chalcogenides. This dependence illustrates the interrelationship between these characteristics during sequential anionic and cationic substitution of components forming several analogous compounds with the general formula I_2VI (I here is Cu or Ag, while VI is S, Se, or Te). Analysis of the periodic behavior of ΔH_m and ΔS_m of simple solids in comparison with the corresponding changes in the nature of the interatomic bonds during the melting yields the important conclusion that changes in the electronic configurations of the atoms at the time of the phase transition contribute to ΔS_m. Here we consider both the suggestion of an electronic component of the entropy of melting ΔS_{el} and

(the more important point) a validation of this suggestion.

Table 3.2 Thermodynamic characteristics of the melting of certain semiconductor compounds (Note that in fact the units of ΔH_m and ΔS_m are kJ·g-atom^{-1} and J·g-atom^{-1}·K^{-1} since the number in a molecule is larger than 1. The data shown in the table have been divided by number of atoms in a molecule, which guarantees the Avogadro constant remains)

Compounds	T_m /K	ΔH_m /(kJ· mol^{-1})	ΔS_m /(J· mol^{-1}· K^{-1})	Compounds	T_m /K	ΔH_m /(kJ· mol^{-1})	ΔS_m /(J· mol^{-1}· K^{-1})
Cu_2S	1403	11.29	7.9	GeS	938	22.57	24.24
Cu_2Se	1386	17.97	12.96	GeSe	943	32.6	34.69
Cu_2Te	1398	24.66	17.56	GeTe	998	40.13	40.55
Ag_2S	1111	8.78	7.9	SnS	1155	31.77	27.17
Ag_2Se	1170	17.56	15.05	SnSe	1133	42.64	38.04
Ag_2Te	1272	21.32	17.14	$SnSe_2$	930	38.46	40.96
CuI	875	10.87	12.12	SnTe	1063	45.14	41.8
ZnS	2123	43.89	20.9	PbS	1393	36.37	26.33
ZnSe	1773	53.5	30.1	PbSe	1361	49.32	40.55
ZnTe	1513	57.68	40.96	PbTe	1190	57.27	48.07
CdS	2023	58.1	20.48	Sb_2S_3	819	65.21	79.42
CdSe	1525	45.56	29.68	Sb_2Si_3	885	77.33	87.36
CdTe	1318	57.27	40.55	GaP	1623	122.06	70.22
Mg_2Si	1375	85.27	61.86	GaAs	15111	96.98	63.95
Mg_2Ge	1388	77.33	55.59	GaSb	985	50.16	48.49
Mg_2Sn	1051	47.65	45.56	InP	1335	50.16	47.65
Mg_2Pb	823	38.87	47.23	InAs	1215	48.49	43.47
AlP	1770	30.93	17.56	InSb	809	40.13	49.74
AlAs	1870	75.66	40.55	HgSe	963	28.01	29.26
AlSb	1327	59.36	43.89	HgTe	943	32.19	34.28
GaSe	1233	38.87	31.77	Sb_2Te_3	894	99.9	111.61
Ga_2Se_3	1273	98.65	76.49	Bi_2S_3	1123	58.94	48.49
GaTe	1097	52.67	48.49	Bi_3Se_3	979	84.85	86.11
Ga_2Te	1063	122.47	115.37	Bi_2Te_3	858	118.71	118.71
InSe	933	19.23	20.9	Zn_3As_2	1288	92.38	71.9
In_2Se_3	1173	63.95	54.34	$ZnAs_2$	1041	40.55	38.87
InTe	969	36.78	37.62	Cd_3As_2	994	71.48	74.4
In_2Te_3	940	88.2	94.05	$CdAs_2$	894	35.11	39.29

It is noteworthy that all the components of entropy of melting were summarized by Ubbelohde in his book [7], where it was shown that one can distinguish vibrational, positional, orientational, configurational, and other components of ΔS_m for various classes of substances, depending on atomic interaction. But which of these components is predominant will depend on the particular features of the physical nature of the substance.

Cusak and Enderby suggested that the analysis of simple substances is limited to three major components of the entropy of melting: the positional, the vibrational, and excess components,

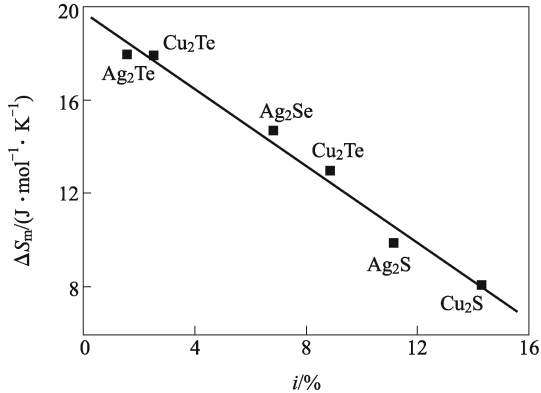$$\Delta S_m = \Delta S_{pos} + \Delta S_{vib} + \Delta S_3 \tag{3.30}$$

Fig. 3.6 ΔS_m as a function of the ionicity of the bonds in copper and silver chalcogenides.

where ΔS_3 should reflect ΔS_el during the melting.

For metals, ΔS_el is negligible in comparison with ΔS_pos and ΔS_vib since the type of binding is preserved without changes in the state of the electronic subsystem when metals melt. When these simple substances formed by subgroup–IVB, VB, and VIB elements undergo melting, there is a disruption of the corresponding system of covalent bonds and a transition to a metallic state. This transition is accompanied by substantial changes in the concentration of free electrons where ΔS_el is extremely substantial. In the case of the group–IVB elements Ge and Si, ΔS_m is nearly twice the sum of $\Delta S_\mathrm{pos} + \Delta S_\mathrm{vib}$. Equally big differences can be observed for elements of subgroup VB (Sb and Bi). Differences, which are slight, but still extremely important, can be seen for the subgroup–VIB elements Te and Po.

For ΔS_m of semiconductors, as stated above, can be represented as the sum of three components,

$$\Delta S_\mathrm{m} = \Delta S_\mathrm{pos} + \Delta S_\mathrm{vib} + \Delta S_\mathrm{el}. \tag{3.31}$$

In light of the discussion above, ΔS_m measured experimentally is of an integrated characteristic, being determined by the three processes associated with changes in these subsystems. These processes can evidently be characterized by corresponding values of thermal effects.

Let us now take a brief look at some independent estimates of these entropies of melting.

3.2.1 Positional Part of Melting Entropy and Its Evaluation [5]

ΔS_pos is the portion of a system's entropy that is related to the position of its constituent particles rather than their velocity of momentum. The idea of

ΔS_{pos} arises in connection with the positional disorder as a substance undergoes a melting transition. It is physically related to the number of ways of arranging all the particles of the system while maintaining some overall set of specified system properties, such as energy. ΔS_{pos} is also known as microscopic entropy or conformational entropy in the study of macromolecules. In general, ΔS_{pos} is the foundation of statistical thermodynamics.

In the case of simple liquids, only two particle species are present: the atoms of the given substance and vacancies. In this case the positional component is found from the expression (details see Sec. 4.5),

$$\Delta S_{\text{pos}} = -R(x_A \ln x_A + x_v \ln x_v) \tag{3.32}$$

where x_A and x_v are the mole fractions of the host material and vacancies, respectively. For a melting process, $x_A = 1/(1 + \Delta V_m/V_s)$ and $x_v = 1 - x_A$ where $\Delta V_m = V_L - V_s$. Equation (3.32) assumes that ΔV_m consists of vacancies with the same size of atoms, which of cause is considerably rough since the size of vacancies must be smaller than atom sizes while the bond length of liquid atoms is larger than that of solid atoms. The above approximation however does not lead to big error when ΔS_{pos} is considered.

In evaluating ΔS_{pos} of semiconductors, we need to consider a post melting effect which arises because the metallization of the bonds is not completed at T_m and instead extends a T above T_m for about ten to dozens of K. In this temperature interval the liquid is assumed to be bistructural. It can be thought of as a solution of clusters which retain structural features inherited from the crystal in a metallic matrix. The presence of clusters in melts should evidently change the number of methods by which a given state can be realized and should therefore influence the thermodynamic probability and thus ΔS_m.

Taking into account the volume fraction of clusters (φ_c) at T_m, we can put the expression for ΔS_{pos} in the following form:

$$\Delta S_{\text{pos}} = -R \left[x_A(1 - \varphi_c) \ln \frac{x_A(1 - \varphi_c)}{x_A(1 - \varphi_c) + x_v} + x_v \ln \frac{x_v}{x_A(1 - \varphi_c) + x_v} \right]. \tag{3.33}$$

For semiconductor compounds, we should also consider the possibility that these compounds will dissociate into their components upon melting. When the crystal is binary, consisting of A and B elements, the following quasichemical reaction could be taken,

$$(AB)_s \leftrightarrow (AB)_L + A_L + B_L + V_L. \tag{3.34}$$
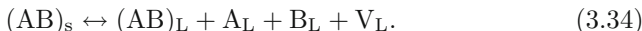
In the quasicrystal approximation, the number of vacancies can be calculated from data on the change in the density due to melting under the condition that the volume per atom is constant in the solid and liquid phases.

The differences among the vacant positions in the liquid phase can be ignored. ΔS_{pos} can evidently be calculated as the entropy of displacement

of the structural units present in the system. Consequently, by analogy with Eq. (3.32), for a system containing structural units in accordance with quasichemical reaction of Eq. (3.34), we can write

$$\Delta S_{\text{pos}} = -R(x_{\text{AB}} \ln x_{\text{AB}} + x_{\text{A}} \ln x_{\text{A}} + x_{\text{B}} \ln x_{\text{B}} + x_{\text{v}} \ln x_{\text{v}}). \tag{3.35}$$

A calculation of the atomic fraction of dissociation products at T_{m} requires calculating the degree of dissociation. The latter calculations can be carried out once we have determined the radius of curvature of the liquidus at T_{m}. Taking account of the dissociation of the compound and the presence of clusters, ΔS_{pos} is shown as

$$\begin{aligned}
\Delta S_{\text{pos}} = -R \Bigg[&x_{\text{AB}}(1-\varphi_{\text{c}}) \ln \frac{x_{\text{AB}}(1-\varphi_{\text{c}})}{x_{\text{AB}}(1-\varphi_{\text{c}}) + x_{\text{A}} + x_{\text{B}} + x_{\text{v}}} \\
&+ x_{\text{A}} \ln \frac{x_{\text{A}}}{x_{\text{AB}}(1-\varphi_{\text{c}}) + x_{\text{A}} + x_{\text{B}} + x_{\text{v}}} \\
&+ x_{\text{B}} \ln \frac{x_{\text{B}}}{x_{\text{AB}}(1-\varphi_{\text{c}}) + x_{\text{A}} + x_{\text{B}} + x_{\text{v}}} \\
&+ x_{\text{v}} \ln \frac{x_{\text{v}}}{x_{\text{AB}}(1-\varphi_{\text{c}}) + x_{\text{A}} + x_{\text{B}} + x_{\text{v}}} \Bigg].
\end{aligned} \tag{3.36}$$

Equation (3.36) reflects the most general case and includes expressions for particular cases. In the case $\varphi_{\text{c}} = 0$, for example, Eq. (3.36) becomes Eq. (3.35), while for $\varphi_{\text{c}} = 1$ (a complete blocking of the particles in a crystal-like structure), $\Delta S_{\text{pos}} = 0$. Calculations of ΔS_{pos}, incorporating clustering and dissociation of semiconductor compounds, have shown that the effect of these processes on ΔS_{pos} is appreciable. As expected, ΔS_{pos} value calculated for the case with clustering is lower, i.e., the partial preservation of a crystal-like structure reduces the positional disorder in the system.

3.2.2 Contribution of Vibrational Part of Melting Entropy of Semiconductors [5]

For metallic and organic crystals, the type of chemical connection does not vary during the melting transition. Thus, $\Delta S_{\text{el}} \approx 0$, and

$$\Delta S_{\text{vib}} = \Delta S_{\text{m}} - \Delta S_{\text{pos}}. \tag{3.37}$$

For some semi-metals, $\Delta S_{\text{el}} \neq 0$, ΔS_{vib} must be determined in a direct way, such as Mott's equation,

$$\Delta S_{\text{vib}} = 3R \ln(\nu_{\text{s}}/\nu_{\text{L}}) = (3/2)R \ln(\vartheta_{\text{s}}/\vartheta_{\text{L}}). \tag{3.38a}$$

If the parameters in the above equations are unavailable, as a first order approximation,

$$\Delta S_{\text{vib}} \approx \Delta S_{\text{m}} - R. \tag{3.38b}$$

The maximum ν_s at T_m is estimated most simply from the Lindemann relation,

$$\nu_s = C_L(T_m/M_w V^{2/3})^{1/2} \tag{3.39}$$

where M_w is the molecular weight, V is the atomic volume, and the constant C_L is $2.06\times10^{12}\text{kg}^{1/2}\cdot\text{m}\cdot\text{s}^{-1}\cdot\text{K}^{-1/2}$.

In addition to Eq. (3.39), several other relations can also be utilized,

$$\nu_s = kT_m^{1/2}/hA'(2n^2 + 1), \tag{3.40a}$$

$$\nu_s = (C_1 k/h)(A'V^{2/3}\alpha)^{1/2}, \tag{3.40b}$$

$$\nu_s = C_2 k(Z/2)^{1/2}/(h\rho_a^{1/3}V^{1/3}). \tag{3.40c}$$

Here ρ_a is the coefficient of the density of the atomic packing as a fraction of one, $C_1 = 19.3\text{K}^{7/4}\cdot\text{m}$, $C_2 = 5.6 \times 10^3\text{K}\cdot\text{m}^{-1}$, and A' is a material constant. Equations (3.40a) to (3.40c) are essentially equivalent. They may be used, regardless of the availability and reliability of corresponding experimental data.

Determining ν_L is a more complicated matter. Since the validity of approximating the collective motion in a melt as primarily a vibrational motion is supported by both theories and experiments, that there is an abrupt appearance of diffusion degrees of freedom at the time of melting is obvious. However, the relative number of these freedom degrees does not exceed 3% for a group of metals. In this connection, ν_L becomes particularly significant, which reflects the dynamics of the vibrational motion of particles in the liquid phase. ν_L in molten semiconductors through the dynamic viscosity η_v is established by

$$\nu_L = (3/4)\eta_v(N_A^2/\rho M_w^2)^{1/3} \tag{3.41}$$

where ρ is the density of the melt, N_A is Avogadro constant. Substituting the values of ν_s and ν_L at T_m (Eqs. (3.39) and (3.41), respectively) into Mott's formula (3.28), we find

$$\Delta S_{\text{vib}} = 3R\ln\frac{4}{3\eta_v}\frac{C(T_m M_w)^{1/2}}{(V N_A)^{2/3}}. \tag{3.42}$$

Note that ν_s can also be obtained from Eq. (3.40) when the corresponding experimental data are available.

Table 3.3 lists ΔS_{vib} values calculated from Eq. (3.42) for some basic semiconductors. ΔS_{vib} values are not only comparable to ΔS_{pos}, but also (frequently) greater than ΔS_{pos} ones. Thus, ΔS_{vib} during the melting plays a substantial role in semiconductors, especially in cases where the melting is accompanied by changes of atomic structures. For organic crystals, ΔV on melting is small and ΔS_{pos} is thus negligible as a first order approximation.

Table 3.3 ν_s, ν_L and ΔS_{vib} values of certain semiconductors at T_m

Substance	$\nu_s \cdot$ 10^{-12} $/s^{-1}$	$\nu_L \cdot$ 10^{-12} $/s^{-1}$	ΔS_{vib} /(J· mol^{-1} $\cdot K^{-1})$	Substance	$\nu_s \cdot$ 10^{-12} $/s^{-1}$	$\nu_L \cdot$ 10^{-12} $/s^{-1}$	ΔS_{vib} /(J· mol^{-1} $\cdot K^{-1})$
Sb	2.08	1.7	5.02	Bi	1.4	1.2	3.76
Si	7.0	5.35	6.69	Ge	2.29	1.9	4.6
GeTe	4.2	2.9	9.07	SnTe	2.8	2.62	0.96
PbTe	2.4	1.5	11.7	PbSe	2.68	1.7	10.45
PbS	3.12	2.09	9.91	GaAs	6.51	3.45	11.20
InAs	5.25	1.43	21.03	AlSb	7.35	2.17	19.35
GaSb	5.67	3.22	10.07	InSb	4.36	2.62	12.75

When one or more solid-state phase transitions of some organic crystals closely precede the melting, the corresponding ΔS_m values are reduced [8]. Herein, the cumulative entropy of fusion ΔS_m^c should be introduced, which is defined as the summation of all entropy changes at all transition temperatures and T_m. Thus,

$$\Delta S_{vib} \approx \Delta S_m^c. \tag{3.43}$$

An additional important equation is the determination of Θ_D of solids using the ultrasound propagation velocity v_u, which was derived from the approximation of an isotropic continuum,

$$\Theta_D = \frac{2h_P}{\pi k} \left(\frac{3N}{4\pi V_A} \right)^{1/3} v_u. \tag{3.44}$$

Taking account of the premises underlying the derivation of Eq. (3.43) and the fact that Eq. (3.43) for cubic crystals agrees well with Θ_D data found in other ways (e.g. from elastic constants or thermal expansion), Eq. (3.43) may be used to calculate Θ_D of the liquid phase. Furthermore, as pointed out by Frenkel in his day, the approximation of an elastic continuum for liquids is even more systematic than for crystals, since in the latter case there will unavoidably be manifestations of anisotropy, even for highly symmetric (in particular) cubic crystals, while liquid is ideally isotropic.

3.2.3 Electronic Component of Melting Entropy [5]

As mentioned above, the idea of a ΔS_{el} follows from an analysis of the periodic law of ΔS_m (Fig. 3.5) and from the set of experimental data (primarily on electrical properties: the electrical conductivity, the thermal electromotive force emf, and the Hall effect, which reflect changes in the nature of the interatomic bonds during melting of a solid). This component essentially reflects the role of changes in the electronic subsystem due to a melting process.

A quantitative calculation of ΔS_{el} for several semiconductors was carried out on the basis of an analysis of thermoelectric effects at the solid-liquid in-

terface. Classically, an applied temperature difference causes charged carriers in materials, no matter whether they are electrons (negative charges) or holes (positive charges), to diffuse from the hot side to the cold side, similar to a gas that expands when heated. Mobile charged carriers migrating to the cold side leave behind their oppositely charged and immobile nuclei on the hot side, which give rise to a thermoelectric voltage. Thermoelectric power of a material is a measure of the magnitude of an induced thermoelectric voltage in response to a temperature difference across that material.

Typically metals have small thermoelectric powers because they have half-filled bands. Electrons and holes both contribute to the induced thermoelectric voltage, thus canceling each other's contribution to that voltage and making it small. By contrast, semiconductors can be doped with an excess amount of electrons or holes and thus can have large positive or negative values of the thermoelectric power depending on the charge of the excess carriers. The sign of the thermoelectric power can determine which charged carriers dominate the electric transport in both metals and semiconductors. The thermoelectric power also measures the entropy per charge carrier in the material. Superconductors have zero thermoelectric power since the charged carriers carry no entropy. Equivalently, the thermoelectric power is zero because it is impossible to have a finite voltage across a superconductor.

Guided by the concept of the reversibility of thermoelectric effects, which is postulated in the thermodynamics of irreversible processes, investigators established a relationship between ΔS_{m} and a change in the Seebeck coefficient in the melting transition. The amount of heat δQ evolved at a solid-liquid interface, which is crossed by a certain number ($\mathrm{d}n$) of electrons at T_{m} for an arbitrarily small current, is given by $\delta Q = \Delta S^* T_{\mathrm{m}} \mathrm{d}n$, or,

$$\Delta S^* = \delta Q/(T_{\mathrm{m}} \mathrm{d}n) \tag{3.45}$$

where ΔS^* is the change in entropy per electron. On the other hand, we have, $\delta Q = \Delta \phi e \mathrm{d}n$ where e is the electron charge, and $\Delta \phi$ is the Peltier heat, which is evolved at the interface due to a change in the Seebeck coefficient upon melting. $\Delta \phi / T = \Delta a_{\mathrm{emf}}$ with Δa_{emf} being the change in emf coefficient due to the melting. Comparison of these relations yields

$$\Delta S^* = e(a_{\mathrm{emf,s}} - a_{\mathrm{emf,L}}). \tag{3.46}$$

If we know the change in the carrier concentration upon melting, Δn, in light of Eq. (3.46),

$$\Delta S_{\mathrm{el}} = e\Delta n(a_{\mathrm{emf,s}} - a_{\mathrm{emf,L}}). \tag{3.47}$$

With determined ΔS_{el} values of Si, Ge, Sb, Bi, and several semiconductor compounds in terms of Eq. (3.31), Δn can be calculated by Eq. (3.47), which corresponds to measurements from the Hall-effect. This result is convincing evidence that changes in the electronic subsystem contribute substantially to ΔS_{m}, when a substance undergoes a semiconductor-metal melting. Since the mechanism for carrier scattering in the liquid phase has not been finally

resolved, and since calculations of the carrier concentration from measurements of the Hall coefficient are not completely rigorous, Eq. (3.47) is thus meaningful.

ΔS_{el} can also be calculated by a purely thermodynamic method. The general expression for ΔS_m with covalent–metallic interatomic binding is read as

$$\Delta S_m = f_c \Delta S_{met} + \Delta S_{cov} \qquad (3.48)$$

where subscripts "met" and "cov" denote typical metals (e.g., Cs) and purely covalent crystals (e.g., diamond), and f_c is the number of free electrons in a real crystal at its T_m, divided by the total number of electrons. f_c has been determined by

$$f_c = \exp(-E_g/2kT) \qquad (3.49)$$

where E_g is the band gap width at T_m. Assuming that all the excess entropy of melting for a purely covalent crystal over that of a good metallic crystal is determined by the difference $\Delta S_{cov} - \Delta S_{met}$, Chakraverty [9] suggested calculating it from the Boltzmann equation incorporating the change in the number of bound electrons,

$$\Delta S_{cov} - \Delta S_{met} = k \ln \frac{(4N)!}{[(2N)!]^2}. \qquad (3.50)$$

A covalent crystal is regarded as a solid having $4N$ electrons, where N is the number of atoms in the crystal. The melting of such a crystal is accompanied by a "depairing" of $2N$ electron pairs and the complete liberation of the electrons. Calculation from Eq. (3.50) yields a value of 23.07 J·mol^{-1}·K^{-1}, in satisfactory agreement with the difference between ΔS_m of diamond and ΔS_m of cesium: 31.35–7.52 = 23.83 J·mol^{-1}·K^{-1}. A closer look reveals that this difference is essentially the maximal possible ΔS_{el}, which is an obvious characteristic of diamond. A graphic illustration of the conclusion of Chakraverty shows that electron delocalization plays a decisive role in ΔS_m. The corresponding relationship is shown in Chakraverty's plot of ΔS_m versus the fraction of electrons in the crystal f_c for several simple solids, which is localized at T_m (Fig. 3.7).

We see an inverse proportionality. As f_c in the solid phase increases, the possible destruction of homeopolar bonds in the course of melting becomes progressively less significant for ΔS_m. Clearly not conforming to this behavior is Se. This circumstance indicates that the nature of the interatomic bond remains the same as this substance goes into the liquid phase. Thus, there is essentially no delocalization of electrons when Se melts. This effect was used to calculate the number of electrons in the liquid phase. Taking account of φ_c in the melt of semiconductors, which goes into a metallic state upon melting, ΔS_{el} can be determined by

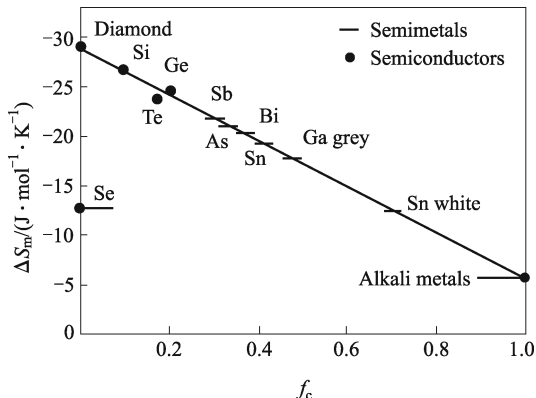$$\Delta S_{el} = k \ln \frac{[4N(1 - \varphi_c)(1 - f_c)]!}{\{[2N(1 - \varphi_c)(1 - f_c)]!\}^2}. \qquad (3.51)$$

Fig. 3.7 ΔS_m of semiconductors and of semimetals versus the change in the relative number of bound electrons at a melting transition.

ΔS_{el} values of five substances in terms of Eq. (3.51) are shown in Fig.3.8 as a function of the relative number of paired electrons, which become free in the molten state. The origin of coordinates here corresponds to an ideal metal, with $f_c = 1$ and $\Delta S_{el} = 0$. The uppermost point on this plot is the largest possible ΔS_{el}, characteristic of a hypothetical covalent crystal. Diamond can apparently be regarded as such a substance. The data of the five semi-conductors of Si, Ge, AlSb, GaSb, and InSb conform almost perfectly to the straight line connecting these two extreme points.

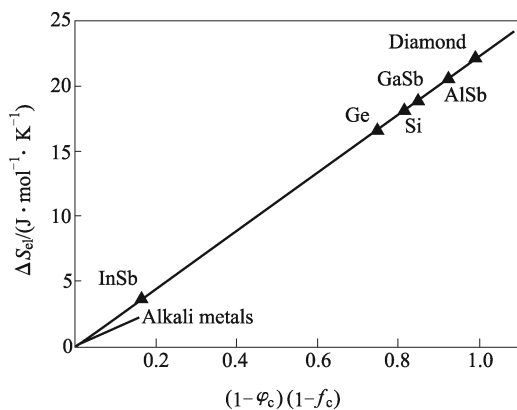**Fig. 3.8** ΔS_{el} of certain semiconductors versus the relative number of electrons which are delocalized at the time of melting.

All the approaches discussed above ΔS_{el} values produce similar results. The proposition that there is a significant ΔS_{el} passing from melting in a semiconductor-metal fashion can be thus regarded as a demonstrated fact: physical reality.

Let us look at yet another approach for calculating ΔS_{el}. This approach is based on the argument that a semiconductor–metal transition observed during the melting of the most important semiconductors forces us to switch from MB statistics to FD statistics in describing the behavior of the electrons in the liquid phase.

We now examine the entropy of a closed, equilibrium system, which can be written as $S = R \ln \Omega$. The increment in entropy due to the change in the carrier energy spectrum upon melting can thus be described by

$$\Delta S_{\text{el}} = S_{\text{el}}^{(\text{L})} - S_{\text{el}}^{(\text{s})} = R \ln(\Omega_{\text{L}}/\Omega_{\text{s}}). \qquad (3.52)$$

For a metallic melt, we write the density of states in the form for a system of a degenerate electron gas,

$$\Omega_{\text{el}}(\varepsilon) = (2\pi/h_{\text{P}}^2)(2m)^{3/2}\sqrt{\varepsilon_{\text{e}}}. \qquad (3.53)$$

Here ε_{e} is the energy of the electron. The density of states for an electron gas in a crystal in the premelting region can be written in a way, which reflects the circumstance that a semiconductor at such temperature behaves as if it had an intrinsic conductivity,

$$\Omega_{\text{s}}(\varepsilon_{\text{n}'}, \varepsilon_{\text{p}}) = [\Omega(\varepsilon_{\text{n}'})\Omega(\varepsilon_{\text{p}})]^{1/2} \qquad (3.54)$$

where $\Omega(\varepsilon_{\text{n}'})$ and $\Omega(\varepsilon_{\text{p}})$ are the densities of one-particle states for electrons and holes, respectively.

According to Eq. (3.53), $\Omega(\varepsilon_{\text{n}'}) = \dfrac{\sqrt{2}m_{\text{n}}^{*3/2}}{2\pi^2 h_{\text{P}}^3}\sqrt{\varepsilon_{\text{n}'}}$ and $\Omega(\varepsilon_{\text{p}}) = \dfrac{\sqrt{2}m_{\text{p}}^{*3/2}}{2\pi^2 h^3}$ $\sqrt{\varepsilon_{\text{p}}}$ where m_{n}^* and m_{p}^* are the effective masses, and $\varepsilon_{\text{n}'}$ and ε_{p} are the kinetic energy of the electrons and holes, respectively. Using Eqs. (3.52)–(3.54) and the above equations, there is

$$\Delta S_{\text{el}} = \frac{R}{2}\left[\ln\left(\frac{m_{\text{n}}^* m_{\text{p}}^*}{m^2}\right)^{-3/2} + \ln\frac{\varepsilon_{\text{e}}}{\sqrt{\varepsilon_{\text{n}'}\varepsilon_{\text{p}}}}\right]. \qquad (3.55)$$

The total energy of the electrons and holes in an intrinsic semiconductor with an E_g can be written as

$$\varepsilon = 2\int_0^\infty \varepsilon f_0(\varepsilon)\Omega(\varepsilon)\mathrm{d}\varepsilon + 2\int_0^\infty (\varepsilon' + E_g)f_0(\varepsilon')\Omega(\varepsilon')\mathrm{d}\varepsilon' \qquad (3.56)$$

where the first integral corresponds to electrons, and the second to holes. Replacing $f_0(\varepsilon)$ and $f_0(\varepsilon')$ by the corresponding distribution functions, and replacing $\Omega(\varepsilon)$ and $\Omega(\varepsilon')$ by the above mentioned equations, there is

$$\varepsilon = \frac{\sqrt{2}}{\pi^2}\frac{m_{\text{n}}^{*3/2}}{h^3}\exp\frac{\mu}{kT}\int_0^\infty \exp\left(-\frac{\varepsilon}{kT}\right)\varepsilon^{3/2}\mathrm{d}\varepsilon +$$
$$\frac{\sqrt{2}}{\pi^2}\frac{m_{\text{p}}^{*3/2}}{h^3}\exp\left(-\frac{\mu}{kT}\right)\exp\left(-\frac{E_g}{kT}\right)\int_0^\infty \exp\left(-\frac{\varepsilon'}{kT}\right) \times$$
$$(\varepsilon' + \Delta E)\mathrm{d}\varepsilon'. \qquad (3.57)$$

Using the value of the chemical potential of an electron for a semiconductor,

$$\mu = -\frac{E_g}{2} + \frac{3}{4}kT \ln \frac{m_p^*}{m_n^*}, \tag{3.58}$$

and integrating Eq. (3.57), there is

$$\varepsilon = \frac{(2\pi\sqrt{m_n^* m_p^*}kT)^{3/2}}{4\pi h^3}(3kT + \Delta E)\exp\left(-\frac{\Delta E}{2kT}\right) = \frac{3}{2}kTn + \frac{n}{2}(3kT + 2\Delta E). \tag{3.59}$$

In the one-particle approximation, we have

$$\varepsilon_{n'} = 3kT/2, \tag{3.60}$$

and

$$\varepsilon_p = (3kT + \Delta E)/2. \tag{3.61}$$

In the liquid state, $\varepsilon_{n'}$ can be found as the energy a degenerate electron gas (i.e., introducing an FD distribution),

$$\varepsilon_e = \frac{h_P^2}{2m_L^*}\left(\frac{3n_i}{8\pi}\right)^{2/3}. \tag{3.62}$$

An analysis of Eq. (3.55) led us to conclude that a calculation of ΔS_{el} requires knowledge of not only certain physical constants of a crystal, but also the concentration of free carriers in the melt. The latter can be determined from measurements of the Hall coefficient. Accordingly, some precise experimental studies were carried out for the temperature dependence of the Hall coefficients of Ge, Si and III-Sb compounds in the solid and liquid states with error being less than 4%. The abrupt change observed in the Hall coefficient at T_m corresponds to a metallization of the bonds of these substances with melting.

The so calculated ΔS_{el} values of some substances are shown in the last column of Table 3.4 while ΔS_{el} values obtained by other methods are also shown, based on measurements of the thermal emf at T_m ($\Delta S_{el}(I)$), the difference between ΔS_m and the sum of ΔS_{vib} and ΔS_{pos} ($\Delta S_{el}(II)$), and a calculation of the change in the configurational entropy of the binding electrons ($\Delta S_{el}(III)$). The obtained results are similar to errors within 10%.

Table 3.4 ΔS_{el} of Ge, Si, and III-Sb compounds calculated in various ways. The meanings in parentheses for ΔS_{el} see the text

Substance	Entropy units			
	$\Delta S_{el}(I)$	$\Delta S_{el}(II)$	$\Delta S_{el}(III)$	$\Delta S_{el}(IV)$
Ge	21.32	20.06	16.72	20.48
Si	15.05	21.32	19.23	15.05
AlSb	14.21	–	20.9	11.29
GaSb	18.81	12.96	18.81	18.81
InSb	21.74	11.29	15.88	22.99

Note also that this calculation has disregarded the possibility of a temperature dependence of the effective masses of the density of states. Accordingly, this calculation qualifies as only a first approximation.

From data on ΔS_{el}, we can solve the inverse problem, i.e., to calculate the effective masses of the density of states in the crystal and the melt near T_m. Such calculations would make it possible to draw certain conclusions about a model for describing the electronic states in molten semiconductors.

3.3 Nanothermodynamics

In the last decade, we have seen the explosive development of a new scientific field, now commonly known as nanoscience [10]. Nanoscience could be defined as the activity aiming at the understanding of natural laws of matter at a nanoscale level (say, $1-100$ nm). Nanomaterials are thus intermediate between single atoms (molecules) and bulk matters. This result in the so-called specific and smooth size effects due to the larger surface-to-volume ratio of nanomaterials than that of their bulky counterparts [11]. The former is responsible for the existence of "magic numbers" and related irregular variation of properties in clusters, whereas the latter pertains to nanostructures in the size domain between clusters and bulk systems [12]. It has also been found that the electronic structure of small particles is generally very discrete and not overlapping as the case with bulk materials, i.e. quantum effect occurs. Two aspects of nanomaterials above render them fundamentally different in their behavior from those of their constituent parts (either atoms or molecules) and from those of macroscopic pieces of matters [11]. One particular phenomenon, size-dependent melting point depression, occurs when the particle size is of the order of nanometers, as first demonstrated by Takagi [13] by means of transmission electron microscope (TEM) observation. Indeed, depending on the size, metallic, semiconductor, and organic nanocrystals with a clean surface all melt below the bulk melting point $T_m(\infty)$. For example, the melting point $T_m(r)$ of Au nanoparticles can be 300 K lower than its $T_m(\infty)$ [14] where r denotes the size of low dimensional materials. Consequently, nanomaterials possess direct and potentially technological implications related to the thin film preparation and the thermal stability of the nanosized materials and devices.

As a major goal in materials physics and chemistry, to quantify the size dependent changes associated with the nanocrystals, a reasonable thermodynamic model in terms of experimentally measurable physical parameters is clearly indispensable. The classical thermodynamics on macroscopic systems describes adequately the macroscopic behavior of bulk systems with the change of macroscopic parameters where the astrophysical objects and small systems at the nanometer scale are excluded. However, the basic thermodynamic relationships of a macroscopic system (such as Eqs. (1.35) to (1.38))

with a statistic basis are only valid for materials being at least larger than submicron size while the parameter "size" is actually a constant of bulk [12].

Is thermodynamics applicable to nanosystems? The answer is *yes* because the thermodynamic limit has not been fulfilled and Gibbs free energy contains more contributions. Since a nanosystem has an extra degree of freedom, size, the study of equilibrium nanosystems requires modification of macroscopic thermodynamics. This subject appropriately is called nanothermodynamics, which has the potential to become an important contributor to nanoscience and technology. It is noteworthy that, in the context of some modern experimental techniques such as the atomic force microscopy, the thermodynamic method is equally promising as a theoretical and empirical description of the experimentally investigated nanosystems. Indeed in many cases, experimental data on nanoparticle properties are rather scanty and contradictory since experimental arrangements can affect measuring results when the particle is not entirely rigid. Thus, thermodynamic consideration on nanoscale becomes an urgent task due to the requirement of the development of nanoscience and nanotechnology.

There are recently three kinds of fundamental approaches to open up the nanothermodynamics, which are based on the fluctuations of the temperature, the Tsallis' entropy, and the Laplace-Young equation in small systems. The first one is a generalized thermodynamic model dealing with nanosystems, which was first studied by Hill [15] in 1961–1964, where only the first law was considered. The second one is on the basis of the Tsallis' generalization of the ordinary Boltzmann-Gibbs thermo-statistics by relaxing the additive properties of the thermodynamic quantities (the entropy, in particular) to include non-extensivity of nanosystems [16, 17]. The last one considers the size-induced internal pressure $P_{in} = 2f_{sv}/r$, where f_{sv} denotes the surface stress of solid, which may also be extended to a general case for the pressure effect on properties of bulk materials since any pressure source should have the same effect on materials properties [18]. These approaches developed from various perspectives can contribute significantly to understanding of properties of nanosystems. However, a consistent insight and a quantitative and unified model on nanothermodynamics are still highly desirable. This task can be performed by deeply analyzing the size dependence of a typical known process of thermodynamic phase equilibrium [12], such as melting, which is so obvious in nature that even the ancient speculative physicists might expect to discuss it and stimulated the development of classical thermodynamics in the nineteenth century [19]. Before the detailed consideration on size dependence, it is necessary to introduce firstly the most general bulk melting.

3.4 Melting Thermodynamics

3.4.1 A Melting Criterion [20]

An alternative for studying the melting transition was carried out in 1910 by Lindemann for single component crystals with a kinetic consideration: Solids liquefy when the amplitude of atomic thermal vibrations exceeds a fraction of the interatomic spacing, which is much simpler than the usual phase equilibrium consideration based on the thermodynamics and will be used as the base of the size-dependent melting model. According to the Lindemann model, at the melting for a given bulk crystal, the typical vibrational displacement $\sigma(\infty)$, or the root-mean-square (rms) average amplitude of atomic thermal vibration, should be some fixed fraction of the atomic or molecular diameter (the nearest atomic or molecular spacing) h, or $\sigma(\infty)/h = 1/2$. This implies that direct collisions between the atoms constituting the lattice would become possible, leading to the lattice demise. Lindemann's quantitative model made use of Einstein's explanation of the low-temperature specific heats of solids, which proposed that the atoms vibrate as quantized harmonic oscillators and the corresponding $\Theta_E(\infty)$ is proportional to $\nu_E(\infty)$ by $h_P\nu_E(\infty) = k\Theta_E(\infty)$. Einstein's theory was published in 1907, and its adoption by Lindemann appears to be the first application of quantum theory to condensed matter after Einstein's own paper.

The theory is quite simple, which averages thermal vibrational energy to the temperature by the equipartition relation [19],

$$m[(2\pi\nu_E(\infty)]^2\sigma^2(\infty) = kT \tag{3.63}$$

where m is the atomic mass. The modern form of Lindemann's criterion has been given by, $\Theta_D(\infty) = c[T_m(\infty)/(M_wV_s^{2/3})]^{1/2}$, where c denotes a fraction of the nearest-neighbor spacing at which melting occurs. Based on the above equation, $\Theta_D^2(\infty) \propto T_m(\infty)$. Now it is known that c varies slightly with crystal structure: It is 0.13 for an fcc crystal and 0.18 for a bcc crystal [21]. This difference is partly due to the change of h, which depends on CN of the specific structure. The h reduces with CN [22]. In order to eliminate or reduce this difference among distinct lattices or CN s, h can not be determined by h itself, but by atomic volume that depends little on the lattice structure, and hence c is almost lattice-independent [23].

There are also other classic kinetic models for melting. Grüneisen correlates $T_m(\infty)$ with the reciprocal of the linear thermal expansion coefficient [24], while Born relates $T_m(\infty)$ to the absence of elastic resistance against shearing stress [25]. Both of the models share a similar physical nature of Lindemann's one [26] and thus will not be further discussed.

However, the Lindemann's model has its limitation. The model is based on harmonic forces, whereas melting must involve bond breaking or loosening

[22, 27]. The model, which depends on properties of the solid phase alone, cannot predict T_m convincingly. In fact, Lindemann did not intend to provide a "melting criterion" at all in his original paper, but rather pointed out the possibility to estimate the frequency of oscillators to support Einstein's model for explaining C_P drop of solids at low T.

Melting may be due to the intrinsic disorder created by thermal excitations, such as vibrational modes, point defects such as vacancies and interstitials, dislocations, and, in the case of molecular crystals, orientational defects [28, 29]. Each type has a characteristic excitation energy dictating an exponential increase of the energy of solid with T. This leads also to lowering of T_m, where solid and liquid have the same Gibbs free energy value. In addition, as we now understand, a proper analysis of dynamical melting should proceed with reference to process at the solid-liquid interface.

Despite the unsolved problems for the modeling of melting, Lindemann's criterion has provided the most bases for predicting the melting behavior as it has been experimentally confirmed. In the following, the criterion will be used as a starting point to model the size dependence of the melting. There are many models for other types of size-dependent phase transition temperatures, such as magnetic transitions, various phase transition models will be discussed further in Chapter 5.

3.4.2 Existing Models for Size-dependent Melting of Crystals [12]

$T_m(r)$ functions have been experimentally measured since 1954 by Takagi. A linear relationship of $T_m(r) \sim 1/r$ is usually modeled, which is simply deduced in terms of a ratio of the surface volume to the entire volume $\zeta = \Delta V/V$. Contrary to observed depression in T_m for substrate-supported small crystals with a relatively free surface, it has been observed that small crystals embedded in the matrix can melt below $T_m(\infty)$ in one matrix (undercooling), while in another matrix the same nanocrystals can be greatly superheated above $T_m(\infty)$ (superheating). The apparent contradictory experimental observations require further definite experiments as well as a clear physical understanding of the melting phenomena of nanocrystals. The correspondent size dependence is function of r and dimension d. In addition, since 1940's, surface melting below $T_m(\infty)$ with a thickness of several atomic layers of a solid is widely studied, which is a process proceeding under the condition of $\gamma_{sv} > \gamma_{sL} + \gamma_{Lv}$ where γ is interface energy with subscripts sv, sL, and Lv being the corresponding interfaces. Note that s, v, and L denote solid, vapor and liquid, respectively. The physical nature of the surface melting is that although $\Delta G(T < T_m) = G_l(T < T_m) - G_s(T < T_m) > 0$, the condition of $\gamma_{sv} > \gamma_{sL} + \gamma_{Lv}$ leads to formation of a liquid surface layer, which neutralizes the positive $\Delta G(T < T_m)$. This effect has naturally been enhanced due to the increase of ζ.

The earliest thermodynamic consideration for $T_m(r)$ function was derived by Pawlow in 1909 where the relative change from $T_m(\infty)$ was taken into account, which was even one year earlier than the modeling of $T_m(\infty)$ by Lindemann in 1910 and much early than the experimental result in 1954, which has the following form:

$$T_m(r)/T_m(\infty) = 1 - 2V_s[\gamma_{sv} - \gamma_{Lv}(\rho_s/\rho_L)^{2/3}]/(r\Delta H_m) \qquad (3.64)$$

where ρ denotes mass density. For the most cubic metals,

$$\gamma_{sv} - \gamma_{Lv} \approx \gamma_{sL} \qquad (3.65)$$

with $\rho_s \approx \rho_L$ and thus $(\rho_s/\rho_L)^{2/3} \approx 1$ and in terms of Eq. (3.65), Eq. (3.64) can be expressed as

$$T_m(r)/T_m(\infty) \approx 1 - 2V_s\gamma_{sL}/(r\Delta H_m). \qquad (3.66)$$

Actually, Eq. (3.66) is identical to the Gibbs-Thomson equation,

$$T_m(r)/T_m(\infty) \approx 1 - (1/r_1 + 1/r_2)V_s\gamma_{sL}/\Delta H_m \qquad (3.67)$$

where r_1 and r_2 are principal radii of curvature of the interface that bound a solid. For a spherical particle, $1/r_1 = 1/r_2 = 1/r$, Eq. (3.67) = Eq. (3.66).

Before the most experimental results were present in 1990's, Couchman and Jesser quantitatively modeled $T_m(r)$ in 1977,

$$T_m(r)/T_m(\infty) = 1 - [3(V_s + V_L)(\gamma_{sM} - \gamma_{LM})/2r - \Delta U]/\Delta H_m \qquad (3.68)$$

where subscript "M" denotes matrix, ΔU shows energy density difference between the nanocrystal and the nanoliquid. If ΔU is negligible, $T_m(r)$ can either higher or lower than $T_m(\infty)$, depending on the sign of $\gamma_{sM} - \gamma_{LM}$, which is closely related to the nature of the interface. Generally, $\gamma_{LM} - \gamma_{sM} = \gamma_{sL}\cos\theta$, where θ is the contact angle between a particle and the matrix ranging from $0°$ to $180°$. For a particle wetted by the matrix, $0° \leqslant \theta < 90°$ and $0 < \gamma_{LM} - \gamma_{sM} \leqslant \gamma_{sL}$ where the matrix/particle interface should be coherent or semi-coherent. Consequently, superheating happens and $T_m(r)$ increases with decreasing r. For a nanocrystal with $\theta \geqslant 90°$, $\gamma_{LM} - \gamma_{sM} \leqslant 0$ and undercooling occurs.

Superheating has also been interpreted through various pressure effects, such as a capillary effect due to the decreasing of r, the differential thermal expansion between the matrix and the nanocrystals, and the effect due to volume change during the melting. However, these models underestimate experimental observations since they can only predict a very small superheating up to 6 K. The reason is that they have only considered mechanical effects while the dominant chemical interfacial effect is neglected.

If the surface-melting phenomenon is taken into account, $T_m(r)$ function has different expressions,

$$T_m(r)/T_m(\infty) = 1 - 2V_s[\gamma_{sL}/(1 - t_s/r) - \gamma_{Lv}(1 - \rho_s/\rho_L)]/(r\Delta H_m), \quad (3.69)$$

$$\frac{T_m(r)}{T_m(\infty)} = 1 - \frac{2V_s\gamma_{sL}[1 - \exp(-t_s/\xi)]}{rH_m(1 - t_s/r)}$$

$$- \frac{V_s[(\gamma_{sv} - \gamma_{Lv}) - \gamma_{sL}(1 - t_s/r)^2]\exp(-t_s/\xi)}{\xi H_m(1 - t_s/r)^2}, \quad (3.70)$$

$$T_m(r)/T_m(\infty) = 1 - 2V_s\gamma_{sL}/[r\Delta H_m(1 - t_s/r)] \quad (3.71)$$

where t_s is surface melting layer thickness and ξ in Eq. (3.70) shows the correlation length of solid-liquid interface. Note that when $t_s \ll r$, $t_s \gg \xi$, $\rho_s \approx \rho_L$, and in terms of Eq. (3.65), Eqs. (3.69)–(3.71) have essentially predicted the same trend as given by Eq. (3.66). This result implies that when r is large enough, the surface-melting phenomenon does not change the melting behavior of the nanocrystals although it indeed exists. However, when t_s is comparable with r being in the size range of $r < 5$ nm ($\zeta > 10\%$), Eqs. (3.69)–(3.71) indicate a stronger melting point depression than Eq. (3.66) does. Note that once Eq. (3.66) comes into play, the surface-melting phenomenon disappears.

Another way to calculate $T_m(r)$ was made by Semenchenko who has considered melting of a small solid particle embedded in the corresponding liquid, which has an exponential form,

$$T_m(r)/T_m(\infty) = \exp[-2V_s\gamma_{sL}/(r\Delta H_m)]. \quad (3.72)$$

Equation (3.72) almost gives the same $T_m(r)$ value of Eqs. (3.69)–(3.71) in the full size range of nanocrystals. As r increases, with a mathematical relation of $\exp(-x) \approx 1 - x$ is valid where x is small, Eq. (3.72) $\approx$ Eq. (3.66). Since some variables in Eqs. (3.69)–(3.71) come from fitting experimental results, Eq. (3.72) is more convenient to predict $T_m(r)$ when $r <5$ nm with the same level of accuracy.

In the above equations, γ_{sL} value, as an important thermodynamic amount to determine $T_m(r)$ function, has been deduced recently according to Gibbs-Thomson equation,

$$\gamma_{sL} = 2h\Delta S_{vib}(\infty)\Delta H_m/(3V_sR). \quad (3.73)$$

Equation (3.73) is capable of predicting γ_{sL} values quite accurately for element and compound crystals when the crystalline anisotropy is negligible, Substituting Eq. (3.73) into Eq. (3.66), one gets

$$T_m(r)/T_m(\infty) = 1 - 4h\Delta S_{vib}(\infty)/(3Rr). \quad (3.74)$$

Note that although any surface reconstruction decreases γ_{sv}, such as roughing and surface melting, which seems to be neglected in Eq. (3.74), $\Delta S_{vib}(\infty)$

itself indeed has included the surface relaxation phenomenon. This is because $\Delta S_{\text{vib}}(\infty)$ value measured at $T_{\text{m}}(\infty)$ has included various surface relaxations since this has occurred in the corresponding solid. However, Eq. (3.74), or Eq. (3.66) still fails for correct description of $T_{\text{m}}(r)$ function of smaller nanocrystals where $\zeta > 20\%$.

In Eq. (3.74), there is a size limit of $r = (\alpha_r - 1)r_0$, at which $T_{\text{m}}(r) = 0$ K. If $r \leqslant (\alpha_r - 1)r_0$, $T_{\text{m}}(r) \leqslant 0$, which is strictly forbidden in physics. As indicated above, when $r < (5 \sim 10)r_0$, Eq. (3.66) or (3.74) is no longer valid. By contrast, Eqs. (3.69)–(3.72) can be applied to $(\alpha_r - 1)r_0 < r < (5 \sim 10)r_0$ due to the nonlinear parts between $T_{\text{m}}(r)$ and $1/r$ in these equations. Note also that r must be larger than $(\alpha_r - 1)r_0$ since $T_{\text{m}}(r)$ has to be larger than the Kauzmann temperature T_{K} where $\Delta S_{\text{m}}(r)$ is equal to zero. The related details will be considered in Sec. 4.6.

It is interesting that although ΔH_{m} function appears in the above equations, it disappears in Eq. (3.74) since it is included in $\Delta S_{\text{vib}}(\infty)$. Thus, the detailed form of ΔH_{m} is not of immediate concern. Based on an analogy with the liquid-drop model and empirical relations between the bulk cohesive energy $E_{\text{c}}(\infty)$, γ, and $T_{\text{m}}(\infty)$, $T_{\text{m}}(r)$ functions are determined as follows:

$$T_{\text{m}}(r)/T_{\text{m}}(\infty) = 1 - (c_2/r)(1 - \gamma_{\text{Ms}}/\gamma_{\text{sv}}) \tag{3.75}$$

where c_2 is a constant relating to atomic volume, $T_{\text{m}}(\infty)$ and γ_{sv}. Equation (3.75) is very similar to Eq. (3.68) and could describe both undercooling and superheating of nanocrystals. For the case of undercooling, $\gamma_{\text{Ms}} = 0$. When superheating occurs, $\gamma_{\text{Ms}}/\gamma_{\text{sv}} > 1$.

Sun et al. connects $T_{\text{m}}(r)$ function directly to the CN-imperfection effect on atomic cohesive energy of the lower coordinated atoms near the surface. It is suggested that the CN-imperfection causes the remaining bonds of the lower-coordinated atoms to contract spontaneously with an association of magnitude increase of the bond energy, i.e., bond-order-length-strength (BOLS) correlation, which contributes to E_{c} (the sum of bond energy ε over all coordinates of a specific atom with the coordination z, $E_{\text{c}} = z N_{\text{A}} \varepsilon/2$), and hence to G that determines the thermodynamic behavior of a system. The thermal energy required to loosen the bonds of the specific atom is a portion of E_{c}. Thus, $T_{\text{m}}(r) \propto E_{\text{c}}(r)$, which leads to

$$T_{\text{m}}(r)/T_{\text{m}}(\infty) = 1 + \sum_{i \leqslant 3} \beta_{ij}(z_{\text{ib}} c_{\text{i}}^{-m'} - 1) \tag{3.76}$$

where β_{ij} is the volume or number ratio of the i-th atomic layer to that of the entire crystal, $z_{\text{ib}} = z_{\text{i}}/z_{\text{b}}$ where z_{i} and z_{b} are the coordinates with and without CN imperfection, c_{i} shows CN-dependent reduction of bond length, and m' is a parameter varying with the bond nature. The model indicates that T_{m} change arises from the change of atomic cohesion of the under-coordinated atoms in the superfacial skins while the atoms in the core interior remain as they are in the bulk.

Moreover, the surface-phonon instability model suggests that $T_m(r)$ is a function of two bulk parameters: $T_m(\infty)$ and the energy of formation of intrinsic defects. The shape effect on $T_m(r)$ for polyhedral nanocrystals, which is in nature also related to ζ, is also considered and the corresponding shape factor is introduced.

In summary, all the above models predict the same linear relationship between $T_m(r)$ and $1/r$ due to the surface effect when r is large enough. However, as $\zeta > 10\%$, the dramatic drop of $T_m(r)$ is present because the energetic states of internal atoms also change, which has been considered by Eqs. (3.69)–(3.72) in different approaches although their considerations are not directly related to energetic state of atoms, but ζ. Since the superheating phenomenon was realized later than the undercooling one, the later models of Eqs. (3.68), (3.75), (3.76) attempted to determine both undercooling and superheating with also a similar linear relationship of $T_m(r) \sim 1/r$. The sign of the $1/r$ term is negative for undercooling but positive for superheating. Note that if the CN imperfection of the second surface layer is considered, Eq. (3.76) becomes a nonlinear function and could describe the melting behavior of smaller size of nanocrystals.

However, it is often that a single phenomenon corresponds to numerous models. A unified model dealing with not one, but all related phenomena, is required. This unification certainly brings out comprehension of interdependence of among different phase transitions, which is given in the next section where we will present a melting model of nanocrystals and give a systematical analysis of both modeling considerations and experimental observations in order to discover the mechanism for the melting transition in a thermodynamic approach.

3.4.3 Size-dependent Melting Thermodynamics of Crystals [12]

The following consideration is at the heart of various models based on Lindemann's criterion for $T_m(r)$ [30],

$$\sigma^2(r) = \sigma_{va}^2(r) + [\sigma_{sa}^2(r) - \sigma_{va}^2(r)]n_{sa}/n_{va} \qquad (3.77)$$

where the subscripts "sa" and "va" denote atoms/molecules at the surface and located within the particle, respectively. $n_{sa}/n_{va} = \zeta = (4\pi r^2 h)/[(4/3)\pi r^3 - 4\pi r^2 h] = r_0/(r - r_0)$ with $r_0 = 3h$ for a spherical or a quasi-spherical particle. Equation (3.77) states that the rms of the particle is the average of its "surface" and "bulk" values. For bulk crystals, atoms in the surface layers can oscillate with larger amplitude than atoms in the interior of the crystals, and the average amplitude of the whole crystal is independent of the size of the crystal. However, both $\sigma_{va}^2(r)$ and $\sigma_{sa}^2(r)$ are larger than the corresponding $\sigma_{va}^2(\infty)$ and $\sigma_{sa}^2(\infty)$. It is assumed that $\sigma_{sa}^2(r)/\sigma_{va}^2(r) = \sigma_{sa}^2(\infty)/\sigma_{va}^2(\infty) = \alpha_r$ is size-independent although $\sigma_{sa}^2(r)$ and $\sigma_{va}^2(r)$ are size-

dependent. Moreover, since the cooperative coupling between the surface and the interior atoms/molecules of small particles may be important, it is phenomenologically considered that the variation of $\sigma^2(r)$ is dependent on the value of $\sigma^2(r)$ itself. Thus, a change in σ^2 with ζ can be given by $\sigma^2(\zeta + \mathrm{d}\zeta) - \sigma^2(\zeta) = (\alpha_\mathrm{r} - 1)\sigma^2(\zeta)\mathrm{d}\zeta$ [30]. Integrating this equation yields

$$\sigma^2(r)/\sigma^2(\infty) = \exp[(\alpha_\mathrm{r} - 1)\zeta] = \exp\{(\alpha_\mathrm{r} - 1)/[(r/r_0) - 1]\} \qquad (3.78)$$

where r_0, at which all atoms/molecules are located on the surface, can be extended for different dimensions d with $d = 0$ for nanospheres, $d = 1$ for nanowires and $d = 2$ for thin films. For a nanosphere and a nanowire, r has the usual meaning of radius. For a thin film, r denotes its half thickness. r_0 is given by:(1) $r_0 = 3h$ for $d = 0$ since $4\pi r_0^2 h = 4\pi r_0^3/3$; (2) $r_0 = 2h$ for $d = 1$ since $2\pi r_0 h = \pi r_0^2$; and (3) $r_0 = h$ for $d = 2$ since $2h = 2r_0$. Note that for disk-like nanoparticle, its quasi-dimension has been defined as $d = 1$ since its ζ is between that of particles and that of thin films [31]. In short,

$$r_0 = c_1(3 - d)h. \qquad (3.79)$$

In Eq. (3.79), c_1 is added as an additional condition for different surface states. $c_1 = 1$ for nanocrystals with free surface. When the interface interaction between the nanocrystals and the corresponding substrate is weak, such as thin films deposited on inert substrates, the film/substrate interaction is van der Waals forces while the inner interactions within the thin films are strong chemical bonds, $c_1 = 1$ too. If this strength on the interface is comparable with that within films, c_1 varies somewhat. When these are similar, which is equal to the case that one of the two surfaces of the films disappears, $c_1 = 1/2$ is thus got (the side surfaces of the thin films are neglected due to the low thickness). For more complicated interfaces, c_1 may be considered case by case between $1/2$ and 1.

Since usually $T_\mathrm{m}(\infty) > \Theta_\mathrm{D}(\infty)$, the high temperature approximation can be utilized, $\sigma^2(r, T) = f(r)T$, where $f(r)$ is a T-independent but r-dependent function. Thus, at any T, $\sigma^2(r, T)/\sigma^2(\infty, T) = f(r)/f(\infty)$. Moreover, when $T = T_\mathrm{m}$, $f(r)/f(\infty) = \{\sigma^2[r, T_\mathrm{m}(r)]/h^2\}/\{\sigma^2[\infty, T_\mathrm{m}(\infty)]/h^2\} \cdot [T_\mathrm{m}(\infty)/T_\mathrm{m}(r)] = T_\mathrm{m}(\infty)/T_\mathrm{m}(r)$ in terms of Lindemann's criterion. In the above equation, h is assumed to be a size-independent constant, namely, $\Delta V_\mathrm{s} = V_\mathrm{s}(\infty) - V_\mathrm{s}(r) \approx 0$ or $\Delta h = h(\infty) - h(r) \approx 0$. It is known that $\Delta h/h = \Delta V_\mathrm{s}/(3V_\mathrm{s}) = 0.1\% - 2.5\%$ when $r < 10$ nm and it is negligible when $r > 10$ nm. Thus, even $r < 10$ nm, $[V_\mathrm{s}(r)/V_\mathrm{s}(\infty)]^{2/3} \approx 0.95 - 0.97$. Note also that $\Theta_\mathrm{D}(r)$ function can be obtained as a generalization of relationship, $\Theta_\mathrm{D}^2(\infty) \propto T_\mathrm{m}(\infty)$, i.e., $\Theta_\mathrm{D}^2(r)/\Theta_\mathrm{D}^2(\infty) = T_\mathrm{m}(r)/T_\mathrm{m}(\infty)$. According to Eq. (3.78),

$$T_\mathrm{m}(r)/T_\mathrm{m}(\infty) = \sigma^2(\infty)/\sigma^2(r) = \Theta_\mathrm{D}^2(r)/\Theta_\mathrm{D}^2(\infty)$$
$$= \exp\{-(\alpha_\mathrm{r} - 1)/[(r/r_0) - 1]\}. \qquad (3.80)$$

Based on Mott's expression for $\Delta S_\mathrm{vib}(\infty)$ of bulk crystals at $T_\mathrm{m}(\infty)$ [5, 32] and the above model, $\Delta S_\mathrm{vib}(r)$ of metallic crystals and α_r in Eq.

(3.80) could also be developed [33, 34]. $\Delta S_{\mathrm{vib}}(r)$ of nanocrystals can be obtained as a generalization of Eq. (3.42), i.e., $\Delta S_{\mathrm{vib}}(r)$ - $\Delta S_{\mathrm{vib}}(\infty) = (3R/2)\ln\{[T_{\mathrm{m}}(r)/T_{\mathrm{m}}(\infty)][C_{\mathrm{s}}(r)/C_{\mathrm{L}}(r)]^2/[C_{\mathrm{s}}(\infty)/C_{\mathrm{L}}(\infty)]^2\}$. Instead of treating $C_{\mathrm{L}}(r)$ and $C_{\mathrm{s}}(r)$ to be size-dependent, respectively, the ratio of $C_{\mathrm{L}}(r)/C_{\mathrm{s}}(r) \approx C_{\mathrm{L}}(\infty)/C_{\mathrm{s}}(\infty)$ is approximately taken as a size-independent value. Hence,

$$\Delta S_{\mathrm{vib}}(r) - \Delta S_{\mathrm{vib}}(\infty) = (3R/2)\ln\{[T_{\mathrm{m}}(r)/T_{\mathrm{m}}(\infty)]. \qquad (3.81)$$

Substituting Eq. (3.79) into Eq. (3.81), it reads

$$\Delta S_{\mathrm{vib}}(r) = \Delta S_{\mathrm{vib}}(\infty) - (3R/2)(\alpha_{\mathrm{r}} - 1)/[(r/r_0) - 1]. \qquad (3.82)$$

It is known that $\Delta S_{\mathrm{m}}(r)$ for metallic crystals is mainly vibrational in nature. Hence, although $\Delta S_{\mathrm{vib}}(r)$ represents only one of several contributions to $\Delta S_{\mathrm{m}}(r)$, one may suggest that $\Delta S_{\mathrm{m}}(r)$ follows the same size dependence as $\Delta S_{\mathrm{vib}}(r)$,

$$\Delta S_{\mathrm{m}}(r) = \Delta S_{\mathrm{m}}(\infty) - (3R/2)(\alpha_{\mathrm{r}} - 1)/[(r/r_0) - 1]. \qquad (3.83)$$

In Eq. (3.83), the smallest size of crystals is assumed to be $2r_0$ where a half of atoms of a crystal are located on the surface with $\zeta = 1$. $T_{\mathrm{m}}(2r_0) = T_{\mathrm{m}}(\infty)\exp(1-\alpha_{\mathrm{r}})$ where both have almost the same short range order and the structure difference between crystal and liquid is little. As a result, melting disappears, $\Delta S_{\mathrm{m}}(2r_0) = \Delta S_{\mathrm{vib}}(2r_0) = 0$ is thus assumed for the smallest nanocrystal, which leads to

$$\alpha_{\mathrm{r}} = 2\Delta S_{\mathrm{m}}(\infty)/(3R) + 1 = 2\Delta S_{\mathrm{vib}}(\infty)/(3R) + 1. \qquad (3.84)$$

Eliminating the parameter α_{r} from Eq. (3.83) by means of Eq. (3.84), one has

$$\Delta S_{\mathrm{m}}(r)/\Delta S_{\mathrm{m}}(\infty) = 1 - 1/(r/r_0 - 1). \qquad (3.85)$$

Equation (3.85) is remarkably simple and more importantly, free of any adjustable parameter. Equation (3.85) has been supported by the experimental results of Sn [35] and Al [36]. It is also utilized for organic nanocrystals due to their similar melting nature, i.e., $\Delta S_{\mathrm{m}}(r)$ of organic crystals are essentially contributed by a vibrational part [23]. However, since organic crystals are molecular ones, h or r_0 stated above must be newly defined. A simple generalization is that h is defined as the mean diameter of the organic molecule, which implies that a molecule in organic crystals takes a similar effect of an atom in metallic crystals. Hence, when a molecule is located on the surface of the organic crystal, the amplitude of the thermal vibration of the full molecule is larger than that of molecules within the crystal.

Since the shape of an organic molecule is usually not spherical, h as a mean diameter of a molecule is defined as $h = \dfrac{1}{3}\sum\limits_{i=1}^{3} h_i$ where h_i is the length of the molecule along three axis directions. For the organic molecules not

having any regular shapes, the direction of the longest size is defined as the x-axis and the shortest size is defined as another axial direction. Different choices of the axes only lead to little difference of h, which changes $T_m(r)$ and $S_m(r)$ functions little specially when r/h is large enough (for instance, usually $r > 2$ nm in experiments and $h < 0.5$ nm for most organic crystals).

After determination of h by consideration of the geometric shape based on the bond length and bond angle of organic molecules, $\Delta S_m(r)$ of organic nanocrystals may be calculated in terms of Eqs. (3.80) and (3.85). Figure 3.9 presents a comparison between the prediction of Eq. (3.85) and experimental results of four organic nanocrystals [37].
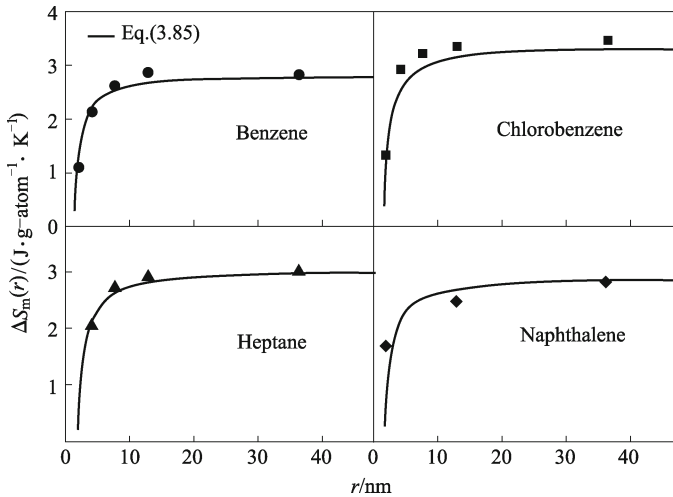

Fig. 3.9 $\Delta S_m(r)$ functions of benzene, chlorobenzene, heptane, and naphthalene. The lines are Eq. (3.85). ●, ■, ▲, and ◆ denote the experimental results of benzene, chlorobenzene, heptane, and naphthalene, respectively. $\Delta S_m(\infty)$ values of benzene, chlorobenzene, heptane, and naphthalene in J·g-atom^{-1}·K^{-1} are 2.842, 3.375, 3.042, and 2.920, respectively. r_0 is taken as $2h$ (for the calculations of h values, see ref. [23]). The corresponding r_0 values in nm are 0.7584, 0.8036, 0.9650, and 0.9024.

For nanocrystals embedded in a matrix with coherent or semi-coherent interfaces, it is expected that the msd value of interfacial atoms of nanocrystals $(\sigma_{ia}^2(r))$ falls between that of the interior atoms of nanocrystals $(\sigma_{va}^2(r))$ and that of the matrix $(\sigma_M^2(r))$, under the assumption that $\sigma_{ia}^2(r)$ of the interfacial atoms of the nanocrystals has an algebraic average value between $\sigma_{va}^2(r)$ of interior atoms and $\sigma_M^2(r)$ and combining the assumption of $\sigma_{va}^2(r) \approx \sigma^2(\infty)$, α_r is determined as

$$\alpha_r = \{[\sigma_M^2(r) + \sigma_{va}^2(r)]/2\}/\sigma_{va}^2(r) = [\sigma_M^2(r)/\sigma^2(\infty) + 1]/2. \qquad (3.86)$$

As stated above, the high-temperature approximation for $\sigma_M^2(T)$ at a T is utilized. Substituting $T = T_M(\infty)$ and $T = T_m(r)$ into Eq. (3.63), one gets

$\sigma_{\mathrm{M}}^2[T_{\mathrm{m}}(r)]/\sigma_{\mathrm{M}}^2[T_{\mathrm{M}}(\infty)] = T_{\mathrm{m}}(r)/T_{\mathrm{M}}(\infty)$. According to the Lindemann criterion, or $\sigma(\infty)/h = c, \sigma_{\mathrm{M}}(T_{\mathrm{M}}(\infty))/h_{\mathrm{M}} = \sigma_{\mathrm{m}}(\infty)/h$, where $\sigma_{\mathrm{M}}[T_{\mathrm{M}}(\infty)]$ denotes the rms displacements of atoms of the matrix at the corresponding T_{m}, and h_{M} shows atomic diameters of the matrix, $\sigma_{\mathrm{M}}^2[T_{\mathrm{M}}(\infty)] = (h_{\mathrm{M}}/h)^2\sigma_{\mathrm{m}}^2(\infty)$ or $\sigma_{\mathrm{M}}^2(T_{\mathrm{m}}(r))/\sigma_{\mathrm{m}}^2(\infty) = (h_{\mathrm{M}}/h)^2[T_{\mathrm{m}}(r)/T_{\mathrm{M}}(\infty)]$ and thus $\alpha_{\mathrm{r}} = \{(h_{\mathrm{M}}/h)^2 [T_{\mathrm{m}}(r)/T_{\mathrm{M}}(\infty)] + 1\}/2$ in terms of Eq. (3.86). Since the difference between $T_{\mathrm{m}}(r)/T_{\mathrm{M}}(r)$ and $T_{\mathrm{m}}(\infty)/T_{\mathrm{M}}(\infty)$ is little, α_{r} is a weak function of r. As a first order approximation, $T_{\mathrm{m}}(\infty)$ takes the place of $T_{\mathrm{m}}(r)$, or α_{r} takes its smallest value. Finally, it reads

$$\alpha_{\mathrm{r}} = \{[T_{\mathrm{m}}(\infty)/T_{\mathrm{M}}(\infty)](h_{\mathrm{M}}/h)^2 + 1\}/2. \qquad (3.87)$$

Substituting Eq. (3.87) into Eq. (3.80), the superheating of nanocrystals can be predicted by Eq. (3.80). As shown in Eq. (3.80), $T_{\mathrm{m}}(r)$ depends on r and α_{r}. Only when $\alpha_{\mathrm{r}} < 1$, which is related to the relative size of h and $T_{\mathrm{m}}(\infty)$ between the nanocrystals and the matrix, does $T_{\mathrm{m}}(r)/T_{\mathrm{m}}(\infty) > 1$ apply and $T_{\mathrm{m}}(r)$ increases as r decreases. Thus, necessary conditions for superheating of the nanocrystals embedded in the matrix are $T_{\mathrm{m}}(\infty)/T_{\mathrm{M}}(\infty) < 1$ and there are the coherent or semi-coherent interfaces between them. Another sufficient, but not necessary condition is that the atomic diameter of the matrix is smaller than that of the nanocrystals ($h_{\mathrm{M}}/h < 1$). For the superheating case, when $T_{\mathrm{m}}(\infty)/T_{\mathrm{M}}(\infty) = (h/h_{\mathrm{M}})^2$, $\alpha_r = 1$. However, this is physically impossible since $T_{\mathrm{m}}(\infty) \propto 1/h$. If $\alpha_{\mathrm{r}} > 1$, which is determined solely by $\Delta S_{\mathrm{vib}}(\infty)$ for free nanocrystals, $T_{\mathrm{m}}(r)$ decreases with decreasing r. $T_{\mathrm{m}}(2r_0)$ is the lowest melting temperature and vice versa.

The physical nature for depression and enhancement of $T_{\mathrm{m}}(r)$ may essentially be induced by different surface/interface conditions. For crystals with free-standing surface, the increase of the coherent energy of surface atoms of crystals is larger than that of the corresponding liquid, which renders that $T_{\mathrm{m}}(r)$ and $\Delta S_{\mathrm{m}}(r)$ drop. For crystals embedded in a more stable matrix with coherent or semi-coherent interfaces, the chemical bonds of the atoms on the coherent nanocrystals/matrix interface have more or less ionic characteristic, which leads to the enhancement of the bond strength on the interface. Since the surface melting of the nanocrystals is avoided, a superheating arises due to the suppression of thermal vibration of atoms on the coherent interface between the matrix and the nanocrystals. Thus, $T_{\mathrm{m}}(r)$ and $\Delta S_{\mathrm{m}}(r)$ increase.

The coherent interface can exist between the same or different atomic structures related to definite epitaxial relations between the nanocrystals and matrix where the atomic distances, on the interface are similar. For instance, for Pb/Al system, they have the same structure, this relation is given by $(111)_{\mathrm{Al}}//(111)_{\mathrm{Pb}}$, and $[110]_{\mathrm{Al}}//[110]_{\mathrm{Pb}}$. When structures are different, such as Pb/Zn and In/Al systems, their epitaxial relations are given by $(0001)_{\mathrm{Zn}}//(111)_{\mathrm{Pb}}, [11\overline{2}0]_{\mathrm{Zn}}//[110]_{\mathrm{Pb}}$, and $\{111\}_{\mathrm{Al}}//\{111\}_{\mathrm{In}}, [110]_{\mathrm{Al}}//[110]_{\mathrm{In}}$ respectively.

Figure 3.10 presents $T_{\mathrm{m}}(r)$ of semimetal In nanocrystals in different dimensions and different surroundings. $T_{\mathrm{m}}(r)$ is indeed a function of d especially

when r is small. When $r/r_0 > 5 - 10$, $\exp(-x) \approx 1 - x$. Equation (3.80) is simplified as Eq. (3.74) with $d = 1$. Since $T_m(r, d = 0) < T_m(r, d = 1) < T_m(r, d = 2)$, Eq. (3.74) is a good approximation of Eq. (3.80) when the dimension effect on $T_m(r)$ is neglected. This is true when r is large enough. In addition, according to Eq. (3.87), α_r decreases as $T_m(\infty)/T_M(\infty)$ and h_M/h decrease, both are essential and determine the superheating tendency of nanocrystals. The nonlinear relationship between $T_m(r)$ and $1/r$ in Eq. (3.80) implies that besides ζ, the interior atoms of nanocrystals have additional contribution to $T_m(r)$. This result shows good evidence that the macroscopic rules cannot simply be extended to the microscopic size range with a linear relationship of $1/r$ when ζ is large.
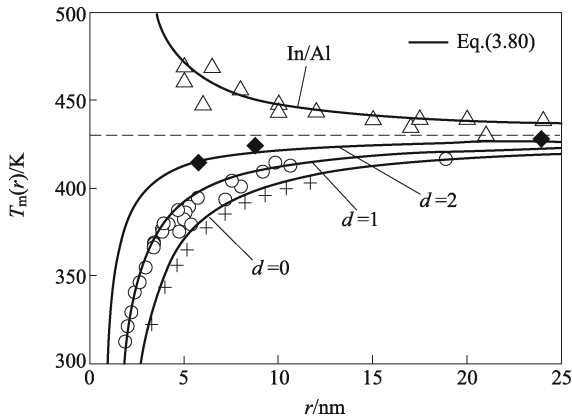

Fig. 3.10 $T_m(r)$ of semi-metal In nanocrystals in terms of Eqs. (3.80), (3.81), (3.85), and (3.89) shown as solid lines. The dash line presents $T_m(\infty) = 429.75$ K. For In, $\Delta S_{vib}(\infty) = 6.58$ J·mol^{-1}·K^{-1} in terms of Eqs. (3.31) and (3.32) where $\Delta V_m/V_s = 2.7\%$ and $\Delta S_m(\infty) = 7.59$ J·mol^{-1}·K^{-1} with $\Delta H_m(\infty) = 3.26$ KJ·mol^{-1}, $h = 0.3684$ nm. For Al, $T_M(\infty) = 933.47$ K and $h_M = 0.3164$ nm. The symbols ◆, ○, and + denote experimental results with $d = 2, d = 1$, and $d = 0$ for In nanocrystals with free surface or deposited on inert substrates. The symbol △ shows experimental results for the In/Al system. (Reproduced from Ref. [12] with permission of Bentham Science Publisers Ltd.)

An emphasis should be again laid on that although the surface melting phenomena have not been directly considered in Eq. (3.80), they have been included in $\Delta S_{vib}(\infty)$ value since $\Delta S_{vib}(\infty)$ is experimentally determined in the existence of surface melting. Thus, Eq. (3.80) correlates to Eqs. (3.69)–(3.71) well but without fitting parameters. Hence, Eq. (3.80) is more convenient to predict $T_m(r)$ function.

Another thermodynamic function of melting besides $T_m(r)$ and $\Delta S_m(r)$ is $\Delta H_m(r)$. From the general thermodynamics,

$$\Delta H_m(r) = T_m(r)\Delta S_m(r). \tag{3.88}$$

Based on Eqs. (3.80), (3.83) and (3.88), $\Delta H_m(r)$ function is determined,

$$\frac{\Delta H_m(r)}{\Delta H_m(\infty)} = \left[1 - \frac{1}{(r/r_0) - 1}\right] \exp\left[-\frac{2S_{vib}(\infty)}{3R} \frac{1}{(r/r_0) - 1}\right]. \qquad (3.89)$$

$\Delta H_m(r)$ function as a general one is suitable for all kinds of the first order transition and has been extended to the second order transition, such as glass transition. For the contents of that see Chapter 5.

A comparison between Eq. (3.89) and experimental results for $\Delta H_m(r)$ function of In nanocrystals is shown in Fig. 3.11. A pretty agreement between them is got. Since both of $T_m(r)$ and $\Delta S_m(r)$ functions are linearly proportional to $1/r$, $\Delta H_m(r)$ should drop more considerably than this linearity as r decreases especially when r is small.
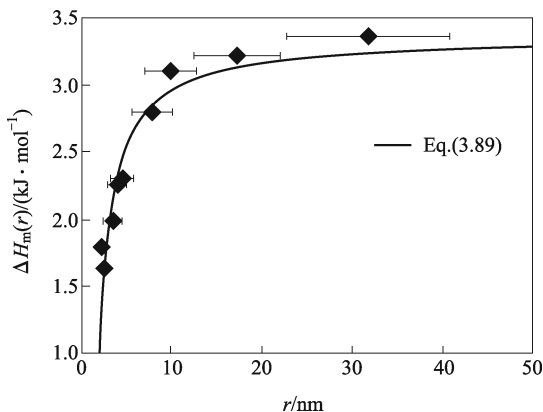

Fig. 3.11 $\Delta H_m(r)$ functions of disk-like In nanoparticles in terms of Eqs. (3.89) shown as the solid line and the symbol ◆ denotes the corresponding experimental results where $\Delta H_m(\infty) = 3.36$ kJ·mol^{-1}, $d = 1$ and other parameters are the same as the caption of Fig. 3.10. (Reproduced from Ref. [12] with permission of Bentham Science Publishers Ltd.)

3.5 Cohesive Energy

3.5.1 Size-dependent Cohesive Energy of Crystals [12]

The nature of the thermal stability of nanocrystals is determined directly by the size-dependent cohesive energy of nanocrystals $E_c(r)$. $E_c(r)$ is the energy required to break the atoms of the solid into isolated atomic species,

which can be obtained experimentally by measuring the latent heat of sublimation at various low temperatures, and extrapolating to zero Kelvin. The first experimental data on $E_c(r)$ function of Mo and W have been determined through measuring the oxidation enthalpy of nanocrystals. The results show that as r decreases, $E_c(r)$ increases (or its absolute value decreases).

As a natural consideration, $\Delta H_m(r)$ function of Eq. (3.89) should be applicable to the determination of $E_c(r)$ function if the corresponding transition entropy term for the solid-vapor transition $\Delta S_b = E_b/T_b$ (E_b denotes the bulk cohesive energy at T_b with T_b being the bulk solid-vapor transition temperature) is used to substitute $\Delta S_{vib}(\infty)$. In light of this consideration, $E_c(r)$ function in terms of Eq. (3.91) is given as follows:

$$\frac{E_c(r)}{E_c(\infty)} = \left[1 - \frac{1}{(r/r_0) - 1}\right] \exp\left[-\frac{2\Delta S_b}{3R} \frac{1}{(r/r_0) - 1}\right]. \tag{3.90}$$

In Eq. (3.90), $E_c(2r_0) = 0$ where the structures of the solid and the vapor are indistinguishable, which here is a single atom or molecule since a single atom or molecule cannot be identified whether it is in a solid or a vapor state. Thus, $2r_0 = h/2$. Accordingly, $r_0 = h/4$. Note that although for the solid-liquid transition r_0 is dimension-dependent, r_0 is dimension–independent for solid-vapor transition due to the structural characteristic of the vapor.

Figure 3.12 compares Eq. (3.90) and experimental observations for $E_c(r)$ functions of Mo and W nanocrystals. Except the $E_c(r=0.5$ nm) value of W nanoparticles, which will be discussed in Sec. 3.5.2, it is evident that Eq. (3.90) is consistent with the experimental observation: $E_c(r)$ increases with a decrease in size due to the increase of the surface/volume ratio while the
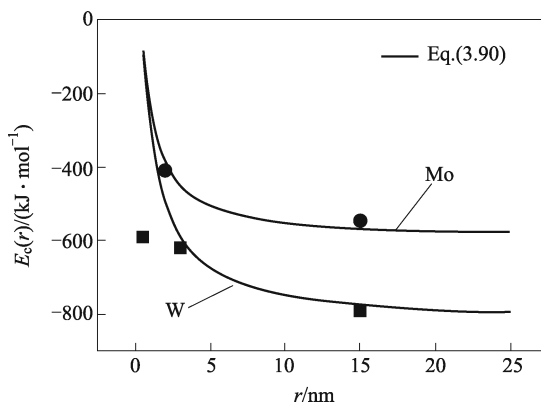
Fig. 3.12 The size dependence of $E_c(r)$ for Mo and W nanocrystals where the solid lines denote Eq. (3.90) and the symbols ● [$E_c(r=2$nm) $= -410$ kJ·mol^{-1}, $E_c(r=15$ nm) $= -544$ kJ·mol^{-1}] and ■ [$E_c(r=0.5$ nm) $= -590$ kJ·mol^{-1}, $E_c(r=3$ nm) $= -619$ kJ·mol^{-1}, $E_c(r=15$ nm) $= -791$ kJ·mol^{-1}] show experimental data of Mo and W nanocrytals, respectively. (Reproduced from Ref. [12] with permission of Bentham Science Publishers Ltd.)

surface atoms have lower CN and thus higher energetic state. Because the energetic state of the vapor phase is size-independent and referenced as zero, it is conceivable that the above size dependence of $E_c(r)$ is solely induced by averaged energetic state of atoms of the nanocrystals.

Considering the mathematical relation of $\exp(-x) \approx 1-x$ when x is small, Eq. (3.90) can be rewritten as $[E_c(\infty) - E_c(r)]/[E_c(\infty)\Delta S_b] \approx 2r_0/(3Rr)$. This result is in agreement with the general consideration that the decrease of any size-dependent thermodynamic amount is proportional to $1/r$ or the surface/volume ratio. However, as r further decreases to the size comparable with h, namely, about several nanometers, the size effect of the thermodynamic amount is more powerful than the above simplified form from Eq. (3.90) because the energetic state of interior atoms of the nanocrystals in this size range is higher than that of the corresponding bulk ones too.

The size dependence of E_c is not much more than that of the latent heat. This is because although ΔS_b in Eq. (3.90) is one order larger than $\Delta S_m(\infty)$, $r_0 = h/4$ for solid-vapor transition is one order smaller than $r_0 = 3h$ for solid-liquid transition. As a result, the exponential term in Eq. (3.90) has a similar size to the solid-liquid transition.

It has been assumed up to now that nanoparticles have the same structure of the corresponding bulk crystals even if r is small. As r of the particles decreases to a size of $0.5h < r < 5h$, or $r < 1-1.5$ nm where the particles consist of only dozens of or several hundred atoms, the structure of the particles, which usually are called clusters, differs from that of the corresponding bulk crystals with even negative specific heat in some cases. The prediction of Eq. (3.90) thus may be no longer fully correct. This is the case of the experimental values of E_c $(0.5-1\text{nm})$ of W nanoparticles shown in Fig. 3.12. However, the limit case of Eq. (3.90) is still correct because a particle consisting of one atom cannot be considered as a solid and the corresponding cohesive energy value must be zero. A detailed discussion about $E_c(r)$ of clusters will be held in the following section.

3.5.2 Vacancy Formation Energy and Cohesive Energy of Clusters

Clusters have shown unique chemical and physical properties compared with their counterpart in bulk [38]. One of the applications of these materials is to act as catalysts with certain $E_c(N)$ and $\gamma_{sv}(N)$ due to huge surface-volume ratio, where N is the number of atoms in a cluster [39]. If a metallic cluster has a spherical shape, the corresponding N value is named magic number. These kinds of clusters are easy to study where some rules could be found, which will be considered in this section. The best known structures of this kind of structure or cluster with magic number are quasi-crystalline structures such as icosahedron (IH), truncated decahedron (DH), and truncated octahedron (TO) with large proportion of atoms located at edges and vertices [40].

The basic understanding of energetic term of clusters is the cohesive energy of atoms at surface and interior, $E_{cs}(N)$ and $E_{ci}(N)$, which are the mean values of all surface and interior atoms of clusters. Both can be determined by computer simulation techniques. As a result, $E_c(N)$ and $\gamma_{sv}(N)$ are obtained. More exactly, the cohesive energy of atoms at a special x site, $E_{cx}(N)$, is more complicated and in some cases is more important than $E_c(N)$ one. This is because many properties, such as adsorption, catalysis and optical behavior of clusters, are exhibited by atoms at special surface locations of clusters [41]. Moreover, alloy clusters show superior performance compared with a single element cluster in catalytic and optical properties [42]. To determine the degree of segregation or mixing in an alloy cluster, besides the surface sites, $E_{cx}(N)$ of the interior sites also needs to be understood.

$E_{cx}(N)$ values cannot be directly obtained by using simulation techniques. The vacancy formation energy of the x site $E_{vx}(N)$ in a cluster however could be determined using simulation techniques [43], which can be related to $E_{cx}(N)$. For bulk crystals, the vacancy formation energy $E_v(\infty)$ is approximately a fraction of $E_c(\infty)$, such as $E_v(\infty)/E_c(\infty) \approx -0.3$ for the transitional metals [44]. For nanocrystals, a thermodynamic relationship has been deduced as $E_v(N)/E_c(N) = E_v(\infty)/E_c(\infty)$ where $E_v(N)$ is the average value of $E_{vx}(N)$ [45]. Since clusters usually have non-crystalline and quasi-crystalline structures, this linear relationship may be invalid and $E_{cx}(N) \sim E_{vx}(N)$ relationship still needs to be clarified.

In the following, Ag clusters with the magic number are introduced as examples to illustrate the situations of clusters and the corresponding $E_c(N)$ and $E_v(N)$ where the typical IH ($N = 13, 55$ and 147), DH ($N = 75$ and 101) and TO ($N = 38$) structures are taken as shown in Fig. 3.13. The specific surface and interior sites are marked with numbers.

$E_v(\infty)$ denotes the lowest energy to remove an atom from a selected site, and usually the atom is brought to an assumed reservoir which determines the atomic chemical potential [46]. For single element crystals, this potential is $E_c(\infty)$. The physical meaning behind this is that the removed atom is brought to a kink site at surface [46]. Although the cohesive energy of the under-coordinated kink site $E_{ck}(\infty)$ is greater than $E_c(\infty)$, it has been widely reported that the binding energy of the atoms at the kink site $E_{bk}(\infty)$ is just equal to $-E_c(\infty)$ [47]. This is mainly because when an atom is bound at the kink site, besides its cohesive energy turning from 0 to $E_{ck}(\infty)$, the cohesive energy of the coordinated atoms also decreases since these atoms all gain one extra bond. Thus, in Density Functional Theory (DFT) simulation, $E_v(\infty)$ has been deduced as [46]

$$E_v(\infty) = E(1) + E(\infty, N - 1, 1) - E(\infty, N, 0) + E_c(\infty) \qquad (3.91)$$

where $E(1)$ is the total energy of a single atom, $E(\infty, N, 0)$ and $E(\infty, N-1, 1)$ are separately the total energy of the super cell and that after the atom at x site is removed. Since clusters are quite different from bulk crystals in both structure and energy, a new reservoir should be assumed to calculate $E_{vx}(N)$.
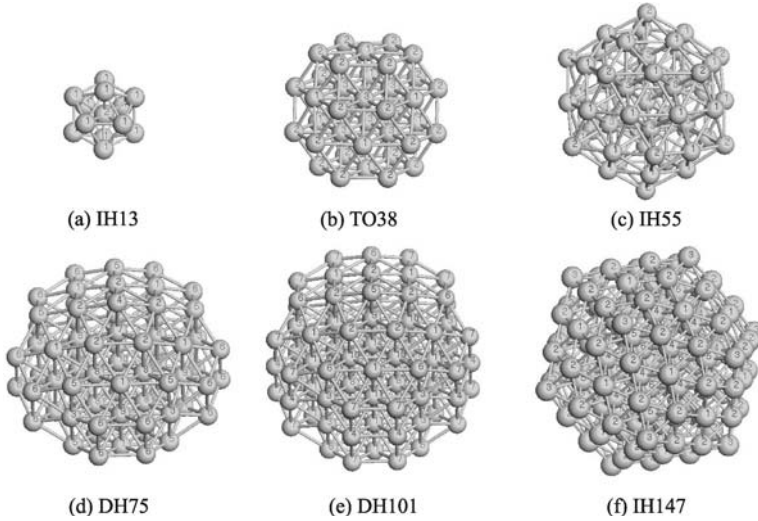
(a) IH13   (b) TO38   (c) IH55

(d) DH75   (e) DH101   (f) IH147

Fig. 3.13 Ag cluster structures with different magic numbers N. The different surface and interior sites are marked with numbers and the corresponding site names are shown in Table 3.5.

With the same consideration as bulk crystals, it is simply assumed that the new reservoir is determined by $E_c(N)$ where $E_{bk}(N) = -E_c(N)$.

Table 3.5 $E_c(N)$ and $E_{cx}(N)$ in eV.atom^{-1}, $E_{vx}(N)$ in eV, N_x and $Z_x(N)$ of Ag clusters obtained from DFT simulation and Eqs. (3.92) and (3.95)

Cluster	$-E_c(N)$	Atomic sites	N_x	$Z_x(N)$	$E_{vx}(N)$	$-E_{cx}(N)$
IH13	2.13	(1) vertex	12	6	0.44	2.10
		(2) core	1	12	0.79	2.44
TO38	2.64	(1) (111) facet	8	9	1.21	3.10
		(2) vertex	24	6	0.5	2.39
		(3) sub-layer	6	12	1.16	3.05
IH55	2.79	(1) edge	30	8	1.05	2.77
		(2) vertex	12	6	0.84	2.56
		(3) sub-layer	12	12	1.33	3.05
		(4) core	1	12	1.15	2.87
DH75	2.82	(1) (111) facet	10	9	1.15	3.05
		(2) top edge	10	8	0.9	2.80
		(3) notch edge	5	10	1.35	3.25
		(4) top vertex	2	6	0.4	2.3
		(5) notch vertex	10	7	0.84	2.74
		(6) lateral vertex	20	6	0.5	2.4
		(7) sub-top vertex	2	12	1.18	3.08
		(8) sub-top edge	10	12	1.36	3.24
		(9) sub-(111) facet	5	12	1.04	2.94
		(10) core	1	12	1.32	3.22

Continue

Cluster	$-E_c(N)$	Atomic sites	N_x	$Z_x(N)$	$E_{vx}(N)$	$-E_{cx}(N)$
DH101	2.9	(1) (111) facet	10	9	1.04	3.08
		(2) top edge	10	8	0.82	2.86
		(3) notch edge	10	10	1.24	3.28
		(4) lateral edge	10	7	0.61	2.65
		(5) top vertex	2	6	0.32	2.36
		(6) notch vertex	10	7	0.65	2.69
		(7) lateral vertex	20	6	0.37	2.41
		(8) sub-notch edge	10	12	1.43	3.47
		(9) sub-top vertex	10	12	1.06	3.10
		(10) sub-top edge	2	12	1.16	3.20
		(11) sub-(111) facet	5	12	1.16	3.20
		(12) core	2	12	1.31	3.35
IH147	2.99	(1) (111) facet	20	9	1.14	3.18
		(2) edge	60	8	0.81	2.85
		(3) vertex	12	6	0.3	2.34
		(4) sub-edge	30	12	1.25	3.29
		(5) sub-vertex	12	12	0.99	3.03
		(6) second sub-layer	12	12	1.28	3.32
		(7) core	1	12	0.42	2.46

To confirm the validity of the above relationship, more detailed discussion is given. At bulk surfaces, CN of the atoms at the close packed (111) facet and at the kink site are separately $Z_{s(111)} = 9$ and $Z_{sk} = 6$ [48]. Hence, three neighboring bonds of an atom should be broken when making a kink at the plane. For clusters, the average CN of the atoms at the close packed surface $Z_s(N) = 6 - 8$ [49], which brings out the CN of corresponding kink sites $Z_{sk}(N)$ being $3 - 5$. For instance, for Ag IH13 and DH75 clusters, $E_c(13)/E_c(\infty) = 0.61$ and $E_c(75)/E_c(\infty) = 0.8$ with $Z_s(13) = 6$ and $Z_s(75) = 7.4$ [49]. Thus, $Z_{sk}(13) \approx 3$ and $Z_{sk}(75) \approx 4$. It has been reported that at Cu bulk surfaces, the binding energy of the Cu adatoms at the hollow sites of the (111) and (100) facets keeps the ratios of $E_{b(111)}(\infty)/E_c(\infty) = -0.64$ and $E_{b(100)}(\infty)/E_c(\infty) = -0.8$ [47]. Since the CN of these sites are separately $Z_{s(111)}(\infty) = 3$ and $Z_{s(100)}(\infty) = 4$ while the crystalline structure of Ag is also fcc, these sites should be similar to the kink sites of Ag IH13 and DH75 clusters. Thus, $E_{bk}(13)/E_c(\infty) \approx -0.64$ and $E_{bk}(75)/E_c(\infty) \approx -0.80$ are approximately valid and the assumption of $E_{bk}(N) \approx -E_c(N)$ is reasonable. With the above consideration for the new reservoir, $E_{vx}(N)$ is defined as

$$E_{vx}(N) = E(1) + E_x(N - 1, 1) - E(N, 0) + E_c(N) \qquad (3.92)$$

where $E(N, 0)$ and $E_x(N - 1, 1)$ are the total energy of the cluster with N atoms and that after the atom at x site is removed. For transitional metals, it has been found that $E_v(\infty) - E_{v(111)}(\infty) \approx E_{cb}(\infty) - E_{c(111)}(\infty) = \gamma_{(111)}(\infty)$ where γ is the surface energy, which says that the difference of E_v between the bulk surface and interior is essentially induced by the corresponding discrepancy in E_c. Following the same consideration, the difference of $E_{vx}(N)$ in the same cluster is assumed to be mainly decided by the discrepancy in

$E_{cx}(N)$, there is

$$E_{vy}(N) - E_{vx}(N) \approx E_{cy}(N) - E_{cx}(N) \qquad (3.93)$$

where subscript "y" denotes another site in the cluster, which differs from "x". Moreover, $E_{cx}(N)$ could also be deduced as

$$E_{cx}(N) = [NE_c(N) - \sum_z N_z E_{cz}(N)]/N_x \qquad (3.94)$$

where N_x and N_z are the numbers of atoms of the x and z sites. Inserting Eq. (3.94) into Eq. (3.93), it reads

$$E_{cx}(N) = E_c(N) - \{\sum_y N_y [E_{vy}(N) - E_{vx}(N)]\}/N. \qquad (3.95)$$

In Eq. (3.95), $E_c(N)$ values could be obtained by simulations, $E_{vy}(N)$ and $E_{vx}(N)$ values are calculated in terms of Eq. (3.92) and simulation results. Moreover, $\gamma(N)$ is defined as [49]

$$\gamma(N) = E_{cs}(N) - E_{ci}(N) \qquad (3.96)$$

where $E_{cs}(N)$ and $E_{ci}(N)$ are separately the average cohesive energy of the surface and interior atoms of the considered clusters.

Based on Eq. (3.91), $E_v(\infty) = 1.18$ eV, which agrees with experimental and simulation results of $1.11 - 1.24$ eV for bulk Ag crystals [45]. The calculated $E_{vx}(N)$ values of Ag clusters in light of Eq. (3.92) are shown in Table 3.5. The vertex sites have comparatively small $E_{vx}(N)$ values as $E_{v\text{-vertex}}(N) = 0.3 - 0.84$ eV, or the sites are easy to form vacancy compared with other surface sites. This result is not difficult to understand since $Z_{\text{vertex}}(N) = 6$ except at the notch vertex sites of DH structures. In addition, $E_{vx}(N)$ firstly increases with increasing N until a maximum appears at $E_{v\text{-vertex}}(55) = 0.84$ eV and then it decreases. Namely, vacancy is easier to form at the vertex sites with increasing N when $N > 55$.

Clusters would transform to nanocrystals as N further increases. Although nanocrystals usually keep the TO structure thermodynamically, the IH and DH structures could also be metastable due to some kinetic factors [50]. Simulation results show that Au nanocrystals in a size range of 3–8 nm have the "Chui icosahedron" (c-IH) structure [51], which is truncated from the IH structure where all atoms at the vertex site are removed. A thermodynamic model suggests that there is a critical size beyond which the c-IH structure is energetically more favorable than the IH structure [52]. This conclusion corresponds to the result that clusters or nanocrystals with larger size tend to form vacancies at the vertex sites.

For the atoms at (111) facets $[Z_{(111)}(N) = 9]$ and edge $[Z_{\text{edge}}(N) = 8]$ sites, $E_{v(111)}(N) = 1.04 - 1.21$ eV and $E_{v\text{-edge}}(N) = 0.81 - 1.05$ eV, which are much larger than those of the bulk (111) and (100) facets of $E_{v\text{-}(111)}(\infty)$

= 0.77 eV and $E_{\text{v-}(100)}(\infty) = 0.53$ eV. Hence, vacancies are more difficult to form at these sites for clusters than for the corresponding bulks. For the interior sites of Ag clusters, most $E_{\text{v-interior}}(N)$ values are in the range of $1 - 1.43$ eV, which is approximately equal to or even larger than $E_{\text{v}}(\infty) = 1.18$ eV. Accordingly, vacancies are more difficult to form at some interior sites of clusters than those at the interior of bulk crystals. The exceptions are the core sites of IH13 and IH147 with $E_{\text{v-core}}(13) = 0.79$ eV and $E_{\text{v-core}}(147) = 0.42$ eV. Therefore, the core site of the IH structure may be unoccupied.

On the other side, the calculated $E_{cx}(N)$ values in terms of Eq. (3.94) are also shown in Table 3.5. For the surface sites with $Z_{sx}(N) = 6, E_{\text{c-vertex}}(N)$ values are in the range of $(-2.3) - (-2.56)$ eV with only exception of $E_{\text{c-vertex}}(13) = -2.10$ eV. $E_{\text{c-vertex}}(N)$ does not show obvious size dependence like $E_{\text{v-vertex}}(N)$. Similarly, $E_{cx}(N)$ keeps almost the same with the same $Z_{sx}(N)$ when $Z_{sx}(N) = 7 - 10$. For the bulk surface, $E_{cs}(\infty) \approx [Z_s(\infty)/Z(\infty)]^{1/2}E_c(\infty)$ has been demonstrated using simulation techniques [53]. $E_{cx}(N) \sim Z_x(N)$ relationship is similar to $E_{cs}(\infty) \sim E_c(\infty)$ one. Thus, for the most surface sites of clusters, $E_{cx}(N) \approx E_{cs}(\infty)$ when $Z_{sx}(N) = Z_s(\infty)$. As mentioned above, even if $E_{cx}(N) \approx E_{cs}(\infty)$, surface atoms of clusters could not easily be separated to form vacancy. This is because for forming a vacancy at the cluster surface, chemical potential of the assumed reservoir has been changed from $E_c(\infty)$ to $E_c(N)$, which increases difficulty of the vacancy formation.

For most interior atoms of clusters, $E_{cix}(N) = (-2.87) - (-3.35)$ eV with $Z_{ix}(N) = 12$. Although $E_{cix}(N) > E_c(\infty)$, some interior sites are harder to form vacancy than bulk due to the change of the chemical potential of the reservoir from $E_c(\infty)$ to $E_c(N)$. The exceptions are the core sites of IH13 and IH147 with $E_{\text{c-core}}(13) = 2.44$ eV and $E_{\text{c-core}}(147) = 2.46$ eV where there are smaller vacancy formation energy of $E_{\text{v-core}}(13) = 0.79$ eV and $E_{\text{v-core}}(147) = 0.42$ eV.

Through averaging the $E_{csx}(N)$ and $E_{cix}(N)$ values, $E_{cs}(N), E_{ci}(N)$ and $\gamma(N)$ values in terms of Eq. (3.96) are calculated and shown in Table 3.6. Both $E_{cs}(N)$ and $E_{ci}(N)$ increase as N decreases. $\gamma(N)$ values are in the range of $0.46 - 1.06$ J·m^{-2}, which is smaller than the corresponding bulk value $\gamma(N) = 1.2$ J·m^{-2} [53]. Since the surface atoms are mostly located at the edge and vertex sites, they should have more broken bonds and higher

Table 3.6 $E_{cs}(N), E_{ci}(N), \gamma(N)$ and $Z_s(N)$ of Ag clusters obtained from DFT simulation and Eqs. (3.95) and (3.96)

Clusters	$Z_s(N)$	$\gamma_{sv}(N)$ /(eV·atom^{-1})	$\gamma_{sv}(N)$ /(J·m^{-2})	$-E_{cs}(N)$	$-E_{ci}(N)$
IH13	6	0.34	0.46	2.1	2.44
TO38	6.75	0.48	0.85	2.57	3.05
IH55	7.43	0.33	0.6	2.71	3.04
DH75	7.4	0.43	0.86	2.71	3.14
DH101	7.53	0.51	1.06	2.76	3.27
IH147	7.96	0.36	0.75	2.86	3.22

$E_{cs}(N)$ values. However, due to the high pressure existing in the cluster, $E_{ci}(N)$ would also increase. According to Table 3.6, the increasing extent of $E_{ci}(N)$ is large than $E_{cs}(N)$, which induces the decreasing of corresponding $\gamma_{sv}(N)$. Since both cohesive values of surface $E_{cs}(N)$ and interior $E_{ci}(N)$ would change for clusters, $\gamma_{sv}(N)$ is different from the corresponding bulk value $\gamma_{sv}(\infty)$.

3.6 Size Effect on Bandgap of II-VI Semiconductor Nanocrystals [54]

Semiconductor nanocrystals show tunability of their electronic and optical properties by the three-dimensional confinement of carriers. One of their characteristics is the increase of the valence-conduction band-gap $E_g(r)$ function (the so-called blue-shift) with decreasing r, or $\Delta E_g(r) = E_g(r) - E_g(\infty) > 0$. According to the nearly-free-electron approach, E_g is a function of the crystalline field E_{cr}, which depends on the total number of atoms and the interatomic interaction of the solids and indicates that the bandgap is determined by the first Fourier coefficient of the crystalline field $E_{cr,1}$, namely, $E_g = 2|E_{cr,1}|$. If ΔE_g is supposed to be proportional to $\Delta E_{cr}, \Delta E_g(r)/E_g(\infty) = |\Delta E_{cr}(r)/E_{cr}(\infty)|$. Because E_c is also related to both the total CN of an atom and the interatomic interaction, such as E_{cr}, the relationships of $E_c \propto E_{cr}$ and $\Delta E_c(r) \propto \Delta E_{cr}(r)$ must also exist. As a result,

$$\frac{\Delta E_g(r)}{E_g(\infty)} = \left| \frac{\Delta E_{cr}(r)}{E_{cr}(\infty)} \right| = \left| \frac{E_c(r) - E_c(\infty)}{E_c(\infty)} \right| = 1 - \frac{E_c(r)}{E_c(\infty)}. \qquad (3.97)$$

Substituting Eq. (3.90) for $E_c(r)/E_c(\infty)$ function into Eq. (3.97), it reads

$$\frac{\Delta E_g(r)}{E_g(\infty)} = 1 - \left[1 - \frac{1}{(4r/h) - 1} \right] \times \exp\left(-\frac{2\Delta S_b}{3R} \frac{1}{(4r/h) - 1} \right). \qquad (3.98)$$

Equation (3.97) denotes that only two parameters ΔS_b and h are needed in order to predict the $\Delta E_g(r)/E_g(\infty)$ value. h and ΔS_b values of elements are easy to find in literature. For compounds, even if their h values cannot be found, algebraic-averaged h values of elements consisting of the compounds may be utilized and this substitution leads to little error. However, ΔS_b values of compounds, especially those of semiconductor compounds, are difficult to find since many of them are unstable and are broken down before T_m is reached. Thus, $\Delta S_b = 13R$, which is the mean values of all elements in the periodic table $(70 - 150 \text{ J·g-atom}^{-1}\text{·K}^{-1})$, will be taken for II-VI semiconductor nanocrystals.

For II-VI semiconductors with zinc-blend structure, $h = (3^{1/2}/4)a$ with a being the lattice parameters (0.541 nm, 0.567 nm, 0.610 nm, 0.582 nm, 0.605 nm and 0.648 nm for ZnS, ZnSe, ZnTe, CdS, CdSe and CdTe, respectively).

There is little difference of h values for them since the difference of the lattice constants a is small, thus they should have the similar size dependence of bandgap expansion. If simply $h = 1/4$ nm is taken and take that $\Delta S_b \approx 13R$,

$$\frac{\Delta E_g(r)}{E_g(\infty)} \approx 1 - \left[1 - \frac{1}{16r - 1} \right] \times \exp\left(-\frac{26}{3} \frac{1}{16r - 1} \right). \qquad (3.99)$$

In Eq. (3.99), there is no any thermodynamic quantity, which implies that all II-VI semiconductors concerned have similar electronic structures. Comparisons of $\Delta E_g(r)/E_g(\infty)$ of II-VI semiconductor nanocrystals CdSe between Eq. (3.99) and available experimental results are shown in Fig. 3.14. As expected, $\Delta E_g(r)$ increases with a decrease in size. In the figure, there still exists a little deviation between Eq. (3.99) and experimental results. A possible reason for this is that parts of the experimental data were directly determined based on the photoluminescence (PL) or the photoabsorption (PA) measurements, where the corresponding energy E_{PL} and E_{PA} differs from each other with a difference called Stoke shift, or $E_{PL} = E_g - E_s$ and $E_{PA} = E_g + E_s$ with E_s denoting the energy for electron-phonon coupling. Thus, for PL and PA, the mentioned bandgap should be joint contributions of both crystal potential and electron-phonon coupling. Only the crystals potential contributes to the actual bandgap ($E_g = (E_{PL} + E_{PA})/2$), yet the electron-phonon coupling causes the Stoke shift ($2E_s$). For bulk semiconductors, $E_s(\infty)$ is far smaller than $E_g(\infty)$ and hence is negligible. As a result, $E_g(\infty) \approx E_{PL}(\infty)$ (or $E_{PA}(\infty)$). However, with decreasing of r, $E_s(r)$ abruptly increases, which induces the enhanced difference between $E_g(r)$ and $E_{PL}(r)$ (or $E_{PA}(r)$) especially when $r < 1$ nm.

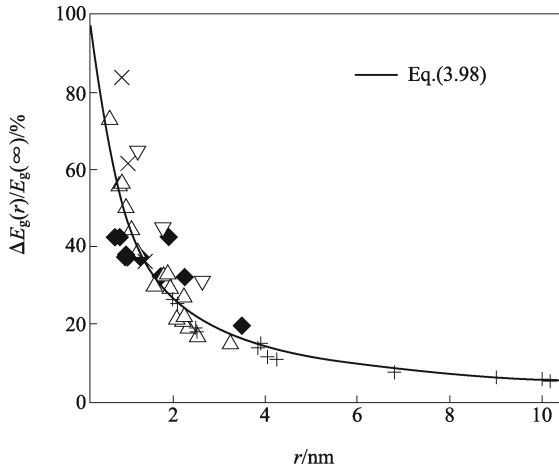**Fig. 3.14** A comparison of $\Delta E_g(r)/E_g(\infty)$ of CdSe between Eq. (3.99) (solid line) and experimental results shown as ◆, △, ▽, × and +. The $E_g(\infty)$ value used in Eq. (3.99) is 1.74 eV. (Reproduced from Ref. [54] with permission of Elsevier)

References

1   http://en.wikipedia.org/wiki/Material_properties_(thermodynamics);
       http://www.calculatoredge.com/calc/exp.htm. Accessed 12 January 2009
2   Hsieh J S. Principles of Thermodynamics. Scripta Book Company, (1975)
3   Francis W S, Gerhard L S. Thermodynamics, Kinetic Theory and Statistical
       Thermodynamics. Addison-Wesley Publishing Company, London (1975)
4   Chang L T, John H L. Statistical Thermodynamics. Hemisphere Publishing
       Corporation, Washington London (1979)
5   Regel A R. Entropy of melting of semiconductors. Semiconductors, **29**, 405-
       417 (1995) and references therein
6   http://secondlaw.oxy.edu. Accessed 23 March 2009
7   Ubbelohde A R. The Molten State of Matter. Wiley, New York (1979)
8   Tiwari G P, Juneja J M, Iijima Y. Role of entropy of fusion in phase transfor-
       mation and self-diffusion. J. Mater. Sci., **39**, 1535-1546 (2004)
9   Chakraverty B K. On the excess entropy of fusion of semiconducting and
       semimetallic elements. J. Phys. Chem. Solids, **30**, 454-459 (1969)
10   Nalwa H S. Encyclopedia of Nanoscience and Nanotechnology. American Sci-
       entific, New York (2004)
11   Otto D P, de Villiers M M. Physicochemical principles of nanosized drug de-
       livery system. In: Nanotechnology in Drug Delivery. American Association of
       Pharmaceutical Scientists, (2009)
12   Jiang Q, Yang C C. Size effect on the phase stability of nanostructures. Curr.
       Nanosci., **4**, 179-200 (2008) and references therein
13   Takagi M. Electron-diffraction study of liquid-solid transition of thin metal
       films. J. Phys. Soc. Japan, **9**, 359-363 (1954)
14   Buffat P H, Borel J P. Size effect on the melting temperature of gold particles.
       Phys. Rev., A **13**, 2287-2298 (1976)
15   Hill T L. Thermodynamics of Small Systems. Part 1 and 2. W. A. Benjamin
       and Co., New York (1964)
16   Tsallis C. Possible generalization of Boltzmann-Gibbs statistics. J. Stat. Phys.,
       52, 479-487 (1988)
17   Rajagopal A K. Von Neumann and Tsallis entropies associated with the Gen-
       tile interpolative quantum statistics. Phys. Lett., A **214**, 127-130 (1996)
18   Yang C C, Li J C, Jiang Q. Effect of pressure on melting temperature of silicon
       determined by Clapeyron equation. Chem. Phys. Lett., **372**, 156-159 (2003)
19   Dash G. History of the search for continuous melting. Rev. Mod. Phys., **71**,
       1737-1743 (1999)
20   Lindemann A. Üder die Berechnung Molekularer Eigenfrequenzen. Z. Phys.,
       11, 609-610 (1910)
21   Stillinger F H. A topographic view of supercooled liquids and glass formation.
       Science, **267**, 1935-1939 (1995)
22   Sun C Q, Wang Y, Tay B K, Li S, Huang H, Zhang Y B. Correlation between
       the melting point of a nanosolid and the cohesive energy of a surface atom. J.
       Phys. Chem., B **106**, 10701-10705 (2002)
23   Jiang Q, Shi H X, Zhao M. Melting thermodynamics of organic nanocrystals.
       J. Chem. Phys., **111**, 2176-2180 (1999)
24   Cahn R W. Melting and the surface. Nature, **323**, 668-669 (1986)
25   Born M. Thermodynamics of crystals and melting. J. Chem. Phys., **7**, 591-603
       (1939)

26 Jin Z H. Gumbsch P, Lu K, Ma E. Melting mechanisms at the limit of super-heating. Phys. Rev. Lett., **87**, 055703 (2001)

27 Hoffmann H J. Reasons for melting of chemical elements and some consequences. Materialwiss. Werkst., **34**, 571-582 (2003)

28 Pauchard L, Bonn D, Meunier J. Dislocation-mediated melting of a two-dimensional crystal. Nature, **384**, 145-147 (1996)

29 Burakovsky L, Preston D L. Analysis of dislocation mechanism for melting of elements. Solid State Commun., **115**, 341-345 (2003)

30 Shi F G. Size dependent thermal vibrations and melting in nanocrystals. J. Mater. Res., **9**, 1307-1313 (1994)

31 Zhang Z, Li J C, Jiang Q. Modelling for size-dependent and dimension-dependent melting of nanocrystals. J. Phys. D: Appl. Phys., **33**, 2653-2656 (2000)

32 Mott N F. The resistance of liquid metals. Proc. R. Soc., A **146**, 465-472 (1934)

33 Jiang Q, Shi F G. Entropy for solid-liquid transition in nanocrystals. Mater. Lett., **37**, 79-82 (1998)

34 Jiang Q, Tong H Y, Hsu D T, Okuyama K, Shi F G. Thermal stability of crystalline thin films. Thin Solid Films, **312**, 357-361 (1998)

35 Lai S L, Guo J Y, Petrova V, Ramanath G, Allen L H. Size-dependent melting properties of small tin particles: nanocalorimetric measurements. Phys. Rev. Lett., **77**, 99-102 (1996)

36 Eckert J, Holzer J C, Ahn C C, Fu Z, Johnson W L. Melting behavior of nanocrystalline aluminum powders. Nanostruct. Mater., **2**, 407-413 (1993)

37 Jackson C L, Mckenna G B. The melting behavior of organic materials confined in porous solids. J. Chem. Phys., **93**, 9002 (1990)

38 Halperin W P. Quantum size effects in metal particles. Rev. Mod. Phys., **58**, 553-606 (1986)

39 Coquet R, Howard K L, Willock D J. Theory and simulation in heterogeneous gold catalysis. Chem. Soc. Rev., **37**, 2046-2076 (2008)

40 Baletto F, Ferrando R. Structural properties of nanoclusters: Energetic, thermodynamic, and kinetic effects. Rev. Mod. Phys., **77**, 371-423 (2005)

41 Lopez N, Nørskov J K. Catalytic CO oxidation by a gold nanoparticle: A density functional study. J. Am. Chem. Soc., **124**, 11262-11263 (2002)

42 Wang A Q, Chang C M, Mou C Y. Evolution of catalytic activity of Au-Ag bimetallic nanoparticles on mesoporous support for CO oxidation. J. Phys. Chem., B **109**, 18860-18867 (2005)

43 Wilcoxon J P, Provencio P P. Heterogeneous growth of metal clusters from solutions of seed nanoparticles. J. Am. Chem. Soc., **126**, 6402-6408 (2004)

44 Itoh M, Kumar V, Kawazoe Y. Ab initio calculations of the stability of a vacancy in Na clusters and correlation with melting. Phys. Rev., B **73**, 035425 (2006)

45 Yang C C, Li S. Investigation of cohesive energy effects on size-dependent physical and chemical properties of nanocrystals. Phys. Rev., B **75**, 165413 (2007)

46 Neugebauer J, Scheffler M. Adsorbate-substrate and adsorbate-adsorbate interactions of Na and K adlayers on Al(111). Phys. Rev., B **46**, 16067-16080 (1992)

47 Karimi M, Tomkowski T, Vidali G, Biham O. Diffusion of Cu on Cu surfaces. Phys. Rev., B **52**, 5364-5374 (1995)

48   Liu Z P, Hu P, Alavi A. Catalytic role of gold in gold-based catalysts: A density functional theory study on the CO oxidation on gold. J. Am. Chem. Soc., **124**, 14770-14779 (2002)

49   Liu D, Zhu Y F, Jiang Q. Cohesire energy in several Ag clusters. J. Phys. Chem. C **113**, 10907-10912 (2009)

50   Grochola G, Russo S P, Snook I K. On morphologies of gold nanoparticles grown from molecular dynamics simulation. J. Chem. Phys., **126**, 164707 (2007)

51   Chui Y H, Grochola G, Snook I K, Russo S P. Molecular dynamics investigation of the structural and thermodynamic properties of gold nanoclusters of different morphologies. Phys. Rev., B **75**, 033404 (2007)

52   Barnard A S, Opletal G, Snook I K, Russo S P. Ideality versus reality: Emergence of the Chui icosahedron. J. Phys. Chem., C **112**, 14848-14852 (2008)

53   Jiang Q, Lu H M. Size dependent interface energy and its applications. Surf. Sci. Rep., **63**, 427-464 (2008)

54   Yang C C, Jiang Q. Size effect on the band-gap of II-VI semiconductor nanocrystals. Mater. Sci. Eng., B **131**, 191-194 (2006)

Chapter 4 Phase Diagrams

In this chapter, one of the most important applications of thermodynamics to materials, namely the phase diagram, is described based on the phase diagram thermodynamics as the physical basis of phase diagrams. The series of phase diagrams with different variables, different bonding natures, and distinct component numbers (one and two) are introduced in detail. In addition, recent extension and progress of thermodynamics in nanoscience and nanotechnology, such as size-dependent phase diagram and size-dependent band gap of semiconductor alloys, are also introduced.

4.1 Gibbs Phase Rule and Phase Diagram of Unary System [1−3]

A phase is a portion of matter that is uniform throughout, not only in chemical compositions but also in physical states. Thermodynamic stability of phases is an important issue for the users and producers of materials, which depends on such variables as T, P, composition, and r in a system. A change in T, P, r, and/or composition for the system in equilibrium will result in transition from one stable phase to another. Note that there are also other variables, which affect the phase stability, such as external fields (electric, magnetic, electrochemical, etc.). We neglect them in this chapter while these factors could be considered in a similar way. Note also that the variable, r has a similar effect of surface; we in this chapter take however a more general form, namely, r, to study this effect. Our goal is to figure out how T, P, r, and composition changes affect the equilibrium between phases, which results in that we can make maps of the existing phases at various variables or phase diagrams. Much of the information about the control of microstructures or phase structures of a particular alloy system is conveniently and concisely displayed in a phase diagram, which is the mainstay of materials science and technology. Of course, many useful materials involve thermodynamically unstable structures whose physical stability is maintained by limiting the rate at which the structure approaches equilibrium. Even in those cases, however, it is important to know how many phases may exist at equilibrium, given a set of specified physical constraints. The phase rule addresses that ques-

tion. Although in recent days there are also metastable phase diagrams for related phase equilibriums, we have not considered them while these kinds of phase diagrams follow the same rule of the phase diagram for phases in thermodynamic equilibria.

The constructions of phase diagrams as well as some of the principles governing the conditions for phase equilibria are dictated by laws of thermodynamics. One of these is the Gibbs phase rule. This rule represents a criterion for the number of phases that will coexist within a system at equilibrium, and is expressed by the simple equation,

$$fi = C - \Pi + N \tag{4.1}$$

where Π is the number of phases presented. The parameter fi is termed the number of degree of freedom or the number of externally controlled variables (e.g., T, P, composition) which must be specified to completely define the state of the system. Or, expressed another way, fi is the number of these variables that can be changed independently without altering the number of phases that coexist in equilibrium. The parameter C represents the number of components in the system. Finally, N in Eq. (4.1) is the number of noncompositional variables (e.g., T and P).

The phase diagram of a one-component system ($C = 1$), such as pure water, is shown in Fig. 4.1. In the region containing only one phase ($\Pi = 1$), $fi = C - \Pi + 2 = 2$. Thus in the gas region, both T and P may be arbitrarily fixed while the phase remains.
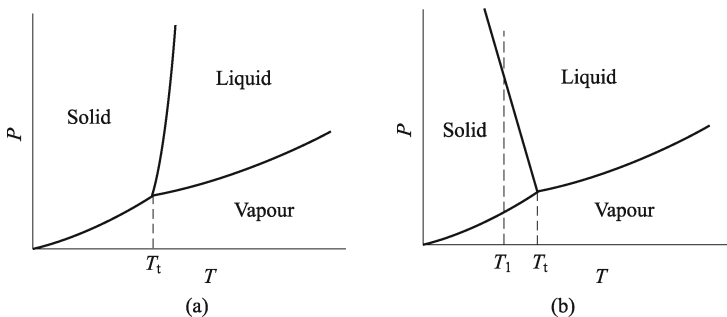
Fig. 4.1 Phase diagrams of a most simple substance (a), water which expands on freezing (b).

The lines of equilibria or phase boundaries separate the three phases of solid, liquid, and gas in Fig. 4.1 in three two-phase regions ($\Pi = 2$), where there is only one degree of freedom, $fi = C - \Pi + 2 = 1$. On these two-phase lines, we may arbitrarily fix either P or T. Once that has been done, another variable cannot be changed freely. Let us consider the slope of the lines of equilibria. Suppose two phases, i and ii, are in contact with each other and in equilibrium. Then the Gibbs free energy is related to $G(i) =$

$G(\text{ii})$. Along the phase line, we also have $dG_i = dG_{ii}$. Inserting the condition of equilibrium $dG = -SdT + VdP$ into the line, we obtain $-S_i dT + V_i dP = -S_{ii} dT + V_{ii} dP$. Rearranging the equation, $dP/dT = (S_i - S_{ii})/(V_i - V_{ii})$. From the relation between heat and change of entropy in a reversible process, there is $\Delta H_{i \to ii}(T, P) = T \Delta S_{i \to ii}(T, P)$. Combining the last two equations where all amounts are in molar units, it reads

$$\frac{dP}{dT} = \frac{\Delta H_{i \to ii}(T, P)}{T \Delta V_{i \to ii}(T, P)}. \tag{4.2}$$

Equation (4.2) is the Clapeyron equation, which, geometrically speaking, not only expresses the slope of the equilibrium line, but also gives the rate, where the P must change with T for two phases to remain in equilibrium. It applies to all changes of phases where there is a discontinuity in S and V at the transition that is the first order phase change.

4.2 Clapeyron Equation in Condensed State Equilibria [3, 4]

For the most substances, the slope of the solid-liquid line is positive. The greater the P on a given substance, the closer the molecules of the substance are brought to each other, which increases the effect of the substance's intermolecular forces. Thus, the substance requires a higher T for its molecules to have enough energy to break out the fixed pattern of the solid phase and enter the liquid phase. The reason is also interpreted qualitatively from Eq. (4.2), which shows that this is associated with the fact that the most substances expand on melting and therefore have both ΔV and ΔH positive. Water is an exception in that it expands on freezing so that the solid-liquid boundary has a negative slope. Thus, in the case of water, it is possible by increasing P isothermally to pass from vapor to solid to liquid (e.g. at T_1 in Fig. 4.1(b)) whereas for most substances, the solid is the high-pressure phase. As stated in Chapter 3, when chemical bonding is changed, such as semiconductors, ΔV could also be negative where coherent bonding with $CN \approx 4 - 8$ in solids changes to metallic bonding with $CN \approx 10 - 11$ in liquids.

To utilize Eq. (4.2) for determination of the phase diagram, one is frequently interested in knowing the relation between the equilibrium values of P and T instead of their mutual rate of change. This leads to trying and integrating Eq. (4.2) where experimental $\Delta H_{i \to ii}(T, P)$ and $\Delta V_{i \to ii}(T, P)$ functions for a certain material are needed. Since both $\Delta H_{i \to ii}(T, P)$ and $\Delta V_{i \to ii}(T, P)$ are functions of T and P, and the necessary separation of variables cannot be accomplished in any direct and known manner, the integration of Eq. (4.2) has been carried out through approximate methods ever since the equation was first established in the 19th century.

The crudest approximation is to take $\Delta H_{i \to ii}$ and $\Delta V_{i \to ii}$ as constants.

When $\Delta P = P - P_0$ and $\Delta T = T - T_0$ are small where the subscript "0" denotes the initial point, $\Delta H_{i \to ii}(T,P) \approx \Delta H_{i \to ii}(T_0, P_0)$ and $\Delta V_{i \to ii}(T,P) \approx \Delta V_{i \to ii}(T_0, P_0)$ have a minor error. Equation (4.2) then integrates to give $P = (\Delta H_{0,i \to ii} \ln T / \Delta V_{0,i \to ii}) + a'$ with a' being a constant.

Instead of assuming that $\Delta H_{i \to ii}$ was constant, we may make the better approximation that $\Delta H_{i \to ii}$ is a function of T while $\Delta V_{i \to ii}$ is a function of $P, \Delta H_{i \to ii}(T,P) \approx \Delta H_{i \to ii}(T)$ and $\Delta V_{i \to ii}(T,P) \approx \Delta V_{i \to ii}(P)$, which brings out a simplification of Eq. (4.2) [5],

$$\frac{\mathrm{d}P}{\mathrm{d}T} = \frac{\Delta H_{i \to ii}(T)}{T \Delta V_{i \to ii}(P)}. \qquad (4.3)$$

In fact, the P and T dependent molar volumes of the both phases for wide ranges of P and T are rarely known. Simple analytical forms of $\Delta V(T,P)$ have to be used.

In order to assess the P effect on T, the surface stress-induced internal pressure P_{in} for a spherical particle is extended to the bulk case. Let P denote the sum of P_{in} and the external pressure $P_e, P = P_{in} + P_e$. When $P_e \approx 0$, $P = P_{in}$. This is the case for the size-dependent transition of low-dimensional materials. When $P_{in} \approx 0$ with $r \to \infty, P = P_e$, which is the usual situation of pressure-dependent transition for bulk materials. Since any pressure source should have the same effect on materials properties, P_{in} can be substituted by P_e. In our case, we will use the expression of P_{in} as that of P in the following [6, 7].

As an example, the T-P phase diagram of Ge determined by Clapeyron equation is introduced [8]. In the T-P phase diagram of Ge, there are together three transitions with the corresponding $T(P)$ functions, which are the melting of Ge-I, the solid transition between Ge-I and Ge-II where I and II denote different solid states, and the melting of Ge-II. These transitions are identified by subscripts of I-L, I-II and II-L, respectively. According to Eq. (4.3), three $T(P)$ curves are obtained by integrating Eq. (4.3) after suitable considerations for initial points and $\Delta H(T)$ and $\Delta V(P)$ functions, which are described here. The first one in consideration is the I-L transition. For this transition, $\Delta H_m(T)$ function can be determined by Helmholtz function, $\Delta H_m(T) = \Delta G_m(T) - T \mathrm{d} \Delta G_m(T)/\mathrm{d}T$. For semiconductors, $\Delta G_m(T) = \Delta H_{m,0} T (T_{m,0} - T)/(T_{m,0})^2$ where the subscript "0" denotes the reference state [9] (for details see Sec. 4.6). Thus,

$$\Delta H_m(T) = \Delta H_{m,0}(T/T_{m,0})^2. \qquad (4.4)$$

When $T < T_K$ with $T_K = T_{m,0}/2$ being the Kauzmann temperature or isentropic temperature where $\partial \Delta G_m(T)/\partial T = 0$ [10], $\Delta H_m(T) = \Delta H_m(T_K)$. As a result, at $T < T_K$,

$$\Delta H_m(T) = \Delta H_{m,0}/4. \qquad (4.5)$$

Another function of Eq. (4.3) is $\Delta V_{I-L}(P_I) = (V_{L,0} - V_{I,0}) + (\Delta V_L - \Delta V_I)$ where $V_{L,0}$ and $V_{I,0}$ as molar volumes of liquid and solid are known data

while $\Delta V_L = -V_L P_L \beta_L$ and $\Delta V_I = -V_I P_I \beta_I$ with the available compressibility $\beta = -\Delta V/(VP)$. P_L and P_I in the above equations are considered by assuming a spherical particle with a radius r where there exists a curvature-induced pressure. In light of the Laplace-Young equation, $P_I = 2f_I/r$ and $P_L = 2\gamma_{sv}/r$ [11]. Essentially γ_{sv} describes a reversible work per unit area to form a new surface while f denotes a reversible work per unit area due to the elastic deformation, which equals the derivative of γ_{sv} with respect to the strain tangential to the surface. For solid, $f \neq \gamma$ while for liquid $f = \gamma_{sv}$. Thus, $\Delta V_L = -V_{L,0} P_I(\gamma/f_I)\beta_L$ because $P_I/P_L = f_I/\gamma_{sv}$. Substituting this relationship into $\Delta V_{I\text{-}L}(P_I)$ function, it reads

$$\Delta V_{I\text{-}L}(P_I) = V_{L,0} - V_{I,0} + [V_{I,0}\beta_I - V_{L,0}(\gamma_{sv}/f_I)\beta_L]P_I \qquad (4.6)$$

where f has been expressed as

$$f = (h/2)[3\Delta S_{vib}\Delta H_m(T)/(\beta V R)]^{1/2}. \qquad (4.7)$$

When the initial point of (P_0, T_0) is selected as $(0, T_{mI,0})$ where $T_{mI,0}$ is the melting temperature of Ge-I under ambient pressure, integrating Eq. (4.3) with $\Delta H_{I\text{-}L}(T_{I\text{-}L})$ and $\Delta V_{I\text{-}L}(P_I)$ functions in terms of Eqs. (4.4) and (4.6),

$$\int_0^{P_I} \{V_{L,0} - V_{I,0} + [V_{I,0}\beta_I - V_{L,0}(\gamma_{sv}/f_I)\beta_L]P_I\}\mathrm{d}P_I$$
$$= [\Delta H_{I\text{-}L,0}/(T_{mI,0})^2]\int_{T_{mI,0}}^T T\mathrm{d}T, \quad \text{or,}$$

$$T(P_I) = T_{mI,0}\sqrt{1 + \{2(V_{L,0} - V_{I,0})P_I + [V_{I,0}\beta_I - V_{L,0}(\gamma_{sv}/f_I)\beta_L]P_I^2\}/\Delta H_{I\text{-}L,0}}. \qquad (4.8)$$

Note that Eq. (4.8) is also applicable to nanosized material if $T_{mI,0}$ in Eq. (4.8) is substituted by $T_m(r)$ at $P = 0, T_{mI,0}(r)$. Thus, $T_{mI,0}(r)$ is a function of r and P. The value of $T_{mI,0}(r)$ has been deduced as Eq. (3.80). In Sec. 4.5.2, we will discuss the size-dependent phase diagram in detail.

For I-II transition, the subscript "I'" is used to substitute I for distinguishing this P-induced transition from melting transition of the Ge-I phase since the initial point as the boundary condition is selected as $(P_{I\text{-}II,0}, 273)$, where $P > 0$ and related parameters have been affected by P. Since $P_{I'}$ varies a little in the full transition temperature range, as a first order approximation, $\Delta V_{II} \approx \Delta V_{I'}$ is assumed and thus $V_{II,0}f_{II}\beta_{II} \approx V_{I',0}f_{I'}\beta_{I'}$. As a result,

$$\Delta V_{I\text{-}II}(P_{I'}) \approx V_{II,0} - V_{I',0}, \qquad (4.9)$$

and

$$f_{II} \approx (V_{I',0}/V_{II,0})(\beta_{I'}/\beta_{II})f_{I'}. \qquad (4.10)$$

The corresponding thermodynamic parameters of Ge-II differ from Ge-I due to their distinct structures. Since the specific heat difference between different polymorphous solid phases ΔC_P is small, it is assumed that

$$\Delta S_{\text{vibII-L}} \approx \Delta S_{\text{vibI-L}} + \Delta S_{\text{vibI-II}} \tag{4.11}$$

where $\Delta S_{\text{I-II}} = \Delta H_{\text{I-II},0}/T_{\text{I-II},0}$, which may be determined by

$$\Delta S_{\text{vibI-II}} = (\Delta H_{\text{I-II},0}/T_{\text{I-II},0})(\Delta S_{\text{vibI-L}}/\Delta S_{\text{mI}}) \tag{4.12}$$

where $\Delta S_{\text{vibI-II}}/\Delta S_{\text{I-II}}$ is supposed to be equal to $\Delta S_{\text{vibI-L}}/\Delta S_{\text{mI}}$ as a first order approximation.

With the neglect of $\Delta C_P, \Delta H_{\text{I-II},0} \approx \Delta H_{\text{II-L}} - \Delta H_{\text{I-L}}$. As the transition occurs at $T < T_{\text{K}}$, in terms of Eq. (4.5),

$$\Delta H_{\text{I-II},0} = (\Delta H_{\text{II-L}} - \Delta H_{\text{I-L},0})/4. \tag{4.13}$$

Note that Eqs. (4.4) and (4.5) are also applicable to $\Delta H_{\text{II-L}}(T)$. In terms of Eqs. (4.5), (4.7) and (4.10), $(V_{\text{I}',0}/V_{\text{II},0})(\beta_{\text{I}'}/\beta_{\text{II}})h_{\text{I}'}[\Delta S_{\text{vibI-L}}\Delta H_{\text{mI},0}/(\beta_{\text{I}'}V_{\text{I}',0})]^{1/2} = h_{\text{II}}[\Delta S_{\text{vibII-L}} \times \Delta H_{\text{mII}}/(\beta_{\text{II}}V_{\text{II},0})]^{1/2}$, it yields

$$\Delta H_{\text{II-L}} = (V_{\text{I}',0}/V_{\text{II},0})(\beta_{\text{I}'}/\beta_{\text{II}})(h_{\text{I}'}^2/h_{\text{II}}^2)(\Delta S_{\text{I-L}}^{\text{vib}}/\Delta S_{\text{II-L}}^{\text{vib}})\Delta H_{\text{I-L},0}. \tag{4.14}$$

In terms of Eqs. $(4.11)-(4.14)$, $\Delta H_{\text{I-II},0}$ is obtained as

$$\begin{aligned}
\Delta H_{\text{I-II},0} = \{&[(4T_{\text{I-II},0}\Delta S_{\text{mI}} - \Delta H_{\text{I-L},0})^2 \\
&+16\Delta H_{\text{I-L},0}T_{\text{I-II},0}\Delta S_{\text{mI}}(V_{\text{I}',0}/V_{\text{II},0})(\beta_{\text{I}'}/\beta_{\text{II}})(h_{\text{I}'}^2/h_{\text{II}}^2)]^{1/2} \\
&-\Delta H_{\text{I-L},0} - 4T_{\text{I-II},0}\Delta S_{\text{mI}}\}/8. \tag{4.15}
\end{aligned}$$

Integration of $P_{\text{I}'}$ from $P_{\text{I-II},0}$ to $P_{\text{I}'}$ and T from $T_{\text{I-II},0}$ to T in terms of Eqs. (4.9) and (4.15) gives $\displaystyle\int_{P_{\text{I-II},0}}^{P_{\text{I}'}} (V_{\text{II},0} - V_{\text{I}',0})\mathrm{d}P_{\text{I}'} = \Delta H_{\text{I-II},0}\int_{T_{\text{I-II},0}}^{T} \frac{1}{T}\mathrm{d}T$, which brings out

$$T(P_{\text{I}'}) = T_{\text{I-II},0} \exp[(V_{\text{II},0} - V_{\text{I}',0})(P_{\text{I}'} - P_{\text{I-II},0})/\Delta H_{\text{I-II},0}]. \tag{4.16}$$

Letting Eq. (4.8) = Eq. (4.16), the Ge-I/Ge-II/liquid triple point $(P_{\text{t}}, T_{\text{t}})$ is obtained, which is considered as the known threshold point for the melting curve of Ge-II. Since all the three phases $(\Pi = 3)$ coexist there, there is no freedom in the system and the condition for thermodynamic equilibrium leads to unique T and P defining the triple point, or there is only one combination of T and P where three phases coexist in a single-component system.

If it is assumed that Eqs. (4.4) and (4.6) are applicable to the $\Delta H_{\text{II-L}}(T)$ and $\Delta V_{\text{II-L}}(P)$ functions through substituting the initial point of $(0, T_{\text{mI},0})$ by $(P_{\text{t}}, T_{\text{t}})$, Eq. (4.3) is integrated from P_{t} to P_{II} for P_{II} and from T_{t} to T for T to

give $\displaystyle\int_{P_{\mathrm{t}}}^{P_{\mathrm{II}}} \{V_{\mathrm{L}} - V_{\mathrm{II}} + [V_{\mathrm{II}}\beta_{\mathrm{II}} - V_{\mathrm{L}}(\gamma/f_{\mathrm{II}})\beta_{\mathrm{L}}]P_{\mathrm{II}}\}\mathrm{d}P_{\mathrm{II}} = (\Delta H_{\mathrm{II\text{-}L}}/T_{\mathrm{t}}^2)\int_{T_{\mathrm{t}}}^{T} T\mathrm{d}T,$

which in turn results in

$$
\begin{aligned}
&T(P_{\mathrm{II}}) \\
&= T_{\mathrm{t}}\sqrt{1 + \{2(V_{\mathrm{L}} - V_{\mathrm{II}})(P_{\mathrm{II}} - P_{\mathrm{t}}) + [V_{\mathrm{II}}\beta_{\mathrm{II}} - V_{\mathrm{L}}(\gamma/f_{\mathrm{II}})\beta_{\mathrm{L}}](P_{\mathrm{II}} - P_{\mathrm{t}})^2\}/\Delta H_{\mathrm{II\text{-}L}}}.
\end{aligned}
\tag{4.17}
$$

Figure 4.2 presents functions of Eqs. (4.8), (4.16) and (4.17) and experimental results of T-P phase diagram of Ge where the necessary parameters are listed in Table 4.1. Note that P_{in} in tiny droplets of a few molecules may reach GPa range studied here where the pressure has a real effect on V of solid and liquid.
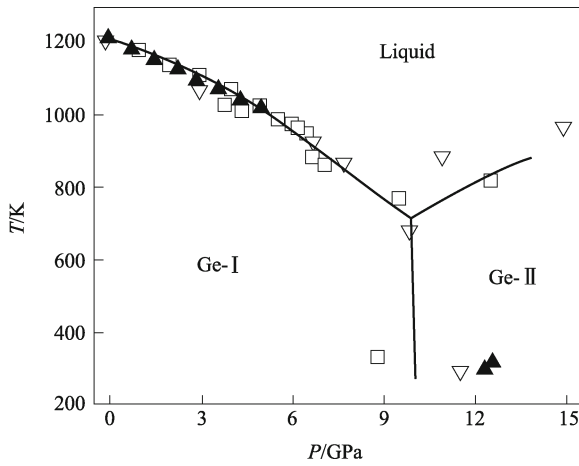

Fig. 4.2 A comparison of T-P phase diagrams of Ge between Eqs. (4.8), (4.16) and (4.17) (solid line) and experimental results shown with different symbols come from distinct sources.(Reproduced from Ref. [8] with permission of Elsevier)

The P-T relationship in Fig. 4.2 is established by a generalization from the consideration of internal pressure on small particles to the bulk case. Thus, the low size limit of nanoparticles for P_{in} at $6h$ in Eqs. (4.8) and (4.17) must be considered. For I-L transition, at $6h_{\mathrm{I}} = 1.47$ nm, $P_l = 6.12$ GPa in terms of Eq. (4.7). As shown in the figure, $P_{\mathrm{t}} = 9.915$ GPa. In order to predict the P-T relationship from 6.12 GPa to 9.915 GPa, the value of $T(P = 6.12$ GPa) and the corresponding slope are linearly extended up to P_{t} point. This consideration is based on the experimental results shown in the figure where when P is large enough, the melting curve approximately changes linearly. With a similar consideration, for II-L transition, at $6h_{\mathrm{II}} = 1.62$ nm, $P_2 = 3.92$ GPa in terms of Eq. (4.10) and the largest applicable pressure is 13.835 GPa, which is the sum of P_{t} and P_2.

Table 4.1   Necessary parameters for calculating $T(P)$ phase diagram of Ge in terms of Eqs. (4.8), (4.16) and (4.17). T is in K, P in GPa, V in cm$^3 \cdot$mol^{-1}, β in 10^{-11}Pa^{-1}, γ and f in J$\cdot$m^{-2} and ΔH is in kJ$\cdot$mol^{-1}

I-L transition		I-II transition		II-L transition	
$T_{\mathrm{mI},0}$	1210.4	$T_{\text{I-II},0}$	273[d]	T_t	714[f]
		$P_{\text{I-II},0}$	10[d]	P_t	9.915[f]
$V_{\mathrm{I},0}$	13.64[a]	$V_{\mathrm{I}',0}$	11.93[a]	V_{II}	9.66[a]
$V_{\mathrm{L},0}$	12.94[a]	$V_{\mathrm{II},0}$	9.66[a]	V_{L}	12.94[a]
β_{I}	1.33[b]			β_{II}	1.19[b]
β_{L}	10.00			β_{L}	10.00
f_{I}	2.252[c]			f_{II}	1.589[c]
γ	0.581			γ	0.581
$\Delta H_{\text{I-L},0}$	36.94	$\Delta H_{\text{I-II},0}$	0.2[e]	$\Delta H_{\text{II-L}}$	37.74[e]

[a] $V_{\mathrm{I},0} = M_\mathrm{w}/\rho_\mathrm{I}$ and $V_{\mathrm{L},0} = M_\mathrm{w}/\rho_\mathrm{L}$ with $M_\mathrm{w} = 72.59$ g$\cdot$mol^{-1} being the molar weight and ρ being the density, $\rho_\mathrm{I} = 5.32$ g$\cdot$cm^{-3} and $\rho_\mathrm{L} = 5.61$ g$\cdot$cm^{-3}·$V_{\mathrm{II},0} = N_\mathrm{A} v_{\mathrm{II}}$ and $V_{\mathrm{I}',0} = N_\mathrm{A} v_{\mathrm{I}'}$ where N_A denotes the Avogadro's constant and v is the mean atom volume within the corresponding crystalline structures. $v_{\mathrm{II}} = a_{\mathrm{II}}^2 c_{\mathrm{II}}/4 = 0.016{,}053$ nm^3 with the lattice constants $a_{\mathrm{II}} = 0.4884$ nm and $c_{\mathrm{II}} = 0.2692$ nm for β-Sn structure and $v_{\mathrm{I}'} = (a_{\mathrm{I}'})^3/8 = 0.019{,}815$ nm^3 where the lattice constant $a_{\mathrm{I}'} = 0.5412$ nm for diamond structure.

[b] $\beta_\mathrm{I} = 1/B_{\mathrm{m},\mathrm{I}}$ and $\beta_{\mathrm{II}} = 1/B_{\mathrm{m},\mathrm{II}}$ with B_m being the bulk modulus, $B_{\mathrm{m},\mathrm{I}} = 75.0$ GPa and $B_{\mathrm{m},\mathrm{II}} = 84.0$ GPa. Note that as the first-order approximation, $\beta_{\mathrm{I}'} \approx \beta_\mathrm{I}$ is assumed.

[c] f_I is calculated by Eq. (4.7) with $h_\mathrm{I} = (3^{1/2}/4)a_\mathrm{I} = 0.2450$ nm due to its diamond structure where $a_\mathrm{I} = 0.5658$ nm denoting the lattice constant and $\Delta S_{\text{I-L}}^{\text{vib}} = 4.6$ J$\cdot$mol$^{-1}\cdot$K^{-1}.f_{II} is calculated through Eq. (4.10) where $f_{\mathrm{I}'} = 1.151$ J$\cdot$m^{-2} determined by Eqs. (4.5) and (4.7) with $\beta_{\mathrm{I}'} \approx \beta_\mathrm{I} = 1.33 \times 10^{-11}$ Pa^{-1} being a weak function of pressure and $h_{\mathrm{I}'} = (3^{1/2}/4)a_{\mathrm{I}'} = 0.2343$ nm for diamond structure.

[d] This value is the more recent value and approximately the mean value among the experimental results.

[e] $\Delta H_{\text{I-II},0}$ is calculated by Eq. (4.15) where $\Delta S_{\mathrm{mI}} = \Delta H_{\text{I-L},0}/T_{\mathrm{mI},0} = 30.52$ J$\cdot$mol$^{-1}\cdot$K^{-1} and $h_{\mathrm{II}} = c_{\mathrm{II}} = 0.2692$ nm due to its β-Sn structure. The value of $\Delta H_{\text{II-L}}$ is determined by Eq. (4.13).

[f] The triple point $(P_\mathrm{t}, T_\mathrm{t})$ is determined by letting Eq. (4.8) = Eq. (4.16).

High pressure work on Ge is plagued with the problems of sluggish phase transitions and possible metastable phases. Thus, the I-II phase boundary in the T-P diagram is very indefinite with a wide reported transition pressure where the transition with hysteresis is very slow, especially at the lower temperature range. As shown in the figure, although a mean value of $P_{\text{I-II},0}$ among different experiments has been selected to ascertain the I-II transition curve, the predicted I-II phase boundary in terms of Eq. (4.16) is indeed approximately equal to the mean value of the experimental results.

4.3 Solution, Partial Molar Properties and Chemical Potential [1, 12, 13]

Until now we have confined our discussion to closed physical systems, which cannot exchange matter with their surroundings. Now it is time to extend our discussion to open systems, in which the quantity of matter is not fixed and matter can move in or out of the system.

Many interesting properties of materials, important phase equilibria and

phase transitions take place not among pure elements or compounds, but among elements of compounds dissolved in one another's solutions. A solution is a homogeneous mixture of two or more substances, in which particles of one or more substances (the solute) are distributed uniformly throughout another substance (the solvent), so that the mixture is homogeneous at the molecular or ionic level. A solution may exist in any phase, which may be solids, liquids, gases, or a combination of these. Brass, aqueous hydrochloric acid and air are examples of the solid, liquid and gas solution, respectively.

A solution that has uniform physical and chemical characteristics is defined as one homogeneous phase. We know that a system may consist of more than one phase and the concentration of chemical species throughout the system is typically inhomogeneous. To describe the phase equilibria of system with many chemical species, and with non-uniform distributions of those components in the different phases, we need to generalize our treatment of phase equilibria and phase transitions. In order to understand the thermodynamic properties of these multicomponent systems, the key idea here is that we need to develop a method of describing the properties of solutions. This strategy for describing solutions is heavily based on the concept of partial molar properties, which will be considered here.

Partial molar properties are thermodynamic quantities, which indicate how any extensive property of a solution or a mixture varies with changes in the molar composition of the mixture at constants T and P. Stated another way, it is the change rate of that quantity as mass of a particular component is added to a system at constants T and P. Thus, a partial molar quantity is expressed mathematically as the partial derivative of that quantity with respect of number of moles n at constant T, P, and n of all other materials in the system. Every extensive property of a solution has a corresponding partial molar property.

Let us consider the Gibbs free energy of a solution consisting of materials A and B at constants T and P. $G = G(n_A, n_B)_{T,P}$ is a function of the amounts of $A(n_A)$ and $B(n_B)$. Because G is a state function, there is

$$dG = \left(\frac{\partial G}{\partial n_A}\right)_{T,P,n_B} dn_A + \left(\frac{\partial G}{\partial n_B}\right)_{T,P,n_A} dn_B.$$

$(\partial G/\partial n_A)_{T,P}$ is named the partial molar volume of A, and is written as

$$G_A = \left(\frac{\partial G}{\partial n_A}\right)_{T,P,n_B}. \tag{4.18}$$

Then,

$$dG = G_A dn_A + G_B dn_B. \tag{4.19}$$

Similarly, G of a solution with i components can be expressed as $dG = \Sigma_i G_i dn_i$. The partial molar property is thus an intensive property without mass dependence of the system. As a limiting case, the partial molar Gibbs

free energy of pure A is just the molar one of A, $G_{m,A}$, where the subscript "m" denotes the molar amount.

The significance of Eq. (4.18) is shown in Fig. 4.3. It is the change rate of the volume of the solution with respect to the moles of B added. The partial molar volume of a component in a solution is the volume change of a very large amount (infinite, in fact) of the solution when one mole of the particular component is added to it, at constants T and P.
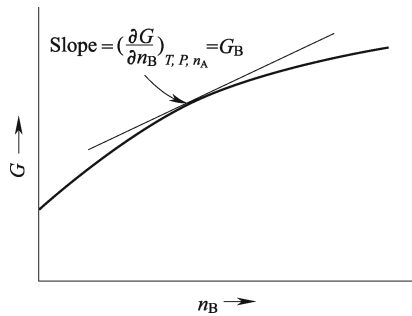

Fig. 4.3 Gibbs free energy of solution A-B as a function of moles of B added to the solution.

We can integrate Eq. (4.19) along a special path where n_A/n_B remains constant. If the composition is constant, G_A and G_B are constants, and $G = G_A n_A + G_B n_B$. Dividing this by the total number of moles, $n_A + n_B, G_m$ is got,

$$G_m = G_A x_A + G_B x_B \qquad (4.20)$$

where x_A and x_B are the mole fractions of A and B in the solution. The same principle applies to other quantities, such as H, S, and F. Generaly, for a generic extensive property of a solution Γ', we have $\Gamma'_m = \sum_i \Gamma'_i x_i$.

For a system with variable composition, the thermodynamic energy is also a function of n of each of the substance present at a given time. To be more useful, the thermodynamic basic equations with Eqs. (1.36)–(1.39) are extended to deal with changes in composition through additions of mass. For $U = U(S, V, n_i), H = H(S, P, n_i), F = F(T, V, n_i)$, and $G = G(T, V, n_i)$, we have

$$dU = TdS - PdV + \sum_i \left(\frac{\partial U}{\partial n_i}\right)_{S,V,n_j \neq n_i} dn_i,$$

$$dU = TdS + VdP + \sum_i \left(\frac{\partial H}{\partial n_i}\right)_{S,P,n_j \neq n_i} dn_i, \qquad (4.21)$$

$$dF = -SdT - PdV + \sum_i \left(\frac{\partial F}{\partial n_i}\right)_{T,V,n_j \neq n_i} dn_i,$$

$$dG = -SdT + VdP + \sum_i \left(\frac{\partial G}{\partial n_i}\right)_{T,P,n_j \neq n_i} dn_i.$$

Since $G = F + PV, dG = dF + PdV + VdP$. Combining with the equations above,

$$dG = -SdT + VdP + \sum_i \left(\frac{\partial G_i}{\partial n_i}\right)_{T,P,n_j \neq n_i} dn_i$$

$$= -SdT + VdP + \sum_i \left(\frac{\partial F}{\partial n_i}\right)_{T,V,n_j \neq n_i} dn_i.$$

Thus,

$$\sum_i \left(\frac{\partial G_i}{\partial n_i}\right)_{T,P,n_j \neq n_i} = \sum_i \left(\frac{\partial F_i}{\partial n_i}\right)_{T,V,n_j \neq n_i}.$$

By repeating the procedure for each of the defined thermodynamic variables, we have

$$\sum_i \left(\frac{\partial G_i}{\partial n_i}\right)_{T,P,n_j \neq n_i} = \sum_i \left(\frac{\partial F_i}{\partial n_i}\right)_{T,V,n_j \neq n_i} = \sum_i \left(\frac{\partial H_i}{\partial n_i}\right)_{S,V,n_j \neq n_i}$$

$$= \sum_i \left(\frac{\partial_i U}{\partial n_i}\right)_{T,V,n_j \neq n_i} = \mu_i$$

where μ_i is the chemical potential of the component i and $\mu_i = G_i$. This implies that the partial molar Gibbs free energy and the chemical potential, one of the most important properties in thermodynamics and chemistry, are the same in quantity.

In real systems, it is usually difficult to hold the entropy fixed, since this involves good thermal insulation. It is therefore more convenient to use μ as the partial derivative of F or G with respect to n_i with constants T, V, and T, P, respectively. Under isobaric and isothermal conditions, knowledge of μ_i yields every property of mixture as it completely determines G_i.

μ_i as a fundamental parameter is conjugate to the composition, being used extensively in the treatment of the thermodynamics of solutions and of chemical reactions. In modern statistical physics, μ_i is the Lagrange multiplier (see Eq. (2.18)) for the average particle constraint, when maximizing S. This is a precise and abstract scientific definition, just like T is defined as the Lagrange multiplier for the average energy constraint. μ at $T = 0$ K of a system of electrons is also called the Fermi level.

4.4 Graphical Representation, Ideal and Regular Solutions [1]

If we know a property of a two-component solution as a function of n_i, we can determine the partial molar values of that property. Taking V_m as an

example, we have $V_m = V_A x_A + V_B x_B$. From this equation, the result would look something like the solid line in Fig. 4.4. Because $x_A + x_B = 1$, $dx_A + dx_B = 0$, and $dx_A/dx_B = -1$, Eq. (4.20) can also be written as $(\partial V_m/\partial x_B)_{T,P} = V_B - V_A$. Multiplying this equation by x_A and x_B, respectively, two equations are present. Subtracting them from V_m, it reads

$$V_A = V_m - x_B \left(\frac{\partial V_m}{\partial x_B}\right)_{T,P}, \tag{4.22a}$$

$$V_B = V_m + x_A \left(\frac{\partial V_m}{\partial x_B}\right)_{T,P}. \tag{4.22b}$$

This is a kind of abstract at this point and it may be difficult to realize what this is telling us. Equation (4.22a) says that V_A can be thought of as the intersection of the tangent of V_m as a function of x_B with V_m axis at $x_B = 0$. V_B on the other hand is the intersection of that tangent with V_m axis at $x_B = 1$. Figure 4.4 shows this graphically.
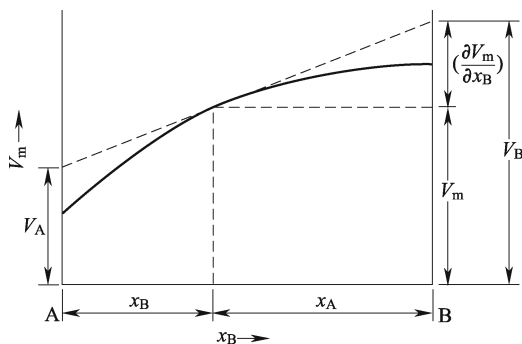

Fig. 4.4 Plot of V_m versus x_B to show geometrical relationships to an A-B solution.

Substituting G for V in Eqs. (4.22a) and (4.22b) and combining the relationship of $G_A = \mu_A$, the chemical potentials of each species in solution as a function of composition are got,

$$\mu_A = G_m - x_B \left(\frac{\partial G_m}{\partial x_B}\right)_{T,P}, \tag{4.23a}$$

$$\mu_B = G_m + x_A \left(\frac{\partial G_m}{\partial x_B}\right)_{T,P}. \tag{4.23b}$$

The functions that are of special importance for expressing μ in detail and to construct a phase diagram for a multicomponent material are G, H, S. Thus, we will concentrate on them. There are various standard models for solutions that provide approximations to the above functions. Let us consider firstly the thermodynamics of ideal solution.

Ideality of solutions is analogous to that of gases, with the important difference that intermolecular interactions in condensed phases are strong and can not simply be neglected as they can in an ideal gas. What is meant by "ideal" in these cases is that the interactions between the constituents of the solution are the same, regardless of their nature. More formally, for a mix of molecules of A and B, the interaction energy between unlike neighbors (ε_{AB}) is the same as that between neighbors ε_{AA} and ε_{BB}, i.e. $\varepsilon_{AB} = \varepsilon_{AA} = \varepsilon_{BB}$. It follows that there is no enthalpy change (enthalpy of mixing $\Delta_{mix}H = 0$) when the substances are mixed, then the solution is automatically ideal. The more dissimilar the nature of A and B, the more strongly the solution is expected to deviate from ideality.

Why do the components of the ideal solution mix with each other? The reason is the existence of the entropy of mixing of an ideal solid solution, which consists of atoms labeled A and B. Using Boltzmann equation written for each of the components and the mixture, all the configurations are at the same energy level, all are equally probable, and then the positioning of atoms on a lattice is random where $\Delta_{mix}H = 0$. For one mole of atoms (the sum of N_A and N_B is Avogadro's number of atoms, N_m), the way number of microstates is $N_m!$ to introduce the atoms onto the lattice. Not all these different configurations are distinguishable. To account for this, we must divide by the number of different ways that the N_A atoms can be distributed on their sites. Using an argument similar to the one above, rearranging the atoms labeled A on the lattice can be done in $N_A!$ ways. A similar relationship applies for N_B. The entropy of this configuration, the entropy of mixing N_A and N_B, is $\Delta_{mix}S_m = k\ln\Omega = k\ln[N_m!/(N_A!N_B!)] = k\ln[N_m!\text{-}N_A!\text{-}N_B!]$. Using Stirling approximation,

$$\begin{aligned}
\Delta_{mix}S_m &= k[N_m \ln N_m - N_m - N_A \ln N_A + N_A - N_B \ln N_B + N_B] \\
&= k[(N_A + N_B)\ln N_m - N_A \ln N_A - N_B \ln N_B] \\
&= -k[N_A \ln(N_A/N_m) + N_B \ln(N_B/N_m)] \\
&= -kN_m[(N_A/N_m)\ln(N_A/N_m) + (N_B/N_m)\ln(N_B/N_m)] \\
&= -R[x_A \ln x_A + x_B \ln x_B].
\end{aligned}$$

The above expression can be generalized to a mixture of i components, starting with $\Omega = N_m!/(\prod_i N_i!)$, namely,

$$\Delta_{mix}S_m = -R\sum_i x_i \ln x_i. \tag{4.24}$$

Since $\Delta_{mix}H_m = 0$, there is $\Delta_{mix}G_m = \Delta_{mix}H_m - T\Delta_{mix}S_m = RT\sum_i x_i \ln x_i$, or for a two-component solution, $\Delta_{mix}G_m = RT(x_A \ln x_A + x_B \ln x_B)$. Since the mole fraction is always smaller than unity, the ln terms are negative, and $\Delta_{mix}G_m < 0$. This becomes more negative as T increases. As a result, ideal solutions are always completely miscible.

Gibbs free energy of the mixture equals the sum of Gibbs free energy of individual components and Gibbs free energy of mixing. This yields a fundamental expression for μ as a function of x_i. Now by mixing A and B to form an ideal solution, it reads $G_m = G_{\text{initial}} + \Delta_{\text{mix}}G_m = x_A G_{m,A} + x_B G_{m,B} + RT(x_A \ln x_A + x_B \ln x_B)$. Substituting the above equation into Eqs. (4.23a) and (4.23b), it reads

$$\mu_A = G_{m,A} + RT \ln x_A, \qquad (4.25a)$$

$$\mu_B = G_{m,B} + RT \ln x_B. \qquad (4.25b)$$

If the chemical potential of a pure component i is denoted μ_i^*, $G_{m,i} = \mu_i^*$ and the chemical potential of i in an ideal solution is $\mu_i = \mu_i^* + RT \ln x_i$.

Only the difference of chemical potential, $\Delta \mu_i = \mu_i - \mu_i^*$, has a physical meaning. The absolute value of μ_i depends on the location of zero of the potential energy scale, which is also called the standard state. For an ideal solution system, it is convenient to choose the pure component as its standard state. Note that the standard state is defined for each T.

Figure 4.5 shows the graphs of G_m as a function of x_B, with the two points representing $G_{m,A}$ and $G_{m,B}$ of pure A and B taken at different levels. Using the partial molar operator, we can convert general thermodynamic relationships to the coefficient one,

$$\left(\frac{\partial G_i}{\partial P} \right)_{T,n_i} = \left[\frac{\partial}{\partial P} \left(\frac{\partial G}{\partial n_i} \right)_{T,P,n_j \neq n_i} \right]_{T,n_i} = \left[\frac{\partial}{\partial n_i} \left(\frac{\partial G}{\partial P} \right)_{T,n_i} \right]_{T,P,n_j \neq n_i}$$

$$= \left[\frac{\partial V}{\partial n_i} \right]_{T,P,n_j \neq n_i} = V_i,$$

and the change in the partial molar volume is

$$\Delta_{\text{mix}}V_i = V_i - V_{m,i} = \left(\frac{\partial G_i}{\partial P} \right)_{T,n_j} - \left(\frac{\partial G_{m,i}}{\partial P} \right)_{T,n_j} = \left(\frac{\partial \Delta_{\text{mix}}G_i}{\partial P} \right)_{T,n_j}.$$

Now, if the mixture is ideal, we have

$$\Delta_{\text{mix}}V_i = \left(\frac{\partial (RT \ln x_i)}{\partial P} \right)_{T,n_j} = 0,$$

and thus

$$\Delta_{\text{mix}}V_m^{\text{ideal}} = \sum_i x_i \Delta_{\text{mix}}V_i = 0.$$

For an ideal solution, the change of the partial molar volume is absent as we form the mixture. In other words, the partial molar volume is independent of composition. If that is the case, the volume of the mixture is just the weighted average of the molar volumes of the pure substances. Thus, for an
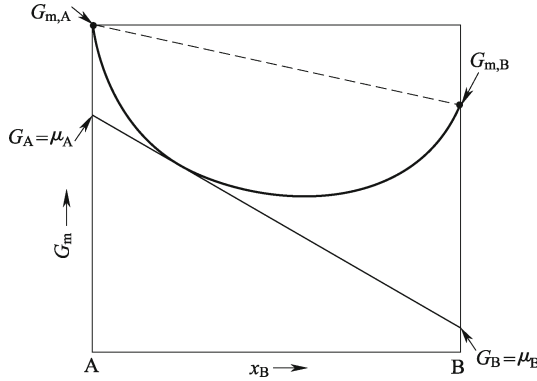
Fig. 4.5 Plot of G_m versus x_B to show their geometrical relationships.

ideal mixture, there is no change in V, U, or H from the total values of the pure states of all the components.

Better model of the Gibbs free energy of solution comes from consideration of the interactions between atoms in the system. The simplest version is called the regular solution model–it averages the interactions between like and unlike atoms to calculate $\Delta_{\text{mix}}H$ and uses the ideal solution to calculate $\Delta_{\text{mix}}S$. The regular solution model can predict "unmixing" and this results in a spinodal phase diagram.

For a solid solution consisting of randomly distributed A and B on the lattice sites, $\Delta_{\text{mix}}S$ of A and B is equal to the entropy of mixing of an ideal solution. Each atom will be assumed to have an energy interaction only with its nearest neighbors numbered by CN or z. We will mix N_A atoms of A with N_B atoms of B. Before mixing, the number of N_{AA} bonds among the A atoms (in pure A) is $N_A z/2$. We arrive at this conclusion by counting the number of bonds emanating from each A atom (z), multiplying by N_A, then dividing by 2 because the bonds are doubly counted. After mixing, the number of AA bonds will be $(N_A)^2 z/2N$ with $N = N_A + N_B$. To count the number of AA bonds we multiply N_A by two factors: z and the probability that its nearest neighbor is an A atom, N_A/N. The same procedure is followed for calculating the number of BB bonds and AB bonds. Thus, $\Delta_{\text{mix}}U = z[(N_A)^2 z\varepsilon_{AA}/(2N_T)+(N_B)^2 z\varepsilon_{BB}/(2N_T)+N_A N_B z\varepsilon_{AB}/N_T - N_A\varepsilon_{AA}/2 - N_B\varepsilon_{BB}/2]$. The resulting energy after mixing is listed in Table 4.2.

Table 4.2 Bond energy after mixing atoms A and B in a solid solution

	Number of bonds	Energy per bond	Energy
N_{AB}	$N_A N_B z/N$	ε_{AB}	$N_A N_B z\varepsilon_{AB}/N$
N_{AA}	$(N_A)^2 z/(2N)$	ε_{AA}	$(N_A)^2 z\varepsilon_{AA}/(2N)$
N_{BB}	$(N_B)^2 z/(2N)$	ε_{BB}	$(N_B)^2 z\varepsilon_{BB}/(2N)$

Since $x_A = N_A/N$, the above equation can be rewritten as $\Delta_{\text{mix}}U =$

$zN[(x_A^2 - x_A)\varepsilon_{AA} + (x_B^2 - x_B)\varepsilon_{BB}]/2 + x_A x_B \varepsilon_{AB} = zN x_A x_B[\varepsilon_{AB} - (\varepsilon_{AA} + \varepsilon_{BB})/2]$, or

$$\Delta_{\text{mix}} U = \omega x_A x_B \qquad (4.26)$$

where $\omega = zN[\varepsilon_{AB} - (\varepsilon_{AA} + \varepsilon_{BB})/2]$ is called the interaction parameter.

All ε values are negative, decreasing in absolute value with reducing r or decreasing N [14–16]. If decreasing rates of different ε values are distinct, ω is size-dependent. According to general quantum chemistry consideration, all thermodynamic quantities are roughly a linear function of $1/r$ that corresponds to the surface/volume ratio of particles. ω is assumed to have the same relationship. Because $\Delta H_{\text{m}}(2r_0) = 0$ in terms of Eq. (3.88), $\omega(r)$ should have the same limit and thus is assumed to have the following form:

$$\omega(r)/\omega(\infty) = 1 - 2r_0/r. \qquad (4.27)$$

Equation (4.26) for the $\Delta_{\text{mix}} U$ is equal to $\Delta_{\text{mix}} H$ for solids because the volume change influencing the PV term in the definition of enthalpy is very small. Therefore,

$$\Delta_{\text{mix}} G_{\text{m}} = \Delta_{\text{mix}} H_{\text{m}} - T\Delta_{\text{mix}} S_{\text{m}} = RT(x_A \ln x_A + x_B \ln x_B) + \omega x_A x_B. \quad (4.28)$$

From Eq. (4.26) it can be seen that the solution will behave as ideal ($\Delta_{\text{mix}} H = 0$) when $|\varepsilon_{AB}| = (|\varepsilon_{AA}| + |\varepsilon_{BB}|)/2$. If $|\varepsilon_{AB}| > (|\varepsilon_{AA}| + |\varepsilon_{BB}|)/2, \omega < 0$ and $\Delta_{\text{mix}} H < 0$. (Remember that $\varepsilon < 0$). A negative $\Delta_{\text{mix}} H$ favors stable homogeneous solutions and a positive $\Delta_{\text{mix}} H$ makes a system separate and has a miscibility gap at lower T.

To make adjustment for the non-ideality of the solution, a new property called the activity is used instead of x in the fundamental equation for μ. If materials A and B form a continuous set of solutions, but are non-ideal, the activity of material B is usually expressed as $a_B = f_B x_B$. Consequently,

$$\mu_B = \mu_B^* + RT \ln a_B = \mu_B^* + RT \ln x_B + RT \ln f_B \qquad (4.29)$$

where f is called the activity coefficient. If the solution itself is ideal, $a_B = x_B$ and $f_B = 1$ in light of Eqs. (4.25) and (4.29). Thus, departure of f from unity indicates a non-ideal behavior of the regular solution from the ideal solution, and f should account for the changes in the enthalpy during mixing.

Substituting Eq. (4.28) into Eqs. (4.23a) and (4.23b), μ of the individual components in a regular solution is shown to be

$$\mu_A = \mu_A^* + RT \ln x_A + \omega x_B^2, \qquad (4.30a)$$

$$\mu_B = \mu_B^* + RT \ln x_B + \omega x_A^2. \qquad (4.30b)$$

Comparing Eq. (4.29) and Eq. (4.30), it reads

$$f_A = \exp \frac{\omega x_B^2}{RT}, \quad f_B = \exp \frac{\omega x_A^2}{RT}. \qquad (4.31)$$

4.5 Equilibrium Conditions of Phases and Phase Diagram of Binary Systems [1, 3, 17]

Conventional equilibrium phase diagrams represent the relationships between T, P, x and the quantities of phases in equilibrium. When two or more phases are in equilibrium, there is no driving force for change, and the phases are stable. It is important to understand the criteria for equilibrium because the usefulness of many metallic, polymeric, and ceramic systems depends on the presence of various different equilibrium phases in materials. To approach this subject, the equilibrium conditions of phases need to be considered.

When a thermodynamic system is in thermal equilibrium, mechanical equilibrium, and diffusional (or chemical) equilibrium, it is said to be in thermodynamic equilibrium. The first two equilibria require the system to have constants T and P.

For a multicomponent (A, B, etc.), multiphase (α, β, etc.) system, all phases are in direct contact with each other where there are no surface effects or chemical reactions. The only displacement accessible to the system is that involving the transfer of mass from one phase to another. Suppose, for example, that we transfer dn_A moles (with $dn_A > 0$) of the Ath constituent from phase α to phase β. $dn_A^{\alpha} = -dn_A^{\beta}$. From Eq. (4.21), we know that $dG = -SdT + VdP + \sum_i \mu_i dn_i$. At constants T and P for the entire system, we have $dG_{T,P} = dG_\alpha + dG_\beta = -\mu_A^{\alpha} dn_A + \mu_A^{\beta} dn_A = (\mu_A^{\beta} - \mu_A^{\alpha})dn_A$. The equilibrium criterion of $dG_{T,P} \leqslant 0$ [Eq. (1.34)], is valid for any type of homogeneous or heterogeneous system. Now it is however more meaningful to restrict the initial use of this criterion to a study of phase equilibrium, which occurs in the multiphase system. Since dn_A is positive by construction, we conclude that $\mu_A^{\beta} - \mu_A^{\alpha} \leqslant 0$ or $\mu_A^{\beta} \leqslant \mu_A^{\alpha}$. If the system is not in equilibrium, $\mu_A^{\beta} < \mu_A^{\alpha}$, which indicates that a system can minimize its Gibbs free energy by transforming to the phase with the lowest chemical potential. When the system is in equilibrium, $\mu_A^{\beta} = \mu_A^{\alpha}$, there is only one chemical potential defined for the system. Our conclusion is that two phases in equilibrium must have the same T, P and μ. The above sequence of derivations can easily be extended to include more phases and/or extended to include mixtures, where we would find that the T, P, and μ of each component must be the same in every phase, i.e. $\mu_A^{\alpha} = \mu_A^{\beta} = \mu_A^{\gamma} = \cdots$. with similar conditions for each of the other components.

We know that systems like to minimize their energy. In solids, components are usually rearranged by diffusion. Thus, a chemical potential gradient of a component means that there is a driving force for diffusion of that material to regions of lower μ value. Just like temperature gradients are the potential for heat transfer, and pressure gradients are the driving force for bulk mass transport, chemical potential governs the flow of particles between distinct phases. μ can therefore be used to determine whether or not a system is in

equilibrium.

In a binary system containing gases, P changes are important. In condensed systems, however, the thermodynamic properties are relatively insensitive to changes in P and modest variations in P do not appreciably alter phase relationships. Thus, when dealing with relationships in solids, it is common to assume that the P of the system is one atmosphere pressure and is neglected. Now the phase rule is reduced to $fi = C - \Pi + 1$. At least $\Pi = 1, fi_{\max}$ accommodated is two. In such a condensed phase system, it is possible to plot phase stability regions for two-component systems in two dimensions. In binary diagrams, composition is generally plotted on the abscissa and T is drawn on the ordinate.

4.5.1 Complete Miscibility, Continuous Binary Solution Phase Diagram and Related Size Dependence

For a two-component system A-B, in which A and B are completely miscible in both solid and liquid states, an ideal solution is present. Based on our knowledge of the thermodynamics of the ideal solution (Sec. 4.4), we could predict the equilibrium phase diagram of this system, given information about T_{m} and ΔH_{m} of the two components.

At $T < T_{\mathrm{m}}$, for the melting of pure A, $\Delta G_{\mathrm{m}} = \Delta H_{\mathrm{m}} - T\Delta S_{\mathrm{m}}$. For simplicity, assume $\Delta C_P = 0$ between liquid and solid where ΔH_{m} and ΔS_{m} are T−independent. At T_{m}, the two phases are in equilibrium where $\Delta G_{\mathrm{m}} = 0$ and $\Delta S_{\mathrm{m}} = \Delta H_{\mathrm{m}}/T_{\mathrm{m}}$. ΔG_{m} can thus be rewritten as

$$\Delta G_{\mathrm{m}} = \Delta H_{\mathrm{m}}(T_{\mathrm{m}} - T)/T_{\mathrm{m}} = \mu_{\mathrm{L}}^* - \mu_{\mathrm{s}}^*. \tag{4.32}$$

Let $\Delta T = T_{\mathrm{m}} - T$ be the degree of supercooling. μ of A and B in the ideal liquid solution is $\mu_{\mathrm{A,L}} = \mu_{\mathrm{A,L}}^* + RT \ln x_{\mathrm{A,L}}$ and $\mu_{\mathrm{B,L}} = \mu_{\mathrm{B,L}}^* + RT \ln x_{\mathrm{B,L}}$. In light of these relations, $G_{\mathrm{m,L}} = x_{\mathrm{A,L}}\mu_{\mathrm{A,L}} + x_{\mathrm{B,L}}\mu_{\mathrm{B,L}} = x_{\mathrm{A,L}}\mu_{\mathrm{A,L}}^* + x_{\mathrm{B,L}}\mu_{\mathrm{B,L}}^* + RT(x_{\mathrm{A,L}} \ln x_{\mathrm{A,L}} + x_{\mathrm{B,L}} \ln x_{\mathrm{B,L}})$. $G_{\mathrm{m,s}}$ has a similar form. If we now choose the pure liquids A and B as the standard states, the terms $\mu_{\mathrm{A,L}}^*$ and $\mu_{\mathrm{B,L}}^*$ are each zero. Combining the equations above, the $G_{\mathrm{m,L}}$ and $G_{\mathrm{m,s}}$ are

$$G_{\mathrm{m,L}} = RT(x_{\mathrm{A,L}} \ln x_{\mathrm{A,L}} + x_{\mathrm{B}} \ln x_{\mathrm{B,L}}),$$
$$G_{\mathrm{m,s}} = RT(x_{\mathrm{A,s}} \ln x_{\mathrm{A,s}} + x_{\mathrm{B,s}} \ln x_{\mathrm{B,s}})$$
$$\quad - x_{\mathrm{A,s}}[\Delta H_{\mathrm{m}}(T_{\mathrm{m,A}} - T)/T_{\mathrm{m,A}}] - x_{\mathrm{B,s}}[\Delta H_{\mathrm{m}}(T_{\mathrm{m,B}} - T)/T_{\mathrm{m,B}}].$$

The $G_{\mathrm{m,L}}$ and $G_{\mathrm{m,s}}$ values are plotted from (a)–(d) in Fig. 4.6 at various T. At $T > T_{\mathrm{m,A}}$ and $T_{\mathrm{m,B}}, G_{\mathrm{m,L}}$ curve (Fig. 4.6(a)) lies below the curve for the solid across the entire composition range. Hence, the liquid exists in equilibrium across the phase diagram, as expected. The reverse is true for $T < T_{\mathrm{m,A}}$ and $T < T_{\mathrm{m,B}}$ (Fig. 4.6(b)).

At $T_{\mathrm{m,A}} < T < T_{\mathrm{m,B}}, G_{\mathrm{m,L}}$ and $G_{\mathrm{m,s}}$ intersect at a point away from the vertical axes. If, at a given T, $G_{\mathrm{m,L}}$ and $G_{\mathrm{m,s}}$ curves intersect, there is a

range of compositions over which the two may exist in equilibrium, $x_{B,1}$ and $x_{B,2}$. In the equilibrium where μ values are equal in all phases, the tangent of the curves is the same at the equilibrium compositions (i.e., a common tangent). This result allows equilibrium to be determined by a geometrical construction: drawing the common tangent line between the two curves as illustrated in Fig. 4.6(c). The intercepts of the tangent to G_m versus x_B curve on the vertical axes $x_A = 0$ and $x_B = 0$ are μ_B and μ_A, respectively, and $\mu_{A,s} = \mu_{A,L}$ and $\mu_{B,s} = \mu_{B,L}$. The result of a calculation based on this principle is a phase diagram of the type shown in Fig.4.6(d), with a lens-like stability region for the coexistence of liquid and solid.
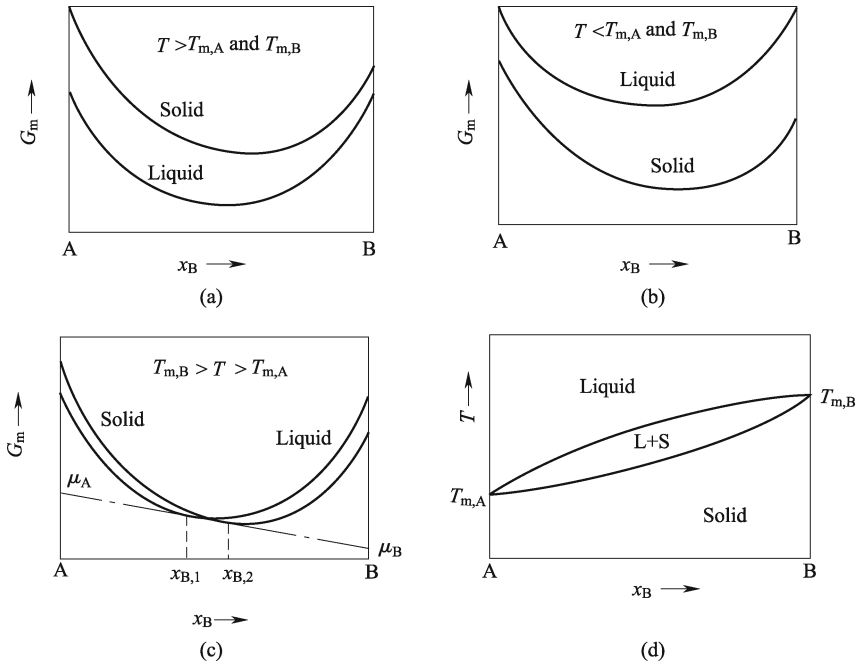

Fig. 4.6 G_m and phase diagram for ideal solutions (solid and liquid) of a system A – B: (a) at $T > T_{m,A}$ and $T > T_{m,B}$, (b) at $T < T_{m,A}$ and $T < T_{m,B}$, (c) at $T_{m,A} < T < T_{m,B}$, (d) phase diagram.

If the solid and liquid solutions of A and B are non-ideal, their thermodynamic properties can be described by a regular solution. $\mu_{A,L}$ and $\mu_{A,s}$ in the regular solution can be expressed from Eq. (4.29),

$$\mu_{A,L} = \mu_{A,L}^* + RT \ln a_{A,L}, \tag{4.33a}$$

$$\mu_{A,s} = \mu_{A,s}^* + RT \ln a_{B,s}. \tag{4.33b}$$

Combining Eqs. (4.32), (4.33a), (4.33b), and the condition of phase equilib-

rium, $\mu_{A,s} = \mu_{A,L}$, we have

$$\ln(a_{A,s}/a_{A,L}) = \Delta H_{m,A}(T_{m,A} - T)/(T_{m,A}RT). \qquad (4.34)$$

Similarly, for component B,

$$\ln(a_{B,s}/a_{B,L}) = \Delta H_{m,B}(T_{m,B} - T)/(T_{m,B}RT). \qquad (4.35)$$

It is known from Eq. (4.31) that $\ln f_A = (\omega/RT)x_B^2$ and $\ln f_B = (\omega/RT)x_A^2$. Substituting the above relations into Eqs. (4.34) and (4.35), it reads

$$\Delta H_{m,B}(T_{m,B} - T)/T_{m,B} = \omega_s(1 - x_{B,s})^2 - \omega_L(1 - x_{B,L})^2 + RT\ln(x_{B,s}/x_{B,L}), \qquad (4.36)$$

and

$$\Delta H_{m,A}(T_{m,A} - T)/T_{m,A} = \omega_s(x_{B,s})^2 - \omega_L(x_{B,L})^2 + RT\ln[(1 - x_{B,s})/(1 - x_{B,L})]. \qquad (4.37)$$

$x_{B,L}$ and $x_{B,s}$ in a bulk phase diagram are respectively unique at a certain T, and can be determined through Eqs. (4.36) and (4.37) when other quantities are known. The equations can in return be utilized to determine $\omega_s(\infty)$ and $\omega_L(\infty)$ when $T, x_{B,L}$ and $x_{B,s}$ are at hand from the corresponding bulk phase diagrams besides ΔH_m and T_m [18]. Although the chemical bonds between components in the phase diagrams are different in nature, they can be utilized in a unified form. However, the assumption that ω is composition-independent is only valid for the continuous solution phase diagram where the electronegativity difference between two components is small. Since $\omega_s(\infty)$ and $\omega_L(\infty)$ are weak functions of composition, as a first order approximation, they are determined at $T \approx (T_{m,A} + T_{m,B})/2$ with the corresponding $x_{B,L}$ and $x_{B,s}$ in the bulk phase diagram.

As an example, Fig. 4.7 shows a continuous solution phase diagram of binary systems of ceramic Al_2O_3-Cr_2O_3 in terms of Eqs. (4.36) and (4.37) where $\omega_s(\infty)$ and $\omega_L(\infty)$ are firstly determined by Eqs. (4.36) and (4.37) through introducing the corresponding known bulk phase diagram [19]. To determine $\omega_s(\infty)$ and $\omega_L(\infty), T = 2430$ K, $x_{Cr_2O_3,L} = 0.44$ and $x_{Cr_2O_3,s} = 0.67$ are used in calculation in Fig. 4.7. With the determined $\omega_s(\infty)$ and $\omega_L(\infty)$ values, the bulk phase diagram is replotted in Fig. 4.7.

Table 4.3 Related parameters and data used in Fig. 4.7. To determine h value, the related data are $V_{c,Al_2O_3} = 0.2548$ nm^3, $V_{c,Cr_2O_3} = 0.2898$ nm^3.

$r/$ nm		$T_m/$ K	$\Delta H_m/$ (J·mol^{-1})	$\omega_s/$ (J·mol^{-1})	$\omega_L/$ (J·mol^{-1})	$h/$nm	$\Delta S_{vib}/$ (J·g-atom^{-1}·K^{-1})
∞	Al$_2$O$_3$	2327	113040	22371.72	22733.72	0.634	9.716
	Cr$_2$O$_3$	2512	117230			0.6618	9.344
10	Al$_2$O$_3$	1937.66	72032.54	13488.36	13706.61		
	Cr$_2$O$_3$	2086.4	73269.45				
4	Al$_2$O$_3$	1148.04	5253.64	163.31	165.96		
	Cr$_2$O$_3$	1200.68	882.46				

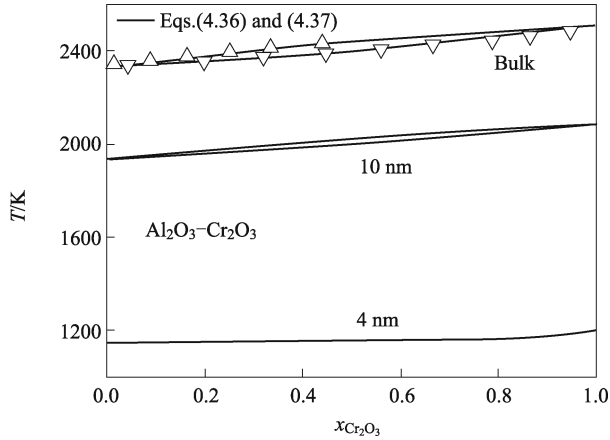**Fig. 4.7** Al_2O_3-Cr_2O_3 nano phase and bulk phase diagrams where the solid lines show the theoretical results in terms of Eqs. (4.36) and (4.37), and the symbol denotes the bulk experimental results. For the necessary parameters used see Table 4.3. (Reproduced from Ref. [18] with permission of IOP Publishing Ltd.)

Since the bulk solidus and liquidus curves in the binary regular solution phase diagrams correspond to experimental results, the fitted $\omega_s(\infty)$ and $\omega_L(\infty)$ values in return should have minor error.

One consideration of the size effect on phase diagrams is to separate the thermodynamic quantities into bulk and surface items, related to the contribution of ζ [20]. Since the nanophase equilibrium is metastable in nature and is difficult to measure, theoretical work may be an alternative. In addition, metastable nanophases of a substance could not be exclusive where several metastable phases are present in different size ranges, which could be even absent in bulk [21]. Thus, the size-dependent phase diagrams also draw great interest of researchers.

To calculate nanophase diagrams, $T_m(r)$, $\Delta H_m(r)$ and $\omega(r)$ functions of components are basic thermodynamic quantities. The former two have been determined in Chapter 3 while $\omega(r)$ is determined by Eq. (4.27). Taking $T_m(r)$, $\Delta H_m(r)$ and $\omega(r)$ functions into Eqs. (4.36) and (4.37), binary continuous solution nanophase diagrams can be calculated as shown in Fig. 4.7. In the figure, $\Delta S_{vib}(\infty) \approx \Delta S_m(\infty) = \Delta H_m(\infty)/[nT_m(\infty)]$ where n is the atom number in a molecule since the unit of $\Delta S_{vib}(\infty)$ is J·g-atom^{-1}·K^{-1} [22]. $n = 5$ in ceramic Al_2O_3-Cr_2O_3 system. Since $2r_0 = 6h$ in terms of Eq. (3.79) where h is component-dependent, different components have different r_0 values, a larger h value of the two components will be taken to calculate $2r_0$, which avoids physically unreasonable negative $\Delta H_m(r)$ in terms of Eq. (3.88) without evident error. For molecules, $h = V_c^{1/3}$ where V_c is volume of the cell. For organic molecules, there is no direct value of V_c. V_c is determined by $V_c = M_w/(\rho N_A)$. Other necessary parameters during the calculations and the calculated results are shown in Table 4.3. In light of Eq. (4.27), $\omega_s(r)$ and

$\omega_\mathrm{L}(r)$ have the same size dependence.

As r decreases, solidus and liquidus curves drop since $T_\mathrm{m}(r)$ of each component decreases. When $r \to 2r_0$, $T_\mathrm{m}(2r_0) = T_\mathrm{m}(\infty)\exp[-2\Delta S_\mathrm{vib}(\infty)/(3R)]$ in terms of Eq. (3.80), which implies that $T_\mathrm{m}(2r_0)$ is determined by $T_\mathrm{m}(\infty)$ and $\Delta S_\mathrm{vib}(\infty)$. Another evident change comparing with the bulk phase diagram is that the two-phase zone of the nanophase diagram becomes small. As $r \to 2r_0$, which is about several nanometers, the zone even approaches zero. This is a direct result of $\omega(2r_0) = 0$ where the regular solution deteriorates into the ideal solution and the structures of liquid and the solid become similar since they have a similar short range order.

Since the second phase strengthening is one of the strengthening methods for all structural materials, the above equations could be extended to deal with this kind of problem where only the size of one component with size-dependent thermodynamic quantities decreases and another remains the bulk.

4.5.2 Immiscibility–Two Mechanisms of Phase Transitions [1, 23, 24]

There may be partial miscibility between two components in the solid state, which is usually proportional to T, unless the individual components undergo a phase change. To examine this phenomenon, a regular solid solution of two components is considered, which can be used to predict the pattern of the phase separation of the two partially miscible components. In light of Eq. (4.28), $\Delta_\mathrm{mix}G_\mathrm{m} = RT(x_\mathrm{A}\ln x_\mathrm{A} + x_\mathrm{B}\ln x_\mathrm{B}) + \omega x_\mathrm{A}x_\mathrm{B}$. The first term of $RT(x_\mathrm{A}\ln x_\mathrm{A} + x_\mathrm{B}\ln x_\mathrm{B})$ is the one that applies to $\Delta_\mathrm{mix}G_\mathrm{m}$ for an ideal solution. The second term $\omega x_\mathrm{A}x_\mathrm{B}$ represents the nonideality of the mixture. If ω has a small positive value, $\Delta_\mathrm{mix}S_\mathrm{m}$ ensures that the two components of A and B mix in more or less all proportions. As ω increases, $\Delta_\mathrm{mix}S_\mathrm{m}$ is less able to dominate the positive $\Delta_\mathrm{mix}H_\mathrm{m}$ and $\Delta_\mathrm{mix}G_\mathrm{m}$, although remaining negative overall, acquires a shape with two minima and one maximum, i.e., becoming partially immiscible as illustrated in Fig. 4.8(a).

The compositions of the two immiscible phases, $x_\mathrm{B,1}$ and $x_\mathrm{B,2}$, are easily determined using the common tangent method described in the preceding section, which are those corresponding to the two minima in the curve of $\Delta_\mathrm{mix}G_\mathrm{m}$, where the first derivative of the curve is zero and the second is positive. This method has been used to calculate the phase diagram as illustrated in Fig. 4.8(b). Differentiating with respect to x_B, $\dfrac{\partial \Delta_\mathrm{mix}G_m}{\partial x_\mathrm{B}} = RT\ln\left(\dfrac{x_\mathrm{B}}{1-x_\mathrm{B}}\right) + \omega(1-2x_\mathrm{B}) = 0$. To satisfy the equation needs two x_B values denoting the minima corresponding to the two immiscible phases in equilibrium. The equation has a maximum at $x_\mathrm{B} = 1/2$. The solution of this equation, when plotted against T, yields a line of miscibility gap in Fig. 4.8(b).

Further differentiation gives

$$\frac{\partial^2 \Delta_{\text{mix}} G_{\text{m}}}{\partial x_{\text{B}}^2} = RT \left\{ \frac{1}{x_{\text{B}}} + \frac{1}{(1 - x_{\text{B}})} \right\} - 2\omega = 0. \tag{4.38}$$
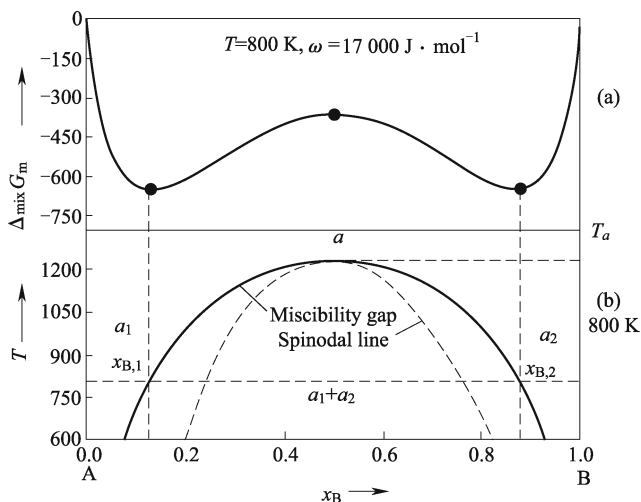

Fig. 4.8 Plots of $\Delta_{\text{mix}} G_{\text{m}}$ versus x_{B} for a regular solution (a) and the corresponding phase diagram having the miscibility gap, showing spinodal line (b).

This can be solved to give the upper consolute temperature (the temperature at which the two solutions just become miscible) as $T_a = \omega/2R$, i.e., the plot has no curvature. In this phase diagram, the single-phase region, $T > T_a$, indicates that A and B are completely miscible. At $T < T_a$, the solution is separated into two phases of α_1 and α_2. At points under the miscibility gap, the phase compositions vary with T. For example, at 800 K the phase compositions $x_{\text{B},1}$ and $x_{\text{B},2}$ are in equilibrium.

Another feature of the phase behavior is related to the points of inflection in the curves of $\Delta_{\text{mix}} G_{\text{m}}$ with respect to x_{B} when their second derivative equals zero (Eq. (4.38)). These inflection points, called spinodal points, have a special significance in the study of phase transitions. The locus of spinodal points can be indicated with a dash line in phase diagrams as in Fig. 4.8(b).

To appreciate the importance of the spinodal curve, we consider the region to the right of the spinodal point in Fig. 4.9, where $\Delta_{\text{mix}} G_{\text{m}}$ curve is concave downward and has regions of a negative curvature ($\partial^2 \Delta_{\text{mix}} G_{\text{m}}/\partial x_{\text{B}}^2 < 0$). In this region the solution may begin the process of decomposition into the equilibrium phases by incremental changes in composition without increasing G_{m} of the system, called the spinodal decomposition mechanism. A different situation exists in the region to the left of the spinodal point (the inflection point), in which the curvature is positive ($\partial^2 \Delta_{\text{mix}} G_{\text{m}}/\partial x_{\text{B}}^2 > 0$). Hence, as

the material is separated into two phases, G_{m} of the system must increase before it can finally decrease, called the nucleation and growth mechanism. This difference in path for G_{m} during decomposition results in a difference in phase transition behavior, which is important for kinetics. It will be useful to discuss the two different phase transition mechanisms in the context of G_{m} curves.
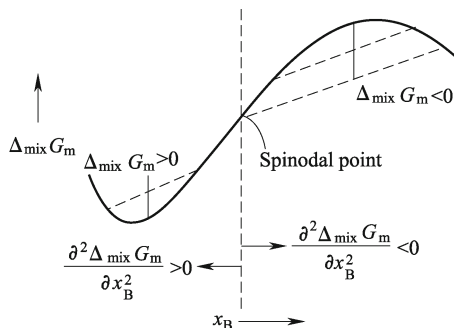

Fig. 4.9   The relation between $\Delta_{\mathrm{mix}}G_{\mathrm{m}}$ and composition on either side of the spinodal point.

The dynamics of phase separations is driven by fluctuations. In general, if a fluctuation leads to a decrease in $\Delta_{\mathrm{mix}}G_{\mathrm{m}}$, it will happen spontaneously. Consider a part of $\Delta_{\mathrm{mix}}G_{\mathrm{m}}$ curve where the curvature is negative, $\partial^2\Delta_{\mathrm{mix}}G_{\mathrm{m}}/\partial x_{\mathrm{B}}^2 < 0$. Suppose that a very small fluctuation occurs and consider what happens to $\Delta_{\mathrm{mix}}G_{\mathrm{m}}$ for the small fluctuation. Apparently, $\Delta_{\mathrm{mix}}G_{\mathrm{m}}$ change is negative for an arbitrarily small fluctuation in a composition that one part of the system gets more concentrated at the expense of another. The system is inherently unstable and this process is called spinodal decomposition under a condition,

$$\frac{\partial^2\Delta_{\mathrm{mix}}G_{\mathrm{m}}}{\partial x_{\mathrm{B}}^2} < 0. \tag{4.39}$$

Now we consider the part of the curve where the curvature is positive but inside the miscibility gap (two-phase region). Apparently, $\Delta_{\mathrm{mix}}G_{\mathrm{m}}$ here increases. Therefore, small fluctuations in this region do not lead to phase separation and the system is "stable". In other words, it is metastable with respect to infinitesimal composition fluctuations. Such a system is clearly unstable to the separation into the limiting compositions given by the common tangent construction. How does the system phase separate? Clearly an average composition within the two-phase region, but outside of the spinodal curves, requires large composition fluctuations to decrease the energy. A process requiring a large composition fluctuation is called "nucleation". Nucleation is a phase transition that is large in degree (composition change) but small in extent (size). After a nucleus forms, the new phase grows. Together,

the process is called nucleation and growth and the transition is discontinuous, whereas spinodal decomposition is small in degree but large in extent and it is continuous.

Nucleation is a topic of wide interest in many scientific studies and technological processes, which is the starting of a phase transition in a small region. It is used heavily in industry. The most widely used examples are directional solidification of vanes in different engines and the growth of monocrystalline silicon in semiconductor industry. Recently, these ideas are also utilized in the growth of quantum dots, nanowires, nanobelts, single crystalline thin films, etc. in nanotechnology.

In solidification, nucleation is the formation of a crystal phase from liquid phase. Nucleation without preferential nucleation sites is a homogeneous one, which occurs spontaneously and randomly, but it requires supercooling or superheating of the medium. The creation of a nucleus implies the formation of an interface at the boundaries of a new phase. The change in Gibbs free energy is balanced by the energy gain of creating a new volume, and the energy cost due to appearance of a new interface, expressed as $\Delta G = -(4\pi/3)r^3 \Delta G_{\mathrm{v}} + 4\pi r^2 \gamma_{\mathrm{sL}}$ where $\Delta G_{\mathrm{v}} = G_{\mathrm{L}} - G_{\mathrm{s}}$ being a change in Gibbs free energy per unit volume between the two phases, which relate to the ΔT as described in Eq. (4.32). The greater the supercooling or ΔT, the larger the ΔG_{v}, which favors phase transition. When the solid nucleus is spherical in a radius r, we have

$$\Delta G(r, T) = -(4\pi/3)r^3 \Delta G_{\mathrm{v}}(T) + 4\pi r^2 \gamma_{\mathrm{sL}}. \tag{4.40}$$

The first and second terms of the right hand of Eq. (4.40) and their addition ($\Delta G(r, T)$) are given in Fig. 4.10. ΔG achieves maximum ΔG^* at $r = r^*$, which means that the nucleus will certainly grow when $r > r^*$. The nucleus with r^* is termed the critical nucleus. Letting $\mathrm{d}\Delta G/\mathrm{d}r = 0$, it reads

$$r^* = \frac{2\gamma_{\mathrm{sL}}}{V \Delta G_{\mathrm{v}}} = \frac{2\gamma_{\mathrm{sL}} T_{\mathrm{m}} V}{\Delta_{\mathrm{s}}^{\mathrm{L}} H_{\mathrm{m}} \Delta T}. \tag{4.41}$$

Equation (4.41) shows that $r^* \propto 1/\Delta T$. Substituting Eq. (4.41) into Eq. (4.40) gives the nucleation barrier energy or the driving force for nucleation ΔG^*,

$$\Delta G^* = \frac{16}{3} \frac{\pi \gamma_{\mathrm{sL}}^3 T_{\mathrm{m}}^2 V^2}{\Delta H_{\mathrm{m}}^2 \Delta T^2}. \tag{4.42}$$

ΔG^* is an amount to overcome the additional energy associated with the interface or the interfacial energy, which will be discussed in Chapter 6 in detail.

Heterogeneous nucleation occurs much more often than homogeneous nucleation. It forms at preferential sites such as phase boundaries or impurities like dust and requires less energy than homogeneous nucleation. At such preferential sites, the effective interface energy is lower, thus diminishing ΔG^* and facilitating nucleation. An interface promotes nucleation because $\gamma_{\mathrm{ss}} < \gamma_{\mathrm{sL}}$
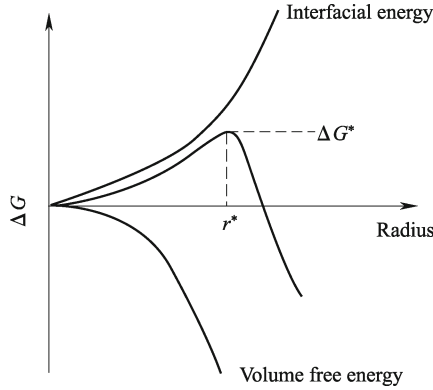
Fig. 4.10 $\Delta G(r,T)$ function during solidification.

where subscript ss denotes solid-solid interface, which encourages particles to nucleate. The above inequation can be quantitatively described by another amount – the wetting contact angle θ between two phases, which is always greater than zero. The Gibbs free energy needed for heterogeneous nucleation is equal to the product of homogeneous nucleation and a function of θ,

$$\Delta G_{\text{hetero}} = \Delta G_{\text{homo}} \times f(\theta) \tag{4.43}$$

where $f(\theta) = 1/2 + 3\cos\theta/4 - \cos^3\theta/4 < 1. \Delta G_{\text{hetero}} < \Delta G_{\text{homo}}$ leads to less ΔT needed. θ determines the ease of nucleation by reducing the energy needed. It is important to note that r^* remains unchanged while volume of the critical nucleus can be significantly small for heterogeneous nucleation where θ affects the shape of the nucleus. During the heterogeneous nucleation, some energy is released by the partial destruction of the previous interface. For example, precipitate particles can be formed at grain boundaries of a solid. This can interfere with precipitation strengthening, which relies on homogeneous nucleation to produce a uniform distribution of precipitate particles.

4.6 On Approximation of Gibbs Free Energy Change of Crystallization [25]

For a solidification process of an undercooled liquid, $\Delta G_{\text{v}} = \Delta H_{\text{v}} - T\Delta S_{\text{v}}$, which is an important parameter in the nucleation theory. Because the nucleation frequency has an exponential dependence on ΔG_{v}, the accuracy of an estimate of ΔG_{v} is often critically important when we analyze nucleation phenomena. It is known that

$$\Delta H_{\text{v}} = T_{\text{m}}\Delta S_{\text{m}} + \int_{T_{\text{m}}}^{T} \Delta C_P \mathrm{d}T, \tag{4.44a}$$

$$\Delta S_{\mathrm{v}} = \Delta S_{\mathrm{m}} + \int_{T_{\mathrm{m}}}^{T} \frac{\Delta C_P}{T} \mathrm{d}T \tag{4.44b}$$

where ΔC_P is the heat capacity difference of supercooled liquid and solid. Since C_P of the undercooled liquid, C_P^{L}, is rarely available, the functional dependence of $\Delta G_P(T)$ on undercooling must often be estimated, which can be satisfactorily described by a linear relation,

$$\Delta C_P = AT + B \tag{4.45}$$

where A and B are unknown constants. In light of this equation,

$$\Delta G_{\mathrm{v}} = \Delta S_{\mathrm{m}} \Delta T - \left[\frac{A}{2}(\Delta T)^2 + B \left(\Delta T - T \ln \frac{T_{\mathrm{m}}}{T} \right) \right]. \tag{4.46}$$

This can be simplified by using the approximation, $\ln(T_{\mathrm{m}}/T) \cong 2\Delta T/(T_{\mathrm{m}} + T)$, which is strictly valid only for small ΔT. However, in the temperature range of interest here ($T_{\mathrm{m}}/2 < T < T_{\mathrm{m}}$), this leads to errors in ΔG_{v} of less than 4% at the largest undercooling. Equation (4.46) then can be simplified to

$$\Delta G_{\mathrm{v}} = \frac{\Delta H_{\mathrm{m}} \Delta T}{T_{\mathrm{m}}} - (\Delta T)^2 \left[\frac{A}{2} + \frac{B}{T_{\mathrm{m}} + T} \right]. \tag{4.47}$$

Moreover, Jones and Chadwick proposed that ΔC_P can most simply be approximated as a constant, i.e. $A = 0$ and $B = \Delta C_P$, which brings out

$$\Delta G_{\mathrm{v}} = \frac{\Delta H_{\mathrm{m}} \Delta T}{T_{\mathrm{m}}} - \frac{\Delta C_P (\Delta T)^2}{T_{\mathrm{m}} + T}. \tag{4.48}$$

Although authors do not specifically indicate how the constant value for ΔC_P should be chosen, usually the best value available is $\Delta C_P(T_{\mathrm{m}})$. If ΔC_P values are unavailable at all, the simplest assumption made by Turnbull [26] is $\Delta C_P = 0$,

$$\Delta G_{\mathrm{v}} = \Delta H_{\mathrm{m}} \Delta T / T_{\mathrm{m}}. \tag{4.49}$$

This is the oldest linear approximation. Although the assumption of $\Delta C_P = 0$ is a bad one for polymers, it is not unreasonable for metallic systems where ΔC_P is very small.

In studies of glass forming liquids, Hoffman treated ΔC_P as a constant which could be evaluated [9], in terms of the temperature T_∞ at which $\Delta H_{\mathrm{v}} = 0$, being slightly below the T_{g} of the liquid, given in Fig. 4.11 sketchily.

A linear function of $\Delta H_{\mathrm{v}} = \Delta H_{\mathrm{m}} - \Delta C_P(T_{\mathrm{m}} - T)$ is often adequate in a considerable temperature range. Since $\Delta H_{\mathrm{v}} = 0$ at $T = T_\infty$, Hoffman's estimate is

$$\Delta C_P = \Delta H_{\mathrm{m}} / (T_{\mathrm{m}} - T_\infty). \tag{4.50}$$

Substituting Eq. (4.50) into the above equation, we have $\Delta H_{\mathrm{v}} = \Delta H_{\mathrm{m}}[(T - T_\infty)/(T_{\mathrm{m}} - T_\infty)]$. Equation (4.47) now becomes, after rearranging the terms,

$$\Delta G_{\mathrm{v}} = \frac{\Delta H_{\mathrm{m}} \Delta T}{T_{\mathrm{m}}} \left[\left(\frac{T}{T_{\mathrm{m}}} \right) + \left(\frac{\Delta T}{T_{\mathrm{m}} + T} \right) \times \left(\frac{T}{T_{\mathrm{m}}} - \frac{T_\infty}{T_{\mathrm{m}} - T_\infty} \right) \right]. \tag{4.51}$$
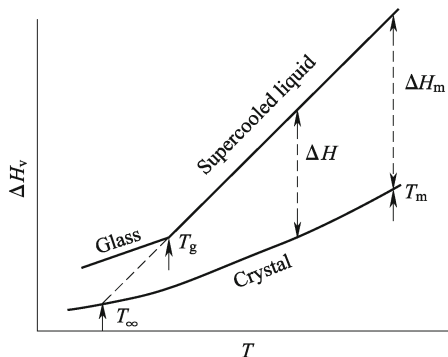
Fig. 4.11 Idealized enthalpy-temperature diagram showing definition of T_∞, and decrease of ΔH as T falls below T_m.

At this point, Hoffman indicated that $\Delta T/(T_\mathrm{m} + T)$ is small for small ΔT and assumes that $T/T_\mathrm{m} \cong T_\infty/(T_\mathrm{m} - T_\infty)$ when $T \cong T_\mathrm{g}$, so that the last term in his estimate can be neglected, leading to his final result,

$$\Delta G_\mathrm{v} = \frac{\Delta H_\mathrm{m} \Delta T}{T_\mathrm{m}} \left(\frac{T}{T_\mathrm{m}} \right). \tag{4.52}$$

The validity of this approximation depends critically on his original assumption that T_∞ is close to T_g. However, if Eq. (4.50) is used to estimate T_∞ by equating ΔC_P with the measured $\Delta C_P(T_\mathrm{m})$, it becomes clear that at least for metals with a small ΔC_P value, $T_\infty \ll 0$. Thus, the assumption of $T_\infty \approx T_\mathrm{g}$ is invalid for metals and alloys but is appropriate for some organic substances, which have a large ΔC_P value at T_m so that ΔH_v at T_g can be much smaller than ΔH_v at T_m.

However, an appropriate adaptation of Hoffman's approach can be made as follows [25]: When ΔC_P is small, although ΔH_v with decreasing T does not become much smaller than ΔH_m around T_g, ΔS_v decreases more quickly. As Kauzmann has pointed out, ΔS_v seems to vanish at T_K being somewhat below T_g. This fairly universal phenomenon, observed in many materials, has its physical basis that ΔS_v is primarily configurational in nature and hence decreases very quickly around T_g due to the rapid increase in configurational order associated with the rise in viscosity. For constant ΔC_P, Eq. (4.44b) becomes $\Delta S_\mathrm{v} = \Delta H_\mathrm{m}/T_\mathrm{m} + \Delta C_P \ln(T/T_\mathrm{m})$, and since ΔS_v vanishes at $T = T_\mathrm{K}$, $\Delta C_P = [\ln(T_\mathrm{K}/T_\mathrm{m})]\Delta H_\mathrm{m}/T_\mathrm{m}$. For metallic glass forming systems, $T_\mathrm{g} \approx T_\mathrm{m}/2$, and hence T_K is probably somewhere between $T_\mathrm{m}/2 < T_0 < T_\mathrm{m}/3$. As a result, the best constant approximation is $\ln(T_\mathrm{K}/T_\mathrm{m}) \cong 1$ or $\Delta C_P = \Delta H_\mathrm{m}/T_\mathrm{m}$. Substituting this result into Eq. (4.46) leads to

$$\Delta G_\mathrm{v} = \frac{\Delta H_\mathrm{m} \Delta T}{T_\mathrm{m}} \left(\frac{2T}{T_\mathrm{m} + T} \right) \tag{4.53}$$

which should be fairly accurate for materials with constant ΔC_P such as

some easy glass forming alloys.

Singh and Holz [27] have proposed a new expression for the change in free energy by making the following expression for the last term in Eq. (4.46),

$$\frac{A}{2}(\Delta T)^2 + B\left(\Delta T - T\ln\frac{T_\mathrm{m}}{T}\right) = \Delta S_\mathrm{m}\frac{(\Delta T)^2}{T_\mathrm{m} + 6T}. \tag{4.54}$$

This brings out

$$\Delta G_\mathrm{v} = \frac{\Delta H_\mathrm{m}\Delta T}{T_\mathrm{m}}\left(\frac{7T}{T_\mathrm{m} + 6T}\right). \tag{4.55}$$

Equation (4.55) takes into account the temperature dependence of ΔC_P suitably, which reproduces ΔG_v function of metallic elements of experimental results as shown in Fig. 4.12. Note that although Eq. (4.55) is well described ΔC_P of metallic elements, Eq. (4.53) is much better for glass forming alloys.
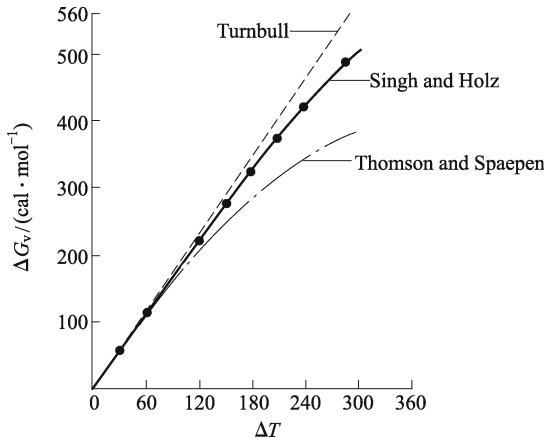

Fig. 4.12 ΔG_v on crystallization for Pb vs ΔT. The filled circles are the experimental results obtained by extrapolation of available data. The names and related curves denote the model predictions of the corresponding authors from Eq. (4.49) (dash line), Eq. (4.54) (solid line) and Eq. (4.53) (dot ted dash line). (Reproduced from Ref. [27] with permission of Elsevier)

The rising value of C_P^L with increased ΔT is a common feature of liquids which exhibits a continuous hardening to a glass [28]. The termination of the rise in C_P^L represents the thermal manifestation of the glass transition. From this viewpoint, Chen and Turnbull have suggested that this fact denotes the loss of S_pos of the liquid. In terms of the free volume approach refined by Cohen and Grest, this behavior is related to the fraction of liquid-like cells available for configurational adjustment. Other similar defect-based models reported involve a number of parameters, which can be adjusted to fit the C_P^L behavior.

4.7 Bandgap Energy of Binary Nanosemiconductor Alloys [29]

Now size-tunable properties are a hallmark of quantum dots and related nanostructures due to the potential applications to optoelectronics, high-density memory, quantum-dot lasers, vivo imaging, and lately biosensing and biolabeling. Size also plays a role when nanocrystals must be incorporated into larger superstructures such as mesoporous materials in photovoltaics [30]. However, the tuning of physical and chemical properties only by changing r could cause problems in many applications, particularly, if unstable small particles (less than ~ 2 nm) are used. One effective way to solve the problem of dual requirements is to employ alloy nanocrystals. As a valid method, alloying could tune the spectrum continuously since the interatomic interactions among different elements or compounds are different. Actually, tuning bandgap of nanocrystals by alloying could result in high luminescence and stability compared to the case for the component with narrower bandgap. An example to illustrate the advantages of alloying is the comparison of $(ZnSe)_x(CdSe)_{1-x}$ with CdSe nanocrystals. A proven strategy for increasing the luminescence and stability of CdSe nanocrystals is to grow a thin inorganic layer of a wider bandgap semiconductor on the surface of the core nanocrystals, where r is very small. By contrast, r of $(ZnSe)_x(CdSe)_{1-x}$ nanocrystals increases and thus the nanocrystals have better thermal stability with high crystallinity (or less defects). Note that subscript "x" shown in the alloy composition denotes the fraction of the first component in the alloy with $0 < x < 1$. For example, blue-emitting $(ZnSe)_x(CdSe)_{1-x}$ nanocrystals have particle sizes of over 3.5 nm, which is 3 times larger than that of the blue-emitting CdSe/ZnS nanocrystals. In addition, the stronger ZnSe bond stabilizes the weaker CdSe bond, and the shorter bond length of ZnSe introduces stiff struts into the system. Both lead to an increase of the dislocation energy. The addition of ZnSe into the CdSe lattice results in an increased covalency and a reduced ionicity, thus inhibiting plastic deformation and the generation of defects. Moreover, although inorganic-capped CdSe can provide a potential step for electrons and holes originating in the nanocrystals, and reduce the probability of the carriers to migrate to the sample surface, spatial compositional fluctuations in $(ZnSe)_x(CdSe)_{1-x}$ nanocrystals can produce atomically abrupt jumps in the chemical potential that can further localize free exciton states in the crystalline alloy.

After the above alloying, $E_g(x,r)$ with a bowing behavior induced by interatomic interactions is however a nonlinear function of x [31], which leads to difficulty for materials design because the $E_g(x,r)$ value could be determined only by experiments. If the $E_g(x,r)$ function is a linear one, a certain spectrum could be predicted only by that of two components with the additive rule. Note that for semiconductor alloys, the component could be compounds as shown in the above.

On the basis of assumption that a bulk ternary semiconductor alloy or psedo-binary semiconductor compound alloy is a regular solution of components, $E_g(x, \infty)$ has been given by [32],

$$E_g(x, \infty) = xE_g(0, \infty) + (1 - x)E_g(1, \infty) + \omega(x, \infty)x(1 - x). \qquad (4.56)$$

According to a virtual-crystal approximation model [33], $\omega(x, \infty)$ essentially originates from the intersubstitutional crystalline structure with the normal CN. Up to now, although some experimental results have been brought about, the theoretical way to quantitatively determine $\omega(x, \infty)$ values is still immature. Theoretical $E_g(x, r)$ functions of alloys cannot be determined either.

As r decreases from bulk, surface/volume ratio of the compound increases while the component and the structure are retained. Under this condition, $E_g(0, r)$ function varies continuously as r drops. This continuity of $E_g(0, r)$ function terminates at the lowest limit value of $r_0(0)$, as stated early. Thus, r can vary from ∞ to $r_0(0)$ continuously. The cases for $E_g(1, r)$ and $\omega(x, r)$ functions should be similar. Under the above considerations, $E_g(x, r)$ function can be obtained from Eq. (4.56) by simply substituting ∞ by r, namely,

$$E_g(x, r) = xE_g(0, r) + (1 - x)E_g(1, r) + \omega(x, r)x(1 - x). \qquad (4.57)$$

$E_g(0, r)$ function of unary nanosemiconductor in terms of $E_c(0, r)$ function has been described in Sec. 3.5 without any adjustable parameter, which is shown in a little modified form as

$$\frac{E_g(0, r)}{E_g(0, \infty)} = 2 - \left(1 - \frac{1}{12r/r_0(0) - 1}\right) \exp\left(-\frac{2\Delta S_b(0, \infty)}{3R} \frac{1}{12r/r_0(0) - 1}\right). \qquad (4.58)$$

In the original work, the calculation is deduced for the solid-vapor transition of particles where $d = 0$ is defined. To suit a more general case for all low dimensional materials, $r_0(0) = (3 - d)h(0)$ is used in Eq. (4.58). To balance this modification, a constant of 12 is added in Eq. (4.58). At the smallest crystal size $2r_0(0) = 2(3 - d)h(0)$, $E_g(0, r)/E_g(0, \infty) \rightarrow 2$. Thus, $E_g(0, r)$ is an ascending function with r. Equation (4.58) is simple since only two variables of $\Delta S_b(0, \infty)$ and $h(0)$ are needed in order to predict $E_g(0, r)/E_g(0, \infty)$ or $E_g(1, r)/E_g(1, \infty)$ value when 0 in the function is substituted by 1. Moreover, $\omega(x, r)$ function has been determined in Eq. (4.27), namely, $\omega(x, r)/\omega(x, \infty) = 1 - 2r_0(x)/r$ where $r_0(x) = (3 - d)h(x)$ and $h(x) = xh(0) + (1 - x)h(1)$. h is less dependent on composition concerned here with data given in Table 4.4 since both components are in the same group in the Periodic Table of Elements.

Substituting Eqs. (4.58) and (4.27) into Eq. (4.57) gives rise to an analytic $E_g(x, r)$ function,

$$E_g(x, r) = xE_g(0, r) + (1 - x)E_g(1, r) + [1 - 2r_0(x)/r]\omega(x, \infty)x(1 - x). \quad (4.59)$$

In order to determine $\omega(x, \infty)$ values of IIB–VIB semiconductors, $E_g(x, \infty)$ functions of some bulk pseudo-binary IIB–VIB chalcogenide semiconductors

are plotted in Fig. 4.13. The unknown $\omega(x, \infty)$ values of WZ-$(CdS)_x(CdSe)_{1-x}$, WZ-$(ZnS)_x(CdS)_{1-x}$, and WZ-$(ZnSe)_x(CdSe)_{1-x}$ used in Eq. (4.59) are determined from Fig. 4.13 (WZ denotes the wurtzite structure).
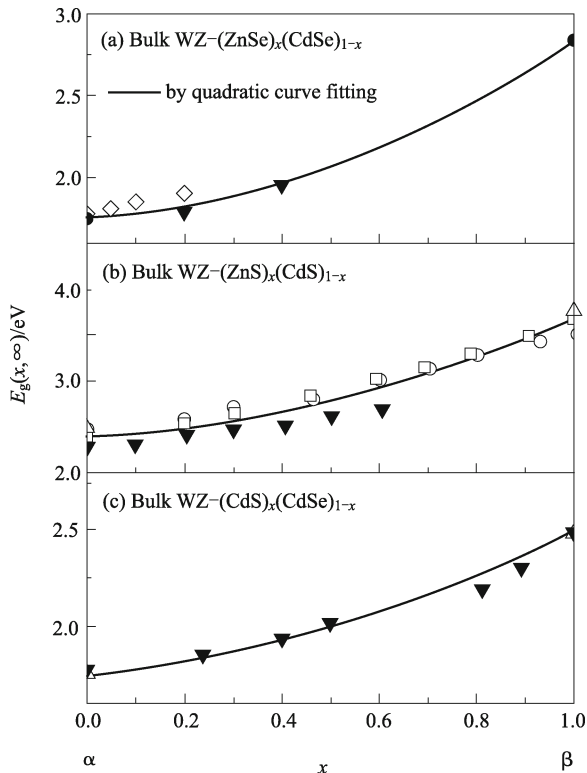

Fig. 4.13 $E_g(x, \infty)$ functions of some bulk pseudo-binary IIB–VIB chalcogenide semiconductors of experimental (symbols) and fitting results (curves). (a) WZ-$(ZnSe)_x(CdSe)_{1-x}$, (b) WZ-$(ZnS)_x(CdS)_{1-x}$, (c) WZ-$(CdS)_x(CdSe)_{1-x}$. The mean $\omega(x, \infty)$ values for WZ-$(ZnSe)_x(CdSe)_{1-x}$, WZ-$(ZnS)_x(CdS)_{1-x}$, and WZ-$(CdS)_x(CdSe)_{1-x}$ are respectively identified as -0.92 eV, -1.01 eV and -0.50 eV by quadratic curve fitting. The curves are shown in terms of Eq. (4.27) using the mean $\omega(x, \infty)$ values derived from quadratic curve fitting and $E_g(0, \infty)$ and $E_g(1, \infty)$ values listed in Table 4.4. (Reproduced from Ref. [29] with permission of Wiley-VCH)

Figure 4.14 shows comparisons of $E_g(x, r)$ functions of some homogeneously alloyed pseudo-binary IIB–VIB chalcogenide semiconductor nanoparticles with $r < 10$ nm ($d = 0$) in terms of Eq. (4.59) and available experimental results while Fig. 4.15 presents the related cases for the nanocrystals at $r \geqslant 20$ nm ($d = 0$ or $d = 1$).

It is shown that $E_g(x, r)$ functions increase on deceasing r, similar to the cases of $E_g(0, r)$ and $E_g(1, r)$. An obvious increase in $E_g(x, r)$ is observed for

Table 4.4   The relevant data used in the calculations of Eq. (4.59)

	Structure	$\Delta S_b(\infty)/$ (J·g-atom^{-1} ·K^{-1})	Lattice constant/nm	h/nm	$E_g(\infty)$/eV
CdS	ZB	67.11	$a = 0.582$	0.253	2.42
	WZ		$a = 0.4160$, $c = 0.6756$	0.212	2.50
CdSe	ZB	67.63	$a = 0.608$	0.262	1.76
	WZ		$a = 0.430$, $c = 0.701$	0.219	1.74
CdTe	ZB	68.79	$a = 0.648$	0.281	1.51
ZnS	ZB	68.01	$a = 0.541$	0.235	3.68
	WZ		$a = 0.3811$, $c = 0.6234$	0.195	3.51
ZnSe	ZB	68.53	$a = 0.567$	0.245	2.72
GaN	ZB	61.43	$a = 0.3189$, $c = 0.5178$	0.196	3.20
	WZ		$a = 0.498$	0.162	3.39
AlN	WZ	61.55	$a = 0.311$, $c = 0.498$	0.157	6.02
InN	ZB	58.37	$a = 0.3533$, $c = 0.5693$	0.216	1.80
	WZ		$a = 0.452$	0.179	0.70

the size range of $r < 10$ nm shown respectively in Fig. 4.14 while this increase is less obvious for $r \geqslant 10$ nm shown in Fig. 4.15. For a given r, $E_g(x,r)$ shifts higher from the narrower bandgap side $\alpha_1 (x = 0)$ to the wider bandgap side $\beta_1 (x = 1)$ with the increase of x. This blue shift [or increase in $E_g(x,r)$] is ascribed to the formation of alloyed nanocrystals via the intermixing of the wider bandgap β_1 with the narrower bandgap α_1. Moreover, bowing shape of $E_g(x,r)$ curves drops with r; in contrast to the prediction curves with $r \geqslant 10$ nm in Fig. 4.15, an almost linear relationship as x varies is interestingly observed for the curves shown in Fig. 4.14 especially when $r < 2.5$ nm.

For clarity, Fig. 4.16 shows $\omega(x,r)$ of IIB-VIB chalcogenide semiconductors as function of r in terms of Eq. (4.59), which determines the bowing shape of $E_g(x,r)$ curves. Corresponding to the bowing shape of $E_g(x,r)$ curves in Fig. 4.14 ($r < 10$ nm) and Fig. 4.15 ($r \geqslant 10$ nm), $\omega(x,r) \approx \omega(x,\infty)$ when $r \geqslant 10$ nm, but it lowers clearly as $r < 5$ nm. Especially, $\omega(x,r) \to 0$ when $r \to 2r_0(x) \approx 1.4$ nm for $d = 0$ or $r \to 2r_0(x) \approx 1$ nm for $d = 1$. Now $E_g[x, 2r_0(x)]$ function deteriorates into Végard's Law where about a half of atoms are located on the particle surface, which leads to evident enhancement of solubility due to the lack of elastic energy induced by solute atoms within a solution.

Although $E_g(x,r)$ curves determined experimentally have a bowing shape, which leads to difficulty of materials design, the bowing shape of $E_g(x,r)$ curves becomes weak and deteriorates into an almost linear function of x as r decreases. This is especially true when $r < 2.5$ nm at $d = 0$ or 1. Since the requirement of miniaturization of electronic and optic parts or devices is gradually enhanced, a smaller r value is asked in materials design where $\omega(x,r) \to 0$. This result suggests that when $r \to 2r_0(x)$, even if we do not know the exact $\omega(x,\infty)$ value, we can still determine $E_g(x,r)$ function of the alloys in terms of Végard's Law. Note that at $r > 10$ nm (Fig. 4.15), the size effect on $E_g(x,r)$ is much weak, and $\omega(x,r) \approx \omega(x,\infty)$ in this regime. In this

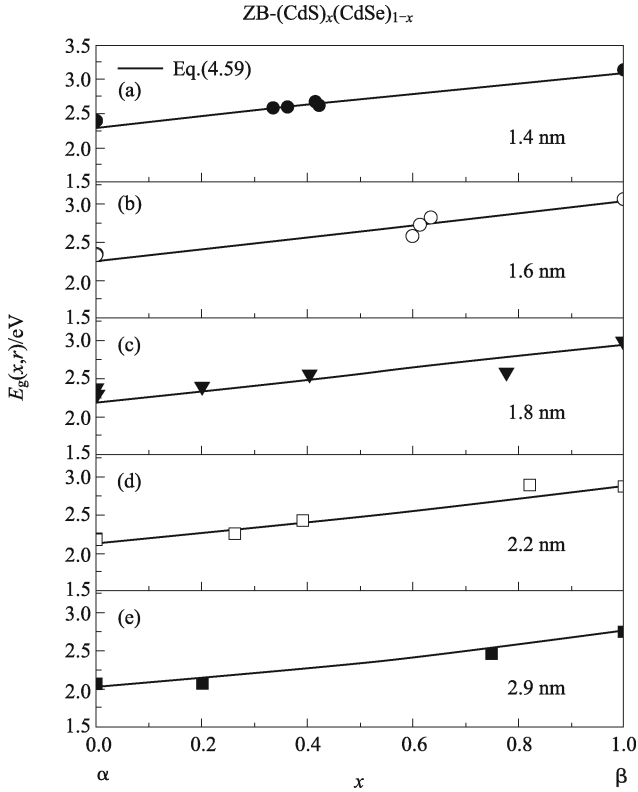case, Eq. (4.56) should be directly used to estimate $E_g(x, r)$ value.

Fig. 4.14 $E_g(x, r)$ functions of zinc blende ZB–$(CdS)_x(CdSe)_{1-x}$ nanoparticles ($d = 0$) of Eq. (4.59) (curves) and experimental results (symbols). α and β denote the compounds with narrower bandgap at $x = 0$ and wider bandgap at $x = 1$, respectively. r values are selected based on known experimental results. Different r values are shown respectively in (a)–(e). The mean $\omega(x, \infty) = -0.53$ eV is taken for simplicity. $h(x) = xh(0) + (1 - x)h(1)$. For $\Delta S_b(0, \infty), \Delta S_b(1, \infty), E_g(0, \infty)$, $E_g(1, \infty), h(0)$ and $h(1)$ values see Table 4.4. (Reproduced from Ref. [29] with permission of Wiley-VCH)
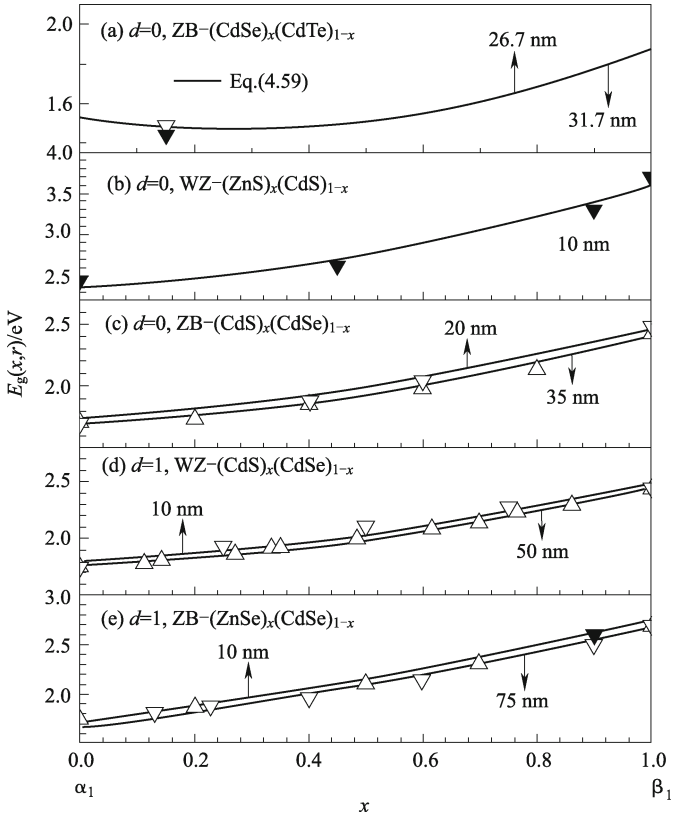
Fig. 4.15   A comparison of $E_g(x, r)$ functions of nanostructured materials between Eq. (4.59) (curves) and experimental results (symbols) for (a) ZB-$(CdSe)_x(CdTe)_{1-x}$ $(d = 0)$, (b) WZ-$(ZnS)_x(CdS)_{1-x}(d = 0)$, (c) ZB-$(CdS)_x(CdSe)_{1-x}(d = 0)$, (d) WZ-$(CdS)_x(CdSe)_{1-x}(d = 1)$ and (e) ZB-$(ZnSe)_x(CdSe)_{1-x}$ $(d = 1)$. r values are selected based on known experimental results. (Reproduced from Ref. [29] with permission of Wiley-VCH)
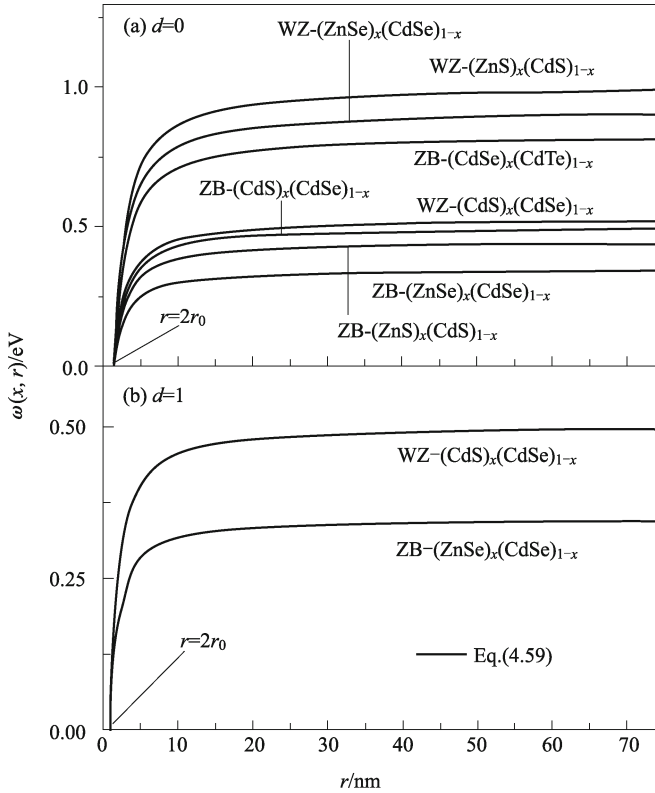
Fig. 4.16 $\omega(x,r)$ of some pseudo-binary IIB–VIB chalcogenide semiconductors as function of r in terms of Eq. (4.59). $r_0(x)$ is calculated by the relationship $r_0(x) = (3-d)h(x)$ with $d=0$ or $d=1$. The averaged h values of all cited IIB–VIB chalcogenides semiconductor compounds are about 0.24 nm as shown in Table 4.4. For simplification, this value will be taken as a rough estimate of h to determine the corresponding $2r_0(x)$. (Reproduced from Ref. [29] with permission of Wiley-VCH)

References

1   David V R. Thermodynamics of Materials. John Wiley & Sons, New York (1994)

2   Callister W D Jr. Fundamentals of Materials Science and Engineering. John Wiley & Sons, New York (2000)

3   Adkins C J. Equilibrium Thermodynamics. McGraw-Hill Book Company, UK (1975)

4   Jiang Q, Yang C C. Size effect on phase stability of nanostructures. Curr. Nanosci., **4**, 179-200 (2008) and references therein

5   Lobo L Q, Ferreira A G M. Phase equilibria from the exactly integrated Clapeyron equation. J. Chem. Thermodyn., **33**, 1597-1617 (2001)

6   Yang C C, Li J C, Jiang Q. Effect of pressure on melting temperature of silicon

determined by Clapeyron equation. Chem. Phys. Lett., **372**, 156-159 (2003)

7   Yang C C, Li J C, Jiang Q. Temperature-pressure phase diagram of silicon determined by Clapeyron equation. Solid State Commun., **129**, 437-441 (2004)

8   Yang C C, Jiang Q. Temperature-pressure phase diagram of germanium determined by Clapeyron equation. Scripta Mater., **51**, 1081-1085 (2004)

9   Hoffman J D. Thermodynamic driving force in nucleation and growth processes. J. Chem. Phys., **29**, 1192 (1958)

10   Kauzmann W. The nature of the glassy state and the behavior of liquids at low temperatures. Chem. Rev., **43**, 219-256 (1948)

11   Jiang Q, Liang L H, Zhao D S. Lattice contraction and surface stress of fcc nanocrystals. J. Phys. Chem., B **105**, 6275-6277 (2001)

12   http://en.wikipedia.org/wiki/Partial_molar_property. Accessed 15 June 2009

13   http://en.wikipedia.org/wiki/Chemical_potential. Accessed 19 June 2009

14   Sun C Q, Tay B K, Lau S P, Sun X W, Zeng X T, Li S, Bai H L, Liu H, Liu Z H, Jiang E Y. Bond contraction and lone pair interaction at nitride surfaces. J. Appl. Phys., **90**, 2615-2617 (2001)

15   Jiang Q, Li J C, Chi B Q. Size-dependent cohesive energy of nanocrystals. Chem. Phys. Lett., **366**, 551-554 (2002)

16   Müller H, Opitz Ch, Strickert K, Skala L. Abschätzung von eigenschaften der materie im hochdispersen zustand-praktische anwendungen des anylytischen clustermodells. Z. Phys. Chemie. Leipzig., **268**, 625-646 (1987)

17   Musgrave C B. Solid State Thermodynamics. Stanford University, Stanford (1998)

18   Liang L H, Liu D, Jiang Q. Size-dependent continuous binary solution phase diagram. Nanotechnology, **14**, 438-442 (2003)

19   Kim S S, Sanders T H. Thermodynamic modeling of the isomorphous phase diagrams in the Al_2O_3-Cr_2O_3 and V_2O_3-Cr_2O_3 systems. J. Am. Ceram. Soc., **84**, 1881-1884 (2001)

20   Vallée R, Wautelet M, Dauchot J P, Hecq M. Size and segregation effects on the phase diagrams of nanoparticles of binary systems. Nanotechnology, **12**, 68-74 (2001)

21   Tanaka T, Hara S. Thermodynamic evaluation of nano-particle binary alloy phase diagrams. Z. Metallkd., **92**, 1236-1241 (2001)

22   Jiang Q, Shi H X, Zhao M. Melting thermodynamics of organic nanocrystals. J. Chem. Phys., **111**, 2176-2180 (1999)

23   http://pruffle.mit.edu/3.00/Lecture_32_web/. Accessed 26 July 2009

24   http://en.wikipedia.org/wiki/Nucleation. Accessed 10 August 2009

25   Thompson C V, Spaepen F. On the approximation of the free energy change on crystallization. Acta Met., **27**, 1855-1859 (1979)

26   Turnbull D, Cech R E. Microscopic observation of the solidification of small metal droplets. J. Appl. Phys., **21**, 804 (1950)

27   Singh H B, Holz A. Stability limit of supercooled liquids. Solid State Commun, **45**, 985-988 (1983)

28   Perepezko J H, Paik J S. Thermodynamic properties of undercooled liquid metals. J. Non-crystalline Solids, **61-62**, 113-118 (1984)

29   Zhu Y F, Lang X Y, Jiang Q. The effect of alloying on the bandgap energy of nanoscaled semiconductor alloys. Adv. Funct. Mater., **18**, 1422-1429 (2008) and references therein

30   Robel I, Subramanian V, Kuno M, Kamat P V J. Quantum dot solar cells. Harvesting light energy with CdSe nanocrystals molecularly linked to mesoscopic TiO_2 films. J. Am. Chem. Soc., **128**, 2385-2393 (2006)

31   Willardson R K, Goering H L. Compound Semiconductors, Vol.I. Preparation
      of Ⅲ-V Compounds. Reinhold Publishing Corp., New York (1962)
32   Thompson A G, Woolley J C. Energy-gap variation in mixed III–V alloys.
      Can. J. Phys., **45**, 255-261 (1967)
33   Hill R. Energy-gap variations in semiconductor alloys. J. Phys. C: Solid State
      Phys., **7**, 521-526 (1974)

Chapter 5 Thermodynamics of Phase Transitions

Understanding how to predict and describe the existence of these transitions, their characteristics and consequences for everyday phenomena is one of the more important roles of statistical and condensed matter physics. In this chapter, thermodynamics of phase transitions is described, which are ubiquitous in nature and are widely used to realize, improve or extend the materials properties. Examples include magnets, liquid crystals, superconductors, crystals, amorphous solids, and liquid condensation. These transitions occur between equilibrium states as functions of $T, P, H_{\mathrm{mag}}, r$, etc.; and define the nature of the matters we deal with on a day-to-day basis.

5.1 Thermodynamic Classification of Phase Transitions [1, 2]

The first attempt at classifying phase transitions was the Enrenfest classification scheme, which grouped phase transitions based on the degree of non-analyticity involved. In other words, even though μ of the component undergoing phase transition remains unchanged, its derivative with respect to a state variable (for instance T) changes. The nature of this change is the basis of the Ehrenfest classification scheme, under which phase transitions were labeled by the lowest derivative of the G that is discontinuous in the transition.

For the various solid/liquid/gas transitions, such as vaporization, fusion, or sublimation of pure substance, T and P remain constants while S and V show finite changes. Since $\mathrm{d}G = -S\mathrm{d}T + V\mathrm{d}P$ in terms of Eq. (1.38), it is apparent that there will be no change in G function during such a phase transition. However, since $(\partial G/\partial T)_P = -S$ and $(\partial G/\partial P)_T = V$, it follows that the first-order derivatives of G must have finite changes. Such a transition is therefore called a first-order phase transition. The left part of Fig. 5.1 illustrates the main characteristics of first-order transitions.

In contrast to first-order transitions there are phase changes taking place at constants T and P without changes of S and V, or the first-order derivatives of G function exhibit continuity as illustrated in the right part of Fig.

5.1. If the second-order derivatives of G function have finite variations during the transition however, such a transition is defined as a second-order phase transition. From Eqs. $(3.1)-(3.3)$, C_P, α, and β in the related second-order phase transitions vary finitely. The higher derivatives of G function, however, are not all continuous. In light of Ehrenfest, an n-th order phase transition has a discontinuity in the n-th derivative of G function with respect to T, $\partial^n G/\partial T^n$.

The Ehrenfest scheme is an inaccurate method of classifying phase transitions since it does not take into account the case where a derivative of free energy diverges. For instance, in the ferromagnetic transition, C_P diverges to infinity. In the modern classification scheme, phase transitions are divided into two broad categories, named similarly for the Ehrenfest classes: the first-order phase transitions are those that involve a latent heat. During such a transition, a system either absorbs or releases a fixed (and typically large) amount of energy while T stays constant as heat is added. The second class of phase transitions is the continuous phase transitions, also called second-order phase transitions. These have no associated latent heat and correspond to divergent susceptibility, an infinity correlation length, and a power law decay of correlations. Lev Davidovich Landau has given a phenomenological theory for this kind of phase transition.
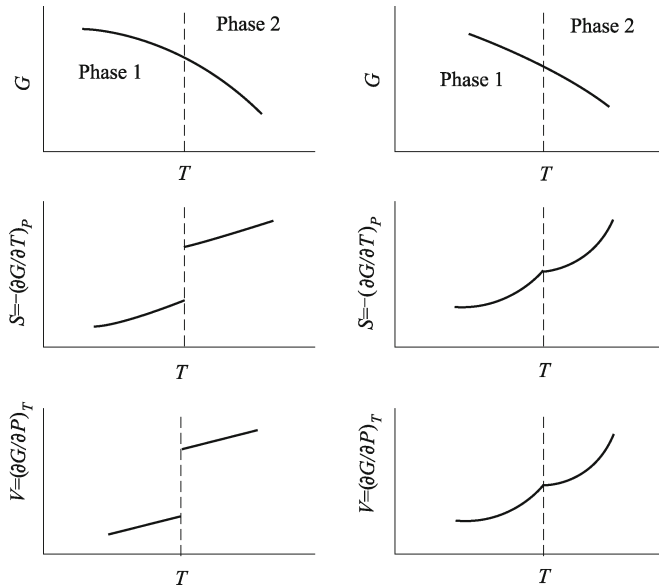

Fig. 5.1 Several thermodynamic functions during the first-order (left) and second-order (right) phase transitions.

In a first-order phase transition, the slope of the $P \sim T$ equilibrium curve is given by the Clapeyron equation (Eq. (4.2)), $dP/dT = (S^2 - S^1)/(V^2 - V^1)$, where the superscripts "1" and "2" denote the initial and final phases of a transition. In a second-order transition, the right side of this equation becomes indeterminate. To determine its slope dP/dT, we now use the conditions that there are no changes in S and V.

The entropy change for a simple compressible system may be expressed as a function of any pair of the variables P, V, and T, thus forming three general equations, the derivations of which are as follows: When S is considered as a function of T and P, we have $dS = (\partial S/\partial T)_P dT + (\partial S/\partial P)_T dP$. Since $(\partial S/\partial T)_P = C_P/T$ and $(\partial S/\partial P)_T = -(\partial V/\partial T)_P, dS = C_P dT/T - (\partial V/\partial T)_P dP$. This is the second dS equation. Starting from the condition that $S^1 = S^2$ or $dS^1 = dS^2$ and through the use of the second dS equation, we obtain $C_P^1 dT - TV\alpha^1 dP = C_P^2 dT - TV\alpha^2 dP$ where we have used $V = V^1 = V^2$. Therefore,

$$\frac{dP}{dT} = \frac{C_P^2 - C_P^1}{TV(\alpha^2 - \alpha^1)}. \tag{5.1}$$

Alternately, starting from the condition that $V^1 = V^2$ or $dV^1 = dV^2$ and noting that $dV = (\partial V/\partial T)_P dT + (\partial V/\partial P)_T dP = V\alpha dT - V\beta dP$, we obtain $V\alpha^{(1)} dT - V\beta^{(1)} dP = V\alpha^{(2)} dT - V\beta^{(2)} dP$. Thus,

$$\frac{dP}{dT} = \frac{\alpha^2 - \alpha^1}{\beta^2 - \beta^1}. \tag{5.2}$$

Equations (5.1) and (5.2) are known as Ehrenfest's equations for the second-order phase transitions. Interestingly, the only phase transition known to exhibit distinct jumps in C_P and α and obey Eq. (5.2) is the normal superconductor transition [3]. For the most systems undergoing continuous phase transitions, instead of jumps in C_P and α, critical behavior is observed.

The transition from ferromagnetism to paramagnetism at the Curie point, and that from ordinary liquid He to superfluid liquid He at λ point were originally thought to be a second order. These transitions satisfy the conditions that T, P, G, S, and V (and therefore U, H, and F) remain constants. More precise experimental data however indicate that the conditions of finite changes in C_P, β, and α are not satisfied. Instead, these properties would become infinite at the transition temperature. It was the resemblance of this curve to the Greek letter λ that led to the name of λ transition for such a transition.

5.2 Landau and Ising Models for the Second-order Phase Transitions

5.2.1 Landau Model [4, 5]

Continuous, or the second-order, phase transitions can be very spectacular, because they give rise to a diverging correlation length and hence to behavior known as critical phenomena. Landau theory in physics was introduced by Landau in an attempt to formulate a general theory of the second-order phase transitions. He was motivated to suggest that the free energy of any system should obey two conditions: the free energy is analytic, and the free energy obeys the symmetry of the Hamiltonian.

A generic system to discuss the transitions is the magnet. Uniaxial ferromagnet is a simplest example of phase transitions. As we know, $G = U - TS - H_{\mathrm{mag}}M$ has to be minimized at constants P and T. The big question is a minimum with respect to variables. When symmetry is broken, one needs to introduce one or more extra variables to describe the state of the system. In the ferromagnic phase, magnetization M vanishes at certain temperature T_{c} at $H_{\mathrm{mag}} = 0$. Below T_{c} a spontaneous M is observed, its direction can be "up" and "down" with equal likelihood. The nearest neighbors interact in a way favorable to point in the same direction. At $H_{\mathrm{mag}} = 0, G$ consists of two terms of U and $-TS$. At low T, U is more important and the system is a ferromagnet. At high T, G is minimized by disordered state in which S is large. It is the fight between the order and disorder that makes the critical state specifically interesting. We can denote the variables by M; in a generic case, it is called the order parameter θ. In some cases it is difficult to specify θ and in general it can be a scalar, a vector, a tensor, etc. A basic element of Landau's theory for continuous phase transitions is the presence of a θ.

θ is a measure of the degree of order in a system; the extreme values are 0 for total disorder and 1 for complete order. Landau supposes here that a given system can be described by a single θ, which should be zero at high T, usually above T_{c}, for disordered phase, and it is non-zero in an ordered phase. Examples include the dielectric polarization in a ferroelectric system, the fraction of superconducting electrons in a super conductor, or the fraction of neighbor-A-B bonds to total bonds in an alloy AB.

Landau's unified theory of all the second-order phase transitions concerns itself with what is happening in the vicinity of the phase transition. In this region the magnitude of θ will be small as $T \to T_{\mathrm{c}}$. The Landau approach expands the free energy as a power series in these small parameters where the free energy is assumed to be an analytic function of θ, which leads to a phenomenological expression for G,

$$G(P,T,\theta) = G_0(P,T) + a(P,T)\theta + b(P,T)\theta^2 + c(P,T)\theta^3 + d(P,T)\theta^4 + \cdots.$$

First we note that $G_0(P,T)$ can be ignored here since the origin of the energy is entirely arbitrary. The coefficients in the Landau expansion a, b, c, and d are function of P and T. We know that above T_c, θ is vanished and θ has some finite value below T_c. The minimum of the free energy below T_c should therefore occur at $\theta \neq 0$ and above T_c at $\theta = 0$ ($\partial G/\partial\theta = 0$). From this we conclude immediately that $a = 0$ (for systems without external fields), because otherwise $\theta \neq 0$ at any T. Also b in front of the quadratic term in the free energy should be positive for $T > T_c$ (minimum at $\theta = 0$) and negative at $T < T_c$ (minimum of G at $\theta \neq 0$). The simplest choice is

$$b(P,T) = a_0(T - T_c) \tag{5.3}$$

where a_0 is positive constant and Eq. (5.3) is only valid in a neighborhood of T_c. The condition that θ is finite below T_c requires $d(P,T) > 0$ and that a_0 and d are sufficiently large that all the interesting behavior occurs for small θ. Thus, we don't have to worry about higher order functions. Furthermore, Landau's idea is to forget the details of the microscopic model and consider just the symmetries. Hence, the power series of the G must only contain terms which respect the symmetry of the $\theta(c = 0)$, so that G can be expanded into

$$G(P,T,\theta) = a_0(T - T_c)\theta^2 + d\theta^4. \tag{5.4}$$

To find the minimum, we set the derivative with respect to θ to zero, $(\partial G/\partial\theta)_T = 2a_0(T - T_c)\theta + 4d\theta^3 = 0$, which has the roots

$$\theta = \begin{cases} 0 & T > T_c \\ \left[\dfrac{-a_0}{2d}(T - T_c)\right]^{1/2} & T < T_c \end{cases}$$

with a_0 and d positive. $\theta = 0$ corresponds to the minimum of the G function (Eq. (5.4)) at $T > T_c$ where $G(T) = G_0$. The other root, $\theta = [a_0(T_c - T)/(2d)]^{1/2}$, is related to the minimum of $G(T)$ at $T < T_c$ where

$$G(P,T) = G_0 - a_0^2(T_c - T)^2/(4d).$$

The variation of $G(\theta, T)$ as a function of θ^2 for three representative T is shown in Fig. 5.2 (a), and $\theta(T)$ function is shown in Fig. 5.2 (b).

Landau model describes a phase transition in which $\theta \to 0$ as $T \to T_c$. $S = -\partial G(\theta, T)/\partial T = S_0 - a_0\theta^2$ where $S_0 = -\partial G_0/\partial T$, which is the entropy drop as the ordered phase is entered and it is continuous at the transition,

$$T > T_c, \quad \theta = 0, \quad S = S_0(T);$$

$$T < T_c, \quad \theta^2 = \frac{a_0(T_c - T)}{2d}, \quad S = S_0(T) + \frac{a_0^2(T - T_c)}{2d}.$$

$C_P = T(\partial S/\partial T)_P$ is then,

$$C_P = \begin{cases} T(\partial S_0/\partial T)_P = C_{P,0} & T > T_c \\ C_{P,0} + \dfrac{a_0^2 T}{2d} & T < T_c \end{cases}$$
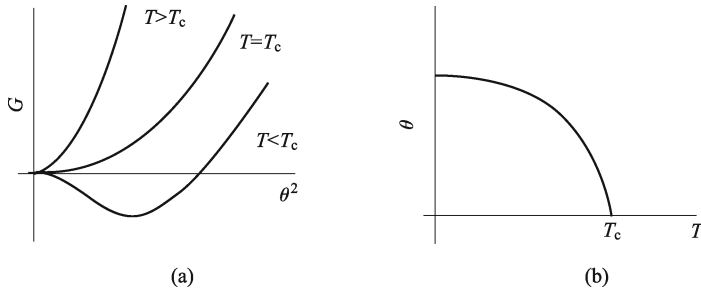
Fig. 5.2 (a) Landau G function versus θ^2 at representative T. As T drops below T_c the equilibrium value of θ^2 gradually increases, as defined by the position of $G_{\min}$. (b) Typical behavior of θ as a function of T. Below T_c, θ is finite, which vanishes at $T > T_c$.

At the transition there is a discontinuity in C_P given by $\Delta C_P = a_0^2 T_c / 2d$, in accord with the mean field theory. However, the magnitude of the discontinuity can be obtained in terms of the Landau parameters.

Taking the magnetization as an example, we can specify M as an order parameter. As a result, G depends on T, H_{mag}, M. Those are the intensive parameters characterizing the state. Landau's theory corresponds to a mean field theory that ignores the effect of fluctuations, and hence gives incorrect predictions of critical exponents and, occasionally, fluctuations may even prevent the transition from being continuous. In spite of this, the application of Landau's theory to predicting and understanding the symmetry changes at the transition point and the qualitative behavior of the system seems to be quite successful so far. The great virtue of Landau's theory is that it makes specific predictions for what kind of non-analytic behavior one should see when the underlying free energy is analytic.

5.2.2 Ising Model [6, 7] and its Applications

Far and away the most influential model of a system capable of a phase transition is the Ising model. This was invented by Lenz in 1920 as a simple model of a ferromagnet, though we shall see that it can be interpreted as a model of other systems too. Magnetism (or electromagnetism) is one of the fundamental forces of nature. A field of magnetic force is produced by the motion of an electrically charged particle, so electric current (which consists of moving electrons) produces a magnetic field. In 1925 Uhlenbeck and Goudsmit hypothesized that the electron has a "spin", and thus behaves like a small bar magnet. In an external magnetic field, the direction of the electron's magnetic field is either parallel or antiparallel to that of the external field.

In the same year Lenz suggested to his student Ising that if an interaction

was introduced in between spins so that parallel spins in a crystalline lattice attracted one another, and antiparallel spins repelled one another, then at sufficiently low T the spins would all be aligned and the model might provide an atomic description of ferromagnetism. Thus the "Ising model" arose in which "spins", located on the sites of a regular lattice, have one of two values, +1 and –1, and spins with spin values s_i and s_j on adjacent sites interact with an energy $-J's_i s_j$ where J' is a positive real number. Thus, spins with similar values interact with an energy $-J'$, and those with dissimilar values interact with the (higher) energy J'. The magnetization per spin of a system of N spins is defined as $\sum_i (s_i/N)$ which thus lies between -1 and $+1$ and the total energy function (the "Hamiltonian") is defined as the sum of the interaction energy, i.e.,

$$E = -\frac{1}{2}\sum_{ij} J'_{ij} s_i s_j - H_{\text{mag}} \sum_i s_i \qquad (5.5)$$

where H_{mag} breaks the symmetry, the subscripts label lattice sites, and J_{ij} is defined that $J'_{ij} = J'$ where i and j are neighbouring sites, otherwise $J'_{ij} = 0$.

The model's partition function can now be written as

$$Z_{\text{Ising}} = \sum_{\{s_i\}} \exp\left[\beta\left(\frac{1}{2}\sum_{ij} J'_{ij} s_i s_j + H_{\text{mag}} \sum_i s_i\right)\right]$$

where $\{s_i\}$ indicates that the sum should be extended over all possible assignments of ± 1 to lattice sites.

Ising studied the simplest possible model consisting simply of a linear chain of spins, and showed that for this $d = 1$ case there is no (non-zero) T_c (i.e., the spins become aligned only at $T = 0$). In 1944, Onsager solved the model for $d = 2$ in the absence of an externally applied magnetic field and showed that the model's critical exponents were quite different from those predicted by Landau's theory, which had been thought correct. An exact solution for the $d = 2$ model in non-zero external field has only recently appeared. Despite decades of intensive effort, we still have no exact solution for $d = 3$.

The Ising model can be mapped into the lattice gas, which is a simple model of density fluctuations and liquid-gas transitions. Since the kinetic energy doesn't depend on the position only on the momentum, the statistics of the positions only relate with the potential energy, and the thermodynamics of the gas only relies on the potential energy for each configuration of atoms. We divide the d-dimensional space occupied by the gas up into cells of just the same size as an individual atom. Each atom is obliged to occupy a single cell, and no cell may contain more than one atom. Let $\mathfrak{R}_i$ be 0 or 1 decided by whether the cell is occupied or not. Since the gas is non-ideal, atoms attract each other and the energy of the gas is lower when atoms are

in adjacent cells than when each lives in glorious isolation. If the attraction is only between nearest cells, the energy is reduced by $-4J\Re_i\Re_j$ for each occupied neighboring pair.

The density of the atoms can be controlled by adding a chemical potential, which is a multiplicative probability cost for adding one more atom. A multiplicative factor in probability can be reinterpreted as an additive term in the logarithm energy. The extra energy of a configuration with N atoms is changed by μN. The probability cost of one more atom is a factor of $\exp(-\beta\mu)$. As a result, the energy of the lattice gas is $E = -2\sum_{ij} J'\Re_i\Re_j - \mu\sum_i \Re_i$. In order to show the correspondence between the lattice gas and the Ising model, we make the variable transition $\Re_j = (s_i + 1)/2$ and obtain

$$E = -\frac{1}{2}\sum_{ij} J's_is_j - \frac{1}{2}\sum_i (4J' - \mu)s_i.$$

Therefore, the lattice model is isomorphic with the Ising model: "spin up" in the Ising model corresponds to an occupied cell in the lattice model, "spin down" is related to an empty cell. In the Ising model, H_{mag} depends (within constants) on μ and the coupling constant is $4J'$.

β-brass is an alloy consisting of equal numbers of Cu and Zn atoms. At $T = 0$ the alloy consists of two interpenetrating cubic lattices, one of Cu and one of Zn atoms, in such arrangement that each Cu atom is surrounded by eight Zn atoms, and vice versa for each Zn atom. As T is raised, more and more Cu atoms stray onto the Zn sub-lattice and vice versa, until at 739 K the division into two distinct sub-lattices breaks down altogether. Above 739 K, both sub-lattices contain equal numbers of each kind of atoms. This system can be described by the Ising model as follows:

At low T, the system is ordered because it is energetically preferable to unlike atoms to become the nearest neighbours rather than the like atoms. Suppose that the system's energy is lowered by an amount J' for every bond between unlike atoms on adjacent sites, and raised by J'' for every bond between like atoms on adjacent sites. By a suitable choice of the arbitrary zero point of the energy scale, we can ensure that $J' = J''$.

Now we set the order parameter on the i-th site s_i to $+1$ if the site is occupied by a Cu atom, and to -1 if it is occupied by a Zn atom. Then the system's energy function becomes $E = -\frac{1}{2}\sum_{ij} J'_{ij}s_is_j$, which is identical with Eq. (5.5) for the Ising model's energy function in the case of $H_{\mathrm{mag}} = 0$.

5.2.3   Critical Exponent [8, 9]

Critical exponents describe the behavior of physical quantities near continuous phase transitions, which are associated with the emergence of power

law distributions of certain physical quantities. A power law is a special kind of mathematical relationship between two quantities, which is some polynomial relationship that exhibits the main property of scale invariance. In physics and mathematics, scale invariance is a feature of objects or laws that do not change if length scales (or energy scales) are multiplied by a common factor. The most common power laws relate two variables and have the form of $f(x) = ax^K + o(x^K)$, where a and K are constants, K is typically called the scaling exponent, and $o(x^K)$ is an asymptotically small function of x^K. Given a relation of $f(x) = ax^K$, scaling the argument x by a constant factor causes only a proportionate scaling of the function itself. That is, $f(cx) = a(cx)^K = c^K f(x) \propto f(x)$.

Suppose $f(T_r)$ is a function describing the behavior of a physical quantity, such as magnetization, where $T_r = (T - T_c)/T_c$, the reduced temperature T_r is zero at the phase transition. As $T_r \to 0$, the limit Λ of $\ln[f(T_r)]/\ln t_r$, if it exists, is called the critical exponent associated with f. In this case, we write $f \sim T_r^\Lambda$ ("$\sim$" is read as "is asymptotically equal to"). It is important to remember that this only represents the asymptotic behavior of the function $f(T_r)$ as $T_r \to 0$. In other words, a number of quantities show a power law behavior close to T_c, e.g. $M(T) \sim (T_c - T)^{\beta_c}$.

Other examples of critical exponents for thermodynamic quantities are

$$C \sim |T_c - T|^{-\alpha_c},$$
$$\chi = (\partial M/\partial H_{mag})_T \sim |T_c - T|^{-\gamma_c},$$
$$M(H_{mag}, T_c) \sim H_{mag}^{1/\delta_c}.$$

There was an astonishing empirical fact to explain the coincidence of the critical exponents in very different phenomena, such as magnetic systems, superfluid transition (λ transition), alloy physics $\cdots$. These phenomena, whereby dissimilar systems exhibit the same critical exponents, are called universality. Universality is an important concept of the theory of continuous phase transition. Systems of the same dimension and with a phase transition into an ordered state with the same symmetry belong to the same universality class. They have essentially the same critical properties.

One of the successes of the modern theories of critical phenomena is in finding relations between the various critical exponents-scaling theories. Thus phase transitions in many different systems may be described by the same underlying scale-invariant theory. In fact, Scale invariance is a feature of phase transitions in diverse systems. The key observation is that near a phase transition or critical point, fluctuations occur at all length scales. Diverse systems with the same critical exponents, which display the identical scaling behavior as they approach criticality, can be shown to share the same fundamental dynamics. For instance, among the critical exponents for magnetic systems are α_c, β_c, γ_c and ν_c. They are not all independent, and it is possible to derive inequalities such as $\alpha_c + 2\beta_c + \gamma_c \geqslant 2$.

5.3 Thermodynamics of Martensitic [10] and Bainite Transitions [11]

Martensitic phase transitions are first order, diffusionless, shear (displacive) solid state structural changes, which can be induced either by variation of T or by application of stress. It is the origin of properties such as shape memory effect, superelasticity, and high damping capacity (internal friction). The application of thermodynamics to understanding the martensite transition has been extremely productive over the last several decades in moving towards the generalization of effects in several steel systems.

During such transitions, a parent phase (the austenite phase γ_A) transforms into a crystallographic different product phase (the martensitic phase α_M) without any change of composition where γ_A is the high temperature phase. On cooling at a proper rate, α_M starts to nucleate at the martensite start temperature M_s. Upon further cooling, further nucleation of other γ_A and growth occur in such a way that α_M progressively invades γ_A. The transition finishes when all γ_A has been replaced by α_M at the martensite finish temperature M_f. Depending on the final temperature reached on cooling ($T > M_f$), the transition could stop before the whole system has changed into α_M, i.e., a mixture of γ_A and α_M is obtained. On heating, the reverse transition occurs starting at the austenite start temperature (A_s) and finishing at the austenite finish temperature (A_f).

A general scheme of G function of γ_A and α_M and their difference ΔG is reported in Fig. 5.3 as a function of T. At high T, γ_A has lower G and thus is more stable than α_M.

Kaufman and Cohen, in their pioneering work, first introduced the useful concepts of T_0 temperature and driving force, and established a thermodynamic framework, which can be applied to martensitic transitions. As shown in Fig. 5.3, G of γ_A and α_M at T_0 are equal, or thermodynamically in (metastable) equilibrium, i.e.,

$$G(\gamma_A, T_0) = G(\alpha_M, T_0). \tag{5.6}$$

At any other T, there is a difference in G between α_M and γ_A, which is a quantitative measure of the driving force for the martensitic transition, the larger in a positive sense the greater the driving force. According to the scheme in Fig. 5.3(b), for $\gamma_A \rightarrow \alpha_M$ transition, this driving force can be defined as

$$\Delta G(\gamma_A \rightarrow \alpha_M, T) = G(\alpha_M, T) - G(\gamma_A, T), \tag{5.7}$$

whereas for the reverse transition,

$$\Delta G(\alpha_M \rightarrow \gamma_A, T) = G(\gamma_A, T) - G(\alpha_M, T). \tag{5.8}$$

The experimental determination of T_0 depends on bracketing it between M_s and A_s. The hysteresis between M_s and A_s can be reduced by plastic deformation, thus closing the gap to a few degrees. However, in non-thermoelastic
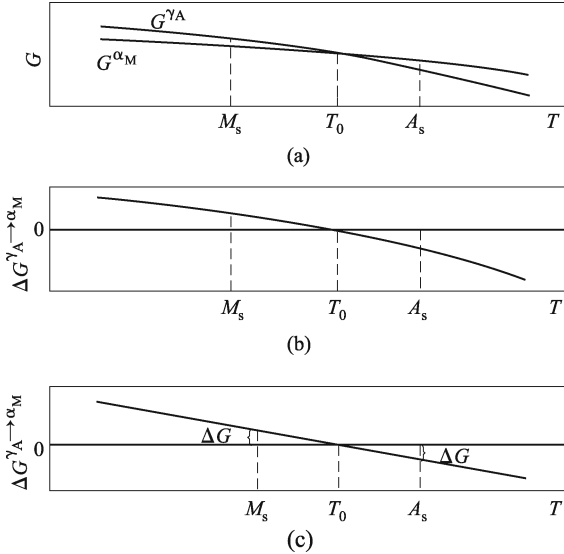
Fig. 5.3 Schematic representation of G functions of the parent (γ_A) and martensitic (α_M) phases (a), ΔG function between the above two phases (b) and ΔG function where $\Delta G(\gamma_A \rightarrow \alpha_M, M_s) = \Delta G(\alpha_M \rightarrow \gamma_A, A_s)$ (c). (Reproduced from Ref. [10] with permission of Elsevier)

alloys, as in Fe-C system, hysteresis between M_s and A_s can be as large as hundreds of degrees.

When the entropy difference between the two phases is constant, and $\Delta G(\gamma_A \rightarrow \alpha_M, M_s) = \Delta G(\alpha_M \rightarrow \gamma_A, A_s)$ [Fig. 5.3(c)], the following equation holds for non-thermoelastic transitions,

$$T_0 = (M_s + A_s)/2. \tag{5.9}$$

When there are no magnetic contributions to G, C_P of a solid pure element or an alloy presents a smooth trend, and is approximately equal in the considered temperature range where martensitic transitions usually occur. This implies that the $\Delta S(\gamma_A \rightarrow \alpha_M)$ can be assumed to be constant. On the contrary, when magnetic transitions occur, C_P shows the so-called λ shape, i.e. a sharp peak at Curie or Néel temperature. As a consequence, the difference in C_P between the parent and martensitic phases can be large, $\Delta G(\gamma_A \rightarrow \alpha_M, T)$ is not a linear function of T and the driving forces $\Delta G(\gamma_A \rightarrow \alpha_M, M_s) \neq \Delta G(\alpha_M \rightarrow \gamma_A, A_s)$. Eq. (5.9) is invalid. This occurs indeed very often. For instance, magnetism is present in Fe-base alloys. Even when the aforementioned hypotheses are not fulfilled, however, Equation (5.9) is commonly used as a reasonable approximation for obtaining T_0 in non-thermoelastic martensitic alloys.

In thermoelastic alloys, hysteresis between M_s and A_s is limited, and thus bracketing is not required to estimate T_0. Unfortunately, it has been

found for some β-brass that $A_s < T_0$, and thus the determination of T_0 requires special care. The origin of this behavior is related to the accumulation of strain energy in the direct reaction (on cooling), which is sufficient to "prematurely" start the reverse transition on heating. However, it has been recognized that for several thermoelastic transitions, it can be assumed that the elastic contribution becomes negligible at M_s and A_f, i.e. for the first plate of martensite to form during the direct transition, and for the last plate to disappear during the inverse transition. Thus, T_0 should lie at half way between M_s and A_f and Eq. (5.9) should be modified to

$$T_0 \approx (M_s + A_f)/2. \qquad (5.10)$$

Figure 5.4 reports $G(T)$ functions of equilibrium phases. For the purpose of illustration, a generic Fe-X system is considered and G curves of γ_A and α_M as a function of composition at different T are shown. For an alloy composition x_0 at a temperature T_1 being higher than T_0 (Fig. 5.4(a)), γ_A is stable, and its $G(T_1)$ is given by point A'. When T is decreased down to T_0 (Fig. 5.4(b)), the G values of both γ_A and α_M are equal (point B). However, according to the common tangent rule, the equilibrium state of the system is a mixture of γ_A and α_M, whose G is given by point B'. At any lower T_3 (Fig. 5.4(c)), γ_A (point C) has the possibility to transform into α_M without composition change (point C') or into the more stable mixture of $\alpha_M - \gamma_A$ (point C''), whose compositions are given by the tangent points C''' and C''''. Although a thermodynamic driving force exists for a transition of γ_A into the stable mixture of $\alpha_M - \gamma_A$ (line CC''), this reaction requires diffusion of the components and can be hindered by rapid cooling at low T. Thus, the martensitic reaction, being diffusionless, can occur even with a lower driving force (CC').

The previous thermodynamic scheme is simplified in some regards: (1) In most cases, both γ_A and α_M are metastable when the martensitic transition occurs. This implies that in the schemes of Figs. 5.3 and 5.4, curves for one or more other phases which have lower $G(T)$ values should be included, i.e. the "true" thermodynamic equilibrium is different from that including only γ_A and α_M. However, this "true" equilibrium can be avoided by quenching and the schemes in Figs. 5.3 and 5.4 are therefore useful to the purpose of describing the martensitic transition. (2) As previously described, the martensitic transition and its reverse occur at different T on cooling and heating, with respect to T_0. This is due to the effect of other energetic terms, such as elastic and plastic energy or irreversible frictional energy, which hinder the formation of the martensite and its reverse.

The major non-chemical contributions are: (1) An elastic stored energy $E_{el}(\gamma_A \rightarrow \alpha_M)$, i.e. the energy necessary to accommodate the residual strain after the martensite transition, and the subsequent slip or twinning at the habit plane. E_{el} is reversibly accumulated during the direct reaction and released in the reverse transition. In non-thermoelastic transitions, irreversible plastic deformation also occurs. (2) An irreversible frictional energy or fric-
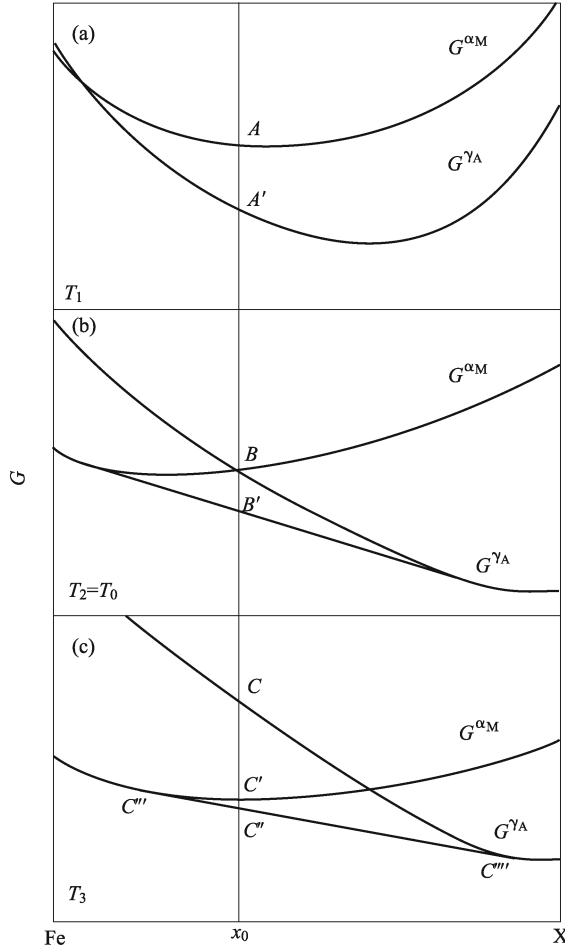
Fig. 5.4 $G(T)$ functions for parent and martensitic phases in a generic Fe-X system as a function of composition at three different temperatures: (a) $T_1 > T_0$; (b) $T_2 = T_0$; (c) $T_3 < T_0$. (Reproduced from Ref. [10] with permission of Elsevier)

tional work E_{fr}, which is related to the motion of the interface and the creation of defects during the transition. (3) An interfacial energy contribution $\gamma_{ss}A$, i.e. the energy released due to the creation of the interface between γ_A and α_M. In non-thermoelastic transitions this term is rather small in comparison with the total driving force, the interface being coherent or semicoherent, and is often neglected.

Both E_{el} and E_{fr} are of the order of $50-100$ J·mol^{-1} in thermoelastic transitions, whereas higher values appear in non-thermoelastic ones. The driving force for the martensitic transition can thus be expressed as $E_{el} + E_{fr} + \gamma_{ss}A$. At M_s combining this equation and Eq. (5.7), the following energy balance

is established,

$$\Delta G(\gamma_A \rightarrow \alpha_M) = E_{el} + E_{fr} + \gamma_{ss}A. \tag{5.11}$$

In light of the aforementioned non-chemical contributions to the energy balance, the different behaviors of thermoelastic and non-thermoelastic martensites can be rationalized, and experimental observations can be explained. It has been observed experimentally that the growth and shrinkage of thermoelastic martensitic phases take place in a well defined sequential order, with the first plate forming during cooling being the last one to disappear during heating. A necessary condition for this behavior is the absence of plastic accommodation of the transitional shape and volume changes. $E_{el}(\gamma_A \rightarrow \alpha_M)$ accumulated in the direct reaction is reversibly recovered during the reverse transition, and therefore helps the reversion of the martensite. In the early stages of the reverse reaction, it can be large enough to promote the transition, even without the help of $\Delta G(\gamma_A \rightarrow \alpha_M)$. As a consequence, A_s may lie below the T_0. Moreover, the hysteresis in thermoelastic martensites is limited because of the absence of nucleation and the lower value of elastic energy in comparison with plastic accommodation.

Salzbrenner and Cohen have carried out a complete series of experiments, in order to clarify the role of different contributions to these transitions. Their main results are: (1) If a single crystal is forced to transform with a single interface, no E_{el} is accumulated, and the transition proceeds up to completion with the same T at the interface. The thermal hysteresis observed is totally due to E_{fr}, which can be assumed constant since the dimensions of the interface do not change during the transition. Since $M_s = M_f$, and $A_s = A_f$, Eq. (5.9) is valid for determination of T_0. (2) Multiple interfaces, single crystal samples transform with increasing storage of E_{el}. Since the transitional shape and volume are constrained, a progressive depression of the transition curves to lower T in the thermal hysteresis cycle. If nucleation takes place at a free corner, the specimen can be considered unconstrained at M_s and A_f and Eq. (5.10) can be used. (3) If polycrystalline specimens are considered, E_{el} is operative even at M_s and A_f. Consequently, while T_0 is not changed, these temperatures are shifted to lower values and Eqs. (5.9) and (5.10) are invalid.

In the non-thermoelastic case, E_{el} is not a controlling factor of the reaction, and both the direct and reverse transitions require separate nucleation to start. Now the critical driving force to nucleate martensite from the parent phase is the same as that in the reverse transition, i.e. $\Delta G(\gamma_A \rightarrow \alpha_M, M_s) = \Delta G(\alpha_M \rightarrow \gamma_A, A_s)$. With the further assumption that C_P values of the both phases are similar, Eq. (5.9) is generally considered valid and widely applied.

There is another similar transition in steel, namely, bainite transition. In a far-reaching paper, Zener (1946) attempted to give a rational thermodynamic description of the phase transitions in steel. He assumed that bainite growth is diffusionless, any carbon supersaturation in bainitic ferrite is relieved subsequent to growth, by partitioning into the residual austenite. He

believed that unlike martensite, there is no E_{el} associated with the growth of bainite. Thus bainite should form at a temperature just below the corresponding equilibrium temperature T_{0b}, where γ_A and ferrite (α_F) of the same composition have an identical G value. This is schematically shown in Fig. 5.5.
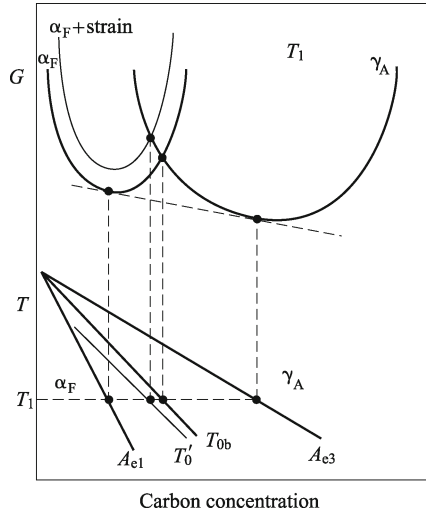

Fig. 5.5 Schematic illustration of the origin of the T_{0b} curve on the phase diagram. The T_0' curve incorporates a strain energy term for the ferrite, illustrated on the diagram by raising the Gibbs free energy curve for ferrite by an appropriate quantity.

Hultgren at the time proposed a model for the role of substitutional alloying elements in steel; at high T where diffusion rates are reasonable, these elements can redistribute during transition in a way consistent with equilibrium. The transition was then said to occur under "orthoequilibrium" conditions. This contrasts with "paraequilibrium" in which the substitutional alloying elements are unable to partition, although C, which is a fast diffusing interstitial element, redistributes between the phases until its chemical potential is uniform throughout.

Another important solid transition in steel is the eutectoid transition with the product phase peralite, which consists of cementite and ferrite. The mechanism of pearlite transition was believed to be initiated by the nucleation of cementite. This led to the contrasting suggestion that bainite is initiated by the nucleation of ferrite. Hultgren put these ideas together and proposed that upper bainite begins with the nucleation and growth of ferrite with a paraequilibrium C concentration, causing the residual austenite to become enriched in C. This bainitic ferrite, unlike the ferrite associated with pearlite, was considered to have a rational Kurdjumov-Sachs or Nishiyama-Wasserman orientation relationship with γ_A in which it grows. This was used to illustrate

the observed difference in ferrite morphologies in bainite and pearlite. Bainitic ferrite was always found to consist of individual plates or sheaves whereas the ferrite in pearlite apparently formed alternating plates of a regularly spaced two-phase lamellar aggregate. The enrichment of austenite with C should eventually cause the paraequilibrium precipitation of cementite from austenite in a region adjacent to the bainitic ferrite. At this time, pearlitic cementite was thought to bear a rational orientation relation to the austenite grain into which the pearlite colony grows whereas bainitic cementite should be randomly orientated to the austenite in which it precipitated. This process of ferrite and subsequent cementite precipitation then repeated, giving rise to the sheaf of bainite. Thus, the upper bainite is similar to pearlite but growing under paraequilibrium conditions and different in the orientation relations with austenite. Later, Hillert pointed out an important distinction between pearlite and upper bainite; in the former case, the ferrite and cementite phases grow cooperatively, whereas in the latter case, the plates of bainitic ferrite form first with the precipitation of cementite being a subsequent reaction.

A bainitic microstructure is far from equilibrium. The free energy change accompanying the formation of α_F in a Fe-0.1C wt% alloy at 813 K is -580 J·mol^{-1}, whereas that for the formation of an equilibrium mixture of allotriomorphic ferrite and austenite at the same T is -1050 J·mol^{-1}. Consequently, the excess energy of α_F is about 470 J·mol^{-1} relative to allotriomorphic ferrite, equivalent to about 0.04 in units of RT_m. This is about an order of magnitude larger than the stored energy of a severely deformed pure metal. It is small, however, when compared with highly metastable materials such as rapidly-quenched liquids which solidify as supersaturated solutions, or multilayered structures having a high density of interface (Table 5.1). Thus, bainitic steel can be welded whereas all the other materials listed with higher stored energy would not survive the welding process.

Table 5.1 Excess energy of metastable materials adapted from Turnbull

Example	Excess energy (RT_m)
Highly supersaturated solution	1
Amorphous solid	0.5
Artificial multilayers	0.1
Bainite	0.04
Cold-deformed metal	0.003

The concepts of equilibrium, metastable equilibrium and indeed constrained equilibrium remain useful in spite of the large excess energy, which can be applied to α_F in the interpretation of the transition mechanism and to the design of modern steel.

The atom-probe experiments have established that there is no redistribution of substitutional solutes during the bainite transition. These experiments cover the finest conceivable scale for chemical analysis. They rule out any mechanism which requires the diffusion of substitutional solutes. This includes the local equilibrium modes of growth. By contrast, all experimen-

tal data show that pearlite grows with the diffusion of substitutional solute atoms. Cr, Mo, Si, and Co have been shown to partition at the reaction front. The extent of partitioning is smaller for Mn and Ni, especially at large undercoolings, but there is localised diffusion. These observations are expected because pearlite is the classic example of a reconstructive transition.

Solutes in iron affect the relative stabilities of γ_A and α_F. This thermodynamic effect is identical to all transitions. We have seen, however, that substitutional solutes do not diffuse at all during displacive transitions whereas they are required to do so during reconstructive transition. It is for this reason that the observed effect of solutes, on the rate of transition, is larger for reconstructive than for displacive transition as shown in Fig. 5.6.
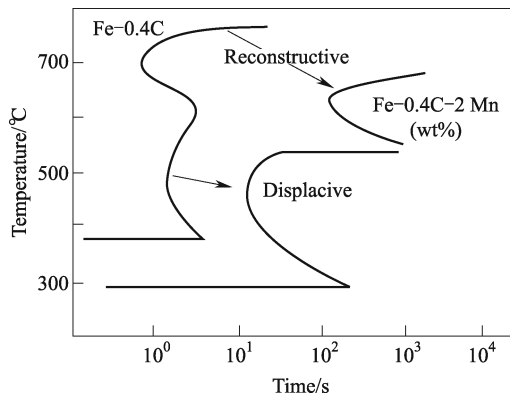

Fig. 5.6 Time-temperature-transition (TTT) diagrams showing the greater retarding effect that Mn has on a reconstructive transition compared with its influence on a displacive transition.

Bainite forms at somewhat higher T where C can escape from the plate within a fraction of a second. Its original composition cannot thus be measured directly. There are three possibilities. C may partition during growth so that the ferrite may never contain any excess C. The growth may on the other hand be diffusionless with C being trapped by the advancing interface. Finally, there is intermediate case in which some C may diffuse with the remainder being trapped to leave the ferrite partially supersaturated.

Diffusionless growth requires that transition occurs below T_{0b}, when the free energy of α_F becomes smaller than that of γ_A of the same composition. Growth without diffusion can only occur if C concentration of γ_A lies to the left of the T_{0b} curve. It is found experimentally that transition to α_F does stop at T_{0b} boundary. The balance of evidence is that the growth of α_F below B_s involves the successive nucleation and martensitic growth of subunits, followed in upper α_F by the diffusion of C into the surrounding γ_A. The possibility that a small fraction of C is nevertheless partitioned during growth cannot entirely be ruled out, but there is little doubt on whether α_F

is at first substantially supersaturated with C.

The chemical potential is not uniform in steel when the bainite reaction stops. The reaction remains incomplete in that the fraction of α_F is less than expected from a consideration of equilibrium between γ_A and α_F. This "incomplete reaction phenomenon" explains why the degree of transition to α_F is zero at B_s (starting transition temperature of bainite) and increases with undercooling below B_s in steel where other reactions do not overlap the formation of α_F.

Although the bainite reaction stops before equilibrium is reached, the remaining γ_A continues to decompose by reconstructive transition, albeit at a greatly reduced rate. Pearlite often forms sluggishly after α_F. The delay between the cessation of α_F and the start of pearlite varies with the steel composition and transition temperature. In one example, the bainite reaction stopped in a matter of minutes, with pearlite growing from the residual γ_A after some 32 h at $T = 723$ K. In another example, isothermal reaction to lower α_F at 751 K was completed within 30 min, but continued heat treatment for 43 days caused the incredibly slow reconstructive transition to two different products. One of these was alloy-pearlite which nucleated at the austenite grain boundaries and developed as a separate reaction. The other involved the irregular, epitaxial and reconstructive growth of ferrite from the existing α_F. The extent of ferrite growth in 43 days was comparable to the thickness of the bainite plates, which took just a few seconds to form. The two-stage decomposition of γ_A is more difficult to establish for plain carbon steel where the reaction rates are high, with the pearlite reaction occurring a few seconds after α_F.

5.4   Glass Transition

5.4.1   Freezing into Solid State: Glass Formation versus Crystallization [12, 13]

A wide variety of materials ranging from metals to polymers can solidify as glasses rather than crystals. In order to obtain solid, we can do the following experiment, that is, cooling the vapor of the material until it condenses into the liquid state, and then further gradually cooling the liquid until it solidifies. Results of such an experiment, for a given quantity of the material, may be represented on a $V(T)$ plot such as the one schematically shown in Fig. 5.7.

Figure 5.7 should be read from right to left, since time runs in that direction during the course of the quenching (T-lowering) experiment. A sharp break or bend in $V(T)$ marks a change of phase occurring with decreasing T. The first occurs when the gas condenses to the liquid phase at T_b. Continued
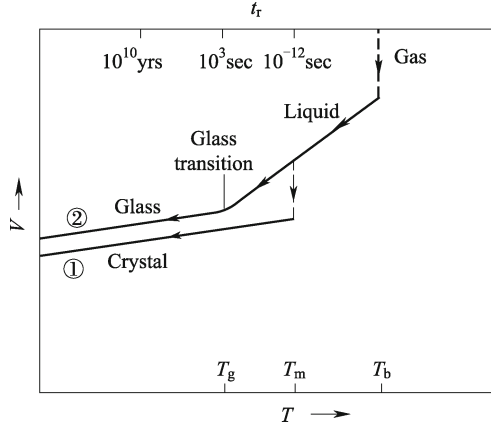
Fig. 5.7 The two general cooling paths by which an assembly of atoms can condense into the solid state. Route ① is the path to the crystalline state; route ② is the rapid-quench path to the amorphous solid state.

cooling now decreases the liquid volume in a continuous fashion, the slope of the smooth $V(T)$ curve defining the liquid's $\alpha = (1/V)(\partial V/\partial T)_P$ (The experiment is assumed to take place at $P \approx 0$). Eventually, when T is brought low enough, a liquid→solid transition takes place with the exception of liquid He, which remains liquid as $T \to 0$ under $P \to 0$. The solid then persists in $T = 0$, its signature in terms of $V(T)$ being a small slope corresponds to the low α value which characterizes a solid. A liquid may solidify in two ways: One is discontinuous with a crystalline solid, the other is continuous with an amorphous solid (glass).

The two solids resulting from these two quite different solidification scenarios are labeled, correspondingly, ① and ② in Fig 5.7. The former occurs at T_m. The liquid→crystal transition is marked by a discontinuity in $V(T)$, an abrupt contraction of the volume of the crystalline solid. But crystallization takes time through nucleation and growth by outward propagation of the crystal/liquid interfaces. In a quenching experiment carried out at a sufficiently low cooling rate, this is usually the route taken to arrive at the solid state. At sufficiently high cooling rates however, most materials alter their behavior and follow route ② to the solid phase. T_m is bypassed without incident, and the liquid phase persists until a lower glass transition temperature T_g is reached and the second solidification scenario is realized. The liquid→glass transition occurs in a narrow temperature interval near T_g. There is no volume discontinuity, instead $V(T)$ bends over to acquire the small slope characteristic of the low α of a solid.

With the liquid being cooled at a finite rate, the liquid may be taken below T_m along the $V(T)$ trajectory, which smoothly continues the curve from higher T. In the temperature interval between T_m and T_g, the liquid is referred to as the undercooled liquid. If its temperature can be taken below T_g before

crystallization has time to occur, the undercooled liquid solidifies as the glass and remains in this form essentially indefinitely. Glass formation, therefore, is a matter of bypassing crystallization. The channel to the crystalline state is evaded by quickly crossing the dangerous temperature regime between T_m and T_g. For a material to be prepared as an amorphous solid, cooling must proceed "fast enough and far enough". "Far enough" means that the quenching must be taken to $T < T_g$, and "fast enough" implies that $T_g < T < T_m$ must be crossed in a time too short for crystallization to occur. In contrast to crystallization, which is heterogeneous (pockets of the solid phase appear abruptly within the liquid and then grow at its expense), the glass transition occurs homogeneously throughout the material. This transition (i.e., all liquids would form glasses) would be observed for any liquid when sufficiently undercooled and the amorphous state is a universal property of condensed matter, no matter whether ceramic, polymeric or metallic.

The fundamental difference between crystals and glasses comes from their microscopic, atomic-scale structure. In crystals, the equilibrium positions of the atoms form a translationally periodic array. The atomic positions exhibit long-range order. In amorphous solids, long-range order is absent; the array of equilibrium atomic positions is strongly disordered. For crystals, the atomic-scale structure is securely known at the outset from the results of diffraction experiments, and it provides the basis for the analysis of such properties as electronic and vibrational excitations. For amorphous solids however, the atomic-scale structure is itself one of the key mysteries.

Roughly speaking, a glass is a material that is out of equilibrium, having the disordered molecular structure of a liquid and the rigidity of a solid. An amorphous solid is metastable with respect to some crystalline phase with the thermodynamic equilibrium state of the lowest energy. While this statement itself is correct, the emphasis is misplaced because experience teaches that the crystalline ground state is normally kinetically inaccessible. Once formed, glasses can persist without practical limit ($> 10^n$ year). The situation is similar to that of crystalline metastable diamond (the most stable crystalline structure is graphite at ambient T and P). Since the same is true of a glass well below T_g, metastability becomes an academic matter. But the underlying physics of the glass transition remains one of the most fascinating open questions in materials science and condensed-matter physics. A hotly debated issue is whether the glass transition involves an underlying thermodynamic or kinetic phase transition. The Monte Carlo simulation [14] provides further evidence that the glass transition is not thermodynamic in origin.

A thermodynamic phase transition must involve abrupt changes in certain thermodynamic properties, such as V. According to the thermodynamic viewpoint, the experimentally observable glass transition is a kinetically controlled manifestation of an underlying thermodynamic transition. A detailed view of the vicinity of the liquid→glass transition is shown in Fig. 5.8 for the case of the organic glass polyvinylacetate ($CH_2CHOOCCH_3$). $V(T)$ functions

are cooling rate dependent where two experimental time scales are 0.02 and 100 hr while the the fixed initial temperature is well above T_g. Change this time by a factor of 5000 shift T_g by only 8 K. Thus this effect, while quite real, is small.
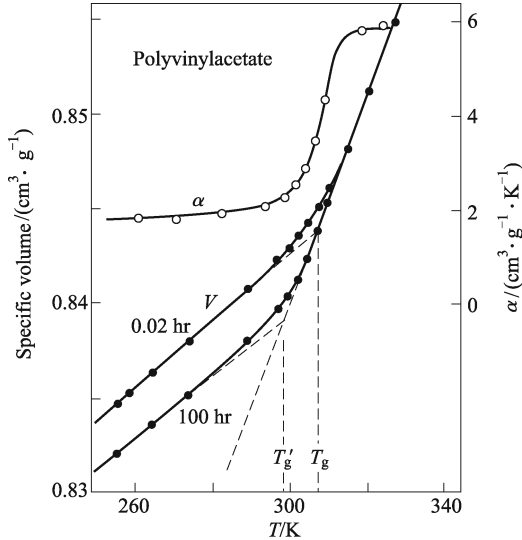

Fig. 5.8 $V(T)$ functions of an organic material with two different cooling rates in the neighborhood of the glass transition while $\alpha(T)$ function is under the fast-cooling rate (0.02 hr). The slope changes in the curves signal the occurrence of the liquid→glass transition.

The reason that T_g shifts to lower T when the cooling process is extended over longer time resides in the temperature dependence of a typical molecular relaxation time t_r. The quantity $1/t_\mathrm{r}$ characterizes the rate at which the molecular configuration of the condensed system adapts itself to a change in T. This quantity varies enormously during the cooling process. An indication of this dramatic variation is given at the top of Fig. 5.7 where in crude order-of-magnitude terms, values of t_r are associated with three temperatures: T_m, T_g, and a temperature well below T_g (say, T_g-50 K). The structural-rearrangement response time may increase from the order of 10^{-12} sec at T_m to 10^{10} years at T_g-50 K. As T traverses the region near T_g, $t_\mathrm{r}(T)$ becomes comparable to the time scale of the measurement. As T is lowered below T_g, t_r becomes much longer than any experimentally accessible time, so that the material loses its ability to rearrange its atomic configuration in harmony with the imposed decline of T. The atoms get frozen into well defined positions (equilibrium positions, about which they oscillate), which correspond to the configuration they had at T_g: If a longer experimental time t is available, then a lower T is needed to achieve the condition $t_\mathrm{r}(T) > t$, which freezes the atoms into the configuration that they maintain in the amorphous solid

state. Note that the mildness of the t dependence on T_g is simply the other side of the coin with respect to the severity of the exceedingly steep function $t_r(T)$.

While kinetic effects clearly play a role in the operational definition of T_g, it is generally believed that the observed glass transition is a manifestation of an underlying thermodynamic transition viewed as corresponding to the limit $t \to \infty$, the average cooling rate $-\overline{dT/dt} \to 0$.

5.4.2 Characteristic Properties of Glass Transition [12]

The basic thermodynamic response function to be experimentally examined in connection with a temperature-induced change of phase is C_P. Figures 5.9(a) and 5.9(b) shows $C_P(T)$ data for two very different amorphous solids, the covalent glass As_2S_3 and the metallic glass $Au_{0.8}Si_{0.1}Ge_{0.1}$. In each case, the glass transition clearly appears as a "step" in the C_P. For As_2S_3, $C_P(T)$ can be followed continuously from low temperature up through T_g and well into the liquid regime to T_m and beyond. For $Au_{0.8}Si_{0.1}Ge_{0.1}$, a portion of the liquid curve (shown with dash line in the figure) is extrapolated between measured values taken just above T_g and below T_m, because crystallization intervenes shortly after passing these temperatures at the relatively slow heating or cooling rates required for measuring C_P. Figure 5.9 provides the first thermodynamic evidence of a glass transition in an amorphous metal, observed upon warming a splat quenched sample through T_g.
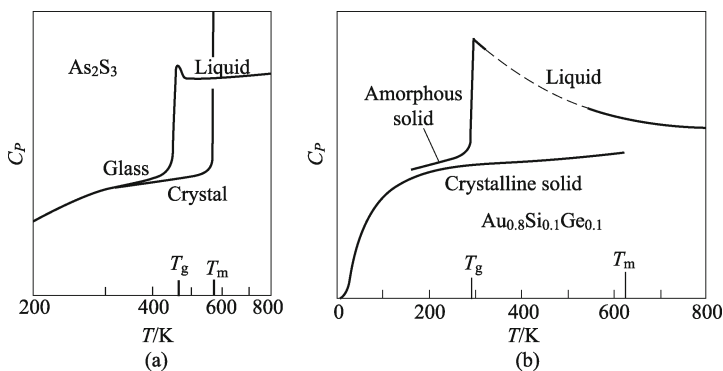
Fig. 5.9 (a) C_P of the crystalline, amorphous, and liquid forms of a covalent As_2S_3, which is a prototypical galss former. (b) C_P signature of the glass transition in a metallic glass.

The behavior of $C_P(T)$ near T_g in Figs. 5.9(a) and 5.9(b) is qualititavely the same as that of $\alpha(T)$ in Fig. 5.8: Both the C_P and the α step up, in a narrow temperature interval, from a low value characteristic of the glass to a high value characteristic of the liquid. This observation characterizes the glass

transition closely resembling a second-order thermodynamic transition. While $V(T)$ is continuous through the vicinity of $T_g, \alpha(T)$ and $C_P(T)$ definitely change their values upon passing through this region. However, these changes are not sharp (as they should be in a true second-order transition) but instead are diffuse, occurring over a small temperature interval rather than at a single sharply definable T. Thus the kink in $V(T)$, separating the undercooled liquid from the amorphous solid in Fig. 5.7, is rounded, so that the corresponding step in $\alpha(T)$, while steep, is not a vertical discontinuity. Similar statements apply to the bend in the $S(T)$ function and to the corresponding step in $C_P(T)$. Nevertheless, the steps exhibited near T_g in Figs. 5.9(a) and 5.9(b) are certainly quite clear and pronounced. It is therefore convenient, in order to further distinguish the solidification transition which occurs at T_g from that which occurs via crystallization (in a true first-order transition) at T_m, to phenomenologically characterize the glass transition as an apparent, diffuse, second-order transition.

The confluence of both the thermodynamic and the kinetic dimensions of the glass transition presents one of the most formidable problems in condensed matter physics. The two best known theoretical treatments, with both adopting an equilibrium thermodynamic viewpoint, are the polymer-configuration model of Gibbs and DiMarzio [15] and the free-volume model of Turnbull and Cohen [16, 17].

Strong empirical support for the idea that the observed glass transition is the kinetically modified reflection of an underlying equilibrium transition is contained in data of the type displayed in Fig. 5.10. The curve shown here, obtained by integrating $C_P(T)$ heat capacity data for the hydrogen-bonded glass-forming liquid $H_2SO_4 \cdot 3H_2O$, tracks $S(T)$ of the liquid from T_m down to T_g. The quantity plotted is the excess entropy $S_{ex} = S_{liquid} - S_{crystal}$, the amount by which the entropy exceeds that of the crystal at the same T. As T decreases from T_m to T_g, S_{ex} drops sharply, which comes from the fact that just as in Fig. 5.9(a), the C_P of the liquid is substantially larger than that of the crystal. Data are not shown here for the glass $(T < T_g)$, but since we know that both the crystalline and amorphous solids have nearly equal C_P, it follows immediately that S_{ex} levels off at low T to a nearly constant value close to $S_{ex}(T_g)$.

The significant point about Fig. 5.10, the key feature which bears materially on the question of an underlying thermodynamic transition, is the dash line that extrapolates the liquid curve below T_g. However, were we to adopt a view of the glass transition as a purely kinetic phenomenon, it would be possible to probe the dash curve by shifting T_g to lower T, thereby extending the life of the liquid phase. Extend the curve to $S_{ex} = 0$, where $t \to \infty$, at a T not far from the observed T_g in Fig. 5.10, and still quite far from $T = 0$. Further extending leads to the extrapolated $S_{liquid} < S_{crystal}$ or $S_{ex} < 0$, which creates an "entropy crisis". This explanation originates in the famous work of Kauzmann [18]. Since the existence, at the same temperature, of an amorphous phase with lower S than the stable crystalline
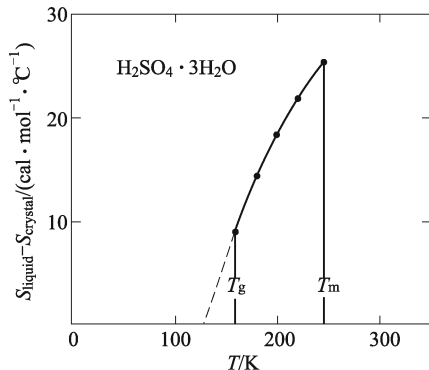
Fig. 5.10 The excess entropy of a glass-forming liquid in the region between T_m and T_g, showing the extrapolation to zero excess entropy at a temperature near T_g.

phase is physically implausible, the extrapolated curve cannot be followed beyond the $T(S_{ex} = 0)$ at which the excess entropy vanishes. $T(S_{ex} = 0)$ is defined as Kauzmann temperature T_K, which is a lower bound of T_g. Thus thermodynamic constraints do strongly limit the influence of kinetic effects upon T_g since $T_g \rightarrow T_K$ as cooling rate goes to zero.

5.4.3 Size Effect on Glass Transition [19]

An attractive choice for studies of finite size effects on the glass transition is polymer thin films since they are experimentally easy to access. The first study of this issue was done by Bares in 1975, where it was observed that T_g of styrenebutadiene-styrene triblock copolymer decreases as its ζ increases and its molecular weight M_w decreases. Now we know that T_g of a free-standing polymer thin film decreases as r decreases. However, T_g of a substrate-supported film can increase or decrease depending on the strength of chemical interaction between the support and the film and the thickness of the film while M_w has little effect on T_g. This observation leads to an argument that the radius of gyration of a molecule R_g, which depends on M_w, has no effect on T_g when r of the film is equal to or smaller than R_g (dozens of to hundred nanometers). In light of this, it is hypothesized that the correlation length for intermolecular cooperative rearrangement ξ, which determines the glass transition behavior, is independent of M_w.

One way to find a unified model for the size-dependent glass transition is to utilize an analogy between the glass transition and the melting transition. The both reflect a common tendency toward order, even if the transitions have different classes (second and first order transitions, respectively). Thus, finite size effects of T_g may be related to these on crystal melting. According to Lindemann's criterion for melting, as long as σ of atoms or molecules

reaches a critical fraction of interatomic distance, a crystal will melt. During the transition, the viscosity of the crystal will drop sharply. In fact, this is also the transition characteristic of a glass transition. Since glasses and crystals as solids have the same solid feature, their vibrational characteristics should be similar at their melting temperatures of T_g and T_m [19]. As a phenomenological observation, it is assumed that $\sigma_g^2(\infty) \approx \sigma^2(\infty)$ where the subscript "g" denotes T_g although there is no rigorous justification for this. Substituting this relationship into Eq. (3.80), namely, letting $T_g(r), T_g(\infty), \sigma_g^2(r)$ and $\sigma_g^2(\infty)$ replace $T_m(r), T_m(\infty), \sigma^2(r)$ and $\sigma^2(\infty)$, it reads

$$T_g(r)/T_g(\infty) = \sigma_g^2(\infty)/\sigma_g^2(r) = \exp\{-(\alpha_r - 1)/[(r/r_0) - 1]\}. \qquad (5.12)$$

In Eq. (5.12), for free-standing films or those supported by a passivated substrate where there is a weak chemical film/substrate interaction of van der Waals force, the corresponding $\alpha_r(\alpha_s)$ has been determined by

$$\alpha_s = [2\Delta C_{pg}(\infty)/(3R)] + 1 \qquad (5.13)$$

where $\Delta C_{pg}(\infty)$ is the heat capacity difference between the bulk glass and the bulk liquid at $T_g(\infty)$. This generalization of Eqs. (3.80) and (3.84) is based on consideration of the transition order. As a melting transition, it is a first order transition characterized by a discontinuous change of the first derivative of the Gibbs free energy, or ΔS_m. Although there are kinetic aspects to be consistent in a narrow temperature range near T_g, the glass transition is still an equilibrium thermodynamic transition with little diffuse heat capacity change. Thus, a glass transition as a second order one behaves with a discontinuous change of the second derivative of the Gibbs free energy, or ΔC_{pg}. $\alpha_s > 1$ in Eq. (5.13) since $\Delta C_{pg}(\infty)$ is positive. Thus, $T_g(r)$ decreases as r decreases in light of Eq. (5.12). Note that h in Eq. (3.79) is defined as the smallest unit in crystals, which has different vibration properties when the unit is located on the surface or within the crystals.

For a polymer film deposited on a substrate, the substrate could produce long-range effects on chain connectivity owing to the chemical interaction between the substrate and the film. If this chemical interaction is similar in strength to van der Waals force among the chain molecules, this interaction will only lead to a disappearance of one surface, which lets Eq. (3.79) be $r_0 = (3-d)h/2$. When the chemical interaction between the substrate and the film is stronger than the van der Waals force, such as hydrogen bonding between the polymer and the SiO_2 surface, $\alpha_i = \sigma_i^2(r)/\sigma_v^2(r)$, where the subscript "i" denotes the interface. Since $\alpha_s = \sigma_s^2(r)/\sigma_v^2(r), \alpha_i = \alpha_s \sigma_i^2(r)/\sigma_s^2(r)$. It is assumed that the bond strength ε is inversely proportional to σ^2, namely, $\sigma_s^2(r) \propto 1/\varepsilon_s$ and $\sigma_i^2(r) \propto 1/\varepsilon_i$. Thus, $\sigma_i^2(r)/\sigma_s^2(r) = \varepsilon_s/\varepsilon_i$, or [20],

$$\alpha_i = \alpha_s \varepsilon_s/\varepsilon_i. \qquad (5.14)$$

If $\varepsilon_s = \varepsilon_i$, this is possible when nanoparticles are embedded into a certain liquid, $\alpha_i = \alpha_s = 1$ and $T_g(r) = T_g(\infty)$. When ε_s and ε_i have comparable

sizes, assuming that the total effect of both surfaces and the film/substrate interface on $T_g(r)$ is additive, there is

$$\frac{T_g(r)}{T_g(\infty)} = \left\{ \exp\left(-\frac{\alpha_s - 1}{(r/r_0) - 1}\right) + \exp\left(-\frac{\alpha_i - 1}{(r/r_0) - 1}\right) \right\} \bigg/ 2. \qquad (5.15)$$

Figure 5.11 compares $T_g(r)$ function of polystyrene (PS) films with different surface conditions. As shown in the figure, when the molecular force at the interface (surface) is stronger than that within the film, a superheating is present. In an opposite case, an undercooling occurs. Note again that the size dependence of $T_g(r)$ is much weaker than $T_m(r)$ since the glass transition is a second order transition where $C_{pg}(\infty)$ value in a size about $(1/4 - 1/5)$ R in Eq. (5.13) is much smaller than the usual $\Delta S_{vib}(\infty) \approx R$.
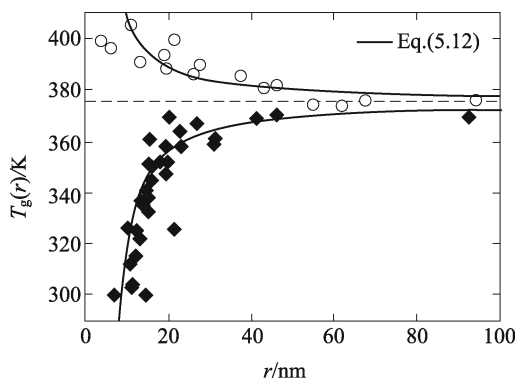

Fig. 5.11 $T_g(r)$ function of free-standing polystyrene (PS) films and PS films supported by Si substrate with hydrogen bonding in terms of Eqs. (5.12), (5.13), (5.15) and (3.79). The dash line denotes $T_g(\infty)$ of PS. For free-standing PS films, $d = 2, \alpha_s = 1.154$ determined by Eq. (5.13) where $C_{pg}(\infty) = 30.7$ J·mol^{-1}·K^{-1} = 1.919 J·g-atom^{-1}·K$^{-1}, T_g(\infty) = 375.15$ K, $r_0 = \xi = 5$ nm with $c_1 = 1$ in terms of Eq. (3.79) where $\xi = \xi[T < T_g(\infty)] = 5$ nm, which is used to substitute h for polymers. The symbol $\blacklozenge$ shows the experimental results. For PS films supported by Si substrate with hydrogen bonding, $\varepsilon_i = 4.5$ kcal·mol^{-1} is the mean hydrogen bonding strength of $4 - 5$ kcal·mol$^{-1}, \varepsilon_s = 1.5$ kcal·mol^{-1} shows the mean van der Waals force of $1 - 2$ kcal·mol^{-1}. Thus, $\alpha_i = 0.388\,5$ in terms of Eq. (5.14). $r_0 = \xi = 2.5$ nm with $c_1 = 1$ in light of Eq. (3.79) where $\xi = \xi[T_g(\infty)] = 2.5$ nm. The symbol. $\circ$ denotes the experimental evidence. (Reproduced with permission from Ref. [19])

When a blend as a compatible system consists of two polymers where their interaction is essentially van der Waals force, the blend could be considered as a mixture and their properties may be additive. Let w' be the weight fraction of the second polymer component, the corresponding $T_g(w', r)$ function of thin films may be determined by the Fox equation,

$$1/T_g(w', r) = (1 - w')/T_g(0, r) + w'/T_g(1, r). \qquad (5.16)$$

Equation (5.16) supplies an easy way to determine $T_g(w', r)$ function of polymer alloys when $T_g(0, r)$ and $T_g(1, r)$ are known from Eq. (5.12) or Eq. (5.15) where $w' = 0$ or $w' = 1$ is considered for components. Note that Eq. (5.16) for bulk is simply extended for thin films due to their interaction of two polymer components.

Figure 5.12 presents $T_g(w', r)$ function of poly(2,6-dimethyl-1,4-phenylene oxide)/polystyrene (PPO/PS) blended films supported by a passivated Si substrate [21]. Good correspondences between Eq. (5.16), experimental results, and computer simulation results are shown where $T_g(w', r)$ decreases as r decreases and decreases as w' increases since $T_g(1, \infty) < T_g(0, \infty)$. The successful application of Eq. (5.16) implies that the chemical interaction between polymer films is weak. Thus their interaction nature of van der Waals force is not necessary to be specially considered. The properties of the composite can be simply determined by an algebra sum of the components.
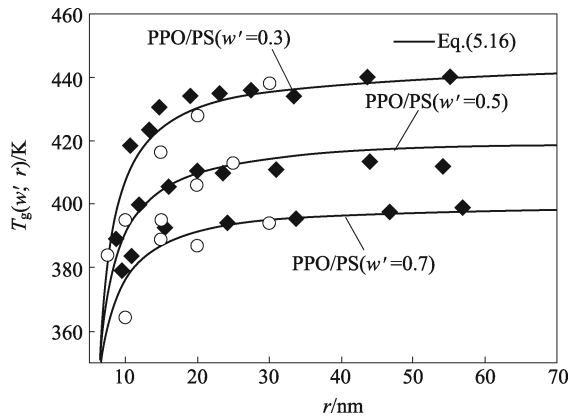
Fig. 5.12 $T_g(w', r)$ function of PPO/PS [poly(2,6-dimethyl-1,4-phenylene oxide)/polystyrene] blend films supported by a passivated Si (100) substrate in terms of Eqs. (5.12), (5.13), and (5.16) with $c_1 = 1/2$ in Eq. (3.79) since the interaction between the film and the substrate interface is similar to that within polymer. For PPO, $T_g(0, \infty) = 483$ K, $C_{pg}(\infty) = 1.591$ J·g-atom^{-1}·K^{-1}, and $r_0 = \xi = 9$ nm. For PS, $T_g(1, \infty) = 375.15$ K, $C_{pg}(\infty) = 1.919$ J·g-atom^{-1}·K^{-1}, and $r_0 = \xi = 5$ nm. The symbols ◆ and ○ denote experimental and computer simulation results, respectively. (Reproduced with permission from Ref. [19])

5.5 Ferromagnetic and Antiferromagnetic Phase Transitions of Nanocrystals

5.5.1 Size-dependent Ordering Temperatures of Ferromagnetic and Antiferromagnetic Nanocrystals [22]

The Curie temperature T_C and the Néel temperature T_N are the most important properties to characterize ferromagnetic (FM) and antiferromagnetic (AFM) phase stabilities, which are mostly present in low-dimension. such as thin films deposited on substrates of Fe/Au(100), Co/Cu(111), and Ni/Cu(100) systems. Interest in the thin films, superlattices, nanoparticles and nanorods of AFM insulators has grown for both fundamental studies and device application, for example, Ho/Nb/Y, Ho/Y/Nb, CoO/SiO$_2$, CoO/MgO, CoO/NiO, CoO/Fe$_3$O$_4$, NiO/MgO thin films and CuO nanoparticles and nanorods.

Generally, for free nanocrystals and thin films deposited on nonmagnetic substrates, $T_C(r)$ and $T_N(r)$ functions are almost size-independent at $r > 5$ nm; as r is further reduced, $T_C(r)$ and $T_N(r)$ decrease; finally, $T_C(r)$ and $T_N(r)$ approaches 0 K for small enough r (usually a few monolayers). Furthermore, due to the different ζ values of free nanocrystals, the change of the $T_C(r)$ function of nanorods or nanowires with r is less than that of nanoparticles, but greater than that of thin films. Whereas the $T_N(r)$ of CoO thin films supported by NiO and Fe$_3$O$_4$ substrates increases as r decreases, which is attributed to the vicinity effect at the NiO/CoO and Fe$_3$O$_4$/CoO interfaces, where the exchange coupling of CoO is enhanced. This differs from the experimental results of Fe/Cr(001), where $T_N(r)$ decreases with dropping r, which could be induced by the spin-frustration effect in the vicinity of the rough Fe/Cr(001) interfaces, where the interfacial exchange energy can be minimized only locally and frustration of the interfacial spins occurs since Fe and Cr have magnetically long-range order.

To understand the underlying mechanisms for $T_C(r)$ and $T_N(r)$ functions, the pioneering theoretical work of Fisher and his co-workers strongly influences our general understanding [23], in which ξ is defined as the distance from a point beyond which there is no further correlation of a physical property associated with that point, and follows the temperature-dependent function $\xi(T) = \xi_0 T_r^{v_c}$, where $T_r = 1 - T/T_C$ is the reduced temperature, ξ_0 is a macroscopic length, and v_c is a universal critical exponent. This scaling relationship leads to shift of $T_C(r)$ to lower temperature than that of the bulk when ξ exceeds $2r$. As far as thin films concerned, when $2r > \xi$,

$$T_C(r)/T_C(\infty) = 1 - [(\xi + t_f)/(4r)]^{JI}, \qquad (5.17a)$$

with $J I = 1/v_c$, t_f denotes the thickness of a monolayer. When $2r < \xi$,

$$T_C(r)/T_C(\infty) = (2r - t_f)/(2\xi). \tag{5.17b}$$

Since nanoparticles have different characteristics of $T_C(r)$ functions from those of thin films, a unified model should be considered. In light of the effect of the breaking of exchange bonds, $T_C(r)$ function of nanoparticles has been proposed,

$$T_C(r)/T_C(\infty) = 1 - (3\Delta L)/(4r) \tag{5.18}$$

where ΔL is the thickness of surface layer of nanoparticles. However, Eq. (5.18) differs from experiment data of $T_C(r)$ function of Fe_3O_4 nanoparticles since a constant ΔL cannot satisfactorily describe this case in the full size range.

Since the dimension of nanocrystals d significantly affects the $T_C(r)$ function, while Eqs. (5.17) and (5.18) consider the cases of $d = 2$ for thin films and $d = 0$ for particles respectively, they thus exhibit different forms. Sun established a unified model to consider the dimension effect on $T_C(r)$ by incorporating the bond order-length-strength (BOLS) correlation mechanism into the Ising premise,

$$T_C(r)/T_C(\infty) = 1 + \sum_{i \leqslant 3} x_i (z_{ib} q_i^{-w} - 1) \tag{5.19}$$

where $q_i = h_i/h = 2/\{1 + \exp[(12 - z_i)/(8z_i)]\}$ shows a CN dependent reduction of h, $z_{ib} = z_i/z_b$ with z_i and z_b being the coordinates with and without CN imperfection, respectively, and $x_i = \tau' h q_i/D$ is the portion of atoms in the i-th atomic layer from the surface compared to the total number of atoms of the entire solid. $i = 1, 2, 3$ corresponds to thin films, nanorods, and nanoparticles, respectively, although the physical background of this definition is unclear. The power index w as an indicator of the bond nature is an adjustable parameter. Equation (5.19) has a good correspondence with experimental results when w ≈ 1.

Since Eq. (5.19) has an adjustable parameter, further efforts need to be made. Based on the size-dependent cohesive energy function, $T_C(r)$ of thin films can be given as

$$T_C(r)/T_C(\infty) = \{1 - 1/[4r/(c_1 h) - 1]\} \exp\{[-2\Delta S_b/(3R)]/[4r/(c_1 h) - 1]\} \tag{5.20}$$

where ΔS_b is the bulk evaporation entropy of crystals. c_1 is added as an additional condition to different surface states. $c_1 = 1$ for the nanocrystals with free surface. When the interface interaction between the nanocrystals and the corresponding substrate is weak, such as thin films deposited on inert substrates, the film/substrate interaction is weak van der Waals forces while the inner interactions within the thin films are strong chemical bonds, $c_1 = 1/2$. If this strength on the interface is comparable with that within films, c_1 varies somewhat. When these are similar, which is equal to the case that

one of the two surfaces of the films disappears, $c_1 = 1/2$ is thus got (the side surfaces of the thin films are neglected due to the low thickness). For more complicated interfaces, c_1 may be considered case by case between $1/2$ and 1. Equation (5.20) has presented a qualitative explanation for drop of $T_C(r)$ function of nanocrystals with decreasing of r.

In addition to Eqs. (5.17)–(5.20), another theoretical model, a finite-size scaling relationship, has also been proposed for reproducing $T_C(r)$ functions of Co/Ni alloys,

$$[T_C(\infty) - T_C(r)]/T_C(r) = [(r - r')/\xi_0]^{-w} \tag{5.21}$$

with r' denoting the finite half-thickness of films at $T_C(r) = 0$. Although Eq. (5.21) can also fit the experimental data of Co, Co_1Ni_1, Co_1Ni_3 and $CoNi_9$, it strictly holds only in the large size limit of r through help of three adjustable parameters r', ξ_0 and w and their physical meanings are unclear.

In the explanations of $T_N(r)$ functions, besides the empirical law that is of similar form of Eq. (5.21), the finite-size scaling law has also been employed to analyze the experimental data [24],

$$T_N(r)/T_N(\infty) = 1 - (\xi_0/2r)^w, \tag{5.22}$$

and $\xi(T) = \xi_0[1 - T/T_N(\infty)]^{-v}$, where ξ_0 is the extrapolated correlation length at $T = 0$ K.

In magnetic materials, the spins are coupled through the strong, short-range exchange interactions and the long-range magnetic dipolar interactions. It is well known that near T_C, there exist two opposite forces: the ordering force due to the exchange interaction of magnetic moments, and the disordering force of lattice thermal vibrations. Based on the mean-field approximation,

$$k_B T_C(\infty) = E_{exc}(\infty) \tag{5.23}$$

where E_{exc} is the spin-spin exchange interaction energy.

The average thermal vibrational energy is related to T by an equipartition relation of $m(2\pi v_E)^2\sigma^2(T) = kT$ (Eq. (3.63)). In terms of this relationship and Eq. (5.23), at $T_C(\infty)$, the thermal vibration of atoms will destroy the magnetic ordering due to the exchange interaction of nearest-neighbor atoms with $\sigma^2[T_C(\infty)] = kT_C(\infty)/[m(2\pi v_E)^2] = E_{exc}(\infty)/[m(2\pi v_E)^2]$. Similarly, based on Lindemann's basic assumption that melting occurs when σ reaches a fraction of atomic diameter c at $T_m(\infty)$, $\sigma^2[T_m(\infty)] = kT_m(\infty)/[m(2\pi v_E)^2] = (ch)^2$ and $\Theta_D(\infty) = c[T_m(\infty)/(mh^2)]^{1/2}$. In terms of the above three relationships and an assumption that $E_{exc}(\infty)/(2\pi v_E c^2)^2 = A'$ with A' being a material constant, one can obtain

$$T_C(\infty) \propto \Theta_D^2(\infty). \tag{5.24}$$

If FM and AFM nanocrystals have the same crystal structure of the corresponding bulk, Eq. (5.24) can be extended to nanometer size, $T_C(r) \propto \Theta_D^2(r)$.

Thus, $T_C(r)/T_C(\infty) = \Theta_D^2(r)/\Theta_D^2(\infty)$. Substituting Eq. (3.80) into this equation leads to $T_C(r)/T_C(\infty) = E_{exc}(r)/E_{exc}(\infty) = \exp[-(\alpha_r - 1)/(r/r_0 - 1)]$. The same case should occur for $T_N(r)/T_N(\infty)$ function. Therefore,

$$T_C(r)/T_C(\infty) = T_N(r)/T_N(\infty) = E_{exc}(r)/E_{exc}(\infty)$$
$$= \exp[-(\alpha_r - 1)/(r/r_0 - 1)]. \qquad (5.25)$$

For metallic or compound crystals with free surfaces, α_r is determined by Eq. (3.84). While FM or AFM films are epitaxially grown on substrates, the effect of such epitaxial film/substrate interfaces on α_r must be considered since the atomic vibration at interfaces differs from that at free surfaces. Based on the Ising model, the simplest case is that only the surface and interface coupling constants (J_s and J_i) are different from the rest, where the subscript "i" denotes the interface. For the sake of simplicity, the effect induced by the exchange interface thickness is neglected while $J_i = J_s + J_{sub}$ is assumed to be a first approximation with the subscript "sub" denoting the substrate. Thus, $\alpha_i = \sigma_i^2(r)/\sigma_v^2(r) = \alpha_s\sigma_i^2(r)/\sigma_s^2(r)$ in light of the definition of α where $\alpha_s = \sigma_s^2(r)/\sigma_v^2(r)$. Since the magnitude of the exchange interaction is proportional to the bond strength ε, the bond strength is reversely proportional to σ^2, $\sigma^2(r) \propto 1/J$, $\sigma_s^2(r) \propto 1/J_s$ and $\sigma_i^2(r) \propto 1/J_i$. As a consequence, $\sigma_i^2(r)/\sigma_s^2(r) = J_s/J_i$, or,

$$\alpha_i = \alpha_s J_s/J_i. \qquad (5.26)$$

If the effects induced by surface and interface on $T_C(r)$ and $T_N(r)$ are additive, according to Eq. (5.25), it reads

$$T_C(r)/T_C(\infty) = T_N(r)/T_N(\infty)$$
$$= \{\exp[-(\alpha_s - 1)/(r/r_0 - 1)]$$
$$+ \exp[-(\alpha_i - 1)/(r/r_0 - 1)]\}/2. \qquad (5.27)$$

Note that Eq. (5.27) is only valid for the case of thin films while the side surface is neglected due to its small percentage of the total surface. For nanoparticles and nanorods, the contribution of substrates on $T_C(r)$ is neglected since the corresponding interface has only a small percentage of the total surface. In this case, Eq. (5.25) is directly used. In the following, although $T_C(r)$ and $T_N(r)$ functions are denoted by Eq. (5.27), when the considered systems are nanoparticles and nanorods, $\alpha_s = \alpha_i$, and Eq. (5.27) = Eq. (5.25).

Figure 5.13 compares $T_C(r)$ functions of Eq. (5.27) and experimental results of magnetic transition metals and their alloys and compounds, such as Ni, Fe_3O_4 and $MnFe_2O_4$ nanoparticles, Ni nanorods, and Fe, Co, Co_1Ni_1, Co_1Ni_3, Co_1Ni_9, Ni thin films, which are deposited on a nonmagnetic metal substrate. For an epitaxial FM film on a magnetic inert substrate with negligible lattice mismatch, exchange interaction between them is assumed to be absent since it is assumed that the surface and the film/substrate interface

are magnetically similar. Thus, $\alpha_i = \alpha_s$ in terms of Eq. (5.26) with $J_i = J_s$ and $J_{sub} = 0$. On the other side, for this kind of epitaxial film, the interaction strength at the film/substrate interface is comparable with the inner one, which results in disappearance of one of the two surfaces of films. Thus, the critical size of the epitaxial films is r_0.
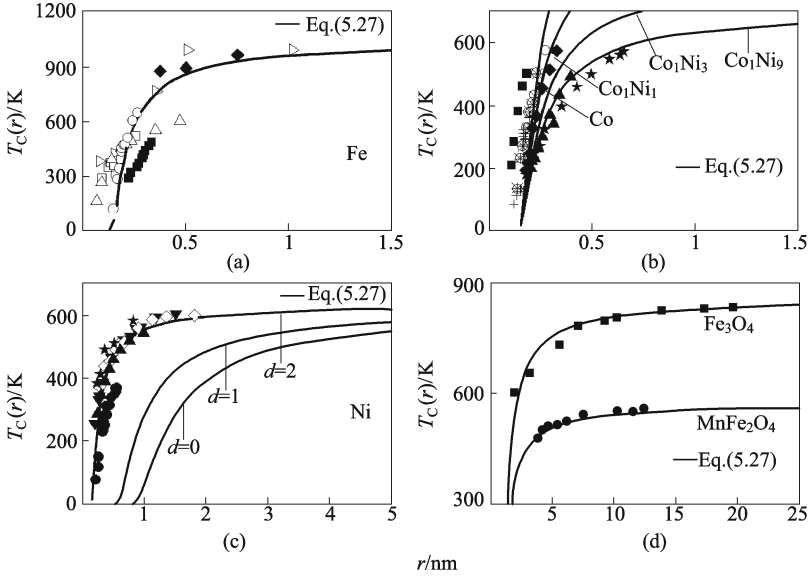
Fig. 5.13 Comparisons of $T_C(r)$ functions of Eq. (5.27) and experimental measurements for Fe, Co, Co_1Ni_1, Co_1Ni_3, Co_1Ni_9, Ni, Fe_3O_4 and $MnFe_2O_4$ nanocrystals. The necessary parameters: (a) the symbols ◆, ▷, □, △, ○, and ■ denote the experimental results of Fe/SiO, Fe/Ag(001), Fe/Au(100), Fe/Pd(100), Fe/Ag(111) and Fe/Ag(100) epitaxial films, respectively; (b) for Co, Co_1Ni_1, Co_1Ni_3 and Co_1Ni_9 alloy films, ○, *, ■, + denote the experimental evidence of Co/Cu(100), Co/Cu(111), Co/Cu(001) epitaxial films and ◆, ▲ and ★ denote the Co_1Ni_1/Cu(100), Co_1Ni_3/Cu(100), Co_1Ni_9/Cu(100) epitaxial thin films; (c) for Ni, the symbols ◆, * denote Ni nanoparticles, ○, ■, ▽ the nanorods, and ▲, ●, ★, ▼ and ◇ the experimental evidence of Ni/Cu(100), Ni/Cu(001), Ni/Cu(111), Ni/W(110) epitaxial films; (d) for Fe_3O_4 and $MnFe_2O_4$, the symbols ■ and ● denote Fe_3O_4 and $MnFe_2O_4$ nanoparticles, respectively. The other necessary parameters used in the calculations are listed in Table 5.2.

As shown in this figure, Eq. (5.27) is quantitatively consistent with the experimental data of thin films epitaxially grown on silicon oxide glass, or nonmagnetic metallic substrates. The depressed $T_C(r)$ of FM nanocrystals should be attributed to the reduction in the number of spin interactions at the surface in comparison with that in the interior. Although Eqs. (5.17) – (5.19) can also fit the experimental results of FM nanocrystals, some adjustable parameters, such as ξ and Л in Eq. (5.17), ΔL in Eq. (5.18) and w in Eq. (5.19), are present. The utilization of these experimentally fitting parameters

could mislead understanding of the related physical nature since the fitting parameters actually consist of several factors. It should be noted that for alloys the corresponding $T_C(\infty)$ and $\Delta S_m(\infty)$ values are roughly estimated by their algebraic sum of elements. As shown in Fig. 5.13(b), Eq. (5.27) corresponds to experimental evidence well.

Table 5.2 The parameters utilized in the calculations of Eq. (5.27) for FM materials. $T_C(\infty)$ is in K, $\Delta S_m(\infty)$ in J·g-atom^{-1}·K^{-1}, h and r_0 are in nm

	$T_C(\infty)$	$\Delta S_m(\infty)$	h	r_0	α_r
Fe films	1 043	7.628	0.248 3	0.124 2	$\alpha_i=\alpha_s = 1.612$
Co	1 404	9.157	0.249 7	0.124 9	$\alpha_i=\alpha_s = 1.734$
Ni	630	10.12	0.249 2	0.747 6(d =0); 0.498 4(d=1); 0.124 6(d=2)	$\alpha_s = 1.811(d =0,1)$ $\alpha_i =\alpha_s = 1.811$
CoNi	1 018	9.638[a]	0.249 5	0.124 8	$\alpha_i=\alpha_s = 1.773$
Co$_1$Ni$_3$	824.3	9.879[a]	0.249 3	0.124 7	$\alpha_i =\alpha_s = 1.792$
Co$_1$Ni$_9$	708.3	10.02[a]	0.249 3	0.124 7	$\alpha_i =\alpha_s = 1.803$
Fe$_3$O$_4$	860	10.55	0.222 0	0.669	$\alpha_s = 1.845 8$
MnFe$_2$O$_4$	573	10.55[b]	0.222 3	0.666	$\alpha_s = 1.845 8$

[a] $\Delta S_m(Co_1Ni_n, \infty) = [\Delta S_m(Co, \infty) + n\Delta S_m (Ni, \infty)]/(n + 1)$ as a first approximation, where n denotes the number of Ni atoms in the compounds.

[b] Since no experimental data of $\Delta S_m(MnFe_2O_4, \infty)$ or $\Delta S_{vib}(MnFe_2O_4, \infty)$ are in hand, $\Delta S_m(MnFe_2O_4, \infty) \approx \Delta S_m(Fe_3O_4, \infty)$ is taken.

Figure 5.13(c) shows the comparisons of $T_C(r)$ function of Ni nanocrystals with different dimensions ($d = 0$, 1 and 2) between experimental results and Eq. (5.27). As seen in this figure, $T_C(r)$ decreases with r and d while the surface/volume (A/V) ratios of free nanocrystals are $3/r, 2/r$ and $1/r$ for $d = 0, 1, 2$, respectively. Since the freestanding materials have larger A/V, their size dependence is more than that of the substances supported by substrates. However, this dimension effect has been neglected in Eqs. (5.17), (5.18) and (5.20).

In addition to the aforementioned metallic substances, $T_C(r)$ functions of nanocompounds such as Fe$_3$O$_4$ and MnFe$_2$O$_4$ nanoparticles are given in Fig. 5.13(d). As shown in the figure, the depressed $T_C(r)$ of compound nanocrystals also follows Eq. (5.27) in the full size range.

$T_N(r)$ has a similar form of $T_C(r)$ function. Similar results for CoO thin films epitaxially grown on SiO$_2$ or MgO substrate have been shown in Fig. 5.14. In light of the properties of magnetic exchange interaction of AFM, the nearest spacing of the parallel spin-spin coupling of AFM $h = 2a_l$ with a_l being the lattice parameter since the lattice of AFM can be considered to consist of two sublattice with opposite spin direction. Whereas for CoO thin films supported by Fe$_3$O$_4$ and NiO substrates, there exist strong exchange couplings at CoO/Fe$_3$O$_4$ or CoO/NiO interface where the thermal vibration of interface atoms is suppressed and much higher energy is required to disorder the ordering force. Therefore, $T_N(r)$ increases as r decreases. Equation (5.27) is qualitatively consistent with experimental evidence Although the free surface of such CoO film has still a tendency to lower the value of $T_N(r)$

of films, the total effect of the free surface and the interface leads to the drop of the total energy, thus increasing $T_N(r)$ function with decreasing r. Furthermore, the stronger the interaction at the interface is, the more the $T_N(r)$ function will increase Thus, different substrates lead to the distinct $T_N(r)$ and $T_N(\infty)$ values of CoO. For the sake of simplicity, exchange bias effect from FM/AFM interface, existence of easy and hard axes, and magnetocrystalline anisotropy are neglected.
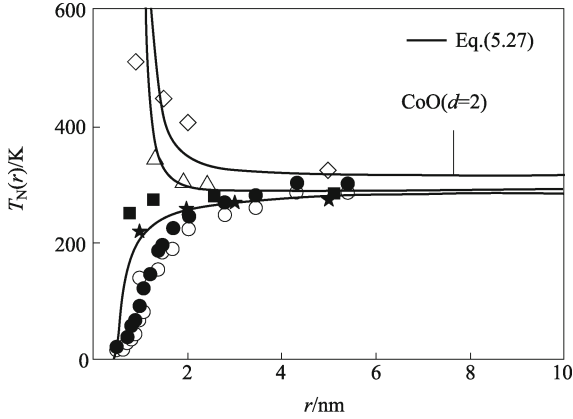
Fig. 5.14 Comparisons between $T_N(r)$ functions of Eq. (5.27) and experimental evidence for CoO thin films epitaxially grown on SiO_2 or MgO substrates ($\bullet$ and $\circ$, $\blacksquare$ and $\star$), and on Fe_3O_4 ($\triangle$) and NiO ($\diamond$) substrates, respectively. For CoO deposited on nonmagnetic substrates, the parameters $r_0 = h/2 = 0.426\,0$ nm in terms of Eq. (3.79) with $d = 2$, and $\alpha_i = 1.544$ according to Eq. (5.26) with $J_s \approx J_i$, $J_{sub} \approx 0$ and $\alpha_s = 1.544$; for CoO supported by Fe_3O_4 and NiO substrates, $\alpha_i = 0.4139$ and 0.5544 in terms of Eq. (5.26) with $\alpha_s J_s/(J_s+J_{sub}) \approx \alpha_s T_C(\infty)/[T_C(\infty)+T_{C,sub}(\infty)]$, which is achieved based on the mean-field approximation, $J_s \propto T_C(\infty)$ and $J_{sub} \propto T_{C,sub}(\infty)$ or $J_s \propto T_N(\infty)$ and $J_{sub} \propto T_{N,sub}(\infty)$. $\Delta S_m(\infty)$ of metallic oxides are given as $\Delta S_{m,MO}(\infty) = [\Delta S_{m,M}(\infty) + \Delta S_{m,O}(\infty)]/2$ as a first approximation since no experimental data are found, where the subscripts "M" and "O" denote the metal and oxygen atoms, respectively.

Considering the mathematical relationship of $\exp(-x) \approx 1 - x$ with small x, under the condition that $r \gg r_0$, Eq. (5.27) can be simplified to

$$T_C(r)/T_C(\infty) = T_N(r)/T_N(\infty) \approx 1 - (\alpha_s + \alpha_i - 2)r_0/(2r). \qquad (5.28)$$

Comparing Eq. (5.28) with the scaling law of Eq. (5.17a) for thin films with $2r > \xi$, $T_C(r)$ follows a power law curve with $\lambda = 1$. Thus, Eq. (5.17a) can be rewritten as $T_C(r)/T_C(\infty) = T_N(r)/T_N(\infty) = 1 - [(\xi + r_0)/(4r)]$. Associated with this relationship and Eq. (5.28), $\xi = (\alpha_s + \alpha_i - 2)2r_0 - r_0$. For Fe, Co, Ni thin films, $\xi = 0.4048$ nm, 0.5531 nm, 0.6322 nm, respectively, which are approximately consistent with experimental and theoretical values of 0.4583, 0.3962, 0.7048.

Equation (5.28) is similar to Eq. (5.18) for nanoparticles. Combining Eqs. (5.18) and (5.28),

$$\Delta L \approx 4(\alpha_s - 1)r_0/3, \tag{5.29}$$

which indicates that ΔL is related to two parameters of ΔS_{vib} and h. Substituting these parameters into Eq. (5.29), $\Delta L = 0.8084$ nm, 0.9692 nm, 0.7521 nm, 0.7512 nm and 1.541 nm for Ni, Gd, $MnFe_2O_4$, Fe_3O_4 and CuO nanoparticles, respectively, or $\Delta L \approx 3h$. Thus, when r is larger than several nanometers, Eq. (5.18) can be rewritten as

$$T_C(r)/T_C(\infty) = T_N(r)/T_N(\infty) \approx 1 - (9h)/(4r). \tag{5.30}$$

Equation (5.30) becomes a pure geometrical equation and emphasizes the surface contribution to $T_C(r)$ function.

In light of Eqs. (5.19) and (5.28),

$$\sum_{i\leqslant 3} q_i(z_{ib}q_i^{-w} - 1) \approx -(\alpha_s + \alpha_i - 2). \tag{5.31}$$

Obviously, w is functions of materials and interface conditions. According to Eq. (5.31), $\sum_{i\leqslant 3} q_i(z_{ib}q_i^{-w} - 1) = 0.0421$ for the case of CoO epitaxial films on Fe_3O_4 substrates. With this value, $T_N(r)$ function of Eq. (5.19) is predicted to increase as r is reduced, which is qualitatively consistent with the experimental evidence.

In short, Eq (5.27) without any adjustable parameter can be utilized to predict dimension and interface effects on $T_C(r)$ or $T_N(r)$ function through introducing the parameter r_0 and α_r. When $0 < \alpha_r < 1, T_C(r)$ or $T_N(r)$ increases with decreasing r, while the contrary occurs when $\alpha_r > 1$, which is determined by both effects of surface and film/substrate interface with different interface interaction strengths. Furthermore, when Eq. (5.28) is reasonable, the adjustable parameters appearing in Eqs. (5.17)–(5.19) could be quantitatively determined and more exact physical meaning of these parameters may be found.

5.5.2 Thermal Stability in Exchange-biased FM/AFM Bilayers [22]

Exchange bias refers to a shift of hysteresis loop along a magnetic field axis, which can be observed in exchange interacting FM/AFM materials. Materials exhibiting the exchange bias and related effects have been proposed and utilized in applications, such as permanent magnet materials, high density recording media, domain stabilizers in recording heads, spin-valve devices and giant magnetoresistance (GMR) type devices. However, the microscopic origin of this effect is not well understood yet.

One important property of exchange bias is its thermal stability indicated by the blocking temperature T_{bl}, which is of concern for the design of magnetic heads and governs the choice of the biasing materials. At T_{bl}, the exchange bias field H_e, which is equal to the shift of the hysteresis loop, approaches zero. T_{bl} is a function of r. As r decreases, $T_{bl}(r)$ function decreases in bilayer systems. One empirical $T_{bl}(r)$ function based on the thermal fluctuation model for polycrystalline AFM films has been given as follows:

$$T_{bl}(r)/T_{bl}(\infty) = 1 - (\xi_1/r_g)^w \qquad (5.32)$$

where $\xi_1 = J_{int}/(4K_{AFM}ra_l)$ is the correlation length and J_{int} is the interface coupling exchange between the FM and AFM spins, K_{AFM} is the magnetic anisotropy constant, r_g and a_l are the grain size and the lattice constant of AFM, respectively. Equation (5.32) is valid for larger r_g values.

For an exchange-biased FM/AFM system comprising a thick FM layer with a thickness t_{FM} and an AFM layer with infinite thickness, $r_g \to \infty$, the magnitude of the exchange bias field at 0 K, $H_{e0}(\infty)$, is related to the FM/AFM interfacial energy, $E_0(\infty)$, where $H_{e0}(\infty) = E_0(\infty)/(M_{FM}t_{FM})$ [22]. In this relationship, M_{FM} is the fixed saturation magnetization of the FM layer because the effect of t_{FM} on H_e is here assumed to be constant. To estimate the value of $H_{e0}(\infty)$, two theoretical approaches have been pursued to determine the value of $E_0(\infty)$. On the basis of the idea of planar domain walls at a smooth FM/AFM interface, $E_0(\infty) = 2[A_{AFM}(\infty)K_{AFM}(\infty)]^{1/2}$, where $A_{AFM}(\infty) = 2J_{AFM}(\infty)s^2/a_l$ is the exchange stiffness, with J_{AFM} being the exchange integral and s the s-spin of AFM. Another theory argued that the assumption of an ideal interface was unrealistic, and the roughness of the interface leads to magnetic defects, which gives rise to local random fields. Therefore, $E_0(\infty)$ was determined by, $E_0(\infty) = 2z[A_{AFM}(\infty)K_{AFM}(\infty)]^{1/2}/\pi^2$, with z being a number of order unity. A common characteristic of both deductions is $E_0(\infty) \propto [J_{AFM}(\infty)s^2K_{AFM}(\infty)]^{1/2}$. According to this relationship and the mean field approximation, $J_{AFM}(\infty)s^2 \propto E_{exc,AFM}(\infty)$, and thus,

$$E_0(\infty) \propto [E_{exc,AFM(\infty)}K_{AFM}(\infty)]^{1/2}. \qquad (5.33)$$

where $E_{exc,AFM}(\infty)$ denotes the spin-spin exchange interaction on the sublattice of AFM.

It is understandable that with increasing T the thermal energy $E_{th}(T)$ is introduced to decrease the FM/AFM interfacial energy, namely, $E(T,\infty) = E_0(\infty) - E_{th}(T,\infty)$, where $E_{th}(T) = k_B T$ in light of the Einstein's relationship. At $T_{bl}(\infty)$, taking $E(T_{bl},\infty) = 0$ as reference, in terms of Eq. (5.33),

$$k_B T_{bl}(\infty) \propto [E_{exc,AFM}(\infty)K_{AFM}(\infty)]^{1/2}. \qquad (5.34)$$

If AFM nanocrystals have the same crystalline structure as the corresponding bulks, and the domain walls of the AFM layer are perpendicular to the FM/AFM interface, $T_{bl}(r)$ can be obtained as a generalization of Eq. (5.34),

i.e., $k_B T_{bl}(r) \propto [E_{exc,AFM}(r) K_{AFM}(r)]^{1/2}$. Combining this relationship and Eq. (5.34) brings out

$$T_{bl}(r)/T_{bl}(\infty) = \{[E_{exc,AFM}(r) K_{AFM}(r)]/[E_{exc,AFM}(\infty) K_{AFM}(\infty)]\}^{1/2}$$
(5.35)

where $K_{AFM}(r)/K_{AFM}(\infty) = E_{exc,AFM}(r)/E_{exc,AFM}(\infty)$ is assumed if the size dependence of $K_{AFM}(r)$ is mainly induced by $E_{exc}(r)$ for the coherent FM/AFM interface. Therefore, Eq. (5.35) can be rewritten as

$$T_{bl}(r)/T_{bl}(\infty) = E_{exc,AFM}(r)/E_{exc,AFM}(\infty). \qquad (5.36)$$

For coherent FM/AFM structures, $T_{bl}(r)$ function is dependent not only on the FM/AFM interface interaction strength but also on the AFM field. The former determines the magnitudes of $T_{bl}(\infty)$, and the latter the size dependence of the $T_{bl}(r)$ function. Since we consider only the relative difference of $T_{bl}(r)$ and $T_{bl}(\infty)$, while the value of $T_{bl}(\infty)$ is taken directly from experiments, the contribution of the FM/AFM interface interaction strength to $T_{bl}(\infty)$ is ignored. Based on this consideration and the mean-field approximation for AFM with sublattice magnetization, in terms of Eqs. (5.25) and (5.36),

$$T_{bl}(r)/T_{bl}(\infty) = \exp\{-2\Delta S_{vib}(\infty)/[3R(r/a_l - 1)]\}. \qquad (5.37)$$

The comparisons of $T_{bl}(r)$ functions between Eq. (5.37) and experimental data of Fe_3O_4/CoO, NiO/NiFe, CoNiO/NiFe, FeMn/NiFe, MnPt/CoFe and FeF_2/Fe bilayer systems are shown in Fig. 5.15(a) and (b), where $T_{bl}(r)$ functions decrease to 0 K as r is reduced from bulk to thin enough AFM layers (usually a few nanometers). Equation (5.37) agrees quantitatively with experimental evidence.
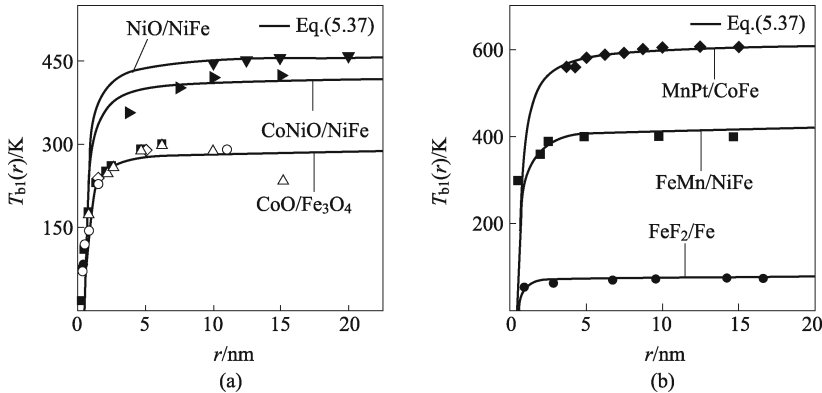
Fig. 5.15 Comparisons of $T_{bl}(r)$ functions between Eq. (5.37) and experimental evidence: (a) Fe_3O_4/CoO (■, ♦, ●, ▲, ○, △, ◇), NiO/NiFe (▼) and CoNiO/NiFe bilayers (▶); (b) FeMn/NiFe (■), MnPt/CoFe (♦) and FeF_2/Fe bilayers systems (●). The necessary parameters are listed in Table 5.3.

Table 5.3 Parameters utilized in calculations using Eq. (5.37) for the AFM materials. $T_{bl}(\infty)$ is in K, $\Delta S_{vib}(\infty)$ is in J·g-atom^{-1}·K^{-1}, r_0 and ξ_1 are in nm

	$T_{bl}(\infty)$	$\Delta S_{vib}(\infty)$[a]	$r_0 = a_l$[b]	ξ_l	δ
CoO	292	6.789	0.4260	1.8	1.20
NiO	463	7.271	0.4210	1.92	1.40
CoNiO	423	7.899	0.4235	2.17	1.65
FeMn	425	7.786	0.7140	1.00	1.60
MnPt	616	8.764	0.7736	2.48	1.62
FeF$_2$	79	5.724	0.9380	0.73	0.62

[a] For alloys AB, $\Delta S_{vib}(\infty) = [\Delta S_{A,vib}(\infty) + \Delta S_{B,vib}(\infty)]/2$, where A and B denote different metallic atoms, and $\Delta S_{vib}(\infty) = 7.493, 7.628, 9.584$ (J·g-atom^{-1}·K^{-1}) for Mn, Fe, Pt, respectively.

[b] $a_l = 0.426\,0, 0.421\,0, 0.376\,0, 0.357\,0, 0.386\,8$ and $0.469\,0$ (nm) for CoO, NiO, IrMn, FeMn, MnPt, and FeF$_2$, respectively. $r_0 = 0.211\,8$ nm for CoNiO is the mean value of CoO and NiO.

According to the definition of T_{b1}, it is natural to consider that T_{b1} should be (at least slightly) below T_N and should depend on the strength of FM/AFM interface exchange field. This results from the unidirectional exchange anisotropy and the spin-spin exchange interaction of AFM with sublattice magnetization. It is well known that $T_{b1}(r)$ corresponds to the situation at which the AFM spins follow the motion of the FM layer. Thus, $H_{eTb}(r) = 0$ because the unidirectional exchange anisotropy energy is less than E_0, where $H_{eTb}(r)$ denotes the exchange bias at $T_{b1}(r)$. This differs from the finite-size scaling of $T_N(r)$ of AFM in FM/AFM system, where J_{AFM} at the FM/AFM interface is enhanced, which results in increasing of $T_N(r)$ function with dropping r. Equation (5.37) also sheds light on the $H_{e0}(r)$ function in the following form:

$$H_{e0}(r)/H_{e0}(\infty) = T_{b1}(r)/T_{b1}(\infty) = \exp\{-2\Delta S_{vib}(\infty)/[3R(r/a_l - 1)]\} \tag{5.38}$$

where the effect of FM layers is set as an invariable. Both $H_{e0}(r)$ and $T_{bl}(r)$ functions have the same trend with dropping r. $H_{e0}(r)$ function of Eq. (5.38) is presented in Fig. 5.16. As shown in the figure, $H_{e0}(r)$ decreases with decreasing r. The results qualitatively correspond to available experimental evidence with large scatters. Note that since their $\Delta S_{vib}(\infty)$ values, in a size of R, are similar (although the substances are different), the curves based on Eq. (5.38) are almost the same.

Since there exists different degree of spin-spin interactions between the inner and surface atoms because of the reduction in the number of spin interactions at the AFM surface, the $E_{exc,AFM}(r)$ function decreases with dropping r. Thus, the decreasing $T_{bl}(r)$ and $H_{e0}(r)$ functions should be attributed to decreasing exchange interaction field of AFM layer with r because both $T_{b1}(r)$ and $H_{e0}(r)$ functions are influenced by AFM layers. As shown in Figs. 5.15 and 5.16, although the related compounds show different spin structures, for example, FeMn and MnPt have the non-collinear spin structure and the collinear spin structure, respectively, $T_{b1}(r)$ and $H_{e0}(r)$ in light of Eqs. (5.37) and (5.38) are still in agreement with experimental data, respectively.

Following the mathematical relation of $\exp(-x) \approx 1 - x$ when x is small
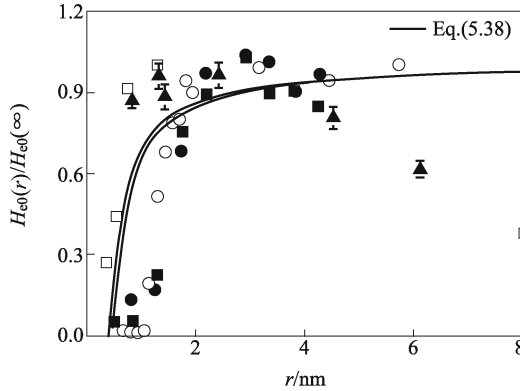
Fig. 5.16 Comparisons of $H_e(r)$ functions between Eq. (5.38) and available experimental results: CoO/Fe_3O_4 ($\square$ and $\blacktriangle$), IrMn/NiFe ($\circ$), FeMn/FeNi bilayers ($\blacksquare$ and $\bullet$).

enough, Eq. (5.37) can be simplified to

$$T_{bl}(r)/T_{bl}(\infty) \approx 1 - C/r \tag{5.39}$$

where $C = 2a_l\Delta S_{vib}(\infty)/(3R)$. Equation (5.39) indicates that the most important size effect on $T_{bl}(r)$ relates closely to A/V ratio or $1/r$ of AFM layer, when $r > 5a_l \approx 3.5 - 4$ nm. Comparing Eq. (5.39) with Eq. (5.32), w$(r) = \{\ln[2a_l\Delta S_{vib}(\infty)/(3R)] - \ln r\}/(\ln\xi_1 - \ln r)$. As $r \to \infty$, w$(\infty) = 1$. Thus,

$$\text{w}(r)/\text{w}(\infty) = \{\ln[2a_l\Delta S_{vib}(\infty)/(3R)] - \ln r\}/(\ln\xi_1 - \ln r). \tag{5.40}$$

It is known that w(r) in Eq. (5.32) depends on the non-universal value of the actual coupling strength in ultrathin films while w(r) function in Eq. (5.40) further indicates that this dependence is related to ξ_1 at the FM/AFM interface coming from the balance between the anisotropy energy of AFM and the FM-AFM spins exchange coupling energy, $\xi_1 \propto J_{int}/K_{AFM}$. In the mean-field theory, a similar relationship can be given as $\xi_0 \propto J_{int0}/K_{AFM0}$, with subscript "0" denoting the corresponding values of the mean-field approximation. As a result,

$$\xi_1/\xi_0 = (J_{int}K_{AFM0})/(J_{int0}K_{AFM}). \tag{5.41}$$

As $\xi_1 = 2a_l\Delta S_{vib}(\infty)/(3R)$ for $r > 5a_l$ where Eq. (5.39) is valid, w$(r) = 1$ in terms of Eq. (5.40), which corresponds to the w value of the mean-field theory and leads to $\xi_0 = 2a_l\Delta S_{vib}(\infty)/(3R)$ in terms of Eq. (5.32). With a good approximation, $\Delta S_{vib}(\infty) \approx R$ for compounds and metallic elements, and $a_l = \sqrt{2}h$ with h being the atomic diameter for face-centered cubic (fcc) structure, $\xi_0 \approx 2\sqrt{2}h/3$, which is related to the expected value of FM/AFM exchange interface thickness restricted to $h - 2h$. Note that ξ_0 is a little different for distinct crystalline structures of AFM due to different relationships between h and a_l, such as $h = \sqrt{2}a_l/2$ for NaCl structure

and $h = (2a_l^2 + c^2)^{1/2}/2$ for the body-centered tetragonal (bct) structure, respectively.

Obviously, the experimentally overestimated J_{int} value in comparison with J_{int0} results in $\xi_1 > \xi_0$ according to Eq. (5.41) while J_{int} is strongly affected by experimental conditions. In light of the ξ_1 values of CoO, NiO, CoNiO, IrMn, FeMn and MnPt, w(r) function determined by Eq. (5.40) generally increases with decreasing r, which is shown in Fig. 5.17.
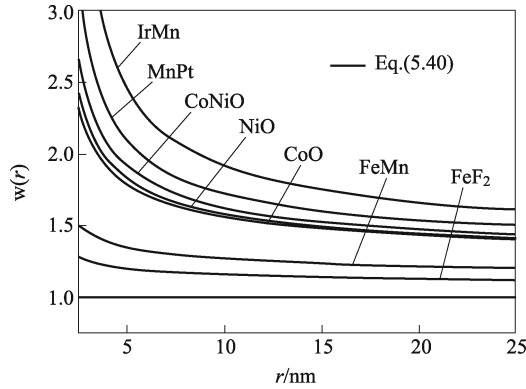
Fig. 5.17   Shift exponent w(r) function in terms of Eq. (5.40) for CoO, NiO, CoNiO, IrMn, FeMn, MnPt and FeF$_2$ FM/AFM bilayers. The used parameters in Eq. (5.40) are listed in Table 5.3.

If J_{int} value is derived from the Heisenberg model, where the spin-spin exchange coupling in thin films is assumed to be uniform throughout the films, $J_{int} > J_{int0}, \xi_1 > \xi_0$ and w > 1 are also obtained since the exchange coupling near surfaces of thin films in mean-field approximation is expected to be weaker than that in the bulk. Nevertheless, for AFM materials with much higher anisotropy, such as FeF$_2$, ξ_1 is predominantly determined by K_{AFM}, and the effect of J_{int} is negligible. Thus, $\xi_1 \approx \xi_0$ in terms of Eq. (5.41) with $J_{int}/K_{AFM} \approx J_{int0}/K_{AFM0}$, and w($r$) ≈ 1 with a much weak apparent size dependence in light of Eq. (5.40).

If $\xi_1 = \xi_0 = 2a_l\Delta S_{vib}(\infty)/(3R)$ and w = 1 in Eq. (5.32), Eq. (5.32) is the same as Eq. (5.40), in which the parameters are definitely physical in describing all $T_{bl}(r)$ functions in the exchange-biased FM/AFM bilayers although Eqs. (5.32) and (5.40) are only valid for thicker film limit. As $r \rightarrow h/2$, Eq. (5.37) is more suitable for predicting $T_{bl}(r)$ function since when r is comparable with $h/2$, energetic changes of internal atoms in AFM materials also contribute to T_{bl}.

In light of the analysis above, the size-dependent phase and thermal stabilities for low dimensional FM and AFM nanocrystals and FM/AFM systems are still related with $1/r$, which suggests a progressively increasing role of the surface layer with decreasing r. As a key thermodynamic quantity, $\Delta S_{vib}(\infty)$

determines the atomic vibration and the interaction strength among atoms. This brings out an interesting result that the phase and thermal stabilities of FM and AFM nanocrystals are also related to the natural properties of substances: ΔS_{vib}, size of nanocrystals, and the corresponding bulk values that embody most properties of materials.

5.5.3 Ferroelectric Phase Transition of Nanocrystals [22]

Ferroelectric (FE) crystals are characterized by a displacement of ions from their centrosymmetric positions. This displacement leads to a net dipole moment of the unit cell and to a spontaneous static polarization. With increasing T this polarization decreases until, at the ferroelectric phase-transition temperature, T_{ce}, the crystal undergoes a phase transition from the polarized ferroelectric phase to the nonpolarized paraelectric phase.

Since its discovery in 1920 by Valasek, ferroelectricity has attracted considerable interest from a fundamental point of view due to its wide range of potential applications. In view of the sustained trend towards further miniaturization of microelectronic devices, investigations of the scaling effects in ferroelectrics acquire great practical importance. For such cooperative phenomena, a different degree of ordering is expected to occur near surface or interface, leading to an intrinsic dependence on r.

The surface spontaneous polarization temperature of free nanocrystals is lower than that of the bulk, or $T_{ce}(r) < T_{ce}(\infty)$. However, some recent experiments demonstrated that substrates impart mechanically on ultrathin epitaxial thin films, and may affect their phase transition characteristics and the order of the transition. This is induced by the elastic interaction with the transition strain, which may assist or obstruct the transition, and thus raise or lower the $T_{ce}(r)$ value accordingly. The mechanisms of the concerned phenomena may be regarded as interface effect.

The Landau phenomenological theory and the transverse Ising models have been used to develop the surface and size effects of ferroelectrics. The former has been more fruitful, in which the free energy expansion coefficients are assumed to be size-independent, and the extrapolation length δ' is introduced to qualitatively illustrate the difference between the surface and the interior. When $\delta' > 0$, polarization is reduced at the surface and $T_{ce}(r) < T_{ce}(\infty)$. When $\delta' < 0$, polarization is enhanced at the surface and $T_{ce}(r) > T_{ce}(\infty)$. However, the existence of several adjustable parameters in the related models leads to the hard understanding of the physical natures. In the transverse Ising model, two-spin interaction constant and tunneling frequency are modified near the surface, which consequently results in the size dependence of ferroelectric properties. In this model, only the decreased $T_{ce}(r)$ functions with r have been predicted where the interface effect and dimension dependence are neglected, such as the difference of $T_{ce}(r)$ functions

of thin films, nanowires or nanorods, and nanoparticles. In fact, the both effects on $T_{ce}(r)$ functions still remain open. Recently, Sun et al. and Yang et al. have obtained $T_{ce}(r)$ functions by combining the BOLS correlation mechanism and the size-dependent cohesive energy with the Ising premise, respectively, which are of the same forms of Eqs. (5.19) and (5.20). Besides, as an empirical $1/r$ relation,

$$T_{ce}(r)/T_{ce}(\infty) = 1 - A'/r \qquad (5.42)$$

is widely pursued, where A' is a material constant. In addition, based on the model for $T_m(r)$, $T_{ce}(r)$ equation of the perovskite ferroelectric nanocrystals with a first-order transition has been given by

$$T_{ce}(r)/T_{ce}(\infty) = \exp\{-[2\Delta S_{ce}/(3R)]/[r/r_0 - 1]\}, \qquad (5.43)$$

where ΔS_{ce} denotes the transition entropy, r_0 is the critical particle size where the ferroelectric phase cannot exist or the Curie transition is absent.

From a fundamental point of view, the displacive ferroelectric materials characterized by macroscopic spontaneous polarizations P_s are caused by atomic off-center displacement, which results from a delicate balance between long-range Coulomb interaction and short-range covalent interaction. It is well known that the ferroelectric properties in low dimensions are mainly determined by the truncation of Coulomb interaction, which affects the dipoles located both at surfaces and inside the materials and results in the alteration of P_s. As a particular case of tetragonal phase, P_s being normal to the surface ($P_x = P_y = 0, P_z = P_s \neq 0$, where the subscripts denote the polarization axis directions) is expected to be stable and the largest, which is typically the desired polarization direction in devices.

It is worth emphasizing that the termination of the lattice periodicity in the surface normal has two effects. One is the reduction of *CN* of surface atoms and the other is the creation of a surface potential barrier. Both bring out a large number of physical quantities, such as $\sigma^2(r)$, $\Theta_D^2(r)$, $E_{exc}(r)$, and $P_s(r)$, and at the surfaces differ from their interior counterparts. Now suppose that there exists a surface layer on a nanocrystal with a size r, in which the surface spontaneous polarization $P_{ss}(r)$ differs from the interior one $P_{sv}(r)$. Following a similar deduction for the size dependent function of atomic thermal vibrations of nanocrystals in Chapter 3, one can obtain

$$P_s(r)/P_s(\infty) = \exp[(\alpha_r - 1)/(r/r_0 - 1)] \qquad (5.44)$$

where r_0 is determined by Eq. (3.79), in which h denotes the critical size of basic structural unit required for ferroelectric activity at which $P_s = 0$.

For freestanding perovskite ferroelectric nanosolids, α_r is determined as

$$\alpha_r = 1 - \Delta S_{ce}(\infty)/(3R) \qquad (5.45)$$

The coupling effect between the mechanical deformation or strain ς and P_s in the ferroelectric materials can be described via the electrostrictive coefficient

Q_{ij}, namely, $\varsigma = Q_{12}P_s^2$. For thin films eptiaxially grown on substrates, P_{si} at the interface can be expressed as $Q_{12}P_{si}^2 = Q_{12}P_{sv}^2 + \varsigma_i$, with $\varsigma_i = (a'_{lt} - a_{lt})/a_{lt}$ and $Q_{12}P_{si}^2 \approx -|a_{ls} - a_{lc}|/a_{ls}$, where $a'_{lt} = a_{lt}\{\beta(a_{ls} - a)/[3a_{ls}(s_{11} + s_{12})] + 1\}$ is the lattice constant of the tetragonal phase of the film under the stress $\sigma = (a_{ls} - a_{lc})/[a_{ls}(s_{11} + s_{12})]$, where a_{lt} and a_{lc} are, respectively, the lattice constants of tetragonal and cubic phase of ferroelectrics, β is the compressibility, a_{ls} is the lattice constant of the substrate, s_{11} and s_{12} are the elastic compliance constants. If some interface relaxation takes place, the real substrate lattice parameter a_{ls} should be replaced by the effective substrate lattice parameter a_{ls}^*. Based on the above relationships, in terms of the definition of α, let subscript "i" denote this interface, the corresponding $\alpha_i = P_{si}/P_{sv}$, namely,

$$\alpha_i = \{1 - [(a'_{lt} - a_{lt})/a_{lt}]/[-|a_{ls} - a_{lc}|/a_{ls}]\}^{-1/2}. \tag{5.46}$$

It should be noted that Eq. (5.46) has neglected the contribution of the strain gradients, which may be important in proper ferroelastics, and the coupling between these gradients and polarization.

Based on the effective field theory developed to describe the lattice dynamics of ferroelectric systems, $T_{ce}(\infty) = k'P_s^2(\infty)$ with $k' = \rho'V_x(\Sigma_b\gamma_b/\lambda_s)/k_B$ where ρ' is the parameter relating T_{ce} to ionic polarization $P_{ion}(\infty)$, V_x is the volume of a primitive cell in the crystal lattice, γ_b is a Lorentz-field tensor, $\lambda_s = P_s^2(\infty)/P_{ion}^2(\infty)$. This relationship is valid over a wide range of materials. From a simple physical consideration, this simple relationship between experiments and theories may be interpreted as equivalence between the lattice vibrational energy and the displacive energy of the ferroelectric state. Note that here the influence of depolarizing field is neglected because the remnant surface charge near the critical point is so small that the influence of the relevant depolarizing field becomes a secondary factor for the structural instability. If this relationship may be generalized for the corresponding size-dependent function, $T_{ce}(r)/T_{ce}(\infty) = P_s^2(r)/P_s^2(\infty)$. In terms of Eq. (5.44), $T_{ce}(r)$ is established as

$$T_{ce}(r)/T_{ce}(\infty) = P_s^2(r)/P_s^2(\infty) = \exp[2(\alpha_r - 1)/(r/r_0 - 1)]. \tag{5.47}$$

The existence of a free surface and substrate constraint destroy the macroscopic symmetry of the system and can significantly affect $T_{ce}(r)$. Under the assumption that the surface and interface effects on $T_{ce}(r)$ are additive,

$$\begin{aligned} T_{ce}(r)/T_{ce}(\infty) &= P_s^2(r)/P_s^2(\infty) \\ &= \{\exp[2(\alpha_s - 1)/(r/r_0 - 1)] \\ &\quad + \exp[2(\alpha_i - 1)/(r/r_0 - 1)]\}/2. \end{aligned} \tag{5.48}$$

According to Eq. (5.48), $P_s(r)$ function (solid line) of $SrRuO_3/BaTiO_3/SrRuO_3$ capacitors is shown in Fig. 5.18 and good agreement between Eq. (5.48) and available experimental measurements is found, which sharply

deviates from that of free $BaTiO_3$ films (dash line). This indicates that $SrRuO_3/BaTiO_3$ interface not only results in smaller critical size, but also takes different roles in impacting on the ferroelectric stability of films in comparison with that of free films.

Figure 5.19 shows the $T_{ce}(r)$ functions of the freestanding $PbTiO_3$ nanocrystals according to Eq. (5.48). The main effect of a free surface is to alter the environment of surrounding polarizable groups of atoms. This can result in the loss of translational invariance of the structure, and the modifications of the phonon spectrum and soft modes, as well as dipole-dipole interaction. Therefore, it is reasonable to assume the existence of surface layer of ferroelectric crystals in which the spontaneous polarization is lower than that of interior, thus the suppression of $T_{ce}(r)$ is present. Similar to $T_C(r)$ functions of FM nanocrystals, as r is reduced, the change strength of $T_{ce}(r)$ functions follows the order of thin films, nanorods, and nanoparticles due to different ξ or d values in Eq. (3.79).
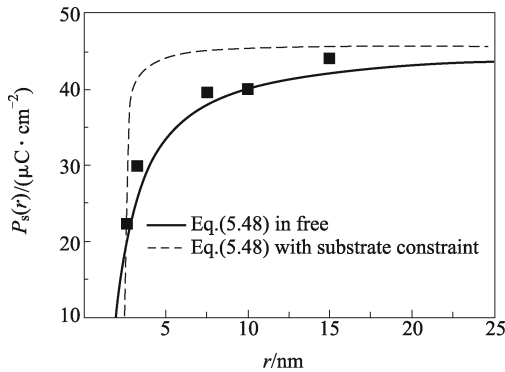
Fig. 5.18 Comparisons of $P_s(r)$ function of $BaTiO_3$ thin films between Eq. (5.48) (solid line) and available experimental results of $SrRuO_3/BaTiO_3/SrRuO_3$ (■). The necessary parameters are $\alpha_i \approx 0$ according to Eq. (5.46) since both $SrRuO_3$ and $BaTiO_3$ have the approximately same lattice constants, $r_0 = (2h)/2 = 2.4$ nm with $d = 2$, $P_s(\infty) = 46$ μC·cm^{-2}. The dash line denotes $P_s(r)$ function of the free $BaTiO_3$ thin films, where $\alpha_s = 0.992$ in terms of Eq. (5.45) with $\Delta S_{ce}(\infty) = 0.1$ J·g-atom^{-1}·K^{-1}.

The comparisons between the predicted $T_{ce}(r)$ functions in terms of Eq. (5.48) (solid line) and experimental evidence of $BaTiO_3$ and $PbTiO_3$ epitaxial grown thin films on different substrates are shown in Fig. 5.20. Equation (5.48) corresponds well to available experimental results. As shown in Fig. 5.20, the tensile stress induced by the positive misfit strain ε_i at coherent ferroelectrics/substrate interface will also result in the decrease of $T_{ce}(r)$ with r. Although this coherent interface brings out the disappearance of a free surface of the films, the tensile stress still constrains the ferroelectricity. Comparing with $T_{ce}(r)$ function of the freestanding thin films with two free surfaces, this
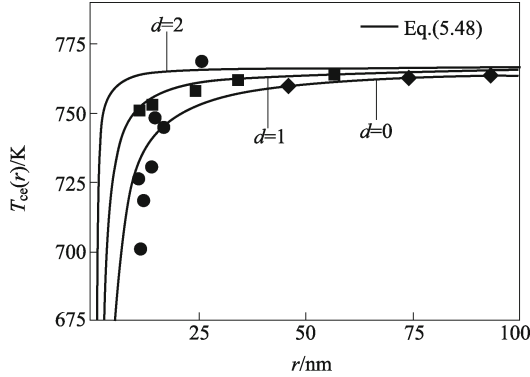
Fig. 5.19 Comparisons of $T_{ce}(r)$ functions between Eq. (5.48) (solid lines) and experimental evidence ($\blacklozenge$, $\bullet$, $\blacksquare$) for PbTiO$_3$ free nanocrystals. The necessary parameters are as follows: $T_{ce}(\infty) = 769$ K is the average value of the corresponding experiments, $\alpha_s = 0.963$ in terms of Eq. (5.45) with $\Delta S_{ce} = 0.46$ J·g-atom^{-1}·K^{-1}, r_0 = 0.79, 1.59 and 2.38 (nm) in terms of Eq. (3.79) with $d = 2$, 1 and 0, respectively, and $h \approx 0.8$ nm.

decrease of $T_{ce}(r)$ may be sharper or slighter, depending on the magnitude of misfit strain. As $\varepsilon_i > \varepsilon_v > 0$, the decrease of $T_{ce}(r)$ of epitaxial grown thin films is bigger as shown in Fig. 5.20(a); while $0 < \varepsilon_i < \varepsilon_v$, the related drop of $T_{ce}(r)$ is weaker as shown in Fig. 5.20(b). This implies that when a tensile stress is applied, the ferroelectricity can be stabilized only in thicker films.

Because of the electrostrictive coupling between lattice strain and polarization in ferroelectrics, the deformation of the lattice along the a_{lt} and c_{lt} tetragonal directions is proportional to P_s^2. Therefore, the tetragonal distortion η can be written, with good approximation, as $\eta_t(\infty) = (c_{lt} - a_{lt})/a_{lt} = (Q_{11} - Q_{12})P_s^2(\infty)$. If this relationship can be extended to nanometer size, in the light of Eq. (5.48), there is

$$\eta_t(r)/\eta_t(\infty) = P_s^2(r)/P_s^2(\infty) = T_{ce}(r)/T_{ce}(\infty) \qquad (5.49)$$

which is obtained via assuming that $Q_{11} - Q_{12}$ is size-independent. $\eta_t(r)$, $P_s^2(r)$ and $T_{ce}(r)$ have the same trends as the dropping r.

Since the low-dimensional ferroelectric materials are particularly prone to processing-induced defects, which include microstructural heterogeneities, variations in crystalline quality, and mechanical stresses imposed on the materials by the substrates, the values of parameters in Eq. (5.48) are taken from the corresponding experimental values for better correspondences.

Taking again the relation of $\exp(x) \approx 1 + x$ with small x, Eq. (5.42) in fact has the same form as that of Eq. (5.47), namely, $T_{ce}(r)/T_{ce}(\infty) \approx 1 + 2(\alpha_r - 1)r_0/r$, which indicates that the most important size effect is still related with $1/r$.

On the other hand, P_s at the surface and the interface is introduced through α_r in Eq. (5.47). When $\alpha_r < 1, T_{ce}(r)$ increases with decreasing r,
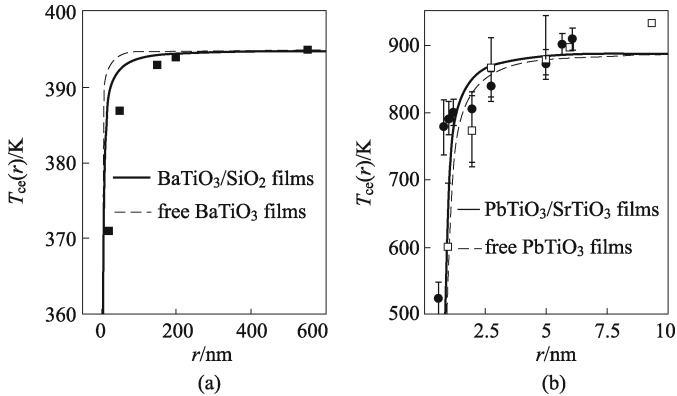
Fig. 5.20 Comparisons of $T_{ce}(r)$ functions between Eq. (5.48) for BaTiO$_3$ and PbTiO$_3$ thin films epitaxially grown on different substrates (solid line) and experimental results. The dash lines are for the freestanding BaTiO$_3$ and PbTiO$_3$ thin films, respectively. (a) For BaTiO$_3$/SiO$_2$ (■) system with $T_{ce}(\infty) = 395$ K, the parameters: $\alpha_i = 0.876\,6$ for BaTiO$_3$/SiO$_2$ interface in terms of Eq. (5.46) with $a_{ls} = 0.417\,9$ nm of SiO$_2$, respectively, and $\beta = 5.1 \times 10^{-3}$ GPa^{-1}, $a_l = 0.400\,96$ nm and $a_{lt} = 0.400\,51$ nm, $s_{11} + s_{12} = 5.62 \times 10^{-12}$ m^2·N^{-1}·$r_0 = 2.41$ nm in terms of Eq. (3.79) with $d = 2$. (b) For PbTiO$_3$/SrTiO$_3$ epitaxial thin films (□ and ●), where $\alpha_s = 0.892$ in terms of Eq. (5.45), $\alpha_i = 0.983\,8$ in terms of Eq. (5.46) with $a_{ls} = 0.390\,5$ nm of SrTiO$_3$, and $\beta = 4.9 \times 10^{-3}$ GPa^{-1} $a_{lc} = 0.390\,5$ nm and $a_{lt} = 0.389\,9$ nm, $s_{11} + s_{12} = 5.5 \times 10^{-12}$ m^2·N^{-1}, $r_0 = 0.792$ nm in terms of Eq. (3.79) with $d = 2$, $T_{ce}(\infty) = 895$ K is the average value of the corresponding experiments. The other parameters are the same as those in Fig. 5.19.

while contrary when $\alpha_r > 1$. Although complicated, the size dependence of $T_{ce}(r)$ can also be analyzed by Eq. (5.48) as long as the surface or interface conditions of the nanocrystals and relative thermodynamic parameters are clear.

5.5.4   Superconductive Phase Transition of Nanocrystals

The BCS theory had played an important role in understanding the role of the electron-phonon interaction in normal and superconducting metals and compounds. According to BCS theory of superconductivity, T_{cs} depends on the electron-phonon interaction of superconducting metals and compounds. In light of McMillan, $T_{cs}(\infty) = [\Theta_D(\infty)/1.45] \times \exp\{-1.04(1 + J_{ep})/[\phi - \mu^*(1+0.62J_{ep})]\}$, where J_{ep} and μ^* are the electron-phonon coupling constant and the Coulomb pseudopotential of Morel and Anderson, respectively. If $\mu^* \ll J_{ep}$, this relationship can be approximated as

$$T_{cs}(\infty) \propto \Theta_D(\infty). \tag{5.50}$$

It is assumed that $T_{cs}(r)$ has the same size dependence of $\Theta_D(r)$, or

$$T_{cs}(r)/T_{cs}(\infty) = \Theta_D(r)/\Theta_D(\infty). \qquad (5.51)$$

Substituting Eq. (3.80) into Eq. (5.51) leads to

$$T_{cs}(r)/T_{cs}(\infty) = \exp[-[(\alpha_r - 1)/2]/(r/r_0 - 1)] \qquad (5.52)$$

where α_r is determined by Eq. (3.84) for free nanocrystals. For metallic nanosolids with oxide at the surface, such as Al, because the metal-oxygen bonding is stronger than metal-metal bonding, $\alpha_r < 1$ according to the definition of $\alpha_r = \sigma_s^2(r)/\sigma_v^2(r)$. Under the assumption that the bond strength ε is reversely proportional to σ^2, namely, $\sigma_s^2(r) \propto 1/\varepsilon_s$ and $\sigma_v^2(r) \propto 1/\varepsilon_v$, α_r in this case is taken as

$$\alpha_r = \varepsilon_v/\varepsilon_s. \qquad (5.53)$$

Equation (5.52) and experimental results of Pb thin films are shown in Fig. 5.21 and $T_{cs}(r)$ decreases as r drops where good correspondence within the experimental error range is observed. Once $r \to t_0$ where t_0 is the critical size at which the superconductivity vanished and t_0 can be determined in terms of Kubo formula, $T_{cs}(r)$ functions decrease dramatically although t_0 does not appear in Eq. (5.52). Note that since Pb thin films may refer to finely granular structures with high densities of inner surfaces/grain boundaries and cannot be described by a continuous film, this granular structure is similar to a random structure of a chain polymer modelled by a trajectory of a self-avoiding walk with a fractal dimension of $d' = (2+d)/3$. For thin films, since $d = 2$, $d' = 4/3$ in terms of the above equation.

In Figs. 5.21 and 5.22, $T_{cs}(r)$ functions of nanoparticles are also predicted in terms of Eq. (5.52) by introducing dimension-dependent r_0 values determined by Eq. (3.79), where Eq. (5.52) corresponds to experimental evidence. This extension in crystal shape from films to particles or rods is valid only when the crystal has a continuous, rather than discrete, electron spectrum, which, however, may be questionable for nanoparticles since their discreteness of the electron spectrum changes the effective electron density states and coupling strength. The deviations between Eq. (5.52) and experimental evidence shown in Figs. 5.21 and 5.22 may indeed be attributed to this effect. Nevertheless, since superconductive thin films and nanoparticles have the similar forms of the external field dependence of E_b, and if their surface atoms are assumed to have the same vibrational mode, the mechanisms of the superconducting transition of thin films could qualitatively be utilized for nanoparticles without big error.

The comparisons of enhanced $T_{cs}(r)$ functions between Eq. (5.52) and experimental evidence for Al thin films and nanoparticles are shown in Fig. 5.22 where α_r is determined by Eq. (5.53). Equation (5.52) is roughly in agreement with experimental results in experimental error range. This enhancement of $T_{cs}(r)$ is induced by existing alumina on the surface of Al nanosolids with
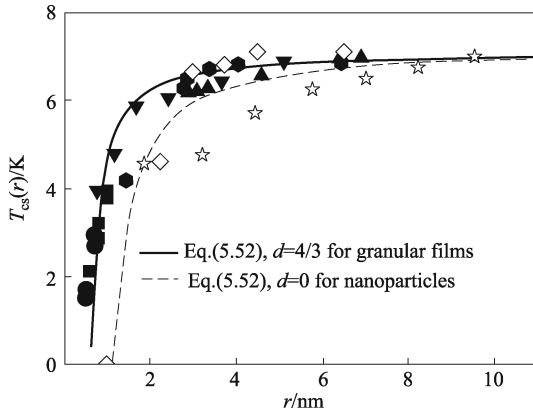
Fig. 5.21 Comparisons of $T_{cs}(r)$ functions between Eq. (5.52) and experimental results for Pb nanoparticles ($\diamond$, $\star$) and films ($\blacktriangle$, $\bullet$, $\blacktriangledown$, $\blacksquare$, $\hexagon$). The necessary parameters are: $T_{cs}(\infty) = 7.2$ K, $r_0 = 0.65$, 1.17 nm in terms of Eq. (3.79) with $d = 4/3$ and $d = 0$ for granular films and nanoparticles, respectively, and $h = 0.3900$ nm, $\alpha_r = 1.6406$ in terms of Eq. (3.84) with $\Delta S_{vib} = \Delta S_m = 7.99$ J·mol^{-1}·K^{-1}.
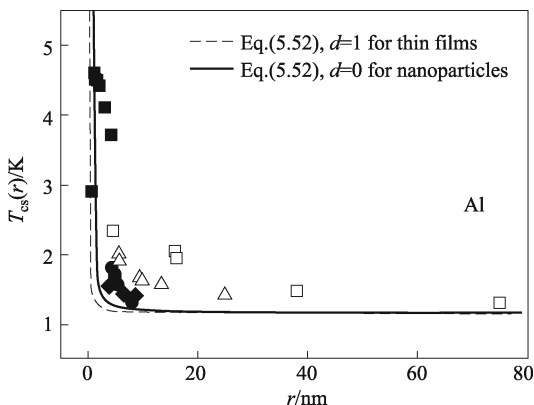
Fig. 5.22   Comparisons of $T_{cs}(r)$ of Al nanoparticles (solid line) and thin films (dash line) between Eq. (5.52) and experimental measurements ($\blacksquare$ and $\blacklozenge$, $\bullet$ for nanoparticles, $\square$, $\triangle$ for thin films). The parameters in Eq. (5.52) are: $T_{cs}(\infty) = 1.175$ K, $r_0 = 0.9498$ nm or 0.3166 nm in terms of Eq. (3.79) for nanoparticles with $d = 0$ or for thin films with $d = 2$ where $h = 0.3166$ nm. $\alpha_r = 0.3636$ in terms of Eq. (5.53) with $\varepsilon_{Al-Al} = \varepsilon_v = 186.2$ kJ·mol^{-1} and $\varepsilon_{Al-O} = \varepsilon_s = 512.1$ kJ·mol^{-1}.

Al–O bonding, which leads to the vibrational suppression of surface Al atoms and thus $\alpha_r < 1$.

For nanosolids, not only the electronic properties but also the phonon spectrum will certainly be influenced by size. Because of the favorable surface/volume ratio in nanosolids, also possible electron-electron interaction will be affected via surface phonons. The two parameters Θ_D and σ describ-

ing the vibrational lattices or atoms are useful in determining the role of phonons in its superconducting mechanism. In light of modern field theory, an electron will have a self-energy in this vibrational field since it produces a lattice deformation that in turn reacts on the electron, which can be considered as the attractive interaction among the electrons. The interaction brings out energy lowering of systems below E_b, where these electrons are in long-range order, namely, in superconducting state. As shown in the figures, the complicated $T_{cs}(r)$ functions for nanocrystals can be described in a simple and unified form with related thermodynamic parameters.

It is worth emphasizing that the above nanothermodynamics functions predict the relative difference of nanocrystals and bulk counterparts, while most of the properties of the materials have been embodied in bulk properties. Thus, the modelling could be realized in a simple and unified form. However, since thermodynamics can only describe statistical behavior of large number of molecules, this top-down method cannot be utilized to depict the action of clusters with only a few molecules or atoms. Once r decreases to r_0, quantum effect is important, which results in the disability of this method. In addition, if the structure of nanocrystals differs from that of the corresponding bulk, where the electronic distribution varies, the above equations are also invalid since we assume that the crystalline structure is remained.

References

1   Hsieh J S. Principles of Thermodynamics. Scripta Book Company, (1975)

2   http://en.wikipedia.org/wiki/phase_transition. Accessed 26 August 2009

3   Souza J A, Yu Y D, Neumeier J J, Terashita H, Jardim R F. Method for analyzing second-order phase transitions: Application to the ferromagnetic transition of a polaronic system. Phys. Rev. Lett., **94**, 207209 (2005)

4   http://www.springerlink.com/content/gh89q45726683247/fulltext.pdf. Accessed 15 September 2009

5   http://grothserver.princeton.edu/~groth/phys301f02/lect25.pdf. Accessed 18 September 2009

6   http://www.hermetic.ch/compsci/thesis/chap1.htm. Accessed 9 October 2009

7   Binney J J, Dowrick N J, Fisher A J, Newman M E J. The Theory of Critical Phenomena: An Introduction to the Renormalization Group. Oxford Science Publications, USA (1992)

8   http://en.wikipedia.org/wiki/critical_exponent. Accessed 12 October 2009

9   http://web.edu.ioffe.ru/register/?doc=statphys/phasetr.tex. Accessed 17 October 2009

10   Palumbo M. Thermodynamics of martensitic transitions in the framework of the CALPHAD approach. Calphad., **32**, 693-708 (2008) and references thererin

11   Bhadeshia H K D H. Bainite in Steels. 2nd Edition. The Institute of Materials, (2001)

12   Zallen R. The Physics of Amorphous Solids. John Wiley & Sons, New York (1983) and references therein

13   Torquato S. Hard knock for thermodynamics. Nature, **405**, 521-523 (2000)

14   Santen L, Krauth W. Absence of thermodynamic phase transition in a model glass former. Nature, **405**, 550-551 (2000)

15   Gibbs J H, DiMarzio E A. Nature of the glass transition and the glassy state. J. Chem. Phys., 28, 373-383 (1958)

16   Turnbull D, Cohen M H. Free-volume model of the amorphous phase: Glass transition. J. Chem. Phys., 34, 120-125 (1961)

17   Turnbull D, Cohen M H. On the free-volume model of the liquid-glass transition. J. Chem. Phys., 52, 3038-3041 (1970)

18   Kauzmann W. The nature of the glassy state and the behavior of liquids at low temperatures. Chem. Rev., 43, 219-256 (1948)

19   Jiang Q, Yang C C. Size effect on the phase stability of nanostructures. Curr. Nanosci., **4**, 179-200 (2008) and references therein

20   Jiang Q, Lang X Y. Glass transition of low-dimensional polystyrene. Macromol. Rapid Comm., **25**, 825-828 (2004)

21   Ao Z M, Jiang Q. Size effects on miscibility and glass transition temperature of binary polymer blend films. Langmuir, **22**, 1241-1246 (2006)

22   Lang X Y, Jiang Q. Size dependence of phase transition temperatures of ferromagnetic, ferroelectric and superconductive nanocrystals. Front. Phys. China, **2**, 289-311 (2007) and references therein

23   Fisher M E, Barber M N. Scaling theory for finite-size effects in the critical region. Phys. Rev. Lett., **28**, 1516-1519 (1972)

24   Ambrose T, Chien C L. Finite-size effects and uncompensated magnetization in thin antiferromagnetic CoO layers. Phys. Rev. Lett., **76**, 1743-1746 (1996)

Chapter 6   Thermodynamics of Interfaces

In this chapter, one important application field of thermodynamics in recent years, the thermodynamics of interfaces, is introduced. The bulk and size-dependent interface energy values, which include interface energy of solid-vapor, liquid-vapor, and solid-solid, are considered. Another important related phenomenon, interface stress, is also described and quantitatively modeled. Based on these quantitative results, several typical surface phenomena, such as crystal growth, surface reconstruction, adsorption, and surface phase transition, are analyzed. These results could benefit us to understand and utilize the interfaces or crystalline defects as tools for better materials properties. Also, the given data may promote the development of nanotechnology due to the large surface/volume ratio of nanomaterials.

If a perfect crystal could be obtained, atoms would only exist on lattice sites, every lattice site would be occupied by one atom, each atom would have its full quota of electrons in the lowest energy levels, and the atoms would be stationary. However, as an example, experimentally it has been found that there is discrepancy between the stress theoretically needed to deform a perfect crystal plastically and the actual stress measured on ordinary crystals. The latter is much lower than the former, which denotes that the atomic structures of the most crystalline materials are not perfect: The regular pattern of atomic arrangement is interrupted by crystalline defects. This is also the case of the electric conduction. Nowadays, using various electronic microscopes, the existance of different defects in crystalline structures has been confirmed and observed. The detailed messages about them are known.

There are many types of defects in crystals and all defects are of great importance to the materials scientists as they affect properties of materials in different ways. Defects are classified according to their dimension d. In ascending order of d, they are point defects (vacancies with $d = 0$), line defects (dislocations with $d = 1$), and planar defects (interfaces and surfaces (solid-vapor interface) with $d = 2$). Defects may also be classed as intrinsic defects, when they occur in an otherwise perfect substance; or they may be termed extrinsic defects, when they derive from the presence of impurities. The vacancy is a thermodynamic stable defect, which results in the decrease of Gibbs free energy and thus exists certainly in crystals. Planar defects are unavoidable since any material has a certain size with a boundary. As a result, although we could drop the amount of defects in crystalline structures, such

as rods of single crystals in a diameter of 450 mm, being the case in silicon industry, the essesntial decreases are dislocations and grain boundaries. Since the most progressive fields in materials science and nanotechnology now are related interfaces, we in this chapter will consider the thermodynamics of interfaces at full length.

6.1 Point Defect Thermodynamics [1, 2]

Point defects are defects which are not extended in space in any dimension. At $T > 0$ K, the atoms in a solid are subject to thermal vibrations where they continuously vibrate in their equilibrium positions in the lattice with average amplitude of vibration that increases with increasing T. At a given T, there is always a wide spectrum of vibration amplitudes due to the energetic fluctuations. Thus, the vibrations occasionally in a localized region may be so intense that an atom is displaced from its lattice site and a vacancy is formed. The displaced atom can move either into an interstice, in which it is called a self-interstitial, or on to a surface lattice site. The vacancy self-interstitial is known as a Frenkel defect and the simple vacancy itself as a Schottky defect (Fig. 6.1).

(a)   (b)
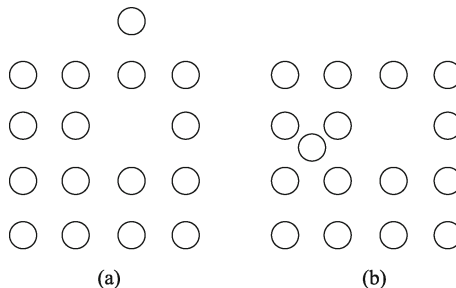
Fig. 6.1 The formation of a Schottky defect (a) and a Frenkel defect (b)

Consider a fixed volume of crystal and let n vacancies be distributed over N lattice sites. The vacancies can take up many different possible positions in the crystal, which leads to configurational entropy associated with their distributions. The vacancies thus not only increase the degree of disorder of the crystal, but also raise the entropy, which favours decrease in free energy. The total number of arrangements of the n vacancies is given $N!/(N-n)!$. However, vacancies are indistinguishable from one another: We cannot differentiate between vacancies i and j on a given site. There are n indistinguishable ways of obtaining the first vacancy, $(n-1)$ ways of obtaining the second, $(n-2)$ ways of obtaining the third, and so on, and in all $n!$. As a result, the total number of arrangements, or probability Ω of the system, is $\Omega =$

$N!/[(N-n)!n!]$. Using relationship of Eq. (2.4) and Stirling's approximation for factorials, we obtain

$$\Delta S = k \ln \Omega = k \ln\{N!/[(N-n)!n!]\}.$$

On the other hand, the introduction of defects into a perfect solid requires an expenditure of energy on the system. If the defects are truly isolated from each other, then the internal energy should just be proportional to the number of defects. Let Δu represent the internal energy change for the formation of a single defect; then $\Delta G = n\Delta u + \Delta(PV) - T\Delta S \approx n\Delta u - T\Delta S$ for the formation of the n vacancies. Positive Δu is related to an increase in the internal energy of the crystal. The relative contributions of two terms, ΔU and ΔS, to ΔG of the crystal given as a function of n are shown in Fig. 6.2 where c_e is the equilibrium concentration, ΔU is molar vacancy formation energy.

We can see that as n increases, ΔG falls to a minimum with $n = n_e$ and then increases where n_e is the equibrium number of vacancies. In equilibrium, $(\partial\Delta G/\partial n)_T = 0$, there is $\Delta u - kT \ln[(N-n_e)/n_e] = 0$. If we assume that N is very large, then $n << N$ and the above equation rearranges to

$$n_e/N = c_e = \exp[-\Delta u/(kT)] = \exp[-\Delta U/(RT)]. \tag{6.1}$$

As indicated in Eq. (6.1), c_e is a function of T. As T increases, c_e increases dramatically when ΔU remains constant. Up to T_m, c_e reaches the maximum.
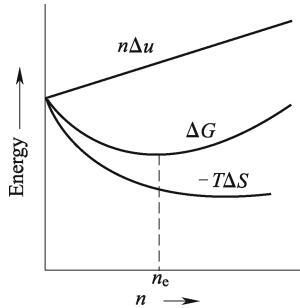
Fig. 6.2 $\Delta G, -T\Delta S$ and $n\Delta u$ as functions of n at a certain T.

Many important solid state processes, such as recovery, recrstallization, and precipitation, proceed from atoms moving (diffusing) from one lattice site to another in the crystal. One of the reasons for our interest in c_e is the diffusion, which leads to occurance of the above phenomena. Both of atoms from the host material and from substitutional atoms diffuse by a vacancy mechanism, i.e., atoms diffuse by jumping into vacant lattice sites. n_e thus decides the diffusion rate.

To accelerate the above mentioned solid state processes in materials engineering, sometimes we need to change n. In light of Eq. (6.1), this can be realized by heating the material to $T \approx T_{\mathrm{m}}$, keeping the material there for a certain time to guarantee $c_{\mathrm{e}}(T)$ is reached. After that, a quenching technique is used to remain $n_{\mathrm{e}}(T_{\mathrm{m}})$ at the room temperature T_{room}. Since $n_{\mathrm{e}}(T_{\mathrm{m}})$ is several orders of $n_{\mathrm{e}}(T_{\mathrm{room}})$, the time of the later diffusion treatment is evidently shortened.

Concerned with solid state diffusion, we introduce the basic laws of diffusion which were discovered by Adolf Fick on a phenomenological base long before point defects were known. The starting point is Fick's first law , stating that the flux J of diffusing particles (not necessarily atoms) is proportional to the gradient of their concentration (for ideal mixtures). In one spatial dimension, this is $J_i = -J_{\mathrm{d}}(\partial C_{\mathrm{d}i}/\partial x)$, where the index "$i$" refers to the particular particle with number i observed, and J_{d} is the diffusion coefficient of that particle. The driving force of the one-dimensional diffusion for ideal mixture is the concentration gradient, $-\partial C_{\mathrm{d}}/\partial x$ where C_{d} denotes the concentration. In systems other than ideal solutions or mixtures, the driving force for diffusion of each species is the gradient of chemical potential of this particle. Then Fick's first law can be written as $J_i = -(J_{\mathrm{d}}C_{\mathrm{d}i}/RT)(\partial \mu_i/\partial x)$. Since the gradient of μ_i may differ from zero even for constant concentrations, special effects as, e.g., uphill diffusion, are contained within this formulation.

The next basic equation is the continuity equation. It says that the changes of C_{d} within a volume element must express the difference between what goes in and what goes out–we have conservation of the particle number here. In mathematical terms, this means $\partial C_{\mathrm{d}}/\partial t = -\partial J/\partial x$. Substituting Fick's first law to this equation and assuming J_{d} to be a constant, we obtain Fick's second law : $\partial C_{\mathrm{d}}/\partial t = J_{\mathrm{d}}(\partial^2 C_{\mathrm{d}}/\partial x^2)$, which predicts how diffusion causes the concentration field to change with time.

We now must link the phenomenological description of diffusion (that only works on averages and thus only if many particles are considered) with the basic diffusion event, the single jump of a single atom or defect. We describe the net flux of particles as the difference in the number of particle jumps to the left and to the right. With the jump frequency Γ, i.e. the number of jumps per second from one position to a neighboring one, we obtain $J_{\mathrm{d}} = g'a\,\Gamma$ for cubic crystals, where a is the lattice constant, g' is the geometry factor of the lattice type considered. $\Gamma = \Gamma_0 \exp(-\Delta G^*/RT)$, with ΔG^* being the Gibbs free energy for the jump or for the migration of the atom or defect, i.e. the Gibbs free energy barrier that must be overcome between two identical positions in the lattice. Γ_0 is the frequency of "attempts" to overcome the energy barrier for a jump. It is, of course, the vibration frequency of the lattice atoms around 10^{13} s^{-1}. In a simple vacancy mechanism, since only lattice atoms that have a vacancy as a neighbor can jump, or, in other words, the number of lattice atoms jumping per second is identical to the number of vacancies jumping per sec, Γ of atom is expressed as $\Gamma = c_{\mathrm{e}}\Gamma_0 \exp(-\Delta G^*/RT) = \Gamma_0 \exp[-\Delta U/(RT)] \exp(-\Delta G^*/RT)$, where $\Delta G^* = \Delta H^* - T\Delta S^* \approx E^* -$

$T\Delta S^*$ with E^* being migration energy and ΔS^* the migration entropy for diffusion. Combining everything, there is

$$J_{\mathrm{d}} = J_{\mathrm{d}0} \exp[-(\Delta U + E^*)/(RT)]$$

where all constant (or nearly constant) factors have been included in $J_{\mathrm{d}0}$. In fact, the activation energy for diffusion, E_0, consists of two terms, the energy of formation ΔU and the energy of motion E^* of a vacancy: $E_0 = \Delta U + E^*$.

6.2 Line Defects Thermodynamics [2]

The dislocation theory is the core for metallic materials since the dislocation is responsible for their plastic property, while the plasticity guarantees metals and alloys to be widely used as structural materials in industry and in our life. Although the line defect is theoretically modeled and named as the dislocation, it is in 1950's that this linear crystalline defect was experimentally confirmed by direct observation with the electron microscope. The dislocation is long in one direction, while its diameter is only about 1–2 h. It is known that the regularity of a crystal lattice implies that each atom takes its site with minimized potential energy. Thus, a dislocation must represent a rising of the potential energy of all the atoms whose positions are affected by its presence. Thus, an energy may be ascribed to a dislocation which, physically, is the strain energy built into the crystal structure by displacement of the atoms from their regular positions.

Unlike vacancies, linear defects cannot move spontaneously and chaotically. A slight stress, however, is sufficient for a dislocation to start motion. There are essentially two types of dislocations. One is named the screw dislocation developed by Volterra in 1907, the other is called the edge dislocation established by Nabarro in much later 1952. Here we show the dislocation model or the basic geometry of the screw dislocation in Fig. 6.3. The left side is the schematic figure of the screw dislocation in crystalline lattice while the right side presents a cylinder of an elastic material deformed as defined by Volterra. The dislocation is made by slicing off one side of the cylinder along the axis direction and by moving one lattice constant a, or the Burgers vector $\boldsymbol{b}$. This leads to the formation of strain. $\boldsymbol{b}$ can also be obtained by taking a Burgers loop around the axis along the lattice site at a lattice plane. The step number of loops along a direction must be the same. It is found that there is a gap between the starting point and the end point. The difference between the two points as a vector is equal to $\boldsymbol{b}$, whose direction is parallel to the axis of the cylinder or perpendicular to the lattice plane.

With the results of the elasticity theory we can get approximate formula for the energy of a dislocation. The energy of a dislocation comes from the elastic part contained in the elastically strained bonds outside the radius r_{h} of the above cylinder (r_{h} is the radius of the hollow part of right side of Fig.
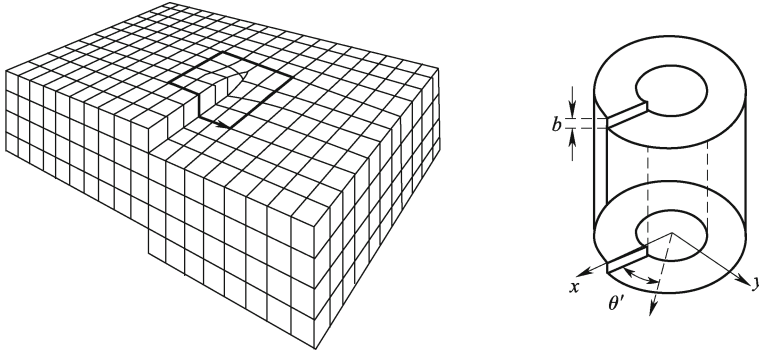
Fig. 6.3 Model for the calculation of the energy of a screw dislocation.

6.3) and from the energy stored in the core, which is of course energy sitting in the distorted bonds. The total energy per unit length E_{ul} is the sum of the energy contained in the elastic field, E_{el}, and the energy in the core, E_{core}, i.e., $E_{ul} = E_{el} + E_{core}$. In the core region the strain is very large and atoms are displaced by about a or $\boldsymbol{b}$. The linear elasticity theory thus is no more valid there. This is the reason why in Fig. 6.3 the cylinder is hollow, which denotes the core region and must be considered separately, which is added to the solutions from the linear elasticity theory.

Further understanding of the above can be built up by analyzing the stress-strain curve along the radius direction of the cylinder. It is interesting to note from this that the stresses and strains are proportional to $1/r$ and therefore diverge to infinity as $r \rightarrow 0$ as shown in the schematic picture in Fig. 6.4. This makes no sense and therefore the cylinder used for the calculations must be hollow to avoid too small r values, i.e. smaller than r_0. Real crystals, of course, do not contain hollow dislocation cores. If we want to include the dislocation core, we must do this with a more advanced theory of deformation or a non-linear atomistic theory. The picture simply illustrates that strain and stress are smooth functions of r where we then have no problem in using the Volterra approach.
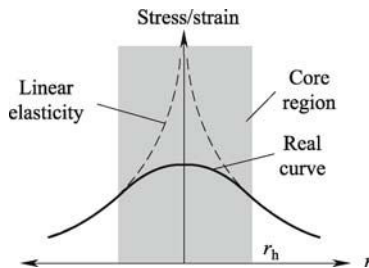
Fig. 6.4 The relationship between both stress and strains and $1/r$.

The elacstic strain energy dE_{el} of a small volume element dV is given by $(1/2)\,\tau_s\varsigma\,dV$ where τ_s is the shear stress with the shear modulus G_{shear} and ς is the strain. Since $\tau_s = Gb/(2\pi r)$ while $\varsigma = b/(2\pi r)$, the work done is

$$dW = \frac{1}{2}\tau_s\varsigma dV = \frac{1}{2}\frac{G_{shear}b}{2\pi r}\frac{b}{2\pi r}dV = \frac{1}{2}G_{shear}\left(\frac{b}{2\pi r}\right)^2 dV.$$

The volume of the annular element dV is $2\pi rldr$ where l denotes the length of the cylinder. Hence, $dW = G_{shear}b^2ldr/(4\pi r)$. E_{el} contained within a cylinder of radius R_c around the dislocation is obtained by integrating this equation up to the limit R_c. The lower limit of integration is taken to be r_h and the region inside r_h is referred to as the dislocation core. We therefore have

$$E = \frac{G_{shear}b^2l}{4\pi}\int_{r_h}^{R_c}\frac{dr}{r} + E_{core}l$$

where $E_{core}l$ is the strain energy within the radius 0 to r_h, i.e., the core energy.

How large is r_h or the extension of the dislocation core? Since the theory used is only valid for small strains, we may equate the core region with the region if the strain is larger than, say, 10%. From the equation above it is seen that the strain exceeds about 0.1% or 10% whenever $r \approx b$. A reasonable value for r_h therefore lies in the range b and $4b$, i.e. $r_h \geqslant 1$ nm in most cases and the reliable estimate of core energy is $G_{shear}b^2l/10$. Thus, on integrating to obtain the elastic strain energy, we get for E

$$E = \frac{G_{shear}b^2l}{4\pi}\ln\frac{R_c}{r_h} + \frac{G_{shear}b^2l}{10}.$$

Since generally $R_c \gg r_h$, the logarithmic term in this expression only varies slowly with R_c/r_h. As an approximation, $\ln(R_c/r_h)$ may be taken as 4π, thus,

$$E \approx G_{shear}b^2l + G_{shear}b^2l/10. \tag{6.2}$$

Equation (6.2) shows that $E \propto b^2$; and E_{core} is only one tenth of E_{el}.

For typical metals, such as Cr or Cu, $G \approx 5 \times 10^{10}$N $\cdot$ m^{-2}. Taking $b = 2.5\times10^{-10}$m, $E \approx 5.5$ eV·atom^{-1} for a screw dislocation. An equation similar to Eq. (6.2) can be derived for an edge dislocation and would give $E \approx 8$ eV·atom^{-1}. These energy is considerably greater than the formation energy of Schottky defects in metals. We have seen how Schottky defects become an equilibrium feature of a crystal due to the entropy effect. Dislocations also increase the entropy, but in this case the entropy change does not outweigh the very large enthalpy increase of $5.5-8$ eV·atom^{-1}, and consequently the free energy of the crystal is increased. As a result, dislocations are non-equilibrium defects. If possible, a crystal will decrease its dislocation density in order to drop its free energy.

6.3 Thermodynamics of Interfaces [3]

Molecules or atoms in an interface (surface) are in different environments from molecules or atoms within bulk materials. If a material is finely divided, interface effects may be quite significant. 1 m^3 of the material divided into 10^{-6}m cubes has a surface area of 6×10^3 m^2. The unsymmetrical force field at a surface gives rise to a surface energy parallel with the surface, a tendency of asymmetric molecules to be oriented in a surface, and a capacity to bind other molecules at the surface either physically or chemically. Such interfacial phenomena may be defined as those related to the interaction between one phase (solid or liquid) and another (solid, liquid, gas or vacuum) in a narrow region where the transition from one phase to another occurs. Our understanding of the nature of the interfacial region and the changes or transitions has historically lagged behind that in many other scientific areas because of the development and implementation of both theoretical and practical concepts. In the late 19th and early 20th centuries, great achievements in thermodynamics have been made in the theoretical understandings of interface interactions. Modern computational and analytical techniques available in the last thirty years have led to significant advances toward a more complete understanding of the inimitable nature of interfaces and the interface interactions due to the rapid increase of computation ability/price ratio of computers. With the computing techniques or computer simulations, the so-called computation materials science considers the interface properties from three different size scales. (1) Atomic and electronic scales where the *ab initio* calculation based on the first principles is used. In this size scale, many-body interaction behavior of dozens of several hundred molecules is considered together. (2) Nanometer to millimeter size scales where the molecular dynamics and Monte Carlo methods are utilized. In these techniques, many-body interaction behavior of several thousand to several hundred million molecules can be calculated. (3) Engineering behavior of large-scale construction problems, or bulk materials. In this case, the finite element method is a powerful tool where averaging constitutive laws are used to incorporate interface microstructures.

When interface size at least in one dimension is at nanometer size range, ζ increases and thus interface effect on materials properties becomes evident. Consequently, the corresponding materials properties could not be readily interpreted based on "classical" atomic or solid solution theories, and the regions of space involved were beyond the scope of existent experimental techniques. Since in the nanosize range the *ab initio* calculation cannot be realized due to the computing ability of present computers, the computer simulations remain many uncertainties. An alternative is the classic thermodynamics, which still holds importance to model the above phenomena. This is because not only the classic thermodynamics has been widely applied to bulk materials, but also people are very familiar with this unique technique.

It is well known that the thermodynamic approach is applicable to a big

system consisting of great number of atoms/molecules. An ensemble of many small objects will also be a macroscopic system, which may be rather speculative or correspond to a real dispersed system (aerosol, micro-emulsion, composed material, etc). However, extension of thermodynamic methods to very small objects, such as nanoparticles, still faces many principal difficulties. In this chapter, the size-dependence of thermodynamic amounts related to interfaces is introduced based on authors' own recent works, which relates the nanothermodynamic amounts directly to the corresponding bulk ones.

6.3.1 Thermodynamic Description of Surface Free Energy of Liquids and Solids [4]

The molecules at the surface of a liquid are attracted into the body of the liquid because the attraction of the underlying molecules is greater than the attraction by the vapor molecules on the other side of the surface. This inward attraction causes the surface to contract if it can give rise to a force in the plane of the surface. The surface energy of a liquid, γ_{Lv}, is responsible for the formation of spherical droplets, the rise of water in a capillary, and the movement of a liquid through a porous solid. γ_{Lv} is the force per unit length on the surface that opposes the expansion of the surface area. This definition is illustrated by the idealized experiment in Fig. 6.5, where the movable bar is pulled with force f_o to expand a liquid film that is stretched like a soap-bubble film on a wire frame. $\gamma_{Lv} = f_o/2l$, where l is the length of the bar, and factor 2 is introduced because there are two liquid surfaces, one at the front and one at the back.
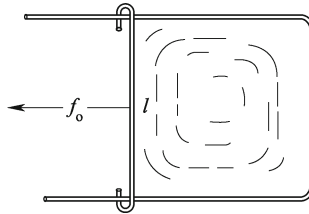
Fig. 6.5 Idealized experiment for the determination of the surface tension of a liquid.

γ_{Lv} decreases as T rises and becomes very small at a few degrees below the critical temperature T_c. It is zero at T_c where the liquid-vapor transition occurs. γ_{Lv} of liquid metals and molten salts is large in comparison with that of organic liquids due to different bond natures.

Surface work W' is required to increase the area of a surface. In Fig. 6.5, W' for the film is $W' = f_o x = 2\gamma_{Lv} l x = \gamma_{Lv} A$, where x is the displacement of the moving bar, A is the total area. The unit of γ_{Lv} is in J·m^{-2}. For

a system in equilibrium, the infinitesimal total work due to the change in area of the surface is $\delta W = -P\mathrm{d}V + \gamma_{\mathrm{Lv}}\mathrm{d}A$. A equation combining the first $(\mathrm{d}U = \delta Q + \delta W)$ and the second $(\delta Q = T\mathrm{d}S)$ laws for an open-component system is expressed,

$$\mathrm{d}U = T\mathrm{d}S - P\mathrm{d}V + \gamma_{\mathrm{Lv}}\mathrm{d}A + \mu\mathrm{d}n \qquad (6.3)$$

where $\mathrm{d}n$ is the change in the number of moles in the system. The equilibrium state of a one-component system consisting of n mole particles at a fixed T and P is the one with the minimum of $G(T, P, n) = U + PV - TS$. Thus,

$$\begin{aligned} \mathrm{d}G &= \mathrm{d}U + P\mathrm{d}V + V\mathrm{d}P - T\mathrm{d}S - S\mathrm{d}T \\ &= -S\mathrm{d}T + V\mathrm{d}P + \gamma_{\mathrm{Lv}}\mathrm{d}A + \mu\mathrm{d}n \end{aligned} \qquad (6.4)$$

where the second form has been obtained by substituting Eq. (6.3). The γ_{Lv} in Eqs. (6.3) and (6.4) is given by

$$\gamma_{\mathrm{Lv}} = \left(\frac{\partial U}{\partial A}\right)_{S,V,n} = \left(\frac{\partial G}{\partial A}\right)_{T,p,n} = \left(\frac{\partial H}{\partial A}\right)_{S,P,n} = \left(\frac{\partial F}{\partial A}\right)_{T,V,n}. \qquad (6.5)$$

Here γ_{Lv} can be identified as the surface excess free energy per unit area or surface free energy for short (but imprecisely), which is also suitable for solid-vapor interface energy or surface energy of solids γ_{sv} since the case is similar. Thus, in the later sections, Eqs. (6.4) and (6.5) are also utilized for γ_{sv}. Note that in this section and later sections we denote sometimes the solid-vapor interface and the liquid-vapor interface as surface for simplicity since simply the interaction force of the vapor phase is much weaker than solid and liquid phases. Thus, solid-vacuum and liquid-vacuum interfaces have similar behavior.

The thermodynamics of the interface/surface as formulated by Gibbs has proven to be one of the most useful and powerful frameworks for studying solid surface phenomena. Central to this approach is the quantity referred to as interface energy. It is equal to the reversible work per unit area needed to create a surface and is the fundamental parameter that determines the behavior of fluid-fluid interfaces. However, Gibbs was the first to point out that for solids, there is another type of surface quantity, differing from γ_{sv}, the surface stress f. f can also critically affect the behavior of surfaces that is associated with the reversible work per unit area needed to elastically stretch a pre-existing surface. The relationship between f and γ_{sv} is derived in the following section.

6.3.2 Thermodynamics of Surface Stress and Intrinsic Stress [4]

The physical origin of f can be qualitatively understood in the following manner. The nature of the chemical bonding (e.g., the number of bonds) of

atoms at the surface differs from that in the interior. Thus, h of the surface atoms differs from that of the interior atoms if the surface atoms were not constrained to remain structurally coherent with the underlying lattice. As a result, the interior of the solid can be considered as exerting a stress f on the surface. There has been some confusion with regard to identifying f of either sign as compressive or tensile. When f is positive, the surface work $f\mathrm{d}A$ is negative if $\mathrm{d}A$ is negative. This indicates that the surface could lower its energy by contracting and is therefore under tension. Namely, a positive (negative) f is referred to as a tensile (compressive) surface stress.

The elastic deformation of a solid surface can be expressed in terms of a surface elastic strain tensor ς_{ij}, where $i, j = 1, 2$. Consider a reversible process that causes a small variation in the area through an infinitesimal elastic strain $\mathrm{d}\varsigma_{ij}$. One can define a surface stress tensor f_{ij} that relates the work associated with the variation in $\gamma_{\mathrm{sv}}A$, the total excess free energy of the surface, owing to the strain $\mathrm{d}\varsigma_{ij}$ (summing over each repeated index):

$$\mathrm{d}(\gamma_{\mathrm{sv}}A) = Af_{ij}\mathrm{d}\varsigma_{ij}. \tag{6.6}$$

Equation (6.6) was first given by Shuttleworth, who derived it by considering the two reversible paths illustrated in Fig. 6.6. In the first path (clockwise), the solid pictured in the upper left is cleaved into two pieces and then both pieces are subjected to the same elastic strain. The work associated with the first step is $w_{\mathrm{r}1} = 2\gamma_{\mathrm{sv}}A$, where A is the area of each of the newly created (unstrained) surfaces. The work of the second step, denoted by $w_{\mathrm{r}2}$, equals the work needed to elastically deform the total bulk volume and four (two original and two newly formed) surfaces. In the second path of Fig. 6.6 (counter-clockwise), the solid is first subjected to the elastic strain and is then cleaved into two pieces. The work of the first step w_1 is equal to that needed to deform the bulk volume and the two surfaces. The difference $w_{\mathrm{r}2} - w_{\mathrm{r}1}$ is
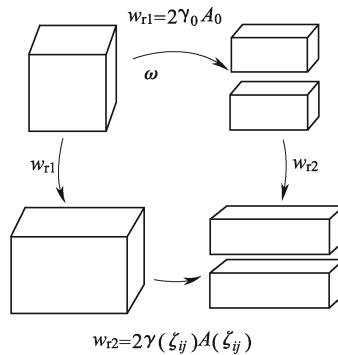
Fig. 6.6 Schematic representation of two reversible paths that illustrate the relationship between surface free energy and surface stress. (Reproduced from Ref. [4] with permission of Elsevier)

the excess work necessary to elastically deform two surfaces of area A to area $A(\varsigma_{ij})$. This difference can be equated with the work performed against f_{ij}.

$$w_{r2} - w_{r1} = 2\int f_{ij}\mathrm{d}A(\varsigma_{ij}) = 2\int A f_{ij}\mathrm{d}\varsigma_{ij}. \tag{6.7}$$

The work associated with the second step of the second path can be expressed as $w_{r2} = 2\gamma(\varsigma_{ij})A(\varsigma_{ij})$, so that $w_{r2} - w_{r1} = 2[\gamma(\varsigma_{ij})A(\varsigma_{ij}) - \gamma_{sv}A]$. Equating the total works of the two reversible paths leads to $W_2 - W_1 = w_{r2} - w_{r1}$. Therefore,

$$2[\gamma(\varsigma_{ij})A(\varsigma_{ij}) - \gamma_{sv}A] = 2\int A f_{ij}\mathrm{d}\varsigma_{ij}, \tag{6.8}$$

which is equivalent to Eq. (6.6). Since $\mathrm{d}(\gamma A) = \gamma\mathrm{d}A + A\mathrm{d}\gamma$, and $\mathrm{d}A = A\delta_{ij}\mathrm{d}\varsigma_{ij}$ (where δ_{ij} is the Kronecker delta), f_{ij} can be expressed as

$$f_{ij} = \gamma\delta_{ij} + \partial\gamma_{sv}/\partial\varsigma_{ij}. \tag{6.9}$$

In contrast to γ_{sv}, which is a scalar, f_{ij} is a second rank tensor. For a general surface, it can be referred to such a set of principal axes that the off-diagonal components are identically zero. Furthermore, the diagonal components are equal for surface possessing three-fold or higher rotation axis symmetry. This means that f_{ij} for high symmetry surfaces is isotropic and can be taken as a scalar $f = \gamma_{sv} + \partial\gamma_{sv}/\partial\varsigma$. Rewrite this as

$$f - \gamma_{sv} = \partial\gamma_{sv}/\partial\varsigma. \tag{6.10}$$

Equation (6.10) shows that the difference between f and γ_{sv} is equal to the change in surface free energy per unit change in elastic strain of the surface. For most solids, $\partial\gamma/\partial\varsigma \neq 0$. $\partial\gamma/\partial\varsigma$ has usually the same order of magnitude as γ_{sv} and can be positive or negative, while γ_{sv} (for a clean plane surface) is always positive. Thus, f has also generally the same order of magnitude as γ_{sv} and can be positive or negative.

   Both f and γ_{sv} can each be considered as representing a force per unit length, the former (latter) is exerted by a surface during elastic (plastic) deformation. As a result, both f and γ_{sv} have been referred to as "surface tension". This has undoubtedly contributed to some of the confusion in the literature concerning the difference between them, and it is probably best not to use the term when discussing solid surfaces. It is often stated that in contrast to solids, f_{Lv} and γ_{Lv} are the same for fluids (to identify the difference between the surface stresses of solid and liquid, the subscript "Lv" for f is added). This is due to the fact that when a fluid such as a soap film is stretched, the atoms or molecules in the interior move to the surface to accommodate the new area created. In this case γ_{Lv} remains constant during the stretching process, and according to Eq. (6.10), $f_{Lv} = \gamma_{Lv}$. This has led some to claim by the same reasoning that at high T where there is sufficient atomic mobility, $f = \gamma_{sv}$ for solids during processes such as creep.

However, this is not correct. During the initial elastic deformation in a creep experiment, the work per unit area needed to stretch the solid is f, while during plastic deformation γ_{sv} represents the specific surface work to create new surface. Thus, the quantity being measured in a creep test, where the plastic strain is much greater than the elastic strain, is γ_{sv}, not f.

For many processes, the easiest and most unambiguous way of determining whether f or γ is the relevant parameter is the following: If a small variation in area does not change the surface atomic density, then the specific surface work is equal to γ_{sv}; if the variation is due to an elastic strain that changes the surface density of atoms, then the specific surface work is f. According to this rule, plastic deformation and crack propagation are examples of processes where γ_{sv} equals the surface work, independent of mechanism. On the other hand (as will be discussed in more detail later), the Laplace pressure associated with a small solid particle in a fluid is proportional to f. In the case of liquids, all processes of interest involve variations in area without varying the surface density, and the surface work represents γ_{Lv} (However, in the case of a compressible liquid, it is possible to conceive of a surface stress-like quantity that denotes the surface work when a liquid is subjected to a hydrostatic pressure).

Cahn pointed out that the expression for f can be simplified by using a Lagrangian measure of the area A_L. The relation between A_L and the physical area A is $A = A_L(1+\varsigma_{ij})$, where ς_{ij} represents the trace of the elastic strain ε_{ij}. A_L is the surface area measured with respect to a standard state of strain, and remains unchanged during elastic deformation. In the Lagrangian coordinate system, it is necessary to define the surface free energy γ_L so that $\gamma_L A_L = \gamma_{sv} A$,

$$\gamma_L = \gamma_{sv}(1 + \varsigma_{ij}). \tag{6.11}$$

The two types of surface work that can be performed on solid to change its A can be taken as either changing A_L and holding ς_{ij} constant, or changing ς_{ij} and holding A_L constant. The former surface work is equal to γ_L, while the latter is equal to f_{ij},

$$f_{ij} = \partial \gamma_L / \partial \varsigma_{ij}. \tag{6.12}$$

Substituting Eq. (6.11) into Eq. (6.12) leads to Eq. (6.9). For many problems, the use of the Lagrangian coordinate system greatly simplifies the analysis.

Surface and interface stresses influence the structure and properties of thin films. These stresses are often important factors in determining behavior of thin films with high surface/volume ratio, and can result in a significant intrinsic stress, induce higher order elastic behavior, and affect the thermodynamics of epitaxy.

There exists stress in almost all deposited thin films. These stresses develop because certain processes occur, which would result in the films changing their in-plane dimensions if they are located on substrates. A well-known example is thermal stress which develops in response to a change in T when the thermal expansion coefficients of a film and a substrate are different. In-

trinsic stresses are defined as those developing during film growth. Consider an isotropic film of thickness t_h that is constrained to have its bulk lattice parameter. Assume that there is not a strong film-substrate interaction so that $f \gg \sigma_{in}$, the interface stress σ_{in} can be interpreted as the specific interface work associated with changing disolcation density. When the constraint is removed, the film elastically deforms on the substrate in response to f. Letting ς represent the resultant elastic in-plane radial strain, the elastic energy per unit area in the film is given by $Yt\varsigma^2$, where Y is the biaxial modulus equal to $E_Y/(1-\nu_P)$, where E_Y is Young's modulus and ν_P is Poisson's ratio. The work per unit area performed against f can be expressed as $2f\varsigma$. The total work per unit area is therefore: $W' = 2f\varsigma + Yt\varsigma^2$. The equilibrium strain ς^* is determined by setting $\partial W'/\partial\varsigma = 0$,

$$\varsigma^*(t_h) = -f/E_Y t_h. \tag{6.13}$$

Based on this result, it has been sometimes argued that the intrinsic stress resulting from opposing this deformation would equal $-E_Y\varsigma^*(t_h)$, and therefore should be of the same sign as f and be inversely proportional to t_h. However, this is an incorrect physical picture with regard to generating an intrinsic stress in a film. A film on a substrate that displays an equilibrium strain relative to bulk does not have to be under a state of intrinsic stress. Instead, if at some point during deposition, the film is firmly attached to the substrate, intrinsic stress will subsequently be generated by f as t_h increases.

This idea can be carried out quantitatively. Consider a film that has firmly attached to a substrate with a thickness t_0. Assuming no intrinsic stress generating mechanisms have operated, the deposited film is in a stress-free state with its equilibrium in-plane lattice parameter equaling $a_0[1+\varsigma^*(t_0)]$, where a_0 is the bulk lattice parameter. During further deposition, if the film was not constrained by the substrate, the equilibrium strain relative to bulk $\varsigma^*(t_h)$ is determined by Eq. (6.13), and there is a difference of $\Delta\varsigma = \varsigma^*(t_h) - \varsigma^*(t_0)$. However, since t_0 was constrained by the substrate, it could not elastically deform in the plane of the film, the substrate must impose an in-plane biaxial stress to oppose the latent strain $\Delta\varsigma$ as t increases. As a result, σ generated in the film due to the effect of f is equal to

$$\sigma(t_h) = -E_Y\Delta\varsigma = f(1/t_h - 1/t_0). \tag{6.14}$$

As $t_h \to \infty$, $\sigma \to -f/t_0$. Even though the above analysis considered just the effect of f while the film with t_0 was assumed to be stress-free, the result given in Eq. (6.24) is, nevertheless, of general validity. That is, Eq. (6.14) represents the contribution to the overall σ resulting from f, independent of other stress generating mechanisms (and even if the lattice parameter differs from $a_0[1 + \varsigma^*(t_0)]$ at $t = t_0$).

Consideration is now given to the proper value of t_0. It would appear plausible that growing crystals first become constrained when substantial impingement occurs. t_0 would depend in part on the thermodynamics of the

film-substrate interface, in particular, on how well the film wets the substrate. t_0 would also be dependent in large part on kinetic factors, such as the deposition rate and the surface mobility of the adatoms (which in turn relies on the deposition temperature). Experimental studies have indicated that a metal film deposited by physical vapor deposition can become continuous at $t_{\mathrm{h}}{=}1$ nm. Referring to Eq. (6.14), and using reasonable values of $f = 2$ N·m^{-1} and $t_0 = 5$ nm, $\sigma(t_{\mathrm{h}})$ generated when $t_{\mathrm{h}} \gg t_0$ is of the order of -4×10^8 Pa. Note that $\sigma(t_{\mathrm{h}})$ has an opposite sign of f.

Since most experimental and theoretical investigations on f of metals give positive values, the proposed mechanism would be expected to produce a compressive σ. It is generally found that at the end of nonepitaxial growth, metallic films exhibit a positive σ. However, during the early stages of deposition the film often shows a compressive stress, which increases in magnitude with increasing t, up to a certain thickness. After that a competing tensile stress generating mechanism appears and eventually dominates. Two popular models to explain generation of a tensile stress in metal films are the grain growth model and the grain boundary relaxation model. In both processes the total grain boundary volume reduces with decreasing time, which, not constrained by the substrate, leads to a densification of the film. Kinetic analyses of these processes have been given by Doerner and Nix. They showed that in both cases a significant amount of time can elapse before a perceptible tensile stress is developed. During this period of time, the film can grow to a thickness many times larger than t_0. As a result, a compressive σ due to f can develop before the other processes generate a competing tensile stress that eventually dominates. Of course, $f < 0$ for some thin films, which leads to $\sigma > 0$.

In the above discussion, the effect of σ_{in} was not considered. If there is a strong epitaxial relationship between a film and substrate, σ_{in} could be very important and in fact dominate the behavior. However, if a strong epitaxial relationship is absent (for example, metal deposition on an amorphous substrate), σ_{in} plays little role. In either case, the effect of σ_{in} can be formally taken into account by considering f to be a net surface stress, which is the sum of f and σ_{in}. If the film is a polycrystal, the interface stress of the grain boundaries could contribute a term to σ. In the case of films with a columnar microstructure, this term is a function of grain sizes but not t. As a result, the interface stress has little effect on development of σ until significant grain growth occurs, and it is therefore not expected to be important during the early stages of deposition.

6.3.3 Real Surface: Reconstruction and Relaxation [5–7]

The 2D translational symmetry of ideal surfaces and half-spaces with bulk atomic positions are characterized by the primitive Bravais vectors. In addi-

tion to point and line defects, on a real surface of a crystal there are other reasons why the assumption of an ideal surface is not valid in general. Such a picture does not fully account for the bonding behavior of the atoms in a crystal. In an ideal infinite crystal, the equilibrium position of each individual atom is determined by the forces exerted by all other atoms in the crystal, resulting in a periodic structure. If a surface is introduced to the system by terminating the crystal along a given plane, these forces will be altered, changing the equilibrium positions of the remaining atoms. This is most noticeable for the atoms at or near the surface plane, as they now only experience inter-atomic forces from one direction. The forces acting on them result in displacements of atomic positions with respect to those of the infinite crystal. Consequently, the atomic structure of the surface is not merely a truncation of a bulk crystal.

The distortion of the ideal bulk-like atomic configuration due to the existence of a surface (more precisely, the non-existence of formerly neighboring atoms in the vacuum) depends on the bonding behavior of the material considered. Let's take the surfaces and interfaces of semiconductors as examples, which play a decisive role in many technologically important device applications and lead to the birth of surface science in the 1960s, In the 1960s and 1970s, the standard method for generating semiconductor surfaces was to cleave a single crystal in an ultra-high vacuum. The natural cleavage plane is the (111) surface for diamond structure semiconductors characterized by purely covalent bonds such as Si and Ge, and the (110) surface for zinc-blende-structure III-V and II-VI semiconductors characterized by partially covalent and partially ionic bonds. In such covalently bonded semiconductors, strong directional bonds are present. Each bond contains two spin-paired electrons. When a surface is created, at least one such bond per atom is "cut". A "cut" bond is called a "dangling" bond and contains less than two spin paired electrons. The lack of electron pairing makes dangling bonds unstable, requiring the surface atoms to "seek new coordinates", so that the free energy of the system reaches its minimum. Sometimes, this process is accompanied by bringing surface atoms closer together. One of these mechanisms resulting in pairs of surface atoms is schematically indicated in Fig. 6.7(a). However such a rearrangement can also yield rough surface layers, the stoichiometry of which is changed with respect to the ideal surface [Fig. 6.7(b)]. In both cases, the 2D Bravais lattice of the surface is changed. Such perturbations destroying the translational symmetry of the fictitious ideal surface are known as surface reconstruction.

In simple metals, instead, one has a gas of quite delocalized electrons and chemical bonds, which are far less directional than in semiconductors. Consequently, there are no preferred directions in the displacements of atoms with the exception of that parallel to the surface normal vector itself. One thus expects a displacement mainly of the first-layer atoms in a vertical direction with respect to the surface as indicated in Fig. 6.7(c). The 2D Bravais lattice and, hence, the 2D translational symmetry remain unchanged. Such a

Reconstruction

(a)   (b)

Relaxation

(c)
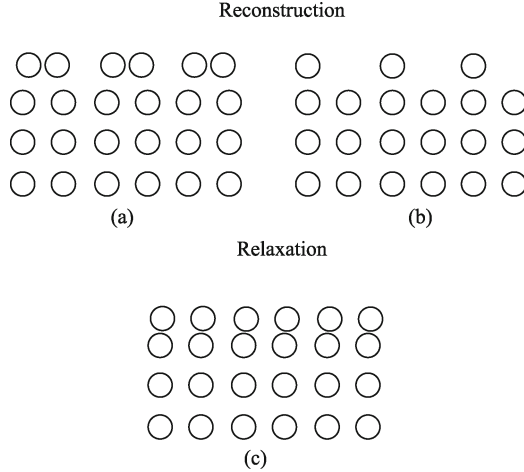
Fig. 6.7 Schematic illustrations of atomic rearrangements in the surface region. (a) pairing reconstruction; (b) missing row reconstruction; and (c) relaxation of the uppermost atomic layer.

translational-symmetry-conserving change of the atomic structure is called surface relaxation, which barely reduces the density of states (DOS) for the surface layer at ε_F. The surface reconstruction is however accompanied by opening of a surface band gap around ε_F where a significant reduction of the DOS is present.

A standard notation has been adopted to describe reduced symmetry structures due to the restruction in which, e.g., a Si(hkl)-($n \times m$) symbol designates the reconstruction of the (hkl) plane (given by its Miller indices) into one, in which the interatomic spacings are multiplied by n and m in the x and y directions respectively. This notation is often used to describe reconstructions concisely, but does not directly indicate changes in the layer symmetry (for example, square to hexagonal).

Semiconductor surfaces are known to reconstruct differently under various conditions such as upon cleavage, upon epitaxial growth and annealing conditions, due to overlayer growth, deposition of passivating or surfactant layers, and induced by defect formation. For example, over 300 phases of Si surfaces have been reported depending on T, on which crystal facet is exposed. The Si(111) facet affords an illuminating example of this fact: Low-temperature cleavage generates a (2×1) structure with alternating rows of depressed and raised surface atoms, shown in Fig. 6.8(a). This would allow the depressed atoms to assume more planar geometry with sp^2-like bonding and the raised atoms to assume a pyramidal geometry with a bonding configuration involving more s characters of the dangling bonds. Since the energetic level of s electrons is lower than that of p electrons, the dangling bonds at the raised atoms would be occupied by two electrons, while the dangling bonds at the depressed atoms would become empty. This would then

make the surface semiconducting in nature. A $(2{\times}1)$ structure is not stable, and depending upon the annealing temperature. Si(111) exhibits a number of irreversible high-temperature reconstructions. When vacuum is annealed above 603 K, the $(2{\times}1)$ reconstruction changes to a mixture of $(5{\times}5)$ and $(7{\times}7)$ reconstructions. When annealed above 873 K, only the $(7{\times}7)$ reconstruction is observed. The $(7{\times}7)$ structure is stable up to around 1173 K and remains so when the sample is cooled down to T_{room}. A first-order reversible $(7{\times}7) \leftrightarrow (1{\times}1)$ phase transition takes place at even higher T. The $(1{\times}1)$ structure can also be stabilized at T_{room} by some other means: such as small amounts of adsorbed chlorine, laser annealing, when the $(7{\times}7)$ structure is quench-cooled from high T. Thus, the kinetic accessibility as well as the ground-state free energy play an important role in determining which of the various possible reconstructions actually occurs under a specified set of preparation conditions.

(a)

(b)
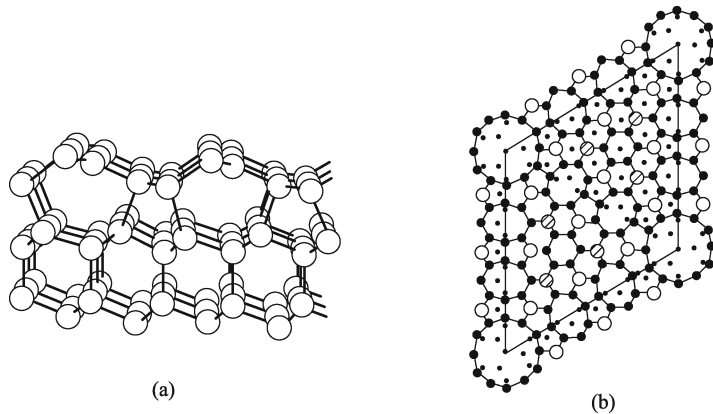
Fig. 6.8 (a) Ball-and-stick model of the $(2{\times}1)$ π-bonded chain structure on Si(111) resulting from the single-bond scission cleavage of silicon. (b) Atomic arrangement on the Si(111)-$(7{\times}7)$ according to the DAS model.

The high-temperature $(7{\times}7)$ reconstruction of Si(111) was first observed in 1959. This reconstruction can be described as the dimer adatoms stacking fault (DAS) model and is characterized by (1) dimerization of second-layer atoms, (2) adatoms, and (3) a stacking fault between the first and second layers over one-half of the $(7{\times}7)$ unit cell. This is shown in Fig. 6.8(b). Notice that the stacking sequence in the right half of the surface unit mesh is the same as in bulk Si while that in the left half is faulted. The ideal (unrelaxed) $7{\times}7$ structure would contain 48 Si atoms in every surface layer. In the DAS model of the $7{\times}7$ reconstruction, there are a total of 102 Si atoms in the top three layers of the $7{\times}7$ unit cell. These are: 12 atoms in the adatom layer, 42 atoms in the rest atom layer, and 48 atoms in the layer containing the stacking fault. Of all these 102 atoms only 19 (the 12 adatoms, six rest atoms and one atom at the bottom of the corner-hole) atoms possess dangling bond. This reduction in the dangling bond number stabilizes the metallic $7{\times}7$

reconstruction, which energetically is favourable compared with the (2×1) reconstruction by 60 meV per 7×7 unit cell.

The driving force for a surface reconstruction changing the density of surface atoms is the difference between f and γ_{sv}, i.e., the strain derivative of the surface energy $\tau_{ij} = \partial \gamma_{sv}/\partial \varsigma_{ij}$. Consequently a surface would tend to reconstruct toward a state in which $f = \gamma_{sv}$ [5]. When $\tau_{ij} > 0$, there is an increasing tendency for the density of surface atoms, and vice versa for a negative value. The conclusion concerning the driving force for surface reconstruction is similar to results of other studies of surface densification. However, in those studies it was shown that this driving force does not result in any reconstruction. The reason for the obviously different findings could be that the above criterion follows within the linear elasticity theory and, hence, applies only for small uniform strains when the surface layer and bulk are strained together. A reconstruction involving straining the surface layer alone necessarily changes the surface-substrate bonding, which generally costs energy. The application of the above criterion to the case of Au (110) surface should therefore fail. This surface undergoes a missing row reconstruction in which alternate $[1\overline{1}0]$ rows of atoms are removed from the surface. The removal of one-half of the surface layer of atoms cannot plausibly be discussed within the linear elasticity theory since the missing row reconstruction involves very great changes in the local environment of some atoms.

6.3.4 Equilibrium of Fluid Droplets and Solid Particles [4]

Consider a fluid (liquid or vapor while we here discuss a liquid) droplet in equilibrium with a different surrounding fluid that can be considered infinite in extent. There will be a pressure difference $\Delta P = P_1 - P_2$ (where the subscripts "1" and "2" refer to the droplet and the surrounding fluid, respectively) acting on the droplet owing to f or γ_{Lv} where $f = \gamma_{Lv}$ as mentioned above. In equilibrium, the virtual work $\Delta P dV$ resulting from a small variation in the volume of the droplet due to transfer of atoms or molecules from the surrounding fluid to the droplet equals γdA, the increase in the total free energy of the surface. For a spherical droplet with radius r, the area of the droplet A is $4\pi r^2$ and $dA = 8\pi r dr$ and $\gamma dA = 8\pi \gamma_{Lv} r dr$. Since the volume change is $dV = 4\pi r^2 dr$, this equality leads to the well-known Laplace-Young Equation,

$$\Delta P = 2\gamma_{Lv}/r. \tag{6.15}$$

Because of this Laplace pressure ΔP, the vapor pressure of a small droplet exceeds that of a plane surface of the liquid, and the vapor pressure of a concave surface of a liquid is smaller than that of a plane surface. When we consider the Gibbs free energy change dG with dn moles of a substance added to the droplet, $\mu_{planar} = (\partial G/\partial n)_{T,P,A}$ for a planar surface. If the surface is

curved, which is our case of the spherical droplet, the surface area varies and $dA = 2dV/r = 2V_m dn/r$ where V_m is the molar volume of the liquid. Combining this equation with Eq. (6.4) yields

$$dG = -SdT + VdP + (2V_m\gamma_{Lv}/r + \mu_{planar})dn. \qquad (6.16)$$

The total chemical potential of the liquid in the droplet is thus given by $\mu = 2V_m\gamma_{Lv}/r + \mu_{planar}$. If the related surrounding vapor behaves like a perfect gas, there is $\mu = \mu_{planar} + RT\ln(P/P_0)$ where P_0 is the vapor pressure for a planar surface. Combining this equation with the preceding one yields the Kelvin equation,

$$\ln\left(\frac{P}{P_0}\right) = \frac{2V_m\gamma_{Lv}}{rRT}. \qquad (6.17)$$

This equation gives the vapor pressure P of a droplet with a radius r.

Equation (6.15) may be used to derive the relation between γ_{Lv} and the rise, or drop of a liquid in a capillary illustrated in Fig. 6.9. If the contact angle θ_a that the liquid makes with the wall is smaller than $90°$, the liquid will rise; when $\theta_a > 90°$, the surface of the liquid will be depressed. If the capillary is of sufficiently small diameter, the meniscus will be a section of
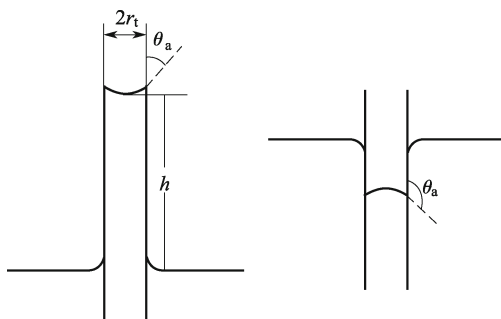
Fig. 6.9   Rise or drop of a liquid in a capillary where h value is equal to the distance between the bottom of the meniscus and the height of the surrounding liquid plane.

a sphere, and the radius of curvature of the liquid surface in the capillary is given by $r = r_t/\cos\theta_a$, where r_t is the radius of the capillary tube. The difference between the pressure in the liquid at the curved surface and that at the flat surface of the liquid is given in light of Eq. (6.15),

$$\Delta P = 2\gamma_{Lv}\cos\theta_a/r_t.$$

Therefore, the atmospheric pressure pushes the liquid up the tube until ΔP is balanced by the hydrostatic pressure due to the liquid column of height h.

$$\frac{2\gamma_{Lv}\cos\theta_a}{r_t} = hg(\rho_L - \rho_v)$$

where ρ_L and ρ_v are the densities of the liquid and the vapor respectively, and g is the acceleration of gravity. Since $\rho_v \ll \rho_L$, ρ_v may be neglected,

$$\gamma_{Lv} = \frac{hg\rho_L r_t}{2\cos\theta_a}.$$

If the above equation is used to determine γ_{Lv} with the measured h value, it is found that the obtained γ_{Lv} value is slightly lower than the real one. This can be corrected by adding $r_t/3$ to the measured h. After that a good agreement between experiments and the above equation could be found.

If the small droplet is changed to a small solid in equilibrium with a surrounding fluid, Eq. (6.15) is still valid. For simplicity, it will be assumed that the solid is spherical and has an isotropic surface stress f. Substituting f as γ_{Lv} into Eq. (6.15), there is

$$\Delta P = 2f/r. \qquad (6.18)$$

In literature, the Laplace pressure for a solid is often incorrectly written as Eq. (6.15) rather than Eq. (6.18).

As discussed by Gibbs, and more recently by Cahn, the chemical potential of the solid phase will contain the term $2fV_s/r$ (Eq. (6.16)), where V_s is the molar volume of the solid. This is because a transfer of atoms from the fluid to the solid phase will change the Laplace pressure acting on the solid. However, μ_L contains the term $2\gamma_{Lv}V/r$, reflecting the fact that the transfer changes the physical area of the solid-fluid interface. This leads to

$$\mu_s - \mu_L = 2(f - \gamma_{Lv})V/r. \qquad (6.19)$$

Note that, except for the special case of $f = \gamma$, the chemical potentials of the two phases in equilibrium are not the same. Gibbs restricted his attention to a single component solid in equilibrium with a multicomponent fluid. Cahn extended the analysis for the case of a multicomponent solid with both substitutional and interstitial components. The analysis is simplified if the Lagrangian coordinate system is used. In the case of an interstitial component, the transfer of atoms from the fluid to the solid does not change the Lagrangian surface area but can induce an elastic strain if the component has a nonzero partial molar volume. Cahn showed that for interstitial components, the chemical potential is the same for solid and fluid phases ($\mu_s - \mu_f = 0$), while for the substitutional components the difference is given by Eq. (6.19), where V is now the volume of the solid divided by the number of moles of substitutional lattice sites.

Various thermodynamic derivations employing correct expression for the Laplace pressure of solids have been given by Cahn. Some of them are given below in order to illustrate under what circumstances the equilibrium behavior is determined by γ_{Lv} and/or f. The Lagrangian measure of the surface free energy γ_L is used in order to emphasize the fact that Cahn used the Lagrangian coordinate system in his derivations, which significantly reduced

the complexity of his analysis. The difference between T_m and the melting temperature of a finite-sized single component solid $T_m(r)$ is

$$T_m - T_m(r) = 2\gamma_{Lv}V/r(S_L - S_s) \tag{6.20}$$

where S is the molar entropy. Melting or freezing a surface layer of atoms changes the Lagrangian area. The relevant surface parameter is γ_{Lv}. Similarly, the solubility of a dilute single component solid in a multicomponent fluid is given by

$$C = C_0 \exp(2\gamma_{Lv}V/rRT) \tag{6.21}$$

where C is the concentration in the fluid for a particle of radius r, C_0 is the bulk saturation concentration, R is the gas constant. Again, γ_{Lv} is the appropriate parameter since dissolving a layer from the solid changes the Lagrangian area. Similar to Eq. (6.21), the equilibrium vapor pressure P for a single component solid sphere with a radius r, assuming that the vapor is monatomic, is shown as

$$P = P_0 \exp(2\gamma_{Lv}V/rRT) \tag{6.22}$$

Consideration is now given to P of a dilute interstitial component. Assuming the component vaporizes in monatomic form, there is

$$P = P_0 \exp(2fV_i/rRT) \tag{6.23}$$

where V_i is the partial molar volume of the component in the solid. In this case, f is valid because transfer of interstitial component atoms does not change the Lagrangian area but does work against f if the component has a nonzero partial molar volume.

As a final example, the vapor pressure of a dilute substitutional component that vaporizes in monatomic form has the following equation,

$$P = P_0 \exp\{2[\gamma_{Lv}V + f(V - V_i)]/rRT\}. \tag{6.24}$$

The term involving γ_{Lv} accounts for the change in Lagrangian area, while the term involving f reflects the work performed against the surface stress when V_i of the substitutional component differs from V.

Many derivations in literature do not employ correct expression for the Laplace pressure of a solid, using γ instead of f in Eq. (6.18). As a result, they apply only to the rare special case of $f = \gamma$. Even though some derivations using the incorrect expression for the Laplace pressure for the solid can produce the correct result (as is often the case for many derivations of Eqs. (6.21) and (6.22)), it is obviously impossible to obtain Eqs. (6.23) and (6.24) without considering effect of f.

6.3.5 Wulff Construction and Adsorption on Solid Surfaces [5, 8]

The anisotropy of γ_{sv} determines the equilibrium shape of small crystals at a particular T. The crystal is assumed to be of macroscopic (or at least) size so that edge and apex effects can be neglected. The equilibrium crystal shape (ECS) at constant T with fixed V and μ is determined by minimizing the sum of $\gamma_{sv}A$, namely, $G = \oint \int\limits_{A(V)} \gamma_{sv}(n)\mathrm{d}A$ with a fixed V. The Wulff theorem states that ECS is not necessarily the state of the minimum surface area. It may be a complex polyhedron with the lowest total surface energy for a given V. A minimal surafce only occurs for a perfectly spherical Wulff plot with a sphere ECS, i.e., an isotropic excess surface free energy. This has been experimentally shown for water droplets in the absence of gravity. For crystals, the variation of γ_{sv} with the normal $\boldsymbol{n}$ produces, on each surface element dA, a force proportional to $\partial\gamma_{sv}/\partial\boldsymbol{n}$, which alters its direction at the same time as γ_{sv} would like to shrink its area. Consequently, ECS can be no longer a sphere. Figure 6.10 schematically shows Wulff plot $\gamma_{sv}(\boldsymbol{n})$ in two dimensions, which governs the equilibrium shape and the morphological stability of a crystal. In a real three-dimensional crystal the situation is more complicated.
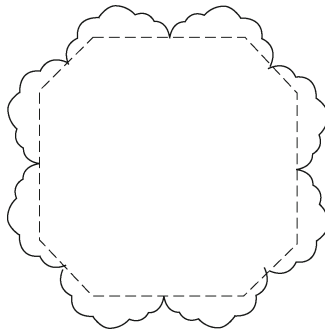
Fig. 6.10 A polar plot of the surface free energy for a 2D crystal (solid line) and the ECS based on the Wulff construction (dotted line).

Besides the variation of γ_{sv} with the surface normal, also the strength of the variation plays a role. This is demonstrated in Fig. 6.11. The ECS is constructed for Si taking into account γ_{sv} values of four orientations, namely, [001], [011], [113], and [111]. In Fig. 6.11(a) and (b) the same energetic ordering of $\gamma_{111} < \gamma_{100} < \gamma_{110} < \gamma_{113}$ but different values have been used. The first parameter set is derived from measurements while the second one has been calculated by an *ab initio* method. Qualitatively the shapes in Fig. 6.11(a) and (b) are the same. However, the relative areas of the crystalline facets vary with the absolute numbers of the various energy. Considering only the

two lowest γ_{sv} values for (111) and (100) orientations, the cubic symmetry suggests that the Wulff shape is a regular octahedron with (111) facets truncated at each apex by (100) planes perpendicular to the cube axes at the same distance from the octahedron center. The inclusion of the (113) energy destroys the octahedral shape discussed frequently for homopolar semiconductors. On the other hand, the (110) facets in the tetrakaidecahedron (Fig. 6.11(a)) disappear completely in Fig. 6.11(b), indicating the influence of the absolute values of γ_{sv}.

(a)   (b)
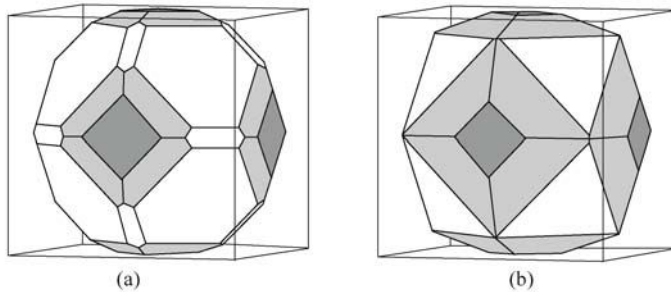
Fig. 6.11   Equilibrium shapes of a Si crystal based on the Wulff construction using (a) experimental values or (b) calculated values. Four surface orientations are considered. The areas with the orientation sequence (100), (311), (110), and (111) vary from black to white.

Crystalline facets, part of a Wulff construction, are thermodynamically stable. Since all four orientations considered appear on the ECSs to a certain extent in Fig. 6.11, the four reconstructed or relaxed surfaces (111), (110), (100), and (311) are stable surfaces in this respect. Of course, the (110) areas in Fig. 6.11(b) are negligibly small because of the high value of γ_{110}. The inclusion of the $16{\times}2$ reconstruction of the Si(110) surface should, however, lower this value.

The existence of γ_{sv} leads to adsorption. In a bulk material, all the bonding requirements (be ionic, covalent, or metallic) of the constituent atoms of the material are filled by other atoms in the material. However, atoms on the surface of the adsorbent are not wholly surrounded by other adsorbent atoms and therefore can attract adsorbates. The exact nature of the bonding depends on the details of the species involved, but the adsorption process is generally classified as physisorption (characteristic of weak van der Waals forces) or chemisorption (characteristic of covalent bonding). The heat evolved in the physisorption process is of the order of magnitude of the heat evolved in the process of condensing the gas, and the amount adsorbed may correspond to several monolayers. Physical adsorption is readily reversed by lowering the pressure of the gas or the concentration of the solute, and the extent of physical adsorption is smaller at higher T due to the entropy ef-

fect. Chemisorption involves the formation of chemical bonds, which may be so tight that the original species may not be recovered. For example, when oxygen is adsorbed on graphite, heating the surface in a vacuum leads to the formation of carbon monoxide. The rate of chemisorption may be fast or slow, depending on the activation energy. Physical adsorption of a gas may occur at a low T and the gas may become chemisorbed when T is raised. Chemisorbed gases cannot be removed by simply exposing a solid surface to a vacuum.

Adsorption is usually described through isotherms, that is, the amount of adsorbate on the adsorbent as a function of its P (if it is a gas phase) or concentration (if it is a liquid phase) at constant T. The quantity adsorbed is nearly always normalized by the mass of the adsorbent to allow comparison of different materials. To discuss the theory of adsorption we first consider a very simple model treated by Langmuir. It is a semi-empirical isotherm derived from a proposed kinetic mechanism based on four assumptions: (1) The surface of the adsorbent is uniform, that is, all the adsorption sites are equivalent. (2) Adsorbed molecules do not interact. (3) All adsorption occurs through the same mechanism. (4) At the maximum adsorption, only a monolayer is formed: molecules of adsorbate do not deposit on other already adsorbed molecules of adsorbate, only on the free surface of the adsorbent.

If θ_s is the fraction of the surface occupied by gas molecules, the rate of evaporation from the surface is $k_{-1}\theta_s$, where k_{-1} is the rate of evaporation from the completely covered surface at a certain T. The rate of adsorption of molecules on the surface is proportional to the fraction of the area that is not covered $(1 - \theta_s)$ and to P of the gas. Thus the rate of condensation is expressed as $k'(1 - \theta_s)P$, where k is a constant at a given T and includes a factor to allow for the fact that not every gas molecule that strikes an unoccupied space will stick.

In equilibrium, the rate of evaporation of the adsorbed gas is equal to the rate of condensation,

$$k_{-1}\theta_s = k'(1 - \theta_s)P. \tag{6.25}$$

We have thus

$$K = \frac{k'}{k_{-1}} = \frac{\theta_s}{(1 - \theta_s)P}, \quad \text{or} \quad \theta_s = \frac{KP}{1 + KP} \tag{6.26}$$

where P is the partial pressure of the gas or the molar concentration of the solution. $\theta_s \approx KP$ at very low P and $\theta_s \approx 1$ at larger P. Since the volume V of gas adsorbed is proportional to $\theta_s, \theta_s = V/V_m$ and we obtain a straight line,

$$\frac{1}{V} = \frac{1}{V_m} + \frac{1}{V_m KP}. \tag{6.27}$$

Through its slope and y-axis intercept we can obtain V_m and K, which are constants for each adsorbent/adsorbate pair at a given T. In fact, some data do not show asymptotic saturation and do not give a linear plot except at low

P. Thus adsorption on solids is more complicated than that the Langmuir theory has indicated.

In physical adsorption, molecules of a gas may be adsorbed to the depth of many monolayers. In 1938, Brunauer, Emmett, and Teller developed an isotherm model, or BET theory, that takes that possibility into account. The derivation of the formula is more complicated than Langmuir's. The result is

$$\frac{x}{V(1-x)} = \frac{1}{V_{\mathrm{m}}c} + \frac{x(c-1)}{V_{\mathrm{m}}c}$$

where x is the pressure divided by the vapor pressure for the adsorbate at a T (usually denoted by P/P^0), $c = KP$ where K is determined by Eq. (6.26). The key assumption used in deriving BET equation is that the successive adsorption heat for all layers except the first one equals the condensation heat of the adsorbate.

6.4 Solid-liquid Interface Energy

6.4.1 Bulk Solid-liquid Interface Energy and That at Melting Points [3, 9, 10]

The bulk solid-liquid interface free energy γ_{sL0}, which is defined as the reversible work required to form or to extend a unit area of interface between a crystal and its coexisting fluid plastically, is one of the fundamental materials properties. It plays a key role in many practically important physical processes and phenomena like homogeneous nucleation, crystal growth from the melt, surface melting and surface roughening, etc. Thus, a quantitative knowledge of γ_{sL0} values is necessary. However, direct measurements of γ_{sL0} are not at all easy even for elements in contrast to the case of interface energy of bulk liquid-vapor γ_{Lv0}. Some attempts are made to obtain γ_{sL0} by theoretical approaches or computer simulations. A widely used technique in an indirect way to determine γ_{sL0} value is nucleation experiments of undercooled liquid based on the classical nucleation theory (CNT), which was made firstly by Turnbull. According to CNT, the undercooled liquid crystallizes at nucleation temperature T_{n} with a critical nucleation size r^* induced by a localized structural and energetic fluctuation where the thermodynamic properties of nanometric aggregates of the newly nucleated phase are the same as those of the corresponding bulk one. Thus, the nucleus-liquid interface energy $\gamma_{\mathrm{sL}}(r^*, T_{\mathrm{n}})$ at T_{n} is treated as the respective value for a planar interface γ_{sL0}' being temperature-independent (this assumption is known as the capillarity approximation), which makes it possible to consider the Gibbs free-energy difference of a spherical nucleus in the liquid $\Delta G(r, T)$ as a sum

of a volume term and an interface term as Eq. (4.40). With a consideration for homogeneous nucleation rate, γ_{sL0} in Eq. (4.40) can be determined, which as an empirical relationship is proportional to ΔH_{m},

$$\gamma_{\mathrm{CNT}} = \tau \Delta H_{\mathrm{m}}/(V_s^{2/3} N_{\mathrm{A}}^{1/3}) = \tau h \Delta H_{\mathrm{m}}/V_s \qquad (6.28)$$

where Turnbull coefficient τ is considered to be 0.45 for metals (especially closed-packed metals) and 0.34 for nonmetallic elements at about 20% of undercooling below T_{m}, V_s is the g-atom volume of the crystal, h is the atomic diameter, and N_{A} is the Avogadro constant. A computer simulation confirms this empirical relationship where τ calculated for the interfaces of (111), (100) and (110) of an fcc crystal is 0.36, 0.35, 0.37, respectively, or γ_{CNT} for the fcc crystal has a small anisotropy. According to the review papers of Eustathopoulos and Kelton, $\tau = 0.55 \pm 0.08$ and $\tau = 0.49 \pm 0.08$ for metals while τ increases noticeably for molecules having more asymmetry. Equation (6.28) would seem capable of predicting γ_{CNT} quite accurately for many crystals.

However, the droplet technique has been modified and improved recently. The results of maximum supercooling are much more than those found by Turnbull before, which in many cases are about twice as much. According to CNT, this means that the γ_{CNT} values measured by Turnbull are lower than real γ_{sL} ones for metals. In addition, the existence of τ to be determined also weakens the theoretical meaning of this equation, and makes it only an empirical rule. Moreover, Eq. (6.28) overlooks some important pieces of physics and will be considered later.

Although Eq. (6.28) underestimated γ_{sL} values, Eq. (6.28) has been rationalized in terms of interfacial bonding models by Ewing, thus it reads

$$\gamma_{\mathrm{sL}} = h \Delta H_{\mathrm{m}}/(4V_s) + (N_{\mathrm{A}} b' k/V_{\mathrm{L}}) \int_0^{b'} g_{\mathrm{L}}(r) \ln g(r) \mathrm{d}r \qquad (6.29)$$

where $g_{\mathrm{L}}(r)$ is the liquid radial distribution function, b' is the cut-off distance beyond which $g_{\mathrm{L}}(r)$ shows no significant deviation from unity, k is Boltzmann's constant, and V_{L} is the g-atom volume of the liquid. The approach of Miedema and den Broeder results in

$$\gamma_{\mathrm{sL}} = 0.211 \Delta H_{\mathrm{m}}/(V_s^{2/3} N_{\mathrm{A}}^{1/3}) + 0.52 \times 10^{-7} T/V_s^{2/3} \qquad (6.30)$$

while that of Gránásy and Tegze yields

$$\gamma_{\mathrm{sL}} = \phi(\Delta H_{\mathrm{m}} + T \Delta S_{\mathrm{m}})/[2(V_s^{2/3}/N_{\mathrm{A}}^{1/3})]. \qquad (6.31)$$

In Eq. (6.31), ϕ is a geometric factor ranging from 0.29 to 0.63 for cubic or hcp structure, depending on the interface orientation.

It is known that the most powerful method available for theoretically estimating γ_{sL} is to directly use the so-called Gibbs-Thomson equation (known

also as the Kelvin equation), which describes the equilibrium between a small solid nucleus and the infinite amount of its liquid, as follows:

$$T_{\mathrm{m}}(r, r')/T_{\mathrm{m}} = 1 - V_{\mathrm{s}}\gamma_{\mathrm{sL}}(1/r + 1/r')/\Delta H_{\mathrm{m}}. \tag{6.32}$$

r and r' in Eq. (6.32) are principal radii of curvature of the crystal in equilibrium on the interface with the liquid at $T_{\mathrm{m}}(r, r')$. Equation (6.32) is valid when r and r' are large enough (say 10 nm) and thus the crystal retains its bulk values of γ_{sL0}, V_{s} and ΔH_{m}. For an actual γ_{sL} measurement, $r = r'(d = 1$ and $r_0 = 2h)$ or $r = r$ and $r' = \infty(d = 2$ and $r_0 = h)$ can be taken.

$T_m(r)$ function has been described by Eqs. (3.80) and (3.84),

$$T_{\mathrm{m}}(r)/T_{\mathrm{m}}(\infty) = \exp\{-[2\Delta S_{\mathrm{vib}}/(3R)]/[(r/r_0) - 1]\}. \tag{6.33}$$

When $r > 10r_0 \approx 10$ nm, in terms of the mathematical relationship of $\exp(-x) \approx 1 - x$, equation (6.33) is written as

$$T_{\mathrm{m}}(r)/T_{\mathrm{m}} \approx 1 - 2r_0\Delta S_{\mathrm{vib}}/(3Rr). \tag{6.34}$$

Through comparing Eqs. (6.32) and (6.34) with respect to Eq. (3.79),

$$\gamma_{\mathrm{sL0}} = 2h\Delta S_{\mathrm{vib}}\Delta H_{\mathrm{m}}/(3V_{\mathrm{s}}R). \tag{6.35}$$

Equation (6.35) is similar to the Turnbull's empirical equation (Eq. (6.28)) where $\tau = 2\Delta S_{\mathrm{vib}}/3R$. Thus, τ is not a constant, but dependent on ΔS_{vib}. Since for all kinds of crystals except the semiconductors, there is $\Delta S_{\mathrm{vib}} \approx \Delta S_{\mathrm{m}}$, each parameter in Eq. (6.35) is known. Thus, Eq. (6.35) can predict γ_{sL0} values directly.

To confirm the generality of Eq. (6.35), the values of $\gamma_{\mathrm{sL0}}(T_m)$ for different types of elemental crystals including true metals, semi-metals, and semiconductors are predicted and shown in Table 6.1. For comparison, the corresponding experimental γ_{exp} and γ_{TS} based on the Turnbull-Spaepen relation are also shown in Table 6.1 noting that the Turnbull-Spaepen relation is read as

$$\gamma_{\mathrm{TS}} = 0.6[M/(\rho_{\mathrm{liq}}N_{\mathrm{A}})]^{1/3}\Delta H_{\mathrm{m}} \tag{6.36}$$

with M being the atomic mass.

Although Eq. (6.35) overestimates γ_{sL0} of metals at T_m typically by 50% to 100% in comparison with that obtained from CNT or the undercooling experiments of liquid droplets of elements, typically from the Turnbull's work, the predicted γ_{sL0} values are in agreement with those of γ_{exp} and γ_{TS} except for Si (the reason will be explained later) and Mo where the reason remains unknown. As for Cr, the larger deviation between γ_{sL0} and γ_{TS} may result from lower ΔS_{m} value, which is thought not to present its true value. When 151, 215, 85, 48 and 88 (mJ·m^{-2}) for Al, Au, Sn, Pb and Bi in light of Eq. (6.35) are compared with the corresponding experimental values of 131–151, 270±10, 62±10, 40±7 and 55–80 (mJ·m^{-2}) derived from measurements of

T_m depression, the theoretical data are 120, 151, 83, 71 and 95 (mJ·m^{-2}). It is obvious that Eq. (6.35) corresponds better to the experimental results than the latter theoretical results especially for Al, Au, Pb and Bi. Thus, Eq. (6.35) can quantitatively estimate γ_{sL0} values of metals.

Table 6.1 Comparisons of $\gamma_{sL0}(T_m)$ among Eq. (6.35), γ_{TS} by Eq. (6.36), and γ_{exp}. ΔS_{vib} is determined by Eq (3.38a) for Al and Sn, by Eq. (3.38b) for Ga, by Eq. $S_{vib} \approx S_m - S_{el}$ for Ge, Si, Sb, Te and Bi. Since ΔS_{el} of Si, Sb, Te and Bi are unknown, $\Delta S_{el}/\Delta S_m$ for these semiconductors are assumed to be the same as those for Ge with $\Delta S_{el} = 16.8$ J·g-atom^{-1}·K^{-1}. ΔS_{vib} for the rest elements is determined by Eq. (3.37). γ in mJ·m^{-2}, h in nm, ρ in g·cm^{-3}, V in cm^3·g-atom^{-1}, ΔH_m in kJ·g-atom, T_m in K, $\Delta V/V$ in %, ΔS_{vib} in J·g-atom^{-1}·K^{-1}

	γ_{sL0}	γ_{TS}	γ_{exp}	h	ρ_{liq}	ρ_s	V_s	ΔH_m	T_m	$\Delta V/V$	ΔS_{vib}
Ti	216	234		0.290	4.11		10.6	15.5	1943	3.2	6.80
V	364	354		0.262	5.56		8.8	20.9	2175	5.2	7.86
Cr	272	326		0.250	6.28	7.20	7.2	16.9	2130	7.2	6.08
Mn	243	246		0.273	5.73		7.4	12.1	1517	1.7	7.26
Fe	236	276	221	0.248	7.01		7.1	13.8	1809	3.4	6.47
Co	353	338		0.251	7.76		6.7	16.1	1768	3.5	7.85
Ni	421	367	326	0.249	7.91		6.6	17.2	1726	5.4	8.11
Cu	297	261	270	0.256	8.00		7.1	13.0	1358	4.2	7.75
Zn	137	122	141	0.267	6.58		9.2	7.3	693	4.3	8.60
Zr	192	208		0.318	6.24		14.1	16.9	2125	3.5	6.69
Nb	402	400		0.286	7.62	8.55	10.9	26.4	2740	5.5	7.73
Mo	626	533		0.273	9.00	10.2	9.4	32.0	2890	6.4	9.01
Tc	441	425		0.270	10.2	11.5	8.5	24.0	2473	5.8	7.74
Ru	431	434		0.265	10.7	12.2	8.3	24.0	2523	7.0	7.51
Rh	387	391		0.269	10.7	12.4	8.3	21.5	2236	8.9	7.41
Pd	311	304		0.275	10.5		8.9	17.6	1825	5.9	7.64
Ag	199	176		0.289	9.34		10.3	11.3	1234	3.8	7.82
Cd	92	81		0.298	8.02		13.1	6.1	594	3.8	8.87
Hf	341	310		0.313	11.9	13.1	13.7	24.0	2500	3.2	8.45
Ta	472	477		0.286	14.6	16.6	10.9	31.6	3287	6.7	7.60
W	511	582		0.274	16.2	19.3	9.5	35.4	3680	12	6.62
Re	541	581		0.274	18.0	21.0	8.8	33.2	3453	9.7	6.91
Os	525	572		0.268	19.2	22.4	8.5	31.8	3300	9.7	6.93
Ir	468	464		0.271	20.0	22.5	8.6	26.0	2716	5.5	7.67
Pt	336	333		0.278	19.0		9.1	19.6	2045	6.6	7.58
Au	215	201	270±10 190	0.288	17.4		10.2	12.5	1338	5.2	7.62
Hg	29	28		0.301	13.4		14.8	2.3	234	3.7	8.51
In	35	38		0.325	7.02		15.7	3.3	430	2.7	6.70
Tl	39	45		0.341	11.2		17.2	4.2	577	3.2	6.13
Pb	48	49	40±7	0.350	10.7		18.2	4.8	601	3.6	6.77
Se	72	78		0.232	3.99	4.80	16.5	6.7	494	13	10.2
Al	151	170	149	0.286	2.39		10.0	10.8	933		6.15
Sn	89	79	62±10	0.281	7.00		16.7	7.0	505		9.22
Ga	87	76		0.244	6.09		11.8	5.6	303		10.1
Ge	412	453		0.245	5.60		13.6	31.8	1210		9.40
Si	738	672	332	0.235	2.51		12.1	50.0	1685		10.3
Sb	185	200		0.290	6.48		18.2	19.7	904		7.80
Te	158	168		0.286	5.71		20.5	17.5	723		8.65

Continue

	γ_{sL0}	γ_{TS}	γ_{exp}	h	ρ_{liq}	ρ_s	V_s	ΔH_m	T_m	$\Delta V/V$	ΔS_{vib}
Bi	88	101	55–80	0.309	10.1		21.3	10.9	545		7.20
Li	31	38	30	0.304	0.51		13.1	3.0	454	2.2	5.77
Na	19	22	20	0.372	0.94		23.7	2.6	371	2.5	6.15
K	11	13		0.454	0.83		45.5	2.3	336	2.6	6.06
Rb	10	11		0.495	1.46		55.9	2.2	313	2.5	6.17
Cs	8	9		0.531	1.84		71.1	2.1	302	2.6	6.06
Be	287	303		0.223	1.69	1.85	5.0	12.2	1560	2.5	6.96
Mg	115	113		0.320	1.59		14.0	8.7	922	3.6	8.15
Ca	60	61		0.395	1.37		26.2	8.5	1112	4.1	6.24
Sr	56	58		0.430	2.37	2.60	33.7	8.3	1041	2.7	7.06
Ba	45	49		0.435	3.20	3.50	39.2	7.8	1002	2.4	6.94

The dependence of γ_{sL0} on crystal structure is crucial to understand the role of metastable structures in nucleation pathways. In 1897, Ostwald formulated his "step rule", which states that nucleation from the melt occurs to the phase with the lowest activation barrier, but not necessarily to the thermodynamically most stable bulk phase. In the case of the nucleation of fcc crystals, there is evidence that crystallization often proceeds first through the formation of bcc nuclei, which transforms to fcc crystals later in the growth process. This phenomenon has been observed in experiments on metal alloys, in computer simulations of Lennard-Jones particles and weakly charged collides. These results could be interpreted as that if γ_{sL0} for bcc crystals were significantly lower than those for fcc crystals in these systems, substantially lower activation barriers would be brought out. Using a simple model of interfacial structure, Spaepen and Meyer predicted that γ_{sL0} for bcc-melt interfaces (γ^{bcc}) should be about 20% lower than that for fcc-melt interfaces (γ^{fcc}), based on packing considerations. Molecular dynamics (MD) simulation results of Fe also show that $\gamma^{bcc}/\gamma^{fcc} = 65\%$–$70\%$. Equation (6.35) can also easily confirm this difference. Since the difference of V between bcc and fcc iron is only 1.3%, the effect of the change of V can be neglected. Thus, $\gamma^{bcc}/\gamma^{fcc} \approx (\Delta H_m^{bcc}/\Delta H_m^{fcc})(\eta^{bcc}/\eta^{fcc})^{1/3}$ in terms of Eq. (6.35). With the known values of $\Delta H_m^{bcc}/\Delta H_m^{fcc} \approx 0.72$ and $\eta^{bcc}/\eta^{fcc} \approx 0.92$, $1 - \gamma^{bcc}/\gamma^{fcc} \approx 0.3$, which is consistent with the reported values of 30%–35%. Moreover, from the viewpoint of the internal energy change, the change from the melt to bcc structure should be smaller than that to fcc structure, which leads to also small activation barrier.

Table 6.2 shows γ_{sL0} values of 15 organic molecular crystals, the predictions in terms of Eq. (6.35) partly correspond to the latest experimental results but are less than the early experimental results. Organic crystals as molecular crystals differ from metallic and ionic ones, whose chemical bonds are covalent within molecules but consist of van der Waals forces or hydrogen bonds among molecules. The former, being responsible for stability of individual molecules, is much stronger than the latter, being primarily responsible for bulk properties of matter, such as γ_{sL0}. Because bond strength of van der Waals forces or hydrogen bonds is weaker than that of metallic

or ionic bonds, γ_{sL0} values of organic crystals are also smaller than those of metallic and ionic crystals, such as Pb with $\gamma_{sL0} \approx 40\pm7$ mJ·m^{-2} (this value in fact is one of the smallest γ_{sL0} values among metallic or ionic crystals due to its small ΔS_m and ΔH_m values in terms of Eq. (6.35)). Moreover, γ_{sL0} values of compounds composed of full hydrogen bonds, such as H_2O with $\gamma_{sL0} \approx 25$–45 mJ·m^{-2}, should also be larger than those of organic crystals since organic crystals consist of hydrogen bonds and van der Waals force. Thus, $\gamma_{sL0} < 30$–40 mJ·m^{-2} for organic crystals.

Table 6.2 Comparisons of $\gamma_{sL0}(T_m)$ between Eq. (6.35) and available experimental results γ_{exp} for ice and organic crystals where γ_{Lv0} values are also listed

	γ_{sL0}	γ_{exp}	γ_{Lv0}	m	n	h	V_s	ΔH_m	ΔS_{vib}
Ice	56	44±10 45±15		3	1	0.310	6.55	2006	7.34
Benzene	15.4	15.7 22±2	28.9	12	1	0.503	6.40	829	2.95
Naphthalene	18.6	8.2 61±11	28.8	18	2	0.452	6.18	1062	2.98
Ethylene dibromide	16.4	19.5 35±7	38.4	8	2	0.509	19.8	1368	5.81
Cis-decalin	8.5	11.6	32.2	28	2	0.503	5.48	515	2.24
Trans-decalin	9.6	18.4	29.9	28	2	0.509	5.67	516	2.59
Chlorobenzene	15.7	14.1	33.6	12	1	0.534	7.66	802	3.50
Cyclohexane	3.1	4.6	25.5	18	1	0.547	5.46	150	2.55
Heptane	10	17.1	20.1	23	7	0.302	5.04	616	3.34
Stearic acid	14.3	106–151 151±10 135–180	28.9	56	18	0.294	7.83	1010	2.95
Myristic acid	16.0	81 116±10	28.6	44	14	0.292	10.8	1031	3.15
Lauric acid	13.9	71 ±15 100±15	28.5	38	12	0.299	4.90	964	3.05
Pivalic acid	2.4	2.8 2.7±0.2		17	1	0.572	6.60	146	2.33
Carbontetrabromide	10.6	10–20 28±4		5	1	0.540	19.0	790	5.89
Succinonitrile	7.3	8.9 7.9±0.8	47	10	2	0.402	6.20	370	3.78
Diphenyl	14.4	24 50±10	34.5	22	2	0.505	7.06	905	2.78

It is known that organic molecules mostly consist of C-H bonds with intermolecular dispersion forces caused by relative movement between electrons and the atomic nucleus. Their relative movements change the electron density within the molecule. Generally, the larger the number of electrons and the more diffuse the electron cloud in the molecule, the greater the dispersion forces in the molecule. However, the forces hardly affect the net attraction

applied to a unit area of interface, the size difference of γ_{sL0} values for organic molecules thus is smaller than that of metallic and ionic crystals (for other three that of intermolecular forces, orientation forces and induced forces, a similar discussion may be held).

Although measured γ_{sL0} values of organic crystals composed of chain molecules are much larger than the above limits shown in Table 6.2, their real values should be similar to those composed of spherical molecules since γ_{sL0} denotes excess energy of unit area where molecular weight has negligible effect on it. Even if chain molecules may contain one or more hydrogen bonds, γ_{sL0} values still vary little since the most bonds of the molecules are van der Waals forces. This result also implies that anisotropy of γ_{sL0} of organic crystals is small.

Moreover, for a typical fcc crystal, bond number decrease of molecules on a solid-liquid interface is usually 1–2 while that on a liquid-vapor interface is 3–4. If this bond number is roughly proportional to the corresponding interface energy, with the note that the bond strength difference of molecules between solid and liquid states is only several percent, $\gamma_{sL0} < \gamma_{Lv0}$ while γ_{Lv0} is easy to measure with better measuring accuracy. Thus, γ_{Lv0} value is good reference as an upper limit of γ_{sL0}. For organic crystals, $\gamma_{sL0} \approx \gamma_{Lv0}/2$ as a rough estimation. Since $\gamma_{Lv0} \approx 20$–40 mJ·m^{-2} shown in Table 6.2, $\gamma_{sL0} < 20$ mJ·m^{-2}, which is also smaller than the above-stated limits in terms of considerations of the bond strength of metallic, ionic, and hydrogen bonds. On the basis of the above consideration, it is known that γ_{sL0} values of organic molecules must be smaller than those of the other types of crystals. Equation (6.35) is in agreement with the principles of $\gamma_{sL0} < \gamma_{Lv0}$ and with the upper size limit of γ_{sL0} values.

In Table 6.2, although $\gamma_{sL0} < 20$ mJ·m^{-2} as analyzed for organic crystals in the above discussion, γ_{sL0} values of different organic crystals change from 0.62 mJ·m^{-2} for cyclohexane to 19.7 mJ·m^{-2} for ethylene dibromide, their sizes differences are about 30 times. This difference is analyzed in Eq. (6.35) where the variants are h, $\Delta S_m/R$, and $\Delta H_m/V_s$. Since h varies a little for different substances, $\Delta H_m/V_s$, denoting the energetic difference between crystal and liquid, and $\Delta S_m/R$, showing that the corresponding structural difference is more important. $\Delta H_m/V_s$ values are between 27 and 172 J·cm^{-3} in Table 6.2, while $\Delta S_m/R$ values are in the range from 0.064 to 0.568. Since $\Delta H_m/V_s$ and $\Delta S_m/R$ for one substance do not simultaneously take the largest values induced by different T_m, with the known fact that $\Delta H_m = T_m \Delta S_m$, the real differences in γ_{sL0} values are smaller than the largest possible one.

For intermetallic compounds and oxides listed in Table 6.3, Eq. (6.35) also corresponds to available theoretical results with the absolute deviation smaller than 6%. Although higher T_m and larger $\Delta V/V$ of these substances make ΔS_{vib} comparable with those of elemental crystals, larger ΔH_m and smaller V_s indicate that their $\gamma_{sL0}(T_m)$ values are larger than those of most elemental crystals.

Table 6.3 Comparison of $\gamma_{\mathrm{sL0}}(T_{\mathrm{m}})$ between γ_{sL0} by Eq. (6.35) and other theoretical results γ' for intermetallic compounds and oxides

	γ_{sL0}	γ'	h	ρ_{s}	V_{s}	ΔH_{m}	T_{m}	$\Delta V/V_{\mathrm{s}}$	ΔS_{vib}
α-MoSi$_2$	651	620	0.277	6.27	8.1	28.2	2173	29	8.4
β-MoSi$_2$	538	509	0.460	6.32	8.0	22.9	2303	35	5.1
WO$_3$	233	241	0.193	7.2	8.1	17.9	1743	18	6.8
ZrO$_2$	491	500	0.223	5.89	7.0	29.1	2988	15	6.6
Ref			57,60–61	56–57		56	56–57	57,62	

6.4.2 Size Dependence of Solid-liquid Interface Energy [3]

For comparison, γ_{CNT} values for elemental crystals Au, Al, Sn, Pb and Bi in terms of Eq. (6.28) are 132, 93, 33.6, 54.5 and 54.4 (mJ·m^{-2}), which correspond to the lower limits of the corresponding experimental data for Sn, Pb and Bi, but are by far lower than those for Au and Al. This disagreement results from the two approximations in the CNT: (1) The heat capacity difference between solid and liquid ΔC_p is assumed to be zero. Namely, the influence of ΔC_p is neglected, or $\Delta H_{\mathrm{m}}(T)$ is independent of temperature. (2) The nucleus-liquid interface energy $\gamma_{\mathrm{sL}}(r^*, T_{\mathrm{n}})$ is treated as the value for a temperature-independent planar interface γ_{CNT}, i.e. the capillarity approximation. Since the values of γ_{CNT} in Eq. (6.28) are initially obtained for nuclei-liquid interface while any nucleus during solidification is in nanometer size range, $\gamma_{\mathrm{sL}}(r)$, not γ_{sL0}, has to be considered.

To determine $\gamma_{\mathrm{sL}}(r)$ function, we consider a compressible spherical particle, or a cube with cube side taken as r, immersed in the corresponding bulk liquid. According to Laplace-Young equation, $\Delta P = 2fA/(3V) = 2f/r$ (Eq. (6.18)). Using the definition of $\beta = -\Delta V/(V\Delta P), \varsigma = \Delta r/r = \Delta A/(2A) = \Delta V/(3V)$ under small strain and $A/V = 3/r$ where Δ denotes the difference,

$$\varsigma = -2\beta f/(3r). \tag{6.37}$$

In terms of a scalar definition of f, there exists

$$f = \partial G/\partial A = \partial(\gamma_{\mathrm{sL}} A)/\partial A = \gamma_{\mathrm{sL}} + A\partial\gamma_{\mathrm{sL}}/\partial A \approx \gamma_{\mathrm{sL}} + A\Delta\gamma_{\mathrm{sL}}/\Delta A \tag{6.38}$$

where $G = \gamma_{\mathrm{sL}} A$ states the total excess Gibbs surface free energy, or $\Delta\gamma_{\mathrm{sL}} = (\Delta A/A)(f - \gamma_{\mathrm{sL}})$.

To find mathematical solutions of f and γ_{sL} or $\gamma_{\mathrm{sL}}(r)$, two boundary conditions of $\gamma_{\mathrm{sL}}(r)$ are needed. An understandable asymptotic limit is that as $r \to \infty, \gamma_{\mathrm{sL}}(r) \to \gamma_{\mathrm{sL0}}$. As $r \to \infty$, let

$$\Delta\gamma_{\mathrm{sL}} = \gamma_{\mathrm{sL}}(r) - \gamma_{\mathrm{sL0}}. \tag{6.39}$$

Substituting Eq. (6.39) into Eq. (6.38) and taking in mind that $V/A = r/3$ and $\Delta A/A = 2\beta = -4\beta f/(3r)$ in terms of Eq. (6.16), it reads

$$\gamma_{\mathrm{sL}}(r)/\gamma_{\mathrm{sL0}} = [1 - 4\beta f^2/(3\gamma_{\mathrm{sL0}}r)]/[1 - 4\beta f/(3r)]. \tag{6.40}$$

Equation (6.40) is consistent with general calculations of thermodynamics and quantum chemistry for particles.

Another boundary condition of $\gamma_{sL}(r)$ is γ_{sL0} value at the smallest size r_0 where almost all atoms of a low-dimensional crystal immersed in fluid are located on its surface with a radius of r_0 and the crystal is assumed to be indistinguishable from the surrounding fluid. Thus, the solid-liquid interface is at all diffuse where the crystal is similar to a cluster produced by an energetic fluctuation of the fluid. As a result, $\gamma_{sL}(r_0) \to 0$ where $hA/V = 1 - V_i/V = 1 - [(r_0 - h)/r_0]^{3-d} = 1$ with V_i being the interior volume of the crystal. r_0 depends on the existence of curvature. When a crystal has plane surface, such as films, $r_0 = h$. For crystals with curved surfaces, such as particles or wires, $r_0 > h$. As a first order approximation, $r_0 \approx 3h/2$ where $hA/V = 26/27$ for a spherical particle. In summary,

$$r_0 = 3h/2, \quad \text{for curved surface,} \tag{6.41a}$$

$$r_0 = h, \quad \text{for plane surface.} \tag{6.41b}$$

Now Eq. (6.40) can be rewritten as

$$\gamma_{sL}(r)/\gamma_{sL0} = [1 - r_0/r]/[1 - \gamma_{sL0}r_0/(fr)] \tag{6.42}$$

with $4\beta f^2/(3\gamma_{sL0}) = r_0$ or $f = \pm[(3\gamma_{sL0}r_0)/(4\beta)]^{1/2}$. The different signs of f correspond to the tensile $(+)$ and compressive $(-)$ stress on the surface. The possible physical background of the positive or negative f could be illustrated based on the following mechanism: Atoms at the interface suffer a CN reduction, bond contracts spontaneously, which leads to the enhancement of the atomic binding energy and hence the tensile stress, or $f > 0$. This is the case of free nanoparticles. When the interface atoms of different elements are intermixing, CN or the bond strength may increase, such as alloying or compound formation. The alloying and chemical reaction may alternate the atomic valences, which may introduce repulsive stress of the ions or electronic changes.

The above deduced f is in fact the solid-liquid interface stress f_{sL}, which differs from the solid-vacuum surface stress f_{sv}. It is assumed that $f \approx f_{sL}(T_m) \approx f_{sv}(T_m)$ because the interface stress induced by the elastic strain of a solid remains almost constant when the vacuum is substituted by the liquid on the solid surface where the liquid affects little the elastic strain of the solid. For the most elements, f is one order larger than γ_{sL0}. Although some MD work based on a hard-sphere model shows that f has the same magnitude of γ_{sL0}, the hard-sphere model itself may lead to this result where strain is absent, this and f co-exist Thus, when $f > 10\gamma_{sL0}$, Eq. (6.42) may be simplified to a first order approximation,

$$\gamma_{sL}(r)/\gamma_{sL0} \approx 1 - r_0/r. \tag{6.43}$$

Equation (6.43) denotes $\gamma_{sL}(r) \sim 1/r$ relationship. Figure 6.12 gives an example for comparison between Eq. (6.43) and the computer simulation result of

$\gamma_{sL}(r)/\gamma_{sL0}$ where $\gamma_{sL}(r)$ value reduces as r decreases. The both are in agreement. In Fig. 6.12, since the cited fcc crystal has not given an idiographic substance, the simplified form of Eq. (6.42), namely, Eq. (6.43), is employed.
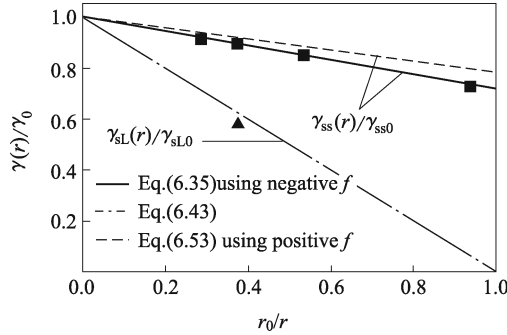
Fig. 6.12 $\gamma(r)/\gamma_0$ as a function of r_0/r in terms of Eqs. (6.43) and (6.53) with $r_0 = 3h/2$. For $\gamma_{ss}(r)/\gamma_{ss0}$ function, the solid line and the dash line are obtained by using negative and positive f, respectively. The symbols ■ and ▲ illustrate the computer simulation results of $\gamma_{sL}(8h)/\gamma_{sL0} = 0.58$ for unknown fcc metal and those for Cu where $\gamma_{ss0} = 594$ mJ·m^{-2}. (Reproduced from Ref. [3] with permission of Elsevier)

At the same time, $\gamma_{sL}(r)$ values of five organic nanocrystals have also been calculated in terms of Eq. (6.42) and are shown in Table 6.4. Equation (6.42) is consistent with experimental observation with the note that there exists a size distribution of nanocrystals. As r decreases, $\gamma_{sL}(r)$ drops. At $r = 2$ nm, the decrease in $\gamma_{sL}(r)$ for different substances is distinct due to different r_0 or r_0/r values. The relative drop of $\gamma_{sL}(r)/\gamma_{sL}(\infty)$ values reaches 20%–40% where r_0 may be near 4 nm. Thus, the energetic resistance to the nucleation process in liquid may be lower than what CNT has estimated. In addition, the success of Eq. (6.42) for $\gamma_{sL}(r)$ values in return confirms again that ΔH_m and ΔS_{vib}, not ΔH_m itself, determine γ_{sL0} values as shown in Eq. (6.35).

Table 6.4 Comparison of $\gamma_{sL}(r)/\gamma_{sL0}$ values between Eq. (6.42) with $r_0 = 3h/2$ and experimental results where the experimental data of $\gamma_{sL}(r = 2$ nm$)$ are obtained by measuring the slope of experimental data of T_m versus $1/r$ with two points of $r = 2$ nm and $r \approx 4.3$ nm in terms of Gibbs-Thomson equation. Since β values of crystals are not found, β values of the corresponding liquid are used, which leads to minor error. Note that β values of naphthalene and trans-decalin have been estimated as those of benzene

	$\gamma_{sL}(r)/\gamma_{sL0}$		$\beta/(\text{MPa}^{-1}\times 10^{-5})$
	Experiments	Eq. (6.42)	
Benzene	0.67	0.66	87
Naphthalene	0.68	0.69	≈ 87
Chlorobenzene	0.89	0.63	67
Heptane	0.63	0.80	134
Trans-decalin	0.60	0.68	≈ 87

6.4.3 Nucleus-liquid Interface Energy [3]

As mentioned in Chapter 4, several improved expressions for $\Delta G_\mathrm{m}(T)$ function have been proposed through considering ΔC_p function below T_m, such as Eqs. (4.52), (5.53) and (4.55), they are adequate for different kinds of substances. These equations predict a steepest variation near T_m, and a much weaker temperature-dependence near T_K, which can be determined by letting $\mathrm{d}\Delta G_\mathrm{m}(T)/\mathrm{d}T = 0$. With these $\Delta G_\mathrm{m}(T)$ functions, the respective $\Delta H_\mathrm{m}(T)$ functions can also be determined in terms of $\Delta H_\mathrm{m}(T) = \Delta G_\mathrm{m}(T) - T\mathrm{d}\Delta G_\mathrm{m}(T)/\mathrm{d}T$ (Helmholtz function),

$$\Delta H_\mathrm{m}^a(T) = 49\Delta H_\mathrm{m}T^2/(T_\mathrm{m} + 6T)^2, \tag{6.44a}$$

$$\Delta H_\mathrm{m}^b(T) = 4\Delta H_\mathrm{m}T^2/(T_\mathrm{m} + T)^2, \tag{6.44b}$$

$$\Delta H_\mathrm{m}^c(T) = \Delta H_\mathrm{m}(T/T_\mathrm{m})^2 \tag{6.44c}$$

where superscripts of "a", "b" and "c" stand for metallic elements, ionic crystals and semiconductors, respectively. Because $\Delta G_\mathrm{m}(T)$ is determined by ΔC_p while ΔC_p between crystal and glass approaches to zero when $T \leqslant T_\mathrm{K}$, the liquid must transform to glass. Thus, Eq. (6.18) is valid only at $T > T_\mathrm{K}$ where $T_\mathrm{K}^{(a)} = (7^{1/2}-1)T_\mathrm{m}/6$, $T_\mathrm{K}^{(b)} = (2^{1/2}-1)T_\mathrm{m}$, and $T_\mathrm{K}^{(c)} = T_\mathrm{m}/2$. Note that $T > T_\mathrm{K}$ is satisfied in undercooling experiments. Combining Eq. (6.25) and Eq. (6.44), the temperature-dependent $\gamma_\mathrm{sL0}(T)$ functions can be expressed as

$$\gamma_\mathrm{sL0}^a(T) = \frac{2h\Delta H_\mathrm{m}\Delta S_\mathrm{vib}}{3RV}\left(\frac{7T}{T_\mathrm{m} + 6T}\right)^2, \tag{6.45a}$$

$$\gamma_\mathrm{sL0}^b(T) = \frac{2h\Delta H_\mathrm{m}\Delta S_\mathrm{vib}}{3RV}\left(\frac{2T}{T_\mathrm{m} + 6T}\right)^2, \tag{6.45b}$$

$$\gamma_\mathrm{sL0}^c(T) = \frac{2h\Delta H_\mathrm{m}\Delta S_\mathrm{vib}}{3RV}\left(\frac{T}{T_\mathrm{m}}\right)^2. \tag{6.45c}$$

$\gamma_\mathrm{sL0}(T)$ in terms of Eq. (6.45) decreases as T drops. As $T \to T_\mathrm{m}, \gamma_\mathrm{sL0}^a \approx \gamma_\mathrm{sL0}^b \approx \gamma_\mathrm{sL0}^c$ due to the decreased effect of ΔC_p on $\Delta G_\mathrm{m}(T)$. Although negative temperature dependence for γ_sL0 has been considered, it differs from the usual understanding that differences of structures and surface states between crystal and liquid decrease with T.

Substituting Eq. (6.45) into Eq. (6.42), the integrated size- and temperature-dependent interface energy can be read as

$$\gamma_\mathrm{sL}^a(r, T) = \frac{2h\Delta H_\mathrm{m}\Delta S_\mathrm{vib}}{3RV}\left(1 - \frac{3h}{2r}\right)\left(\frac{7T}{T_\mathrm{m} + 6T}\right)^2 \tag{6.46a}$$

$$\gamma_\mathrm{sL}^b(r, T) = \frac{2h\Delta H_\mathrm{m}\Delta S_\mathrm{vib}}{3RV}\left(1 - \frac{3h}{2r}\right)\left(\frac{2T}{T_\mathrm{m} + T}\right)^2, \tag{6.46b}$$

$$\gamma_{\text{sL}}^c(r,T) = \frac{2h\Delta H_{\text{m}}\Delta S_{\text{vib}}}{3RV}\left(1-\frac{3h}{2r}\right)\left(\frac{T}{T_{\text{m}}}\right)^2. \tag{6.46c}$$

Substituting Eqs. (4.52), (4.53) and (4.55) into Eq. (4.40) and when γ_{sL0} is replaced by $\gamma_{\text{sL}}(r,T)$ in terms of Eq. (6.46), the critical size of nuclei r^* can be determined by letting $\partial\Delta G(r,T)/\partial r = 0$,

$$r^*(a) = h(A_1 + \sqrt{A_1^2 - 3A_1\theta_{\text{c}}/2})/\theta_{\text{c}}, \tag{6.47a}$$

$$r^*(b) = h(4B_1 + \sqrt{16B_1^2 - 18B\theta_{\text{c}}})/(3\theta_{\text{c}}), \tag{6.47b}$$

$$r^*(c) = h(C_1 + \sqrt{C_1^2 - 3C_1/2}) \tag{6.47c}$$

where $\theta_{\text{c}} = (T_{\text{m}}-T)/T_{\text{m}}$ is the degree of undercooling. $A_1 = 14\Delta S_{\text{vib}}(1-\theta_{\text{c}})/[3R(7-6\theta_{\text{c}})]$, $B_1 = \Delta S_{\text{vib}}(1-\theta_{\text{c}})/[R(2-\theta_{\text{c}})]$ and $C_1 = 2\Delta S_{\text{vib}}(1-\theta_{\text{c}})/(3R\theta_{\text{c}})$. Substituting Eq. (6.47) into Eq. (6.46) with experimentally determined θ_{c} values, $\gamma_{\text{sL}}(r^*,T_{\text{n}})$ can be determined.

Figure 6.13 shows a comparison between $\gamma_{\text{sL}}(r^*,T_{\text{n}})$ values in terms of Eq. (6.46) and experimentally determined γ_{CNT} values in good agreement, which implies that the γ_{CNT} value by Eq. (6.28) is not γ_{sL0}, but γ_{CNT}.
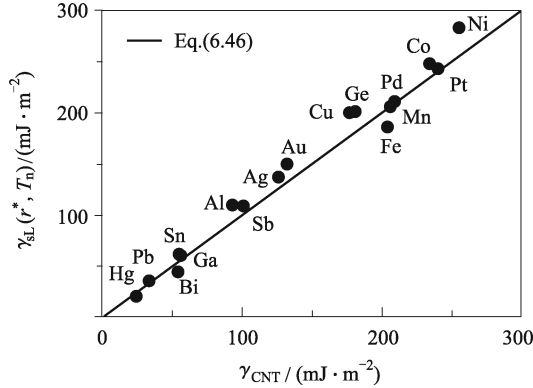
Fig. 6.13 The comparison between $\gamma_{\text{sL}}(r^*,T_{\text{n}})$ in terms of Eq. (6.46) for a variety of elemental systems and γ_{CNT} calculated from the CNT. (Reproduced from Ref. [3] with permission of Elsevier)

Aforementioned T_{n} and $\gamma_{\text{sL}}(r^*,T_{\text{n}})$ correspond well to the Turnbull's undercooling experimental results although both the expressions of $\gamma_{\text{sL}}(r,T)$ and $\Delta G_{\text{m}}(T)$ functions differ from those in CNT. The possible reason may be the mutual compensation for $\gamma_{\text{sL}}(r,T)$ and $\Delta G_{\text{m}}(T)$ functions. However, there is about 40% difference in the value of r^* between CNT ($r^* \approx 4h$) and the above equations ($r^* \approx 5.5h$), which may result from neglecting of derivative of $\gamma_{\text{sL}}(r,T)$ to r in CNT. Although we cannot confirm the above

difference from experiments due to the experimental difficulties, a little larger r^* should be more reasonable. Moreover, according to Eq. (6.47), the size of r^* is decided by ΔS_{vib} and θ_{c} due to the introduction of $\gamma_{\mathrm{sL}}(r, T)$ function, and it increases with an increase in ΔS_{vib} or a decrease in θ_{c}. Since ΔS_{vib} and θ_{c} values for elements with different bond natures are similar, r^* is in fact independent of the elemental types. Thus, $r^* \approx 5.5h$ is here for all concerned elements.

In Eq. (6.28), h also affects γ_{CNT} value. To accurately estimate this influence, h of all elements should be unified to h' where the elements with different structures have the same CN of 12. According to the Goldschmidt premise for lattice contraction, $(1 - h/h')$ will be 3%, 4%, and 12% if CN reduces from 12 to 8, 6, and 4, respectively. From this correlation between h and h' for the elements, whose CN is 4, 6 or 8, replacing h with h', Eq. (6.28) can be simplified to

$$\gamma_{\mathrm{CNT}} = \tau_2 \Delta H_{\mathrm{m}}/V_{\mathrm{s}} \qquad (6.48a)$$

with $\tau_2 \approx 0.11 \pm 10\%$ nm except semi-metals Pb, Sn and Ga as shown in Fig. 6.14. In a similar way, Eq. (6.28) can also be simplified to

$$\gamma_{\mathrm{sL0}}(T_{\mathrm{m}}) = \tau_3 \Delta H_{\mathrm{m}}/V_{\mathrm{s}} \qquad (6.48b)$$

with $\tau_3 = 2S_{\mathrm{vib}}h'/(3R) \approx 0.18 \pm 15\%$ nm except Fe, Al and Ga. Equation (6.48) can represent γ_{CNT} or $\gamma_{\mathrm{sL0}}(T_{\mathrm{m}})$ with a unique τ_2 or τ_3 rather than two different τ values by Eq. (6.28) due to different bond natures of the elements. Moreover, the disappearance of h or h' in Eq. (6.48) implies that the unique parameter deciding γ_{sL0} is ΔH_{m}. This conclusion is confirmed by Fig. 6.14 where we indeed find a good relationship between $\Delta H_{\mathrm{m}}/V_{\mathrm{s}}$ and $\gamma_{\mathrm{sL}}(r^*, T_{\mathrm{n}})$ (γ_{CNT}).
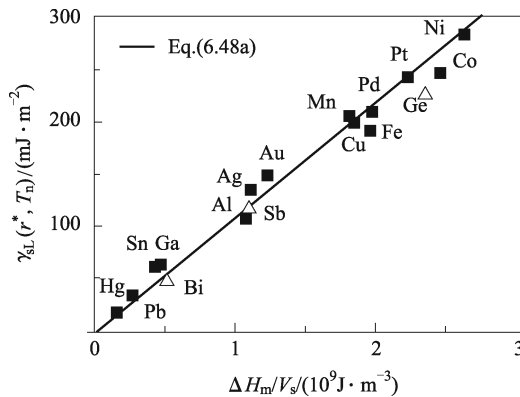

Fig. 6.14 $\gamma_{\mathrm{sL}}(r^*, T_{\mathrm{n}})$ as a function of $\Delta H_{\mathrm{m}}/V_{\mathrm{s}}$ for a variety of elemental systems in terms of Eq. (6.48a) (solid line) while ■ and △ denote $\gamma_{\mathrm{sL}}(r^*, T_{\mathrm{n}})$ values of metals and semiconductors. (Reproduced from Ref. [3] with permission of Elsevier)

Substituting Eq. (6.47) into Eq. (6.48) and plotting the function, the curve can be linearly regressed as a function of θ_c, which leads to

$$\gamma_{sL}(r^*, T_n) \approx (1.78 - 3.83\theta_c) \times 10^{-10} \times \Delta H_m / V_s. \qquad (6.49)$$

The standard deviations for the constants 1.78 and 3.83 are 0.01 and 0.16, respectively. Equation (6.49) indicates that Eqs. (6.48a) and (6.48b) denote two extreme cases where $\theta_c = \theta_n$ (the maximum degree of undercooling, which is nearly a constant of 0.18±0.02 for the most elements) and $\theta_c = 0$, respectively. In fact, at any θ_c value, $\gamma_{sL}(r^*, T_n)$ is always proportional to $\Delta H_m / V_s$.

As an example, Fig. 6.15 shows such a relationship at $\theta_c = 0.1$ where the linearly regressed slope equals 1.40 as indicated by Eq. (6.49). Figure 6.15 implies that ΔH_m is related to bond energy of atoms while γ_{sL} denotes the bond energy difference between surface atoms and interior ones of a crystal. Thus, γ_{sL} is proportional to the cohesive energy E_c, which has been determined by Eq. (3.90) and is also size-dependent. This result is confirmed in Fig. 6.16 where a comparison between $\gamma_{sL}(r, T)/\gamma_{sL0}(T)$ function in terms of Eq. (6.43) and $E_c(r)/E_c(\infty)$ function by Eq. (3.90) ($\Delta S_b \approx 12R$ is assumed except for Sb and Bi) is made. As shown in the figure, there are good agreements between them. Thus, the size dependence of $\gamma_{sL}(r)$ originates from that of $E_c(r)$. In terms of Eq. (6.48) or Eq. (6.49), $\gamma_{sL}(r^*, T_n)/\gamma_{sL0}(T_m)$ is within 10% of the value of $E_c(r^*)/E_c(\infty)$, which also confirms the validity of Eq. (6.48) or Eq. (6.49).
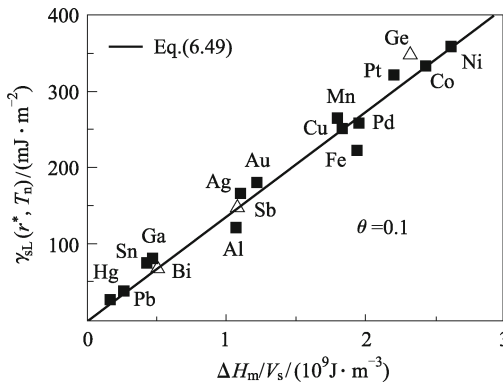
Fig. 6.15 $\gamma_{sL}(r^*, T_n)$ as a function of $\Delta H_m / V_s$ with $\theta_c = 0.1$ for elements in terms of Eq. (6.49) (solid line) where ■ and △ denote the $\gamma_{sL}(r, T)$ values of fcc and non-fcc elements, respectively. (Reproduced from Ref. [3] with permission of Elsevier)

Another linear relationship between $\gamma_{sL}(r^*, T_n)$ or γ_{CNT} and T_m with large scatter among different groups of elements has been rejected as the basis for an empirical rule in favor of the correlation with ΔH_m. However, direct calculations for γ_{CNT} values of transition fcc metals with hard-sphere

systems have shown a high correlation with T_{m}, which can also be extended to $\gamma_{\mathrm{sL0}}(T_{\mathrm{m}})$ for all fcc metals since $\Delta H_{\mathrm{m}} = T_{\mathrm{m}}\Delta S_{\mathrm{m}}$ and $\tau_3\Delta S_{\mathrm{m}} = 1.59 \pm 7\%$ nm·J·mol^{-1}·K^{-1} in terms of Eq. (6.48b). For other elements, $\tau_3\Delta S_{\mathrm{m}}$ values show large scatter in a range of 1.04 to 5.44 (nm·J·mol^{-1}·K^{-1}) due to the scatter of ΔS_{m} values. This indicates a disagreement of a linear relationship between T_{m} and ΔH_{m}. Thus, it is not T_{m}, but ΔH_{m}, which generally characterizes $\gamma_{\mathrm{sL0}}(T_{\mathrm{m}})$ value better.
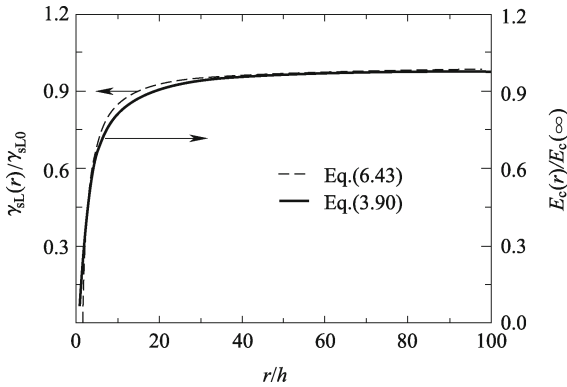
Fig. 6.16   Comparison between $\gamma_{\mathrm{sL}}(r)/\gamma_{\mathrm{sL0}}$ of Eq. (6.43) (dot ted line) and $E_{\mathrm{c}}(r)/E_{\mathrm{c}}(\infty)$ of Eq. (3.90) (solid line). (Reproduced from Ref. [3] with permission of Elsevier)

Note that all of the above considerations for the monotone size-dependent $\gamma_{\mathrm{sL}}(r,T)$ function are based on an essential assumption on $E_{\mathrm{c}}(r)/E_{\mathrm{c}}(\infty)$ function, which supposes that as r decreases, the increase (or decrease in absolute values) of $E_{\mathrm{c}}(r)$ of materials is induced by two effects: One is the increase of the surface/volume ratio, and the other is the increase of the interior atoms of the materials, the increase of the latter is sharper than the former. If the latter is neglected, done especially by computer simulation technique, we could observe a slight increase of $\gamma_{\mathrm{sL}}(r,T)$ as r decreases.

6.5 Solid-solid Interface Energy [3]

For coherent or semi-coherent solid-solid interface, its interface energy can be determined by some classic dislocation models. While for semi-coherent interface, atomic diameter misfit on the interface must be smaller than 0.15–0.25, γ_{ss0} is very strongly dependent on the misorientation of the two crystal halves and remains challenge. However, for high angle grain boundary, γ_{ss0} is almost a constant, which will be considered here.

Since a liquid may be regarded as a solid with such a high concentration of dislocation cores that are in contact everywhere, solid-solid interface energy

γ_{ss0} at T_m is considered to be twice the γ_{sL0} approximately, $\gamma_{ss0}(T_m) \approx 2\gamma_{sL0}(T_m)$. Combining with Eq. (6.35),

$$\gamma_{ss0}(T_m) \approx 4h\Delta S_{vib}\Delta H_m/(3V_sR). \tag{6.50}$$

As shown in Table 6.5, $\gamma_{ss0}(T_m)$ values based on Eq. (6.50) for eleven elements and two organic crystals correspond to available theoretical values γ'_{ss0}. In addition, the listed data of γ'_{ss0} and γ'_{sL0} for Pivalic acid and Succinonitrile determined by the equilibrated grain boundary groove shapes also confirm the validity of $\gamma_{ss0}(T_m) \approx 2\gamma_{sL0}(T_m)$ with the absolute deviation being smaller than 5.5%. Thus, Eq. (6.50) can be used to quantitatively calculate $\gamma_{ss0}(T_m)$ values, at least for metals and organic crystals.

Table 6.5 Comparison of $\gamma_{ss0}(T_m)$ between γ_{ss0} by Eq. (6.25) and available theoretical or experimental results γ'_{ss0} for metals and organic crystals with γ in mJ·m^{-2}

System	γ_{ss0}	γ'_{ss0}	γ'_{sL0}	System	γ_{ss0}	γ'_{ss0}	γ'_{sL0}
Cu	584	601		Ag	398	392,375	
Au	430	400		Al	302	300–380	
Ni	844	866,757		Co	706	650	
Nb	804	760		Ta	944	900	
Sn	158	160,164		Pivalic acid	4.8	5.2±0.4	2.7±0.2
Bi	176	140.5±14.1		Succinonitrile	14.6	15.0±2.0	7.9±0.8
Pb	96	111.5±15.6					

The way to deduce $\gamma_{ss}(r)$ is similar to that to deduce $\gamma_{sL}(r)$ while Eqs. (6.16) and (6.37) must be modified due to different interface conditions. We assume that f as a first order approximation keeps constant for both solid-liquid and solid-solid interfaces at T_m, which leads to the same strain on both sides of the interface when the grains are isotropic. However, elastic modulus of grain boundaries should be larger than that of the solid-liquid interface with less strain under the same stress. This is introduced by the fact that $A = 3V/(2r)$ for solid-solid interface because two solid-liquid interfaces of particles combine to form one grain boundary with

$$\Delta P = 2fA/(3V) = f/r, \tag{6.51}$$

and

$$\varsigma = -\beta f/(3r). \tag{6.52}$$

Both equations indicate that the strain on the grain boundary is only a half of that on the solid-liquid interface and thus $\Delta A/A = 2\varsigma = -2\beta f/(3r)$. Now $\Delta\gamma_{ss} = \gamma_{ss}(r) - \gamma_{ss0} = (\Delta A/A)(f - \gamma_{ss}) = -2\beta f(f - \gamma_{ss})/(3r)$, or

$$\gamma_{ss}(r)/\gamma_{ss0} = [1 - r_0/(4r)]/[1 - \gamma_{ss}r_0/(4fr)]. \tag{6.53}$$

Similar to the simplification of $\gamma_{sL}(r)$, Eq. (6.53) can also be simplified to

$$\gamma_{ss}(r)/\gamma_{ss0} = 1 - r_0/(4r). \tag{6.54}$$

Figure 6.12 shows an agreement between Eq. (6.53) and the computer simulation results for Cu. It is interesting that the use of a negative f for $\gamma_{\mathrm{ss}}(r)$ in Eq. (6.53) leads to a full agreement with the computer simulation results, which implies that $f < 0$ at the grain boundary.

If we compare Eqs. (6.43) and (6.54), $\gamma_{\mathrm{sL}}(r)/\gamma_{\mathrm{sL0}} < \gamma_{\mathrm{ss}}(r)/\gamma_{\mathrm{ss0}}$. This result shows that the stiffer surrounding of grains brings out less decrease of $\gamma_{\mathrm{ss}}(r)$ as r decreases. For the grain boundaries, even if when $r \to r_0$, $\gamma_{\mathrm{ss}}(r)/\gamma_{\mathrm{ss0}} \approx 75\%$ while $\gamma_{\mathrm{sL}}(r)/\gamma_{\mathrm{sL0}} = 0$. Since when $r \approx 2r_0$, the grains are no more stable and will transform to amorphous solids in terms of the computer simulation results, the smallest value of $\gamma_{\mathrm{ss}}(r_0)/\gamma_{\mathrm{ss0}}$ could be about 85%.

6.6 Solid-vapor Interface Energy or Surface Energy

6.6.1 Bulk Surface Energy of Elementary Solids [3]

The surface energy γ_{sv0} of solids usually is defined as the difference between the Gibbs free energy of the surface and that of the bulk or simply as the energy needed to split a solid in two along a plane, which is one of the basic quantities to understand the surface structure and phenomena. Despite of its importance, γ_{sv0} value is difficult to determine experimentally. The most experiments are performed at high T where surface tension of liquid is measured, which is extrapolated from zero Kelvin. This kind of experiment contains uncertainties of unknown magnitude and corresponds to only γ_{sv0} value of an isotropic crystal. Moreover, many published data determined by the contact angle of metal droplets or by peel tests disagree with each other, which can be induced by the presence of impurities or by mechanical contributions, such as dislocation slip or the transfer of material across the boundary. In addition, there are hardly experimental data on the more open surfaces except for the classic measurements on Au, Pb and In to our knowledge. Therefore, a theoretical determination of γ_{sv0} values especially for open surface is of vital importance.

There have been several attempts to calculate γ_{sv0} values of metals using either *ab initio* techniques with tight-binding (TB) parameterizations or semi-empirical methods. γ_{sv0} values, work functions and relaxation for the whole series of bcc and fcc $4d$ transition metals have firstly been studied using the full-potential (FP) linear muffin-tin orbital (LMTO) method in conjunction with the local-spin density approximation to the exchange-correlation potential. In the same spirit, γ_{sv0} values and the work functions of the most elemental metals including the light actinides have been carried out by the Green's function with LMTO method. Later, the full-charge density (FCD) Green's

function LMTO technique in the atomic-sphere approximation (ASA) with the generalized gradient approximation (GGA) was utilized to construct a large database that contains γ_{sv0} values of low-index surfaces of 60 elements in the periodic table. The results denote a mean deviation of 10% for the $4d$ transition metals from FP methods. This database in conjunction with the pair-potential model has been further extended to estimate the formation energy of mono-atomic steps on low-index surfaces for an ensemble of fcc and bcc metals.

On the other side, the traditional broken-bond model is again suggested to estimate γ_{sv0} values of the transition metals and the noble metals at different facets. The simplest approach to get a rough estimation of γ_{sv0} values at $T = 0$ K is to determine the broken bond number Z_{hkl} for creating a surface area by cutting a crystal along certain crystallographic plane with a Miller index (hkl). $Z_{hkl} = Z_b - Z_s$ where Z_s and Z_b are CN of surface atoms and that of the corresponding bulk ones. Multiplying this number with the cohesion energy per bond E_c/Z_b for the non-spin-polarized atom at 0 K, γ_{sv} is determined by [6.11],

$$\gamma_{sv0} = (1 - \upsilon_1)E_c/(N_A A_S) \tag{6.55}$$

where $\upsilon_1 = Z_s/Z_b$ and A_s denotes the area of the two-dimensional unit cell of solid.

In Eq. (6.55), E_c is independent of crystalline structures as a first order approximation since energy differences among crystal structures are several orders of magnitude smaller than E_c when the bond type remains unaltered.

Although the broken-bond rule seems to contradict the basic knowledge about the electronic structure since E_c, in general, does not scale linearly with Z_s, the above estimation provides the order of magnitude of γ_{sv0} and shows a possible relationship between γ_{sv0} and atomic binding strength. Despite the absence of verification from experiments, such a rule has been used to give a reasonable description of γ_{sv0} value of Al.

Since the bond strength becomes stronger for an atom with a smaller CN, this CN-bond-strength relation can be quantified using tight-binding approximation. In the second-moment tight-binding approximation, the width of the local density of states on an atom scales with Z_s, leading to an energy gain to be proportional to the square root of Z_s due to the lowing of the occupied states. Neglecting repulsive terms, there is $E_c/Z_b \propto Z_s^{1/2}$. Since E_c of an atom is a bonding energy sum of all bonds, γ_{sv0} is suggested as

$$\gamma_{sv0} = [1 - \upsilon_1^{1/2}]E_c/(N_A A_S). \tag{6.56}$$

Equation (6.55) does not consider the variation of bond strength with CN while Eq. (6.56) has neglected the repulsive terms of potentials, the both thus need corrections. Namely, the former neglects while the latter overestimates the effect of relaxation on γ_{sv0}, which brings out that Eq. (6.55) can be an acceptable concept for strongly covalent crystals while Eq. (6.56) is especially suitable for noble metals.

Although a direct utilization of Eq. (6.55) or Eq. (6.56) is reasonable, one of them could not alone give satisfied predictions for γ_{sv0} values in comparison with the experimental and theoretical results. To obtain a more general formula, we arbitrarily assume that both Eqs. (6.55) and (6.56) could make up the deficiency with the same weight to both formulae. Thus, γ_{sv0} values may be determined by an averaged effect of them without elaborate estimation on the relaxation energy,

$$\gamma_{sv0} = [2 - v_1 - v_1^{1/2}]E_c/(2N_A A_S). \tag{6.57}$$

Equation (6.57) implies that γ_{sv0} values still depend on the bond-broken rule although they are scaled by both Z_s and $Z_s^{1/2}$. In Eq. (6.31), Z_s is determined by the crystalline structure with the corresponding Z_{hkl} in terms of a geometric consideration. For fcc or hcp structure, $Z_b = 12$. For a bcc lattice, although $Z_b = 8$ is taken according to the nearest-neighbor definition by some authors (probably the majority), others prefer to take $Z_b = 14$ since the difference between the nearest neighbor bond length and the next-nearest neighbor bond length is small. Here, the latter is accepted although the next nearest neighbor bond length is only taken as a fraction of the nearest neighbor bond length. By assuming that the total energy of a surface atom is the sum of contributions from both the nearest neighbor and the next-nearest neighbor atoms, Eq. (6.57) should be rewritten for bcc metals after normalization,

$$\gamma_{sv0} = [(2 - v_1 - v_1^{1/2}) + \varphi(2 - v_1' - v_1'^{1/2})]E_c/[(2 + 2\varphi)N_A A_S] \tag{6.58}$$

where the superscript accent sign denotes the next nearest CN on a surface and φ shows the total bond strength ratio between the next nearest neighbor and the nearest neighbor.

To roughly estimate the size of φ, LJ potential of $u(r) = -4\varepsilon[(\lambda/r)^6 - (\lambda/r)^{12}]$ is utilized with ε being the bond energy and λ insuring $du(r)/dr_{(r=h)} = 0$, i.e. $\lambda = 2^{-1/6}h$ where h is the atomic distance in equilibrium and r is the atomic distance. For fcc crystal, $h = 2^{1/2}a/2$ and $h' = a$, respectively. Let $r = a$, $\varepsilon' \approx \varepsilon/4$, and $\varphi \approx [(1/4) \times 6]/12 = 1/8$. Thus, the effect of the next nearest CN can be neglected as a first order approximation, which is also applicable to hcp crystals. Namely, Eq. (6.58) can be simplified to Eq. (6.57) for fcc and hcp crystals. For bcc crystal, $h = 3^{1/2}a/2$ and $h' = a$, respectively. Let $r = a, \varepsilon' = 2\varepsilon/3$. Thus, $\varphi = [(2/3) \times 6]/8 = 1/2$. Adding this value into Eq. (6.58),

$$\gamma_{sv0} = [3 - v_1 - v_1^{1/2} - v_1'/2 - (v_1'/4)^{1/2}]E_c/(3N_A A_S). \tag{6.59a}$$

Note that the bonding of LJ potential, which is utilized to justify φ value in Eq. (6.58), differs from the metallic bond in its nature. For instance in an LJ bonded system, the surface relaxation is outwards whilst in the transition

metals it is inwards. However, this difference leads to only a second order error in our case and has been neglected.

The effect of next nearest CN also occurs for simple cubic (sc) and diamond crystals (dc) structures because there are twice or thrice as many the second neighbors as the first neighbors, respectively. Similar to the above analysis, for sc crystals: $\varepsilon' \approx \varepsilon/4$ and $\varphi = [(1/4)\times12]/6 = 1/2$, which is the same for bcc and thus Eq. (6.33a) can also hold for sc crystals. For dc structure, $\varepsilon' \approx \varepsilon/10$ and $\varphi = [(1/10)\times12]/4 = 3/10$. With this φ value, Eq. (6.58) is rewritten as

$$\gamma_{sv0} = [26 - 10v_1 - 10v_1^{1/2} - 3v_1' - (9v_1')^{1/2}]E_c/(26N_A A_S). \qquad (6.59b)$$

Z_{hkl} can be determined by some known geometrical rules. For any surface of a fcc structure with $h \geqslant k \geqslant l$,

$$Z_{hkl} = 2h + k \qquad \text{for } h, k, l \text{ being odd,} \qquad (6.60a)$$

$$Z_{hkl} = 4h + 2k \qquad \text{for the rest.} \qquad (6.60b)$$

In a similar way, Z_{hkl} for any surface of a bcc structure is determined with the consideration of the next nearest CN,

$$Z_{hkl} = 2h + (h + k + l) \qquad \text{for } h + k + l \text{ being even,} \qquad (6.61a)$$

$$Z_{hkl} = 4h + 2(h+k+l) \qquad \text{for } h+k+l \text{ being odd and } h-k-l \geqslant 0, \quad (6.61b)$$

$$Z_{hkl} = 2(h+k+l) + 2(h+k+l) \qquad \text{for } h+k+l \text{ being odd and } -h+k+l > 0 \tag{6.61c}$$

where the second item of the right-hand side of Eq. (6.61) denotes the broken bond number of the next nearest neighbors. For sc crystals, Z_{hkl} values of the nearest and the next nearest atoms are 1 and 4 for (100) surface as well as 2 and 5 for (110) surface, respectively. For diamond structure crystals, Z_{hkl} values of the nearest and the next nearest atoms are 1 and 6 for (110) surface. For several surfaces of a hcp structure, Z_{hkl} is obtained by

$$Z_{hkl} = 4(h + k) + 3l \qquad \text{for (0001),} \qquad (6.62a)$$

$$Z_{hkl} = 4(h + k) + (8h + 4k)/3 \qquad \text{for } (10\bar{1}0) \qquad (6.62b)$$

where the first item of the right-hand side of Eq. (6.62) denotes the average number of basal broken bonds while the second item is that of non-basal broken bonds.

Table 6.6 shows some necessary parameters in Eqs. (6.57) and (6.59). Tables 6.7–6.9 give the predicted γ_{sv0} values for fcc, bcc, hcp, diamond and sc structure crystals in terms of Eqs. (6.57) and (6.59) where two sets of experimental results γ_{sv0}'' and the first principle calculations γ_{sv0}' are also shown. Note that the experimental results are not orientation-specific but are averaged values of isotropic crystals. Thus, they should be close to those of the most close-packed surface.

Table 6.6 $A_\mathrm{S}, Z_\mathrm{s}$ and Z_b values for different surfaces and structures where a is lattice constant while Z_s and Z_b are determined by Eqs. (6.60)–(6.62)

Structure	Surface	A_S	Z_s	Z_b
fcc	(111)	$3^{1/2}a^2/4$	9	12
	(100)	$a^2/2$	8	12
	(110)	$2^{1/2}a^2/2$	6	12
bcc	(110)	$2^{1/2}a^2/2$	$Z_\mathrm{s}=6, Z_\mathrm{s}'=4$	$Z_\mathrm{b}=8, Z_\mathrm{b}'=6$
	(100)	a^2	$Z_\mathrm{s}=4, Z_\mathrm{s}'=4$	$Z_\mathrm{b}=8, Z_\mathrm{b}'=6$
	(111)	$3^{1/2}a^2$	$Z_\mathrm{s}=2, Z_\mathrm{s}'=0$	$Z_\mathrm{b}=8, Z_\mathrm{b}'=6$
hcp	(0001)	$3^{1/2}a^2/2$	9	12
	$(10\bar{1}0)$	$(8/3)^{1/2}a^2$	16/3	12
Diamond	(110)	$2^{1/2}a^2/4$	$Z_\mathrm{s}=3, Z_\mathrm{s}'=6$	$Z_\mathrm{b}=4, Z_\mathrm{b}'=12$
sc	(100)	a^2	$Z_\mathrm{s}=5, Z_\mathrm{s}'=8$	$Z_\mathrm{b}=6, Z_\mathrm{b}'=12$
	(110)	$2^{1/2}a^2$	$Z_\mathrm{s}=4, Z_\mathrm{s}'=7$	$Z_\mathrm{b}=6, Z_\mathrm{b}'=12$

Table 6.7 Comparison of γ_sv0 of fcc metals between the predicted values γ_sv0 of Eq. (6.57), FCD calculations γ_sv0', and experimental results γ_sv0''. E_c in kJ·g-atom^{-1}, a in nm, and γ in J·m^{-2}, which are the same as those in Tables 6.8 and 6.9

	E_c	a	$(h\,k\,l)$	γ_sv0	γ_sv0'	γ_sv0''
			(111)	1.83	1.95	1.79, 1.83
Cu	336	0.366	(100)	2.17	2.17	
			(110)	2.35	2.24	
			(111)	1.52	1.28	1.51, 1.50
Au	368	0.420	(100)	1.80	1.63	
			(110)	1.94	1.70	
			(111)	1.85	1.92	2.00, 2.05
Pd	376	0.385	(100)	2.15	2.33	
			(110)	2.35	2.23	
			(111)	2.70	2.47	2.66, 2.70
Rh	554	0.387	(100)	3.15	2.80	
			(110)	3.41	2.90	
			(111)	0.55	0.32	0.59, 0.60
Pb	196	0.511	(100)	0.64	0.38	
			(110)	0.70	0.45	
			(111)	0.43	0.57	0.50, 0.49
Ca	178	0.562	(100)	0.50	0.54	
			(110)	0.55	0.58	
			(111)	0.90	0.87	
Ac	410	0.579	(100)	1.03	0.73	
			(110)	1.14	0.68	
Mn*	282	0.353	(111)	1.65	3.10	1.54, 1.60
			(111)	1.20	1.17	1.25, 1.25
Ag	284	0.418	(100)	1.40	1.20	
			(110)	1.51	1.24	
			(111)	2.44	2.01	2.38, 2.45
Ni	428	0.358	(100)	2.88	2.43	
			(110)	3.11	2.37	

Continue

	E_c	a	$(h\ k\ l)$	γ_{sv0}	γ'_{sv0}	γ''_{sv0}
Pt	564	0.402	(111)	2.54	2.30	2.49, 2.48
			(100)	2.98	2.73	
			(110)	3.24	2.82	
Ir	670	0.391	(111)	3.19	2.97	3.05, 3.00
			(100)	3.74	3.72	
			(100)	4.06	3.61	
Al	327	0.405	(111)	1.45	1.20	1.14, 1.16
			(100)	1.68	1.35	
			(110)	1.84	1.27	
Sr	166	0.617	(111)	0.33	0.43	0.42, 0.41
			(100)	0.39	0.41	
			(110)	0.43	0.43	
Th	598	0.519	(111)	1.61	1.48	1.50
			(100)	1.85	1.47	
			(110)	2.36	1.45	

The symbol *, which has the same meaning in Tables 6.8 and 6.9, denotes that when the low temperature equilibrium crystal structure has a lower symmetry than a close packing phase at high temperature or under a high pressure, the latter is utilized.

Table 6.8 Comparison of surface energy of crystals in bcc, sc and diamond structures between the predicted values γ_{sv0} based on Eq. (6.59), FCD calculations γ'_{sv0}, and experimental results γ''_{sv0}

	E_c	a	$(h\ k\ l)$	γ_{sv0}	γ'_{sv0}	γ''_{sv0}
Li	158	0.399	(110)	0.50	0.56	0.52, 0.53
			(100)	0.58	0.52	
			(111)	0.72	0.59	
K	90.1	0.530	(110)	0.16	0.14	0.13, 0.15
			(100)	0.18	0.14	
			(111)	0.23	0.15	
Cs	77.6	0.626	(110)	0.10	0.08	0.10, 0.10
			(100)	0.12	0.09	
			(111)	0.14	0.09	
Ra	160	0.537	(110)	0.27	0.30	
			(100)	0.32	0.29	
			(111)	0.40	0.32	
V	512	0.302	(110)	2.74	3.26	2.62, 2.56
			(100)	3.26	3.03	
			(111)	4.04	3.54	
Fe	413	0.286	(110)	2.52	2.43	2.42, 2.48
			(100)	2.92	2.22	
			(111)	3.62	2.73	
Mo	658	0.317	(110)	3.20	3.45	2.91, 3.00
			(100)	3.81	3.84	
			(111)	4.62	3.74	
W	859	0.358	(110)	3.36	4.01	3.27, 3.68
			(100)	3.90	4.64	
			(111)	4.84	4.45	
Bi (SC*)	210	0.326	(100)	0.55	0.54	0.49, 0.49
			(110)	0.64	0.54	

Continue

	E_c	a	$(h\ k\ l)$	γ_{sv0}	γ'_{sv0}	γ''_{sv0}
Si	446	0.771	(110)	1.06		1.14
Na	107	0.420	(110)	0.29	0.25	0.26, 0.26
			(100)	0.34	0.26	
			(111)	0.41	0.29	
Rb	82.2	0.571	(110)	0.12	0.10	0.12, 0.11
			(100)	0.15	0.11	
			(111)	0.18	0.12	
Ba	183	0.503	(110)	0.36	0.38	0.38, 0.37
			(100)	0.41	0.35	
			(111)	0.51	0.40	
Eu	179	0.458	(110)	0.43	0.49	0.45, 0.45
			(100)	0.50	0.46	
			(111)	0.61	0.52	
Cr*	395	0.285	(110)	2.39	3.51	2.35, 2.30
			(100)	2.83	3.98	
			(111)	3.50	4.12	
Nb	730	0.376	(110)	2.58	2.69	2.66, 2.70
			(100)	2.99	2.86	
			(111)	3.72	3.05	
Ta	782	0.335	(110)	3.40	3.08	2.90, 3.15
			(100)	4.05	3.10	
			(111)	5.01	3.46	
Sb (SC*)	265	0.336	(100)	0.66	0.61	0.60, 0.54
			(110)	0.77	0.66	
Po (SC*)	144	0.334	(100)	0.38	0.44	
			(110)	0.44	0.37	
Ge	372	0.810	(110)	0.80		0.88

For both noble and transition metals, the predicted γ_{sv0} values agree fully with the experimental results and FCD calculations as shown in Tables 6.7–6.9 although γ_{sv0} for transition metals have slightly larger deviations than those for the noble metals due to the fact that their d-bands are not fully filled and they present peaks at the Fermi level, which can slightly change from one surface orientation to the other and consequently the energy needed to break a bond changes also a little.

As shown in these tables, γ_{sv0} values of transition metals increase along an isoelectronic row where a heavier element has a larger γ_{sv0} value. This is because the d-level of a heavier element is higher in energy and the corresponding d-wave function with a stronger bonding is more extended. This is also true for elements in the same row in the periodic table where a heavier element has more d-electrons. An exception is in VA series where γ_{sv0} value of Nb is smaller than that of V possibly due to the rehybridization of Nb where Nb, whose d shell is less than the half-full, rehybridizes in the opposite direction, i.e., depletes their d_z^2 orbitals based on a charge density difference analysis.

γ_{sv0} values for sp metals except for Be are smaller than those for d-metals

due to their bond nature of *s*- and *p*-electrons, which are more mobile than the localized *d*-electrons and therefore less energy is needed to break these bonds.

Table 6.9 Comparison of γ_{sv0} values of hcp metals between Eq. (6.57), FCD calculations γ'_{sv0}, and experimental results γ''_{sv0}

	E_c	a	$(h\ k\ i\ l)$	γ_{sv0}	γ'_{sv0}	γ''_{sv0}
Be	320	0.222	(0001)	2.40	1.83	1.63, 2.70
			(10$\bar{1}$0)	2.88	2.13	
Mg	145	0.320	(0001)	0.53	0.79	0.79, 0.76
			(10$\bar{1}$0)	0.65	0.78	
Zn	130	0.268 (c/a=1.86)	(0001)	0.66	0.99	0.99, 0.99
			(10$\bar{1}$0)	0.72		
Cd	112	0.306 (c/a=1.89)	(0001)	0.44	0.59	0.76, 0.74
			(10$\bar{1}$0)	0.47		
Tl	182	0.371	(0001)	0.49	0.30	0.60, 0.58
			(10$\bar{1}$0)	0.60	0.35	
Sc	376	0.330	(0001)	1.25	1.83	1.28
			(10$\bar{1}$0)	1.53	1.53	
Ti	468	0.295	(0001)	1.96	2.63	1.99, 2.10
			(10$\bar{1}$0)	2.39	2.52	
Co	424	0.253	(0001)	2.42	2.78	2.52, 2.55
			(10$\bar{1}$0)	2.95	3.04	
Y	422	0.355	(0001)	1.22	1.51	1.13
			(10$\bar{1}$0)	1.49	1.24	
Zr	603	0.325	(0001)	2.08	2.26	1.91, 2.00
			(10$\bar{1}$0)	2.54	2.11	
Tc	661	0.274	(0001)	3.22	3.69	3.15
			(10$\bar{1}$0)	3.93	3.90	
Ru	650	0.272	(0001)	3.20	3.93	3.04, 3.05
			(10$\bar{1}$0)	3.90	4.24	
La*	431	0.387	(0001)	1.05	1.12	1.02
			(10$\bar{1}$0)	1.28	0.92	
Lu	428	0.351	(0001)	1.27	1.60	1.23
			(10$\bar{1}$0)	1.55	1.42	
Hf	621	0.320	(0001)	2.22	2.47	2.19, 2.15
			(10$\bar{1}$0)	2.71	2.31	
Re	775	0.276	(0001)	3.72	4.21	3.63, 3.60
			(10$\bar{1}$0)	4.54	4.63	
Os	788	0.275	(0001)	3.80	4.57	3.44, 3.45
			(10$\bar{1}$0)	4.64	5.02	

For fcc metals except Ca, Sr and Al, the mean-square root error Υ between the predicted and the experimental results for the most close-packed (111) facet is about 7.5%. For Al, the degree of covalent Al–Al bonding increases or the nature of the bonding changes with reduced *CN*, which leads to deviation of Eq. (6.57) from experimental results since Eq. (6.57) neglects

the variation of bonding types. However, the reason of deviations for Ca and Sr is unclear.

For hcp metals, $\Upsilon \approx 10\%$ except Mg, Zn, Cd and Tl. For Cd and Tl, both of the predictions and FCD calculations deviate evidently from the experimental results. In the case of Zn and Cd, c/a ratios (1.86 and 1.89) are larger than the ideal value of $(8/3)^{1/2}$. Thus, the nearest CN values will differ from the ideal condition, which should contribute to the deviation. For sc metals, $\Upsilon = 2.6\%$ where Sb and Bi with the rhombohedral structure are assumed to have slightly a distorted sc structure. For bcc metals, $\Upsilon = 10\%$. The smallest value of Υ in all considered structures appears for diamond structure crystals with $\Upsilon = 1.4\%$, which implies that the pure coherent bond does not change after a CN deduction.

Note that the temperature dependence of γ_{sv0} is ignored here although the experimental results listed in Tables 6.7–6.9 are calculated at 0 K while the most lattice constants cited are measured at T_{room}. This temperature effect deteriorates the prediction accuracy and can be partly responsible for the disagreement with other experimental and theoretical results.

In the FCD calculations, there are often exceptions that the most close-packed surface does not have the lowest γ_{sv0} values or there exists a weak orientation-dependence. These physically unacceptable results are fully avoided here. Moreover, the anisotropy of γ_{sv0} is perfectly considered. $\gamma_{(100)}/ \gamma_{(111)} \approx 1.16$ and $\gamma_{(110)}/\gamma_{(111)} \approx 1.27$ for fcc metals as well as $\gamma_{(0001)}/\gamma_{(10\bar{1}0)} \approx 1.22$ for hcp metals, which show the agreement with theoretical values of 1.15 and 1.22. In addition, $\gamma_{(100)}/\gamma_{(110)} \approx 1.16$ for sc and bcc metals, which is especially comparable with 1.14 for monovalent sp metals based on the jellium model.

If the experimental results are taken as reference, 60% of γ_{sv0} values of the most close-packed surfaces of 52 elements shown in Tables 6.7–6.9 are in better agreement with experimental ones than those of the FCD calculations while 20% of the FCD calculations are in reverse. Note that local density approximation (LDA) is implied here while GGA is used in FCD. Recently, it has been shown that both methods need to be corrected due to the neglect of surface electron self-interactions where GGA is worse than LDA. This is surprising because GGA is generally considered to be the superior method for energetic calculations.

The formula for the transition metals and noble metals works well compared with that for others as the greatest contribution to bonding is from the s-d interaction and the orbital of the others is localized, which is more like a pair interaction. According to Tables 6.7–6.9, the predicted γ_{sv0} values of divalent sp metals have little correspondence with the experimental results since many body (e.g. trimer) terms are here critical to understand the cohesive energy. Thus, the used pair potentials physically may not be fully correct. Possibly the background of the formula, i.e. the broken-bond model, is not universally applicable although the lattice constants used in Eqs. (6.57) and (6.59) have measuring error of about 2%.

According to the first principles calculations, the effect of relaxation on the calculated γ_{sv0} value of a particular crystalline facet may vary from 2% to 5% depending on the roughness. The semi-empirical results indicate further that the surface relaxation typically affects the anisotropy by less than 2%. Surface relaxations for vicinal surfaces have been studied mainly using semi-empirical methods due to the complexity arisen by the simultaneous relaxation of a large number of layers. Here, the relaxation effect is simply considered by adding Eq. (6.56) into Eq. (6.55). According to Tables 6.7–6.9, this measure leads to satisfactory results.

The above formula gives a new insight into and another way to a general estimation of γ_{sv0} of elements, which is difficult to realize by present first principles calculation, and gives a basis of comparison and supplement to further theoretical and experimental considerations for γ_{sv0} values of elements.

Recently, Lodziana et al. have proposed that γ_{sv0} of θ-alumina is negative [12]. Their use of the term "negative solid-vapor interface energy" can cause and has already caused confusion in the scientific community. Mathur et al. nicely summarized and clarified definitions of γ_{sv0} for single- and multi-component systems [13]: γ_{sv0} for single-component systems is always positive, whereas for multi-component systems it can become negative due to chemical effects, which has been confirmed experimentally. The situation in a multicomponent system is slightly more complicated (such as θ-alumina + water), where chemical effects must be considered. In such a system, the Gibbs dividing surface can be located so that there is no excess term for one component, but this only leads to non-zone excess quantities for the other components, which alters the solid's surface energy. Physically, this is a result of the interaction energy between the solid surface and the other components. Thus, in addition to reversible work for creation of new (clean) surface area, surface energy here also includes chemical interactions between the newly formed surface and the surroundings. Adsorption on solid surfaces is typically an exothermic process and it reduces the solid's surface energy. Others have indeed shown that chemical effects can lead to negative surface energy.

6.6.2 γ_{sv0} of Several Ceramics with NaCl Structure [3]

The alkaline metal oxides (AMO) as one kind of three supporting industries in material domain hold the balance in daily life and industrial manufacture. The transition metal carbides (TMC) and the transition metal nitrides (TMN) have been widely applied as surface layers of cutting tools, electrically conducting diffusion barriers in electronic devices, in coatings for solar applications and for corrosion protection. All of these applications due to their unique properties (e.g. high hardness and high T_m) are closely related with their surface states. γ_{sv0} as an important concept changes growth rate, catalytic behavior, adsorption, surface segregation and formation of grain

boundaries. However, it is the ionic character and the hardness of the oxides which result in less reliable experimental data on γ_{sv0} although computer simulations of them have been carried out.

Although Eqs. (6.57) and (6.59) are deduced for elemental crystals, they can be extended for insulators or metallic compounds. The main source of the bonding in these ceramics is the ionic interaction between metal and non-metal atoms in the NaCl structure where $Z_b = 6$ and Z_s are 5, 4, and 3 respectively for (100), (110) and (111) surfaces. Note that because γ_{sv0} values of these compounds under comparison are usually reported in unit of eV·atom^{-1} obtained by computer simulations, γ_{sv0} value in this section is also denoted in this unit.

Table 6.10 gives γ_{100} values of TMCs in terms of Eqs. (6.56) and (6.57). Other computer simulation and theoretical results for TMCs are also shown for comparison. It can be found that the agreement on different methods for stable TMCs is greater than that for metastable TMCs, such as CoC, NiC and OsC. The Fermi levels of both CoC and NiC lie in the upper part of the d region, which may lead to that the simulation results are much lower than those in terms of Eq. (6.57). While for OsC, the Fermi level contains the most d states that do not hybridize with carbon states. Thus, the simulation results represent different trends compared with the theoretical ones. Equation (6.56) is in close agreement with LDA simulation results while those of Eq. (6.57) have good correspondence with other theoretical results based on modification of E_c of the classic broken-bond rule. It is found that all γ_{sv0} values calculated from GGA are smaller than those from LDA, which confirms other similar simulation results.

From Table 6.10, even the largest pseudopotential result (0.68 eV·atom^{-1}) from LDA is about 18.1% lower than the result (0.83 eV·atom^{-1}) from LMTO for TiC due to different approaches during solving the DFT equations. The former treats the effective one-electron potential without any shape approximation and allows one to solve the electronic-structure problem for bulk as well as for the surface from the first principles within a single scheme. LMTO often employs the atomic sphere approximation (ASA) that is clearly inadequate for structures with large interstitial regions or with low coordination symmetry, as in the present surface calculations. Thus, the LMTO approach is generally regarded as an efficient but relatively inaccurate method.

Table 6.11 shows γ_{100} values of twelve existing stable TMNs with the methods as stated above. The calculated results of γ_{100} values of metastable phases have worse accuracy, partly due to their metastable natures with possibly unsuitable potentials. Thus, the corresponding calculations are not shown. γ_{100} values of the stable TMNs determined by GGA-PW91 with the corresponding potential are nearly half of the results in terms of Eq. (6.31) while being larger than other simulation results. LDA results are relatively large and in agreement with the modified broken bond model better. Since the existing results are little, it is difficult to evaluate the accuracy of different simulation methods.

Table 6.10 Comparison of γ_{100} values in eV·atom^{-1} of TMC between γ_1 of Eq. (6.57), γ_2 of Eq. (6.56), γ_3 by using FP-LMTO calculations based on LDA, simulation results γ_4 using GGA-PW91 and γ_5 by LDA, theoretical results γ_6, and other available results γ_7 using pseudopotential plane-wave-based DFT. E_c is in eV·atom^{-1}

	E_c	γ_1	γ_2	γ_3	γ_4	γ_5	γ_6	γ_7
ScC	6.37	0.79	0.57	0.67	0.47	0.56	0.68, 0.86	
TiC	7.16	0.89	0.65	0.83	0.54	0.69	0.84, 0.98	0.50
VC	6.94	0.86	0.62	0.77	0.37	0.55	0.88, 0.92	0.36
CrC	5.80	0.72	0.50	0.71	0.34	0.42	0.88, 0.84	
MnC	5.14	0.64	0.43	0.70	0.30	0.47	0.87, 0.85	
FeC	5.67	0.71	0.47	0.71	0.34	0.55	0.86	
CoC	5.69	0.71	0.48	0.72	0.20	0.32	0.83, 0.85	
NiC	5.65	0.70	0.49	0.45	0.21	0.45	0.75, 0.77	
YC	6.39	0.80	0.43	0.65	0.33	0.44	0.62, 0.78	
ZrC	7.93	0.99	0.64	0.86	0.53	0.66	0.82, 0.94	
NbC	8.26	1.03	0.72	0.87	0.49	0.69	0.90, 0.87	
MoC	7.22	0.90	0.66	0.77	0.38	0.64	0.90, 0.77	
TcC	6.88	0.86	0.66	0.69	0.37	0.61	0.88, 0.77	
RuC	6.73	0.84	0.68	0.69	0.31	0.45	0.86, 0.77	
RhC	6.23	0.77	0.62	0.68	0.38	0.41	0.82, 0.75	
PdC	5.36	0.67	0.52	0.47	0.32	0.48	0.73, 0.65	
LaC	5.74	0.71	0.39	0.70	0.25	0.33	0.63, 0.81	
HfC	8.11	1.01	0.68	0.90	0.52	0.70	0.82, 0.97	
TaC	8.56	1.07	0.70	0.88	0.52	0.68	0.87, 0.89	
WC	8.25	1.03	0.74	0.77	0.47	0.65	0.85, 0.76	
ReC	7.47	0.93	0.73	0.66	0.34	0.44	0.81, 0.73	
OsC	7.36	0.92	0.78	0.62	0.28	0.41	0.77, 0.71	
IrC	6.84	0.85	0.75	0.59	0.31	0.35	0.72	
PtC	6.34	0.79	0.69	0.49	0.14	0.29	0.64, 0.68	

Table 6.11 Comparison of γ_{100} values in eV·atom^{-1} of TMNs between γ_1 of Eq. (6.57), γ_2 of Eq. (6.56), simulation results γ_3 using GGA-PW91 and γ_4 using LDA, and other simulation results γ_5

	E_b	γ_1	γ_2	γ_3	γ_4	γ_5
ScN	6.72	0.84	0.59	0.39	0.54	
TiN	6.69	0.83	0.58	0.38	0.61	0.36
VN	6.25	0.78	0.55	0.29	0.47	0.27
CrN	5.14	0.65	0.44	0.28	0.36	
YN	6.98	0.86	0.61	0.45	0.50	
ZrN	7.52	0.94	0.66	0.48	0.73	
NbN	7.50	0.95	0.66	0.41	0.56	
MoN	6.20	0.78	0.55	0.38	0.45	
TcN	5.48	0.69	0.48	0.36	0.38	
LaN	6.27	0.79	0.55	0.34	0.50	
HfN	7.62	0.96	0.67	0.45	0.69	
TaN	7.63	0.96	0.67	0.39	0.55	

For TMCs and TMNs, the existence of the *d*-electron of transition metals leads to almost the same lattice constants for the same group when the period number of transition metals increases. At the same time, their E_c increases gradually. Thus, γ_{sv0} values increase a little as the period number increases.

On the other side, as the group number in the same period varies, a maximum of E_c values is reached at VB or IVB group. Thus, the corresponding γ_{sv0} values also approach their maxima. It is known that the variation of the bandwidth of compounds should be proportional to that of γ_{sv0} values, which has been confirmed for 4d-TMC by analyzing the density of states (DOS) and the Fermi energy using LMTO method. It is found that the bandwidth developed an early maximum for ZrC and NbC around 11 eV, after which it remains fairly constant, and then shifts downwards for AgC only around 5 eV. The same trend is found in the 3d, 4d and 5d carbides. Considering the chemical similarities between TMNs and TMCs, the variations of γ_{sv0} values in TMN series should follow the same rule.

Table 6.12 gives the calculated γ_{sv0} values of AMOs in terms of Eq. (6.57), Eq. (6.56), LDA and GGA-PW91, and other theoretical results. The packing densities of (100), (110) and (111) surfaces of NaCl structure are roughly in the ratio of 1: 0.71: 0.58, which suggests a sequence of $\gamma_{100} < \gamma_{110} < \gamma_{111}$ where the (100) surface is the most stable surface and the (111) one is the most reactive. As expected, the calculated results agree with the above sequence.

Table 6.12 Comparison of γ_{sv0} values in eV·atom^{-1}of AMOs between γ_1 of Eq. (6.31), γ_2 of Eq. (6.30), simulation results γ_3 using GGA-PW91 and γ_4 using LDA, and other two series of available LDA results γ_5 and GGA results γ_6

	E_c	(hkl)	γ_1	γ_2	γ_3	γ_4	γ_5	γ_6
MgO	5.15	(100)	0.64	0.45	0.24	0.32	0.32	0.29
		(110)	1.32	0.95	0.75	1.03	0.98	0.87
		(111)	2.04	1.51	2.03	2.30		
CaO	5.50	(100)	0.65	0.48	0.24	0.31	0.30	0.24
		(110)	1.41	1.01	0.73	1.05	0.92	0.73
		(111)	2.18	1.61	1.62	2.07		
SrO	5.20	(100)	0.65	0.45	0.23	0.28	0.28	0.25
		(110)	1.34	0.96	0.68	0.96	0.83	0.73
		(111)	2.06	1.53	1.54	1.65		
BaO	5.05	(100)	0.62	0.44	0.21	0.27	0.27	0.20
		(110)	1.23	0.93	0.66	0.88	0.75	0.62
		(111)	2.00	1.49	1.04	1.62		

γ_{111} value of MgO is 2.54 eV·atom^{-1}, which was obtained by the DFT based on full-potential linearized augmented plane-wave method. When it is compared with $\gamma_{100}= 0.26$ eV·atom^{-1}, γ_{111} is one order larger than γ_{100}. This can be induced by its polar nature with instability. From Table 6.12, comparison between Eq. (6.57) and the simulation results shows that the deviation between them increases along the series from MgO to BaO. This may be due to the increase of the crystalline lattice constant with drop of the binding energy induced by the increase of cation repulsion and decrease of anion-anion overlap.

For a certain surface, γ_{sv0} values decrease along the sequence going from

MgO to BaO where the energy loss of MgO is most obvious. MgO has much broader bandwidth and higher dispersion than the rest of the series. The DOS analysis indicates that the O $(2p)$ band becomes narrower along the series going from MgO to BaO. Only the bandwidth of MgO is prominently broader while the bandwidths of CaO, SrO, and BaO are roughly the same. These could be the change cause of γ_{sv0} along the period numbers of the corresponding metals. The above fact can also be considered by Eq. (6.57). The reverse ratio between the period number of the metals and γ_{sv0} values of AMOs is induced by increase of a due to the rapid increase of s-electron orbital as the period number increases while E_c remains almost constant for the same group of elements.

6.6.3 Size-dependent Surface Energy of Solids [3]

The thermodynamic behavior of nanocrystals differs from that of the corresponding bulk materials mainly due to the additional energetic term of $\gamma_{sv}(r)A$–the product of the surface (or interfacial) excess Gibbs free energy and the surface (or interfacial) area. This term becomes significant to change the thermal stability of the nanocrystals due to increasing $A/V \propto 1/r$. When the surfaces of polymorphs of the same material possess different interfacial free energy, a change in phase stability can occur with decreasing r.

In mesoscopic size range, the size dependence of the liquid-vapor interface energy $\gamma_{Lv}(r)$ was thermodynamically considered by Tolman and Buff [14, 15], respectively. The final form of the analytical equation is as follows [14]:

$$\gamma_{Lv}(r)/\gamma_{Lv0} = 1 - 2\delta_v/r + \cdots \tag{6.63}$$

where γ_{Lv0} is the corresponding bulk value of $\gamma_{Lv}(r)$, δ_v denotes a vertical distance from the surface of tension to the dividing surface where the superficial density of fluid vanishes. As a first order approximation, although there is no direct experimental evidence to support Eq. (6.63), Eq. (6.63) should also be applicable to predicting $\gamma_{sv}(r)$ since the structural difference between solid and liquid is very small in comparison with that between solid and gas or between liquid and gas. In addition, it is unknown whether r in Eq. (6.63) can be extended from micron size to nanometer size. Although both the expressions of Eqs. (6.55) to (6.59) and the corresponding results are different, all of them indicate that

$$\gamma_{sv} = \nu E_c/(N_A A_S) \tag{6.64}$$

where $\nu < 1$ is a function of CN.

If the nanocrystals have the same structure as the corresponding bulk, ν is size-independent. Thus, Eq. (6.64) may be extended to nanometer size as

$$\gamma_{sv}(r) = \nu E_c(r)/(N_A A_S). \tag{6.65}$$

Combining Eq. (6.65) with Eq. (3.90), there is

$$\gamma_{sv}(r)/\gamma_{sv} = \left[1 - \frac{1}{4r/h - 1}\right] \exp\left(-\frac{2\Delta S_b}{3R}\frac{1}{4r/h - 1}\right). \tag{6.66}$$

Comparisons of $\gamma_{sv}(r)$ of Be, Mg, Na, Al thin films and Au particles with different facets between Eq. (6.66) and experimental and other theoretical results are shown in Figs. 6.17 and 6.18 where the related parameters in Eq. (6.66) are listed in Table 6.13. It is evident that predictions of Eq. (6.66) are in agreement with the experimental values of Be and Mg (0001), and with other theoretical results of Na (110) and for three low-index surfaces of Au. The deviations in all comparisons are smaller than 5% except the deviation for Al (110) with a deviation of about 10%.

As shown in Figs. 6.17 and 6.18, $\gamma_{sv}(r)$ decreases with a decrease in size. This trend is expected since $E(r)$ of the nanocrystals increases as r decreases. In other words, $\gamma_{sv}(r)$ as an energetic difference between surface atoms and interior atoms decreases as energetic state of interior atoms increases.
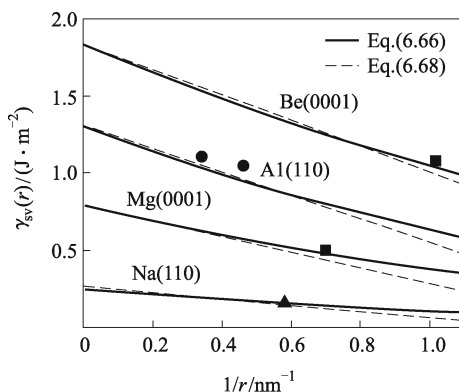
Fig. 6.17 $\gamma_{sv}(r)$ as a function of $1/r$ in terms of Eqs. (6.66) (solid line) and (6.68) (segment line) for nanocrystals Be, Mg, Na and Al with different facets. The symbols ■, ▲ and ● denote the experimental results of Be and Mg (0001), the theoretical values for Na (110) and Al (110). (Reproduced from Ref. [3] with permission of Elsevier)

Since $\exp(-x) \approx 1-x$ when x is small enough, Eq. (6.66) can be rewritten as

$$\gamma_{sv}(D)/\gamma_{sv} \approx 1 - \Delta S_b h/(6Rr). \tag{6.67}$$

Equation (6.67) is in agreement with the general consideration that the decrease of any size-dependent thermodynamic quantity is proportional to $1/r$. If $\gamma_{sv}(r)$ of Eq. (6.67) and $\gamma_{Lv}(r)$ of Eq. (6.63) have the same size dependence, $\delta = \Delta S_b h/(12R) \approx h$ when $\Delta S_b \approx 12R$ as seen in Table 6.13. Namely, the transition zone separating a solid phase and a vapor phase is only one atomic layer, being an understandable result. This δ value is expected since when
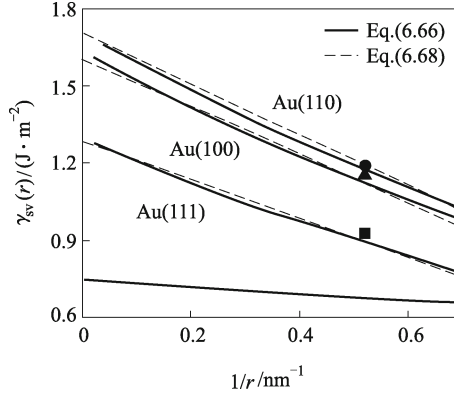
Fig. 6.18 $\gamma_{sv}(r)$ as a function of $1/r$ for nanocrystals Au with different facets in terms of Eq. (6.66) (solid line) and Eq. (6.68) (segment line). The symbols ■, ▲ and ● denote the calculated results of (111), (100) and (110) facets in terms of a modified embedded-atom-method potential. (Reproduced from Ref. [3] with permission of Elsevier)

Table 6.13 Necessary parameters in equations with r and h in nm, E_c in kJ·mol^{-1}, T_b in K, ΔS_b in J·mol^{-1}·K^{-1}, and γ_{sv0} in J·m^{-2}

Element	Surface	r	h	E_c	T_b	ΔS_b	γ_{sv0}
Be	(0001)	0.95	0.222	292.4	2745	106.5	1.83
Mg	(0001)	1.40	0.320	127.4	1363	93.5	0.79
Na	(110)	1.73	0.372	97.0	1156	83.9	0.26
Al	(110)	2.15	0.286	293.4	2793	105.0	1.30
		2.86					
	(111)						1.28
Au	(100)	1.90	0.288	334.4	3130	106.8	1.63
	(110)						1.70

the atomic distance is longer than h, the bond energy decreases dramatically. Thus, Eq. (6.63) can be rewritten as

$$\gamma_{Lv}(r)/\gamma_{Lv0} \approx \gamma_{sv}(r)/\gamma_{sv0} \approx 1 - 2h/r. \qquad (6.68)$$

It is known that the surface energy ratio between different facets is a more important parameter in determining the crystalline shapes. Equation (6.66) indicates that

$$\frac{\gamma_{sv}^1(r)}{\gamma_{sv}^2(r)} = \frac{\gamma_{sv0}^1}{\gamma_{sv0}^2} \qquad (6.69)$$

where the superscripts "1" and "2" denote different facets. Equation (6.67) implies that although the surface energy is size-dependent, the surface energy ratio between different facets is size-independent and is equal to the corresponding bulk ratio. Equation (6.69) can also be compared with the theoretical results for Au where for example, $\gamma_{sv}^{(100)}(3.8nm)/\gamma_{sv}^{(111)}(3.8nm)$

≈ 1.24 and $\gamma_{sv}^{(110)}(3.8nm)/\gamma_{sv}^{(111)}(3.8nm) \approx 1.28$, which correspond well to the corresponding bulk ratios of 1.27 and 1.32.

Note that the structures of Be and Mg, Na, Al and Au belong to hcp, bcc and fcc structures, respectively. Owing to the agreement shown in Figs. 6.17 and 6.18, the model should be applicable to all crystalline structures with different facets. Thus, Eq. (6.66) not only supplies a simple way to determine $\gamma_{sv}(r)$ values of different facets without any free parameter but also has an evident thermodynamic characteristic.

6.7 Liquid-vapor Interface Energy or Surface Tension

6.7.1   Bulk Surface Tension and Its Temperature Coefficient [3]

The γ_{Lv0} function and its temperature dependence are fundamental and important in the theory and practice of materials processing (e.g. crystal growth, welding and sintering), and its temperature coefficient $\gamma'_{Lv0}(T) = d\gamma_{Lv0}(T)/dT$ governs the well-known Marangoni convection on the surface of melt. There are several characteristics for the liquid surface. First, the liquid surface usually takes an equilibrium configuration with the minimum energy due to the high mobility of liquid molecules. Second, because the liquid fails with respect to elastic deformation resistance, $\gamma_{Lv0}(T)$ equals surface stress when surface adsorption is not taken into account. Although early methods of measurement of $\gamma_{Lv0}(T)$ are sufficiently precise, there is still uncertainty regarding its absolute values, particularly the $\gamma'_{Lv0}(T)$ function mainly due to the effect of impurities, which markedly changes the measured results. Therefore, considerable efforts have recently been directed towards the experimental determinations of $\gamma_{Lv0}(T)$ and $\gamma'_{Lv0}(T)$ of metals, and progress has been achieved with the advent of levitation processing and oscillating drop techniques. However, such an experiment often suffers from the ambiguities in the interpretation of the resulting frequency spectra. It is also unlikely that experimental measurements will ever encompass all possible temperature ranges of interest for all metals.

In contrast to the determination of $\gamma_{Lv0}(T_m)$ values, $\gamma'_{Lv0}(T_m)$ values are not well known experimentally even for elemental metallic liquids. A recent analysis of existing data shows that this quantity is known with accuracy better than 50% for only 19 metals while the accuracy is worse for other 28 metals. For the rest 18 metals (mainly refractory metals), there are even no experimental results.

Computer stimulations with Monte Carlo or MD methods are considered to be one of the reliable methods, with which γ_{Lv0} can be calculated either using the mechanical expression for the surface stress or from the viewpoint of

γ_{sv0}. Unfortunately, the former approach suffers from rather high fluctuation and statistical uncertainty, while the latter introduces additional complexity into performance. Thus, the demand of developing reliable prediction methods has never declined.

Semiempirical predictions based on the correlation between the surface and bulk thermodynamic properties are always active. Stephan firstly links γ_{Lv0} to the heat of evaporation $\Delta H'_v$ at $T = 0$ K,

$$\gamma_{Lv0}(T_m) = c' \Delta H'_v / V_L^{2/3} \tag{6.70}$$

with c' being an unknown constant. Equation (6.70) seems to apply only to transition metals. Although Eq. (6.70) has existed for more than 100 years, attempts to theoretically determine c' value are rare.

On the other hand, $\gamma_{Lv0}(T)$ of pure substances may be evaluated from values of critical temperature T_c by the Eötvos or Guggenheim empirical equations,

$$\gamma_{Lv0}(T) V^{2/3} = Q(1 - T/T_c) \tag{6.71a}$$

or

$$\gamma_{Lv0}(T)/\gamma_{Lv0}(T_m) = (1 - T/T_c)^j \tag{6.71b}$$

where the precoefficient Q and the exponent j are system-dependent, e.g. $j = 4/5$ for strongly hydrogen-bonded substances, $j = 11/9$ for H_2, N_2 and CO, etc. However, j value for liquid metals has not been determined. Moreover, unlike those of organic liquids, T_c values of liquid metals are only available for alkali metals and Hg, which severely restricts the use of Eq. (6.71a).

When $\gamma_{Lv0}(T_m)$ and $\gamma'_{Lv0}(T_m)$ values are known, under the assumption that $\gamma'_{Lv0}(T)$ is nearly a constant being equal to $\gamma'_{Lv0}(T_m)$ when T is near T_m, the $\gamma_{Lv0}(T)$ function is expressed simply in a differential form,

$$\gamma_{Lv0}(T) = \gamma_{Lv0}(T_m) + \gamma'_{Lv0}(T_m)(T - T_m). \tag{6.72}$$

However, Eq. (6.72) has not been strictly examined. Thus, both $\gamma_{Lv0}(T)$ and $\gamma'_{Lv0}(T)$ functions need to be further considered.

As stated in Sec. 6.6.1, Eq. (6.58) can be used to calculate γ_{sv0} of elements. Due to the structural similarity of liquid and solid at least near T_m, Eq. (6.58) for γ_{sv0} should give suggestions for γ_{Lv0} modeling and analytical determination of c' value in Eq. (6.70).

About 60 years ago, noting that fusion has only a little effect on V, E_c, and C_P of substance, Frenkel reached the conclusion that "the character of the heat motion in liquid bodies, at least near the crystallization point, remains fundamentally the same as in solid bodies, reducing mainly to small vibrations about certain equilibrium position". The very slight change in volume on melting is also thought to imply that the atoms in a liquid are tightly bound to one another like those in a crystalline solid. Thus, the structural and energetic differences between a solid and a liquid are very small in comparison with those between a solid and a vapor or between a

liquid and a vapor. Consequently, Eq. (6.58) can be extended to determine γ_{Lv0} with several modifications: (1) Since $T \geqslant T_m \gg 0$ for liquids, E_c at 0 K should be replaced by $\Delta H_v(T)$ and A_S should be substituted by $A_L(T)$ where the subscript "L" denotes liquid; (2) The influence of molar excess surface entropy $\Delta S(T)$ should contribute to γ_{Lv0} due to the high temperature condition; (3) CN of liquid is usually determined by integrating the radial distribution function (RDF) up to the first minimum while the distance of the second minimum of RDF is approximately twice that of the first one, the effect of the next nearest neighbors thus may be neglected in terms of the LJ potential, namely $\varphi \approx 0$. Thus, Eq. (6.58) can be rewritten for determining $\gamma_{Lv0}(T)$,

$$\gamma_{Lv0}(T) = [m'\Delta H_v(T) - T\Delta S(T)]/[N_A A_L(T)] \tag{6.73}$$

with $m' = (2 - \nu_1 - \nu_1^{1/2})/2$.

Since metallic liquid is closely packed, the packing density of a random close packing ($\eta_L = 0.637$) can be employed for the liquid. The volume change on melting $\Delta V/V_s$ is not solely determined by the difference in η between two phases, and the Goldschmidt premise for lattice contraction should also be considered. Otherwise, when $\eta_L = 0.637$ is compared with $\eta_{fcc} = 0.74$, $\Delta V/V_s = \eta_{fcc}/\eta_L - 1 \approx 16\%$, which is larger than the experimentally observed value of 2%–6%. Note that $\eta_L = 0.637$ is the maximal value that the single-component liquid can take, which leads to the fact that the specific volume difference between a solid with bcc structure and the corresponding liquid is only 0.2%. Whether a metal can be undercooled depends on the energetic nucleation barrier. When ΔV on crystallization is small, the corresponding nucleation barrier should be also small, as discussed in Sec. 6.4.1. This leads to a small degree of undercooling. If this rule can also be applied to elements, the local order in the metallic liquid is very similar to the bcc-type short-range order, such as liquid Zr. Correspondingly, this consideration can also be applied to the surface structure of liquid metals. Note that the surface of bcc structure is (110) facet to ensure the minimum of the product of $\gamma_{sv0} \sum A_{bcc}$. Thus, the expression of A_{bcc} is assumed to be applicable also to the liquid as a first order approximation. As a result, $\nu_1 = 3/4$ and $A_L = 8^{1/2}h^2/3$. For any pure, isotropic, condensed material, $h = (6\eta V/\pi)^{1/3}$. V can be calculated from the atomic weight M and $\rho(T)$ by $V = M/[N_A\rho(T)]$. Thus, $A_L(T)$ can be determined as

$$A_L(T) = \lambda'\{M/[N_A\rho_L(T)]\}^{2/3} \tag{6.74}$$

with $\lambda' = (8^{1/2}/3)(6\eta/\pi)^{2/3}$. Since $d\rho_L/dT \approx d\rho_L(T_m)/dT$ for liquid metals in the temperature range of $T_m - 2T_m$, $\rho_L(T)$ is equal to $\rho_L(T_m) + (d\rho_L/dT)(T - T_m)$ with $d\rho_L/dT$ being the temperature coefficient of liquid density. This range could be up to $3T_m$ for Rb and Cs and $4T_m$ for Li and K.

It is known that $\Delta H_v(T_c) = 0$ for most substances and reaches the maximum at the triple point T_t where T_t is very close to T_m for metals. Recently, an empirical equation $\Delta H_v(T)/\Delta H_v(T_m) = (1 - t)^{it+j}$ has been proposed

for liquids having a triple point where $t = (T - T_{\mathrm{m}})/(T_c - T_{\mathrm{m}})$, $i = 0.44$ and $j = -0.137$ [16]. In terms of the known $T_{\mathrm{m}}, T_{\mathrm{b}}$ and T_c values for alkali metals (Hg is not involved in this work), it is found that $\Delta H_{\mathrm{v}}(T)$ function between T_{m} and T_{b} is a very weak function of $T (<2\%)$ and thus negligible. Moreover, it is reported that $\Delta H_{\mathrm{v}}(T_{\mathrm{m}})$ values of Cd, Cr, Mn and Zn are 101, 344, 234 and 115 (kJ·mol^{-1}) while the corresponding $\Delta H_{\mathrm{v}}(T_{\mathrm{b}})$ values are 100, 339, 226 and 119 (kJ·mol^{-1}). Their differences are less than 3.5%. Thus, the relation $\Delta H_{\mathrm{v}}(T_{\mathrm{m}} \leqslant T \leqslant T_{\mathrm{b}}) \approx \Delta H_{\mathrm{v}}(T_{\mathrm{m}}) \approx \Delta H_{\mathrm{v}}$ does not lead to big deviation and can be accepted as a first order approximation.

In Skapski's model, the main contribution to ΔS results from the change of oscillation frequency of atoms at the surface. Note that according to Lindemann's criterion, the mean value of oscillation frequency reaches a certain value at T_{m}, which leads to a constant ΔS value at T_{m}. It is known that ΔH_{v} determines the bond strength of liquid atoms, which further determines the size of oscillation frequency. Since $\Delta H_{\mathrm{v}}(T)$ varies little between T_{m} and T_{b}, the temperature dependence of $\Delta S(T)$ is thus negligible and $\Delta S(T) \approx \Delta S(T_{\mathrm{m}}) \approx \Delta S$ can also be assumed.

With these considerations and insertion of Eq. (6.74) into Eq. (6.73), $\gamma_{\mathrm{Lv0}}(T)$ between T_{m} and T_{b} can be determined as

$$\gamma_{\mathrm{Lv0}}(T) = \left[\frac{m'\Delta H_{\mathrm{v}} - T\Delta S}{\lambda N_{\mathrm{A}}^{1/3}} \right] \left(\frac{\rho_{\mathrm{L}}(T)}{M} \right)^{2/3} \tag{6.75a}$$

or

$$\frac{\gamma_{\mathrm{Lv0}}(T)}{\gamma_{\mathrm{Lv0}}(T_{\mathrm{m}})} = \left(1 + \kappa - \kappa\frac{T}{T_{\mathrm{m}}} \right) \left(1 - q + q\frac{T}{T_{\mathrm{m}}} \right)^{2/3} \tag{6.75b}$$

where $\kappa = 1/[m'\Delta H_{\mathrm{v}}/(T_{\mathrm{m}}\Delta S) - 1]$ and $q = (\mathrm{d}\rho_{\mathrm{L}}/\mathrm{d}T)[T_{\mathrm{m}}/\rho_{\mathrm{L}}(T_{\mathrm{m}})]$ are constants for certain metals. Deviation of Eq. (6.75a) with respect to T brings out

$$-\gamma'_{\mathrm{Lv0}}(T) = \frac{\gamma_{\mathrm{Lv0}}(T)}{T} \left[\frac{1}{m'\Delta H_{\mathrm{v}}/(T\Delta S) - 1} - \frac{2}{3}\frac{T}{\rho_{\mathrm{L}}(T)}\frac{\mathrm{d}\rho_L}{\mathrm{d}T} \right]. \tag{6.76}$$

6.7.2 Determination of $\gamma_{\mathrm{Lv0}}(T_{\mathrm{m}})$ and $\gamma'_{\mathrm{Lv0}}(T_{\mathrm{m}})$ Values and $\gamma_{\mathrm{Lv0}}(T)$ and $\gamma'_{\mathrm{Lv0}}(T)$ Functions [3]

Table 6.14 gives the comparison between the predicted $\gamma_{\mathrm{Lv0}}(T_{\mathrm{m}})$ values for 48 liquid metals in terms of Eq. (6.75a) and available mean values of experimental results $\gamma^{\mathrm{e}}_{\mathrm{Lv0}}(T_{\mathrm{m}})$. These experimental data are mainly obtained by the maximum bubble pressure technique for oxidizable metals with low T_{m} like Na, the sessile drop technique for metals with moderate T_{m} like Cu, and the drop weight technique employed at the extremity of a pendant wire with electron bombardment heating for refractory metals like W.

It is found that $\varpi = |\gamma_{\mathrm{Lv0}}(T_{\mathrm{m}}) - \gamma^{\mathrm{e}}_{\mathrm{Lv0}}(T_{\mathrm{m}})|/\gamma^{\mathrm{e}}_{\mathrm{Lv0}}(T_{\mathrm{m}}) < 10\%$ for 40 elements [from Cu to Ba (Table 6.14)]. Note that although $\gamma^{\mathrm{e}}_{\mathrm{Lv0}}(T_{\mathrm{m}}) = 867$ mJ·m^{-2} was proposed for Al, several measurements suggested that the most data for $\gamma^{\mathrm{e}}_{\mathrm{Lv0}}(T_{\mathrm{m}})$ of Al pertain to oxygen-saturated material and those for pure Al could be about $\sim$1070 mJ·m^{-2}. If this result is used, ϖ for Al will only be 3.6%. For divalent metals Mg, Zn and Cd, Eq. (6.75a) is evidently smaller than $\gamma^{\mathrm{e}}_{\mathrm{Lv0}}(T_{\mathrm{m}})$. According to Miedema and Boom, these three metals have an exceptionally stable free atomic configuration, which is close to that of rare gas. Thus, smaller $\gamma_{\mathrm{Lv0}}(T_{\mathrm{m}})$ values in terms of Eq. (6.75a) may be reasonable. Although ϖ values of Ta, Nb, Li, Be, and La range from 13% to 22%, the causes are unknown. The data given above imply that Eq. (6.75a) is suitable for all metals although the errors for transition metals are slightly larger than those for other metals.

Table 6.14 Comparisons of $\gamma_{\mathrm{Lv0}}(T_{\mathrm{m}})$ in mJ·m^{-2} for liquid metals between γ_{Lv0} of Eq. (6.75a) and experimental results $\gamma^{\mathrm{e}}_{\mathrm{Lv0}}$, as well as comparisons of $\gamma'_{\mathrm{Lv0}}(T_{\mathrm{m}})$ in mJ·m^{-2}· K^{-1} between γ'_{Lv0} of Eq. (6.76) and experimental or estimated results $\gamma'^{\mathrm{e}}_{\mathrm{Lv0}}\Delta H_{\mathrm{v}}$ in kJ·g^{-1}·atom^{-1}, ρ_{L} in kg·m^{-3}, and dρ_{L}/dT in kg·m^{-3}·K$^{-1}\Delta S = 5.30$ J·mol^{-1}·K^{-1}, $m' \approx 0.19$. The asterisk * denotes that the accuracy on $\gamma'^{\mathrm{e}}_{\mathrm{Lv0}}$ is better than 50%

	γ_{Lv0}	$\gamma^{\mathrm{e}}_{\mathrm{Lv0}}$	$-\gamma'_{\mathrm{Lv0}}$	$-\gamma'^{\mathrm{e}}_{\mathrm{Lv0}}$	ΔH_{v}	ρ_{L}	dρ_{L}/dT
Cu*	1352	1355, 1310	0.21	0.19, 0.23	300	8000	-0.801
Ag*	925	910, 925	0.18	0.17, 0.21	255	9346	-0.907
Au*	1211	1138, 1145	0.18	0.19, 0.20	330	17360	-1.500
Ni*	1810	1838, 1796	0.33	0.42, 0.35	378	7905	-1.160
Pd	1467	1475, 1482	0.25	0.28, 0.28	380	10490	-1.266
Pt*	1896	1746, 1860	0.31	0.29, 0.31	490	19000	-2.900
Co*	1779	1830, 1881	0.30	0.37, 0.34	375	7760	-0.988
Rh	2010	2000, 1970	0.26	0.30, 0.66	495	10800	-0.896
Ir*	2241	2140, 2250	0.20	0.23, 0.25	560	20000	-0.935
Fe*	1650	1830, 1855	0.26	0.23, 0.39	355	7015	-0.883
Ru	2363	2180, 2250		0.31	580	10900	
Os	2508	2500, 2500		0.23	630	20100	
Mn	986	1152, 1100	0.21	0.20, 0.35	226	5730	-0.700
Tc	2245	2350			550	10300	
Re*	2755	2520, 2700	0.20	0.23	705	18800	-0.800
Cr	1582	1628, 1642	0.19	0.20, 0.20	339	6280	-0.300
Mo	2110	2250, 1915	0.21	0.20, 0.30	600	9340	-0.743
W*	2676	2500, 2310	0.23	0.29, 0.21	800	16200	-1.250
V*	1902	1855, 1900	0.23	0.19, 0.31	453	5700	-0.531
Ti	1520	1525, 1500	0.27	0.26, 0.20	425	4110	-0.702
Zr*	1669	1480, 1435	0.14	0.20, 0.17	580	5800	-0.310
Hf*	1591	1630, 1490		0.21, 0.19	575	11100	
Sc	895	939, 870		0.12, 0.12	318	2846	
Y	899	872, 800		0.09, 0.09	380	4243	
Ce	845	794, 740	0.09	0.07, 0.08	350	6685	-0.227
Pr	782	743, 716	0.09	0.09, 0.08	330	6611	-0.240
Nd	658	689, 687	0.10	0.09, 0.09	285	6688	-0.528
Gd	690	664, 664		0.06, 0.06	305	7140	
Th	1108	1006, 978		0.14	514	10500	
U	1453	1550, 1552	0.15	0.14, 0.27	420	17900	-1.031

Continue

	γ_{Lv0}	$\gamma_{\mathrm{Lv0}}^{\mathrm{e}}$	$-\gamma_{\mathrm{Lv0}}'$	$-\gamma_{\mathrm{Lv0}}'^{\mathrm{e}}$	ΔH_{v}	ρ_{L}	$\mathrm{d}\rho_{\mathrm{L}}/\mathrm{d}T$
Al*	1031	1070, 867	0.19	0.15, 0.16	283	2385	−0.280
Pb*	466	462, 457	0.12	0.11, 0.11	178	10678	−1.317
Tl*	439	461, 459	0.11	0.09, 0.11	165	11280	−1.430
Na*	215	200, 197	0.09	0.10, 0.09	98	927	−0.236
K*	110	112, 110	0.07	0.08, 0.07	79	827	−0.229
Rb	90	90, 85	0.06	0.07, 0.06	76	1437	−0.486
Cs*	73	69, 70	0.05	0.06, 0.05	69	1854	−0.638
Ca*	328	337, 366	0.09	0.11, 0.10	164	1365	−0.221
Sr*	268	289, 286	0.08	0.08, 0.08	144	2480	−0.262
Ba	231	226, 267	0.07	0.07, 0.07	150	3321	−0.526
Mg	359	557, 583	0.14	0.15, 0.26	128	1590	−0.265
Zn	466	789, 815	0.18	0.25, 0.21	119	6575	−1.100
Cd	305	637, 642	0.13	0.20, 0.15	100	8020	−1.160
Ta*	2467	2180, 2010	0.22	0.25, 0.20	735	15000	−1.147
Nb*	2335	2040, 1840	0.27	0.24, 0.18	690	7830	−0.800
Li	465	404, 399	0.15	0.16, 0.15	137	525	−0.052
Be	1637	1350, 1320	0.24	0.29	297	1690	−0.116
La	901	737, 728	0.09	0.11, 0.10	400	5955	−0.237

$\gamma_{\mathrm{Lv0}}(T_{\mathrm{m}})$ values of transition metals increase along an isoelectronic row, where a heavier element has a larger $\gamma_{\mathrm{Lv0}}(T_{\mathrm{m}})$ value. This is because the d level of a heavier element is higher in energy and the corresponding d wave functions with stronger bonding are more extended. Two exceptions are Pd and Zr. For Pd, the full filled d orbital drops the system energy in terms of Hunt's rule, which indicates that its ΔH_{v} value only approaches that of Ni. Since V_{m} and T_{m} values of Pd are obviously larger than those of Ni, $\gamma_{\mathrm{Lv0}}(T_{\mathrm{m}})$ of Pd is thus smaller than that of Ni in terms of Eq. (6.75a). For Zr, its ΔH_{v} and V_{m} values approach those of Hf while its T_{m} value is obviously smaller than that of Hf, $\gamma_{\mathrm{Lv0}}(T_{\mathrm{m}})$ of Zr is therefore larger than that of Hf. The reason of larger ΔH_{v} value of Zr is unclear.

$\gamma_{\mathrm{Lv0}}(T_{\mathrm{m}})$ values of sp metals except the value of Be are smaller than those of d metals due to the bond nature of s and p electrons, which are more mobile than the localized d electrons. Moreover, in contrast to the transition metals, $\gamma_{\mathrm{Lv0}}(T_{\mathrm{m}})$ values of sp metals decrease along an isoelectronic row. This arises because the outmost $n's$ electrons (the number of period $n' = 2$–6) are progressively bound more loosely as they are screened from the nucleus by the increasing number of filled inner shells in the ionic core.

Note that assuming the geometric structure in liquid Si and Ge to be close to that of (100) face of sc structure, their γ_{Lv0} values can be calculated using the above method and reasonable correspondences with experimental or other theoretical results have been found.

To find the similarity between Eq. (6.75a) and Eq. (6.70), the prefactor c' in Eq. (6.70) can be determined by rearranging Eq. (6.75a) at $T = T_{\mathrm{m}}$,

$$\gamma_{\mathrm{Lv0}}(T_{\mathrm{m}}) = c\Delta H_{\mathrm{v}}/V_{\mathrm{s}}^{2/3} \tag{6.77}$$

with

$$c = (m' - T_\mathrm{m}\Delta S/\Delta H_\mathrm{v})/(\lambda N_\mathrm{A}^{1/3}). \tag{6.78}$$

Eq. (6.78) has determined c' value in Eq. (6.70) although Eq. (6.77) differs from Eq. (6.70) a little due to the difference of ΔH_v and $\Delta H_\mathrm{v}'$, or $c = c'\Delta H_\mathrm{v}'/\Delta H_\mathrm{v}$.

Figure 6.19 gives a plot of $\gamma_\mathrm{Lv0}(T_\mathrm{m})$ against $\Delta H_\mathrm{v}/V_\mathrm{s}^{2/3}$ for considered liquid metals in terms of Eq. (6.77) with a linearly regressed slope of $c = 0.174 \times 10^{-8}$ $\mathrm{mol}^{1/3}$ where the correlation coefficient of the fit is 0.998. All metallic elements can thus be estimated by the same c value, which implies that $T_\mathrm{m}/\Delta H_\mathrm{v}$ is almost a constant (since ΔS value has been taken as a constant according to Lindemann's criterion, $m' \approx 0.19$ and $\lambda \approx 1.08$) in terms of Eq. (6.78), which also confirms the correctness of Eq. (6.77). It is known that $\Delta H_\mathrm{v} \propto \Delta H_\mathrm{m}$, and $T_\mathrm{m}/\Delta H_\mathrm{m} = 1/\Delta S_\mathrm{m}$. Since ΔS_m is almost a constant for metallic elements, c value as a constant is reasonable. In terms of the $\Delta H_\mathrm{v}'$ data, it is found that $\Delta H_\mathrm{v}'/\Delta H_\mathrm{v}$ is nearly a constant (≈ 1.09) for transition metals. Thus, $c = c'\Delta H_\mathrm{v}'/\Delta H_\mathrm{v} = 0.174 \times 10^{-8}$ $\mathrm{mol}^{1/3}$ where $c' = 0.16 \times 10^{-8}$ $\mathrm{mol}^{1/3}$ as determined above. In contrary to Eq. (6.70), which is considered to be only suitable for transition metals, all metals are involved in Fig. 6.19. This improvement is only induced by the replacement of $\Delta H_\mathrm{v}'$ by $\Delta H_\mathrm{v}(T_\mathrm{m})$. $\Delta H_\mathrm{v}(T_\mathrm{m})$ describes the atom bonding of stable liquid and can be exactly measured while $\Delta H_\mathrm{v}'$ can be obtained only by extension of experimental results. In addition, since the difference between 0 K and T_m for transition metals are larger than that for non-transition metals, which leads to larger difference between $\Delta H_\mathrm{v}(T_\mathrm{m})$ and $\Delta H_\mathrm{v}'$ for transition metals than for non-transition metals. This results in smaller suitability range of Eq. (6.70) but not Eq. (6.77).
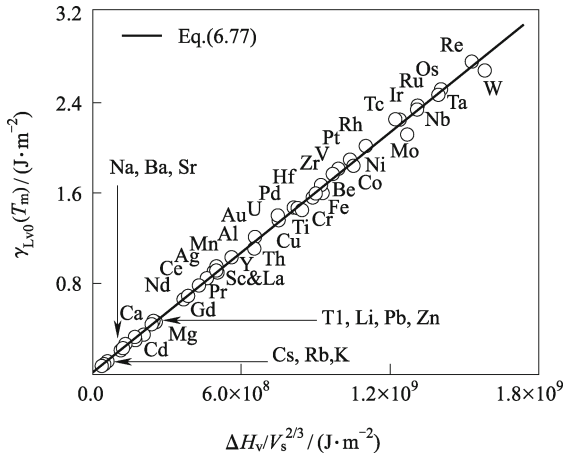
Fig. 6.19 $\gamma_\mathrm{Lv0}(T_\mathrm{m})$ as a function of $\Delta H_\mathrm{v}/V_\mathrm{s}^{2/3}$ for liquid metals in terms of Eq. (6.77) where the solid line is linearly regressed. (Reproduced from Ref. [3] with permission of Elsevier)

In terms of Eq. (6.75a), the introduction of ΔS drops the value of $\gamma_{Lv0}(T)$. At T_m, the decreasing extents range from 8% (for La and Ce) to 20% (for Mg and Sr).

Table 6.14 also shows comparisons between $\gamma'_{Lv0}(T_m)$ values of Eq. (6.76) and available experimental or estimated results $\gamma'^e_{Lv0}(T_m)$. Good agreement is also found, namely, Eq. (6.76) provides a satisfactory description for $\gamma'_{Lv0}(T_m)$.

Equation (6.76) at $T = T_m$ can be written as

$$-\gamma'_{Lv0}(T_m) = (\kappa - 2q/3)\gamma_{Lv0}(T_m)/T_m. \tag{6.79}$$

In terms of the expressions for c and $\kappa, \kappa = m'/(c\lambda N_A^{1/3}) \approx 0.19$. Taking the mean value of –0.17 for $q = (d\rho_L/dT)[T_m/\rho_L(T_m)]$, there is the slope $\kappa_s = \kappa - 2q/3 \approx 0.30$.

The relation between $-\gamma'_{Lv0}(T_m)$ and $\gamma_{Lv0}(T_m)/T_m$ for the fourth, fifth and sixth periods are plotted in Fig. 6.20 in light of Eq. (6.79) with $\kappa_s = 0.30$, where $-\gamma'_{Lv0}(T_m)$ functions increase almost linearly with increasing $\gamma_{Lv0}(T_m)/T_m$ for the A family metals in the same period, and the sequence is nearly the same as that in the Periodic Table of the Elements, although some deviations appear. This is understandable as their outmost electric configurations of $s + d$ electrons undergo nearly the same situation from the leftmost (IA metals) of one to the rightmost (VIIIA metals) of ten in these periods. The exceptions are as follows: (1) In the fourth period (from K to Ni), the anomalies of Mn and Cr are present where their $3d$ orbital is half-filled; (2) Similarly, the appearance of the full $4d$ orbital also results in the anomaly of Pd of the fifth period (from Rb to Pd). On the contrary, the occurrence of half full $4d$ orbital in Mo and the half full $5d$ orbital of Re in the sixth period (from Cs to Pt) do not change the sequence. These may be explained as the
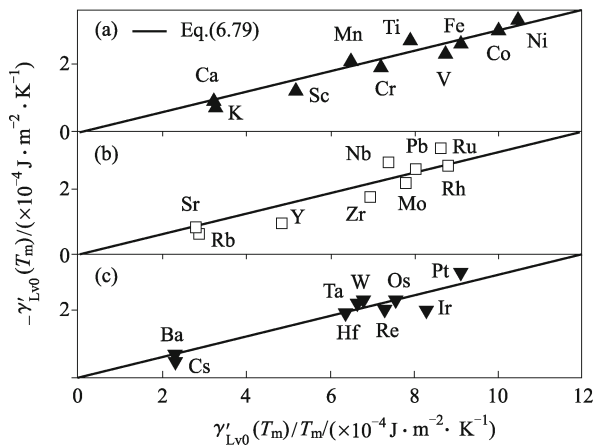
Fig. 6.20 $-\gamma'_{Lv0}(T_m)$ as a function of $\gamma_{Lv0}(T_m)/T_m$ for (a) the fourth (▲), (b) the fifth (□) and (c) the sixth (▼) periods A family metals where the solid lines are determined by Eq. (6.79). (Reproduced from Ref. [3] with permission of Elsevier)

following: In terms of Hund's rule, the half and the full fillings of an orbital usually drop the system energy while the full filling is more effective. For example, ΔH_v values of Cr and Mn are evidently smaller than the neighbor elements V and Fe as shown in Table 6.14. It is also applicable to Pd in comparison with Rh (Ag is not involved because it is a B family metal). While the increase of electronic shell decreases the effect of electric configuration, ΔH_v value of Mo (Re) is thus in between those of Nb (W) and Tc (Os). Since $\gamma_{Lv}(T_m) \propto \Delta H_v$ (the total energetic level of the system), the abnormity only happens in Cr, Mn and Pd.

Note that Tc and La elements are not involved in Fig. 6.20 because $\gamma'_{Lv0}(T_m)$ value of the former is absent while those of the latter are abnormally small possibly due to the effect of f electrons on $\gamma'_{Lv0}(T_m)$ value. Since the $s + d$ electrons of the most lanthanide elements remain constant, their $\gamma'_{Lv}(T_m)$ values hardly change as shown in Table 6.14, and the corresponding κ_s values thus approach zero. In other words, f electrons hardly work as valence electrons.

When elements with empty or full filled electrons of second outmost subshell are considered, only the outermost s electron layer is valence electrons, two groups of elements exist, namely, $s = 1$ (IA and IB metals) and $s = 2$ (IIA and IIB metals). There still exists a linear correlation between $\gamma'_{Lv0}(T_m)$ and $\gamma_{Lv0}(T_m)/T_m$ as shown in Fig. 6.21. In Figs. 6.20 and 6.21, all elements with the sub-shell of $(n' - 1)d$ are located on the right of the figure while all elements with the sub-shell of $(n' - 1)p$ are found on the left of the figure. When the sub-shell is $(n' - 1)s$, the elements are located in the middle or on the right of the figure. When we compare Figs. 6.21 and 6.22, the κ_s value of metals in groups IIA and IIB with $s = 2$ is similar to that of Eq. (6.79). However, the κ_s value of metals in groups IA and IB with $s = 1$ is 30% less than that when n' remains constant.
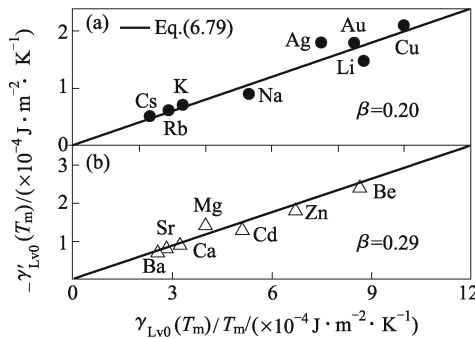
Fig. 6.21 $-\gamma'_{Lv0}(T_m)$ as a function of $\gamma_{Lv0}(T_m)/T_m$ for (a) IA and IB ($\bullet$) and (b) IIA and IIB ($\triangle$) metals. (Reproduced from Ref. [3] with permission of Elsevier)

$\gamma_{Lv}(T_m) = 359, 466, 305 (\text{mJ} \cdot \text{m}^{-2})$ for Mg, Zn and Cd based on Eq. (6.75a) are employed in plotting Figs. 6.19 and 6.21, the existence of related linear

correlations implies that these calculated values may be reasonable. In terms of Eq. (6.76), the contribution of ΔS on $\gamma'_{Lv0}(T_m)$ value ranges from 36% (for metals like Nb and Pt with greater γ_{Lv0} values) to 78% (for metals like Cd, Li and Sr with less γ_{Lv0} values). Neither ΔS nor $d\rho_L/dT$ is thus negligible.

Figure 6.22 shows the comparison of $\gamma_{Lv0}(T)/\gamma_{Lv0}(T_m)$ between Eqs. (6.75b) and (6.72) and experimental evidence for transition metals Ni, Co, Re and W in good agreement. The experimental data for liquid Ni, Co, Re and W in the temperature ranges of 1573–1893 K, 1541–1943 K, 2800–3600 K and 3360–3700 K, respectively, correspond to the undercooling of 155 K, 227 K, 659 K and 320 K as well as the overheating of 165 K, 175 K, 141 K and 20 K. These plots in terms of Eq. (6.72) and Eq. (6.75b) are nearly identical with Co, Re and W. Although it seems that the difference between the two equations is big for Ni, its real difference is only about 1%. The agreement shown in Fig. 6.22 confirms the linear correlation between $\gamma_{Lv0}(T)$ and T in both cases of $T < T_m$ and $T \geqslant T_m$, which denotes the appliance of Eqs. (6.72) and (6.75b) including supercooled liquid metals.
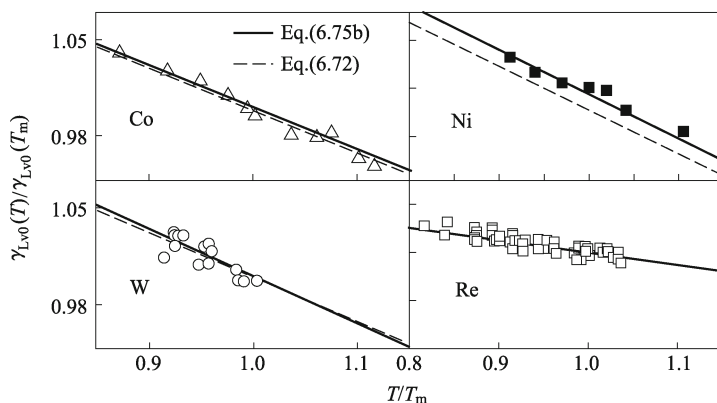
Fig. 6.22 Comparison of $\gamma_{Lv0}(T)/\gamma_{Lv0}(T_m)$ function between the predictions of Eq. (6.75b) (solid line), Eq. (6.72) (dash line) and available experimental data for transition metals Ni (■), Co (△), Re (□) and W (○). (Reproduced from Ref. [3] with permission of Elsevier)

Figure 6.23 presents the comparisons of $\gamma_{Lv0}(T)/\gamma_{Lv0}(T_m)$ between Eq. (6.75b) and experimental results for non-transition metals Na, K, Rb and Cs with a difference of less than 5% at $T_m < T < 3.5T_m$. An approximately linear relation between $\gamma_{Lv0}(T)$ and T occurs again. Equation (6.72) is thus a good approximation of Eq. (6.75b).

Substituting the expression $\rho_L(T) = \rho_L(T_m) + (d\rho_L/dT)(T - T_m)$ into Eq. (6.75b) produces an equation of

$$\gamma_{Lv0}(T) = \left[\frac{m'H_v - TS}{\lambda N_A^{1/3}}\right]\left[\frac{1 + u(T - T_m)}{M/\rho_L(T_m)}\right]^{2/3}$$
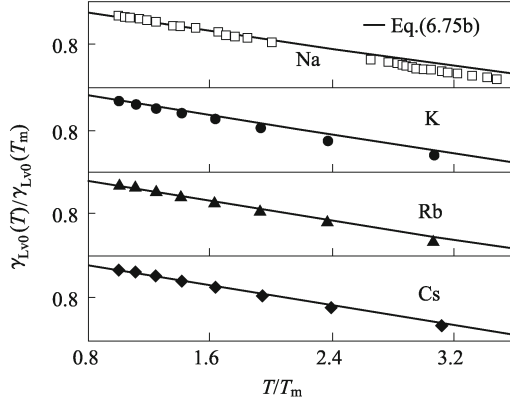
Fig. 6.23 Comparison of $\gamma_{\mathrm{Lv0}}(T)/\gamma_{\mathrm{Lv0}}(T_{\mathrm{m}})$ function between the predictions of Eq. (6.75b) (solid line) and available experimental results for non-transition alkali metals Na ($\square$), K ($\bullet$), Rb ($\blacktriangle$) and Cs ($\blacklozenge$). (Reproduced from Ref. [3] with permission of Elsevier)

where $u' = (\mathrm{d}\rho_{\mathrm{L}}/\mathrm{d}T)/\rho_{\mathrm{L}}(T_{\mathrm{m}})$. Since $u' \approx -10^{-4}\ \mathrm{K}^{-1}$ and $T - T_{\mathrm{m}} < 800\mathrm{K}$ in Fig. 6.23, $u'(T - T_{\mathrm{m}})$ is smaller than 0.1. Considering the mathematical relation of $(1+x)^{2/3} \approx 1 + 2x/3$ when x is sufficiently small (e.g., $x < 0.1$), Eq. (6.75b) can be rewritten as $\gamma_{\mathrm{Lv}}(T) \approx (m'\Delta H_{\mathrm{v}} - T\Delta S)[1 + 2u'(T - T_{\mathrm{m}})/3]/(\lambda N_{\mathrm{A}}^{1/3}V^{2/3})$. Because $(m'\Delta H_{\mathrm{v}} - T\Delta S)[1 + 2u'(T - T_{\mathrm{m}})/3] = v + (T - T_{\mathrm{m}})\{-\Delta S + (2u'v/3)[1 - \Delta S(T - T_{\mathrm{m}})/v]\}$ with $v = m'\Delta H_{\mathrm{v}} - T_{\mathrm{m}}\Delta S$, there is

$$\gamma_{\mathrm{Lv}}(T) \approx \{v + (T - T_{\mathrm{m}})\{-\Delta S + (2u'v/3)[1 - \Delta S(T - T_{\mathrm{m}})/v]\}\}/(\lambda N_{\mathrm{A}}^{1/3}V^{2/3}). \tag{6.80}$$

In terms of $m', \Delta H_{\mathrm{v}}, T_{\mathrm{m}}$ and ΔS values listed in Table 6.14, $\Delta S(T - T_{\mathrm{m}})/v < 0.1$ for most metals at $T - T_{\mathrm{m}} < 800$ K, which thus is negligible as a first order approximation. Thus, Eq. (6.54) can be simplified to $\gamma_{\mathrm{Lv0}}(T) \approx [v + (-\Delta S + 2u'v/3)(T - T_{\mathrm{m}})]/(\lambda N_{\mathrm{A}}^{1/3}V^{2/3})$. Because $v/(\lambda N_{\mathrm{A}}^{1/3}V^{2/3}) = \gamma_{\mathrm{Lv0}}(T_{\mathrm{m}})$ and $(-\Delta S + 2u'v/3)/(\lambda N_{\mathrm{A}}^{1/3}V^{2/3}) = \gamma'_{\mathrm{Lv0}}(T_{\mathrm{m}})$, the correspondence between Eqs. (6.72) and (6.75b) shown in Fig. 6.22 is not only understandable, but also inevitable.

   $\gamma_{\mathrm{Lv0}}(T)$ is related to the bond strength of atoms and its derivative on T corresponds to the bond strength change or electron orbitals change as T varies. As long as the substance remains liquid and $T < T_{\mathrm{c}}$, electron orbitals of liquids change linearly with T. Derivative of Eq. (6.80) with respect to T leads to

$$\gamma'_{\mathrm{Lv0}}(T) \approx \gamma'_{\mathrm{Lv0}}(T_{\mathrm{m}}) + e(T - T_{\mathrm{m}}) \tag{6.81}$$

with $e = -4u'\Delta S/(3\lambda N_{\mathrm{A}}^{1/3}V_{\mathrm{s}}^{2/3})$ being the temperature coefficient of $\gamma'_{\mathrm{Lv0}}(T)$.

Equation (6.81) indicates that $\gamma'_{\mathrm{Lv0}}(T) \propto T$ positively since $e > 0$ ($u < 0$). This tendency against T is the reverse of that of $\gamma_{\mathrm{Lv0}}(T)$ because the energetic difference between liquid and vapor drops as T increases. Although Eq. (6.81) ultimately gives positive temperature dependence, e has only a secondary effect and can be neglected as a first order approximation. For instance, $e \approx 3.0 \times 10^{-5}$ mJ·m^{-2}·K^{-2} for Ni and 1.6×10^{-5} mJ·m^{-2}·K^{-2} for V. Even $T - T_{\mathrm{m}} = 1000$ K, $\gamma'_{\mathrm{Lv0}}(T)/\gamma'_{\mathrm{Lv0}}(T_{\mathrm{m}})$ values of Ni and V are only 1.09 and 1.08, or the error range is smaller than 10%.

Note that the simulated results based on Monte Carlo method in conjunction with the embedded-atom potential show 20%–60% underestimations for Al, Ni, Cu, Ag and Au, and 20% overestimation for Co when they are compared with the experimental data. Thus, this method needs to be further improved. The above theoretical method is therefore a powerful and even unique tool at present to determine $\gamma_{\mathrm{Lv0}}(T)$ function with good accuracy.

6.7.3 Size Dependence of Liquid-vapor Interface Energy [3]

Gibbs defines that γ_{Lv} with a given bulk value γ_{Lv0} depends on pressure P, T and the composition of the two coexisting bulk phases. However, when the liquid-vapor interface is curved, γ_{Lv} is a function of r of the droplet, $\gamma_{\mathrm{Lv}}(r)$. Guggenheim suggested that the $\gamma_{\mathrm{Lv}}(r)$ would change when r falls below 50 nm based on statistical mechanical considerations [17].

A half-century ago, Tolman extended the idea of Gibbs and showed that if the radius R_{s} of the surface of the droplet did not coincide with the equimolar radius $R_{\mathrm{e}}, \gamma_{\mathrm{Lv}}$ varied with size. Moreover, Tolman proposed that the two surfaces must, in general, be distinct from each other. Tolman estimated the Tolman's length $\delta = R_{\mathrm{e}} - R_{\mathrm{s}}$ [18], or the separation between the equimolar surface and the surface of tension. He assumed that δ could be taken as a constant in the nanometer region, and derived the equation,

$$\gamma_{\mathrm{Lv}}(r)/\gamma_{\mathrm{Lv0}} = 1/(1 + 2\delta/r). \qquad (6.82)$$

Kirkwood and Buff developed a general theory based on statistical mechanics for the interfacial phenomena and confirmed the validity of Tolman's approach [19]. For a sufficiently large droplet, Eq. (6.82) may be expanded into power series. Neglecting all the terms above the first order, the asymptotic form was obtained, which has been illustrated as Eq. (6.63). Values for $\gamma_{\mathrm{Lv}}(r)/\gamma_{\mathrm{Lv0}}$ determined by Eqs. (6.63) and (6.82) are close to each other at $r/\delta \geqslant 10$.

Tolman predicted that $\gamma_{\mathrm{Lv}}(r)$ should decrease with decreasing r, indicating a positive δ. The asymptotic Tolman's length in the limit of $r \to \infty, \delta_\infty = h$, is independent of the choice of the dividing surface. However, δ was also predicted to be negative by a rigorous thermodynamic derivation, which would lead to an increase of $\gamma_{\mathrm{Lv}}(r)$ when r drops. It is generally

assumed that $\delta > 0$ for spherical droplets and $\delta < 0$ for bubbles in a liquid. This consideration can also be simply translated as that $\delta > 0$ where $r > 0$ for droplets but $r < 0$ for bubbles. In addition to the uncertainty in the sign of δ, the validity of Eq. (6.82) is considered to be questionable for very small particles.

It is known that for a planar interface of metallic elements at $T_m, \gamma_{sv0}/\gamma_{Lv0}$ $= w = 1.18 \pm 0.03$. Note that in the derivation of $\gamma_{sv}(r)$ the nanocrystal is assumed to have the same structure of the corresponding bulk. Since the structure and energy differences between solid and liquid are little in comparison with those between solid and gas or between liquid and gas, the above expression for the bulk may be extended to nanometer size with the same form,

$$\gamma_{sv}(r)/\gamma_{Lv}(r) = w. \tag{6.83}$$

Combining Eqs. (6.66) and (6.83), there is

$$\frac{\gamma_{Lv}(r)}{\gamma_{Lv0}} = \left[1 - \frac{1}{4r/h - 1}\right] \exp\left(-\frac{2\Delta S_b}{3R} \frac{1}{4r/h - 1}\right). \tag{6.84}$$

Comparisons of $\gamma_{Lv}(r)/\gamma_{Lv0}$ for Na and Al droplets between Eq. (6.84) and the computer simulation results are shown in Fig. 6.24 where agreement is found, which in return confirms the validity of the assumption in Eq. (6.57). As a comparison, Eq. (6.82) with $\delta = h$ is also shown in Fig. 6.24 where obvious derivations between Eq. (6.82) and the computer simulation results occur at $\delta/r > 0.4$ (namely, $r < 0.72$ nm for Al or $r < 0.93$ nm for Na). Although Eq. (6.84) is deduced in light of the relation between γ_{sv0} and CN of surface atoms for metals, this relation should be also applicable to other types of materials. Figure 6.25 shows $\gamma_{Lv}(r)$ function of water by Eq. (6.84) with correspondence of the computer simulation results where h in this case is redefined as O–H bond length. Similarly, the prediction of Eq. (6.84) with $\delta = h$ is also shown in Fig. 6.25.

As shown in Figs. 6.24 and 6.25, $\gamma_{Lv}(r)$ decreases with size, following the trend of $\gamma_{sv}(r)$ and $E(r)$ where Eq. (6.84) provides the same or better accuracy of Eq. (6.82). This is because the energetic state of the interior molecules increases more quickly than that of the surface molecules as r decreases.

Although δ is assumed to be a constant as required by the derivation of Eqs. (6.63) and (6.82), several applications of statistical thermodynamics have indicated that δ depends heavily on r. Since the results of these treatments are based on rather complex numerical calculations, it would be difficult to express $\delta(r)$ analytically. Fortunately, Eq. (6.84) can be used to satisfy this requirement.

Substituting Eq. (6.82) into Eq. (6.84) rather than Eq. (6.63) because the latter is an approximation of Eq. (6.82) and leads to error when $r/\delta \leqslant 5$,

$$\delta(r) = \frac{r}{2}\left[\exp\left(\frac{2\Delta S_b}{3R} \frac{1}{4r/h - 1}\right) \middle/ \left(1 - \frac{1}{4r/h - 1}\right) - 1\right]. \tag{6.85}$$
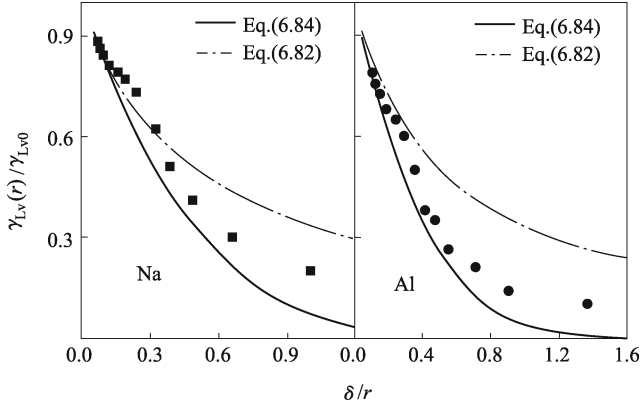
Fig. 6.24 Comparison of the δ/r ($\delta = h$) dependence of $\gamma_{Lv}(r)/\gamma_{Lv0}$ described by various models and computational results for Na and Al.
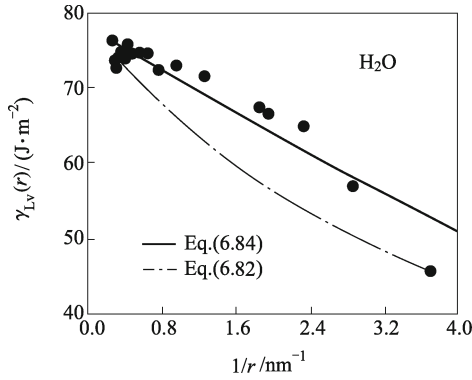
Fig. 6.25 $\gamma_{Lv}(r)$ function with $\delta = h$, for water, where $\gamma_{Lv0}=75$ mJ·m^{-2}.

$\delta(r)/h$ determined by Eq. (6.85) for Na, Al and water droplets are shown as a function of r/h in Fig. 6.26. $\delta(r) > 0$ and decreases when r increases, being consistent with statistical thermodynamics, computer simulations, and other approaches for Lennard-Jones fluids. However, there is an obvious difference between Eq. (6.85) and others. In Eq. (6.85), $\delta(r) > 0$ while it will decrease to a negative limiting value for the planar interface in the others.

The value of δ in Eq. (6.85) is on the verge of infinitude when r reaches its lower limit h. When r is sufficiently large, considering the mathematical relation of $\exp(-x) \approx 1 - x$ when $x < 0.1$, the minimal value $\delta_{\min}$ in terms of Eq. (6.85) can be written as $\delta_{\min} = \delta_\infty = h\Delta S_b/(12R)$, or

$$h\Delta S_b/(12R) < \delta. \qquad (6.86)$$

$\Delta S_b \approx 12R$ for metallic elements leads to $\delta_\infty \approx h$ for Na and Al as indicated

by Tolman while $\delta'_\infty \approx 3h/8$ for water due to $\Delta S_b \approx 9R/2$. This is the reason why the differences of Eqs. (6.82) and (6.84) at $r/h \leqslant 5$ for Na and Al while at $r/h \geqslant 10$ for water are present. Thus, the size dependence of $\delta(r)$ strongly depends on the value of ΔS_b. Eq. (6.86) also implies that the decrease of the bond strength results in the diffusion of the liquid-vapor interface. The corresponding physical picture is that the energetic difference of the molecule on the liquid surface and that in the vapor decreases as the bond strength weakens. Thus, the liquid-vapor interface transition zone becomes narrow.
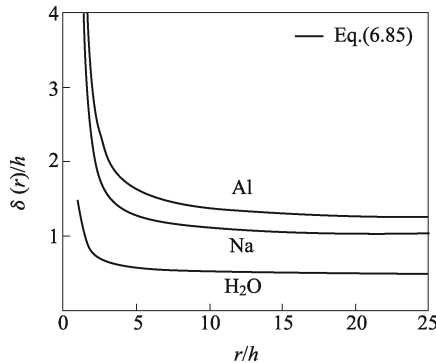
Fig. 6.26 $\delta(r)/h$ as a function of r/h in terms of Eq. (6.85) for Na, Al and H_2O droplets.

6.8 Applications of Size-dependent Interface Energy

6.8.1   Thermodynamic Phase Stability of Nanocarbons [3]

Crystalline carbon is polymorphic in three forms of diamond (D), graphite (G) and fullerenes (F). A recent progress of new structures of carbon is graphene, being a single or several graphite layers with the same structure of G. The carbon bonding of D is sp^3 (tetrahedral) hybridization while that of G is sp^2 (trigonal) one. As a result, D has a three-dimensional structure while G consists of two dimensional layers stacked in an AB sequence, which differs from the AB sequence in a hexagonal close packed (hcp) structure and is linked by a weak van der Waals interaction produced by a delocalized π-orbital. When the materials size is in bulk, G is the stable allotrope of C at atmospheric pressures. $G{\rightarrow}D$ transition only occurs at high T and P according to the equilibrium phase diagram of bulk carbon. As r decreases to nanometer, D can be obtained at low T and P. However, it has been observed that D initially formed with $r < 1.5$ nm transforms into G as it

grows, a size-dependent thermodynamic transition. If r decreases to 1 nm, $\boldsymbol{F}$ or carbon onions ($\boldsymbol{O}$) could be the most stable form of C. Note that $\boldsymbol{F}$ and $\boldsymbol{O}$, which are not true graphitic phases, share many structural characteristics with $\boldsymbol{G}$, e.g. sp^2 hybridization and six-member rings. Between $\boldsymbol{D}$ and $\boldsymbol{F}$ or $\boldsymbol{O}$, an intermediary bucky diamond ($\boldsymbol{B}$) phase with a $\boldsymbol{D}$-like core and a $\boldsymbol{G}$-like outer shell is often found due to the motivation to drop γ_{sv}. The mechanism of relative phase stability of the above phases can be quantitatively determined in a unified thermodynamic form.

The above transitions can be determined by considering effects of surface free energy $G_s(T, r)$ induced by γ_{sv}, elastic free energy $G_e(T, r)$ induced by f, and volume Gibbs free energy $G_v(T, r)$. For solid particles, since the complicated function of free energy difference between i and j nanophases $\Delta G^{i \to j}(T, r)$ cannot be easily considered, a facile way is to distinguish separately the effects of T and r on $\Delta G^{i \to j}(T, r)$. This can be realized by roughly defining that $\Delta G^{i \to j}(T, r)$ function is contributed by the difference sum of a temperature-dependent $\Delta G_v^{i \to j}(T)$, a size-dependent $\Delta G_s^{i \to j}(r)$, and a size-dependent $\Delta G_e^{i \to j}(r)$. $\Delta G_v^{i \to j}(T)$ shows the bulk value and thus is size-independent. The latter two terms denote the size effects. Although they also have temperature effect on $\Delta G^{i \to j}(T, r)$, it is a higher order one since this effect has been partly countervailed as differences where the related two phases have a similar temperature dependence. This consideration certainly leads to errors in the calculation, as shown in the following; these errors however do not evidently affect the ultimate estimation of the phase stability of different carbon polymorphs in nanometer size range, which in return confirms that the above simplification is reasonable.

For a spherical and quasi-isotropic nanocrystal , $\Delta G^{i \to j}(T, r)$ function reads

$$\Delta G^{i \to j}(T, r) = \Delta G_v^{i \to j}(T) + \Delta G_s^{i \to j}(r) + \Delta G_e^{i \to j}(r). \qquad (6.87)$$

$\Delta G_s^{i \to j}(r)$ in Eq. (6.87) can be expressed as

$$\Delta G_s^{i \to j}(r) = A^j \gamma_{sv}^j - A^i \gamma_{sv}^i \qquad (6.88)$$

where $A = 3V_s/r$ is surface area. In Eq. (6.88), γ_{sv} is roughly defined as being isotropic. However, this approximation is not used for strong anisotropic $\boldsymbol{G}$ where $\gamma_b^{\boldsymbol{G}} = 0.13$ J·m^{-2} and $\gamma_h^{\boldsymbol{G}} = 4.80$ J·m^{-2} with subscripts "b" and "h" denoting the basal and high-index planes, respectively. The former is induced by van der Waals force while the latter is present due to the bond deficits. Thus, $\gamma^{\boldsymbol{G}}$ is defined as

$$\gamma^{\boldsymbol{G}} = (\gamma_b^{\boldsymbol{G}} A_b^{\boldsymbol{G}} + \gamma_h^{\boldsymbol{G}} A_h^{\boldsymbol{G}})/(A_b^{\boldsymbol{G}} + A_h^{\boldsymbol{G}}). \qquad (6.89)$$

The experimental γ_{sv} values for single-walled and multi-walled nanotubes are 0.040 J·m^{-2} and 0.045 J·m^{-2}, which are about two orders smaller than $\gamma^{\boldsymbol{D}}$ or $\gamma_h^{\boldsymbol{G}}$. Since the structures of $\boldsymbol{F}$ and $\boldsymbol{O}$ are similar to nanotubes, as a first order approximation, it is assumed that

$$\gamma^{\boldsymbol{F}} \approx \gamma^{\boldsymbol{O}} \approx \gamma_b^{\boldsymbol{G}} \approx 0. \qquad (6.90)$$

$\Delta G_{\mathrm{e}}^{i \to j}(r)$ is expressed as

$$\Delta G_{\mathrm{e}}^{i \to j}(r) = P_{\mathrm{in}}^i V_{\mathrm{s}}^i - P_{\mathrm{in}}^j V_{\mathrm{s}}^j. \tag{6.91}$$

In concerned nanocarbon structures, $V_{\mathrm{s}}^{\boldsymbol{F}}(r)$ is size-dependent and $V_{\mathrm{s}}^{\boldsymbol{F}}(r) = [V^{\boldsymbol{F}}(r)/N^{\boldsymbol{F}}]N_{\mathrm{A}}$ where $V^{\boldsymbol{F}}(r) = 4\pi r^3/3$ is the total volume of $\boldsymbol{F}$, $N^{\boldsymbol{F}} = 4\pi r^2/A_0$ is the corresponding number of C atoms with A_0 being surface atom density. Thus,

$$V_{\mathrm{s}}^{\boldsymbol{F}}(r) = N_{\mathrm{A}} A_0 r/3. \tag{6.92}$$

According to Laplace-Young equation, $P_{\mathrm{in}} = 2f/r$ (Eq. (6.16)), where f is determined by

$$f = [(3\gamma_{\mathrm{sL}}h)/(4\beta)]^{1/2} \quad \text{for plane surfaces,} \tag{6.93a}$$

$$f = [(9\gamma_{\mathrm{sL}}h)/(8\beta)]^{1/2} \quad \text{for curved surfaces.} \tag{6.93b}$$

For the considered cases, $f = 3.54$ J·m^{-2} is determined by Eq. (6.93) for the widely studied C60, which is consistent with $f = 2.36$–4.02 J·m^{-2} by computer simulations where the f values are transformed from eV·atom^{-1} to J·m^{-2} by using $A_0 = 0.027$ nm^2·atom^{-1}. In equilibrium, $\Delta G^{i \to j}(T, r) = 0$. The corresponding critical size $r_{\mathrm{c}}^{i \to j}(T)$ in terms of Eq. (6.87) is obtained as follows:

$$r_{\mathrm{c}}^{i \to j}(T) = [4(f^i V_{\mathrm{s}}^i - f^j V_{\mathrm{s}}^j) + 6(\gamma^j V_{\mathrm{s}}^j - \gamma^i V_{\mathrm{s}}^i)]/\Delta G_{\mathrm{v}}^{i \to j}(T). \tag{6.94}$$

$\Delta G_{\mathrm{v}}^{i \to j}(T)$ of $\boldsymbol{G}, \boldsymbol{D}, \boldsymbol{F}$ and $\boldsymbol{O}$ in Eq. (6.85) are determined one by one. $\Delta G_{\mathrm{v}}^{\boldsymbol{G} \to \boldsymbol{D}}(T)$ of $\boldsymbol{G}$ and $\boldsymbol{D}$ can be found in terms of the bulk $T \sim P$ phase diagram of carbon, and is expressed as

$$\Delta G_{\mathrm{v}}^{\boldsymbol{G} \to \boldsymbol{D}}(T) = P(T)\Delta V_{\mathrm{s}}^{\boldsymbol{G} \to \boldsymbol{D}} \tag{6.95}$$

where $\Delta V_{\mathrm{s}}^{\boldsymbol{G} \to \boldsymbol{D}}$ is approximately a temperature-independent constant, which implies that the dilatability difference between $\boldsymbol{G}$ and $\boldsymbol{D}$ within the considered temperature range has a secondary effect on $\Delta V_{\mathrm{s}}^{\boldsymbol{G} \to \boldsymbol{D}}$.

Since $\boldsymbol{F}$ can be considered as finite two-dimensional analogues of $\boldsymbol{G}$ without interlayer attraction and dangling edge bonds, $\Delta G_{\mathrm{v}}^{\boldsymbol{D} \to \boldsymbol{F}}(T) \approx \Delta G_{\mathrm{v}}^{\boldsymbol{D} \to \boldsymbol{G}}(T) + \Delta E_{\mathrm{c}}^{\boldsymbol{G} \to \boldsymbol{F}}$ where $\Delta E_{\mathrm{c}}^{\boldsymbol{G} \to \boldsymbol{F}}$ is the difference of E_{c} between $\boldsymbol{G}$ and $\boldsymbol{F}$. Note that a lot of isolated pentagon rule structures of $\boldsymbol{F}$ without related thermodynamic parameters deviate from the sphere shape while C60 data can be found in literature, as an example, C60 is used as the typical model molecule of $\boldsymbol{F}$ here. With a similar way, other types of $\boldsymbol{F}$ can also be calculated when necessary parameters are known. The corresponding formation entropy difference has been neglected since the both phases have the same coordination of the sp^2 bonding. Thus, substituting Eq. (6.95) into the above $\Delta G_{\mathrm{v}}^{\boldsymbol{D} \to \boldsymbol{F}}(T)$ expression, there is

$$\Delta G_{\mathrm{v}}^{\boldsymbol{D} \to \boldsymbol{F}}(T) = -P(T)\Delta V_{\mathrm{s}}^{\boldsymbol{D} \to \boldsymbol{G}} + \Delta E_{\mathrm{c}}^{\boldsymbol{G} \to \boldsymbol{F}}. \tag{6.96}$$

As there are no interlayer attractions and dangling edge bonds for $\boldsymbol{F}$, it has no van der Waals interlayer attraction E_{v}. If $\boldsymbol{O}$ is treated as nested $\boldsymbol{F}$ with E_{v},

$$\Delta G_{\mathrm{v}}^{\boldsymbol{F}\to\boldsymbol{O}}(T) = -E_{\mathrm{v}}, \tag{6.97}$$

which can be supported by the fact that as the shell number of $\boldsymbol{O}$ goes up, its stability increases due to the appearance of E_{v}. Since present known experimental and theoretical results consider more about $\boldsymbol{D}\to\boldsymbol{O}$ transition, $\boldsymbol{D}$ is used as a standard state for comparison and $\Delta G_{\mathrm{v}}^{\boldsymbol{D}\to\boldsymbol{O}}(T) = \Delta G_{\mathrm{v}}^{\boldsymbol{D}\to\boldsymbol{F}}(T) + \Delta G_{\mathrm{v}}^{\boldsymbol{F}\to\boldsymbol{O}}(T)$ function is therefore considered in comparison with other known results. The $\Delta G_{\mathrm{v}}^{\boldsymbol{D}\to\boldsymbol{O}}(T)$ function reads

$$\Delta G_{\mathrm{v}}^{\boldsymbol{D}\to\boldsymbol{O}}(T) = -P(T)\Delta V_{\mathrm{s}}^{\boldsymbol{D}\to\boldsymbol{G}} + \Delta E_{\mathrm{c}}^{\boldsymbol{G}\to\boldsymbol{F}} - E_{\mathrm{v}}. \tag{6.98}$$

In terms of Eq. (6.94) and other related equations, $T\sim r$ phase diagram of nanocarbon is calculated and plotted in Fig. 6.27 where necessary parameters are listed in Table 6.15. During the calculation, r values of different structures are unified by those of $\boldsymbol{D}$ where different structures have the same atom number. Moreover, to clarify three contributions towards $\Delta G^{i\to j}(T,r)$ separately, $\Delta G_{\mathrm{v}}^{i\to j}(T), \Delta G_{\mathrm{s}}^{i\to j}(r)$ and $\Delta G_{\mathrm{e}}^{i\to j}(r)$ functions are present in Fig. 6.28 for each transition. Although $\Delta G^{i\to j}(T,r)$ is a temperature-dependent function, Fig. 6.28 only shows a special case at $T = 0$ K where the calculation is the easiest with the largest energetic difference of phases, which benefits the understanding of their relative sizes.

As shown in Fig. 6.27, $r_{\mathrm{c}}^{\boldsymbol{G}\to\boldsymbol{D}}$ decreases from about 7 nm at 0 K to 2 nm at 1500 K, which corresponds to other experimental and theoretical results well. In terms of Eq. (6.90), $\Delta G_{\mathrm{e}}^{\boldsymbol{G}\to\boldsymbol{D}}(r=5\text{ nm}) = 5.80\text{ kJ·mol}^{-1}$, which is ten times $\Delta G_{\mathrm{s}}^{\boldsymbol{G}\to\boldsymbol{D}}(r=5\text{ nm}) = 0.56\text{ kJ·mol}^{-1}$ in light of Eq. (6.87) as shown in Fig. 6.28. Accordingly, f acts as a major driving force for $\boldsymbol{G}\to\boldsymbol{D}$ transition at the nanoscale, which is also the reason why the temperature dependence of $r_{\mathrm{c}}^{\boldsymbol{G}\to\boldsymbol{D}}$ is evident in terms of Eq. (6.94).

For $\boldsymbol{D}\to\boldsymbol{F}$ transition, although f produces P_{in} on particles, f only leads to a negative effect on $\boldsymbol{D}\to\boldsymbol{F}$ transition when r is small since $P_{\mathrm{in}}^{\boldsymbol{F}}V_{\mathrm{m}}^{\boldsymbol{F}} \propto 1/r^{1/2}$ in Eq. (6.90) in terms of Eqs. (6.91) and (6.93) while $P_{\mathrm{in}}^{\boldsymbol{D}}V_{\mathrm{m}}^{\boldsymbol{D}} \propto 1/r$ induced by gradually decreased size of $V_{\mathrm{m}}^{\boldsymbol{F}}$ with r. Thus, there must be a size where $\Delta G_{\mathrm{e}}^{\boldsymbol{D}\to\boldsymbol{F}} = 0$. As shown in Fig. 6.28, this size is about 2.5 nm. Although the same case is present in the calculation of $\Delta G_{\mathrm{s}}^{\boldsymbol{D}\to\boldsymbol{F}}$ based on Eq. (6.87) due to the size dependence of $A_{\mathrm{m}}^{\boldsymbol{F}}$ induced by $V_{\mathrm{m}}^{\boldsymbol{F}}$, this effect on $\Delta G_{\mathrm{s}}^{\boldsymbol{D}\to\boldsymbol{F}}$ is absent where $\gamma^{\boldsymbol{F}} \approx 0$ in terms of Eq. (6.89) has been employed. As a result, $\Delta G_{\mathrm{s}}^{\boldsymbol{D}\to\boldsymbol{F}} \approx -\gamma^{\boldsymbol{D}}A_{\mathrm{m}}^{\boldsymbol{D}}$ is always negative, which is also the case of $\boldsymbol{D}\to\boldsymbol{O}$ transition as shown in Fig. 6.28.
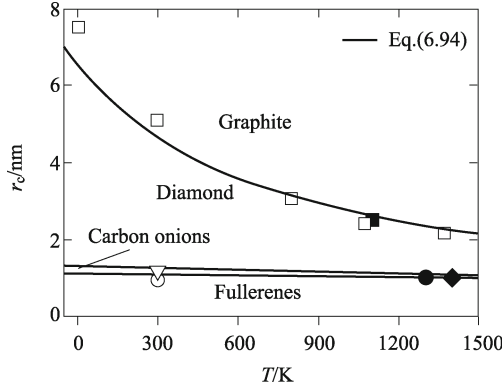
Fig. 6.27 The $r \sim T$ transition diagram of nanocarbon in terms of Eq. (6.94) under $P = 0$ (solid line) where other theoretical ($\circ$, $\triangledown$, and $\square$) and experimental results ($\bullet$, $\blacklozenge$, and $\blacksquare$) are presented for comparison. $P(T) = (2.73T + 2.02 \times 10^3)$ MPa. (Reproduced from Ref. [3] with permission of Elsevier)

Table 6.15 Thermodynamic parameters of the nanocarbon

	h /nm	V_s /(cm³· mol⁻¹)	ΔH_m /(kJ· mol⁻¹)	T_m /K	ΔS_m /(J· mol⁻¹· K⁻¹)	ΔS_{vib} /(J· mol⁻¹· K⁻¹)	β /(10⁻¹⁰ Pa⁻¹)	E_c /(kJ· mol⁻¹)	f /(J· mol⁻¹)	γ /(J· m⁻²)	E_v /(kJ· mol⁻¹)
D	0.154	3.417	125	3723	33.58	6.37	0.088		6.10	3.70	
G	0.142	5.398	120	4800	25.00	4.75	1.000	−714	1.10	3.27	
F	0.157	5.4r	53	1600	33.12	6.29	0.212	−675	2.11 $/r^{1/2}$	0	
O		7.3								0	5.4

The $r_c^{D \to O}(T)$ curve is very close to the $r_c^{D \to F}(T)$ one in Fig. 6.27 due to the competition between a small positive contribution of weak interlayer attraction on $\Delta G_v^{F \to O}$ on one side and a small negative contribution of the size-dependent volume on $\Delta G_s^{F \to O}$ on the other side. The both lead to $\Delta G^{F \to O} \approx 0$ in the considered size range and at the level of the approximation used here. In fact, **O** and **F** as stable states of nanocarbon are indistinguishable within uncertainties when $r < 1.3$ nm. All experimental results of r_c could be considered to be consistent with Eq. (6.94).

The disappearance of dangling bonds in **F** and **O** leads to significant drop of their total free energy G^F and G^O because γ_h^G disappears, which stabilizes **F** and **O** when r is very small. This is clearly shown in Fig. 6.28. The energetic increase caused by the dangling bonds in **D** is greater than the energetic decrease induced by P_{in} at very small r. Because these different contributions of γ_{sv} and f in distinct structures at different r on nanocarbons are distinct, nanocarbons undergo transitions in a series of $\boldsymbol{G} \to \boldsymbol{D} \to \boldsymbol{O}(\boldsymbol{F})$ or bonding of $sp^2 \to sp^3 \to sp^2$ with reducing r.

Note that during $\boldsymbol{D} \to \boldsymbol{O}$ or $\boldsymbol{D} \to \boldsymbol{F}$ transition as well the correspond-
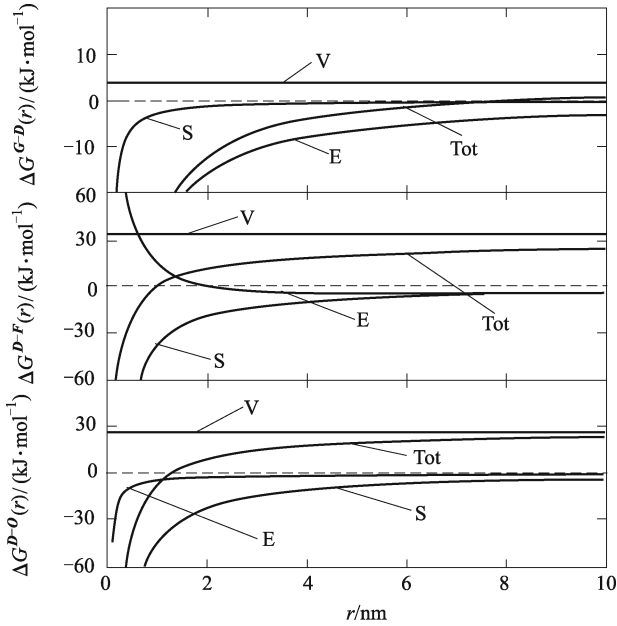
Fig. 6.28 ΔG as a function of r where the solid lines for $\Delta G^{i \to j}(T = 0, r), \Delta G_s^{i \to j}(r), \Delta G_e^{i \to j}(r)$, and $\Delta G_v^{i \to j}(T = 0)$ functions (simplified to Tot, S, E, and V) are determined in terms of Eqs. (6.86), (6.87), (6.90), and (6.95)–(6.98), respectively. The dotted line denotes $\Delta G^{i \to j} = 0$. (Reproduced from Ref. [3] with permission of Elsevier)

ing reverse transitions, an intermediary $\boldsymbol{B}$ phase with a $\boldsymbol{D}$-like core and a $\boldsymbol{G}$-like outer shell is often formed. For $\boldsymbol{D} \to \boldsymbol{B}$ transition, $\Delta G_v^{\boldsymbol{D} \to \boldsymbol{B}}(T) = \Delta G_v^{\boldsymbol{D} \to \boldsymbol{G}}(T)/r, \Delta G_e^{\boldsymbol{D} \to \boldsymbol{B}}(r) = (P_{in}^{\boldsymbol{D}} V_s^{\boldsymbol{D}} - P_{in}^{\boldsymbol{G}} V_s^{\boldsymbol{G}})/r$ and $\Delta G_s^{\boldsymbol{D} \to \boldsymbol{B}}(r) = 6(V_s^{\boldsymbol{G}} \gamma_b^{\boldsymbol{G}} - V_s^{\boldsymbol{D}} \gamma^{\boldsymbol{D}} + V_s^{\boldsymbol{D}} \gamma_i)/r$ when $\boldsymbol{D} \to \boldsymbol{B}$ transition interface is $(111)/(0001)$ faces where γ_i is the interface energy between the $\boldsymbol{D}$-like core and the $\boldsymbol{G}$-like outer shell. $\gamma_i \approx 1.04$ J·m^{-2} is determined for the interface between zigzag $(8,0)$ carbon nanotube and (111) facet of $\boldsymbol{D}$. Inserting necessary parameters listed in Table 6.15 into Eq. (6.87) and letting $\Delta G^{\boldsymbol{D} \to \boldsymbol{B}}(T = 0, r) = 0, r_c^{\boldsymbol{D} \to \boldsymbol{B}}(T = 0) \approx 0.5$nm. Thus, $\Delta G^{\boldsymbol{D} \to \boldsymbol{B}}(T \geqslant 0, r > 0.5nm) \leqslant 0$, which means that $\boldsymbol{D} \to \boldsymbol{B}$ transition is thermodynamically possible. This result is consistent with the theoretical predictions that $\boldsymbol{B}$ and other kinds of C nanoparticles at coexist $r > 0.7$ nm where the coexistence of $\boldsymbol{B}$ and $\boldsymbol{F}$ takes place when $r = 0.7$–0.9 nm, so does that of $\boldsymbol{B}$ and $\boldsymbol{O}$ when $r = 0.9$–1.0 nm, and that of $\boldsymbol{B}$ and $\boldsymbol{D}$ when $r > 1.0$ nm. These results also correspond to the recent experimental results that the surface of $\boldsymbol{D}$ with $r > 0.5$ nm reconstructs in an $\boldsymbol{F}$-like manner, or a $\boldsymbol{D} \to \boldsymbol{B}$ transition.

6.8.2   Static Hysteresis of Solid Transition of CdSe Nanocrystals [3]

As the first-order structural transition, many solids transform to denser structures under applied P, resulting in materials with novel properties without any change in the material composition. The structural transitions are utilized such as for the steel hardening by martensite transition, for shape memory effect, for high fracture toughness ceramics of ZrO, and for diamond film formation.

The microscopic mechanisms of solid-solid phase transition processes are comparatively more complicated to understand due to the inhomogeneous kinetic effect, the complicated effect of grain boundaries, defect formation, and often irreversible transition characteristics. Theoretical estimates for lifetimes of metastable states can be off by many orders of magnitude because they must include generally unknown details of microscopic transition pathways. It is interesting that when r is in nanometer range, the study of phase transitions may be simplified because small crystals can behave as single crystals and reproducibly cycle the transition without appearance of lattice defects, such as dislocations and grain boundaries, where there is only a single transition interface between the parent phase and the formed phase. The existence of the single interface leads to a constant static pressure hysteresis width $P_w(t \to \infty)$(t denotes the time) and this value could be estimated.

High-pressure phases can persist in a metastable state at ambient pressure if sufficiently large energetic barriers and low transition temperature hinder transition to the more energetically favorable structure. The both are characterized by a large kinetic transition hysteresis loop width $P_w(t \to 0)$. Some known examples are the high-energy structures of martensite in carbon steels relative to that of ferrite plus carbide and that of diamond relative to that of graphite. As r decreases, the metastable high-pressure phases and some denser parking phases, which have not been found in bulk state, are easily formed at ambient pressure as found in CdSe, HgS, ZnO, ZnS, GaAs, Fe, Co, Cr, and In. The essential reason is the existence of P_{in} for an isotropic spherical or quasi-spherical nanoparticle induced by f (Eq. (6.16)). Here CdSe nanocrystals are taken as a model system to discuss the phenomenon since experimentally the transition from wurtzite-like phase to the rocksalt-like phase has been carried out in detail.

To determine the thermodynamic solid transition, the thermodynamic amount of the high-pressure phase must be firstly known, which could be obtained from that of the corresponding low-pressure phase. Let subscripts "h" and "l" denote the high-pressure and the low-pressure phases respectively, the pressure-dependent transition volume difference per g-atom $\Delta V(P)$ is expressed approximately as $\Delta V(P) \approx \Delta V_0 + [\Delta V_h(P) - \Delta V_l(P)]$ where $\Delta V_0 = V_h(P=0) - V_l(P=0)$, $\Delta V_h = -V_h P_h \beta_h$ and $\Delta V_l = -V_l P_l \beta_l$ where β is the compressibility. For CdSe crystals, the experimental evidence indicates that $\Delta V(P) \approx \Delta V_0$ or $\Delta V_h(P) \approx \Delta V_l(P)$. Thus, $V_h f_h \beta_h \approx V_l f_l \beta_l$. In light of

Eq. (6.93), this result implies that $f\beta \propto \Delta H_m \beta^{1/2} = $ constant. Since ΔH_m is related to the bond strength, $\beta^{-1/2}$ thus is reasonably proportional to the bond strength. As a result of the above approximation,

$$f_h \approx (V_l/V_h)(\beta_l/\beta_h)f_l. \tag{6.99}$$

Since the discussed solid transition of CdSe occurs at $T < T_K, \Delta H_m(T) = \Delta H_m(T_K/T_m)^2 = \Delta H_m/4$ is taken. Substituting this relation into Eq. (6.8), we have

$$\gamma_{sL} = h(\Delta S_m - R)\Delta H_m/(6V_s R). \tag{6.100}$$

Because ΔC_{pss}, the heat capacity difference between polymorphous solid phases of the same substance, is always small if no Curie transition between them occurs, ΔS_m of such phases are approximately equal. Thus,

$$\Delta H_{mh} = \Delta H_{ml} - \Delta H_s, \tag{6.101}$$

$$\Delta S_{mh} \approx \Delta S_{ml}, \tag{6.102}$$

$$T_{mh} = \Delta H_{mh}/\Delta S_{mh} \tag{6.103}$$

where ΔH_s denotes the solid transition enthalpy. Since ΔH_{mh} may be determined through Eqs. (6.93), (6.99) and (6.100), ΔH_s is given by Eq. (6.101).

According to the first thermodynamic law,

$$\Delta S_s = [\Delta H_s - P_n \Delta V(P)]/T \tag{6.104}$$

where ΔS_s is the solid transition entropy and P_n shows the necessary pressure for the transition in thermodynamic equilibrium. Since the parent phase is the stable one under ambient pressure, $\Delta H_s > 0, \Delta S_s > 0$ and $\Delta V < 0$.

In Eq. (6.104), P_n being an energy barrier going from one phase to another is related with the Gibbs free energy difference between the two phases ΔG_{ss}. In general consideration, any energetic contribution to the phase, such as $\Delta\gamma_{sv}$, is taken as a part of ΔG_{ss}. Thus, $\Delta\gamma_{sv}$ affects the size of P_n through ΔG_{ss}. Since such parameters are unknown, P_e is determined by considering the relationship between P_n and $P_w(t \to 0)$. Based on experimental results, $P_w(t \to 0)$ is observed to be temperature-dependent but size-independent. While the former is understandable due to the kinetic nature of the hysteresis formation, the latter should be valid within a limited size range where only a single transition interface is present with the interface energy γ_{ss}, which is a thermodynamic quantity in a size of $P_w(t \to \infty)$. If the rest hysteresis width of $P_w(t \to 0) \sim P_w(t \to \infty)$ induced by the kinetic effect is contributed from both transition directions in the same size, the total transition barrier in the forward and the reverse transition directions has the same size of $P_w(t \to 0)/2$ as a first order approximation. Therefore, $P_n = P_f + P_{if} - P_w(t \to 0)/2 = P_r + P_{ir} + P_w(t \to 0)/2$ where P_f and P_r are the forward and the reverse transition pressures respectively and $P_w(t \to 0) = P_f - P_r$. In light of Eq. (6.16), $P_{if} = 2f_f/r$ and $P_{ir} = 2f_r/2$. With these relationships and simple mathematical treatments,

$$P_n = \overline{P} + 2\overline{f}/r \tag{6.105}$$

where $\overline{P} = (P_f + P_r)/2$ and $\overline{f} = (f_f + f_r)/2$. Since $\overline{f} > 0$, $P_n > \overline{P}$. With the calculated value of ΔH_s and ΔS_s in terms of Eqs. (6.101) and (6.104), the transition temperature at ambient pressure T_s is obtained as follows:

$$T_s = \Delta H_s/\Delta S_s. \tag{6.106}$$

The static parts of the hysteresis width $P_w(t \to \infty)$ could be determined in light of the equation of $P_w(t \to \infty) = -2\gamma_{ss}A/\Delta V$. According to the standard combining rule for this cross term, $\gamma_{ss} = (\gamma_{ssh} + \gamma_{ssl})/2$ is taken. Since $\gamma_{ss} = 2\gamma_{sL}$ in light of Eq. (6.25), $\gamma_{ss} \approx \gamma_{sLh} + \gamma_{sLl}$. For a spherical or quasi-spherical nanocrystal with a unique transition interface, the maximal A_g value is $n\pi r^2$ with $V = 4n\pi r^3/3$ where n is the nanocrystal number of one gram-atom crystal, or $A = 3V_s/(4r)$. Substituting γ_{ss} and A values into the above equation, it reads

$$P_w(t \to \infty) = -3V_s(\gamma_{sLh} + \gamma_{sLl})/(2r\Delta V_s). \tag{6.107}$$

Since Eq. (6.107) is only applicable to the transition of single crystals with one transition interface without dislocations, $r < 10 - 15$ nm should be satisfied. Note also that although P_n can be determined by $P_w(t \to 0)$ in terms of Eq. (6.105) with some assumptions, $P_w(t \to 0)$ itself is a complicated multi-parameter function of the activation energy, the activation volume and the time cannot directly be calculated.

According to the above equations, the determined thermodynamic quantities for the wurtzite and the rocksalt phases of CdSe and related parameters are shown in Table 6.16. As shown in Table 6.16, $T_{mh} < T_{ml}$ and $\Delta H_{mh} < \Delta H_{ml}$ are understandable due to the metastable nature of the high-pressure phase. $\gamma_{mh} > \gamma_{ml}$ and $f_{mh} > f_{ml}$ because on the surface there is a higher bond density of the high-pressure phase than that of the low-pressure phase. The determined $\Delta H_s = 2.51$ kJ·g-atom^{-1} is similar to the theoretical calculation of $\Delta H_s = 3.16$ kJ·g-atom^{-1}, and is one order smaller than ΔH_m. This is an expected result that the sum of the total bond strengths of two phases is similar. According to the estimated ΔH_s value, ΔS_s and T_s values are also obtained in terms of Eqs. (6.104) and (6.106).

Table 6.16 Necessary parameters for the calculation of the transition behavior of CdSe in terms of Eqs. (6.93), (6.99)–(6.103), (6.105)–(6.107). h is in nm, V in cm^3·g-atom^{-1}, T in K, ΔH in kJ·g-atom^{-1}, ΔS_{ml} in J·g-atom^{-1} K^{-1}, β in 10^{-12} Pa^{-1}, γ in mJ·m^{-2}, f in J·m^{-2}, P_n in GPa, $P_w(t \to \infty)$ in GPa·nm·nm^{-1}

h_l	h_h	V_l	V_h	ΔV	$\Delta V/V$	T_{ml}
0.219	0.286	16.90	14.01	−2.89	−0.171	1525
ΔH_{ml}	ΔS_{ml}	ΔS_{vibl}	β_l	β_h	γ_{sLl}	γ_{sLh}
22.78	14.94	6.624	21.9	17.4	39.20	54.94
f_l	f_h	ΔH_{mh}	ΔS_{mh}	ΔS_{vibh}	T_{mh}	ΔH_s
0.542	0.823	20.27	14.94	6.624	1357	2.51
ΔS_s	P_n	T_s	$P_w(t \to \infty)$			
31.3–40.9	4.59–5.15	62–80	0.83/r			

Under the assumption that the kinetic transition resistance in two transition directions has the same size, ΔS_s and T_s values are determined by two sets of experimental data at different T. It is found that $\Delta S_s > \Delta S_m$, which implies that structural change between two solid phases is greater than that between the solid and liquid. The obtained T_s value is much lower than T_r. This result confirms the above assumption that the positive ΔC_{pss} value is small ($\Delta C_{pss} > 0$ since the high-pressure phase is metastable at the ambient pressure). The larger values of ΔS_s and $\Delta T = T - T_s$ may be the reason why P_n value for the solid transition of CdSe is several orders larger than that for the usual martensite transition.

In the size range of 1.3 nm $< r <$ 6.3 nm, 0.66 GPa $> P_w(t \to \infty) >$ 0.13 GPa in terms of the result of $P_w(t \to \infty) = 0.83/r$. This result implies that the static hysteresis is size-dependent although the validity of Eq. (6.107) is only for single crystals up to a value about $r = 10 - 15$ nm. Since $P_w(t \to 0) \approx 6$ GPa at room temperature and decreases as T increases, which is one order larger than $P_w(t \to \infty)$, the size of $P_w(t \to 0)$ is mainly induced by the kinetic effect.

As r increases, the reverse transition is absent, it is plausible that $P_w(t \to \infty)$ is proportional to bond number on the transition interface which is proportional to the interface area of r^2. Thus, the size contribution to P_n through P_{in} is not evident although $P_{in} \propto 1/r$.

In the above approach, since only general thermodynamic measurable quantities are utilized, this measure seems to be applicable to solid transitions of other semiconductor compounds, such as GaAs, InAs, etc., although there is a lack of necessary experimental data used above.

6.8.3   Critical Layer Number and Critical Misfit of Epitaxial Grown Metallic Thin Films [3]

Ultrathin metallic films epitaxially grown on metallic substrates have been the subjects of many studies because they present very unusual chemical, electronic and magnetic properties, which differ from the corresponding bulk counterparts. The structure of the grown films is affected by the corresponding substrate with certain crystalline facets. To minimize the total G of the film, the film could prefer to take lattice strain at the film/substrate interface $\varsigma_{f/s}$ to avoid the formation of non-coherent interface with a larger interface energy γ_i since a coherent or a semi-coherent interface behaves as a much lower γ_i. However, as the layer number n' increases, or the surface (interface) area $A = V_s/(n'h \sin \theta_1)$ decreases where V_s is the g-atom volume of the film and $h \sin \theta_1$ shows the layer distance of the film from the substrate with θ_1 being the corresponding angle between direction of the nearest atoms at neighbor planes and that of the film surface, the total value of elastic energy of the film G_e will be greater than the total non-coherent interface free energy

$G_i = A\gamma_i$. Subsequently, the stable strain-free structure with a non-coherent interface is recovered at a critical layer number n_c' where a transition from the strained structure to a normal one occurs.

When the epitaxially grown metallic ultrathin films on metallic substrates are remained, the thermodynamic condition is $G_e < G_i$. At $n' = n_c'$,

$$G_i = G_e. \tag{6.108}$$

G_e can be determined by the elastic theory. Let x axis and y axis be horizontal directions along the interface, and z axis be perpendicular to the interface. At n_c', the essential assumptions are as follows: (1) $\varsigma_{xx}(z=0) = \varsigma_{yy}(z=0) = \varsigma_{f/s} = |h_f - h_s|/h_s$ with the subscripts "f" and "s" denoting film and substrate, and $\varsigma_{xx}(z = n'h\sin\theta_1) = \varsigma_{yy}(z = n'h\sin\theta_1) = 0$ at the surface of the film where the interface restriction disappears; (2) The strain along the z-axis varies linearly with the form of $\varsigma_{xx}(z) = \varsigma_{yy}(z) = \varsigma_{f/s}[1 - z/(n'h\sin\theta_1)]$, $\sigma_{xx}(z) = \sigma_{yy}(z) = E_y\varsigma_{f/s}[1 - z/(n_c'h\sin\theta_1)]/(1 - \nu_p)$ in terms of Hooke's law; (3) $\sigma_{zz} = 0$ and $\sigma_{ij} = 0$ where $i \neq j$ since ς_{xx} and ς_{yy} do not produce σ; (4) the film is isotropic as a first order approximation. Under these assumptions, the elastic energy of unit volume u_e is taken as $u_e = (\sigma_{xx} + \sigma_{yy})\varsigma_{f/s}[1 - z/(n'h\sin\theta_1)]/2 = E_y\{\varsigma_{f/s}[1 - z/(n'h\sin\theta_1)]\}^2$. Thus,

$$G_e = \int_V u_e dV = \frac{V_s E_y \varsigma_{f/s}^2}{n'h\sin\theta_1} \int_0^{n'h\sin\varsigma} [1 - z/(n'h\sin\theta_1)]^2 dz = \frac{V_s E_y \varsigma_{f/s}^2}{3(1 - \nu_p)}. \tag{6.109}$$

On the other side,

$$G_i = \gamma_i V_s/(n'h\sin\theta_1). \tag{6.110}$$

It is known that $\gamma_i = 4hS_{vib}\Delta H_m/(3V_s R)$ in terms of Eq. (6.50). For film/substrate interfaces, as a first order approximation, a mean value of the both substances for γ_i is taken,

$$\gamma_i \approx 4\bar{h}\overline{\Delta S}_{vib}\overline{\Delta H}_m/(3\overline{V}_s R) \tag{6.111}$$

where the upper bar on the symbols denotes that the related amount is a mean one. Substituting Eqs. (6.109) and (6.110) into Eq. (6.108) at $n' = n_c'$, there is

$$n_c' = \frac{3(1 - \nu_p)\gamma_i}{E_y h\sin\theta_1 \varsigma_{f/s}^2} = \frac{4(1 - \nu_p)\Delta\bar{S}_{vib}\Delta\bar{H}_m}{\sin\theta_1 \overline{V}_s R E_y \varsigma_{f/s}^2}. \tag{6.112}$$

To understand a general characteristic of Eq. (6.112), a 3D graph for $n_c'(G_i, \varsigma_{f/s})$ function is plotted in Fig. 6.29. It is clear that a thicker epitaxial film can be obtained when ε_i value is small and G_i or γ_i value is larger. As $\varsigma_{f/s}$ decreases, n_c' increases evidently. Thus, as expected, suitable substrates and facets to obtain the smallest $\varsigma_{f/s}$ will be decisive factors for manufacturing thicker epitaxial films. Note that the lattice contraction of the films has been

neglected. If this factor is introduced, the n'_c values will be a little lower than the shown ones.

n'_c values in light of Eq. (6.112) and the corresponding experimental results n''_c of Ni and Cu metallic films grown epitaxially on different metallic substrates are listed in Table 6.17. Agreement is found except for Ni(100)/Pd(100) system where the prediction has a difference of 50%–100% compared with the experimental results. However, even if $n' < n'_c$ and the strained film has a higher energetic state than the corresponding one with non-coherent interface , this strained structure may still exist in a metastable state, which is a usual case for solid transition where there exists a transition hysteresis. Thus, the predicted value of n'_c should be related to the smallest value in experimental experience.
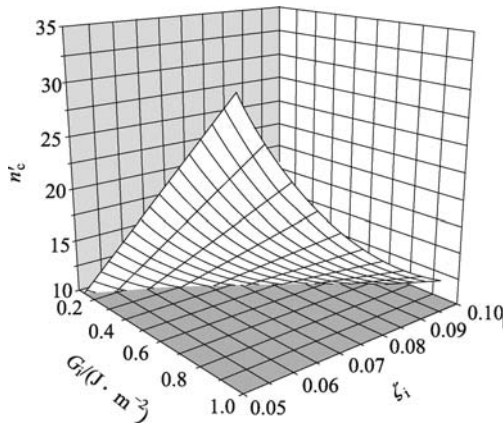
Fig. 6.29 A 3D plot for $n'_c(G_i, \varsigma_{f/s})$ function in terms of Eq. (6.112) where $h \sin \theta_1$ = 0.25 nm, E_y = 100 GPa and ν_p = 0.3 are taken. (Reproduced from Ref. [3] with permission of Elsevier)

Table 6.17 Comparison of n'_c between the predictions of Eq. (6.112) and experimental results n''_c where $\sin\theta_1$ values are $2^{1/2}/2$ and $6^{1/2}/3$ respectively for (100) and (111) planes

Film/substrate	$\varsigma_{f/s}$	ν_f	E_y/GPa	n'_c	n''_c
Ni(100)/Pd(100)	0.095	0.31	200	6	9 − 12
Ni(001)/Cu(001)	0.025	0.31	200	33	> 11
Ni(111)/Pt(111)	0.102	0.31	200	5	6
Cu(111)/Pd(111)	0.071	0.34	130	10	9

All four systems given in Table 6.17 have the same characteristic of $\varsigma_{f/s} >$ 0. It is possible that the energetic increase of atoms by straining is smaller than that by pressing due to the dissymmetrical potential function of atoms.

Since the lattice parameter of an attached film generally differs from that of the substrate, there exist lattice misfits at the film/substrate interface and δ is produced in this system. Usually, the lattice misfit on the film/substrate

interface can be accommodated in two ways: the film is elastically strained in order to accord with the substrate and/or misfit dislocations arise.

The concept of a limiting misfit as the upper limit of misfit, below which epitaxial growth may occur, was related to relevant concepts of misfit strain ς, misfit dislocations, critical misfit λ_c and critical thickness. λ_c is homogeneously strained into registry with the substrate, and the critical thickness is the critical layer thickness above which an interface of given natural misfit loses registry by introducing misfit dislocations. λ_c and the thickness of the eptaxial growth films were widely considered. However, misfit dislocations practically occur in the most eptaxial growth films. As ς increases, the energy of the film increases, ς in the film is relaxed by formation of the misfit dislocations with the misfit dislocation energy G_d. Once it reaches some value being greater than the γ_i, the interface is completely incoherent where $\lambda = \lambda_c$.

The incoherent free interface energy of the film G_i is simply calculated by

$$G_i = \gamma_{ss} A \tag{6.113}$$

where γ_{ss} is determined by Eq. (6.111). When an interface between a fully relaxed film and a substrate consists of dislocations, the corresponding γ_{ss} is equal to $G_d = N_d u_d$ where N_d and u_d denote the dislocation number and the misfit dislocation energy of a single dislocation. As a simplification, it is assumed that the film and the substrate are elastically equivalent, and the dislocation is edge one that is parallel to x-axis or y-axis, thus, $u_d = E_y b^2 l (\ln r_e/b + 1)/[4\pi(1 + \nu_p)(1 - \nu_p)]$ where l is the length of a dislocation. r_e is an effective dislocation stress field radius, which is often approximated as the film thickness t_h. $b \approx \bar{h}$ is the Burgers vector. $N_d = A/(lD)$ with $D = b/\lambda$ being the distance between two neighbor dislocations along $x-$ or $y-$ axis. Thus, the total number along the two axes $N = 2N_i = 2\lambda A/(l\bar{h})$. Thus,

$$G_d = \frac{E_y A \bar{h} \lambda [\ln t_h/\bar{h} + 1]}{2\pi(1 - \nu_p^2)}. \tag{6.114}$$

Let $G_d = G_i$ at λ_c in terms of Eqs. (6.113) and (6.114), where the interface transforms from a semi-coherent interface to an incoherent interface due to the requirement of minimum of the interface energy,

$$\frac{G_d}{G_i} = \frac{3\overline{V}_s R E_y \lambda_c [\ln t_h/\bar{h} + 1]}{8\pi \overline{\Delta S}_{vib} \overline{\Delta H}_m (1 - \nu_p^2)},$$

or,

$$\lambda_c \approx \overline{\Delta S}_{vib} \overline{\Delta H}_m (1 - \nu_p^2)/[\overline{V}_s E_y (\ln t_h/\bar{h} + 1)]. \tag{6.115}$$

In light of Eq. (6.90), λ_c may shift to a greater value through increasing ΔH_m value of the substrate according to the definition of $\overline{\Delta H}_m$.

The calculated λ_c values by Eq. (6.115) for some epitaxial growth thin films on different substrates are listed in Table 6.18 where $t_h/\bar{h} \approx 1$ is taken.

The results indicate that films with epitaxial growth can be obtained except Fe_{bcc}/Au(100) and Co/Pt(111) systems. From Eq. (6.115), the epitaxial growth film exactly depends on the energetic conditions. When the substrate has a larger ΔH_m and the film has a smaller E_y, a thicker film with an epitaxial growth can be obtained.

Table 6.18 Comparison between λ_c by Eq (6.115) and $\lambda_c' = |h_f - h_s|/h_s$ when the solid is isotropic

	ν	E_y /GPa	λ_c	λ_c'		ν	E_y /GPa	λ_c	λ_c'
Ni/Pd(100)	0.31	200	0.102	0.095	Ni/Cu(100)	0.31	200	0.101	0.025
Mo/W(100)	0.293	325	0.085	0.006	Fe_{bcc}/Au(100)	0.29	211	0.055	0.139
Fe_{fcc}/Cu(100)	0.29	200	0.149	0.008	Fe_{fcc}/Ni(100)	0.29	200	0.093	0.018
Ag/Mn(100)	0.37	83	0.118	0.117	Cu/Pd(111)	0.34	130	0.105	0.071
Ni/Pt(111)	0.31	200	0.106	0.102	Co/Cu(111)	0.31	209	0.085	0.017
Co/Pt(111)	0.31	209	0.084	0.099	Ag/Pt(111)	0.37	83	0.156	0.041
Cu/Mo(110)	0.34	130	0.166	0.066	Cu/W(110)	0.34	130	0.170	0.072
Ni/Mo(110)	0.31	200	0.132	0.093	Ni/W(110)	0.31	200	0.134	0.099
Nb/Fe_{bcc}(110)	0.40	105	0.155	0.151					

6.8.4 Reconstruction Possibility of fcc Metallic Surfaces at Room Temperature [3]

The process, in which the atoms in the top monolayer(s) are redistributed to create a surface region with a distinct (and often more complex) structure from the ideally terminated 1×1 surface, is called surface reconstruction, which occurs on various semiconductor and metal surfaces both in the clean state and in the presence of an adsorbate (see Sec. 6.3.3). On low-index metal surfaces, reconstructions are often characterized by a change in the atomic density of the top monolayer. One of them is the commensurate-incommensurate (C-I) phase transition although sometimes neither phase is strictly incommensurate. In all cases an increase in the density is observed, with a concomitant uniaxial or biaxial elastic contraction of surface layers. The surfaces that exhibit these reconstructions belong exclusively to the 4d and 5d transition metals and feature filled or nearly filled d-shells. Note that these structural reconstructions can also be found in other metals.

Frenkel-Kontorova (FK) model has been widely used with some success in describing the incorporative type of reconstructions found on clean, metallic fcc surfaces, especially on (111) facet of Au. For application to two-dimensional systems, FK model assumes that the physical system can be adequately described by a planar array of atoms that interact harmonically with each other and rest with a static, corrugated potential provided by the atoms of the substrate. The structure of the overlayer is then determined from a balance of the interlayer and intralayer interactions. Herring [20] and

Cammarata [21] have considered these using a bulk continuum elastic model,

$$Y_s = (f - \gamma_{sv})/Gh > \mu' \tag{6.116}$$

where $\mu' \cong 1/[4\pi(1 - \nu_p)] \cong 0.1$, and Y_s is the stability parameter. $(f - \gamma_{sv})$ denote the driving force for the reconstruction while the opposing force is due to the disregistry with the underlying lattice. In spite of its simplicity, Eq. (6.116) has successfully predicted surface reconstruction condition, and is consistent with the bulk continuum elastic theory and MD simulations for surface reconstructions on clean Au (111) surfaces. Since f and γ_{sv} are experimentally difficult to determine, Eqs. (6.57) and (6.93) can be employed to determine Y_s. Thus, Y_s can be simply calculated theoretically.

γ_{sv}, f and Y_s of some fcc metals with (111) facets are respectively calculated in terms of Eqs. (6.31), (6.68) and (6.91), and are shown in Table 6.19. As shown in the table, although Y_s values obtained from Eq. (6.91) with the calculated f and γ_{sv} values differ from Y_s' values with cited f and γ_{sv} values, Y_s and Y_s' values have the same predictions for the surface reconstructions of the concerned nine elements. The surface reconstructions are absent for the most elements except Au (111) and Pb (111) where $Y_s > 0.1$. Note also that although both Au and Pb exhibit surface reconstruction at T_r, their T_r/T_m values are different.

Table 6.19 Comparison of Y_s in terms of Eq. (6.116) and other theoretical results Y_s' at $T = 300$ K with related parameters for (111) facets of nine fcc metals where β, G, f, and γ_{sv} are in units of 10^{-12} Pa^{-1}, GPa, J·m^{-2}, and J·m^{-2}.

	β	G	f	γ_{sv}	Y_s	Y_s'
Ir	2.695	209	4.01	3.19	0.034	± 0.034
Ni	5.640	76.0	3.04	2.44	0.032	-0.022
Cu	7.257	48.3	2.23	1.83	0.032	0.007
Ag	9.653	30.3	1.65	1.20	0.051	0.035
Pd	5.348	43.6	2.91	1.85	0.088	0.057
Pt	3.623	60.9	3.71	2.54	0.069	0.087, 0.19*
Pb	21.83	5.59	0.75	0.55	0.102	0.103
Au	5.848	26.0	2.27	1.52	0.100	0.119, 0.19
Al	13.30	26.2	1.65	1.45	0.026	0.041

*Pt(111) can be reconstructed under certain circumstances.

The Y' values of Ir (111) and Ni (111) shown in Table 6.19 are negative, i.e. $f < \gamma_{sv}$. It is known that $f = \gamma + \partial\gamma/\partial A$, while $\gamma_{sv} < f$ for solids is very often although there are exceptions depending on the sign of $\partial\gamma/\partial A$. Thus, $Y_s' < 0$ is inacceptable. In fact, the bond strength of surface atoms and thus f on one side increase while γ_{sv} on the other side decreases after the surface relaxation. Thus, after the reconstruction, even if $Y_s < 0$ before the reconstruction, there must be $\gamma_{sv} < f$ or $Y_s > 0$ after that. Since Eqs. (6.31) and (6.68) for γ_{sv} and f can be approximately applied to any surface of any structure, the surface reconstruction can be in general predicted.

References

1   http://en.wikipedia.org/wiki/Fick's_laws_of_diffusion. Accessed 7 November 2009

2   http://www.tf.uni-kiel.de/matwis/amat/def_en/. Accessed 15 November 2009

3   Jiang Q, Lu H M. Size dependent interface energy and its applications. Surf. Sci. Rep., **63**, 427-464 (2008) and references therein

4   Cammarata R C. Surface and interface stress effects in thin films. Prog. Surf. Sci., **46**, 1-38 (1994) and references therein

5   Bechstedt F. Principles of Surface Physics. Springer, Berlin Heidelberg (2003)

6   Srivastava G P. Theory of semiconductor surface reconstruction. Rep. Prog. Phys., **60**, 561-563 (1997)

7   Duke C B. Semiconductor surface reconstruction: The structural chemistry of two-dimensional surface compounds. Chem. Rev., **96**, 1237-1260 (1996)

8   http://en.wikipedia.org/wiki/adsorption. Accessed 20 November 2009

9   Turnbull D, Fisher J C. Rate of nucleation in condensed systems. J. Chem. Phys., **17**, 71 (1949)

10   Turnbull D. Formation of crystal nuclei in liquid metals. J. Appl. Phys., **21**, 1022 (1950)

11   Haiss W. Surface stress of clean and adsorbate-covered solid. Rep. Prog. Phys., **64**, 591-648 (2001)

12   Lodziana Z, Topsoe N Y, Norskov J K. A negative solid-vapor interface energy for alumina. Nature Mater., **3**, 289-293 (2004)

13   Mathur A, Sharma P, Cammarata R C. Negative surface energy – clearing up confusion. Nature Mater., **4**, 186 (2005)

14   Tolman R C. The effect of droplet size on liquid-vapor interface energy, J. Chem. Phys., **17**, 333-337 (1949)

15   Buff F P. The spherical interface. I. Thermodynamics. J. Chem. Phys., **19**, 1591-1594 (1951)

16   Kuz V A, Meyra A G, Zarragoicoechea G J. An empirical equation for the enthalpy of vaporization of quantum liquids. Thermochimica Acta, **423**, 43-47 (2004)

17   Guggenheim E A. The thermodynamics of interfaces in systems of several components. Trans. Faraday Soc., **36**, 397-412 (1940)

18   Tolman R C. The superficial density of matter at a liquid-vapor boundary. J. Chem. Phys., **17**, 118-127 (1949)

19   Kirkwood J G, Buff F P. The statistical mechanical theory of liquid-vapor interface energy. J. Chem. Phys., **17**, 338-343 (1949)

20   Herring C. The Physics of Powder Metallurgy. McGraw-Hill, New York (1951) p. 143

21   Cammarata R C. Continuum model for surface reconstructions in (111) and (100) oriented surfaces of fcc metals. Surf. Sci., **279**, 341-348 (1992)

Index